

# **Bioreplicated Light-Harvesting Layers for Photovoltaics**

Zur Erlangung des akademischen Grades eines

## **Doktor-Ingenieurs**

(Dr.-Ing.)

von der

KIT-Fakultät für Elektrotechnik und Informationstechnik des  
Karlsruher Instituts für Technologie (KIT)

genehmigte

## **Dissertation**

von

M.Sc. Benjamin Fritz

geboren in Heilbronn

Tag der mündlichen Prüfung:

01.07.2021

Hauptreferent:

Prof. Dr. Ulrich Lemmer

Korreferent:

Prof. Dr. Mathias Kolle



This document is licensed under a Creative Commons Attribution-Share Alike 4.0 International License (CC BY-SA 4.0):

<https://creativecommons.org/licenses/by-sa/4.0/deed.en>





---

# Table of Contents

---

<b>List of Publications .....</b>	<b>V</b>
<b>Abstract .....</b>	<b>1</b>
<b>Kurzzusammenfassung.....</b>	<b>5</b>
<b>1 Introduction.....</b>	<b>9</b>
1.1 Background and Motivation .....	9
1.2 Thesis Outline .....	12
<b>2 Light-Management in Solar Cells and Modules .....</b>	<b>15</b>
2.1 Fundamental Properties of Solar Cells and Modules .....	15
2.1.1 Working Principle .....	15
2.1.2 Efficiency Limits and Loss Mechanisms .....	20
2.1.3 Laboratory vs. Outdoor Operational Conditions .....	25
2.2 Reflection and Refraction of Electromagnetic Waves.....	27
2.3 Antireflective Coatings.....	32
2.3.1 Rayleigh’s Film .....	35
2.3.2 Thin-Film-Interference-Based Antireflection .....	37
2.3.2.1 Single-Layer (Quarter-Wavelength) Antireflective Coatings .....	37
2.3.2.2 Double-Layer Antireflective Coatings .....	43
2.3.2.3 Triple-Layer Antireflective Coatings.....	45
2.3.2.4 Multilayer Antireflective Coatings .....	46
2.3.3 Gradient-Refractive-Index Materials.....	46
2.3.4 Subwavelength Nanostructures.....	48
2.3.5 Microstructured Surfaces .....	50
2.3.6 More Approaches Towards Antireflection and Light-Trapping....	56
2.4 Advanced Light-Management Concepts in PV .....	57
2.5 Computational Methods for Studying the Optical Properties of PV Light-Harvesting Layers.....	60
2.5.1 Transfer-Matrix Method.....	60
2.5.2 Monte-Carlo Ray-Tracing Simulations .....	65
2.5.3 Software .....	70
<b>3 Photonic Structures Found in Living Nature.....</b>	<b>71</b>

## TABLE OF CONTENTS

---

3.1	Optical Micro- and Nanostructures in Animals.....	71
3.1.1	Structural Coloration in Animals.....	71
3.1.2	Antireflective Structures in Animals.....	79
3.2	Optical Micro- and Nanostructures in Plants.....	83
3.2.1	Basic Architecture of (Hierarchical) Plant Surface Structures .....	83
3.2.2	Structural Coloration in Plants.....	89
3.2.3	Antireflective Structures in Plant Leaves.....	92
3.2.4	Antireflective Structures in Flower Petals .....	93
<b>4</b>	<b>Wetting Properties of Micro- and Nanotextured Surfaces.....</b>	<b>97</b>
4.1	Wetting Properties of Rough Surfaces – Classical Theories.....	97
4.2	Wetting Properties of Hierarchically Structured Surfaces.....	99
4.3	Self-Cleaning Surfaces in Photovoltaics .....	103
<b>5</b>	<b>Bioreplication, Bioinspiration, and Biomimetics.....</b>	<b>111</b>
5.1	Replication of Biological Surface Textures.....	111
5.2	Biomimetic and Bioinspired Materials .....	118
5.3	(Optical) Properties of Soft-Imprint Rose Petal Replicas .....	130
5.4	Plant Replicas as PV Light-Harvesting Layers – Current State of Research.....	134
<b>6</b>	<b>Light-Harvesting Properties of Disordered Microstructures on Thin-Film Solar Cells – Optical Simulations.....</b>	<b>137</b>
6.1	Modeling and Simulation Procedures for 3D Disordered Microtextured Surfaces.....	137
6.2	Implementation of Structural Disorder .....	146
6.2.1	Disorder in Cone Height.....	147
6.2.2	Disorder in Cone Positioning .....	147
6.2.3	Disorder in Cone Tilt Angle.....	149
6.3	Model Parameters and Convergence Tests Regarding Number of Rays and Spatial Dimensions .....	152
6.4	Microtextured Surfaces on Top of Thin-Film Solar Cells.....	153
6.5	Results – Influence of Structural Disorder on Petal-Like Microstructures.....	155
6.5.1	Effects of Structural Disorder on Surface Reflectance And In-Coupled Light Angular Distribution.....	155

---

6.5.2 Effects of Structural Disorder on Reflection Losses For Microstructures on CIGS Solar Cells .....	158
<b>7 Advancing the Replication Techniques of Plant Surface Textures Towards Large-Area and High-Throughput Methods.....</b>	<b>163</b>
7.1 Fabrication of Ni Mold Inserts for Rose Petal Replication via Hot-Embossing Lithography .....	164
7.2 Large-Area Embossing Tool Fabrication – Overcoming the Nature-Given Size Limitations in Templating Plant Surfaces.....	167
7.3 Large-Area Hot-Embossing for Upscaled Rose Petal Replication..	171
<b>8 Light-Harvesting and Wetting Properties of Hot-Embossed Rose Petal Replicas – Experimental Analysis.....</b>	<b>177</b>
8.1 Antireflection Properties of Hot-Embossed Rose Petal Replicas on CIGS Single Solar Cells .....	177
8.2 Wetting Properties of Hot-Embossed Rose Petal Replicas .....	182
8.3 Opto-Electrical Properties of Hot-Embossed Rose Petal Replicas on CIGS Solar Cells and Modules.....	185
<b>9 Outdoor Performance and Long-Term Stability of Hot-Embossed Rose Petal Replicas as PV Light-Harvesting Layers.....</b>	<b>191</b>
9.1 Outdoor Performance Monitoring of Rose Petal Textured PMMA on CIGS and Si Solar Modules .....	191
9.2 Long-Term Durability of Rose Petal Textured PMMA Light-Harvesting Layers .....	203
<b>10 Polarized Light Pollution of Solar Panels – Are Polarotactic Insects Maladaptively Attracted by Microtextured Light-Harvesting Layers? ....</b>	<b>209</b>
10.1 Introduction to Polarized Light Pollution .....	210
10.2 Field Experiments for Studying the Maladaptive Attractiveness of PV Cover Layers to Polarotactic Mayflies and Horseflies .....	212
10.3 Imaging Polarimetric Measurements of the Reflection-Polarization Properties of Microstructured PV Light-Harvesting Layers.....	215
10.4 Ray-Tracing-Based Analysis of the Reflection-Polarization Properties of Microstructured Surfaces .....	220
<b>11 Summary and Outlook.....</b>	<b>229</b>
<b>Supplementary Information .....</b>	<b>233</b>

---

## TABLE OF CONTENTS

---

<b>List of Figures .....</b>	<b>245</b>
<b>List of Tables.....</b>	<b>253</b>
<b>List of Abbreviations.....</b>	<b>255</b>
<b>References.....</b>	<b>259</b>
<b>Acknowledgments / Danksagung.....</b>	<b>329</b>

---

# List of Publications

---

## Peer-Reviewed Journals

- [1] **Fritz, B.**<sup>1</sup>, Horváth, G., Hünig, R., Pereszlényi, Á., Egri, Á., Guttman, M., Schneider, M., Lemmer, U., Kriska, G. and Gomard, G. (2020) 'Bioreplicated coatings for photovoltaic solar panels nearly eliminate light pollution that harms polarotactic insects.' *PLOS ONE* **15**(12): e0243296. <https://doi.org/10.1371/journal.pone.0243296>
- [2] Horváth, G., Pereszlényi, Á., Egri, Á., **Fritz, B.**, Guttman, M., Lemmer, U., Gomard, G. and Kriska, G. (2020) 'Horsefly reactions to black surfaces: attractiveness to male and female tabanids versus surface tilt angle and temperature.' *Parasitology Research* **119**(8): pp. 2399–2409. <https://doi.org/10.1007/s00436-020-06702-7>
- [3] **Fritz, B.**, Hünig, R., Guttman, M., Schneider, M., Reza, K. S., Salomon, O., Jackson, P., Powalla, M., Lemmer, U. and Gomard, G. (2020) 'Upscaling the fabrication routine of bioreplicated rose petal light harvesting layers for photovoltaic modules.' *Solar Energy* **201**: pp. 666-673. <https://doi.org/10.1016/j.solener.2020.03.020>
- [4] Jürgensen, N., **Fritz, B.**, Mertens, A., Tisserant, J. N., Kolle, M., Gomard, G. and Hernandez-Sosa, G. (2021) 'A Single-Step Hot Embossing Process for Integration of Microlens Arrays in Biodegradable Substrates for Improved Light Extraction of Light-Emitting Devices.' *Advanced Materials Technologies* **6**(2): 1900933. <https://doi.org/10.1002/admt.201900933>
- [5] Chen, J., **Fritz, B.**, Liang, G., Ding, X., Lemmer, U., & Gomard, G. (2019) 'Microlens arrays with adjustable aspect ratio fabricated by electrowetting and their application to correlated color temperature tunable light-emitting diodes.' *Optics Express* **27**(4): pp. A25-A38. <https://doi.org/10.1364/OE.27.000A25>
- [6] Yu, S., **Fritz, B.**, Johnsen, S., Busko, D., Richards, B. S., Hippler, M., Wiegand, G., Tang, Y., Li, Z., Lemmer, U., Hölscher, H. and Gomard, G. (2019) 'Enhanced Photoluminescence in Quantum Dots–Porous Polymer Hybrid Films Fabricated by Microcellular Foaming.' *Advanced Optical Materials* **7**(12): 1900223. <https://doi.org/10.1002/adom.201900223>

---

<sup>1</sup> Lead author(s) are marked with an underscore

- [7] Schumann, M. F., Fritz, B., Eckstein, R., Lemmer, U., Gomard, G. and Wegener, M. (2018) 'Cloaking of metal grid electrodes on Lambertian emitters by free-form refractive surfaces.' *Optics Letters* **43**(3): pp. 527-530. <https://doi.org/10.1364/OL.43.000527>
- [8] Vüllers, F., Fritz, B., Roslizar, A., Striegel, A., Guttman, M., Richards, B. S., Hölscher, H., Gomard, G., Klampaftis, E. and Kavalenka, M. N. (2018) 'Self-cleaning microcavity array for photovoltaic modules.' *ACS Applied Materials & Interfaces* **10**(3): pp. 2929–2936. <https://doi.org/10.1021/acsami.7b15579>
- [9] Schmager, R., Fritz, B., Hünig, R., Ding, K., Lemmer, U., Richards, B. S., Gomard, G. and Paetzold, U. W. (2017) 'Texture of the viola flower for light harvesting in photovoltaics.' *ACS Photonics* **4**(11): pp. 2687–2692. <https://doi.org/10.1021/acsphotonics.7b01153>
- [10]<sup>1</sup> Fritz, B., Hünig, R., Schmager, R., Hetterich, M., Lemmer, U. and Gomard, G. (2017) 'Assessing the influence of structural disorder on the plant epidermal cells' optical properties: a numerical analysis.' *Bioinspiration & Biomimetics* **12**(3): 036011. <https://doi.org/10.1088/1748-3190/aa6c46>

## Conference Proceedings

- [11] Yu, S., Fritz, B., Theobald, D., Johnsen, S., Busko, D., Richards, B. S., Hippler, M., Wiegand, G., Tang, Y., Li, Z., Lemmer, U., Hölscher, H. and Gomard, G. (2019) 'Foamed polymer/quantum dots composite films with enhanced photoluminescence efficiency.' *OSA Optical Devices and Materials for Solar Energy and Solid-State Lighting*, PT2C-4, <https://doi.org/10.1364/PVLED.2019.PT2C.4>
- [12] Yu, S., Fritz, B., Theobald, D., Wu, K., Johnsen, S., Busko, D., Richards, B. S., Wiegand, G., Tang, Y., Li, Z., Lemmer, U., Hölscher, H. and Gomard, G. (2019) 'Enhanced color conversion of quantum dots - polymer hybrid films in light-emitting diodes.' *Proceedings of ICEPT Hong Kong 2019*. <https://doi.org/10.1109/ICEPT47577.2019.245231>
- [13] Fritz, B., Guttman, M., Casas-Soler, P., Roslizar, A., Langenhorst, M., Schneider, M., Paetzold, U. W., Richards, B. S., Lemmer, U., Hünig, R. and Gomard, G. (2018) 'Towards mass fabrication of hot embossed plant surface texture replicas as photovoltaic cover layers.' *Proceedings of SPIE 10730, Nanoengineering: Fabrication, Properties, Optics, and Devices XV*, 107300J. <https://doi.org/10.1117/12.2320555>

---

<sup>1</sup> awarded by the editorial office as one of the journal's 'Highlights of 2017' [15]

## Other Magazine Contributions

- [14] **Fritz, B.**, Guttman, M., Gomard, G., Hünig, R. (2020) 'Hot embossed large-area plant microstructures for improved photovoltaic light harvesting.' *WOMag* 2020/5, WOTech Technical Media GbR. <https://www.wotech-technical-media.de/womag/>

## Patent Applications

- **Fritz, B.**, Hünig, R., Gomard, G., Guttman, M. (2020) 'Verfahren zum Bereitstellen eines Prägeelements für ein Prägewerkzeug, ein Prägeelement, eine Verwendung eines Prägeelements und ein Prägewerkzeug umfassend ein Prägeelement.' German patent application (reference number 102020209106.4), submitted to the German Patent and Trade Mark Office on 07/21/2020.

## Conference Presentations

- **Fritz, B.**, Hünig, R., Guttman, M., Horváth, G., Schneider, M., Salomon, O., Powalla, M., Lemmer, U. and Gomard, G. (2019) '100 cm<sup>2</sup> bioreplicated photovoltaic cover layers for sunlight harvesting, self-cleaning & reduced polarized light pollution' (**poster**), *Karlsruhe Days of Optics & Photonics 2019*, Karlsruhe, Germany.
- **Fritz, B.**, Guttman, M., Casas-Soler, P., Roslizar, A., Langenhorst, M., Schneider, M., Paetzold, U. W., Richards, B. S., Lemmer, U., Hünig, R. and Gomard, G. (2018) 'Hot embossed bio-replicated surface textures as self-cleaning light harvesting coatings for photovoltaics' (**poster**), *Summer School: Optical Technologies*, Bad Herrenalb, Germany.
- **Fritz, B.**, Vüllers, F., Roslizar, A., Striegel, A., Guttman, M., Richards, B. S., Hölscher, H., Gomard, G., Klampaftis, E. and Kavalenka, M. N. (2018) 'Hot embossed fluorinated polymer films as multifunctional surface coatings for photovoltaic modules' (**oral presentation**), *SPIE Optics + Photonics, NanoScience + Engineering*, San Diego, USA. (A recording of this presentation can be found under <https://doi.org/10.1117/12.2320555>)

- **Fritz, B.** (2017) 'Up-scalable, micro-patterned coatings for improved light management and self-cleaning in photovoltaics' (**poster**), *Karlsruhe Days of Optics & Photonics 2017*, Karlsruhe, Germany.
- **Fritz, B.**, Hünig, R., Schmager, R., Hetterich, M., Lemmer, U. and Gomard, G. (2017) 'Numerical analysis of structural disorder effects for the design of plant-inspired light harvesting coatings' (**poster**), *Spring School: Tailored Disorder*, Karlsruhe, Germany.
- **Fritz, B.**, Hünig, R., Schmager, R., Hetterich, M., Lemmer, U. and Gomard, G. (2017) 'Replicated petal surfaces as light-harvesting layers for photovoltaics: the role of structural disorder' (**poster**), 644. *WE-Heraeus-Seminar on 'Bio-inspired, Nano- and Microstructured Surfaces: New Functionality by Material and Structure'*, Bad Honnef, Germany.
- **Fritz, B.**, Hünig, R., Schmager, R., Hetterich, M., Lemmer, U. and Gomard, G. (2017) 'Numerical analysis of structural disorder effects for the design of plant-inspired light harvesting coatings' (**poster**), *European Materials Research Society (E-MRS) Spring Meeting 2017*, Strasbourg, France.

## International Research Stays

- **Purdue University** (Group of Prof. Peter Bermel)  
West Lafayette, Indiana (USA)  
Oct 2017 - Nov 2017
- **South China University of Technology** (Group of Prof. Yong Tang)  
Guangzhou, Guangdong (China)  
May 2019 - Jun 2019

---

## Abstract

---

The hierarchical micro-/nanotextures, which adorn the petal surfaces of a majority of flowering plant species, have been reported to often exhibit outstanding sunlight-capturing as well as self-cleaning properties. Both of these qualities can be exploited for photovoltaics (PV) via direct replication methods capable of transferring the multi-scale surface structure of a respective flower petal into transparent polymeric materials and onto the front surfaces of solar panels. In recent years, polymer casting and soft-imprint nanolithography have been the most widely used methods for directly copying (artificial as well as) natural micro-, nano-, and multi-scale-structures into an adequate technical material such as a polymer in order to exploit their highly optimized optical and/or wetting properties for optoelectronic devices. However, for large-scale applications, these methods have so far been hampered by the nature-given size limitations immanent in flower petals and by the limited number of high-quality soft-imprint replicas that can be produced from a single (polymeric) mold.

Part of this contribution is dedicated to overcoming both these issues by demonstrating an upscaled bioreplication approach for the hierarchical surface structure of rose petals based on static hot-embossing lithography using metallic mold inserts, thereby paving the way towards a high-throughput production of high-quality replicas of plant surface structures on relevant length scales. After the careful assembly of several natural rose petals into gapless arrays, mechanically stable, temperature resistant, and large-area nickel mold inserts are fabricated based on these upscaled templates by utilizing nickel electroforming. Subsequently, upscaled polymeric replicas are produced from these molds via hot-embossing lithography using three different free-standing thermoplastic foil materials, namely poly(methyl methacrylate) (PMMA), polycarbonate (PC), and fluorinated ethylene propylene (FEP). A high replication fidelity from the sub-micron to the centimeter scale while reaching continuously structured areas of up to 12.5 cm × 10.0 cm per replica is demonstrated for all three polymer materials considered.

Using such hot-embossed rose petal replicas as cover layers of copper indium gallium diselenide (CIGS) solar cells, efficient antireflection and light-trapping properties are observed for a broad spectral range and especially for oblique incidence angles above 50°. For normal light incidence, rose petal textured PMMA

foils are even shown to reduce reflection losses more effectively than state-of-the-art magnesium fluoride ( $\text{MgF}_2$ ) thin-film antireflective layers. Experimental characterizations of the opto-electrical performance of high-efficiency CIGS single solar cells with various cover layer configurations confirm this trend, resulting in an average increase in device efficiency of  $5.7\% \pm 0.6\%$  for CIGS solar cells covered with PMMA rose petal replicas, while  $\text{MgF}_2$  antireflective coatings are found to induce an average performance gain of  $4.5\% \pm 1.6\%$  relative to the respective device efficiencies before applying the antireflective coatings.

It is further demonstrated that, without any additional surface treatment, hot-embossed rose petal replicas can reach strong hydrophobicity with a static water contact angle of  $134.4^\circ \pm 4.3^\circ$  by employing the low surface free energy polymer FEP in the thermal imprinting routine. Experiments with water droplets falling onto tilted FEP rose petal replicas further highlight a pronounced water repellency and indicate their potential for introducing self-cleaning properties in PV devices.

The performance gain induced by applying upscaled PMMA rose petal replicated light-harvesting layers is also assessed for  $10\text{ cm} \times 10\text{ cm}$  silicon-based as well as CIGS mini-modules under realistic operational conditions for fixed installations with various module orientations and tilt angles over a period of nine months in Karlsruhe, Germany. Under conditions where much direct sunlight reaches the modules under oblique incidence angles, daily gains in energy yield relative to a planar cover layer configuration may reach exceptionally high values even well above 10%. Accelerated aging and abrasion tests following several standardized testing protocols widely used throughout the PV industry further promote the long-term applicability of PMMA rose petal replicated PV light-harvesting layers under outdoor conditions.

Moreover, the efficient light-harvesting properties of typical petal surface structures on thin-film solar cells are analyzed in more detail by utilizing a specially developed 3D microstructure modeling routine and a combination of Monte-Carlo ray-tracing simulations and transfer-matrix calculations, mostly with a view on the impact of structural disorder on light in-coupling. Irrespective of the degree of disorder in height, positioning, or tilt angle of the petal-epidermal-cell-mimicking micro-cones, it is shown that the angle-dependent reflectance of such microstructures is mainly governed by the average aspect ratio of the micro-cones, and secondly by their average packing density.

Lastly, the polarization properties of light reflected from solar panels and its harmful impact on populations of polarotactic water-seeking insects are studied.

Typical glass-encapsulated PV modules inadvertently attract various species of water-seeking insects through the linearly polarized light they reflect from their smooth surfaces (the degree of linear polarization depends on the incidence/observation angle, and full linear polarization is observed under Brewster's angle), which may cause a misidentification of solar panels as bodies of water and thereby lead to harmful impacts on the entomofauna. Field experiments studying the maladaptive attractiveness of rose petal replicated PMMA layers to polarotactic mayflies (Ephemeroptera: *Ephemera danica*) and horseflies (Diptera: Tabanidae) demonstrate nearly zero harmful attractiveness of rose petal replicated PMMA surfaces to both polarotactic insect species considered. This observation is linked to the optical properties of microstructured surfaces on the basis of imaging polarimetric measurements as well as Monte-Carlo ray-tracing simulations.



---

## Kurzzusammenfassung

---

Die hierarchischen Mikro-/Nanostrukturen, welche die Blütenblattoberflächen einer Vielzahl von Blütenpflanzen zieren, weisen oftmals hervorragende Lichtsammelungs- sowie Selbstreinigungseigenschaften auf. Diese Qualitäten können mit Hilfe von direkten Replikationsverfahren technisch nutzbar gemacht werden, beispielsweise für die photovoltaische Stromerzeugung. Replikationsverfahren zielen darauf ab die multi-skalige Oberflächenstruktur von Blütenblättern in ein transparentes Polymer zu übertragen und auf der Vorderseite von Solarmodulen aufzubringen. Im Laufe der letzten Jahren haben sich hauptsächlich Polymerabgüsse und die sog. Soft-Imprint Nanolithographie als gängige Verfahren zur direkten Kopie von (sowohl künstlich hergestellten, als auch) natürlichen Mikro-, Nano-, und multi-skaligen Strukturen in adäquate technische Materialien, wie z.B. Polymere zur Ausnutzung ihrer hochoptimierten optischen und/oder Benetzungseigenschaften für optoelektronische Bauteile, etabliert. Eine großflächige Anwendung dieser Verfahren wurde jedoch bislang aufgrund der naturgegebenen Maximalgröße von Blütenblättern nicht etabliert. Des Weiteren kann auf Basis eines einzigen Polymerstempel nur eine limitierte Anzahl an Replikaten mit hoher Strukturqualität mittels Soft-Imprint hergestellt werden.

Ein Teil dieser Arbeit befasst sich mit der Überwindung dieser Hürden durch Weiterentwicklung der Replikationstechniken für pflanzliche Oberflächenstrukturen. Eine solche, in der Fläche hochskalierte Bioreplikationsmethode mit gleichzeitig erheblich gesteigertem Durchsatz wird in dieser Arbeit am Beispiel der hierarchischen Oberflächenstruktur von Rosenblütenblättern als natürliche Strukturvorlage aufgezeigt. Das vorgestellte Verfahren basiert auf der Entwicklung metallischer Prägwerkzeuge, welche in einem statischen Heißprägeprozess eingesetzt werden. Diese Entwicklung ermöglicht die Herstellung von Replikaten pflanzlicher Oberflächenstrukturen mit hoher Strukturqualität, in nie dagewesener Stückzahl, und erstmals auch in einer für eine Integration in kommerzielle Solarmodule relevanten Größe. Die hochskalierten, temperaturstabilen und mechanisch robusten Prägwerkzeuge werden dabei per galvanischer Nickelabscheidung hergestellt. Die primäre Strukturvorlage für diesen Prozess wird dabei durch vorsichtige Aneinanderreihung mehrerer natürlicher Rosenblütenblätter zu einer möglichst

lücken- und nahtlos strukturierten Einheit erzeugt. Der Heißprägeprozess zur Herstellung hochskalierter Polymerreplika der Rosenblütenblattstruktur wird anhand von drei verschiedenen, transparenten Folienmaterialien diskutiert. Sowohl für Polymethylmethacrylat (PMMA), Polycarbonat (PC), und Fluorethylen-Propylen (FEP) wird mit Hilfe des entwickelten Replikationsverfahrens eine hervorragende Strukturtreue über mehrere Längenskalen hinweg, vom sub-Mikrometer Bereich bis hin zu makroskopischen Merkmalen, mit gleichzeitig nahezu durchgängiger Strukturierung bei einer gesamten Strukturfläche von bis zu  $12.5\text{ cm} \times 10.0\text{ cm}$  pro Replikat erzielt.

Als vorderseitige Beschichtung für Kupfer-Indium-Gallium-Diselenid (CIGS) Solarzellen erweisen sich heißgeprägten Rosenreplika als effektive Antireflex- und Light-Trapping-Maßnahme für einen breiten Spektralbereich und besonders für Lichteinfallswinkel  $> 50^\circ$ . Mit heißgeprägten Rosenreplikaten aus PMMA lässt sich sogar bei senkrechtem Lichteinfall eine gegenüber einer optimierten Magnesiumfluorid ( $\text{MgF}_2$ ) Antireflexbeschichtung verbesserte Antireflexwirkung feststellen. Optoelektronische Messungen bestätigen, dass sich diese Reflexionsverminderung auch entsprechend auf die Nennleistung der Solarzellen auswirkt, mit einer um im Mittel um  $5.7\% \pm 0.6\%$  gesteigerten Umwandlungseffizienz (verglichen mit den jeweiligen Solarzellen vor Aufbringung der Antireflexschichten) im Falle von PMMA Rosenreplikaten und  $4.5\% \pm 1.6\%$  für  $\text{MgF}_2$  Dünnschicht-Antireflexbeschichtungen.

Weiter wird gezeigt, dass heißgeprägte Rosenreplika auch mit wasserabweisenden Eigenschaften (mit einem statischer Kontaktwinkel von  $134.4^\circ \pm 4.3^\circ$ ) erzeugt werden können, sogar ohne dabei auf zusätzliche Schritte zur Oberflächenmodifikation zurückgreifen zu müssen. Dazu wird als Ausgangsmaterial für den Heißprägeprozess ein Polymermaterial mit geringer freier Oberflächenenergie benötigt, was beispielsweise bei FEP gegeben ist. Wassertropfen, die auf geneigte FEP Rosenreplika fallen, perlen von diesen sofort und restlos ab, was auf eine potentielle Eignung von FEP Rosenreplikaten zur Produktion selbstreinigender Solarmodule hindeutet.

Der Leistungszuwachs, der durch die Anwendung der hochskalierten PMMA Rosenreplika bewirkt wird, wird des Weiteren auch unter realistischen Betriebsbedingungen über neun Monaten Betrieb unter Außenbedingungen in Karlsruhe (Deutschland) untersucht, und zwar für  $10\text{ cm} \times 10\text{ cm}$  CIGS und siliziumbasierte Solarmodule unter verschiedenen Modulneigungswinkeln und Modulatorientierungen. Besonders hohe Steigerungen der täglichen Energieausbeute verglichen mit einem Referenzmodul ohne strukturierte

Polymerfolie von bis zu deutlich über 10% werden dabei vor allem unter Aufstellbedingungen gemessen, die mit viel direkter Sonneneinstrahlung unter schrägem Lichteinfall einhergehen. Mit Hilfe beschleunigter Alterungs- und Abnutzungstests, welche standardisierten Testprotokollen aus der PV Industrie nachempfunden sind, wird außerdem auf die potentielle Langzeiteignung solch strukturierter Folien auf Solarmoduloberflächen hingewiesen.

Außerdem werden die optischen Eigenschaften typischer Blütenblattstrukturen auf Solarzellen mit Hilfe einer speziell entwickelten 3D Mikrostruktur-Modellierungs- und Simulationsroutine, basierend auf Monte-Carlo-Raytracing und der Transfer-Matrix-Methode, hinsichtlich des Einflusses ungeordneter Strukturbausteine auf die Lichteinkopplungseigenschaften im Detail diskutiert. Durch Variation der Stärke der strukturellen Unordnung sowohl in der Höhe, der Anordnung, als auch der Neigung der Strukturbausteine der betrachteten, Blütenblattepidermis-inspirierten Mikrostrukturen lässt sich zeigen, dass ihre winkelabhängigen Reflexionseigenschaften nur schwach von Unordnung abhängen und in erster Linie vom mittleren Aspektverhältnis und der mittleren Packungsdichte der Strukturbausteine bestimmt werden.

Schließlich werden die Polarisationsseigenschaften von an Solarmodulen reflektiertem Licht hinsichtlich der möglichen schädlichen Auswirkungen auf polarotaktische Insektenarten diskutiert. Die vorderseitige Glasabdeckung herkömmlicher Solarmodule reflektiert aufgrund ihrer glatten Oberfläche linear polarisiertes Licht, wobei der Polarisationsgrad vom Einfallswinkel/Betrachtungswinkel abhängt (vollständige lineare Polarisation bei Betrachtung unter dem Brewster-Winkel). Unbeabsichtigt wird dadurch der Insektenfauna geschadet, da polarotaktische Insekten Solarmodule als solche nicht erkennen und diese fälschlicherweise oft als Gewässer identifizieren, was dann beispielsweise eine Eierablage an einem ungeeigneten Ort und damit den Verlust der Nachkommen zur Folge haben kann. Experimente im Freifeld zeigen jedoch erstmals, dass keinerlei derartige schädliche Anziehungswirkung auf polarotaktische Eintagsfliegen (Ephemeroptera: *Ephemera danica*) und Bremsen (Diptera: Tabanidae) im Falle von PMMA Rosenreplikaten auf Solarmodulen zu befürchten ist. Basierend auf bildgebender Polarimetrie und Monte-Carlo-Raytracing-Simulationen werden diese Resultate auf die optischen Eigenschaften mikrostrukturierter Oberflächen zurückgeführt.



---

# 1 Introduction

---

## 1.1 Background and Motivation

Photovoltaic (PV) electricity generation is one of the key technologies for reducing our dependence on fossil fuels, thereby mitigating global climate change through reducing global CO<sub>2</sub> emissions [16]. Over the last years, PV-generated electricity has become a competitive low-cost option for bulk electricity supply, which is highlighted by the recent downward trend in PV-generated electricity prices, which are given by the lowest bids received for long term electricity supply under power purchase agreements (PPAs) and depicted in Fig. 1.1 A). Over the past decade, PV module costs drastically dropped by a factor of 15, while the annually installed (global) PV capacity has significantly increased from 252 MW<sub>p</sub>yr<sup>-1</sup> in the year 2000 to 109 GW<sub>p</sub>yr<sup>-1</sup> in 2018 [17, 18] and 142 GW<sub>p</sub>yr<sup>-1</sup> in 2020 [19]. In combination with wind-generated energy and battery storage, competitive prices for an ‘on demand’ supply of green electricity have already been reached in several countries, including Australia and the USA [20].

Optimistic renewable energy strategies that would meet the ‘2°C –goal’ set in the 2015 Paris Agreement would require the globally installed PV capacity to reach, for example, 4 TW<sub>p</sub> as soon as 2025, then increase to around 22 TW<sub>p</sub> by 2050, and reach around 70 TW<sub>p</sub> by the end of this century, according to the so-called *Sky* scenario developed by the oil company Shell [18, 21]. The *Sky* scenario, as well as several other recent projections regarding the growth in cumulative (worldwide) installed PV capacity, are illustrated in Fig. 1.1 B). The cost reductions for PV-generated electricity are likely to continue due to numerous factors, including further increases in device efficiency or energy yield, respectively, as well as reductions in material consumption. Such improvements lower the system costs that scale with the total area of a PV installation. Increasing the energy yield of PV installations can be achieved, for example, by minimizing the amount of incident energy lost through reflection or incomplete absorption. Especially in cases where optimum module tilt and orientation is hindered (such as for building-integrated deployment of PV panels), efficiently capturing sunlight from oblique angles of incidence (AOIs) can significantly boost the energy yield of a PV installation. Although cover glasses of commercial solar panels are usually equipped with a

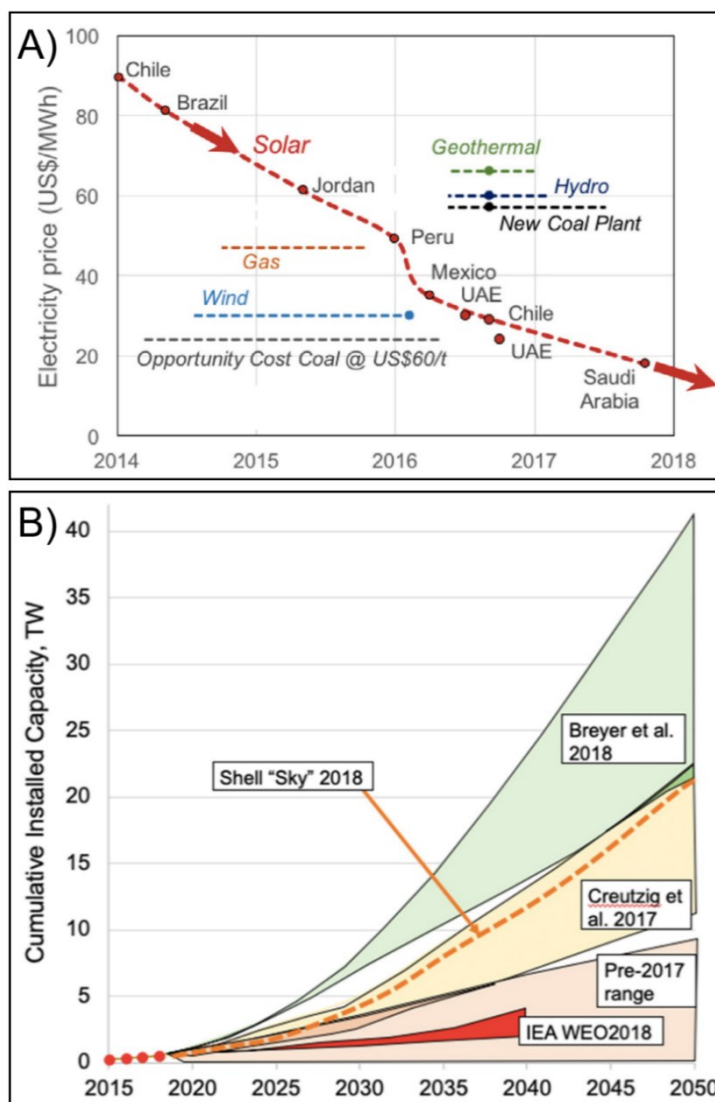


**Fig. 1.1:** Recent records for lowest prices achieved for PV-generated electricity, together with a compilation of projections for the future development of the globally installed cumulative capacity (all original references can be found in [18]). The prices in A) are given by the lowest bids received for long-term electricity supply under power purchase agreements for both photovoltaic and other sources. Both A) and B) were reprinted with permission from reference [18], © 2019 IOP Publishing Ltd.

(quarter-wavelength) antireflective coating, reflection losses are only significantly reduced for a relatively narrow spectral region and only for (close to) normal light incidence. However, obliquely incident light and, as a consequence, a large portion of the diffuse portion of the incident light is still not accessible for the PV energy conversion process due to the reflection losses at the planar front surface of the devices, which lead to a significant glare due to bright specular reflection that many state-of-the-art PV installations cause for oblique incidence of direct sunlight. Relying on structured surfaces for antireflection instead of using planar coatings can lead to improved spectral and angular robustness in antireflection properties, which motivated researchers to develop an incredible variety of reflection-suppressing topographies, spanning several orders of magnitudes in feature sizes, from subwavelength nanostructures to macroscopically patterned glass covers. Inspiration for appropriate structure designs was often found in nature, most famously in the subwavelength nanostructures found on either the compound eyes

or the wings of various insect species like butterflies. However, following the development of straightforward and cost-effective bioreplication methods able to copy the delicate surface micro- and nano-features that comprise the surfaces of plant leaves and flower petals into transparent polymers, these often hierarchical surface structures have come to the attention of more and more researchers for templating their optical and/or wetting properties for improving PV panels.

The *Sky* scenario further predicts that by 2035, solar panels will cover a total area equal to the size of South Korea, and by 2070, this PV-covered total area should have reached the size of Spain [21]. With increasing installed PV capacity, it becomes increasingly essential to thoroughly study the possible ramifications for wildlife of such enormous quantities of PV panels being mass-deployed throughout our planet's wide variety of ecosystems. Unfortunately, it is often overlooked that renewable energy systems including PV can be drivers for various environmental damages. For example, for solar farms located in desert areas, it has been shown that the local climatic conditions in desert regions are affected by the large-area changes in surface albedo [22]. Also, the water demand for cleaning the PV panels' surfaces causes prolonged drying of ephemeral water bodies in arid regions [23]. Further, the large-scale deployment of PV systems also has direct damaging implications for biodiversity [24–28]. For example, it has been reported that utility-scale PV installations are responsible for the high mortality of migratory birds, often through collision-related impact [27]. Furthermore, large-scale solar power installations can also lead to fragmentation or even total loss of habitats [24, 26].

This thesis contributes to advancing the field of bioreplication towards large-scale deployment of plant surface structure replicas as multifunctional cover layers for solar panels in order to boost the devices' energy yield through improved light-management as well as to reduce maintenance and cleaning costs by implementing self-cleaning properties based on a lotus-leaf-like water repellency. Moreover, considering the rapid decline in insect abundance and diversity that is often labeled as the 'global insect crisis' [29–32], this thesis investigates the possible ramifications of PV installations (with and without such bioreplicated cover layers) for the conservation of polarotactic, aquatic insects such as mayflies and horseflies.

## 1.2 Thesis Outline

This dissertation includes **eleven chapters** and presents research efforts that were primarily carried out at the Light Technology Institute (LTI) and the Institute of Microstructure Technology (IMT), both of which are affiliated with the Karlsruhe Institute of Technology (KIT).

The first five chapters provide the theoretical background and describe the current state of research concerning plant-replicated light-harvesting layers in PV. After the brief introduction provided in **chapter 1**, the following **chapter 2** aims to summarize the fundamental principles of light-management in solar cells, including a discussion of the fundamental properties of p-n junction solar cells and introducing various concepts for minimizing reflectance at material interfaces. Next, **chapter 3** presents a broad overview of photonic structures found in living nature, focusing on antireflective surfaces found in animals and plants. In **chapter 4**, the basics of surface wetting and self-cleaning of micro- and nanotextured surfaces are introduced. Furthermore, soiling losses and mitigation strategies are discussed. **Chapter 5** focuses on introducing various techniques for replicating biological surface micro- and nanostructures into technical materials and discussing the two other possible methods of engineered biomimicry, namely bioinspiration and biomimetics.

The following six chapters then summarize the numerical and experimental analyses conducted within the scope of this thesis, starting with **chapter 6**, which is focused on gaining insight into the reflection and light-collection properties of disordered microstructures based on densely packed micro-cones via computational methods. In **chapter 7**, two important advancements towards a mass fabrication of plant surface structure replicas are elaborated in detail, namely the fabrication of metallic molds for hot-embossing-based replication of plant surface structures as well as their areal upscaling to dimensions  $> 100 \text{ cm}^2$ . The following **chapter 8** then covers the experimental characterization of the light-harvesting properties of hot-embossed large-area rose petal replicas, as well as their self-cleaning properties and measurements of their opto-electrical performance for three different polymeric materials atop of copper indium gallium diselenide (CIGS) thin-film solar cells. The performance of  $10 \text{ cm} \times 10 \text{ cm}$  CIGS- and silicon-based solar modules equipped with large-area rose petal replicas as light-harvesting layers under outdoor operational conditions is analyzed in **chapter 9**, as well as a basic experimental assessment of their long-term durability through accelerated aging and abrasion tests designed to mimick the standardized testing procedures generally used in the PV industry. While it is common to study the

light-harvesting, self-cleaning, and radiative cooling properties of PV cover layers, possible ramifications concerning the ecology and conservation of various (polarotactic) insect species have rarely been analyzed thus far. The light reflected from human-made objects (such as, for example, solar panels) can trigger maladaptive behaviors in polarotactic water-seeking insects and thereby ultimately lead to various effects harmful to the insect-fauna. To conclude the main part of this dissertation, **chapter 10** addresses these rarely discussed issues in detail by reporting on behavioral field experiments that explicitly measure the maladaptive attractiveness of (rose petal replicated) PV cover layers to polarotactic horseflies and mayflies. The results of these field experiments are further discussed and interpreted by relying on imaging polarimetric measurements of the reflection-polarization properties of petal replicated PV cover layers as well as their ray-tracing-based analysis.

Lastly, a summary of the key results covered in this thesis is presented in **chapter 11**, together with an outlook regarding all the topics addressed throughout this contribution.



---

## 2 Light-Management in Solar Cells and Modules

---

The following chapter is aimed at providing a brief introduction to the working principles of solar cells and the various light-management concepts that have been established in order to improve device performance. After introducing the basic properties of solar cells in section 2.1 and the theory of light reflection in section 2.2, a rather broad discussion of the various approaches towards minimizing reflection losses at material interfaces follows in section 2.3. Since antireflection and light-trapping are not the only light-management-based methods for improving the performance of PV devices, an assortment of photonics-based approaches which go beyond the concepts of antireflection and light-trapping are introduced in section 2.4. The final section 2.5 is focused on introducing two optical simulation methods – namely ray-tracing and the transfer-matrix method – which are extensively used by researchers for studying light-management in various optoelectronic devices, including solar cells and (organic) light-emitting diodes.

### 2.1 Fundamental Properties of Solar Cells and Modules

#### 2.1.1 Working Principle

Solar cells are electrical devices that exploit the so-called photovoltaic effect for directly converting the energy of incident light into electricity. The photovoltaic effect encompasses several basic steps, namely (i) the absorption of a photon within the respective absorber material, which, through excitation to higher energy levels, leads to the (ii) generation of free charge carriers. Lastly, the (iii) photogenerated charge carriers are separated by a built-in driving force, leading to a voltage build-up across the absorber until the built-in driving force for the charge carrier separation is compensated, and an equilibrium state is reached. By connecting an external load to the opposite sides of the illuminated absorber material, the voltage across the absorber drops to a lower value, and a net current is driven through the circuit. With the exception of dye-sensitized solar cells (further information can be found, for example, in the 2017 review by Gong *et al.* [33]), which follow a

photoelectrochemical approach to induce charge carrier separation, all other types of solar cells are comprised of solid materials only and rely on the special electronic band structure of (doped) semiconductors for achieving PV energy conversion. If a photon carrying an energy  $E_\gamma = E_g + \Delta E > E_g$  is absorbed in a semiconductor with the band gap energy  $E_g$ , an electron can be excited from the valence band to the conduction band, resulting in the generation of a more or less tightly bound electron-hole pair (usually treated as a quasiparticle called exciton) free to move about the semiconductor. However, before any significant movement of the charge carriers can take place, all excess energy  $\Delta E$  is quickly dissipated to the lattice (thermalization) and therefore not available for the PV energy conversion process. The subsequent spatial separation of the thermalized electron-hole pairs is achieved via a built-in electric field, implemented by configuring the semiconductor as a large-area p-n junction. Around a p-n junction, a region depleted of mobile charge carriers forms, driven by diffusion of free electrons and holes across the boundary in opposite directions, leading to many recombination events around the junction. With each electron-hole recombination, more static space charge will build up at each side of the junction, causing a gradient in electrostatic potential that counteracts the diffusion current across the p-n boundary (leveling out the electrochemical potential difference across the junction). At equilibrium, the net current is zero, and a built-in electrostatic field spans across the p-n junction, which is exploited as the driving force for the charge carrier separation in solar cells.

The typical current-voltage characteristic of a solar cell is shown in Fig. 2.1. In the most basic approximation (and under constant irradiation), the IV-curve can be expressed via a photogenerated current  $I_{SC}$  and the current-voltage characteristic of an ideal diode  $I_D(V)$ , yielding the Shockley solar cell equation

$$I(V) = I_{SC} - I_D(V) = I_{SC} - I_0 \left( e^{\frac{qV}{k_B T}} - 1 \right). \quad (1)$$

The overall highest current  $I_{SC}$  is reached under short circuit conditions and, conversely, the overall highest voltage  $V_{OC}$  is reached for an open circuit. The power output of a solar cell is given by the product of voltage and current at the respective operating point on the IV-curve. As illustrated in Fig. 2.1, the extracted power reaches its maximum value  $P_{MPP}$  at the so-called maximum power point (MPP), and the current and voltage at the MPP are denoted as  $I_{MP}$  and  $V_{MP}$ , respectively. The power conversion efficiency (PCE) is defined as the ratio of maximum power output  $P_{MPP}$  and input power  $P_{in}$

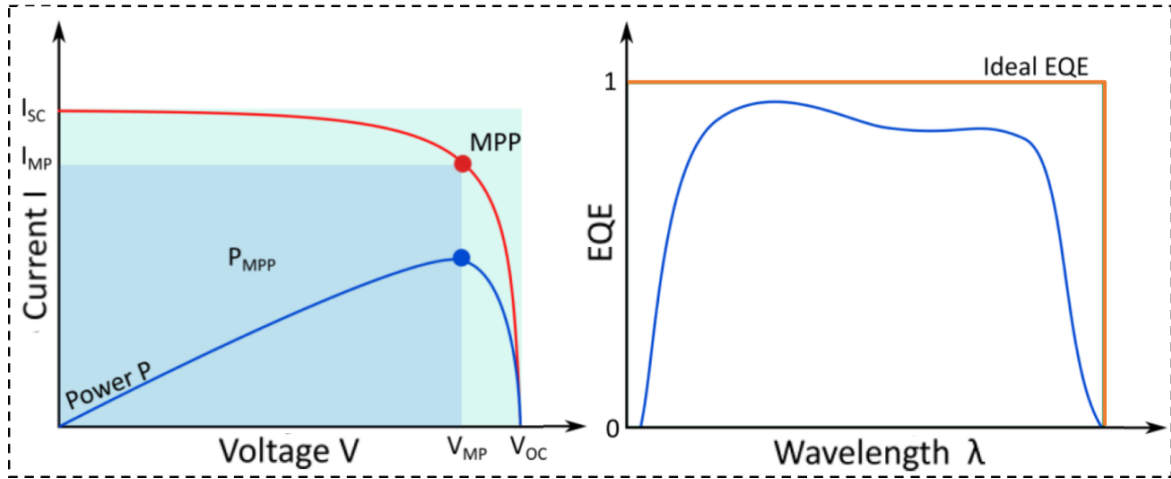


**Fig. 2.1:** Basic opto-electrical properties of solar cells. On the left-hand side, the current-voltage characteristics of a solar cell are schematically depicted. At the maximum power point (MPP), defined by the coordinates  $I_{MP}$  and  $V_{MP}$ , the maximum power  $P_{MPP}$  (represented by the blueish rectangle) can be extracted. The fill factor FF can be obtained as the ratio of  $P_{MPP}$  and the product  $I_{SC}V_{OC}$  (greenish rectangle). The schematic on the right-hand side shows the ideal external quantum efficiency spectrum for PV devices, together with a more realistic example suffering various optical and recombination losses. Adapted with permission from reference [34], © The Author.

$$PCE = \frac{P_{MPP}}{P_{in}} = \frac{I_{MP} \cdot V_{MP}}{P_{in}} = \frac{I_{SC} \cdot V_{OC} \cdot FF}{P_{in}}, \quad (2)$$

where the fill factor FF is defined as

$$FF = \frac{P_{MPP}}{I_{SC} \cdot V_{OC}} = \frac{I_{MP} \cdot V_{MP}}{I_{SC} \cdot V_{OC}}. \quad (3)$$

Another important quantity for characterizing PV devices – the external quantum efficiency (EQE) – provides insight into their spectrally resolved power conversion properties and is defined as the ratio

$$EQE(\lambda) = \frac{N_e}{N_v(\lambda)}, \quad (4)$$

where  $N_e$  describes the number/rate of charge carriers collected at one of the device terminals while  $N_v(\lambda)$  describes the number/rate of incident photons of wavelength  $\lambda$  responsible for the photogeneration of the  $N_e$  charge carrier pairs. A generic solar cell EQE spectrum is depicted in Fig. 2.1. For photon energies below the band gap of the absorber material, the EQE is zero. Concerning short wavelengths, solar cell EQE spectra typically start to drop towards zero for wavelengths  $< 400$  nm due to a rapid increase in parasitic absorption in the front contact material and/or the encapsulation (usually glass or polyvinyl acetate, PVA). For materials that do not support multi-carrier generation, the ideal  $EQE(\lambda)$  spectrum (see Fig. 2.1) follows

the shape of a Heaviside step function  $\text{EQE}(\lambda) = \Theta(\lambda_g - \lambda)$ , where  $\lambda_g$  denotes the absorber material band gap threshold expressed in terms of equivalent photon wavelength. The EQE further links the incident spectral photon flux  $\Phi(\lambda)$  to the short circuit current density  $J_{\text{SC}}$  via the relation ( $q$  denoting the elementary charge)

$$J_{\text{SC}} = q \int \text{EQE}(\lambda)\Phi(\lambda)d\lambda. \quad (5)$$

Due to the combined effects of reflection, incomplete absorption in the active layer, and parasitic absorption outside the active layer, the EQE of real solar cells deviates from the ideal scenario. Besides these optics-related losses taking place prior to the electron-hole pair generation events, recombination (radiative or non-radiative) of charge carriers before their separation and extraction through the device terminals also lead to a reduced EQE in real devices.

After the 1873 discovery that the electrical resistance in selenium can be influenced through irradiation with light [35], the pioneering demonstrations of the first solid-state PV devices based on selenium absorbers followed within a decade [36, 37]. Due to the rather moderate PCEs of these first devices of roughly 1%, research and development efforts regarding solar cells only gained momentum after the first device with a considerably higher efficiency of 6% was achieved at Bell Laboratories and first presented to the public in 1954 [38]. This boost in efficiency was due to their use of Si as the absorber material. Over the following decades, numerous device architectures for Si solar cells, a few examples of which are depicted in Fig. 2.2, have been developed, reaching ever-increasing efficiency records. Roughly six decades after the demonstration of the first Si-based device, researchers boosted the efficiencies of (single-junction) Si solar cells to the current world record of 26.7%, with a cell architecture that can be considered a combination of the configurations shown in Fig. 2.2 B) and D) [39]. Furthermore, today's commercially available Si solar panels (area  $\approx 1.5 \text{ m}^2$ ) can reach efficiencies above 22% [40]. As a side note, it is worth mentioning that, even to this day, selenium solar cells still haven't surpassed maximum efficiencies of 5% – 6% [41]. Current world record efficiencies (as of 2021) for various types and sizes of (single- and multi-junction) solar cells and modules are compiled in reference [42].

Although to date, numerous solar cell technologies based on different absorber materials have been established, Si-wafer-based PV devices (crystalline + polycrystalline) still dominate the global PV market (by far) with a 95% share of production in 2019 [43]. The remaining 5% are governed by several thin-film technologies, namely copper indium gallium diselenide (CIGS) and cadmium

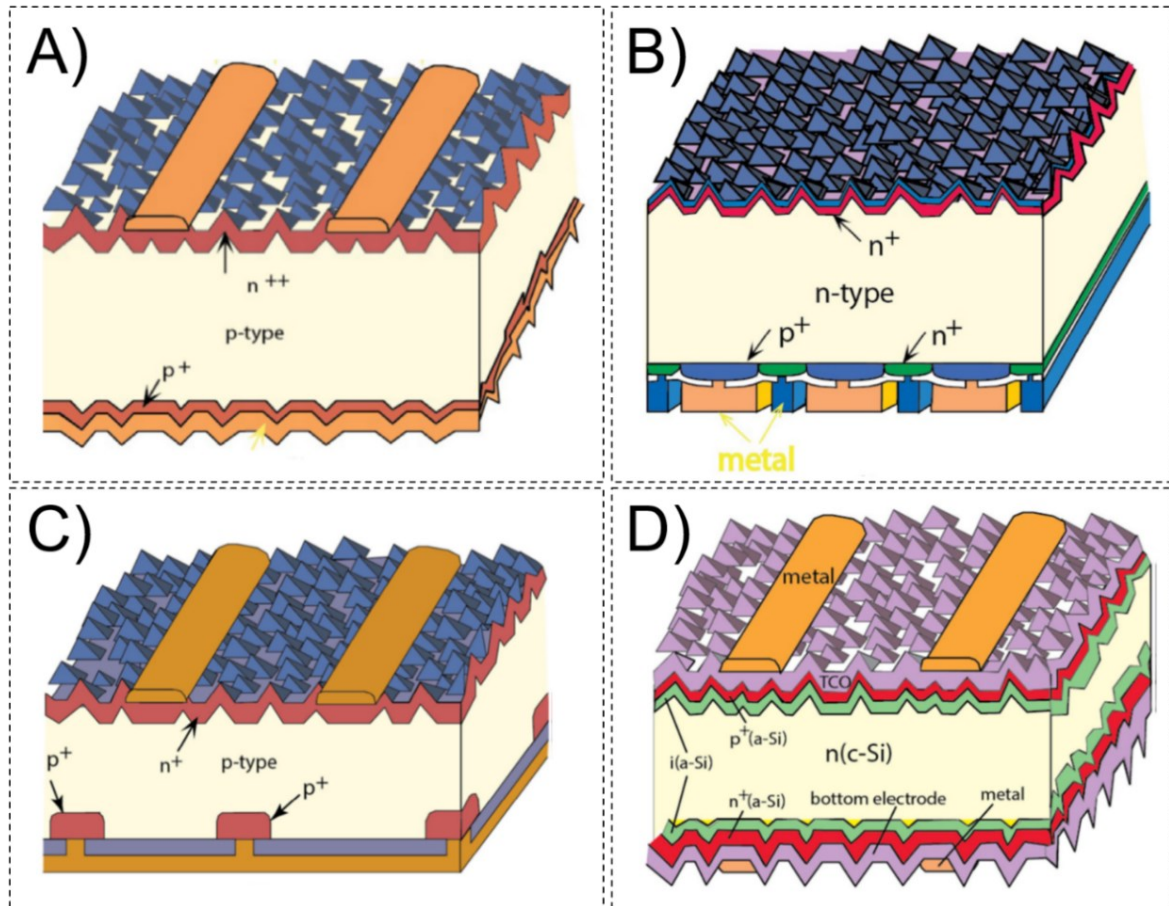


**Fig. 2.2:** Schematic depictions of a selection of high efficiency c-Si solar cell architectures. A) Al-BSF cell design (back surface field produced via doping with Al atoms), which dominated the PV industry for the past three decades. B) Interdigitated back contact solar cell, with both contacts located at the rear side (commercially available). C) Passivated emitter and rear cell (commercially available). D) Heterojunction cell structure using wider-band gap hydrogenated amorphous silicon layers as the contacts. This type of device is not (yet) established in the PV industry. Adapted with permission from reference [18], © 2019 IOP Publishing Ltd.

telluride (CdTe) devices (both polycrystalline), as well as hydrogenated amorphous silicon (a-Si:H) solar cells. An overview of the present (2019) market conditions, the current state of development, as well as drawbacks and advantages concerning all relevant PV technologies can be found in [18].

PV devices based on various other absorber materials have been extensively researched over the years. These include, for example, single-crystalline GaAs or GaInS solar cells, (polycrystalline) copper zinc tin sulfide (kesterite) based devices, organic solar cells, as well as lead halide perovskite solar cells. A detailed discussion of the current state of research for these absorber technologies can be found in reference [44].

### 2.1.2 Efficiency Limits and Loss Mechanisms

The energy conversion mechanism of conventional p-n (single-)junction solar cells inherently suffers several loss mechanisms. The two aforementioned mechanisms related to the electronic band structure of the absorber, namely

- the inaccessibility of the cumulative energy of all incident photons with energies below the absorber band gap ( $E_\gamma < E_g$ ) for PV energy conversion (assuming negligible two-photon absorption), and
- the irreversible loss of the energy portion  $\Delta E$  for absorbed photons with above band gap energies  $E_\gamma = E_g + \Delta E > E_g$  through thermalization,

already strongly suggest that the band gap of the absorber material has a principal impact on the efficiency limit (in terms of converting terrestrial solar radiation to electricity) of the respective type of solar cell. Both these loss mechanisms are unavoidable and are categorized as intrinsic/fundamental losses. Intrinsic losses either cause a reduction in current (as the aforementioned below band gap and thermalization losses do) or a reduction in voltage. Following the naming used in reference [45], the three remaining unavoidable intrinsic loss mechanisms are referred to as

- Carnot loss,
- Boltzmann loss, and
- emission loss,

and are briefly described in the following paragraphs. In analogy to a Carnot heat engine, an ideal solar cell (or more precisely: the electron-hole gas within the absorber) exchanges heat with two reservoirs – a high temperature one and a low temperature one – via thermal radiation, utilizing the uptake of heat from the hot reservoir (absorption of solar photons) in order to convert it into (entropy free) electrical work whilst emitting low-temperature heat radiation into the cold reservoir (atmosphere) [46, 47]. Due to the fundamental principle that the maximum amount of work is extracted if entropy balances out over the cyclical process, a certain portion of the initial energy uptake must be released as waste heat into the cold reservoir, which is basically the price to pay for converting heat into electricity. The amount of energy that is required for converting heat into electricity, and therefore the efficiency, depends only on the two heat reservoir temperatures. Concerning solar energy conversion via PV devices, this fundamental thermodynamic loss mechanism manifests itself in a decrease in open-circuit voltage.

The mechanism termed Boltzmann loss is based on a mismatch in the angular profiles of absorbed and emitted radiation [45]. In more detail, the angular redistribution/randomization inherent to the process of absorbing collimated incident light (2D photon gas) and subsequently re-emitting radiation of equal energy in a random direction (3D photon gas) is accompanied by an irreversible increase in entropy and, as a consequence, a certain amount of heat dissipation to the environment. Like the Carnot losses, this anisotropy-based fundamental loss mechanism leads to a voltage decrease.

Lastly, emission (or radiative recombination) losses are a direct consequence of Kirchhoff's law of thermal radiation, which states that, for an object which absorbs and emits thermal radiation under equilibrium conditions, absorptivity and emissivity are equal at any given direction and at every given wavelength [48, 49]. Based on this famous relation, it becomes clear that radiative recombination can not be fully reduced to zero at finite device temperatures, not even for ideal solar cells. Emission losses lead to reduced currents.

In addition to these five fundamental loss mechanisms, real-life solar cells suffer from several more performance reducing effects such as reflection, incomplete absorption, contact shadowing, and series resistance, as well as (non-radiative) Shockley-Read-Hall [50, 51] and Auger [52] recombination. For a standard CIGS solar cell, Kosyachenko *et al.* reported total optical losses of 17.7%, which amounts to 1.5 times the reported overall recombination losses [53]. Similar studies with a focus on quantifying recombination and/or optical losses have also been conducted for various other solar cell technologies, including, for example, CdTe [54, 55], c-Si (interdigitated back-contact solar cell) [56],  $\mu\text{c-Si:H}$  thin-film (around 1  $\mu\text{m}$  layer thickness) solar cells [57], as well as kesterite and perovskite solar cells [55]. Improving light-management can be considered a promising path for further improving device performance towards their theoretical limit for most types of solar cells, including c-Si and CIGS devices, and further for reducing the absorber thickness whilst still reaching high efficiencies [58, 59].

For an ideal p-n junction solar cell suffering only the five intrinsic loss mechanisms described above, Hirst and Ekins-Daukes [45] analytically calculated the power output and the power consumption of each of the loss channels in dependence of the absorber band gap by evaluating absorbed and emitted radiation using the generalized Planck equation (photon gas with nonzero chemical potential in chemical equilibrium with an excited electron-hole system [60]), which is summarized in Fig. 2.3. The sun and the solar cell were both treated as blackbody

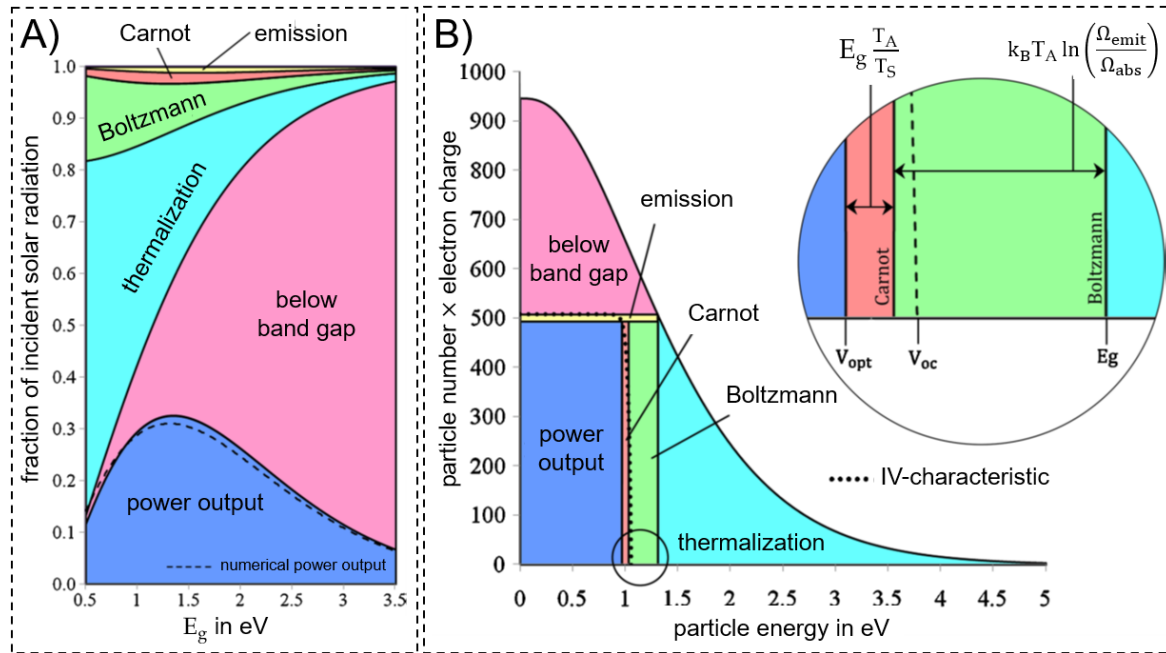


**Fig. 2.3:** Intrinsic loss mechanisms in single-junction solar cells. **A)** Intrinsic loss processes and power output of ideal single-junction solar cells under one sun illumination in dependence of the band gap energy of the absorber. **B)** Intrinsic losses of a single-junction device with (close to) optimum band gap energy  $E_g = 1.31$  eV under one sun illumination. Adapted with permission from reference [45], © 2010 John Wiley & Sons, Ltd.

radiators at temperatures  $T_{\text{sun}} = 6000$  K and  $T_{\text{cell}} = 300$  K, respectively. Fig. 2.3 A) shows that the power output, as well as the relative contributions of each of the loss channels, strongly depend on the absorber band gap. Further, the calculations of Hirst *et al.* yield a PCE limit of  $\approx 33\%$  for single-junction solar cells. For a device with an optimum absorber band gap, the most detrimental loss mechanisms are identified as thermalization and non-absorption of low-energy photons, as illustrated in Fig. 2.3 B).

In a 1961 contribution, Shockley and Queisser were the first to derive a reasonable theoretical efficiency limit that considered some basic properties of the energy conversion process of solar cells through applying the principle of detailed balance to the particle fluxes into and out of the semiconductor [61]. Their approach treats both the sun and the solar cell as blackbody radiators at  $T_{\text{sun}} = 6000$  K and  $T_{\text{cell}} = 300$  K, respectively, and assumes that all incident photons with above band gap energies are absorbed (no reflection losses) and generate exactly one electron-hole pair per photon absorbed. Also, there are no interactions between a solar cell and photons with below band gap energies. Furthermore, the solar cells are assumed to emit heat radiation from both their front and their rear sides.

In the decades that followed, numerous studies focused on deducing theoretical efficiency limits of solar cells under various conditions and for all kinds of device architectures. For example, aiming at more realistic limiting efficiencies, especially for Si-based solar cells, Yablonovitch *et al.* calculated efficiency limits for devices which, besides radiative recombination, include Auger recombination as well as free carrier absorption [62]. Based on a measured optical absorption spectrum and published values of the Auger and free-carrier absorption coefficients, the efficiency limit for Si solar cells was reported at 29.8%. Instead of modeling the sun as a blackbody radiator, Yablonovitch *et al.* used the more realistic AM1.5G spectrum (see also subsection 2.1.3) for these calculations. Since nowadays the standard test conditions (see next subsection 2.1.3) for PV devices require a device temperature of 25°C, it is useful to calculate the Shockley-Queisser efficiency limit for AM 1.5G illumination and a solar cell temperature  $T_{\text{cell}} = 2988.15$  K. Under these conditions, the efficiency limit exhibits local maxima of 32.85% at 1.15 eV (1080 nm) and 33.16% at 1.34 eV (928 nm) [63]. It should be noted that the current world record efficiency for single-junction solar cells is as high as 29.1% (achieved with a GaAs device,  $E_{\text{GaAs}} = 1.42$  eV) [42, 64, 65].

The single-junction solar cell efficiency limitations introduced by Shockley and Queisser can be overcome by utilizing various advanced device concepts. For example, thermalization losses can be reduced by exploiting multi-exciton generation effects or by suppressing interactions of hot charge carriers with phonons and subsequently extracting the hot carriers via energy-selective contacts [66, 67]. Losses through non-absorption of below band gap photons can be reduced with intermediate band solar cells, which are based on introducing an impurity level in the semiconductor band gap [68, 69]. Moreover, increasing the light concentration factor using lenses or mirrors (as well as restricting the emission angle) also leads to higher efficiency limits by reducing the energy lost due to Boltzmann entropy generation [45]. Carnot losses, on the other hand, can only be reduced by operating the PV device in outer space and thereby lowering the temperature of the cold heat sink. Furthermore, reducing radiative recombination losses could only be achieved if there are situations where Kirchhoff's law of thermal radiation, which is a consequence of time-reversal invariance [70], does not hold. It has been proposed that such a scenario could be achieved via time-asymmetrical, magneto-optical devices [71]. It has further been pointed out that nanostructured/nanophotonic solar cells can also reach efficiencies above the Shockley-Queisser limit due to an effect that can be considered the nanoscale equivalent of (optical) concentration in macroscopic systems [72, 73]. Solar thermo-

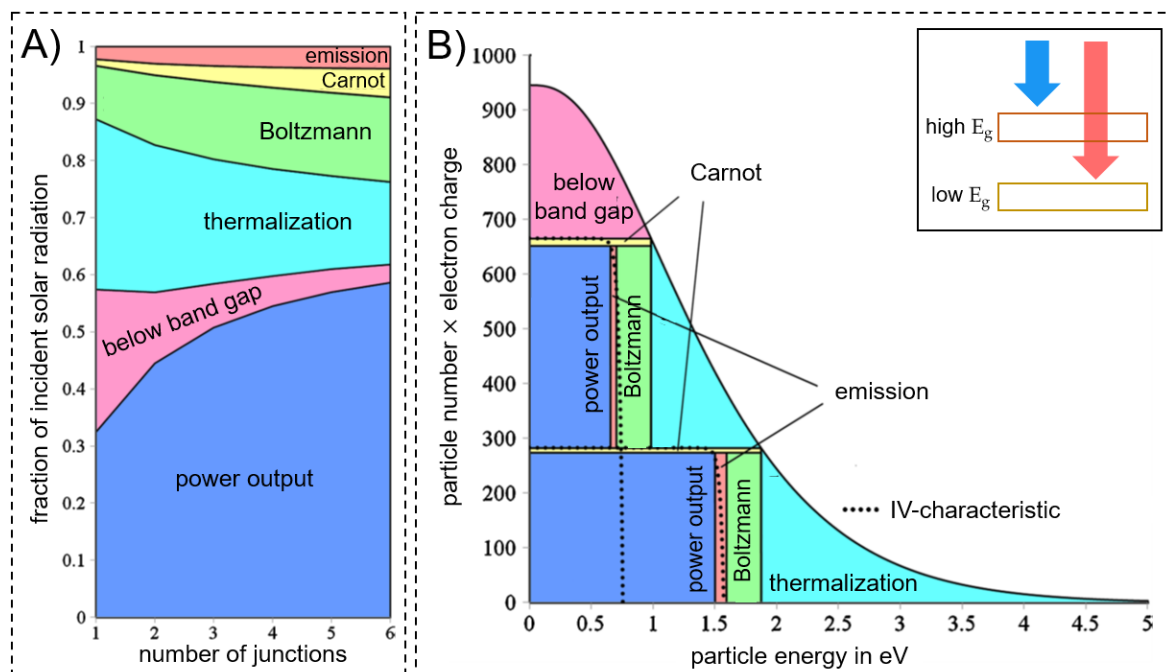


**Fig. 2.4:** Intrinsic loss mechanisms in multi-junction solar cells. **A)** Intrinsic loss processes and power output of ideal unconstrained multi-junction solar cells (optimum band gaps for each sub-cell) under one sun illumination in dependence of the number of junctions in the device. **B)** Intrinsic losses of a two-junction device with optimum band gap energies  $E_g = 0.98$  eV and  $1.87$  eV under one sun illumination. Adapted with permission from reference [45], © 2010 John Wiley & Sons, Ltd.

PV systems are another approach to overcome the Shockley-Queisser limit. Such systems could, in theory, reach efficiencies up to 85.4% by reducing both thermalization losses and loss of sub band gap photons by converting the incident sunlight into (preferably) monochromatic radiation, which is then converted into electricity by a PV cell of equivalent absorber band gap [74, 75]. Another way to reduce thermalization losses and non-absorption of sub-band-gap photons relies on stacking several solar cells with incrementally decreasing absorber band gaps (highest band gap at sun-facing side) on top of each other in order to obtain a multi-junction device, as illustrated in Fig. 2.4. For this type of PV device, extending the Shockley-Queisser approach leads to an efficiency limit of 86.8% for maximum concentration and an infinite number of sub-cells (sun and solar cell are treated as blackbody radiators at  $T_{\text{sun}} = 6000$  K and  $T_{\text{cell}} = 300$  K) [76]. Lastly, it should be noted that numerous authors brought valuable insights and refinements to the considerations on solar cell efficiency limits (and other properties) by relying on a thermodynamics perspective based on energy and entropy fluxes rather than particle fluxes and a detailed balance approach [77–80, 47].

### 2.1.3 Laboratory vs. Outdoor Operational Conditions

Current-voltage-characteristics and nominal power output (as well as PCE) of PV devices are measured under so-called standard test conditions (STC), which encompass the following parameters: module temperature of 25°C, a simulated solar irradiance of 1000 W/m<sup>2</sup> (under normal incidence) following the AM1.5G terrestrial solar spectrum (as specified in IEC 60904-3 [81] or ASTM G173-03 [82]). However, the actual operating conditions of PV modules in the field, for most of the time, differ greatly from STC. For example, variations in the irradiation conditions (spectrum, low irradiance levels, polarization) can lead to changes in annual energy yield of several percent [83, 84]. STC-based examinations also do not provide information about a device's performance under diffuse illumination. Moreover, for a PV installation with a fixed tilt angle, normal incidence of light is a rather rare event. Fig. 2.5 shows the incidence angle distribution and direct solar irradiance for a fixed solar module for an entire year. It can be deduced that the incidence angle is above 45° for around 70% of the time, which corresponds to (only) 19% of the energy share in the module plane due to the reduced projected module area for oblique incidence of light. According to Martin and Ruiz, off-normal incidence of (direct) sunlight leads to a reduction of the annual energy yield by 3% – 3.5% for fixed modules at optimum tilt angle or by 5% – 7% for misoriented modules [85, 86]. These optical losses can be tackled by equipping the front sides of the modules with omnidirectional antireflective layers. It should be noted that these values do not describe the total reflection losses of the devices but rather the additional loss in energy yield relative to an identical device with ideal two-axis solar tracking (only normal light incidence over the entire measurement). Further, the effect of a reduced (projected) module area at oblique incidence of light is also canceled out of these quantities and treated separately. According to King *et al.* [83], module misorientation can lead to a loss in annual energy yield of up to 25% relative to a (fixed) module under optimum tilt towards the south. By utilizing a two-axis solar position tracking system, on the other hand, the improved module orientation with respect to the incidence angle can increase the annual energy yield compared to the fixed installation by up to 30%.

As a rule of thumb, it is often assumed that the optimum tilt and orientation for maximizing the annual energy yield for a fixed PV installation is given by the local latitude as the tilt angle in combination with an orientation towards the south in the northern hemisphere or towards north for the southern hemisphere. It should be noted, however, that deviations of up to 10° (for both tilt and azimuth

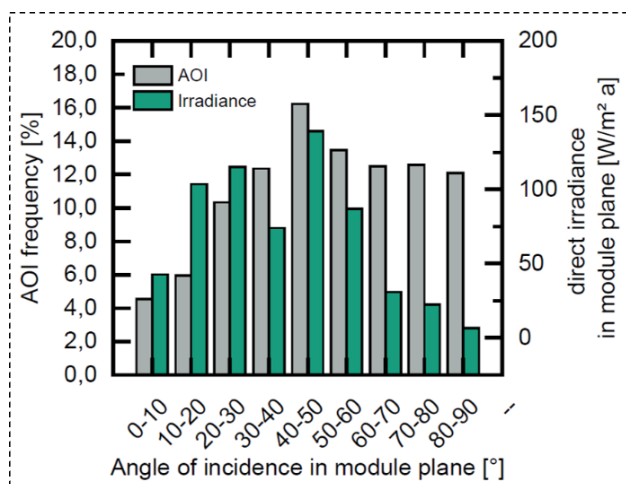


**Fig. 2.5: Incidence angle distribution and direct solar irradiance for a solar module tilted 30° southwards, measured over one year in Freiburg, Germany. Reprinted with permission from reference [87], © 2014 The Authors.**

angle) from this simple estimate have been reported for some locations based on measured solar irradiance data [88]. However, it has also been pointed out that the annual energy yield of fixed PV installations is surprisingly robust against deviations from the optimum parameters for the installation site [89, 90].

The module temperature under field conditions might exceed the STC temperature by far. Based on a one-year survey of a c-Si, poly-Si, and a-Si installation mounted with a 20° tilt towards the south in Takayama (Japan), Nishioka *et al.* determined a maximum value for the monthly average of the module temperature of 44°C in July and peak temperatures throughout the course of a summer day of 60°C – 65°C [91]. With increasing module temperature, the device performance tends to decrease. Typical values for the relative efficiency decrease with every 1 K increase in module temperature of 0.3% – 0.5% are found for c-Si and poly-Si devices [40, 92, 93]. According to King *et al.*, the annual energy yield is reduced by 2% – 10% due to the elevated module temperatures during sunny days [83]. Several active and passive cooling methods have been developed in order to reduce solar module heating, including, for example, the use of phase change materials for temperature stabilization [94, 95] as well as photonics-based approaches such as selective-spectral cooling [96] and passive radiative cooling [97–102]. Selective-spectral cooling aims at minimizing self-heating via free carrier absorption by selectively reflecting sub-band-gap light before it enters the device. Passive radiative cooling, on the other hand, is based on maximizing the emissivity of PV devices in the atmospheric transparency window (between  $\lambda = 8 \mu\text{m}$  and  $13 \mu\text{m}$ ) in order to maximize radiative heat dissipation into outer space. Some more details about these photonics-based approaches for heat-management in PV are provided in section 2.4.

Lastly, another key factor influencing the performance of PV modules in the field is the accumulation of dust on the surfaces of the solar panels over time, which can

easily lead to a 10% loss in annual energy yield. A more detailed discussion of soiling losses and mitigation strategies can be found in chapter 4.

## 2.2 Reflection and Refraction of Electromagnetic Waves

Before the various types of antireflection concepts are introduced in section 2.3, this section aims at providing a brief summary of the theoretical description of light reflection and transmission across material interfaces. Detailed explanations can be found in various textbooks [103–108].

For so-called dispersive materials, the permittivity  $\epsilon$ , which relates the electric induction  $\vec{D}$  to the electric field  $\vec{E}$  is frequency-dependent because the dynamic polarization response of a material can not happen instantaneously if a time-varying electric field is applied. With such a time-dependent material response  $\epsilon(t)$  (and assuming isotropy and a linear response to external fields), the constitutive relation for the electric field  $\vec{E}$  and induction  $\vec{D}$  can be expressed by a convolutional relationship of the form

$$\vec{D}(\vec{r}, t) = \int_{-\infty}^{\infty} \epsilon(t - t') \vec{E}(\vec{r}, t') dt' = \int_{-\infty}^t \epsilon(t - t') \vec{E}(\vec{r}, t') dt', \quad (6)$$

where  $\epsilon(t - t') = 0$  for  $t' > t$  was used (causality). This kind of relationship can be expressed more straightforwardly in the frequency-domain. Assuming an isotropic dielectric and magnetic material, the constitutive relations in the frequency domain can be expressed as follows:

$$\vec{D}(\vec{r}, \omega) = \epsilon(\vec{r}, \omega) \vec{E}(\vec{r}, \omega) = \epsilon_0 \epsilon_{\text{rel}}(\vec{r}, \omega) \vec{E}(\vec{r}, \omega), \quad (7)$$

$$\vec{B}(\vec{r}, \omega) = \mu(\vec{r}, \omega) \vec{H}(\vec{r}, \omega) = \mu_0 \mu_{\text{rel}}(\vec{r}, \omega) \vec{H}(\vec{r}, \omega), \quad (8)$$

and, by using the electric and magnetic susceptibilities  $\chi(\vec{r}, \omega) = \epsilon_{\text{rel}}(\vec{r}, \omega) - 1$  and  $\chi_m(\vec{r}, \omega) = \mu_{\text{rel}}(\vec{r}, \omega) - 1$ , the polarization and magnetization responses  $\vec{P}$  and  $\vec{M}$  can be explicitly introduced into these relations as follows:

$$\vec{D}(\vec{r}, \omega) = \epsilon_0 \epsilon_{\text{rel}} \vec{E}(\vec{r}, \omega) = \epsilon_0 (1 + \chi) \vec{E}(\vec{r}, \omega) = \epsilon_0 \vec{E}(\vec{r}, \omega) + \vec{P}(\vec{r}, \omega) \quad (9)$$

$$\vec{B}(\vec{r}, \omega) = \mu_0 \mu_{\text{rel}} \vec{H}(\vec{r}, \omega) = \mu_0 (1 + \chi_m) \vec{H}(\vec{r}, \omega) = \mu_0 (\vec{H}(\vec{r}, \omega) + \vec{M}(\vec{r}, \omega)) \quad (10)$$

The Maxwell equations can be re-expressed via separation of variables to yield (generally inhomogeneous) wave equations for  $\vec{E}$  and  $\vec{H}$ . For a homogeneous, isotropic, and dispersive material without any free charge carriers and with a linear

response, one finds the form of Helmholtz wave equations for the electric and magnetic fields in the frequency domain, which read

$$(\vec{\nabla}^2 + \omega^2 \mu_0 \mu_{\text{rel}} \epsilon_0 \epsilon_{\text{rel}}) \vec{E}(\vec{r}, \omega) = \left( \vec{\nabla}^2 + \frac{\omega^2}{c^2} \right) \vec{E}(\vec{r}, \omega) = 0 \quad (11)$$

$$(\vec{\nabla}^2 + \omega^2 \mu_0 \mu_{\text{rel}} \epsilon_0 \epsilon_{\text{rel}}) \vec{H}(\vec{r}, \omega) = \left( \vec{\nabla}^2 + \frac{\omega^2}{c^2} \right) \vec{H}(\vec{r}, \omega) = 0 \quad (12)$$

where the speed of light  $c = (\mu_0 \mu_{\text{rel}} \epsilon_0 \epsilon_{\text{rel}})^{-1/2}$  for the propagation through a medium characterized by  $\mu_{\text{rel}}$  and  $\epsilon_{\text{rel}}$  can be identified. The general solution to these equations are superpositions of plane waves  $\vec{E}(\vec{r}, \omega) = \vec{E}_0(\vec{k}, \omega) e^{-i\vec{k} \cdot \vec{r}}$  (or  $\vec{H}(\vec{r}, \omega) = \vec{H}_0(\vec{k}, \omega) e^{-i\vec{k} \cdot \vec{r}}$  respectively).  $\vec{E}_0$  and  $\vec{H}_0$  are complex amplitudes/phasors (product of the real amplitude vector and a phase factor  $e^{i\phi}$ ) orthogonal to  $\vec{k}$ , such that  $\vec{H}_0 = y(\hat{k} \times \vec{E}_0)$  (in non-absorbing materials) with  $y = (\epsilon/\mu)^{1/2}$  describing the characteristic optical admittance. By plugging the plane wave ansatz into the wave equations (11) and (12), one finds that the wave vector  $\vec{k}$  must satisfy

$$\vec{k} \cdot \vec{k} = \omega^2 \mu_0 \mu_{\text{rel}} \epsilon_0 \epsilon_{\text{rel}} = \frac{\omega^2}{c^2} = \frac{\omega^2}{c_0^2} \cdot \mu_{\text{rel}} \epsilon_{\text{rel}} = \frac{\omega^2}{c_0^2} \cdot N^2. \quad (13)$$

Here, the vacuum speed of light  $c_0 = (\mu_0 \epsilon_0)^{-1/2}$  was introduced, as well as the refractive index  $N = (\mu_{\text{rel}} \epsilon_{\text{rel}})^{1/2}$  of the material through which the electromagnetic plane wave is propagating.

Based on the integral representation of Maxwell's equations, a set of conditions (related to the components of the electric and magnetic field vectors normal and tangential to the interface) can be derived, which must be fulfilled when an electromagnetic wave propagates across a material interface. From these interface conditions, the reflection and transmission/refraction properties of electromagnetic waves at abrupt and planar material interfaces can be derived. The amplitude reflection and transmission coefficients  $r$  and  $t$  for p- and s-polarized light incident upon a planar interface between two extended materials 1 and 2 under an angle  $\theta_1$  (commonly called Fresnel coefficients) can be written as

$$r_s = \frac{y_1 \cos \theta_1 - y_2 \cos \theta_2}{y_1 \cos \theta_1 + y_2 \cos \theta_2} \quad t_s = \frac{2y_1 \cos \theta_1}{y_1 \cos \theta_1 + y_2 \cos \theta_2} \quad (14)$$

$$r_p = \frac{y_2 \cos \theta_1 - y_1 \cos \theta_2}{y_2 \cos \theta_1 + y_1 \cos \theta_2} \quad t_p = \frac{2y_1 \cos \theta_1}{y_2 \cos \theta_1 + y_1 \cos \theta_2} \quad (15)$$

where  $y_i = (\epsilon_i/\mu_i)^{1/2}$  denotes the characteristic optical admittance of material  $i$ , which depends on the respective permittivity  $\epsilon_i = \epsilon_0 \epsilon_{i,\text{rel}}$  and permeability  $\mu_i = \mu_0 \mu_{i,\text{rel}}$ , and  $\theta_2$  denotes the propagation angle with respect to the surface

normal in material 2. For non-magnetic materials ( $\mu_{i,\text{rel}} = 1$ ), the optical admittances are directly linked to the refractive index  $N = (\mu_{\text{rel}}\epsilon_{\text{rel}})^{1/2} = \epsilon_{\text{rel}}^{1/2}$  via

$$y_i = (\epsilon_0/\mu_0)^{1/2} \cdot \epsilon_{i,\text{rel}}^{1/2} = y_0 \cdot \epsilon_{i,\text{rel}}^{1/2} = y_0 \cdot N_i, \quad (16)$$

with  $y_0 = (\epsilon_0/\mu_0)^{1/2}$  representing the optical admittance of free space. Therefore, the Fresnel coefficients can be written as

$$r_s = \frac{N_1 \cos \theta_1 - N_2 \cos \theta_2}{N_1 \cos \theta_1 + N_2 \cos \theta_2} \quad t_s = \frac{2N_1 \cos \theta_1}{N_1 \cos \theta_1 + N_2 \cos \theta_2} \quad (17)$$

$$r_p = \frac{N_2 \cos \theta_1 - N_1 \cos \theta_2}{N_2 \cos \theta_1 + N_1 \cos \theta_2} \quad t_p = \frac{2N_1 \cos \theta_1}{N_2 \cos \theta_1 + N_1 \cos \theta_2} \quad (18)$$

and one can find that

$$t_s = r_s + 1 \quad \text{and} \quad \frac{N_2}{N_1} t_p = r_p + 1. \quad (19)$$

In general, the Fresnel-coefficients are of complex value since they not only describe the magnitude-ratios of the transmitted and reflected complex E-field amplitudes but also include the phase-shifts that might occur for the reflected and transmitted waves. While these coefficients describe the relative amplitudes of the reflected and transmitted waves with respect to the incident wave amplitude, the reflected and transmitted power fractions can be derived from the time-averaged Poynting-vectors of the respective partial waves, yielding [103, 104]

$$R_{s/p} = |r_{s/p}|^2 \quad \text{and} \quad T_{s/p} = \left| \Re \left( \frac{N_2 \cos \theta_2}{N_1 \cos \theta_1} \right) \right| |t_{s/p}|^2. \quad (20)$$

The propagation angles  $\theta_2$  and  $\theta_{\text{refl}}$  of the refracted and the reflected wave are determined by using Snell's law

$$N_1 \cdot \sin \theta_1 = N_1 \cdot \sin \theta_{\text{refl}} = N_2 \cdot \sin \theta_2. \quad (21)$$

Detailed descriptions of the various effects that can be derived from the Fresnel equations and Snell's law, including, for example, total internal reflection (TIR) and the related critical angle, as well as the Brewster angle, can be found in various books, such as in [103–107].

The permittivity  $\epsilon_{\text{rel}} = \epsilon'_{\text{rel}} - i\epsilon''_{\text{rel}}$  is generally given by a complex function of the frequency  $\omega$ . Therefore, the refractive index  $N = (\epsilon'_{\text{rel}} - i\epsilon''_{\text{rel}})^{1/2} = n' - in''$  may also generally be of complex value. Real-valued refractive indices therefore only occur for a purely real permittivity  $\epsilon_{\text{rel}} = \epsilon'_{\text{rel}} \in \mathbb{R}$ , which describes the scenario of an absorption-free (lossless) medium. Many classic textbooks, including classics like the Feynman Lectures [109], claim (either explicitly or implicitly) that, in case of complex refractive indices, the expressions for the amplitude reflection and

transmission coefficients given in equations (17) and (18), as well as the reflectance and transmittance (20) and Snell's law (21), can still be used without any alterations. This generally leads to complex propagation angles  $\theta_i$  which can no longer be interpreted intuitively in terms of wave propagation directions. For example, in his book on the *Theory of Reflection*, J. Lekner states on page 234 [107]:

*'Here we consider radiation incident from a non-absorbing medium (real  $\epsilon_1$ ) onto an absorbing medium (complex  $\epsilon_2$ ). Thus the angle of refraction is complex, and has a formal meaning only.'*

It has been pointed out, however, that the conservation of energy for the propagation of an electromagnetic wave across a material interface, which is expressed by the relation

$$R_{s/p} + T_{s/p} = 1, \quad (22)$$

is violated for transitions lossy  $\rightarrow$  lossless and lossy  $\rightarrow$  lossy if the abovementioned equations are kept unaltered for complex refractive indices. The energy conservation mismatch for these scenarios was explicitly calculated by Weber in 2014 [110]. According to Macleod, the source of this difficulty is a coupling between the incident and reflected fields which occurs in lossy materials and needs to be considered when computing energy transport through an interface [105].

The complex angle formalism assumes the following relations to describe the wave propagation in a lossy medium:

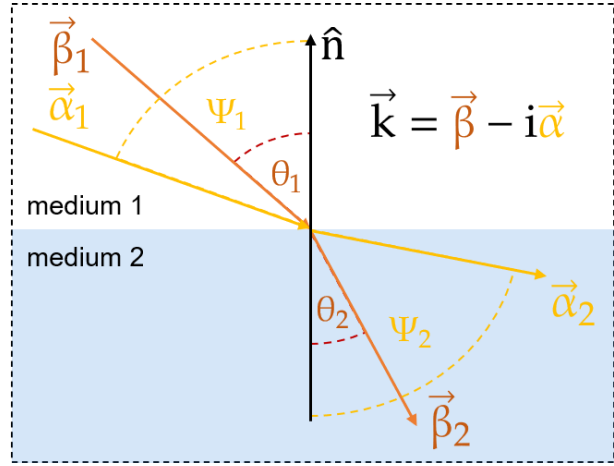
$$\vec{E}(\vec{r}, t) = \vec{E}_0 e^{i(\omega t - \vec{k}\vec{r})} = \vec{E}_0 e^{i(\omega t - k\hat{n}\vec{r})} \quad (23)$$

where  $k = \omega/c_0 \cdot N \in \mathbb{C}$  and  $\hat{n} \in \mathbb{R}^3$ ,  $|\hat{n}| = 1$ . In this description, the direction of wave propagation and attenuation are identical (parallel to the unit vector  $\hat{n}$ ). Such a plane wave is commonly described as homogeneous. As pointed out by Canning [111–113], the assumption that waves propagating in lossy materials will be of such a form is not valid, which can be exemplified by a simple example. It is well known that, in a lossy material, the electric field amplitude will decrease in the direction perpendicular to the interface. Therefore, in case a homogeneous plane wave is obliquely incident upon an interface between a lossless material and a lossy material, the refracted wave propagating through the lossy medium will be of the form

$$\vec{E}(\vec{r}, t) = \vec{E}_0 e^{i(\omega t - (\beta\hat{\beta} - i\alpha\hat{n})\vec{r})}, \quad (24)$$

where  $\hat{\beta}$  denotes the unit vector perpendicular to the planes of constant phase

**Fig. 2.6:** Schematic illustration of the definitions of the (real) angles  $\theta_i$  and  $\Psi_i$  for describing inhomogeneous plane waves.



and  $\hat{n}$  describes the interface normal unit vector, which is perpendicular to the planes of constant wave amplitude. While it has been claimed that the frequently used complex angle description is, in fact, equivalent to the phase and attenuation vector formalism [114, 115], Canning explicitly refuted this equivalency by pointing out discrepancies in the numerical results obtained via the two formalisms [112, 111, 113].

The more suited ansatz for deriving the reflection and refraction properties when lossy materials are involved is given by (harmonic, single-frequency) inhomogeneous plane waves, which take the general form

$$\vec{E}(\vec{r}, t) = \vec{E}_0 e^{i(\omega t - \vec{k}\vec{r})} = \vec{E}_0 e^{i(\omega t - (\vec{\beta} - i\vec{\alpha})\vec{r})} \quad (25)$$

with  $\vec{\beta}, \vec{\alpha} \in \mathbb{R}^3$ . This ansatz is the most general form of a plane wave. In case  $\vec{\beta}$  and  $\vec{\alpha}$  are not collinear (as in (24)), the planes of constant phase and the planes of constant amplitude do not coincide.

Following this ansatz based on harmonic inhomogeneous plane waves, Dupertuis *et al.* demonstrated that the conservation of energy is fulfilled at arbitrary material interfaces [116]. Further, generalized forms of Snell's law of refraction for absorbing (dielectric as well as conductive) media have been studied by various authors [114, 117–124] and can be expressed, for example, as

$$\beta_1 \cdot \sin \theta_1 = \beta_1 \cdot \sin \theta_{\text{refl}} = \beta_2 \cdot \sin \theta_2, \quad (26)$$

$$\alpha_1 \cdot \sin \Psi_1 = \alpha_1 \cdot \sin \Psi_{\text{refl}} = \alpha_2 \cdot \sin \Psi_2, \quad (27)$$

with  $\beta_i, \alpha_i, \theta_i, \Psi_i \in \mathbb{R}$ . Instead of a complex angle, this formalism introduces two real angles which define the directions of phase propagation and attenuation. Both angles  $\Psi_i$  and  $\theta_i$  are measured relative to the surface normal vector  $\hat{n}$

$$\cos \theta_i = \hat{\beta}_i \cdot \hat{n} \quad \cos \Psi_i = \hat{\alpha}_i \cdot \hat{n} \quad (28)$$

$\beta_i$  and  $\alpha_i$  are linked to the complex refractive indices or permittivities of the materials, which can be found by evaluating equation (13) for  $\vec{k} = \vec{\beta} - i\vec{\alpha}$ , which yields

$$\vec{k} \cdot \vec{k} = \vec{\beta}^2 - 2i\vec{\beta}\vec{\alpha} - \vec{\alpha}^2 = \omega^2 \mu_0 \mu_{\text{rel}} \epsilon_0 \epsilon_{\text{rel}} = \frac{\omega^2}{c^2} = \frac{\omega^2}{c_0^2} N^2 = \frac{\omega^2}{c_0^2} (\epsilon'_{\text{rel}} - i\epsilon''_{\text{rel}}) \quad (29)$$

$$\Rightarrow \vec{\beta}^2 - \vec{\alpha}^2 = \frac{\omega^2}{c_0^2} \epsilon'_{\text{rel}} \quad \wedge \quad 2\vec{\beta}\vec{\alpha} = \frac{\omega^2}{c_0^2} \epsilon''_{\text{rel}}. \quad (30)$$

It is worth noting that this formalism includes scenarios where despite the involved materials being lossless ( $\epsilon''_{\text{rel}} = 0$ ), a wave may exist which exhibits a nonzero attenuation vector  $\vec{\alpha}$ . In such a case,  $\vec{\beta}$  and  $\vec{\alpha}$  must be perpendicular in order to fulfill  $\vec{\beta} \cdot \vec{\alpha} = 0$ . By choosing  $\vec{\beta} = \beta_x \hat{x} + \beta_y \hat{y}$  and  $\vec{\alpha} = \alpha_z \hat{z}$ , with  $\alpha_z > 0$  and  $\beta_x^2 + \beta_y^2 > \alpha_z^2$  (due to the first relation in (30)), one finds

$$\vec{E}(\vec{r}, t) = \vec{E}_0 e^{i(\omega t - (\beta_x x + \beta_y y - \alpha_z z))} = \vec{E}_0 e^{i(\omega t - (\beta_x x + \beta_y y))} e^{-\alpha_z z}, \quad (31)$$

which describes an evanescent wave at an interface parallel to the xy-plane with an exponential decay of the amplitude normal to the xy-plane. At an interface between two lossless dielectrics, for example, such evanescent waves are formed in conjunction with TIR processes. Further information about the generalized Fresnel coefficients and related quantities such as the generalized polarization properties and the generalized Brewster angle under various circumstances involving lossy materials can be found, for example, in the following references: [111, 124–130]. Moreover, a discussion of generalizing Snell's law in the context of metasurfaces has recently been published by Rousseau and Felbacq [131].

For the sake of simplicity, the following section 2.3 mostly relies on interfaces between lossless dielectrics for illustrating the working principles of the various types of antireflective coatings.

## 2.3 Antireflective Coatings

After etching different glasses with sulfuric or nitric acid, Joseph von Fraunhofer ascertained that some glass surfaces, after polishing, exhibit a noticeable decrease in surface reflectance compared to the pristine glass surface. He further found that the same treatment can induce a beautiful vivid surface coloration on the etched surface [132]. Although Fraunhofer's discovery predated J. Clerk Maxwell's famous publication [133] by almost 50 years, he still had a remarkably accurate

hunch concerning the origins of these effects, which becomes obvious from the following statement of his, which can be found in his collected works published by E. Lommel [132]. In a 1819 appendix to his 1817 article *Versuche über die Ursachen des Anlaufens und Mattwerdens des Glases und die Mittel, denselben zu vorzukommen*, Fraunhofer stated the following:

English translation [105]	Original quote in German [132]
<p><i>'Colors on reflection always occur with all transparent media if they are very thin. (...) Since the colors, in glasses which have been colored through tarnishing, alter themselves if the inclination of the incident light becomes greater or smaller, there is no doubt that these colors are quite of the same nature as those of soap bubbles, and those which occur through the contact of two polished flat glass surfaces, or generally as thin transparent films of material. Thus, there must be on the surface of tarnished glass that shows colors, a thin layer of glass that is different in refractive power from the underlying. Such a situation must occur if a component is partly removed from the surface of the glass or if a component of the glass combines at the surface with a related material into a new transparent product.'</i></p>	<p><i>'Farben durch Reflexion entstehen allgemein bei allen durchsichtigen Mitteln, wenn sie im hohen Grade dünn sind. (...) Da bei in Farben angelaufenem Glase die Farbe sich ändert, wenn der Neigungswinkel des auffallenden Lichtes grösser oder kleiner wird, so ist es keinem Zweifel unterworfen, dass diese Farben ganz von derselben Natur sind, wie die der Seifenblasen, und die, welche durch Berührung von zwei polirten ebenen Glasflächen entstehen; oder überhaupt wie die dünner durchsichtiger Blättchen. Es muss daher bei angelaufenem Glas, welches Farben zeigt, an der Oberfläche desselben, eine dünne Lage eines Glases sein, welches im Brechungsvermögen von dem des tieferliegenden verschieden ist. Eine solche Lage muss entstehen, wenn dem Glase an der Oberfläche ein Bestandtheil zum Theil entzogen wird, oder wenn ein Bestandtheil des Glases sich mit einer ihm verwandten Materie an der Oberfläche zu einem neuen durchsichtigen Producte verbindet.'</i></p>

In 1886, Lord Rayleigh experimentally studied the reflection of light from various surfaces at close to normal incidence and compared his findings to the theoretical predictions deduced from Fresnel's equations [134]. Based on his observation that only freshly polished glass surfaces reproduce Fresnel's reflection law and older, tarnished samples (even when there is no tarnish visible) actually reflect noticeably less light compared to what Fresnel's equations would predict for an air-glass interface, Rayleigh proposed the explanation that a layer of a material with a

refractive index different from the underlying glass must have formed on the surface of the tarnished samples. Roughly two decades later, Taylor invented the first method for purposefully producing the antireflective tarnish layer on glass by means of chemical etching, paving the way towards the fabrication of highly transparent optical lenses [135]. Further milestones in the development of optical coatings were compiled in reference [136].

Nowadays, antireflective coatings based on several different optical effects have been developed and are extensively used throughout various fields of technology. Depending on the specific application, the preferred strategy for reducing reflection might vary. For example, antireflective coatings for eyeglasses need to be non-scattering since any redistribution of propagation directions would deteriorate the visibility through the coated glass. Similarly, the antireflective coatings applied on optical elements such as lenses for cameras, microscopes, telescopes, and binoculars need to be designed non-scattering as well. Concerning the cover glasses atop solar panels, on the other hand, there is no such general restriction since the only purpose of an antireflective coating in PV is to increase the device efficiency. In fact, for solar cells, especially for devices that suffer from incomplete absorption of light within the active material, it can even be of great advantage to exploit the scattering properties of some antireflection coatings in order to improve light-trapping or to enhance the absorption probability through an increased mean pathlength of the in-coupled photons within the active layer. Since solar cells are exposed to unpolarized light with a broad range of wavelengths and incidence angles, efficient antireflective coatings for PV devices are required to combine polarization insensitivity with broadband and omnidirectional light in-coupling properties.

It should be noted that, in many cases, antireflective coatings are utilized not for enhancing the performance of a device by increasing the light transmission through some barrier, but rather for diminishing the unwanted reflections from a smooth surface (anti-glare effect), as is the case for eyeglasses.

After the introduction of the various concepts for achieving antireflection in the following subsections 2.3.1-2.3.6, the next chapter 3 provides a survey of various antireflective (as well as structural-color-producing) surfaces found on plants and animals

### 2.3.1 Rayleigh's Film

In the following, a planar interface between two (semi-infinite) isotropic, non-magnetic and lossless media is considered. Due to the lack of absorption in both materials, their respective refractive indices  $n_1$  and  $n_2$  can be assumed as real-valued. The most basic way to reduce reflectance at the material interface relies on applying an optically thick (no interference effects) intermediate layer made of another isotropic, non-magnetic, and lossless material (refractive index  $n_{\text{ARC}}$ ). The addition of such a thick-film coating replaces the single interface between material 1 and material 2 with two interfaces (from material 1 to the antireflective coating and from the antireflective coating to material 2). If the refractive index of the coating  $n_{\text{ARC}}$  is chosen properly, the total transmittance through the layered system can be increased despite the additional interface that is generated through the addition of the intermediate layer. The total reflectance  $R_{\text{tot}}$  and transmittance  $T_{\text{tot}}$  of the planar layer system can be derived by adding up an infinite series of contributions caused by light being reflected back and forth within the antireflective layer, as schematically illustrated in Fig. 2.7. For the total reflectance  $R_{\text{tot}}$  one finds

$$\begin{aligned} R_{\text{tot}} &= R_{1 \rightarrow \text{ARC}} + T_{1 \rightarrow \text{ARC}} R_{\text{ARC} \rightarrow 2} T_{\text{ARC} \rightarrow 1} + T_{1 \rightarrow \text{ARC}} R_{\text{ARC} \rightarrow 2} R_{\text{ARC} \rightarrow 2} R_{\text{ARC} \rightarrow 1} T_{\text{ARC} \rightarrow 1} + \dots \\ &= R_{1 \rightarrow \text{ARC}} + T_{1 \rightarrow \text{ARC}} R_{\text{ARC} \rightarrow 2} T_{\text{ARC} \rightarrow 1} \cdot \sum_{m=0}^{\infty} (R_{\text{ARC} \rightarrow 2} R_{\text{ARC} \rightarrow 1})^m \\ &\Rightarrow R_{\text{tot}} = R_{1 \rightarrow \text{ARC}} + T_{1 \rightarrow \text{ARC}} R_{\text{ARC} \rightarrow 2} T_{\text{ARC} \rightarrow 1} \cdot \frac{1}{1 - R_{\text{ARC} \rightarrow 2} R_{\text{ARC} \rightarrow 1}}. \end{aligned} \quad (32)$$

Using  $T_{1 \rightarrow \text{ARC}} = T_{\text{ARC} \rightarrow 1} = T_1$ ,  $T_{2 \rightarrow \text{ARC}} = T_{\text{ARC} \rightarrow 2} = T_2$ ,  $R_{1 \rightarrow \text{ARC}} = R_{\text{ARC} \rightarrow 1} = R_1$ , and  $R_{2 \rightarrow \text{ARC}} = R_{\text{ARC} \rightarrow 2} = R_2$  (see equation (20)), the reflectance can be written as

$$R_{\text{tot}} = R_1 + \frac{T_1^2 R_2}{1 - R_1 R_2}. \quad (33)$$

Analogously, adding up the infinite series of contributions to the total transmittance yields

$$\begin{aligned} T_{\text{tot}} &= T_{1 \rightarrow \text{ARC}} T_{\text{ARC} \rightarrow 2} + T_{1 \rightarrow \text{ARC}} R_{\text{ARC} \rightarrow 2} R_{\text{ARC} \rightarrow 1} T_{\text{ARC} \rightarrow 2} + \dots \\ &= T_{1 \rightarrow \text{ARC}} T_{\text{ARC} \rightarrow 2} \cdot \sum_{m=0}^{\infty} (R_{\text{ARC} \rightarrow 2} R_{\text{ARC} \rightarrow 1})^m = \frac{T_{1 \rightarrow \text{ARC}} T_{\text{ARC} \rightarrow 2}}{1 - R_{\text{ARC} \rightarrow 2} R_{\text{ARC} \rightarrow 1}} \\ &\Rightarrow T_{\text{tot}} = \frac{T_1 T_2}{1 - R_1 R_2}. \end{aligned} \quad (34)$$

Following equation (20), the power transmittances and reflectances for two lossless dielectrics at normal incidence are given by

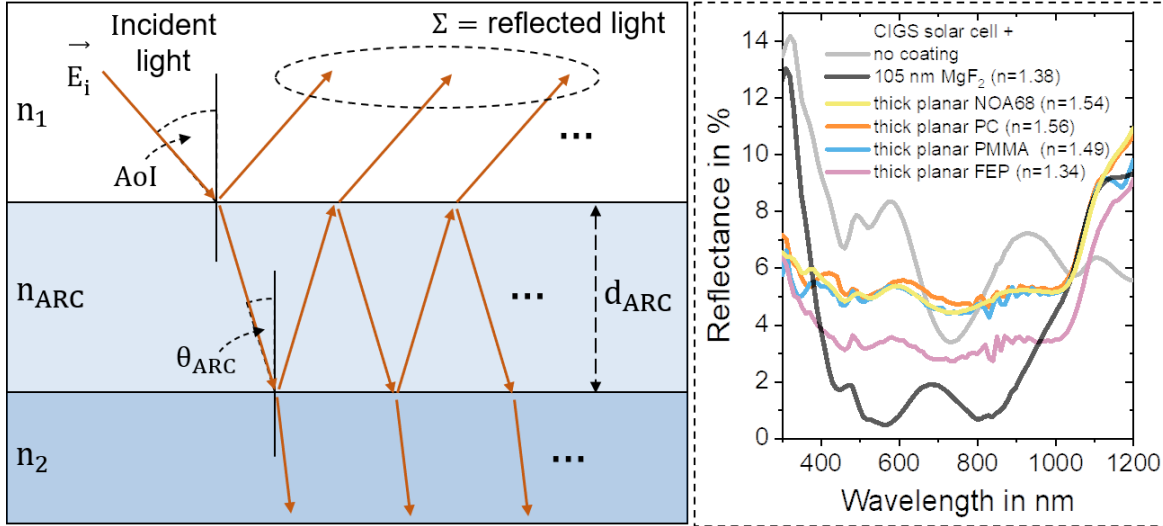


**Fig. 2.7:** Working principle of single-layer antireflective coatings. Left: Schematic depiction of a single-layer antireflective coating with a refractive index  $n_1 < n_{ARC} < n_2$ . If  $d_{ARC}$  is much larger than the wavelength of the incident light, no coherent superposition can take place, and the coating acts as an intermediate layer (Rayleigh's film). If, on the other hand, the antireflective coating is sufficiently thin, destructive interference of the reflected light waves can be exploited to reach zero reflectance for a single wavelength and AoI. Right: Measured reflectance spectra of CIGS solar cells with optically thick planar cover layers based on four different polymers (NOA68, PMMA, PC, FEP), together with the reflectance spectra of an uncoated device and one with an  $MgF_2$  thin-film antireflective coating.

$$R_{1 \rightarrow 2} = \left| \frac{n_1 - n_2}{n_1 + n_2} \right|^2, \quad T_{1 \rightarrow 2} = \frac{n_2}{n_1} \left| \frac{2n_1}{n_1 + n_2} \right|^2. \quad (35)$$

Plugging in these relations into (34) leads to a transmittance through the thick-film layered system of

$$T_{tot} = \frac{4n_1n_2}{n_1 + n_2} \cdot \frac{n_{ARC}}{n_1n_2 + n_{ARC}^2}. \quad (36)$$

By evaluating  $dT_{tot}/dn_{ARC} = 0$ , it can be straightforwardly deduced that a maximum transmittance – and therefore minimum reflectance – is encountered if the refractive index  $n_{ARC}$  of the intermediate layer satisfies

$$n_{ARC} = (n_1 \cdot n_2)^{1/2}, \quad (37)$$

resulting in a maximum transmittance of

$$T_{tot} \left( n_{ARC} = (n_1n_2)^{1/2} \right) = \frac{2(n_1n_2)^{1/2}}{n_1 + n_2}. \quad (38)$$

For the example of an air-glass-interface with  $n_1 = 1$  and  $n_2 = 1.5$ , which exhibits 4% of reflectance for normal light incidence, an intermediate layer with optimum

refractive index reduces the reflectance to  $R \approx 2\%$ . Since, for the case of Rayleigh's film, the coating thickness  $d_{\text{ARC}}$  exceeds the coherence length of the incident light, the quality of the antireflection effect is defined only by  $n_{\text{ARC}}$ , while changes in coating thickness  $d_{\text{ARC}}$  do not have any influence on the optical properties of the layered system.

Based on this principle of incrementally partitioning the refractive index contrast between the two materials into multiple steps of reduced refractive index contrast ('index-matching'), the reflectance could, although impractical, be further reduced by stacking multiple such intermediate thick-film coatings with successively increasing refractive indices between  $n_1$  to  $n_2$  at the respective interface. However, in practice, index-matching-based antireflection is usually achieved via layers with a continuously varying refractive index (see also subsections 2.3.3 and 2.3.4).

Examples for the reduction of reflectance through the addition of an optically thick and planar intermediate layer are provided in Fig. 2.7 (which is comprised of part of the data also shown in Fig. 5.12 and Fig. 8.2) for NOA68, poly(methyl methacrylate) (PMMA), polycarbonate (PC), and fluorinated ethylene propylene (FEP), on unencapsulated CIGS solar cells.

## 2.3.2 Thin-Film-Interference-Based Antireflection

### 2.3.2.1 Single-Layer (Quarter-Wavelength) Antireflective Coatings

In the following, the angle of incidence  $\theta_1$  is renamed  $\theta_1 \rightarrow \text{AoI}$ . In contrast to the case of optically thick coatings as discussed in the previous subsection 2.3.1, the calculation of the reflectance and transmittance of a thin-film coating needs to incorporate the coherent superposition of electromagnetic waves within the layer stack. In such a scenario, reflectance  $R$  and transmittance  $T$  can not be directly constructed from the reflectance and transmittance properties at each individual interface. However, interference effects can be properly factored in by first deriving Fresnel reflection and transmission coefficients  $r_{\text{tot}}$  and  $t_{\text{tot}}$  for the entire thin-film layer stack. Instead of power ratios, these coefficients describe the E-field amplitude ratios of the transmitted/reflected partial wave and the incident E-field amplitude. Adding up the infinite series of contributions to the total reflection coefficient  $r_{\text{tot}}$  yields (in contrast to adding up power reflectance and transmittance as shown in subsection 2.3.1, the derivation of amplitude reflection and transmission coefficients relies on a coherent summation of partial waves and, therefore, the phase change caused by the additional back and forth propagation within the antireflective layer needs to be considered)

$$\begin{aligned}
 r_{\text{tot}} &= r_{1 \rightarrow \text{ARC}} + t_{1 \rightarrow \text{ARC}} r_{\text{ARC} \rightarrow 2} t_{\text{ARC} \rightarrow 1} e^{i2\chi} + t_{1 \rightarrow \text{ARC}} r_{\text{ARC} \rightarrow 2} r_{\text{ARC} \rightarrow 1} t_{\text{ARC} \rightarrow 1} e^{i4\chi} + \dots \\
 &= r_{1 \rightarrow \text{ARC}} + t_{1 \rightarrow \text{ARC}} r_{\text{ARC} \rightarrow 2} t_{\text{ARC} \rightarrow 1} e^{i2\chi} \cdot \sum_{m=0}^{\infty} (r_{\text{ARC} \rightarrow 2} r_{\text{ARC} \rightarrow 1} e^{i2\chi})^m \\
 &\Rightarrow r_{\text{tot}} = r_{1 \rightarrow \text{ARC}} + t_{1 \rightarrow \text{ARC}} r_{\text{ARC} \rightarrow 2} t_{\text{ARC} \rightarrow 1} e^{i2\chi} \cdot \frac{1}{1 - r_{\text{ARC} \rightarrow 2} r_{\text{ARC} \rightarrow 1} e^{i2\chi}}, \quad (39)
 \end{aligned}$$

where  $\chi = 2\pi/\lambda_0 \cdot n_{\text{ARC}} d_{\text{ARC}} \cos \theta_{\text{ARC}}$ . The amplitude transmission coefficient is found analogously (similar to the power transmittance shown in subsection 2.3.1 with the addition of appropriate phase factors). By using the relations introduced in equation (19), as well as  $r_{1 \rightarrow \text{ARC}} = -r_{\text{ARC} \rightarrow 1}$  and  $t_{1 \rightarrow \text{ARC}} = n_{\text{ARC}}/n_1 \cdot t_{\text{ARC} \rightarrow 1}$ , the reflection coefficient  $r_{\text{tot}}$  can be simplified further. For s-polarization (TE), the resulting amplitude coefficients  $r_{\text{tot}}$  and  $t_{\text{tot}}$  can be written as [103]

$$r_{\text{tot}} = \frac{r_{1 \rightarrow \text{ARC}} + r_{\text{ARC} \rightarrow 2} e^{i2\chi}}{1 + r_{1 \rightarrow \text{ARC}} r_{\text{ARC} \rightarrow 2} e^{i2\chi}} \quad \text{and} \quad t_{\text{tot}} = \frac{t_{1 \rightarrow \text{ARC}} t_{\text{ARC} \rightarrow 2} e^{i2\chi}}{1 + r_{1 \rightarrow \text{ARC}} r_{\text{ARC} \rightarrow 2} e^{i2\chi}}. \quad (40)$$

Furthermore, the reflectance  $R_{\text{tot}} = |r_{\text{tot}}|^2$  and transmittance  $T_{\text{tot}} = \frac{n_{\text{ARC}} \cos \theta_{\text{ARC}}}{n_1 \cos \text{AoI}} |t_{\text{tot}}|^2$  can be expressed as

$$R_{\text{tot}} = \frac{r_{1 \rightarrow \text{ARC}}^2 + r_{\text{ARC} \rightarrow 2}^2 + 2r_{1 \rightarrow \text{ARC}} r_{\text{ARC} \rightarrow 2} \cos(2\chi)}{1 + r_{1 \rightarrow \text{ARC}}^2 r_{\text{ARC} \rightarrow 2}^2 + 2r_{1 \rightarrow \text{ARC}} r_{\text{ARC} \rightarrow 2} \cos(2\chi)} \quad (41)$$

$$T_{\text{tot}} = \frac{n_{\text{ARC}} \cos \theta_{\text{ARC}}}{n_1 \cos \text{AoI}} \frac{t_{1 \rightarrow \text{ARC}}^2 t_{\text{ARC} \rightarrow 2}^2}{1 + r_{1 \rightarrow \text{ARC}}^2 r_{\text{ARC} \rightarrow 2}^2 + 2r_{1 \rightarrow \text{ARC}} r_{\text{ARC} \rightarrow 2} \cos(2\chi)}. \quad (42)$$

The Fresnel coefficients for the isolated interfaces can be directly adopted from equations (17) and (18). For s-polarized light at the first interface ( $1 \rightarrow \text{ARC}$ ), for example, the Fresnel coefficients yield

$$r_{1 \rightarrow \text{ARC}} = \frac{n_1 \cos \text{AoI} - n_{\text{ARC}} \cos \theta_{\text{ARC}}}{n_1 \cos \text{AoI} + n_{\text{ARC}} \cos \theta_{\text{ARC}}}, \quad (43)$$

$$t_{1 \rightarrow \text{ARC}} = \frac{2n_1 \cos \text{AoI}}{n_1 \cos \text{AoI} + n_{\text{ARC}} \cos \theta_{\text{ARC}}}. \quad (44)$$

Subsequently, a condition for a local extremum can be easily deduced from the (vanishing) derivative of the total reflectance with respect to the optical thickness via

$$\frac{dR_{\text{tot}}}{d(n_{\text{ARC}} d_{\text{ARC}})} = 0 \Leftrightarrow \sin(2\chi) = 0. \quad (45)$$

For the sine-function to vanish, its argument  $2\chi = 4\pi/\lambda_0 \cdot n_{\text{ARC}} d_{\text{ARC}} \cos \theta_{\text{ARC}}$  must satisfy

$$\frac{4\pi}{\lambda_0} n_{\text{ARC}} d_{\text{ARC}} \cos \theta_{\text{ARC}} = m \cdot \pi \Leftrightarrow n_{\text{ARC}} d_{\text{ARC}} \cos \theta_{\text{ARC}} = m \cdot \frac{\lambda_0}{4}, \quad (46)$$

where  $m \in \mathbb{N}$ . For even values of  $m$ , which corresponds to optical thicknesses of

$$n_{\text{ARC}}d_{\text{ARC}} = \lambda_0/2 \cos \theta_{\text{ARC}}, \lambda_0/\cos \theta_{\text{ARC}}, 3\lambda_0/2 \cos \theta_{\text{ARC}}, \dots, \quad (47)$$

the total reflectance yields

$$R_{\text{tot}} = \left( \frac{r_{1 \rightarrow \text{ARC}} + r_{\text{ARC} \rightarrow 2}}{1 + r_{1 \rightarrow \text{ARC}}r_{\text{ARC} \rightarrow 2}} \right)^2, \quad (48)$$

which, for normal incidence of light ( $\cos \text{AoI} = \cos \theta_{\text{ARC}} = 1$ ), can be further simplified to

$$R_{\text{tot}} = \left( \frac{n_1 - n_2}{n_1 + n_2} \right)^2. \quad (49)$$

For these specific optical thicknesses of the antireflective coating (integer multiples of  $\lambda_0/2$ ), the total reflectance/transmittance does not depend on  $n_{\text{ARC}}$  and is identical to the scenario without the thin-film coating. The more interesting case with respect to antireflection, however, is found for odd values of  $m$ . For the corresponding optical thicknesses of

$$n_{\text{ARC}}d_{\text{ARC}} = \lambda_0/4 \cos \theta_{\text{ARC}}, 3\lambda_0/4 \cos \theta_{\text{ARC}}, 5\lambda_0/4 \cos \theta_{\text{ARC}}, \dots, \quad (50)$$

the total reflectance can be expressed as

$$R_{\text{tot}} = \left( \frac{r_{1 \rightarrow \text{ARC}} - r_{\text{ARC} \rightarrow 2}}{1 - r_{1 \rightarrow \text{ARC}}r_{\text{ARC} \rightarrow 2}} \right)^2, \quad (51)$$

and, for  $\text{AoI} = 0^\circ$ , this relation further simplifies to

$$R_{\text{tot}} = \left( \frac{n_1 n_2 - n_{\text{ARC}}^2}{n_1 n_2 + n_{\text{ARC}}^2} \right)^2. \quad (52)$$

From this relation, it becomes obvious that, by means of a thin-film-interference-based antireflective coating, the reflectance can be reduced to  $R_{\text{tot}} = 0$  if the refractive index of the antireflective coating is chosen as the geometric mean of the refractive indices of the two adjacent materials, hence

$$n_{\text{ARC}} = (n_1 \cdot n_2)^{1/2}. \quad (53)$$

For  $\text{AoI} = 0^\circ$ , the abovementioned condition (46), which defines the optimum coating thickness for minimizing reflectance, simplifies to

$$n_{\text{ARC}} d_{\text{ARC}} = m \cdot \frac{\lambda_0}{4}, \quad (54)$$

which is why such thin-film antireflective layers are commonly called quarter-wavelength or  $\lambda/4$ -antireflective coatings. Due to the enhanced pathlength within the antireflective coating at oblique incidence of light through refraction, the optimum coating thickness for minimizing reflectance depends on the AoI. Using (the square of) Snell's law of refraction

$$\begin{aligned} n_1^2 \sin^2 \text{AoI} = n_{\text{ARC}}^2 \sin^2 \theta_{\text{ARC}} &\Leftrightarrow n_1^2 \sin^2 \text{AoI} = n_{\text{ARC}}^2 (1 - \cos^2 \theta_{\text{ARC}}) \\ &\Leftrightarrow n_{\text{ARC}}^2 \cos^2 \theta_{\text{ARC}} = n_{\text{ARC}}^2 - n_1^2 \sin^2 \text{AoI}, \end{aligned} \quad (55)$$

$\theta_{\text{ARC}}$  can be eliminated from equation (46), yielding an expression that explicitly contains the AoI, which reads

$$(n_{\text{ARC}}^2 - n_1^2 \sin^2 \text{AoI})^{1/2} \cdot d_{\text{ARC}} = m \cdot \frac{\lambda_0}{4}. \quad (56)$$

$\lambda/4$ -antireflective coatings can only be optimized for a single wavelength and a single AoI. For these specific conditions, the reflectance can be effectively reduced. However, broadband and omnidirectional antireflection properties, which would be required for effectively minimizing optical losses in (fixed) PV installations, can not be achieved by relying solely on a single-layer antireflective coating. For an adequate use of single-layer thin-film antireflective coating for solar panels, the coating thickness should therefore be optimized via minimizing reflection losses with respect to the terrestrial solar spectrum and the varying AoI (for a fixed installation) over the course of a day, which can be achieved via computational methods [137].

A widely used material for the fabrication of destructive-interference-based antireflective layers is  $\text{MgF}_2$ , which has a refractive index of  $n_{\text{MgF}_2} \approx 1.38$  [138] at a wavelength of 588 nm. In the context of this thesis,  $\text{MgF}_2$  antireflective coatings were used atop of unencapsulated CIGS thin-film solar cells (see chapter 8), which have an uppermost layer made of Al:ZnO with a refractive index of  $n_{\text{Al:ZnO}} = 1.828$  [139]. The optimum refractive index for a single-layer antireflective coating is therefore given by  $n_{\text{ARC}} = (n_{\text{air}} n_{\text{Al:ZnO}})^{1/2} = (1 \cdot 1.828)^{1/2} = 1.352$ , a value close to  $n_{\text{MgF}_2}$ . Measured reflectance spectra of unencapsulated CIGS solar cells with and without an  $\text{MgF}_2$  antireflective coating are included in Fig. 2.7.

For minimizing reflection losses at an air-glass interface, however, the refractive index of  $\text{MgF}_2$  is too high, since  $n_{\text{ARC}} = (1 \cdot 1.5)^{1/2} \approx 1.22$ . Refractive indices below the one of  $\text{MgF}_2$ , which is the lowest value out of all the existing inorganic and transparent materials [140], can be achieved via composite materials. The effective

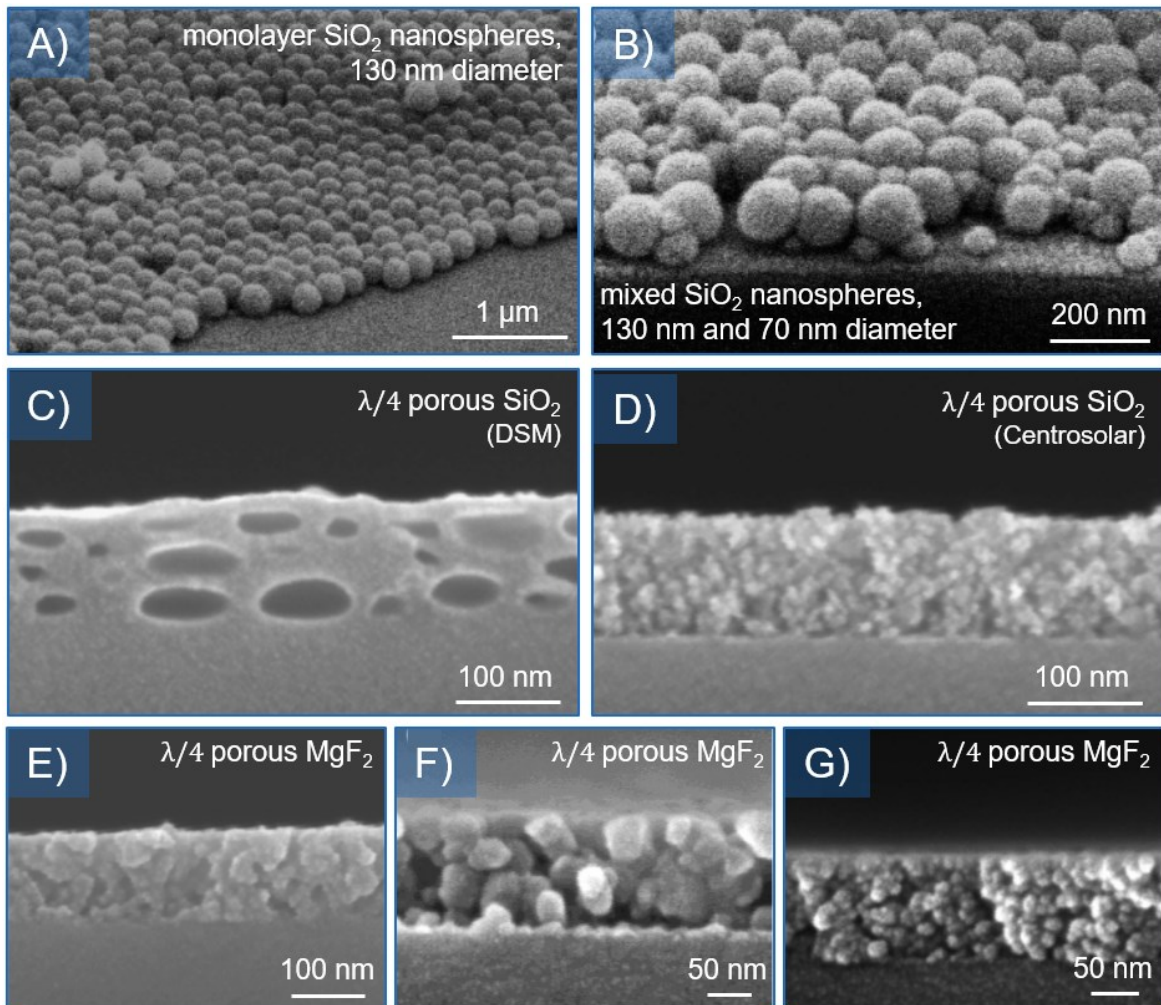


**Fig. 2.8:** SEM micrographs of various thin-film antireflective coatings based on (A, B) silica nanoparticles, porous silica layers (C, D), and based on porous  $\text{MgF}_2$  (E, F, G). The porous silica coatings in C) and D) are commercially available. A) and B) were adapted with permission from reference [141], © 2005 American Chemical Society. C), D), and E) were adapted with permission from reference [142], © 2017 Springer Science Business Media New York. F) and G) were adapted with permission from reference [143], © 2015 Springer Science+Business Media New York.

optical properties of such materials can be tuned by varying the volume filling fraction of the components of the composite. Following this approach, materials with (tunable) refractive indices below  $n_{\text{MgF}_2}$  can be engineered by incorporating subwavelength-scale air voids into a transparent material. By increasing the amount of air in such a porous material, the effective refractive index of the composite can be lowered.

The effective optical properties of such composite materials can be calculated by means of effective medium theory. For a 3D composite material with two constituents, a background medium, and spherical scatterers, the effective optical

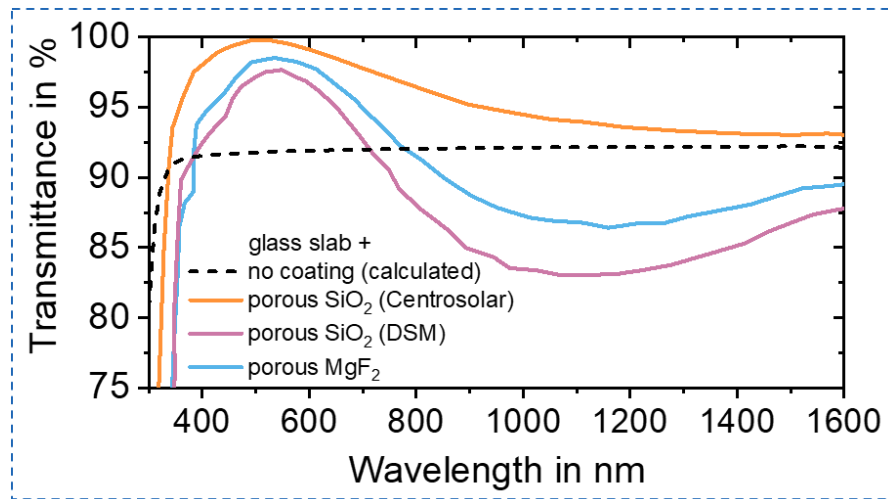


**Fig. 2.9:** Light transmission spectra through planar glass (with  $n = 1.52$ ) coated on both sides with different thin-film antireflective layers based on porous silica and porous  $\text{MgF}_2$ . Regarding porous silica, two commercially available products were utilized. Besides the calculated reference curve, all the data presented in this figure was originally published in reference [142] and was extracted from the original figure with the help of an online tool [144]. © 2017 Springer Science Business Media New York.

properties can be calculated with a so-called mixing formula, such as the

$$\begin{array}{ll}
 \text{Rayleigh mixing formula [145]} & \text{Bruggemann mixing [146]} \\
 \frac{\epsilon_{\text{eff}} - \epsilon_1}{\epsilon_{\text{eff}} + 2\epsilon_1} = f \frac{\epsilon_2 - \epsilon_1}{\epsilon_2 + 2\epsilon_1} & (1 - f) \frac{\epsilon_1 - \epsilon_{\text{eff}}}{\epsilon_1 + \epsilon_{\text{eff}}} + f \frac{\epsilon_2 - \epsilon_{\text{eff}}}{\epsilon_2 + \epsilon_{\text{eff}}} = 0 \quad (57)
 \end{array}$$

where  $\epsilon_1$  and  $\epsilon_2$  denote the relative permittivities of the two constituent materials of the composite,  $\epsilon_{\text{eff}}$  denotes the resulting effective permittivity, and  $f$  denotes the volume fraction occupied by the scatterers.

In the PV industry, a widely used material for thin-film antireflection on the panels' cover glasses is nanoporous silica [147–149]. In 1992, Thomas demonstrated that, by varying the morphology and density of the air inclusions within the porous silica material, the effective refractive indices of such nanoparticle-based composites could be tuned in the range between 1.44 and 1.22 [150]. In more recent years, porous silica layers with even lower refractive indices have been fabricated [151–154]. More detailed explanations concerning the concept of effective refractive indices in subwavelength-textured materials are provided in subsections 2.3.3 and 2.3.4. Scanning electron microscopy (SEM) micrographs of two commercial quarter-wavelength coatings based on porous silica are displayed in Fig. 2.8, together with SEM images of alternative silica-based antireflective coatings comprised of (densely packed) nanoparticle layers. For the two commercial coatings (by DSM and by Centrosolar) together with a porous  $\text{MgF}_2$

layer, their transmittance spectra through (both sides of) a coated glass are shown in Fig. 2.9. Next to coating the cover glasses of solar panels, thin-film antireflective layers can also be applied underneath the encapsulation layer in order to minimize reflection losses between glass (and the respective adhesive layer) and, for example, a (textured) Si solar cell underneath [155, 156].

It should be noted that, besides porous silica, efficient antireflective coatings made of low-refractive-index (porous)  $\text{MgF}_2$  films on glass have also been demonstrated (by means of sol-gel methods) [143]. Cross-sectional SEM micrographs of quarter-wavelength coatings based on porous  $\text{MgF}_2$  are displayed in Fig. 2.8 E), F), and G). In a 2018 study, Chandra Sekhar Reddy *et al.* demonstrated porous  $\text{MgF}_2$  films with refractive indices as low as 1.21 by relying on hollow  $\text{MgF}_2$  nanoparticles [157]. Bao *et al.* even reported a tunable refractive index of 1.10 – 1.35 for  $\text{MgF}_2$  coatings based on hollow nano rod-like nanoparticles [140].

It should further be pointed out that for a thin-film antireflective layer on top of a device like a CIGS solar cell (as in Fig. 2.7), which itself is comprised of a thin-film layer stack (instead of a simple thick planar sheet of glass), calculating the reflection losses for a coated device generally requires the use of optical simulations (in this case the transfer-matrix method, see subsection 2.5.1) for the optimization of the refractive index and thickness of the coating in terms of maximizing light absorption in the active layer of the device. The same can be stated with respect to Multilayer antireflection coatings based on thin-film interference.

### 2.3.2.2 Double-Layer Antireflective Coatings

While single-layer antireflective coatings can induce zero reflectance in a narrow spectral region around a single wavelength, the combination of two quarter-wavelength antireflective coatings with refractive indices  $n_{\text{ARC1}}$  and  $n_{\text{ARC2}}$  to a double-layer system can improve the spectral stability of the antireflection effect.

The reflectance of the  $\lambda/4$   $\lambda/4$  antireflective coating at normal incidence is given by [158–161]

$$R_{\text{tot}} = \left| \frac{n_{\text{ARC2}}^2 n_1 - n_2 n_{\text{ARC1}}^2}{n_{\text{ARC2}}^2 n_1 + n_2 n_{\text{ARC1}}^2} \right|^2. \quad (58)$$

By choosing the refractive indices as

$$n_{\text{ARC1}}^2 = n_1^2 n_2 \quad n_{\text{ARC2}}^2 = n_1 n_2^2 \quad (59)$$

which is equivalent to

$$n_{\text{ARC1}}/n_{\text{ARC2}} = (n_1/n_2)^{1/2} \quad n_{\text{ARC1}}n_{\text{ARC2}} = (n_1n_2)^{3/2}. \quad (60)$$

$R_{\text{tot}} = 0$  is achieved at a particular wavelength. Interestingly, this configuration implies  $n_1 < n_{\text{ARC1}} < n_2 < n_{\text{ARC2}}$  which means that the refractive index of the ‘inner’ layer of the antireflection coating is actually larger than the refractive index of the substrate material.

The spectral tolerance of the antireflection effect induced by a  $\lambda/4 \lambda/4$  coating is noticeably improved compared to the single-layer configuration. However, an effective broadband reduction of reflectance can not be reached. The reflectance spectra of  $\lambda/4 \lambda/4$  coatings are often described as V-shaped [159].

Next to combining two quarter-wavelength layers, a combination of quarter-wavelength and half-wavelength (which might also be interpreted as a  $\lambda/4 \lambda/4 \lambda/4$  triple-layer) coatings can also be fabricated, yielding W-shaped reflectance spectra [162]. Moreover, double-layer antireflective coatings which do not follow the common  $\lambda/4 \lambda/4$  and  $\lambda/4 \lambda/2$  layer thickness configurations can also be designed [163].

Double-layer antireflective coatings have been fabricated based on numerous materials. For example, Lin *et al.* combined two layers of SiO<sub>2</sub>-TiO<sub>2</sub> hybrid films, which can be fabricated with refractive indices between 1.18 and 1.53 by varying the TiO<sub>2</sub> weight ratio from 0 to 1, into a SiO<sub>2</sub>-TiO<sub>2</sub>/SiO<sub>2</sub>-TiO<sub>2</sub> double-layer antireflective coating for solar glass, increasing the transmittance from 91.6% (uncoated glass) to 98.8% [164]. By combining porous MgF<sub>2</sub> with a refractive index of 1.1 and porous SiO<sub>2</sub> on glass with a refractive index of 1.34, Bao *et al.* demonstrated a double-layer antireflective coating for glass, achieving an average transmittance of 99.1% in the spectral range of 400 nm – 1400 nm [140]. Jung *et al.* applied TiO<sub>2</sub>/Al<sub>2</sub>O<sub>3</sub> double-layer antireflective coatings directly on microtextured Si solar cells (random micro-pyramids) and thereby reduced the average surface reflectance at normal incidence in the spectral range between 400 nm and 1000 nm from 28.5% (pristine Si wafer) and 11.85% (textured Si) to 4.98% (textured Si + TiO<sub>2</sub>/Al<sub>2</sub>O<sub>3</sub>) [165]. A comparison of the reflectance spectra of a single-layer TiO<sub>2</sub> and double-layer SiO<sub>2</sub>/TiO<sub>2</sub> (and a SiO<sub>2</sub>/SiO<sub>2</sub>-TiO<sub>2</sub>/TiO<sub>2</sub> triple-layer)  $\lambda/4$  antireflective coating on Si solar cells is depicted in Fig. 2.10.

Next to their use on top of unencapsulated Si solar cells or as a coating for solar glass, double-layer antireflective coatings (with appropriate refractive indices) have also been used to suppress reflections at the glass-Si interface (including an adhesive layer) in encapsulated Si solar cells. Both the cover glass and adhesive material usually exhibit refractive indices close to 1.5. Therefore, an efficient

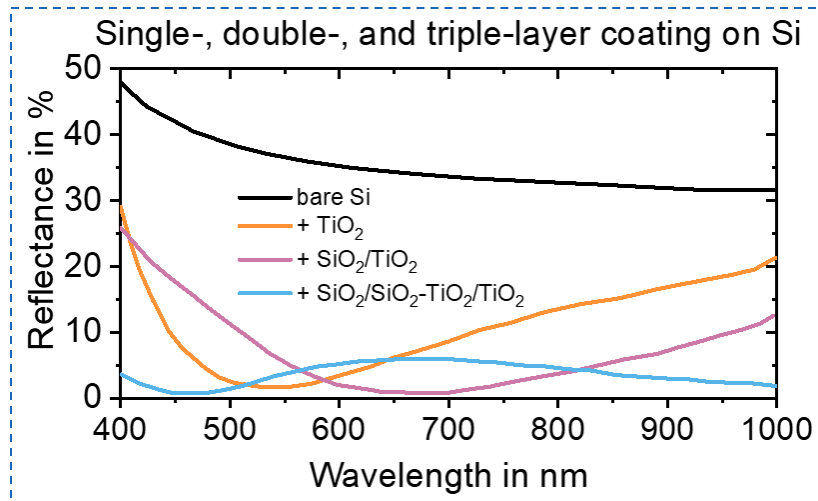


**Fig. 2.10:** Comparison of the reflectance spectra a single-layer  $\text{TiO}_2$ , double-layer  $\text{SiO}_2/\text{TiO}_2$ , and a  $\text{SiO}_2/\text{SiO}_2\text{-TiO}_2/\text{TiO}_2$  triple-layer antireflective coating on Si solar cells ( $n_{\text{TiO}_2} = 2.2$ ,  $n_{\text{SiO}_2} = 1.4$ ,  $n_{\text{SiO}_2\text{-TiO}_2} = 1.8$ ,  $n_{\text{Si}} = 3.4$ ). All data presented in this figure was originally published in reference [166] and was extracted from the original figures with the help of an online tool [144]. © 2006 Elsevier B.V. All Rights Reserved.

suppression of reflection losses at such an interface requires rather high refractive indices, which is usually only fulfilled by materials with strong absorption at short wavelengths [161]. Richards *et al.* demonstrated such a configuration with a double-layer antireflection coating between glass and Si based on  $\text{TiO}_2$  films with refractive indices 1.73 – 2.63 [167]. A similar configuration was demonstrated by Du *et al.* by means of (single- and) double-layer  $\text{SiN}_x\text{:H}$  antireflective coatings between cover glass and Si solar cell [155].

### 2.3.2.3 Triple-Layer Antireflective Coatings

With triple-layer coatings, reflectance can be reduced over a broader spectral range compared to single- or double-layer systems. The conditions for zero reflectance in a  $\lambda/4 \lambda/4 \lambda/4$  coating configurations can be found, for example, in references [168, 169]. With a three-layer system comprised of a  $\lambda/4$  quarter-wavelength low index top layer  $n_{\text{ARC1}}$ , followed by a  $\lambda/2$  coating of refractive index  $n_{\text{ARC2}} > n_{\text{ARC1}}^2/n_2$  and a  $\lambda/4$  high index bottom layer with  $n_{\text{ARC3}}$ , the bandwidth of antireflection can be reduced further [159].

Various material combinations have been utilized for the fabrication of triple-layer antireflective coatings. Kuo *et al.* deposited  $\text{SiO}_x/\text{SiO}_x\text{N}_y/\text{SiN}_x$  triple- $\lambda/4$ -layer systems on textured Si solar cells, resulting in a 10.95% relative increase in device efficiency [168]. Concerning  $\lambda/4$  stacks, a comparison of the reflectance spectra of a single-layer  $\text{TiO}_2$ , a double-layer  $\text{SiO}_2/\text{TiO}_2$ , and a  $\text{SiO}_2/\text{SiO}_2\text{-TiO}_2/\text{TiO}_2$  triple-layer

antireflective coating on Si solar cells has been provided by Lien *et al.* [166] and is depicted in Fig. 2.10. Furthermore, Ye *et al.* utilized the same material system in a different order, with the highest refractive index material as the middle layer ( $\text{SiO}_2/\text{TiO}_2/\text{SiO}_2\text{-TiO}_2$ ) for minimizing reflection losses at a glass-air interface [170].

### 2.3.2.4 Multilayer Antireflective Coatings

Herpin's theorem states that any layer-system comprised of nonabsorbing dielectric materials is equivalent, at one wavelength, to a two-film system, and any symmetric layer system is equivalent to a single film, characterized by an equivalent refractive index and an equivalent thickness [171–173]. The equivalent layer formalism can be used to design broadband antireflective layers by relying on stratified stacking of high index (H) and low index (L) materials. For example, Schulz *et al.* designed a nine-layer antireflective coating (for polymers such as PMMA or PC) based on  $\text{SiO}_2$  and  $\text{Ta}_2\text{O}_5$  (plasma ion-assisted deposition), which can be described as four equivalent layers of incrementally increasing equivalent indices from 1.11 to 1.37 [174]. More complicated designs with up to 27 layers have also been demonstrated [175]. Furthermore, antireflective coatings based on equivalent layers have also been applied underneath the cover glass of solar cells [176].

Using multilayer configurations, antireflective coatings can further be designed to suppress reflectance over a broad spectral range while simultaneously exhibiting high reflectance within a narrow spectral range, resulting in vividly colored solar cells with adequate efficiency. For example, Selj *et al.* demonstrated such a colored antireflective coating based on 36 layers of porous Si (and also based on  $\text{SiN}_x/\text{SiO}_x/\text{SiN}_x$  triple-layer systems for comparison) [177]. Porous Si has the advantage that very large numbers of layers with tunable refractive index can be produced in a very practicable manner, namely by controlling the current density during an electrochemical etching process.

### 2.3.3 Gradient-Refractive-Index Materials

As previously mentioned in subsection 2.3.1, an effective way to minimize surface reflectance is to divide the large refractive index contrast at the respective interface into several smaller index steps by adding intermediate layers. Gradient-index materials take this concept one step further by using coating materials with a gradually changing refractive index in order to abolish the sharp refractive index contrast at the interface.

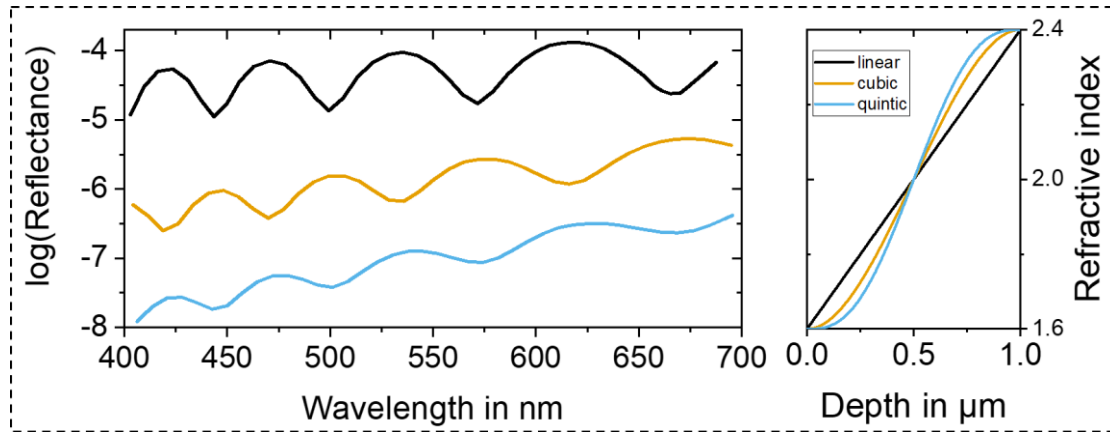


**Fig. 2.11:** Calculated reflectance spectra of different gradient-index antireflective coatings. Left: Linear, cubic, and quintic refractive index profile from  $n_1 = 1.6$  to  $n_2 = 2.4$ . Right: Calculated reflectance/reflectivity spectra for the respective index profiles. Calculating the reflectance for these graded refractive indices, the profiles were approximated as planar layer stacks comprised of fifteen layers per quarter-wave optical thickness for subsequently applying a transfer-matrix-approach. All data presented in this figure was originally published in reference [178] and was extracted from the original figures with the help of an online tool [144]. © 1983 Optical Society of America.

The antireflection capabilities of such layers depend on their refractive index profile. For example, Southwell compared the reflectance at a material interface after applying gradient-index coatings with either linear, cubic, or quintic refractive index profiles of the following form ( $z \in [0, L]$ ) [178]:

$$n(z) = n_1 + (n_2 - n_1) \left( \frac{z}{L} \right) \quad (61)$$

$$n(z) = n_1 + (n_2 - n_1) \left( 3 \left( \frac{z}{L} \right)^2 - 2 \left( \frac{z}{L} \right)^3 \right) \quad (62)$$

$$n(z) = n_1 + (n_2 - n_1) \left( 10 \left( \frac{z}{L} \right)^3 - 15 \left( \frac{z}{L} \right)^4 + 6 \left( \frac{z}{L} \right)^5 \right) \quad (63)$$

For  $n_1 = 1.6$  and  $n_2 = 2.4$ , these three refractive index profiles, together with their respective reflectance spectra, are given in Fig. 2.11. The reflectance was calculated via the transfer-matrix method (see subsection 2.5.1) by approximating the refractive index profiles as planar layer stacks comprised of fifteen layers per quarter-wave optical thickness. The reflectance can be reduced by several orders of magnitude when going from a linear to a cubic and quintic index profile. Next to polynomial index profiles, alternative proposals include an exponential taper

$$n(z) = n_1 \exp \left( \frac{z}{L} \ln \left( \frac{n_2}{n_1} \right) \right) \quad (64)$$

or a Gaussian taper

$$n(z) = \begin{cases} n_1 \exp\left(2\left(\frac{z}{L}\right)^2 \ln\left(\frac{n_2}{n_1}\right)\right); & 0 \leq z \leq \frac{L}{2} \\ n_1 \exp\left(2\left(1 - \left(1 - \frac{z}{L}\right)^2\right) \ln\left(\frac{n_2}{n_1}\right)\right); & \frac{L}{2} < z \leq L \end{cases} \quad (65)$$

It has further been demonstrated that a refractive index profile can be optimized to achieve broadband and angle-tolerant antireflective layers [179]. More detailed information about gradient-index antireflective layers can be found in reference [180].

Graded index antireflection coatings can be fabricated in various ways. The first examples of such inhomogeneous layers were achieved via co-evaporation of CeO<sub>2</sub>-MgF<sub>2</sub>, as well as co-evaporation of Ge-MgF<sub>2</sub>. Furthermore, hollow silica nanoparticles have been used to produce layers of porous silica with a gradual change in pore density on top of PMMA [181]. Also, a linear refractive index profile was achieved with a 4.1 μm thick porous Si layer (24 refractive index steps) has been fabricated by pulsed electrochemical etching, thereby reducing the reflectance of Si below 5% over a broad spectral range (360 nm – 3300 nm) [182]. Combinations of different porous materials have also been used to achieve graded index structures. For example, Kuo *et al.* demonstrated a seven-layer gradient-index structure comprised of porous SiO<sub>2</sub> + porous SiO<sub>2</sub>-TiO<sub>2</sub> + porous TiO<sub>2</sub> as an antireflective coating for Si [183]. SiO<sub>2</sub>-TiO<sub>2</sub> hybrid films have been used to produce graded refractive index profiles (6 layers) for CIGS solar cells (as well as glass) via sol-gel dip-coating [184].

### 2.3.4 Subwavelength Nanostructures

Another method to produce layers with gradually changing refractive index profiles relies on nano-patterning the reflective surface rather than applying a planar coating, as schematically illustrated in Fig. 2.12. If the structural features are considerably smaller than the incident wavelength, the surface nanostructure can not be resolved by the incident light. The patterned interface can then be treated as an effective medium with a gradually changing permittivity tensor  $\hat{\epsilon}_{\text{eff}}(z)$ . In  $z$ -direction (normal to the structured surface), the effective permittivity can be calculated as a weighted average of the form [185]

$$\epsilon_{z,\text{eff}}(z) = f(z)\epsilon_2 + (1 - f(z))\epsilon_1, \quad (66)$$

where  $f(z)$  describes the area filling fraction occupied by the textured material at the depth  $z$  (hence,  $1 - f(z)$  is the filling fraction occupied by the incident medium)

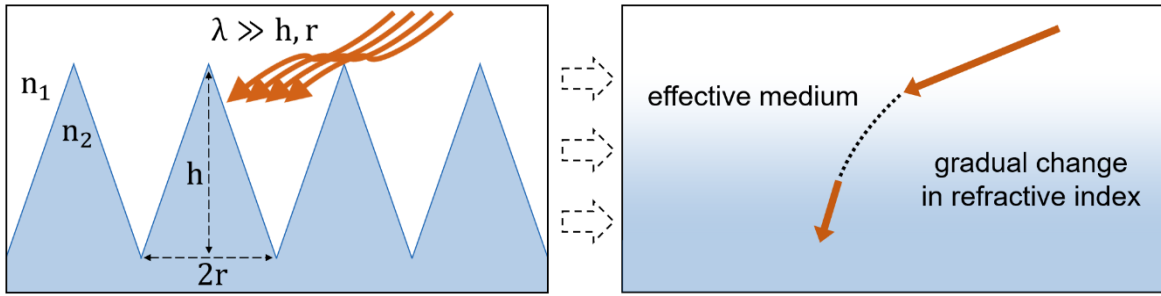


**Fig. 2.12:** Schematic illustration of the working principle of subwavelength nanostructures as antireflective layers.

and  $\epsilon_i$  denotes the permittivity of material  $i$ . The lateral components of the effective permittivity tensor depend on the geometrical shape of the structural components. For subwavelength surface structures comprised of features with a circular base (such as cones), for example, the  $x$ - and  $y$ - components of the effective permittivity can be calculated using the 2D Maxwell Garnett expression [186]:

$$\epsilon_{x,\text{eff}}(z) = \epsilon_{y,\text{eff}}(z) = \epsilon_1 + 2f(z)\epsilon_1 \frac{\epsilon_2 - \epsilon_1}{\epsilon_2 + \epsilon_1 - f(\epsilon_2 - \epsilon_1)} \quad (67)$$

Since this type of surface structure can be found on the eyes of many nocturnal insect species such as moths (see chapter 3), the suppression of surface reflectance through subwavelength nanostructures is commonly called the ‘moth-eye-effect’. Several ways to fabricate moth-eye-like surface structures are discussed in section 5.2. The reflectance properties of a moth-eye-like antireflective structure on glass are depicted in Fig. 2.13. Since their antireflective properties are based on the subwavelength size of the nano-protuberances, broadband antireflection over the visible spectrum is achieved if the feature sizes are sufficiently small. Furthermore, in contrast to antireflection concepts based on planar layers, moth-eye-inspired structures lead to low reflectance even for oblique incidence of light. It is worth noting that moth-eye-mimicking antireflective nanostructures can also be stacked on top of (double-layer) thin-film antireflective coatings for use in, for example, organic solar cells [187], or in InGaP/GaAs/Ge triple-junction solar cells, where an optically thick glass/resin cover is sandwiched between the moth-eye structured front surface and  $\text{TiO}_2/\text{Al}_2\text{O}_3$ -coated rear side [188, 189]. Moreover, a (simulation-based) comparison of the antireflection properties (for normal incidence of light) of subwavelength nanostructures comprised of different geometrical shapes has been provided by Deinega *et al.* [190].

It is worth noting that, in principle, moth-eye-like structures can be described as

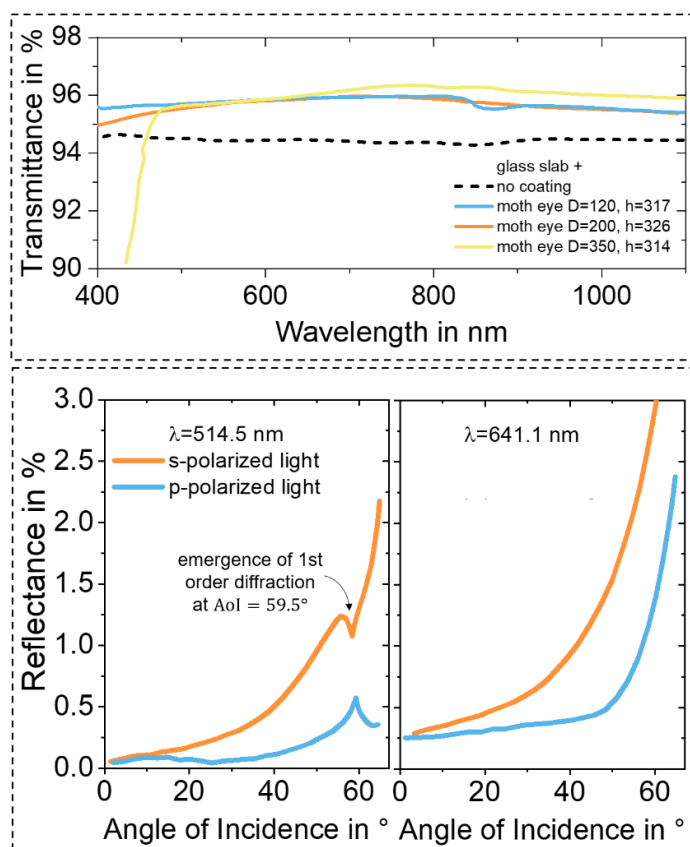


**Fig. 2.13: Optical properties of moth-eye-like antireflective nanostructures. Top: Transmittance spectra of a glass slab covered with moth-eye-structures based on different feature sizes. Adapted with permission from reference [191], © 2013 American Chemical Society. Bottom: Angle-dependent reflectance of moth-eye-covered glass, measured at 514.5 nm and 641.1 nm. Adapted with permission from reference [192], © 1982 British Crown Copyright. All data presented in this figure was extracted from the original figures with the help of an online tool [144].**

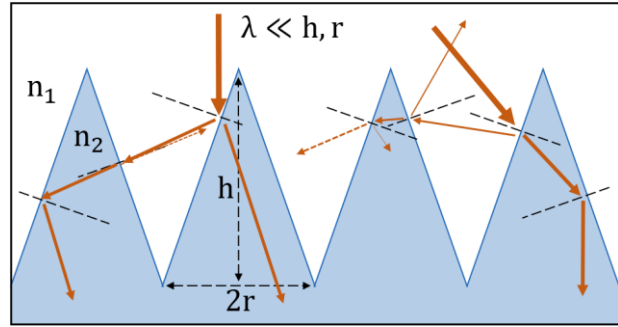
diffraction gratings with periods so small that, except for the zeroth-order diffracted light, all the higher diffraction orders are deflected towards angles above  $90^\circ$  (evanescent waves). For oblique light incidence, however, this condition might not hold anymore, and higher-order diffracted light (starting with the order  $m = 1$ ) might couple into the material, leading to an anomaly in the  $R(\text{AoI})$  reflectance curve (see Fig. 2.13).

Further discussions regarding fabrication techniques for moth-eye (-mimicking) antireflective structures follow in chapters 3 and 5.

### 2.3.5 Microstructured Surfaces

Another way to efficiently suppress reflection losses at material interfaces relies on surface structures with feature sizes much larger than the incident light wavelength. The interaction of light with such large-scale surface structures is governed by ray optics (see also subsection 2.5.2). The working principle of microstructure-based antireflection is illustrated in Fig. 2.14. If the aspect ratio (AR) of the individual structural features is sufficiently large, incident light rays will

**Fig. 2.14:** Schematic depiction of the working principle of antireflective layers based on microstructured surfaces.



often keep their ‘downwards’ propagation direction even after several reflection and refraction events. The combination of multiple chances for light in-coupling, together with TIR preventing out-coupling, results in a highly efficient suppression of surface reflectance, even for oblique light incidence. Since no wave-optical effects occur at such microstructured surfaces, their antireflective effect only depends on the refractive index of the structured material, and therefore naturally exhibits good broadband stability, as indicated by the Fresnel coefficients (17)-(18) and Snell’s law of reflection and refraction (21). For AR = 0.25, 0.5, 0.6, and 1, the AoI-dependent reflectance properties of microstructures composed of cones, pyramids, inverted cones, and inverted pyramids are shown in Fig. 2.15 (calculated using the ray-tracing-based approach introduced in chapter 6). Based on numerical and analytical studies of highly ordered microstructures comprised of different arrangements of micro-cones as well as square, triangular, and hexagonal micro-pyramids, it can be concluded that the antireflective properties of microstructured surfaces are mostly governed by three parameters, namely [190, 193]

- 1) the filling fraction/packing density of the microstructure constituents,
- 2) the AR (or apex angle) of the structural features, and
- 3) the geometrical shape of the structural constituents.

By far, the most important qualities for achieving an effective suppression of reflection losses at microtextured surfaces are filling fraction and AR. In case of a 100% filling fraction (‘full tiling’ configuration) and normal incidence of light, Deinega *et al.* derived a relation for the surface reflectance of the form

$$R_{\text{AoI}=0} \propto e^{-\text{const} \cdot \text{AR}}, \quad (68)$$

which shows that the reflection losses at the microtextured interface asymptotically approach  $R_{\text{AR} \rightarrow \infty} = 0$  with increasing AR of the structural constituents [190]. In case of a (constant) filling fraction below 100% (‘incomplete tiling’ configuration, e.g. hexagonal close packing of micro-cones) and for increasing AR, the reflectance at normal incidence first passes over a local minimum and then asymptotically

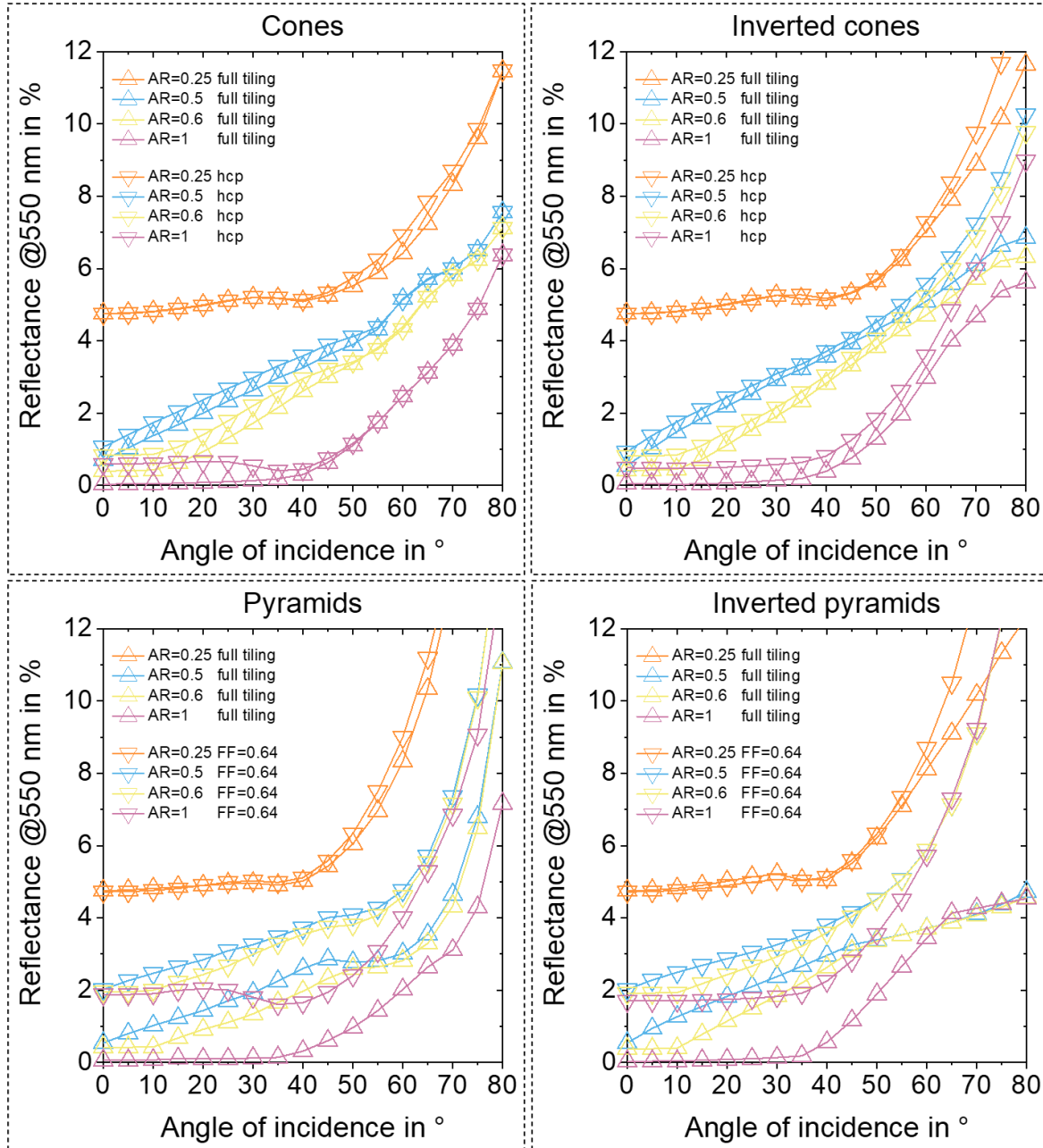


**Fig. 2.15:** AoI-dependent reflectance of a selection of microtextured surfaces based on cones, pyramids, inverted cones, and inverted pyramids of four different ARs and considering two different filling fractions (simulated by using the modeling and simulation scripts introduced in chapter 6).

approaches the reflectance value of the respective planar material interface, hence  $R_{AR \rightarrow \infty} = |(N_1 - N_2)/(N_1 + N_2)|^2$ . An explanation for this behavior can be found in reference [190]. Compared to filling fraction and AR, the geometrical shape of the microstructural constituents exhibits a more moderate impact on the reflection losses of microtextured surfaces. However, for a given AR and filling fraction, sharply tipped geometrical shapes such as pyramids and cones tend to reflect less light compared to analogous microstructures comprised of more rounded shapes

such as (truncated) ellipsoids/spheroids or paraboloids, especially under oblique light incidence [194].

In contrast to the various non-scattering antireflective layers described in the previous subsections (parallel incident light rays lead to parallel rays in reflection and transmission), microstructured surfaces cause a redistribution of the incident light angular profile leading to an increased average path length of light rays within the active material. Moreover, a properly designed microtextured antireflective surface for PV should also exhibit strong retro-reflection capabilities, which decreases the probability of light out-coupling from the textured front side of a device. These effects are commonly summarized under the term light-trapping. Microstructure-based antireflection is therefore especially useful for producing high-efficiency devices whilst reducing the absorber layer thickness for minimizing material consumption. Furthermore, the antireflection and light-trapping properties of microtextured surfaces are famously utilized to overcome losses due to incomplete absorption in the indirect band gap material Si. Most commonly, a microstructure is directly induced in Si via anisotropic etching methods based on, for example, potassium hydroxide (KOH) or sodium hydroxide (NaOH) as aqueous texturing solutions. For example, when the surface of a [100]-oriented Si wafer is exposed to a KOH solution, anisotropic etching can lead to the formation of random micro-pyramids on the Si surface, as depicted in Fig. 2.16. Other Si-based microstructures produced by variations of such anisotropic etching schemes, including triangular grooves, random inverted pyramids, and highly ordered inverted pyramids, are shown in Fig. 2.17. It is worthy of note that computational studies on ultrathin c-Si solar cells have indicated that pseudo-random inverted pyramids outperform their periodic counterparts (at the same filling fraction) [195, 196]. Further information about the impact of (different types of) structural disorder on the light-collection properties of microstructured surfaces can be found in chapter 6.

In addition to wet chemical etching techniques, another type of antireflective Si microstructure can be produced with femtosecond laser pulses (high AR spikes) [197]. More examples for antireflective microtextured Si surfaces, including details about the various fabrication routes, can be found, for example, in reference [198]. It should be noted that some additional approaches for producing micro-, nano-, or hierarchically textured Si surfaces are briefly described in section 5.2.

Next to micro-patterning the active material of a PV device, another widely used method relies on applying a transparent micro-patterned (intermediate) layer at the

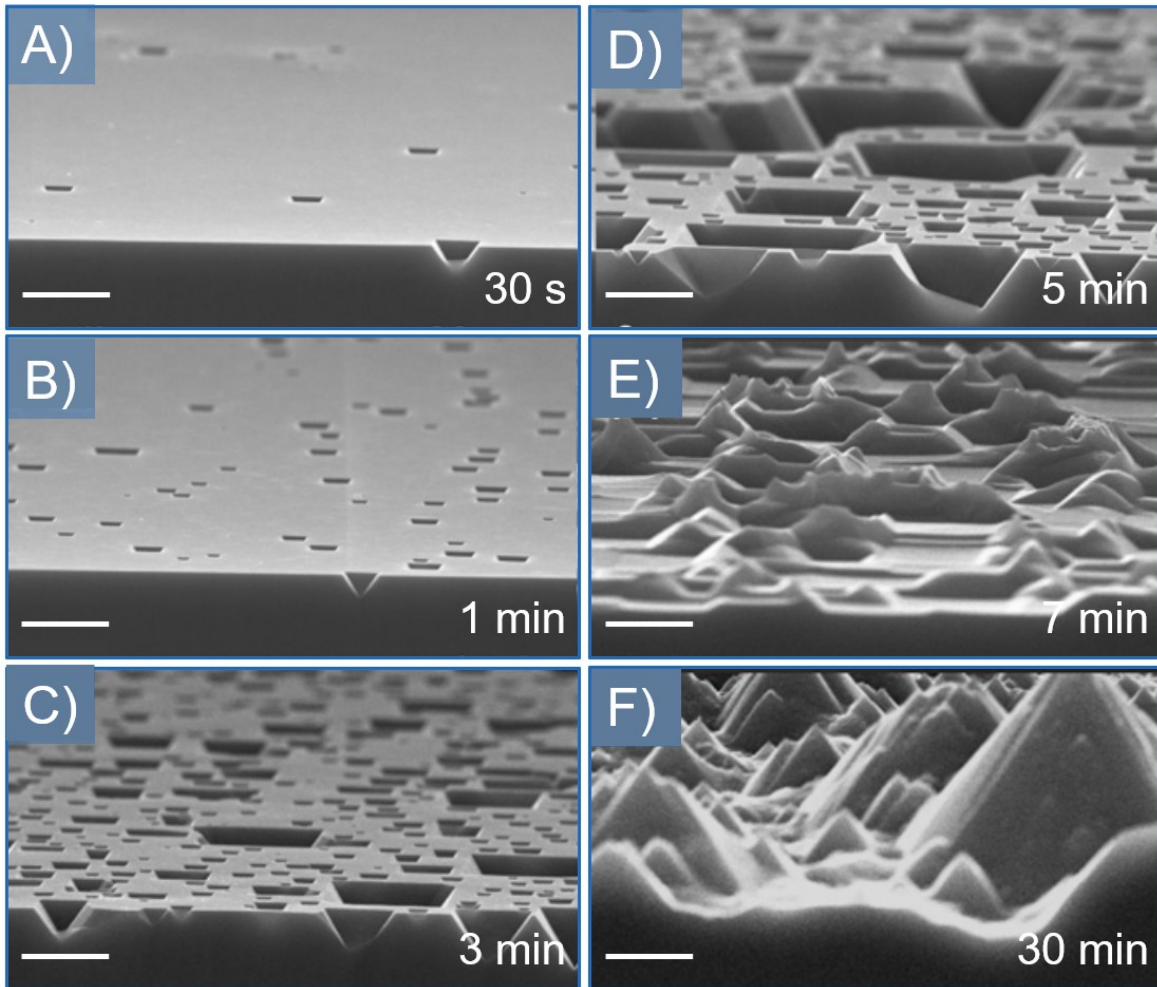


**Fig. 2.16:** Anisotropic etching of Si for producing random micro-pyramids for antireflection and light-trapping. Adapted with permission from reference [199], © 2010 Elsevier B.V. All Rights Reserved.

respective interface. Following this approach, the random pyramid structure of etched Si wafers has been copied into transparent polymers and applied atop of thin-film solar cells [200, 201]. Furthermore, it should be noted that Si micro-pyramids have also been (soft-imprint) replicated into  $\text{TiO}_2$  paste and subsequently utilized in dye-sensitized solar cells [202]. Further information about microstructures obtained by replication techniques (and the optical properties of plant surface structure replicas as antireflective layers for PV devices) can be found in section 5.1.

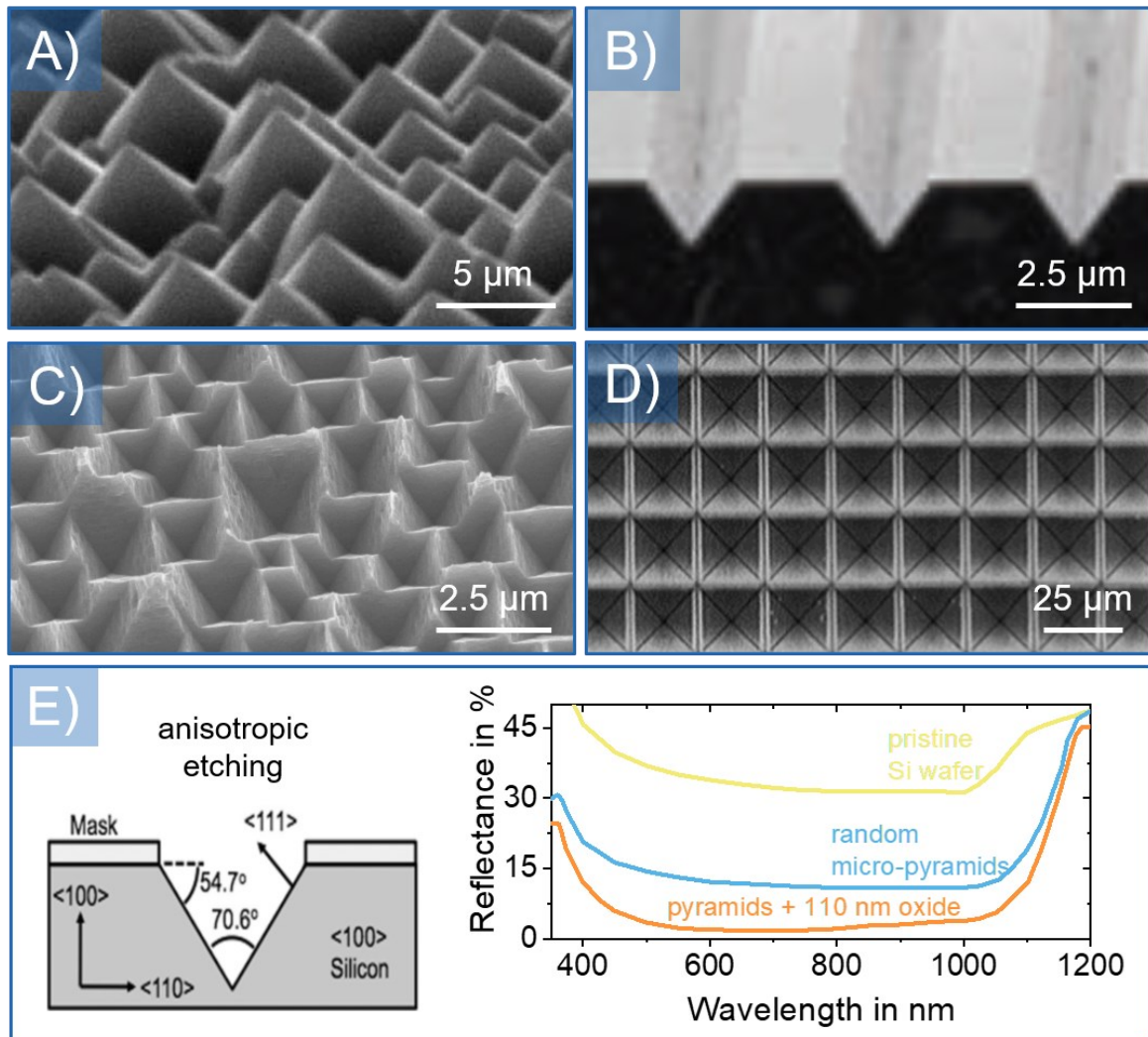


Fig. 2.17: SEM micrographs of Si wafers with different microstructured surfaces: A) Random pyramids. Adapted with permission from [203], © 2006 Elsevier B.V. All Rights Reserved. B) V-shaped grooves. Adapted with permission from [204], © 2009 American Association for the Advancement of Science. C) Random inverted pyramids. Adapted with permission from [205], © 2018 The Authors. D) Highly-ordered inverted pyramids. Adapted with permission from [206], © 2001 Elsevier Science B.V. All Rights Reserved. E) schematic illustration of the anisotropic etching of Si (left) and the reflectance spectra of random-pyramid-structured Si with and without an additional single-layer thin-film antireflective coating, as well as the reflectance of an untreated Si wafer (right) as a benchmark. The schematic was reprinted with permission from reference [207], © 2012 IOP Publishing Ltd. The plotted data was originally published in [208] and extracted via online tool [144] for this illustration.

### 2.3.6 More Approaches Towards Antireflection and Light-Trapping

This subsection summarizes a few more noteworthy strategies towards antireflection and light-trapping that have been demonstrated (or at least proposed).

For Si solar cells, effective sunlight trapping can be achieved with an absorber design based on Si nanowires arrays (photonic crystal), where each Si nanowire encompassed a radial p-n junction [209, 210]. In organic solar cells, light absorption can be enhanced via coherent light-trapping in optical cavities [211, 212].

Numerous research groups utilized metallic nanoparticles of various shapes, sizes, and distributions to scatter or concentrate light into the device's active region in so-called plasmonic enhanced solar cells. However, relying on metal-containing antireflective layers inevitably leads to some parasitic absorption losses, restricting the applicability of plasmonic nanoparticle-based light-harvesting layers to conventional PV (solar thermophotovoltaics as well as solar thermal collectors/absorbers). Plasmonic enhanced light-harvesting layers for solar cells have been implemented at the front surface as well as at the semiconductor-metal interface in the rear section of the device. Further, plasmonic nanoparticles have also been directly integrated into the absorber layer of the device. A more detailed discussion of these architectures can be found, for example, in a 2018 review by Enrichi *et al.* [213].

Relying only on dielectric materials, antireflection can also be achieved through resonant scattering (Mie resonances) at periodic arrays of subwavelength objects of high refractive index at a suitable material interface (front surface, semiconductor-metal interface, or integration directly into the absorber layer), an approach which tends to exhibit rather narrow ranges for operating wavelengths and AoIs [214–216]. Introducing disorder to these subwavelength structures can be exploited to improve spectral and angular stability [217]. Another strategy towards broadband antireflection based on Mie resonances relies on a multiresonant structure, in which differently sized Mie resonators manage antireflection at different wavelengths [218]. Recently, Cordaro *et al.* demonstrated a subwavelength structure in Si, which utilizes both Mie resonances as well as Fabry-Pérot resonances (meaning the thin-film interference effects exploited in traditional antireflective coatings) in order to suppress reflectance at the air-Si interface [219].

A fundamentally different type of antireflective layer has been demonstrated by Yasuda *et al.* and is based on a metasurface comprised of subwavelength Ag nanodiscs, which effectively forms an antireflective layer with a refractive index

below 1.0 (the real part of the refractive index is 0.5 at a wavelength of 550 nm and less than 1.0 over the whole visible wavelength range) [220].

For the transition from an optically thicker to an optically thinner medium, only light rays with an AoI below the critical angle have a chance to be transmitted. Incident light rays with an AoI above the critical angle will always be reflected (total internal reflection). Interestingly, metasurfaces for omnidirectional antireflection from an optically thick to an optically thin medium (overcoming TIR) have therefore been proposed [221].

In bulk optical metamaterials, propagating eigenmodes can have quite complex field profiles, which can't be efficiently excited by simple plane waves. A generalized approach for designing antireflection coatings for such bulk metamaterials, which enable an effective in-coupling of incident plane waves, has been proposed by Maas *et al.* [222].

Another notable optical loss mechanism in PV devices is the shading effect caused by the metallic front contact fingers, which cover a fraction of the front sides of many PV cell types (see Fig. 2.2). These losses can be diminished, for example, via invisibility cloaking [223, 224] or by fabricating triangle-shaped contact fingers [225]. Another notable strategy to overcome these shading losses relies on incorporating air prisms into the encapsulant material directly above the contact fingers [226].

## 2.4 Advanced Light-Management Concepts in PV

Next to antireflection and light-trapping, there are several more photonics-based approaches to enhance solar cell performance. Following a recent 2021 review article by Garnett *et al.*, these methods can be categorized as follows [227]:

- Spectral shaping methods, such as upconversion [228]/downconversion [229] (for reducing sub band gap and thermalization losses) and luminescent down shifting [230] (for improving the spectral response at short wavelengths).
- Spectral splitting in multi-junction devices, for example, by integrating photonic-crystal-based intermediate reflectors into a tandem layer stack [231].
- Fabrication of colored solar cells [177].

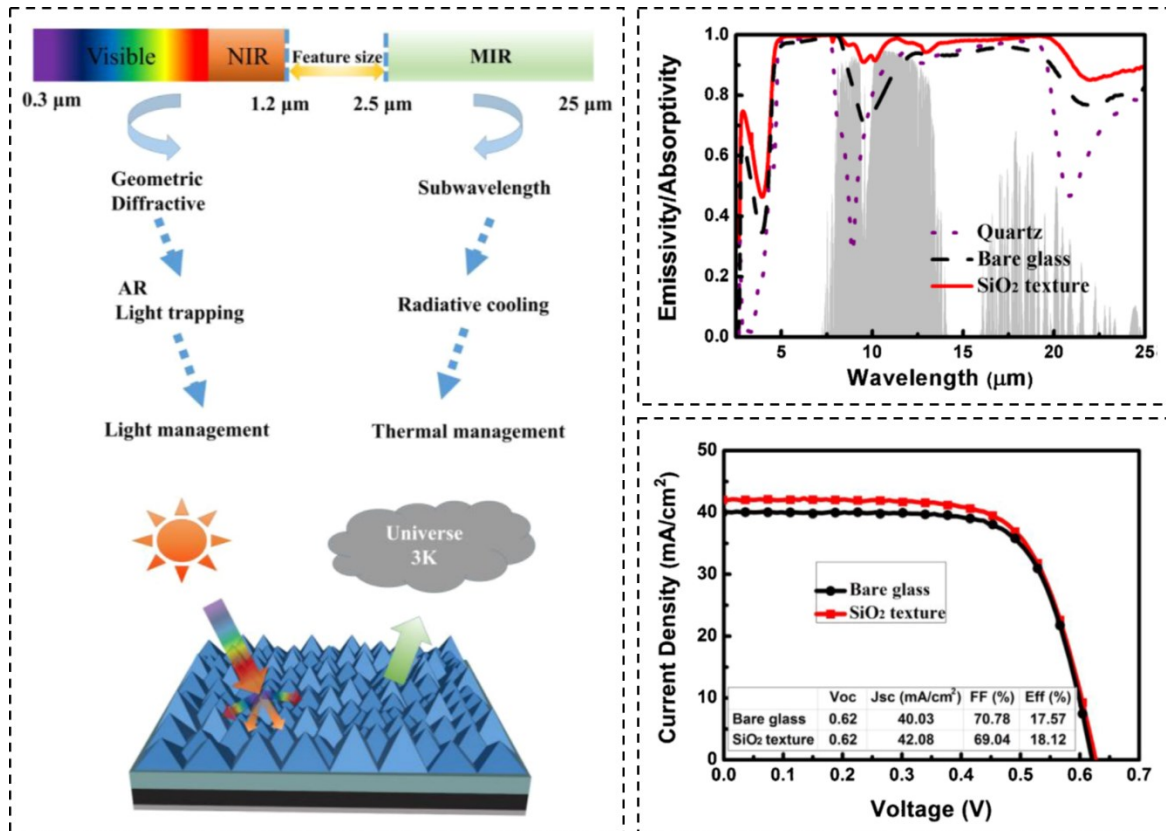
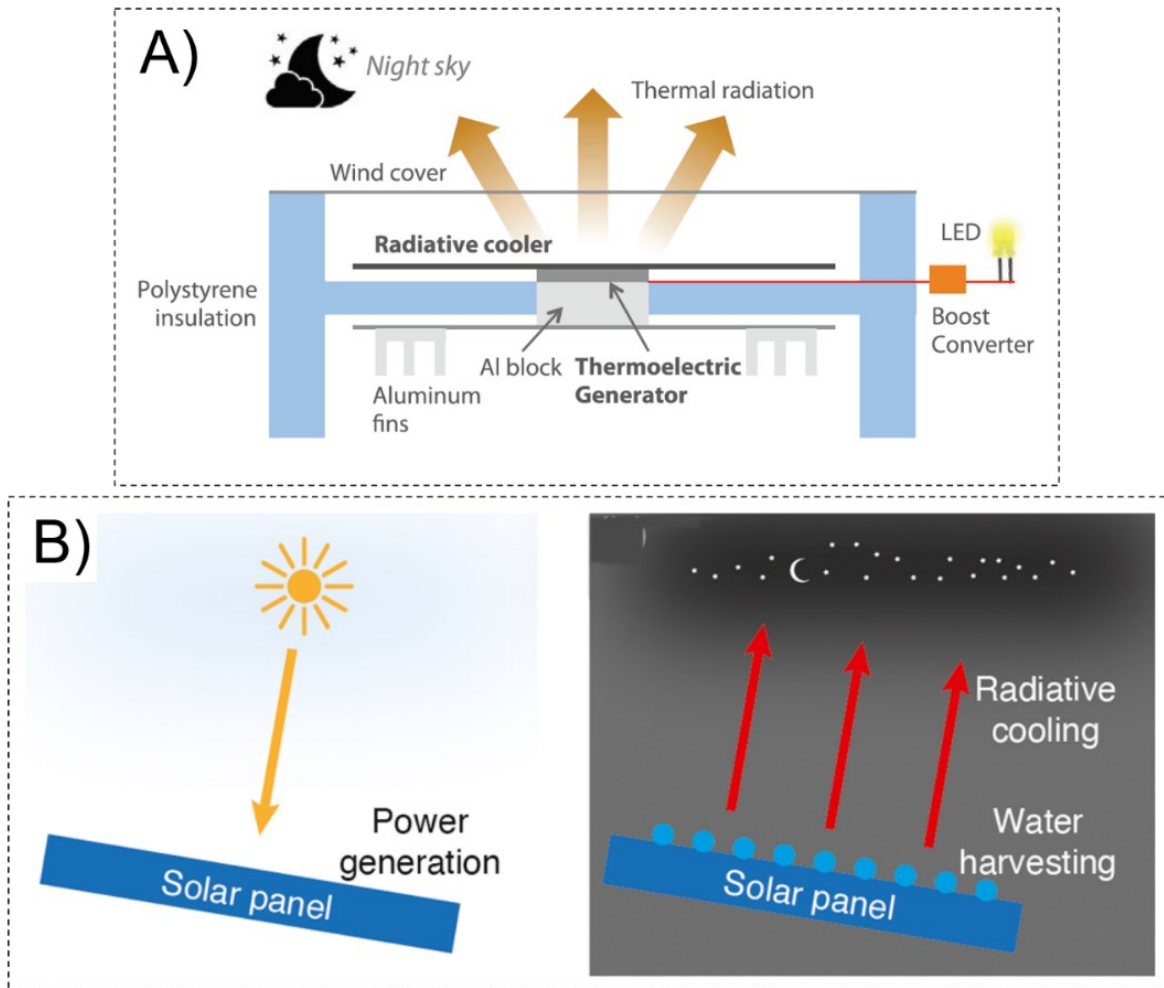


Fig. 2.18: Combined antireflection and radiative cooling effect of random micro-pyramids. On the right, the measured emissivity/absorptivity (top), together with the atmospheric transmittance in shaded grey, and IV characteristics (bottom) of a textured and a reference PV device are shown. Adapted with permission from reference [102], © 2017 WILEY-VCH Verlag GmbH & Co. KGaA, Weinheim.

— Radiative cooling methods [97–102].

The primary challenge in achieving radiative cooling in PV devices is to develop a radiative cooling coating that does not hamper the light in-coupling properties in the visible and near-infrared spectral regions. In Si solar cells, such combined properties have been demonstrated for a square arrangement of cylindrical, low AR micro-pillars comprised of SiO<sub>2</sub> [101]. Furthermore, Lu *et al.* demonstrated that the typical random pyramid structure of KOH-etched Si wafers could be replicated into SiO<sub>2</sub> (via PDMS mold; more details about such micro- and nanostructure replication approaches can be found in section 5.1), resulting in simultaneous antireflection and passive radiative cooling due to the interaction with the visible, near-infrared, and mid-infrared electromagnetic waves via geometric, diffractive, and subwavelength optical effects (see Fig. 2.18) [102]. Moreover, the combined antireflection and radiative cooling properties of random micro-pyramids replicated from etched Si wafers have also been demonstrated for PDMS, reaching



**Fig. 2.19:** Schematic illustration of two strategies to utilize nighttime radiative cooling. A) Electrical power generation at night. Adapted with permission from reference [232], © 2019 Elsevier Inc. B) Water-harvesting at night. Adapted with permission from reference [233], © 2021 American Chemical Society.

near-unity emissivity over the atmospheric transparency window  $8\ \mu\text{m} - 13\ \mu\text{m}$  [100]. In contrast to  $\text{SiO}_2$ -based light-harvesting layers, their PDMS counterparts could be used as an antireflective radiative cooler for flexible thin-film solar cells. It should be noted that a  $200\ \mu\text{m}$  thick planar PDMS layer is already capable of achieving a high emissivity above 0.9 over the entire infrared spectral range of  $4\ \mu\text{m} - 26\ \mu\text{m}$ , even without any surface patterning.

It should be noted that, in recent years, several contributions explored the theoretical efficiency limits for harvesting energy from the (radiative) heat flow between the (terrestrial) ambient and the cold ( $T \approx 3\ \text{K}$ ) outer space, which could be achieved via processes analogous to solar thermal power generation as well as PV power generation [234, 235]. In 2020, Li *et al.* studied thermodynamic performance limits for simultaneous energy-harvesting from the hot sun and cold outer space [236].

During the daytime, radiative cooling in PV aims to decrease the operating temperature, which results in less degradation of the efficiency. Nighttime radiative cooling, on the other hand, can be exploited for various other purposes. Two examples for the utilization of nighttime radiative cooling are schematically illustrated in Fig. 2.19. Based on thermoelectric generators, Raman *et al.* demonstrated a low-cost power generation device where, by facing the night sky, the cold device side radiates heat to the cold of space, as illustrated in Fig. 2.19 A) [232]. The power generated was sufficient to maintain an LED lit at night, enabling battery-free off-grid lighting. Li *et al.*, on the other hand, utilized radiative cooling for water-harvesting from solar panels during the night (Fig. 2.19 B) [233].

Due to the fundamentally different architecture of dye-sensitized solar cells [237] compared to solid-state semiconductor devices (not explained here), light-management strategies for this type of PV device are mostly focused on tuning the morphology and composition of the dye-coated nanocrystalline TiO<sub>2</sub> layer [238, 239].

## 2.5 Computational Methods for Studying the Optical Properties of PV Light-Harvesting Layers

### 2.5.1 Transfer-Matrix Method

The transfer-matrix method (TMM) enables a convenient computation of the reflection, transmission, and absorption properties for plane (electromagnetic or acoustic) waves propagating through stratified media. TMM calculations are extensively used for designing and optimizing (multilayer) thin-film antireflective coatings (see subsection 2.3.2), dielectric mirrors, and other types of optical filters, as well as for analyzing the optical properties of entire thin-film-based optical devices, such as various types of solar cells and organic light-emitting diodes. In the following, it shall be assumed that  $N$  layers are stacked perpendicularly to the  $z$ -axis, as schematically depicted in Fig. 2.20. The lateral ( $xy$ ) dimensions of these layers are assumed to be infinite. The fields are separated into parallel and transverse components with respect to the  $z$ -axis. Next, the transverse components are expressed as superpositions of forward traveling and backward traveling waves, and the continuity conditions for the transverse fields across a material

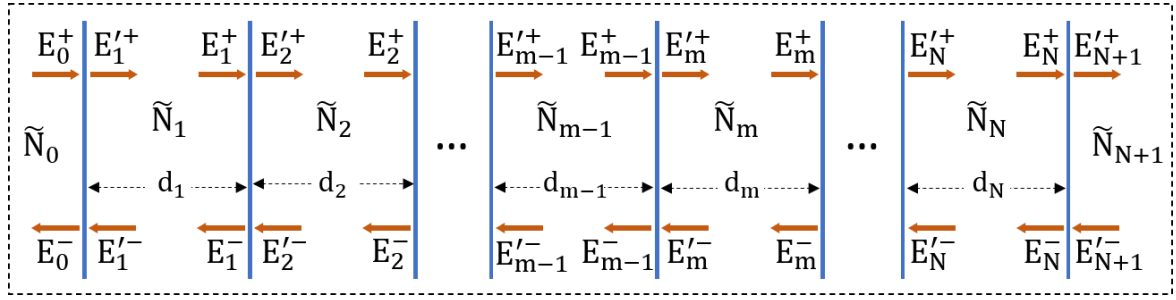


**Fig. 2.20: Schematic illustration of normally incident light propagating through a planar multilayer system.**

interface are applied for all  $N + 1$  material boundaries. In the following, the transfer matrix formalism shall first be discussed for normal incidence of light, while the case of oblique incidence is introduced towards the end of this subsection.

Without loss of generality, the normally incident homogeneous plane wave is assumed to be linearly polarized, following  $\vec{E}(z) = E(z)\hat{x}$  and  $\vec{H}(z) = H(z)\hat{y}$ . Under these conditions, the amplitudes of the electric and magnetic fields are fully transverse and can be expressed as a superposition of forward traveling (+) and backward traveling (-) waves via

$$E(z) = E^+(z) + E^-(z), \quad H(z) = \frac{1}{\eta}(E^+(z) - E^-(z)), \quad (69)$$

$$E^+(z) = \frac{1}{2}(E(z) + \eta H(z)), \quad E^-(z) = \frac{1}{2}(E(z) - \eta H(z)). \quad (70)$$

In matrix notation, these relations can be written in the more compact forms

$$\begin{pmatrix} E^+ \\ E^- \end{pmatrix} = \frac{1}{2} \begin{bmatrix} 1 & \eta \\ 1 & -\eta \end{bmatrix} \begin{pmatrix} E \\ H \end{pmatrix} \quad \text{and} \quad \begin{pmatrix} E \\ H \end{pmatrix} = \begin{bmatrix} 1 & 1 \\ \eta^{-1} & -\eta^{-1} \end{bmatrix} \begin{pmatrix} E^+ \\ E^- \end{pmatrix}. \quad (71)$$

Within the bulk of material  $m$ , the propagation of the forward and backward traveling fields can be described by introducing a propagation matrix  $\mathbf{P}_m$ , which links the field amplitudes at the left interface to the amplitude on the right-hand-side (using the complex angle formalism, see section 2.2), and, using the notation  $\chi_m = 2\pi/\lambda_0 \cdot \tilde{N}_m d_m$  is given by

$$\begin{pmatrix} E_m^+ \\ E_m^- \end{pmatrix} = \mathbf{P}_m \begin{pmatrix} E_m^+ \\ E_m^- \end{pmatrix} = \begin{bmatrix} e^{i\chi_m} & 0 \\ 0 & e^{-i\chi_m} \end{bmatrix} \begin{pmatrix} E_m^+ \\ E_m^- \end{pmatrix}, \quad (72)$$

with  $\tilde{N}_m$  and  $d_m$  denoting the refractive index and layer thickness of material  $m$ . At the interface between material  $m - 1$  and material  $m$ , the forward-backward field amplitudes  $E^\pm$  are linked via the matching matrices  $\mathbf{D}_{m-1,m}$  which ensure the continuous matching of the transverse components of the  $E$  and  $H$  fields across the boundary. The matching matrix  $\mathbf{D}_{m-1,m}$  can be expressed through the amplitude reflection and transmission coefficients  $r_{m-1,m}$  and  $t_{m-1,m}$  yielding the relation

$$\begin{pmatrix} E_{m-1}^+ \\ E_{m-1}^- \end{pmatrix} = \mathbf{D}_{m-1,m} \begin{pmatrix} E_m^+ \\ E_m^- \end{pmatrix} = \frac{1}{t_{m-1,m}} \begin{bmatrix} 1 & r_{m-1,m} \\ r_{m-1,m} & 1 \end{bmatrix} \begin{pmatrix} E_m^+ \\ E_m^- \end{pmatrix}. \quad (73)$$

With the propagation and matching matrices  $\mathbf{P}_m$  and  $\mathbf{D}_{m-1,m}$ , the transfer/transition matrix for the entire layered system can be constructed via matrix multiplication, resulting in

$$\begin{pmatrix} E_0^+ \\ E_0^- \end{pmatrix} = \mathbf{D}_{0,1} \mathbf{P}_1 \mathbf{D}_{1,2} \mathbf{P}_2 \mathbf{D}_{2,3} \dots \mathbf{P}_N \mathbf{D}_{N,N+1} \begin{pmatrix} E_{N+1}^+ \\ E_{N+1}^- \end{pmatrix} = \mathbf{T}_{0,N+1} \begin{pmatrix} E_{N+1}^+ \\ E_{N+1}^- \end{pmatrix}. \quad (74)$$

The amplitude reflection and transmission coefficients for the entire layer stack can directly be derived from the components of the system transfer matrix

$$\mathbf{T}_{0,N+1} = \mathbf{D}_{0,1} \mathbf{P}_1 \mathbf{D}_{1,2} \mathbf{P}_2 \mathbf{D}_{2,3} \dots \mathbf{P}_N \mathbf{D}_{N,N+1} = \begin{bmatrix} T_{11} & T_{12} \\ T_{21} & T_{22} \end{bmatrix} \quad (75)$$

by using the relations

$$r = r_{0,N+1} = \left. \frac{E_0^-}{E_0^+} \right|_{E_{N+1}^- = 0} = \frac{T_{21}}{T_{11}}, \quad t = t_{0,N+1} = \left. \frac{E_{N+1}^+}{E_0^+} \right|_{E_{N+1}^- = 0} = \frac{1}{T_{11}}, \quad (76)$$

$$r' = r_{N+1,0} = \left. \frac{E_{N+1}^-}{E_{N+1}^+} \right|_{E_0^+ = 0} = -\frac{T_{12}}{T_{11}}, \quad t' = t_{N+1,0} = \left. \frac{E_0^-}{E_{N+1}^+} \right|_{E_0^+ = 0} = \frac{\text{Det } \mathbf{T}}{T_{11}}. \quad (77)$$

Conversely, the system transfer matrix  $\mathbf{T}_{0,N+1}$  can be expressed in terms of the amplitude reflection and transmission coefficients of the entire layer stack. By using  $tt' - rr' = T_{22}/T_{21}$ , one finds

$$\mathbf{T}_{0,N+1} = \frac{1}{t} \begin{bmatrix} 1 & -r' \\ r & tt' - rr' \end{bmatrix}. \quad (78)$$

Assuming a lossless incident medium, the amplitude reflection and transmission coefficients of the stratified medium can be linked to power transmittance and reflectance via the well-known relations discussed in section 2.2.

If all the refractive indices (at the wavelength of interest) and layer thicknesses of a multilayer material are known, the individual propagation and matching matrices can be constructed and, following equations (75) - (77), the reflection and transmission properties of the entire layer stack can be straightforwardly determined.

For oblique incidence of light, the electric and magnetic fields are, in general, not fully transverse with respect to the interface, as illustrated in Fig. 2.21. Concerning the electric field, for example, p-polarized light under oblique incidence will exhibit a nonzero parallel component, while the E-field for s-polarized light is fully

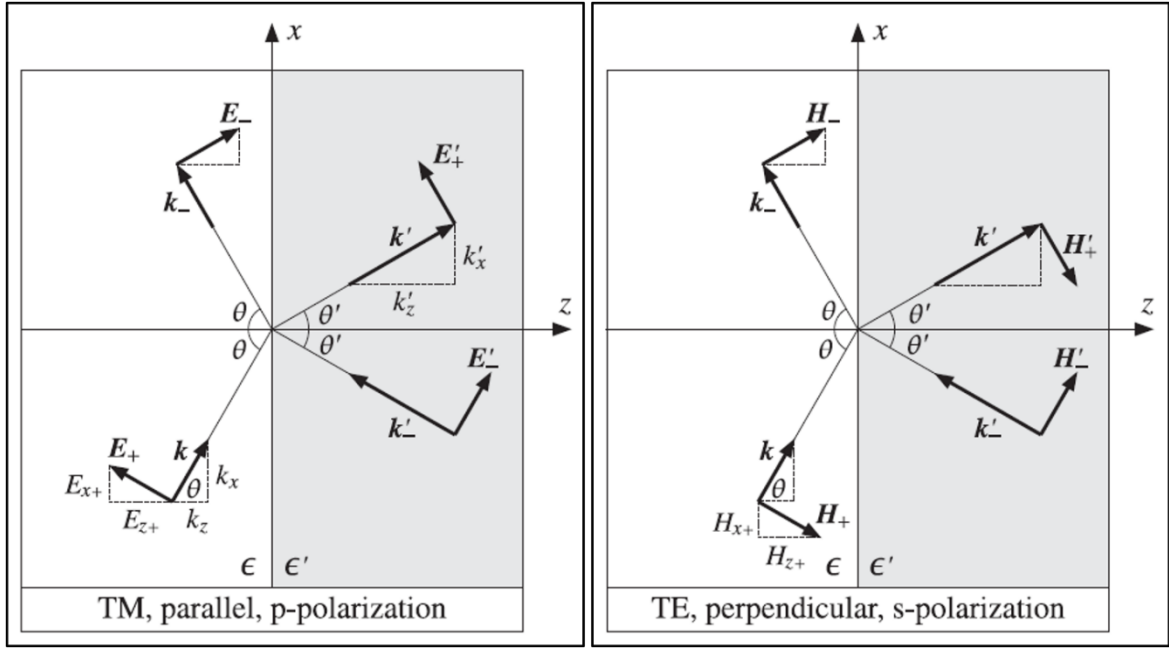


**Fig. 2.21:** Schematic illustration of light propagation through a planar material boundary under oblique incidence for p-polarized and s-polarized light (forward and backward traveling components depicted on both sides of the interface). Reprinted from reference [108], © 1996-2016 Sophocles J. Orfanidis. All Rights Reserved.

transverse. It can be shown that, under some conditions, the transfer matrix formalism for off-normal incidence takes the same basic form as in the normal incidence case. Concerning the propagation matrix, the familiar expression

$$\begin{pmatrix} E_{Tm}^{\prime+} \\ E_{Tm}^{\prime-} \end{pmatrix} = \begin{bmatrix} e^{i\chi_m} & 0 \\ 0 & e^{-i\chi_m} \end{bmatrix} \begin{pmatrix} E_{Tm}^+ \\ E_{Tm}^- \end{pmatrix}, \quad (79)$$

is reestablished, the only alteration is the additional cosine in

$$\chi_m = 2\pi/\lambda_0 \cdot \tilde{N}_m d_m \cos \theta_m, \quad (80)$$

which originates from the projection of the propagation vector onto the z-axis.  $\theta_m$  denotes the (generally complex) propagation angle in material m. The propagation angle follows Snell's law

$$\tilde{N}_0 \sin \theta_0 = \tilde{N}_1 \sin \theta_1 = \dots = \tilde{N}_{N+1} \sin \theta_{N+1} \quad (81)$$

through the entire layer stack. By evaluating the continuity conditions at the material boundaries, a matching matrix for oblique incidence of the form

$$\begin{pmatrix} E_{Tm-1}^+ \\ E_{Tm-1}^- \end{pmatrix} = \frac{1}{\tau_{m-1,m}} \begin{bmatrix} 1 & \rho_{m-1,m} \\ \rho_{m-1,m} & 1 \end{bmatrix} \begin{pmatrix} E_{Tm}^{\prime+} \\ E_{Tm}^{\prime-} \end{pmatrix} \quad (82)$$

can be found. The coefficients  $\rho_{m-1,m}$  and  $\tau_{m-1,m}$  are the transverse amplitude reflection and transmission coefficients. By further introducing a transverse impedance  $\eta_T$  and the related transverse refractive index  $\tilde{N}_T$  via

$$\eta_T = \begin{cases} \eta \cos \theta & \text{p-pol} \\ \eta / \cos \theta & \text{s-pol} \end{cases} \quad \left( \eta = \frac{\eta_0}{\tilde{N}} \Rightarrow \right) \quad \tilde{N}_T = \begin{cases} \tilde{N} / \cos \theta & \text{p-pol} \\ \tilde{N} \cos \theta & \text{s-pol} \end{cases}. \quad (83)$$

$\rho_{m-1,m}$  and  $\tau_{m-1,m}$  can be re-expressed in a compact and familiar way, resulting in

$$\tau_{m-1,m} = \frac{2\eta_{Tm}}{\eta_{Tm} + \eta_{Tm-1}} = \frac{2\tilde{N}_{Tm-1}}{\tilde{N}_{Tm-1} + \tilde{N}_{Tm}}, \quad (84)$$

$$\rho_{m-1,m} = \frac{\eta_{Tm} - \eta_{Tm-1}}{\eta_{Tm} + \eta_{Tm-1}} = \frac{\tilde{N}_{Tm-1} - \tilde{N}_{Tm}}{\tilde{N}_{Tm-1} + \tilde{N}_{Tm}}. \quad (85)$$

It is important to note that these coefficients should not be confused with the Fresnel coefficients introduced in equations (17) and (18), since the latter describe the amplitude reflection and transmission with respect to the total E- and H-field amplitudes instead of focusing only on their transverse components. For s-polarized light, both sets of coefficients are exactly equal due to the fully transverse electric field vector. For p-polarized light, on the other hand, the electric field of an obliquely incident electromagnetic plane wave exhibits a non-zero longitudinal component. In summary, the transformations therefore read

$$r_{m-1,m} = \begin{cases} \rho_{m-1,m} & \text{p-pol} \\ \rho_{m-1,m} & \text{s-pol} \end{cases} \quad \text{and} \quad t_{m-1,m} = \begin{cases} \frac{\cos \theta_{m-1}}{\cos \theta_m} \tau_{m-1,m} & \text{p-pol} \\ \tau_{m-1,m} & \text{s-pol} \end{cases}. \quad (86)$$

For a lossless incident medium like air, glass, or a non-absorbing polymer, the complex angle formalism does not lead to any problems even if absorbing materials are involved in the thin-film layer stack that is analyzed [105]. A straightforward translation of the complex propagation angles into the physically relevant properties (phase propagation direction and attenuation direction), however, can not be achieved in this formalism (see also section 2.1). It should be noted that a generalization of the TMM formalism, which also includes the case of a lossy incident medium, can in principle be deduced by relying on inhomogeneous harmonic plane waves instead of homogeneous ones at the material interface, as has been demonstrated by Mangini and Frezza in a 2016 article [240]. Furthermore, other generalized TMM approaches enable, for example, the treatment of interface current densities [241] or the analysis of layered systems of birefringent materials (using a  $4 \times 4$  matrix formalism) [242]. Similarly, metasurfaces at arbitrary dielectric surfaces were also successfully integrated into a TMM routine [243].

It should be noted that the transfer matrix formalism is also commonly expressed in dependence of the transverse components of the electric and magnetic fields  $E_T$  and  $H_T$  instead of the forward and backward propagating components of the (transverse) electric field  $E_T^\pm$ . The propagation matrix in this alternative notation takes the slightly less intuitive form

$$\begin{pmatrix} E'_{Tm} \\ H'_{Tm} \end{pmatrix} = \begin{bmatrix} \cos \chi_m & i\eta_{Tm} \sin \chi_m \\ i\eta_{Tm}^{-1} \sin \chi_m & \cos \chi_m \end{bmatrix} \begin{pmatrix} E_{Tm} \\ H_{Tm} \end{pmatrix}, \quad (87)$$

while the matching matrix across the material boundary, on the other hand, takes the trivial form

$$\begin{pmatrix} E_{Tm-1} \\ H_{Tm-1} \end{pmatrix} = \begin{pmatrix} E'_{Tm} \\ H'_{Tm} \end{pmatrix} = \begin{bmatrix} 1 & 0 \\ 0 & 1 \end{bmatrix} \begin{pmatrix} E'_{Tm} \\ H'_{Tm} \end{pmatrix}. \quad (88)$$

Further information about the treatment of (partial) incoherence (for arbitrary positions of the optically thick layers), surface roughness, and directional-diffuse light transfers can be found in references [244–247].

In subsection 2.3.2, the total (amplitude) reflection coefficient  $r_{\text{tot}}$  of a two-interface system (single-layer thin-film coating at the planar interface between two materials) was calculated as the (coherent) sum of an infinite number of contributions generated by an increasing number of back and forth reflection events within the thin layer before out-coupling again towards the incident medium, (coherently) contributing to the reflected light. While this approach, in principle, can also be employed for studying more complex multilayer systems, carrying out such calculations is quite cumbersome even for rather simple systems such as a double-layer antireflective coating. Using the TMM, on the other hand, reduces this effort to a series of matrix multiplications which are a lot more convenient to handle. An explicit demonstration of the equivalence of both these routes can be found in [248].

## 2.5.2 Monte-Carlo Ray-Tracing Simulations

Ray-tracing methods are numerical calculation schemes designed for computing light-matter-interactions on the basis of ray optics. Prominently, ray-tracing plays an important role in computer graphics rendering. Instead of photorealistically rendering the visual appearance of objects as seen from certain perspectives and under variable illumination conditions, ray-tracing-based calculations are also commonly employed by scientists and engineers as a facile ray-optics-based simulation method for designing and optimizing, for example, lens systems for

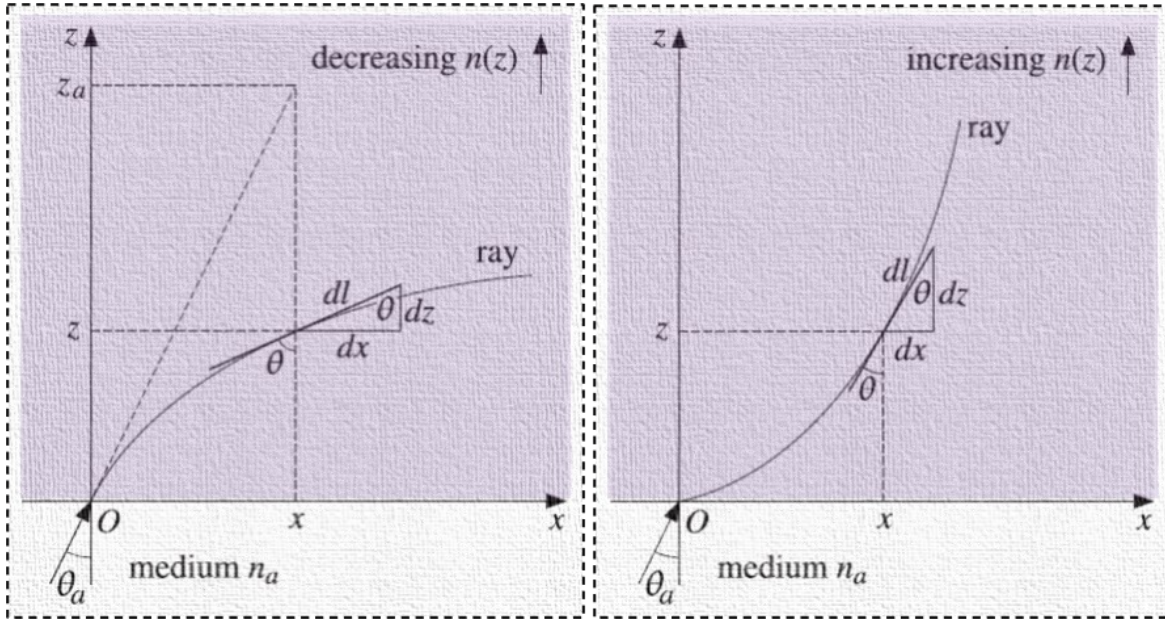


**Fig. 2.22:** Ray propagation in materials with gradually changing refractive indices. Adapted from reference [108], © 1996-2016 Sophocles J. Orfanidis. All Rights Reserved.

imaging purposes. Within the scope of this thesis, however, ray-tracing simulations are mainly utilized for analyzing the reflection and in-coupling properties of visible light interacting with disordered, microstructured surfaces.

In the short-wavelength (or high-frequency) limit, Maxwell's equations can be re-expressed, resulting in a simplified description of light as non-oscillatory entities commonly called rays. The propagation of light rays is governed by the ray equation

$$\frac{d}{dl} \left( n \frac{d\vec{r}}{dl} \right) = \vec{\nabla} n, \quad (89)$$

where  $dl = (d\vec{r} \cdot d\vec{r})^{1/2}$  describes an infinitesimal increment along the ray's propagation direction (see figure above), and  $n$  denotes the refractive index at the respective location. A detailed derivation of the ray optical description of light from Maxwell's equations in the high-frequency limit can be found, for example, in references [103, 108]. In a homogeneous medium, the refractive index is constant, which leads to

$$\frac{d^2\vec{r}}{dl^2} = 0. \quad (90)$$

For constant refractive indices, rays propagate along straight lines. The ray equation implicitly fulfills Fermat's principle of minimized travel time between two points in space. Further, at an interface between two homogeneous materials of different refractive indices, the ray changes its propagation direction following

Snell's law. For materials with continuously varying refractive index  $n(\vec{r})$ , light rays will propagate along curved trajectories, bending away from the lower index regions and toward the higher index regions, as illustrated on the previous page. Further information about ray propagation in materials with graded refractive indices can be found in various textbooks, such as [103, 108].

If a ray is propagating through a lossy (non-magnetic) material defined by the refractive index  $\tilde{N} = n' - in''$  (nonzero extinction coefficient  $n''$ ), the ray's power will exponentially decrease with the distance traveled following Lambert-Beer's-Law, which can be deduced from expressing the intensity as the time-averaged Poynting vector assuming a homogeneous plane wave  $\vec{E}(\vec{r}, t) = \vec{E}(\vec{r})e^{i\omega t}$  with parallel phase propagation and attenuation vectors ( $\vec{k} = k \cdot \hat{k} = \omega/c_0 \tilde{N} \cdot \hat{k} = \omega/c_0 n' \cdot \hat{k} - i \omega/c_0 n'' \cdot \hat{k}$ , see also section 2.2)

$$\vec{E}(\vec{r}) = \vec{E}_0 e^{-i\vec{k}\vec{r}} = \vec{E}_0 e^{-i\frac{\omega}{c_0} n' z} e^{-\frac{\omega}{c_0} n'' z}.$$

The electric field amplitude, therefore, attenuates  $\sim e^{-\frac{\omega}{c_0} n'' z}$ . Since light rays carry irradiance  $I$ , the absorption of light rays propagating through lossy materials can be deduced from the time-averaged Poynting vector  $\vec{S} = \vec{E} \times \vec{H}$  via

$$\begin{aligned} I = \langle \vec{S} \rangle &= \frac{1}{2} |\Re[\vec{E}(\vec{r}) \times \vec{H}^*(\vec{r})]| = \frac{1}{2} |\Re[\vec{E}(\vec{r}) \times y^*(\hat{k} \times \vec{E}^*(\vec{r}))]| = \frac{1}{2} |\Re[(y^*(\vec{E} \cdot \vec{E}^*)\hat{k} - (\vec{E} \cdot \hat{k})\vec{E}^*)]| \\ &= \frac{1}{2} |\Re[y_0 \tilde{N}^*(\vec{E} \cdot \vec{E}^*)\hat{k}]| = \frac{y_0}{2} |\vec{E}|^2 |\Re(\tilde{N})| = \frac{n'}{2} (\epsilon_0/\mu_0)^{1/2} |\vec{E}|^2 \\ &\Rightarrow I \propto |\vec{E}(\vec{r})|^2 = |\vec{E}_0|^2 e^{-2\frac{\omega}{c_0} n'' z} = |\vec{E}_0|^2 e^{-\kappa z}. \end{aligned}$$

Here, the absorption coefficient  $\kappa := 2 \omega/c_0 n''$  was introduced. The intensity, therefore, decreases  $\sim e^{-\kappa z}$  (while the electric field amplitude attenuates  $\sim e^{-\frac{\kappa}{2} z}$ ).

The core principles of a ray-tracing scheme can be described as follows. Materials shall (at first) be assumed to be optically homogeneous and isotropic and are characterized by their complex refractive indices. All objects' surfaces are assumed to be optically smooth. At each interface, a ray is split into a transmitted (refracted) and a reflected ray. The power of each partial ray is calculated via Fresnel's equations. Their propagation directions are determined via Snell's law and the law of reflection. When propagating through the bulk of a lossy/absorbing material, the power a ray carries is exponentially attenuated following Lambert-Beer's-Law. On this basis, a simple (forward) ray-tracing scheme may be conducted as follows:

- 1) Modeling the geometries and optical properties of all objects (including the background material) and object surfaces.

- 2) Definition of the starting points  $(x,y,z)$ , propagation directions (in the form of directional cosines, for example), and initial power values for all rays that shall be traced.
- 3) Running the tracing-loop: For each ray, it is determined if and where an interface with a discontinuous change in (complex) refractive index is intersected.

The tracing-loop of a ray is terminated, if

- 1) the ray does not intersect with any of the modeled objects anymore (and therefore escapes into infinity)
- 2) the ray is fully absorbed at an interface/object surface
- 3) while propagating through an absorbing medium, the ray's power sinks under a certain (predefined) threshold
- 4) the power that a ray carries drops below this power-threshold through a large number of splitting events at interfaces
- 5) the ray surpasses a certain (predefined) maximum number of interactions

The last condition makes sure that rays that are trapped/confined within a certain volume, for example, by TIR and/or perfect (lossless) mirrors, do not lead to an infinite computation time. Comprehensive and detailed explanations concerning the mathematical treatment of these steps, the implementation of 3D shapes, and the various interactions in 3D space can be found in references [249, 250].

In order to feasibly trace the ray paths for light sources with rather complex shapes and (possibly inhomogeneous) emission properties, both regarding the angular distribution of emitted rays as well as their spectral distribution, a probabilistic approach for assigning ray properties (instead of explicitly defining the initial properties of each light ray manually) is needed. Such algorithms, which rely on random number generators to properly initiate ray properties, are commonly called Monte-Carlo ray-tracing methods.

The results of a ray-tracing simulation might be, for example, the total reflectance/transmittance (specular + diffuse) for parallel light incident on a microtextured surface, the areally resolved irradiation/illumination on a specific surface (screen), or an optimized curvature of a parabolic mirror for focusing sunlight, for example in a solar tower configuration.

Ray-tracing can be performed wavelength-dependent. Although the concept of light rays is based on the high-frequency approximation of Maxwell's equations and the resulting light rays are non-oscillating entities that describe the propagation of radiant flux through space rather than the oscillating E- and B-fields

that make up an electromagnetic wave, it nevertheless makes sense to assign a wavelength to each of the rays to trace. If the optical parameters (complex refractive index) of the materials involved are also defined wavelength-dependent, this rather arbitrary assignment of wavelengths to light rays obtains a sensible physical meaning. Following Snell's law, Lambert-Beer's law, and the Fresnel equations, which are all determined by the complex refractive indices of the materials involved, rays of different wavelengths thereby might deviate in their paths. Similarly, it might seem arbitrary to introduce a phase for light rays, but some coherent effects (which don't include diffraction), like the interference pattern that forms when coherent and collimated light passes through a Michelson-interferometer, can also be numerically investigated via ray-tracing based approaches. Furthermore, ray-tracing algorithms also need to faithfully track the polarization state of rays through the 3D models in order to correctly reproduce the polarization-dependent reflection and transmission coefficients described by the Fresnel equations. This can be achieved by assigning each ray a set of Stokes parameters  $S_1$ ,  $S_2$ ,  $S_3$  and  $S_4$  (Jones vectors and polarization ellipse parameters also possible), which defines the initial polarization state of each ray. Generally, if a ray obliquely intersects an object's surface, it needs to be separated into an s-polarized and a p-polarized component in order to apply Fresnel's equations to accurately trace a light ray across an interface.

Instead of splitting the light rays into reflected and transmitted components at sharp material interfaces, ray-tracing simulations can also follow a probabilistic approach where the power of each ray is kept constant, and at material interfaces, the Fresnel equations are used to determine the probabilities for reflection and transmission (the ray-tracing simulations described in chapters 6 and 10 were conducted this way). This approach requires a larger number of (initial) rays to reach convergence.

For all ray-tracing simulations included in this thesis (see chapters 6 and 10), only lossless materials were modeled in LightTools. Absorbing materials were only included in the form of coating files, which were calculated via TMM. It should be noted that in ray-tracing simulations, it is standard practice to consider solely the real part of any medium's refractive index for determining the changes in a ray's propagation direction at an interface between two media (often adequate at optical wavelengths) and absorption is accounted for by reducing the intensity or weight of the ray in accordance with its propagation distance [130].

Lastly, it should be noted that combinations of TMM calculations and ray-tracing simulations can be exploited to numerically study optical systems which

simultaneously rely on multilayer interference effects as well as on light interacting with micron-sized structural features governed by the laws of geometrical optics. For example, the combination of microstructured light-harvesting layers on top of thin-film solar cells makes it necessary to consider both ray-optical interactions and multilayer thin-film interference within a single framework (see chapter 6) [251–254].

### 2.5.3 Software

Transfer-matrix-calculations for analyzing the optical properties of thin-film layer stacks were performed by using ellipsometry software WVASE (J. A. Woollam Co., USA) [255]. All (3D Monte-Carlo) ray-tracing simulations included in this dissertation were performed using the commercial software LightTools (Synopsys Inc., USA) [256]. By using Matlab (The MathWorks, Inc., USA) [257] code to control LightTools via its application programming interface (API), which uses the Microsoft Windows standard Component Object Model (COM) interface, all 3D model construction and simulation procedures, as well as the entire data read-out and data post-processing discussed in chapters 6 and 10, are automatized.

---

## 3 Photonic Structures Found in Living Nature

---

Throughout living nature, a wide variety of photonic structures can be found which are able to manipulate light in various unique ways, resulting in distinctive and exceptional visual appearances. In addition to exceptionally dark, velvety black and brilliantly white coloration, photonic biostructures are also capable of, for example, producing efficient selective reflection properties for narrow spectral regions, resulting in incredibly bright colors. Even metal-like optical properties can be observed in some species. This chapter aims at providing an overview of the various types of photonic structures found throughout our planet's flora and fauna.

The following chapter first provides an overview of light-manipulating micro- and nanostructures found in animals (section 3.1) and plants (section 3.2). Since this thesis is focused on transferring photonic biostructures into PV devices, the subcategory of reflection-minimizing structures is of special relevance. Therefore, the following chapter divides the vast topic of photonic biostructures into the categories of **structural-color**-producing and **antireflective** structures, discussed in separate subsections.

### 3.1 Optical Micro- and Nanostructures in Animals

#### 3.1.1 Structural Coloration in Animals

Almost 200 years before J. Clerk Maxwell published his revolutionary theory of electromagnetism [133], the pioneering works of Robert Hooke [258] and Isaac Newton [259] on the theories of light and the coloration of objects already established that not all colors found in nature can be explained by light-absorbing pigments. Through studying the brilliantly colored tail feathers of male peacocks, Newton deduced that even transparent materials can, under some circumstances, produce color effects that are closely linked to how this non-absorbing material is structured and spatially arranged/assembled on small length-scales [259]:

*'(...) their Colours arise from the thinness of the transparent parts of the Feathers; that is, from the slenderness of the very fine Hairs, or Capillamenta, which grow out of the sides of the grosser lateral Branches or Fibres of those Feathers.'*<sup>1</sup>

---

<sup>1</sup> from page 251 of the 4th edition of 'Opticks', published in 1730.

By the beginning of the 20<sup>th</sup> century, numerous examples of structural coloration (and its combination with absorbing pigments) have been identified throughout the animal kingdom. Although by then, Maxwell's theory had already equipped scientists with the basic tools necessary to grasp the (in most cases) wave-optical effects that lead to structural color effects, the resolution of the best microscopes (diffraction-limited light microscopes) available back then still prohibited a direct observation or morphological study of these micro- and nanostructures. This often led to the simplistic assumption that all structural coloration found in living nature can be attributed to the same basic physical effects, until C. W. Mason's thorough (light-microscopy-based) studies of structural colors in bird feathers [260, 261] and in insects [262–264] for the first time gave a surprisingly accurate overview of the physical basis, even though a direct observation of the structures he studied was still impossible. With the introduction of electron microscopy to biology research in the early 1940s, Anderson and Richards then pioneered the microscopical observation and analysis of structural-color-producing (subwavelength) architectures of insects like *Morpho* butterflies and iridescent beetle species [265], providing the first direct observation of some of Mason's predictions. Over the following decades, a wide variety of intricate photonic biostructures from all throughout the plant and animal kingdoms, including numerous species of beetles [266–268], butterflies [269–273], birds [274, 275], fish [276], spiders [277], and even algae [278], have been explored. Despite this rich supply of photonic biostructures taken from all corners of our living environment and serving various purposes, one major commonality among all these cases can still be deduced: Photonic structures found in living beings rely on hierarchical (multi-scale) structures in order to exploit and combine the different optical effects caused by the interaction of light with structural features which are either small, large or comparable to its wavelength. The structures can include complex architectures (like microlenses, multilayered thin-film-systems, diffraction gratings, helicoidally stacked microfibril-multilayer systems, photonic crystals, scattering layers, and more) on several different length-scales. Further, each of the sub-structures can be composed following either a perfectly ordered, quasi-ordered, or a disordered arrangement. Furthermore, regular and irregular components are also often combined, which enables the creation of even more unique visual appearances. The following paragraphs provide a brief overview of structural coloration in animals and plants.

The wings of many butterfly species are either completely or partly colored by specialized optical nanostructures [269–273]. Two such examples are given in Fig. 3.1 A) and B). In addition to the untreated wings of *Morpho rethenor* and *Cymothoe*

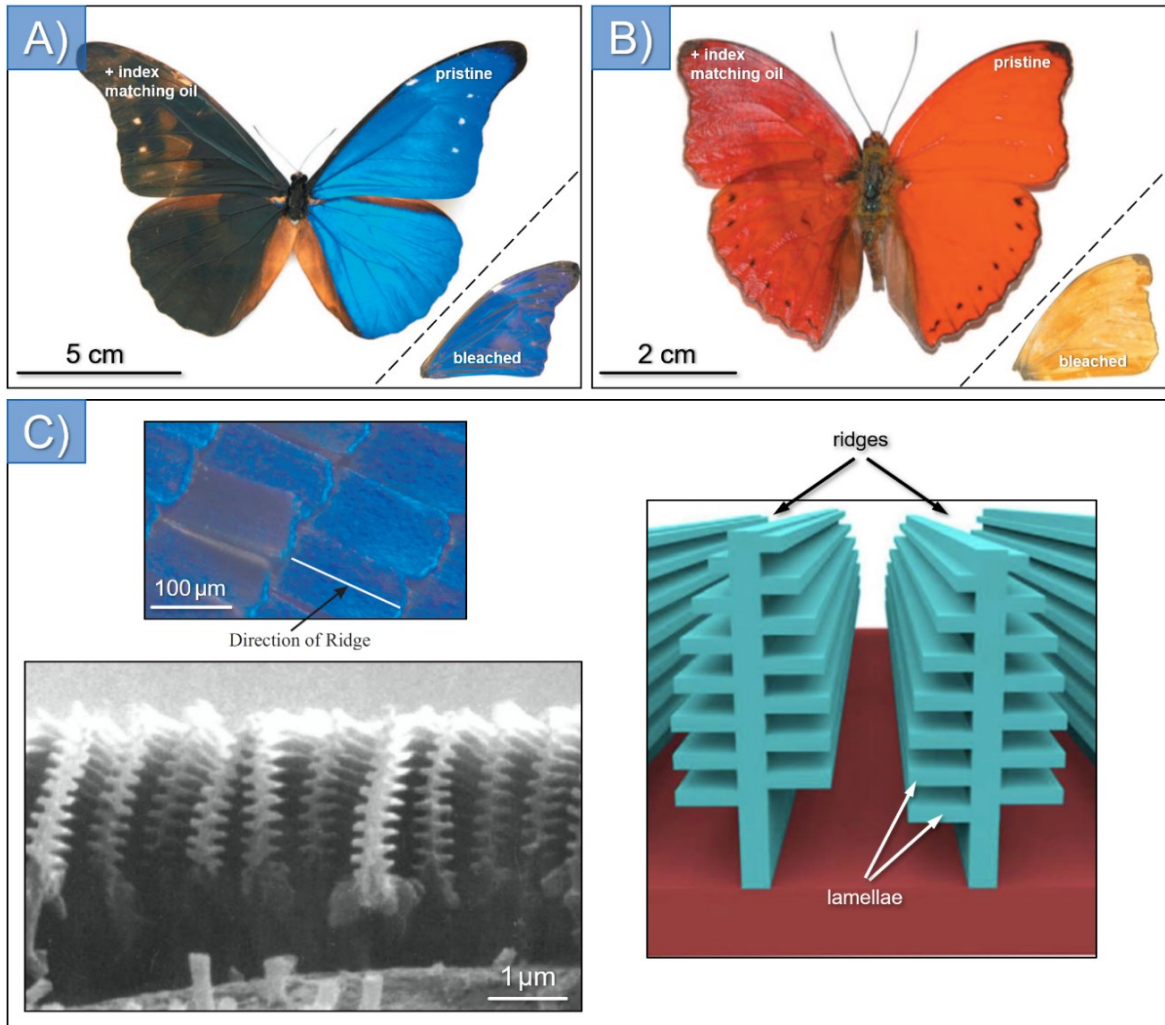


**Fig. 3.1:** Structural vs. pigment-based coloration in butterflies. Photographs of A) a male *Morpho rethenor* butterfly and of B) a male *Cymothoe sangaris* butterfly, where the insects' right wings in both pictures are in their natural state, while their left wings have been saturated with an index-matching liquid to destroy structural coloration. Additionally, photos of a bleached wing (to deactivate the pigments) of either species are included as insets. In C), the picture on the upper left shows an image of the dorsal side of a *Morpho rethenor* wing obtained via light microscopy. On the lower left of C), a cross-sectional SEM image shows a scale of a *Morpho rethenor* wing with its ridged architecture. On the right-hand side of C), this ridged structure is schematically depicted as a simplified 3D drawing (neglecting some of the structural irregularities that are clearly present in the SEM micrograph). The images in A) and B) as well as the optical micrograph in C) were adapted from reference [279], © 2009 American Association of Physics Teachers. The schematic in C) was adapted with permission from reference [280], © 2015 The Authors. The SEM image in C) was adapted with permission from reference [281], © 2008 IOP Publishing Ltd.

*sangaris* in their natural state, specimens that have been either bleached (to selectively eliminate the colors caused by pigmentation), or treated with an index-

matching oil (to selectively eliminate the structure-based colors), are depicted. While the bright red color of *Cymothoe sangaris* is mostly caused by pigments and only slightly intensified by structural optical effects, the exact opposite applies for *Morpho rethenor*'s striking blue complexion. The multi-scale photonic structure responsible for the wing coloration of *Morpho rethenor* is shown in Fig. 3.1 C). Their wings are covered with a single layer of chitin scales, which exhibit a dense concatenation of (longitudinal) high-AR ridges of irregular height and curvature. At subwavelength length-scales, each of these ridges shows a further level of complexity, namely a lamellar sub-structure, which forms a chitin-air multilayer system. The particularly bright and angle-stable blue color of *Morpho rethenor* wings is caused by the ensemble of optical effects resulting from the interaction of (sun)light with these various structural components. In short, the main effects taking place are [270]: The high reflectance over a narrow spectral range is caused by interference effects in the multiple layers of lamellae. The irregular concatenation of ridges causes broadened diffraction effects that increase the angular stability of this uniformly colored light. The pigmentation further increases the color brightness by absorbing erroneous green-red light.

In addition to *Morpho* butterflies, many other genera include structurally colored varieties of butterflies. Although the structure of *Morpho* wings (Fig. 3.1 C) might be the most famous example of photonic structures in butterflies, it should not be assumed that all butterfly structural colors are necessarily caused by similar 3D architectures or even rely on the same basic (combination of) optical principles (like thin-film interference or diffraction). In contrast to the *Morpho*'s bright blue, the green coloration of both *Callophrys rubi* (Fig. 3.2 A) and *Cyanophrys remus* butterflies, for example, is caused by a 3D photonic crystal structure (resembling a gyroid structure) located underneath the surface of the scales, which is segmented into several highly ordered domains with varying domain orientations, similar to the crystallites in a polycrystalline material [282–285]. The *Callophrys rubi* butterfly, together with an optical micrograph of a single wing scale and an SEM micrograph of its subwavelength morphology, is shown in Fig. 3.1. Butterflies commonly rely on such a combination of ordered and disordered structures on different length scales to realize their structural coloration [286]. Besides butterflies, similar types of structures are also found on the wings of some moth species [269].

A fundamentally different example of structural animal coloration can be found in scarab beetles of the genus *Cyphochilus*. These beetles are known for their brilliantly white exoskeleton, as depicted in Fig. 3.3 for *Cyphochilus insulanus*. Their whiteness

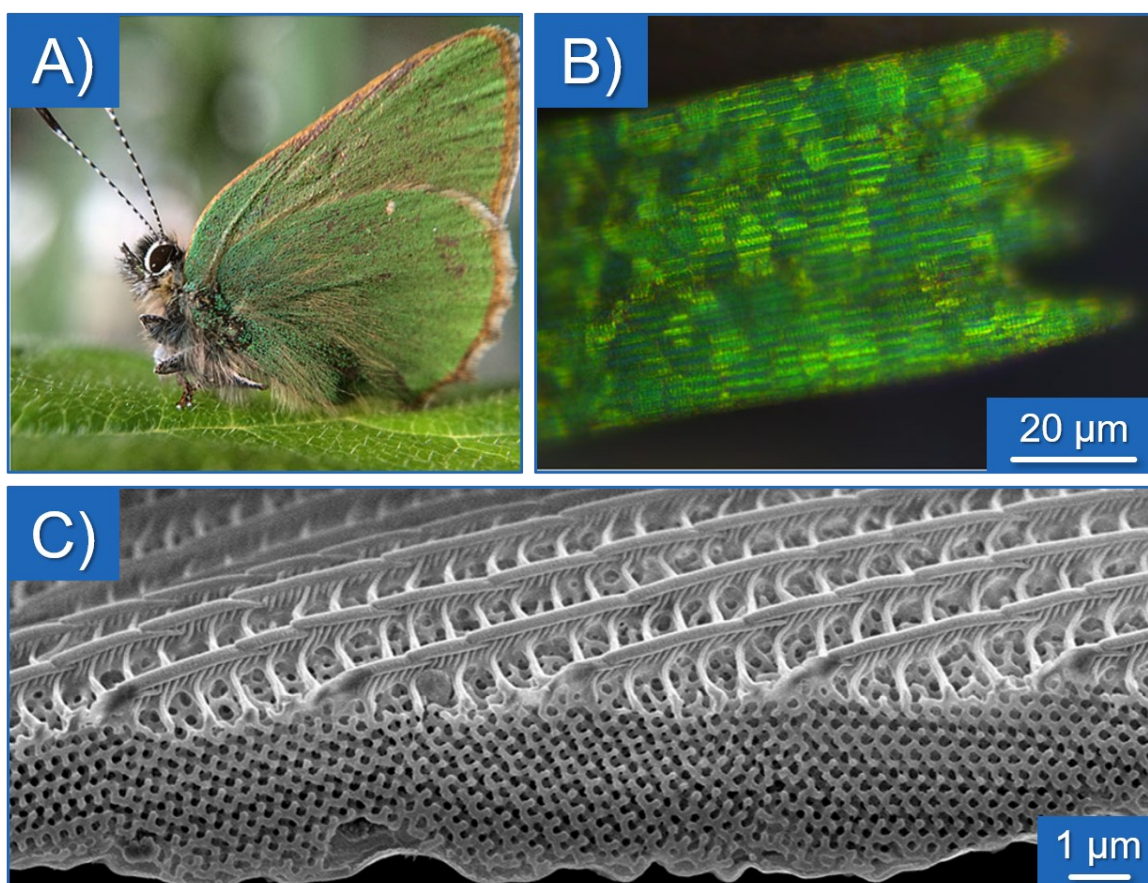


**Fig. 3.2:** Structural coloration of a *Callophrys rubi* butterfly, also known as the green hairstreak. A) Photograph of *C. rubi*. B) Optical micrograph of a green wing scale of *C. rubi*, the scale's bright green color shows slight variations in hue, which are caused by the varying photonic crystal orientations between individual domains. C) SEM image of green wing scale. Underneath the ribbed upper surface, a gyroid photonic crystal structure separated into crystallite domains forms the bulk part of the scale. Five of these domains are included within the picture. Adapted with permission from reference [284], © 2017 The Authors.

is based on wavelength-independent (multiple) incoherent scattering rather than coherent effects (like multilayer Bragg reflectors). A surface is perceived as white if it diffusely reflects incident light of all visible light wavelengths. Although highly reflecting surfaces can be achieved via coherent effects for single wavelengths, it is impossible to exploit a coherent approach for the whole visible spectrum simultaneously. Instead, whiteness can be generated through incoherent scattering events in a disordered and non-absorbing system. Such a scattering layer might, for example, consist of titania (TiO<sub>2</sub>) nanoparticles which are (randomly) dispersed in a transparent (polymeric) host material. If the scattering layer is thick enough to allow a sufficient number of scattering events, all visible light that travels through the layer will eventually be redirected and diffusely backscattered. The large

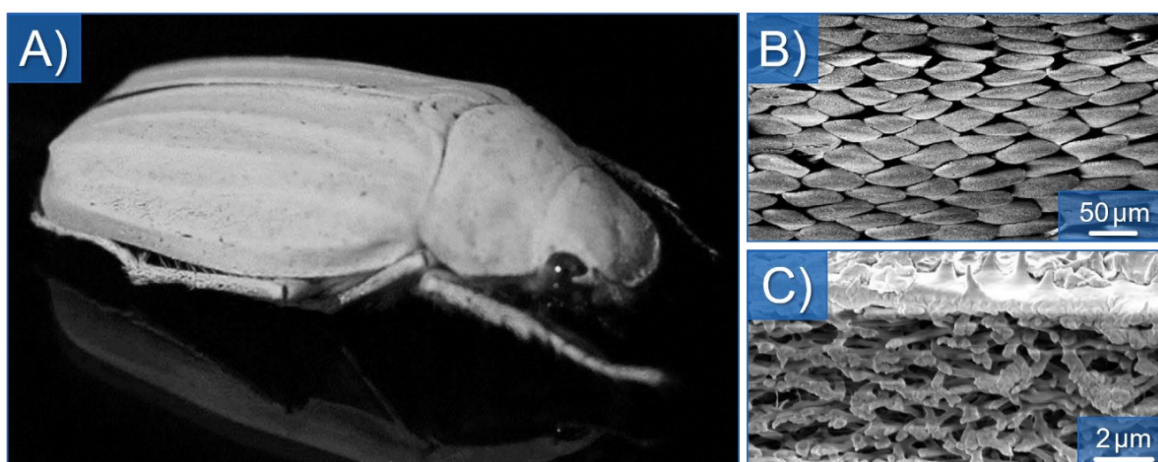


**Fig. 3.3:** Exceptionally white scarab beetle *Cyphochilus insulanus*. A) Photographic depiction of *Cyphochilus insulanus*. This intense whiteness is caused by multiple light scattering events caused by irregular air inclusions within the scales that cover its body. These scales are shown in B) and C) by SEM images at two different magnification factors. Adapted with permission from reference [287], © 2017 The Authors.

contrast in refractive index between host material and  $\text{TiO}_2$  scattering particles leads to the efficient scattering of light for all visible light wavelengths. However, with decreasing refractive index contrast between host and scattering particles, the layer thickness needs to be increased in order to still achieve comparable whiteness. In exoskeletons of *Cyphochilus* beetles, the scattering events occur at irregularly shaped (and interconnected) air voids within the porous chitin material that comprise their scales. Astonishingly, even though the exoskeleton of *Cyphochilus insulanus* consists of porous chitin and therefore exhibits a considerably smaller refractive index contrast compared to titania-based scattering layers, these beetles are still able to produce their brilliant whiteness in scattering layers with a thickness of only  $\approx 5 \mu\text{m}$ , whereas synthetic systems based on nanoparticles typically would need a thickness of at least two orders of magnitude larger in order to achieve a comparable whiteness [288]. Compared to conventional white uncoated wood-free papers, which consist of random networks of bleached cellulose fibers, the *Cyphochilus* beetles' whiteness measures 92% of the paper's value but at only 4% of the paper's thickness [288]. Due to this incredible efficiency in producing white coloration (with only a single material and air voids), understanding and artificially recreating the brilliant whiteness of *Cyphochilus* beetles has caught the attention of an increasing number of researchers over the past decade [288–292]. It is worthy of note that brilliant whiteness in animals can also be found in *Pieris rapae* butterfly wings [293].

Multiple species of scarab beetles famously exhibit a unique type of structural coloration, which gives them a remarkable metal-like appearance. This unusual look is probably most prominently embodied by the golden scarab beetle *Plusiotis resplendens*, depicted in Fig. 3.4 A). The various metallic appearances of scarab beetles are caused by the helicoidal architecture of their cuticle [266]. A schematic depiction of such a helicoidal multilayer structure is given in Fig. 3.4 F). As early as 1911, A. A. Michelson was probably the first to notice the unique property that light reflected from scarab beetles is (left-)circularly polarized, even for normal incidence of polarized as well as natural incident light [294]. After Michelson's discovery, several authors noticed that the distinctive optical properties produced by the helicoidal structure in the scarab beetle's cuticle are very similar to the reflection properties of liquid crystals based on cholesteryl derivatives [295–297]. It was theoretically shown by de Vries in 1951 that helicoidal multilayer systems can act as narrowband wavelength-selective reflectors if the pitch (= distance between two layers with identical orientation) is comparable to the wavelengths of visible light. A helicoidal stack with a pitch  $p$  and a mean refractive index of an individual layer  $n$  will then reflect circularly polarized light (with its handedness being defined by the handedness of the helicoid) with a wavelength of  $\lambda = n \cdot p$  [298]. The following paragraphs briefly summarize a few more noteworthy examples of structural coloration found throughout various species of animals:

A number of mammals exhibit structural coloration of parts of their skin, which is caused by collagen fibers assembled into a 2D quasi-ordered photonic crystal [299].

Some tarantulas exhibit blue structural coloration with remarkable angular stability. Astonishingly, the different types of tarantula show an unexpected variety of different nanostructures that all lead to similar blue iridescence [300]. Other cases of structural coloration in spiders include, for example, male peacock spiders (*Maratus*, Salticidae), which exhibit structurally colored body parts in a variety of colors at once, including a part with a structurally assisted super black [277, 301].

A dense array of triangular hairs gives Saharan silver ants the ability to forage even under the extreme heat and solar irradiance of the African desert. By means of TIR, these hairs cause a unique cooling mechanism by both strongly reflecting visible and near-infrared radiation (responsible for the silvery appearance of these ants) and simultaneously increasing emissivity in the mid-infrared spectral region to enable an efficient radiative heat dissipation [302, 303].

In peacock feathers, coloration is assisted by structural colors created by 2D

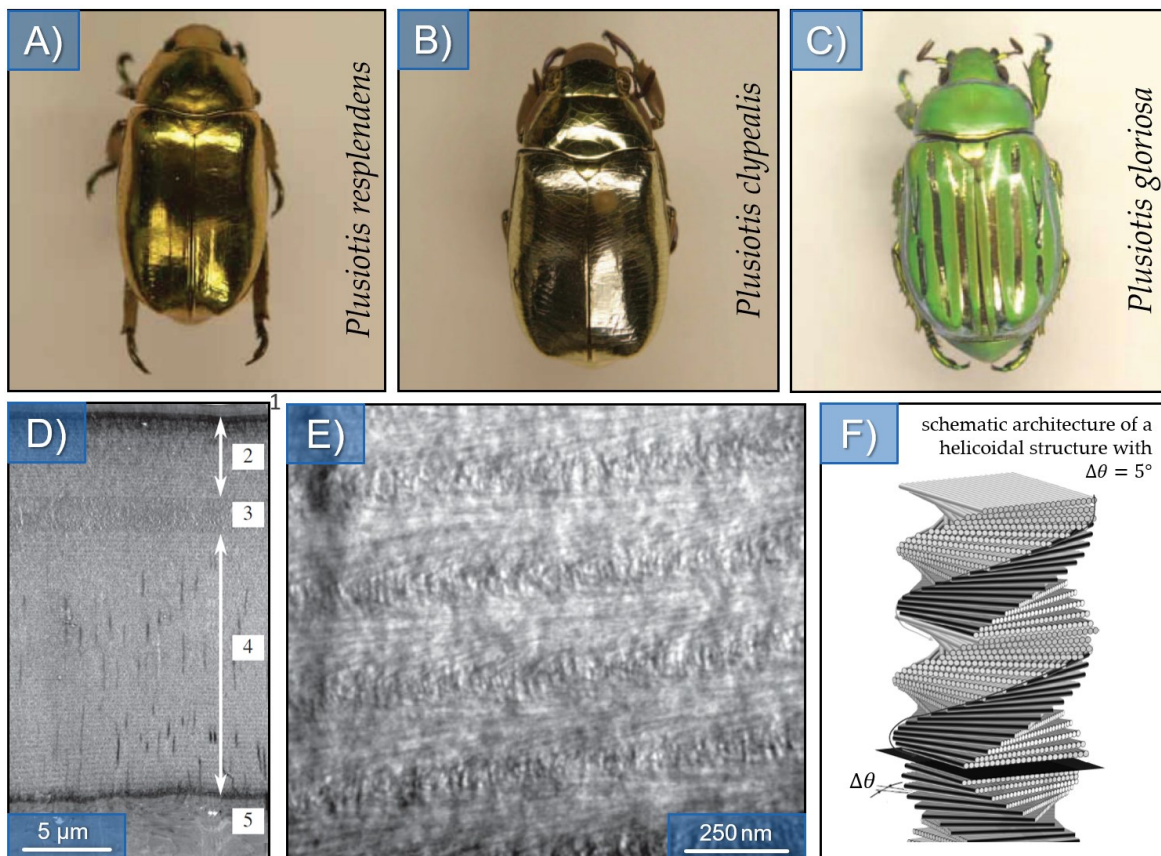


**Fig. 3.4:** Scarab beetles with metal-like structural coloration. A)-C) Photographic depictions of three species of scarab beetles (*Plusiotis resplendens*, *P. clypealis*, and *P. gloriosa*) exhibiting structural coloration. Their distinctive metal-like visual appearances are caused by the helicoidal architecture of their cuticles. Furthermore, the light reflected from such scarab cuticles will always be (partially) left-circularly polarized, even for both extreme cases of either fully polarized or unpolarized incident light. D) depicts a cross-sectional TEM image through the outer part of a *P. resplendens* cuticle, distinguishing the following regions: 1=epicuticle, 2=upper helicoid, 3=unidirectional layer, 4=lower helicoid, 5=endocuticle (with regions 2-4 forming the exocuticle). Obliquely cutting through such a helicoidal section reveals a characteristic pattern of filament orientations, as is exemplified in E) by a TEM micrograph of a *P. resplendens* cuticle. In F), a 3D sketch illustrates how such helicoidal structures are formed by stacking individual filament planes on top of each other while keeping sure that each new layer is rotated by a fixed angle compared to the previous layer. A)-C) were reprinted with permission from reference [304], © 2006 Optical Society of America. D) and E) were adapted with permission from reference [305], © 2017 The Authors. Published by the Royal Society. All Rights Reserved. F) was adapted with permission from reference [306], © 2019 Elsevier Ltd. All Rights Reserved.

photonic crystals [307]. Furthermore, black magpie feathers are also visually enhanced with iridescent colors [308]. Non-iridescent, angle-stabilized structural

colors which rely on quasi-ordered sub-wavelength textures have also been described [274].

Structural colors are also commonly found in many types of jellyfish, like the 2D photonic crystals that cause iridescence in the comb-jellyfish *Beroë cucumis* (Ctenophora) [309, 310]. Further examples of structurally colored marine lifeforms include squids, cuttlefish, and octopuses [311], as well as sea mice [312].

Remarkably, beetles of the genus *Pachyrrhynchus* show structurally colored cuticles of varying color, spanning the entire spectrum from blue → greenish-yellow → yellow → orange → red. Their colors are caused by a 3D photonic (poly) crystal resembling an inverse opal structure [313]. In 2003, a structural color based on an opal-like photonic crystal was, for the first time, discovered in an animal (*Pachyrrhynchus argus* beetle) [314].

It is further worth mentioning that structural coloration in animals was already quite common in prehistoric times, as becomes obvious from various fossils including, for example, insects like wasps [315], springtails [316], or weevils [317]. Researchers have even focused on reconstructing the original colors of fossilized beetles [267] as well as animal feathers [318].

In more recent years, it has been shown that the active color change that chameleons are famous for is produced by a dynamic photonic crystal system, where active tuning of a lattice of guanine nanocrystals within a thick superficial layer of so-called dermal iridophores [319]. Another example of a tunable structural coloration can be found on the fresh water fish neon tetra and was also recently found to be photonic crystal-based [276].

Interestingly, it has been suspected at least as early as 1909 that the wide-spread iridescent properties found throughout the animal kingdom, rather than serving signaling purposes, might help animals to better hide from predators [320]. Although this might seem counterintuitive, recent studies substantiated this idea by showing that diffraction effects and multilayer-interference-based iridescence might confuse predators, for example, by impairing shape-recognition [321, 322].

#### 3.1.2 Antireflective Structures in Animals

Next to structure-based coloration, the animal kingdom also offers micro- and nanotextures that are able to effectively suppress surface reflectance over a wide

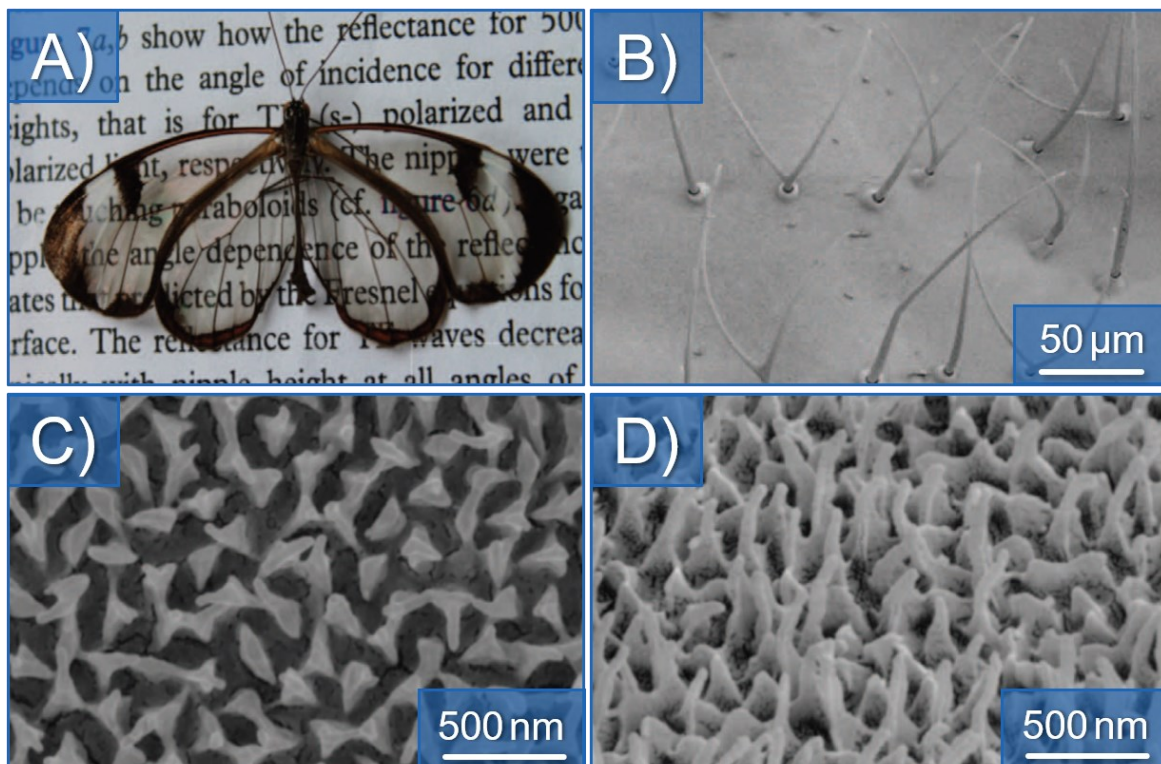


**Fig. 3.5:** Highly transparent wings of the glasswing butterfly (*Greta oto*). A) Photographic depiction of *Greta oto* atop an opened book to highlight the high transparency and low haze of most of its wings. B) SEM image of the transparent wing part with a low magnification factor. Between the individual hairs, the wing surface exhibits a densely packed and disordered array (or network) of sub-wavelength nanopillars, which is shown C) in a top-view and D) in a tilted-view image. Adapted with permission from reference [323], © 2015 Nature Publishing Group, a division of Macmillan Publishers Limited. All Rights Reserved.

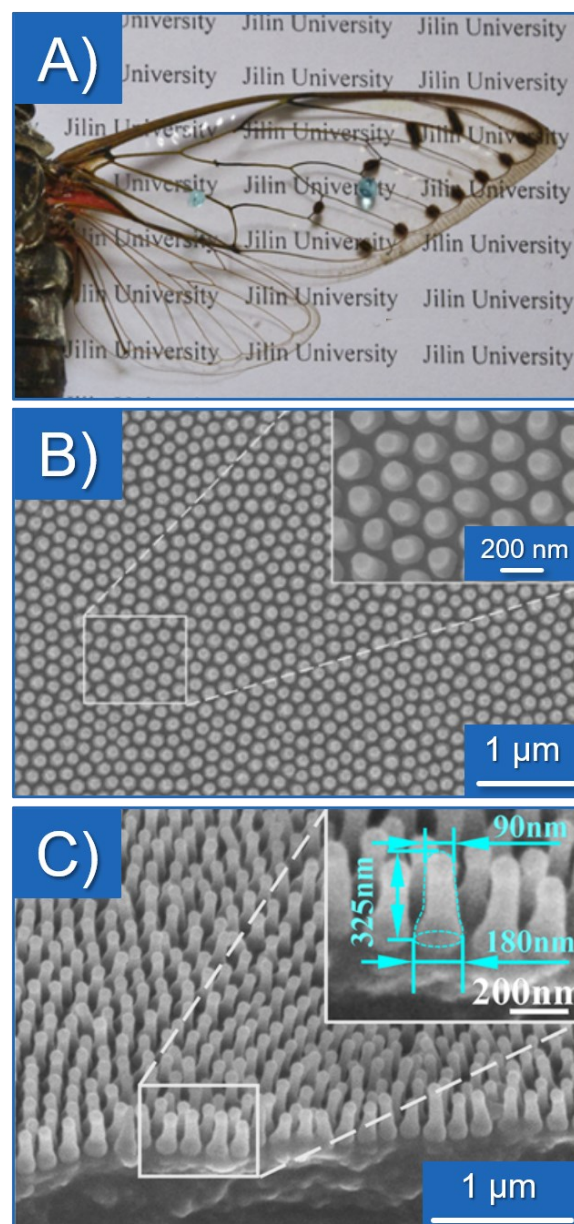
range of angles of incidence and wavelengths. Prominently, such antireflective surfaces are, for example, commonly found on the wings and/or eyes of many species of butterflies and moths [324].

Glasswing butterflies (*Greta oto*), for example, exhibit extraordinarily transparent patches on their wings (see photograph in Fig. 3.5). A densely packed array of disordered subwavelength nano-protrusions on both sides of these wings has been identified to enable this stealthy appearance [323, 325, 326].

The high transparency of the wings of *Megapomponia intermedia* cicadas, on the other hand, is caused by a highly ordered (hexagonal) and densely packed array of cone-shaped subwavelength nano-protuberance [327, 328], which are shown in Fig. 3.6. Moreover, this type of nanostructure can also be found on the transparent wings of a hawkmoth (*Cephonodes hylas*) [329, 330], also shown in Fig. 3.7. Transparent wings help such insects to better blend into the environment in order to hide from predators.

A similar type of highly ordered (at close distances) subwavelength nipple array was already observed decades earlier by the pioneering electron microscopical studies on the corneal surface of many insects' compound eyes, such as various moths and butterflies [331]. Similar subwavelength nano-nipple arrays can also be found on the compound eyes of many other insects, such as flies and mosquitos [160]. The subwavelength protuberances found on many insect eyes and on the transparent wings of many insects are commonly called corneal nipples, and their antireflective quality is based on the gradual change in refractive index that can be described by means of effective medium theory [332, 192], as introduced in the previous subsection 2.3.4. Next to improving the night-vision capabilities of nocturnal insects by enabling an almost lossless photon-collection, the more significant biological purpose of the corneal nipple array might be the camouflage effect caused by minimizing the amount of light that is reflected from their compound eyes back into the environment, making it more difficult for predators to spot the insect. This camouflage might be of special importance for insect species that are inactive during daytime and, therefore, especially vulnerable to predators due to their inability to escape if attacked during their resting phase [331, 333–337]. As shown in the SEM images of a silkmoth compound eye in Fig. 3.8, corneal nipple antireflective structures

**Fig. 3.6:** Highly transparent cicada (*Megapomponia intermedia*) wings. A) Photograph of a *M. intermedia* wing. B), C) Top-view and oblique view SEM images of the highly ordered subwavelength nipple array responsible for the transparent appearance of *M. intermedia* wings. Adapted with permission from reference [328], © 2019 American Chemical Society.



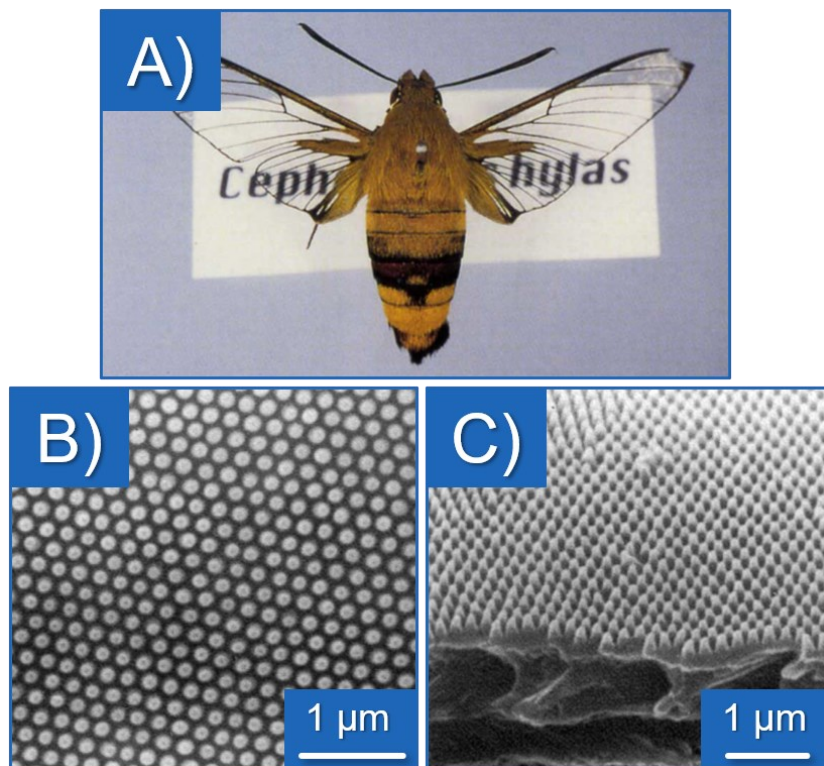


**Fig. 3.7:** Highly transparent wings of hawkmoths (*Cephonodes hylas*). A) Photograph of a hawkmoth *C. hylas* wing. B), C) Top-view and oblique view SEM images of the highly ordered subwavelength nipple array responsible for the transparent appearance of *C. hylas* wings. Adapted with permission from reference [330], © 1997 Zoological Society of Japan.

are segmented into several highly ordered domains with slightly varying nipple orientations. Without such a polycrystal-like quality, a perfectly ordered 2D subwavelength diffraction grating (as introduced in subsection 2.3.4) like a moth-eye-mimicking structure would reflect notable iridescent visible light at certain oblique incidence angles (caused by the  $m = -1$  diffraction order), which would undermine their camouflage effect. Breaking the long-range order by partitioning the corneal surface into several highly ordered but slightly misaligned domains efficiently reduces the intensity of the diffractive glare for all observer perspectives [338].

Although insect eyes and wings might be the most frequently cited examples of animal antireflective structures, lesser-known examples, like the calcitic microlenses that are part of the photoreceptor system in brittlestars, have also been studied [339].

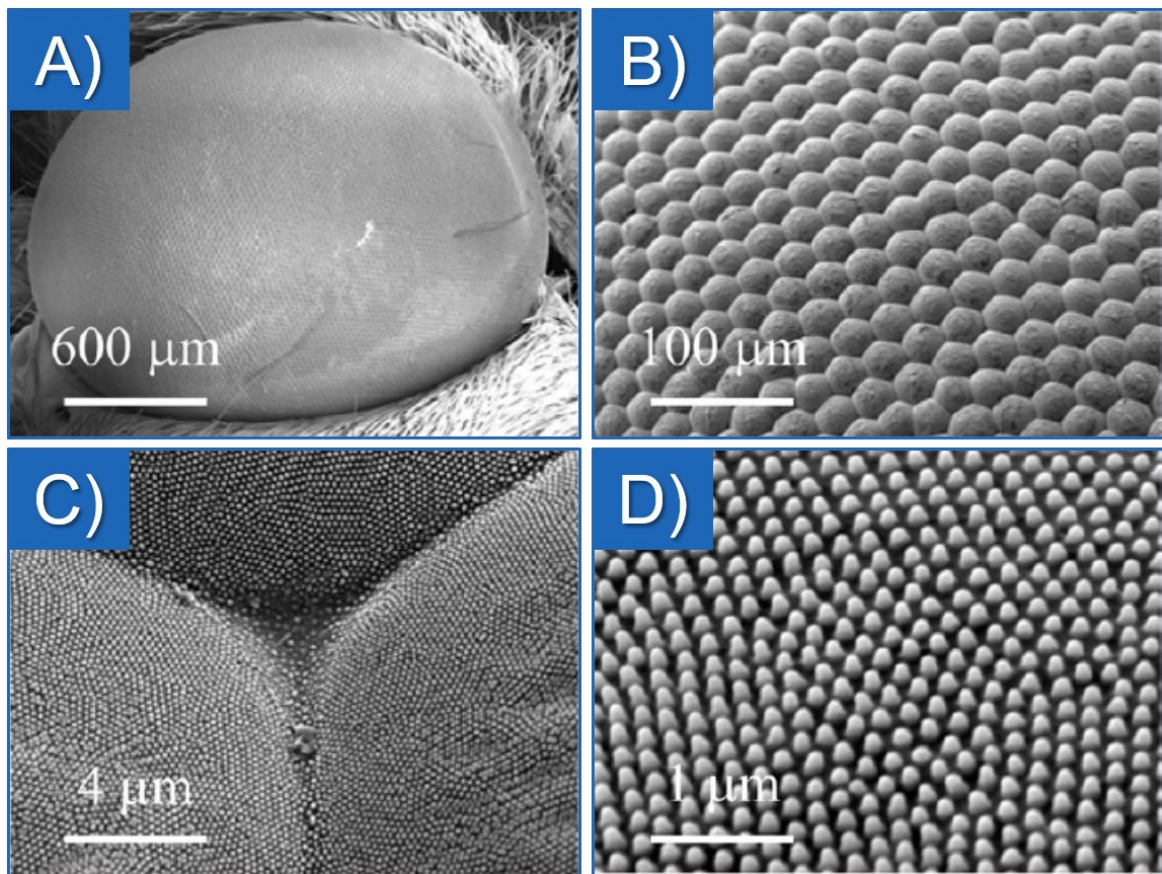


**Fig. 3.8:** SEM images of a compound eye of a silkworm *Philosamia cynthia ricini* at different magnifications. A) depicts the entire compound eye, B) the hexagonal arrangement of ommatidia, C) a more detailed view of the ommatidia, and D) the subwavelength corneal nipple array covering one ommatidium. Adapted with permission from reference [340], © 2016 American Chemical Society.

## 3.2 Optical Micro- and Nanostructures in Plants

### 3.2.1 Basic Architecture of (Hierarchical) Plant Surface Structures

The interface between a plant and its environment is generally formed by its outermost cell layer (epidermis), which is coated with a thin layer of wax (cuticula). Plant epidermal cells come in a variety of shapes and sizes (dimensions typically between several  $\mu\text{m}$  and tens of  $\mu\text{m}$ ). Due to their dense and uninterrupted lateral packing, the epidermal cells generally (except for the case of fully flat epidermal cells) form a microtexture. Due to their slight variations in shape, the surface-microtextures that are formed by plant epidermal cells generally exhibit structural disorder with respect to multiple geometric parameters. Firstly, these

microstructures include a disordered arrangement of individual micro-cones since their lateral spacing does not (closely) follow an ordered grid pattern. Secondly, the cones' height, radius, and (sometimes) tilting angle also show statistical variations. A qualitative description of the 3D morphology of plant epidermal cells (without the cuticula) can be achieved by analyzing the following four geometrical properties (see schematic in Fig. 3.9):

- Basic lateral outline: Either tetragonal, tetragonal elongated, polygonal or polygonal elongated.
- Shape of the anticlinal outline: Either straight, V-undulated, U-undulated,  $\Omega$ -undulated, or S-undulated.
- Sculpturing of the anticlinal outline: Either flat, sunken, or exposed.
- Curvature of the periclinal wall: Either tabular (flat), concave or convex. Tabular cells can either be fully flat or have concave or convex bunches decorating their (lateral) centers. In the case of a convexly shaped periclinal wall, the epidermal cell AR defines another set of sub-categories: Convex, hemispherical, cupola, conical, papilla, hair-papilla, and hair (see Fig. 3.10).

These epidermal cell properties can be considered as the two fundamental components that constitute all hierarchical plant surface structures. The cuticular wax layer that covers the epidermal cells also comes in a variety of shapes. There are three basic types of cuticular wax morphologies:

- Epicuticular wax crystals
- Cuticular (nano-)folds
- Subcuticular (nanoparticle) inserts

The first systematic classification of plant epicuticular waxes with regards to their chemical composition and their structural morphology was conducted by W. Barthlott *et al.* in 1998 on the basis of high-resolution SEM images of 13000 plant species of all major groups of seed plants [341]. Four examples out of the overall 23 distinct epicuticular wax types described by Barthlott *et al.* are given in Fig. 3.11. Wax platelets, for example, can be found on the surfaces of some well-known superhydrophobic plants like taro (*Colocasia esculenta*) or rice (*Oryza sativa*). However, the leaves of the – probably even more widely known – lotus (*Nelumbo nucifera*) plant are equipped with clusters of wax tubules rather than wax platelets.

The formation of the typical nanofolds and -ridges that commonly decorate the petal epidermis (examples displayed in Fig. 3.12) can be explained by a mechanical buckling process, where an anisotropic expansion of epidermal cells and a

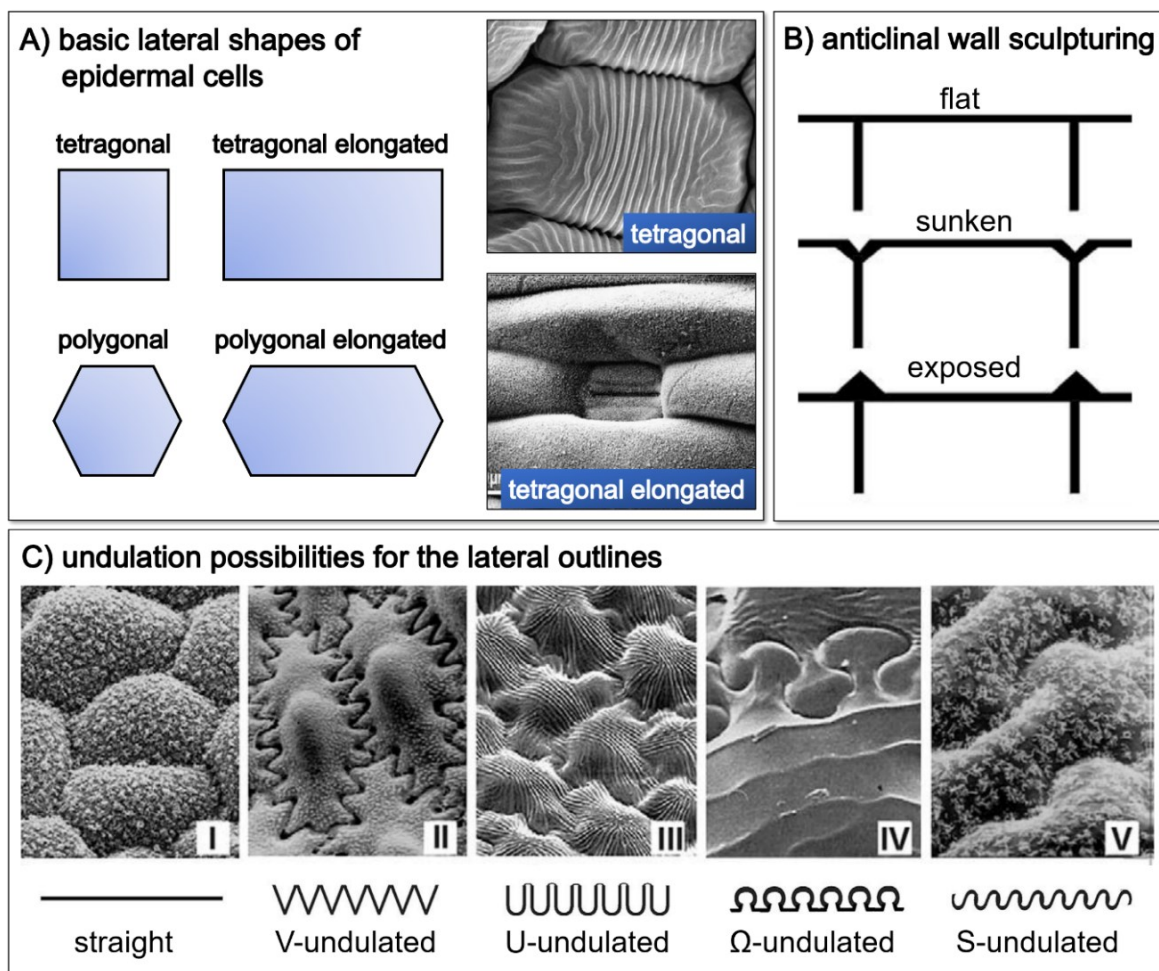


**Fig. 3.9:** 3D morphology of plant epidermal cells (without the cuticula). **A)** Schematic depiction of the four types of basic (lateral) epidermal cell shapes. Tetragonal cells exhibit four anticlines of equal length. Polygonal cells show more than four anticlines of equal length. Furthermore, elongated types of both tetragonal and polygonal epidermal cells are also possible. The SEM insets display examples for tetragonal (leaf of *Chrysanthemum leucanthemum*) and tetragonal elongated (lower (abaxial) leaf side of *Poa annua*) epidermal cells. **B)** Schematic depiction of the three types of anticline sculpturing. **C)** Exemplary SEM images to illustrate the five different types of shape modulation (or undulation) for the outline of the cell boundaries (anticlines). Adapted with permission from reference [342], © 2008 Elsevier Ltd. All Rights Reserved.

simultaneous isotropic cuticle production cause compressive forces [343].

In some cases, the structures atop the epidermal cells can be caused by subcuticular inserts. Such inserts can, as shown in Fig. 3.13, consist of solid SiO<sub>2</sub> crystals. Moreover, calcium oxalate crystals (with multiple possible 3D morphologies) are also commonly found.

The combination of epidermal cell microstructure and cuticular nanostructure

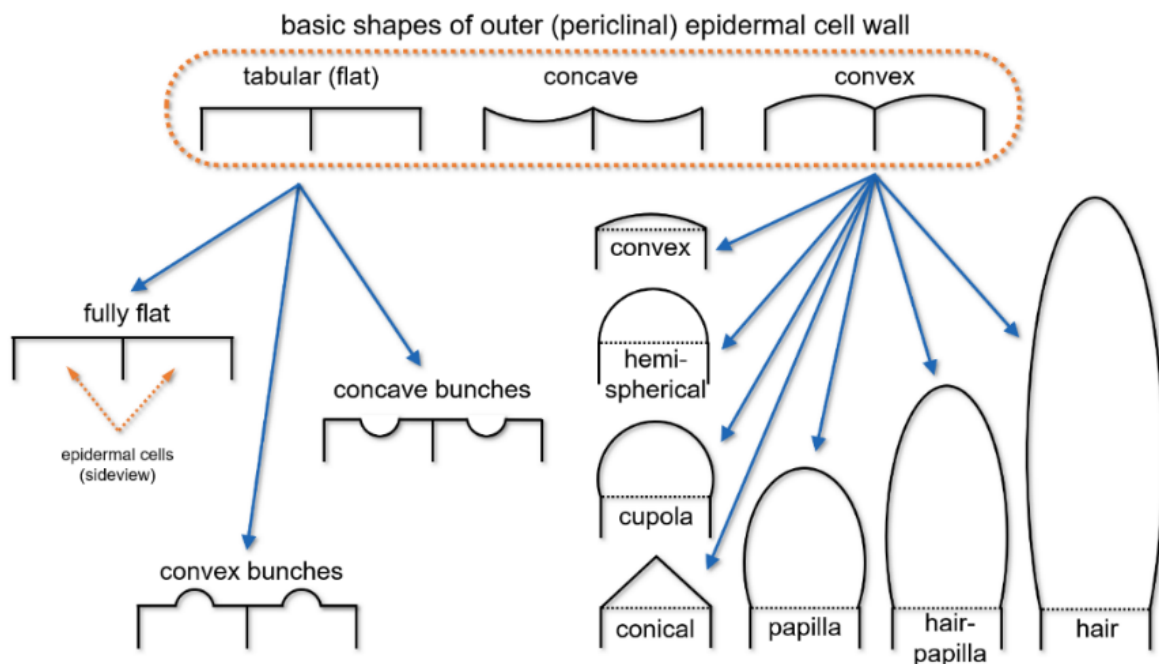


**Fig. 3.10:** Schematic cross-sectional depiction of possible shapes of plant epidermal cells following the classification given in reference [342].

forms hierarchical surface structures. These multi-scale plant structures can be found on leaves, petals, and sometimes even on fruits or seeds, serving a variety of purposes and exhibiting remarkable morphological diversity. The two basic design types of hierarchical plant structures are shown in Fig. 3.14. Convex epidermal cells (or convexly shaped regions of epidermal cells caused by subcuticular inserts) are decorated either with 3D epicuticular wax crystals or with a folded cuticula. In contrast to the 3D wax crystal formations (of numerous different shapes) that commonly decorate leaf epidermal cells (see, for example, Fig. 3.11), the epidermal cells of flower petals are coated with a pattern of irregularly shaped cuticular nanofolds. Astonishingly, a hierarchical architecture consisting of an array of conical epidermal cells (of varying AR, tip sharpness, etc.) and a folded cuticula is found on the petals of 70 – 80 % of all flowering plant species [344, 345].

## epidermal cells decorated with epicuticular waxes

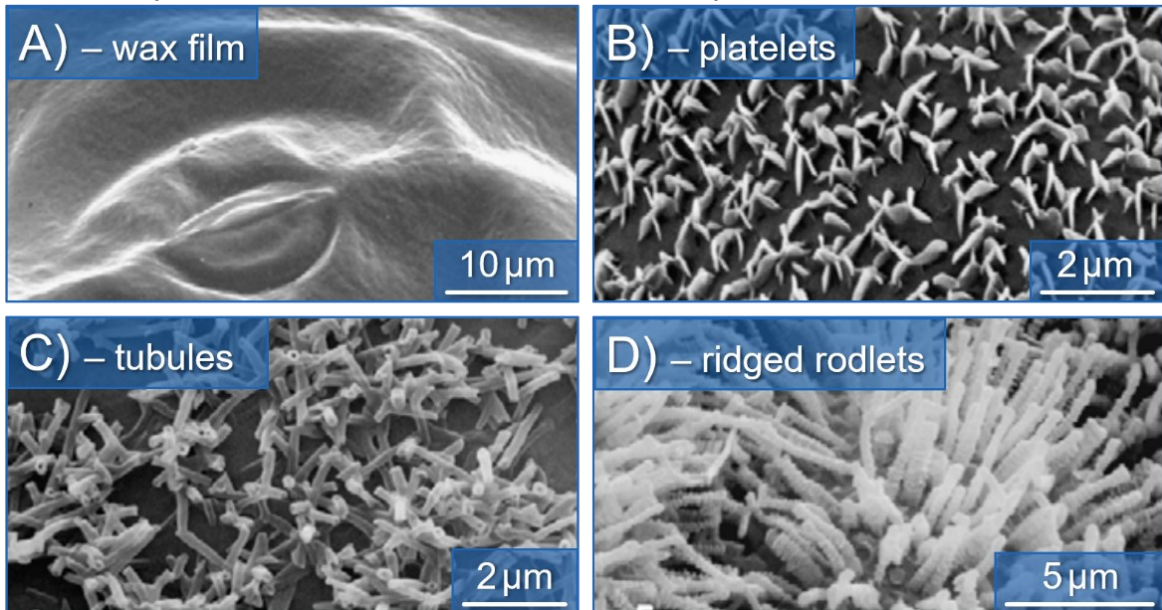


Fig. 3.11: SEM micrographs of four exemplary leaf surfaces showing different types of epicuticular waxes, namely a A) wax film (*Hydrocotyle bonariensis*), B) wax platelets (*Robinia pseudoacacia*), C) wax tubules (*Thalictrum flavum glaucum*), and D) ridged wax rodlets (*Sassafras albidum*). Adapted with permission from reference [342], © 2008 Elsevier Ltd. All Rights Reserved.

## epidermal cells decorated with cuticular folds

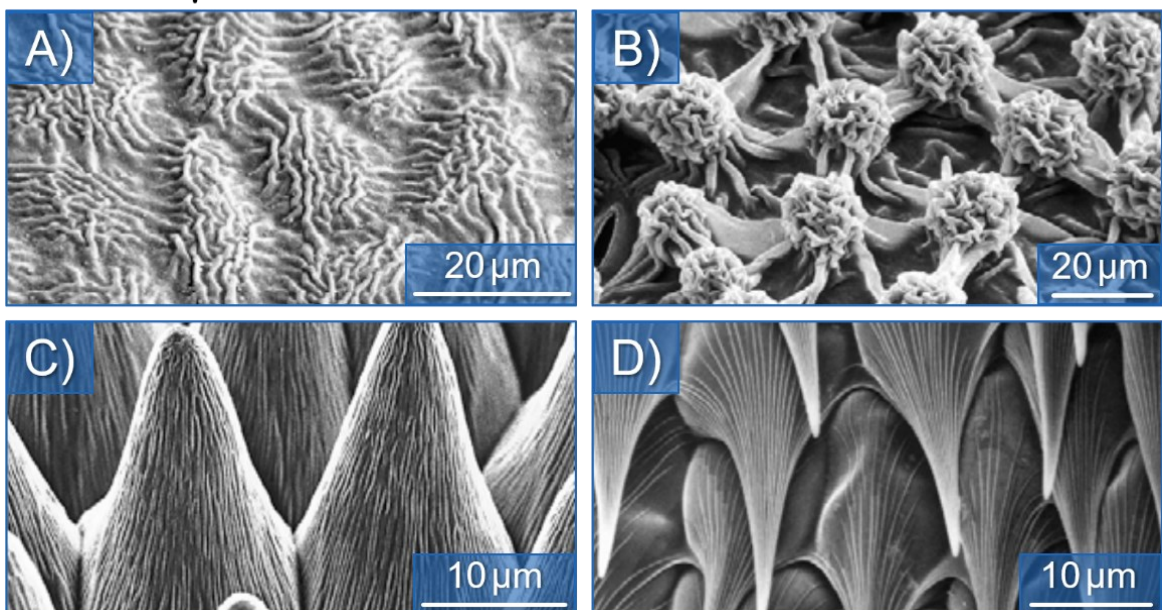
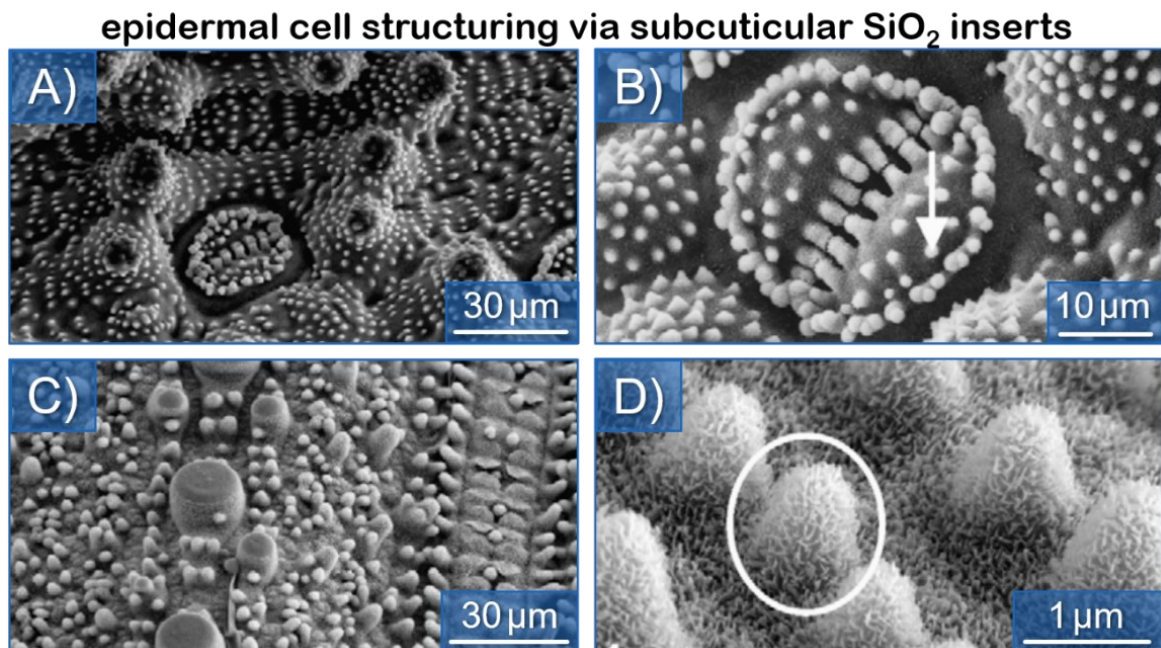
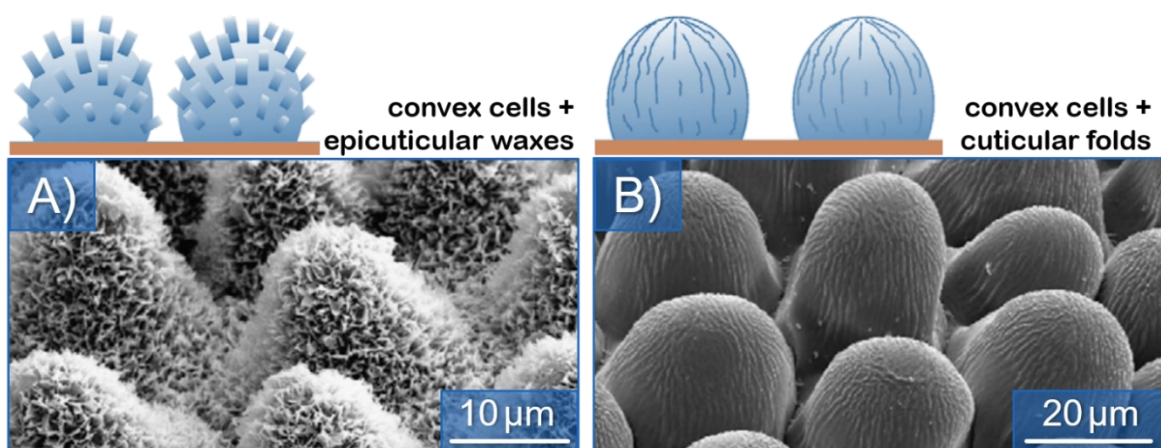


Fig. 3.12: SEM micrographs of epidermal cells covered with cuticular nanofolds. A) Upper leaf side of *Schismantoglottis neoguineensis* B) Lower leaf side of *Alocasia macrorrhizha* C) Upper petal side of *Viola tricolor* D) Trap leaf of *Sarracenia leucophylla*. Adapted with permission from reference [342], © 2008 Elsevier Ltd. All Rights Reserved.



**Fig. 3.13:** Cuticular surface textures caused by sub-cuticular insertions. In A) and B), SEM images of *Equisetum arvense* show that the cells around the stomata (and the stomata themselves) are covered by convex bumps, which are caused by sub-cuticular  $\text{SiO}_2$  crystals. In C) and D), the leaves of *Oryza sativa* show similar bumps covering their surface. Adapted with permission from reference [342], © 2008 Elsevier Ltd. All Rights Reserved.



**Fig. 3.14:** Basic varieties of hierarchically structured plant surfaces, exemplified by A) the upper leaf side of *Euphorbia myrsinites*, which consists of convex epidermal cells decorated with 3D epicuticular wax crystals, and B) the petal surface of *Dahlia spp.*, which is composed of convex epidermal cells covered with cuticular nanofolds. Adapted with permission from reference [342], © 2008 Elsevier Ltd. All Rights Reserved.

### 3.2.2 Structural Coloration in Plants

In plants, features causing structural coloration are by far not as widespread as in animals. On the surfaces of leaves, for example, photonic structures that cause a blue iridescence in reflected light can be found on the leaves of some tropical understory plants [346, 347]. Next to structures that modify the leaf's visual appearance, specialized photonic structures that enhance photosynthetic efficiency inside of plant leaves have also been identified [348]. The cuticular nanostructure that often decorates leaf epidermal cells in the form of 3D wax crystals is usually not causing any structural coloration or other special optical properties. Instead, its purpose is usually more closely linked to controlling the wetting behavior of leaves. Yet, there are still counterexamples found, like the leaves of *Tradescantia pallida* 'purpurea', which reflect a unique golden shine caused by a disordered structure of wax platelets [349]. In some other cases, structural leaf coloration might be less obvious and therefore overlooked. For example, in cases where iridescence is distorted due to interactions with pigments or if the structural color is only reflected from an unusual location on the leaf [350].

As mentioned in the previous subsection 3.2.1, flower petals are usually covered by irregularly shaped nanofolds in close parallel packing. In some rather rare cases, the cuticular nanofolds form a sufficiently regular pattern in order to reflect notably iridescent light [347, 351–355]. Fig. 3.15 depicts a *Queen of the Night* tulip, one of the most famous examples of iridescent flower petals. Its iridescent appearance is caused by parallel nanofolds, which are decorating the tulip's elongated epidermal cells. It is important to note that the strongly iridescent *Queen of the Night* is not a wild-type flower but rather a product of the tulip industry [356]. Other than producing iridescent coloration, some petal photonic structures can further cause a glossy flower appearance through their scattering properties [357, 358]. According to Whitney *et al.*, pollinators, such as bumblebees, can detect such iridescent signals produced by petal nanoridges and can learn to use these signals as a cue to identify rewarding flowers [351]. However, numerous following studies argued that, although Whitney *et al.* were able to actively train bumblebees to directly link the iridescence of artificial diffractive elements with especially rewarding flowers, wild-type flowers usually don't show a sufficiently strong iridescence under natural lighting conditions to enable such a direct visual attraction of pollinators [356, 359–365]. In addition to the debate about such close to ordered cuticular striations, it has also been proposed that disordered, parallel cuticular folding nanostructures in petals create a biologically important scattering effect in the UV-blue spectral region – a blue halo – that is salient to insect pollinators [366].

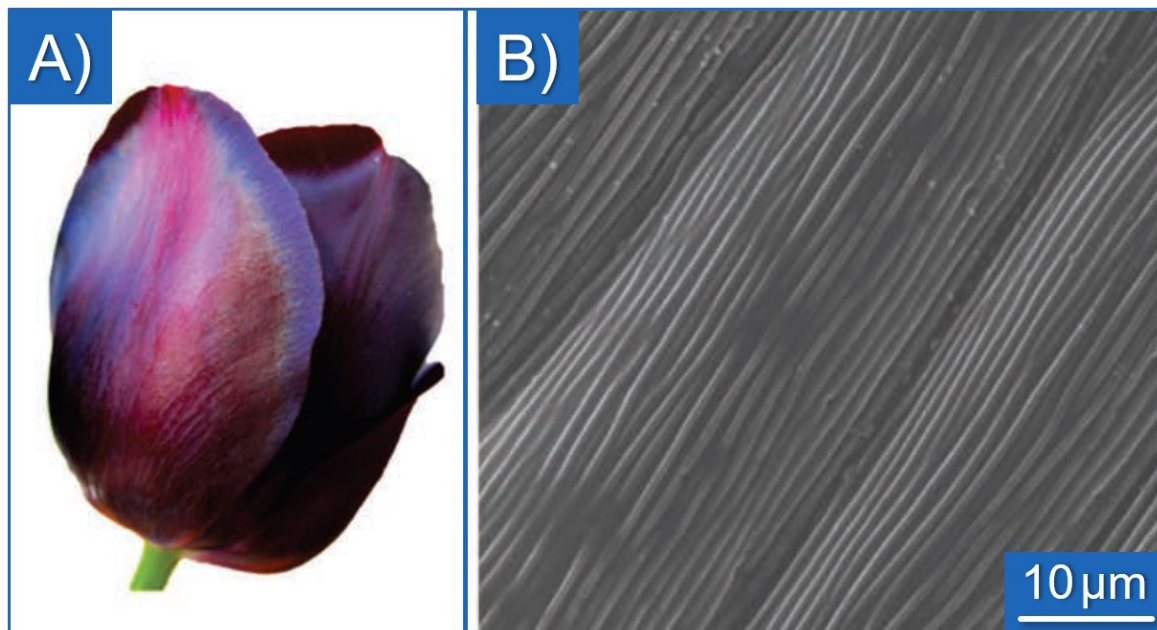


**Fig. 3.15:** Iridescent tulip variety *Queen of the Night*. A) Photograph of *Queen of the Night*. B) SEM image of the hierarchical surface structure, consisting of elongated epidermal cells with parallel nanofolds covering their surface. The high degree of order of the cuticular folds causes iridescence in reflected light. Adapted with permission from reference [355], © 2013 WILEY-VCH Verlag GmbH & Co. KGaA, Weinheim.

Generally, the question of how floral colors are visually perceived by pollinators such as bees has been debated for many decades, especially with respect to their ability to see ultraviolet (UV) light [367].

Leaves and petals are not the only plant parts that are sometimes equipped with structural or structurally assisted coloration. Although quite rare, structural colors can also be found in some fruits. Some species of *Elaeocarpus*, for example, *E. angustifolius*, show a particularly brilliant blue coloration of their fruits, which has been identified as iridescence caused by thin-film interference of a layered epidermal structure three decades ago [368]. A similar blue iridescent color has later been studied in fruits of the rainforest understory plant *Delarbraea michieana* (Araliaceae) [369]. In more recent years, the structures causing two particularly interesting cases of structural fruit coloration have been uncovered by Vignolini *et al.* [347, 370, 371]. The fruits of *Pollia condensata* (see Fig. 3.16 A, B) exhibit a brilliant blue coloration, with little speckles of green and violet/red decorating the whole fruit surface. This bright blue color is more intense than any other color found in biological materials, even surpassing the wings of blue *Morpho* butterflies [370]. Furthermore, the fruits of *Pollia condensata* and the metallic-blue/green fruits *Margaritaria nobilis* (see Fig. 3.16 C) have both been found

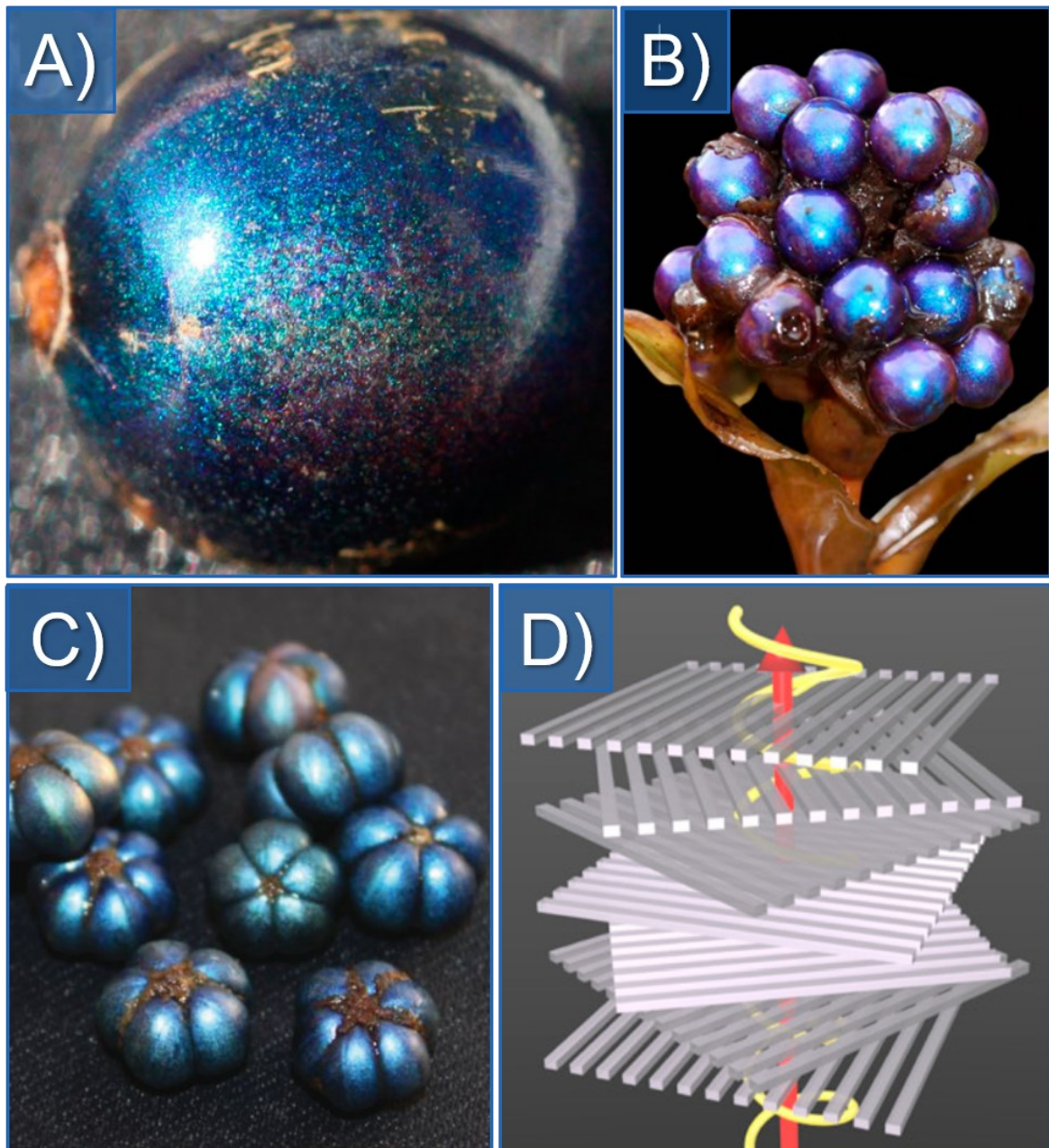


**Fig. 3.16:** Structurally colored fruits of *Pollia condensata* and *Margaritaria nobilis*. A) Photograph of a dried *Pollia condensata* fruit ( $\approx 5$  mm in diameter) with its brilliant pixelated iridescent appearance exhibiting green and purple/red speckles. B) Photograph of a cluster of alcohol-preserved *Pollia condensata* fruits. C) Photograph of fresh fruits of *Margaritaria nobilis* showing their intense metallic coloration. D) Schematic depiction of the helicoidal cell wall architecture causing the distinctive colorations of both kinds of fruits depicted in A)-C), namely a multilayer configuration of Bragg reflectors made from cellulose microfibrils, where each consecutive layer showing an increasingly rotated microfibril orientation. A), B), and D) were adapted with permission from reference [370], © 2012 The Authors. The photograph in C) was reprinted with permission from reference [371], © 2016 The Authors.

to show the unique quality of reflecting circularly polarized light, similar to what was previously found for many scarab beetles. Similar to scarab beetle cuticles, the cell wall architectures of *Pollicia condensata* and *Margaritaria nobilis* fruits were found to be of helicoidal nature [370, 371]. Lastly, it is worthy of note that structure-based coloration can also be found in some species of algae [372, 278].

#### 3.2.3 Antireflective Structures in Plant Leaves

Almost all plants rely on photosynthesis to convert sunlight energy into chemical energy. In order to survive, the leaf epidermis and its cuticula, therefore, need to facilitate the in-coupling of a sufficient amount of light into the leaf. Hence, the surface structures found on leaves (some examples can be seen in the previous section of this chapter) can universally be considered to be a (more or less effective) antireflective structure. In contrast to the subwavelength antireflective structures found on many insects' eyes and wings, the surfaces of plant leaves generally do not involve any sub-micron textural features and, followingly, do not rely on inducing gradually changing (effective) refractive indices.

It seems obvious that some plants that need to survive on low sunlight intensities or under shady (diffuse) conditions have evolved special epidermal cell and cuticular morphologies that improve light capture to manage to thrive under such harsh conditions. In 1985, Bone *et al.* studied the optical properties of the convex epidermal cells found in leaves of many tropical rain-forest shade plants by employing ray-tracing simulations [373]. Based on their numerical analysis, they postulated that the convex cell shape causes a lens-like focusing of in-coupled light, which increases photosynthetic efficiency. Moreover, they hypothesize that overall, the array of epidermal cell lenses exhibits a reduced leaf surface reflectance compared to the sun species. Several other ray-tracing-based studies on epidermal light focusing reached similar conclusions [374–377]. In 1996, Vogelmann *et al.* experimentally studied epidermal cell light focusing of convex leaf epidermal cells and reported concentration factors of up to 15 – 20 [378]. Also, such lens like leaf epidermal cells have also experimentally been shown to enhance diffuse light capture [379].

Next to improving light-capture, the micro- and nanostructures found on leaves fulfill a variety of other (often more) important purposes, including [380]:

- Transport barrier, which regulates the loss of water or foliar uptake
- Providing mechanical stability
- Other optical properties like protection against harmful UV radiation

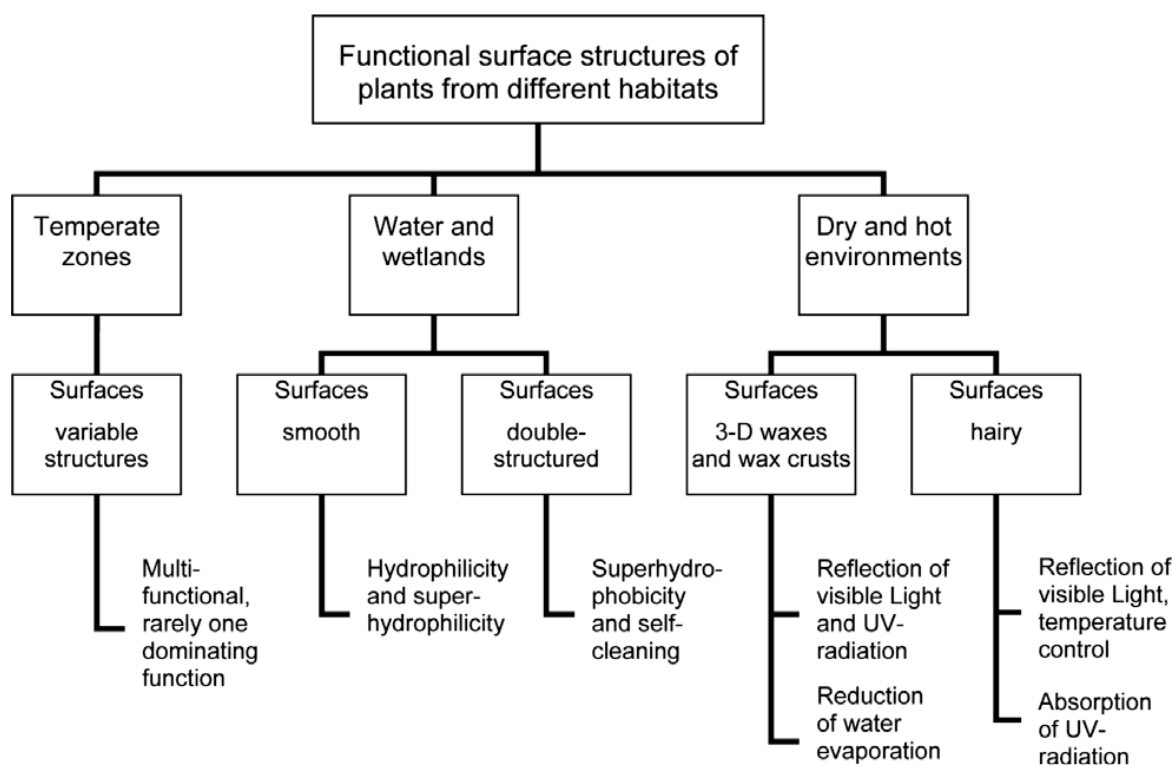


**Fig. 3.17:** Overview of the various functional structures typically found on the surfaces of plants from different habitats. Reprinted with permission from reference [342], © 2008 Elsevier Ltd. All Rights Reserved.

- Controlling the surface wettability of the leaf
- Anti-adhesion for insects

Following K. Koch, B. Bhushan, and W. Barthlott, the functional surface structures of leaves typically follow a small number of basic design principles, which depend on the specific climate zone of the plant's habitat (see Fig. 3.17) [342]. For example, while the typical surface structures found in dry and hot environments often assist cooling, reduce water loss and protect against harmful UV radiation, the surface structures found on the leaves of many water- and wetland-plants mainly control the leaves' wetting properties, thereby achieving the whole range of wetting regimes from superhydrophilicity to superhydrophobicity with either strong (rose-petal-like) or weak (lotus-like) adhesive forces.

### 3.2.4 Antireflective Structures in Flower Petals

Petal surface structures, in contrast to green leaves, do not contain any chlorophyll and therefore do not facilitate a plant's photosynthetic energy production. However, there is another less obvious reason why employing an efficient light-

capture scheme is still of great benefit for flowering plants. As early as 1910, F. Exner and S. Exner conjectured that the dense array of cone-shaped epidermal cells that is typically found on petals might induce two optical effects [381, 382]:

- 1) Increasing the path length of light within the pigment-filled cells and thereby enhancing the spectral purity of the produced color.
- 2) Reducing (specular) surface reflectance due to the multiple chances of in-coupling that a densely packed array of microlenses provides and thereby yielding a more saturated color.

In conclusion, F. Exner and S. Exner proposed that, through creating more vibrant and striking floral colors, conical petal epidermal cells might help to attract more pollinators [381, 382]. Furthermore, based on his studies of the flora of South Africa, R. Marloth came to the same conclusion in 1915, hypothesizing that the convex shape of flower epidermal cells leads to focusing of in-coupled light and an intensified interaction with the embedded pigment molecules [383, 384]. Therefore, similar to the case of leaf surface structures, all hierarchical petal surface structures, which in most cases are composed of conical epidermal cells and the typical nanofold layer on top, can always be considered as (more or less efficient) antireflective surface structures. For natural petals, a theoretical model to calculate petal reflectance depending on epidermal cell shape has even been developed [385].

However, in order to experimentally study the effect of varying epidermal cell shape (from conical to flat) on the color saturation/intensity and further on the pollination success of the respective flower petals, a method to cultivate/engineer individual flowers of the same species with a purposefully manipulated epidermal cell growth behavior and no other distinctions between them is needed. In 1994, Noda *et al.* identified and described a mutant of *Antirrhinum majus* (wild-type snapdragon), which phenotypically only differs from the original line of *Antirrhinum majus* in one aspect: epidermal cell shape [386]. This so-called *mixta* mutant of *Antirrhinum majus* lacks a certain transcription factor that is vital for initiating conical epidermal cell outgrowth and therefore produces only strongly flattened epidermal cells. It was found that *mixta* mutants, although their pigment concentration was not manipulated, exhibit a paler color impression compared to the flower of *Antirrhinum majus* with conical epidermal cells. Flowers of both *Antirrhinum majus* and its *mixta* mutant are photographically depicted in Fig. 3.18, together with SEM images of their respective epidermal cell shapes. Following the study by Noda *et al.*, *Antirrhinum majus* and its *mixta* mutant were utilized to experimentally show an increased pollination success for convex, conical



**Fig. 3.18:** Influence of epidermal cell shape on the flower color saturation in *Antirrhinum majus* petals. The conical epidermal cells that are found on the flower petals of the wild-type (left) lead to a strong increase in petal color saturation compared to the rather flat epidermal cells of the *mixta* mutant (right). The SEM images were reprinted with permission from reference [343], © 2012 The Authors. Published by the Royal Society. All Rights Reserved. The photograph was reprinted with permission from reference [387], © 2007 Springer Science+Business Media B.V.

epidermal cells compared to flat ones [387, 388]. Furthermore, it was shown that petal wettability in *Antirrhinum majus* is decreased for cone-shaped epidermal cells [389]. It is worth noting that a discussion of possible evolutionary pathways in the development of flower coloration through pigments and conical epidermal cells has recently been contributed by P. Rudall [390].

Next to assisting the creation of vibrant floral colors, the conical epidermal cell shape (and the cuticular nanofolds) also directly impact the friction and grip properties of insects landing on petals. Numerous studies have indicated that bees might grip more easily and therefore prefer to land on flower petals exhibiting the typical conical epidermal microtexture, which increases the chance of successful pollination [391–394]. Furthermore, it has been reported that cuticular nanofolds make petals slippery for beetles [395]. Overall, it seems that a pronounced epidermal microstructure increases insect grip, while a pronounced cuticular nanostructure makes petal surfaces more slippery. Both these correlations were further shown for the Colorado potato beetle (*Leptinotarsa decemlineata*) [396]. Another property that can be linked to the petal epidermal cell shape is floral temperature, whereas scent production is not directly affected [397].

While it has been known that bees use the polarization of skylight for navigation [398], it has been further demonstrated that bumblebees can learn the polarization patterns associated with a food source (flower petals), which is the first non-navigational ability related to the polarization-sensitive visual system of bumblebees that has been discovered [399]. Further, it has also been investigated if

the flower-reflected light polarization influences the color perception in polarization-sensitive insects [400].

---

## 4 Wetting Properties of Micro- and Nanotextured Surfaces

---

Depending on the chemical composition and topography on the micro- and nanoscale, solid surfaces may exhibit various possible behaviors when brought into contact with water droplets. This chapter aims at developing a basic understanding of these various possible wetting properties. After first introducing the classical models describing the wetting states of rough surfaces following Wenzel [401] and Cassie and Baxter [402] in section 4.1, the more recently studied and more varied wetting behaviors of hierarchically textured (plant) surfaces are described in section 4.2. In the final subsection 4.3, the different possibilities to realize self-cleaning surfaces in PV are summarized.

### 4.1 Wetting Properties of Rough Surfaces – Classical Theories

A liquid and a solid material, both surrounded by air, are brought into contact. For now, the solid's surface shall be considered perfectly smooth. The basic question then is: Is it energetically more favorable for the solid to be in close contact with the liquid or the surrounding air (and by how much)? Such a scenario can be described utilizing the surface free energies  $\gamma_{SA}$  (solid-air),  $\gamma_{SL}$  (solid-liquid) and  $\gamma_{LA}$  (liquid-air), and by the contact angle  $0^\circ < \theta_0 < 180^\circ$ , a macroscale parameter defined according to the schematic shown in Fig. 4.1. The contact angle at the thermodynamic equilibrium of the solid-, liquid- and gaseous phases is given by the Young equation [403]:

$$\cos \theta_0 = \frac{\gamma_{SA} - \gamma_{SL}}{\gamma_{LA}} \quad (91)$$

The case where it is energetically more favorable for the liquid to wet the solid surface is described by  $\gamma_{SL} < \gamma_{SA} + \gamma_{LA}$  (or equivalently  $-1 < (\gamma_{SA} - \gamma_{SL})/\gamma_{LA}$ ). Otherwise, if it is energetically more favorable for the liquid to surround itself with air and not touch the solid surface is given by  $\gamma_{SA} < \gamma_{SL} + \gamma_{LA}$  (or equivalently

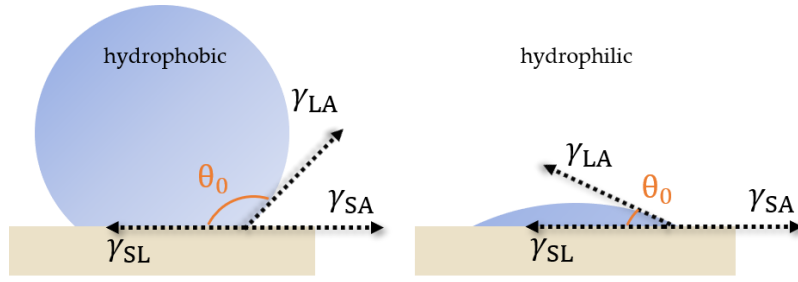


**Fig. 4.1: Definition of the (water) contact angle. Both an example for a hydrophobic surface (left schematic) and a hydrophilic surface (right schematic).**

$1 > (\gamma_{SA} - \gamma_{SL})/\gamma_{LA}$ ). If the liquid considered is water, the extreme cases of a contact angle close to  $\theta_0 = 0^\circ$  and  $\theta_0 = 180^\circ$  are called superhydrophilicity and superhydrophobicity, respectively. Since real materials only asymptotically reach these extreme cases, superhydrophobicity is usually defined via a water contact angle above  $150^\circ$ , while superhydrophilicity, on the other hand, usually refers to surfaces with a water contact angle below  $10^\circ$  [380].

If the solid surface is not microscopically smooth but rather exhibits a (random) roughness, defined by the roughness factor  $R_f > 1$ , the Young equation fails to accurately describe the wetting behavior.  $R_f$  is defined as the ratio of the total surface area and its horizontally projected planar area. Following Wenzel [401], the effective surface free energies of the solid-liquid and the solid-air interface then become  $R_f\gamma_{SL}$  and  $R_f\gamma_{SA}$ , and the contact angle  $\theta$  of the rough surface can be obtained from the contact angle  $\theta_0$  of a smooth surface of the same material using an equation derived by Wenzel in 1936 [401]:

$$\cos \theta = R_f \cos \theta_0 \quad (92)$$

This model assumes that the rough solid surface continuously touches the liquid surface, and no microscopic air pockets are trapped between the solid and the liquid. Such a wetting behavior is schematically displayed in Fig. 4.2 A). Assuming  $0 < f_{SL} < 1$  describes the fraction that constitutes the solid-liquid interface (and therefore  $1 - f_{SL}$  is the fraction that constitutes the solid-air interface), the wetting behavior of a rough surface can be described using the following equation, which was first developed by Cassie and Baxter in 1944 [402]:

$$\cos \theta = R_f f_{SL} \cos \theta_0 - 1 + f_{SL} \quad (93)$$

This type of wetting behavior is shown in the schematic Fig. 4.2 B). A third type of wetting behavior of rough surfaces (Fig. 4.2 C), often called the impregnating Cassie wetting regime, where water fills all the microscopic voids of the rough surface, was also described by Cassie and Baxter [402]:

$$\cos \theta = 1 + f_{SL}(\cos \theta_0 - 1) \quad (94)$$

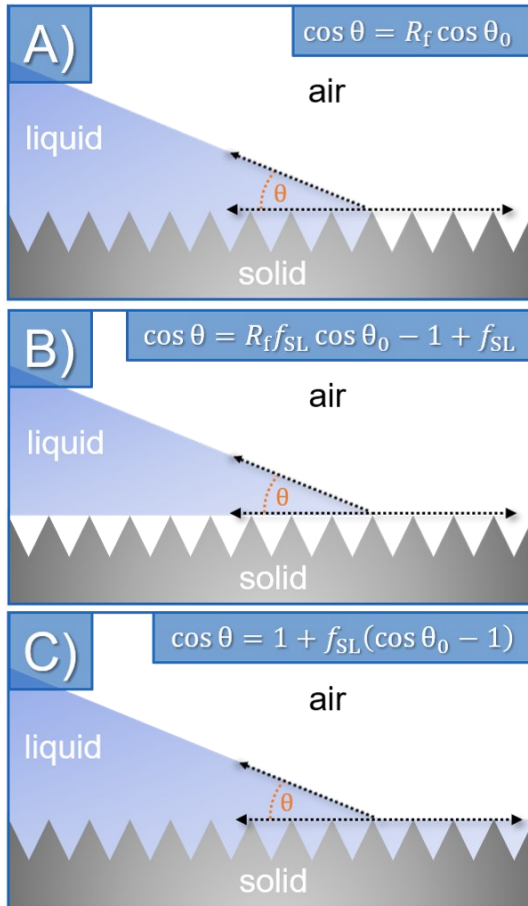


**Fig. 4.2:** Schematics displaying the three classical wetting regimes of rough surfaces. A) Wenzel state. B) Cassie-Baxter state. C) Impregnating Cassie-Baxter state.

A discussion of the relationship between a solid surface's topographical characteristics and its resulting Cassie-Baxter- or Wenzel-wetting properties can be found in reference [404]. Although the three types of wetting behaviors described above already give an accurate description of the wetting properties for various microscale rough surfaces, many recent studies have indicated that hierarchically micro- and nanotextured surfaces exhibit a number of wetting regimes that can't be accurately predicted or described by

employing Wenzel's or Cassie's and Baxter's models, like, for example, a combination of a high contact angle and strong adhesive forces (as will be discussed in the following section 4.2). Therefore, the contact angle doesn't give a full description of the possible wetting properties of hierarchically textured surfaces, like the structures found on the surfaces of plants. In addition to the static water contact angle, other effects like contact angle hysteresis and the roll-off-behavior of water droplets need to be studied to accurately describe the entire realm of possible wetting properties. A more thorough discussion of these concepts can be found in references [405, 406].

## 4.2 Wetting Properties of Hierarchically Structured Surfaces

Following the categorization given by B. Bhushan and M. Nosonovsky [405], considering hierarchically (micro-/nano-) structured surfaces, there are, in total, nine different types of wetting regimes that can be encountered. All these cases are schematically depicted in Fig. 4.3. Basically, these wetting regimes of hierarchical surface structures can be thought of as all the possible ( $3 \cdot 3 = 9$ ) combinations of

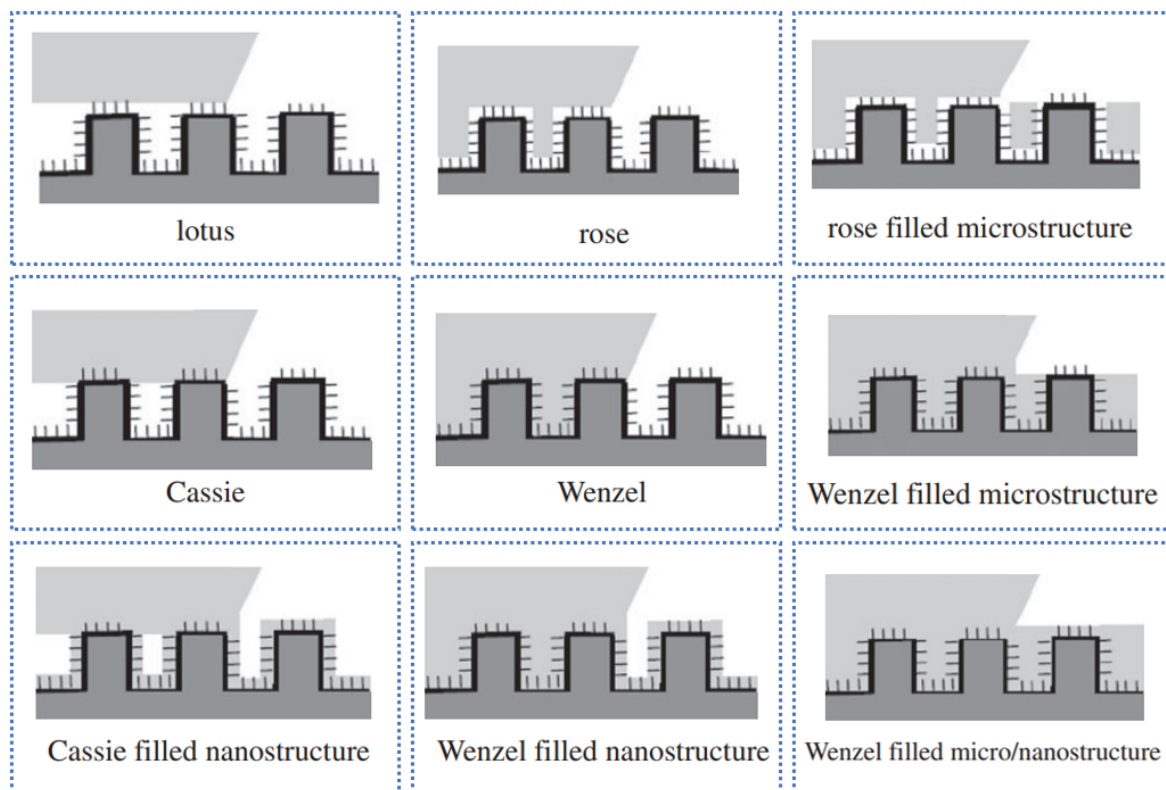


**Fig. 4.3:** Schematic depiction of the nine different types of wetting regimes of hierarchically textured surfaces. Adapted with permission from reference [405], © 2010 The Royal Society.

the classical Wenzel, Cassie, and Cassie-impregnated wetting behaviors taking place on the microstructure level and the nanostructure level separately.

As introduced in subsection 3.2.1, leaf and petal surfaces may exhibit various kinds of hierarchical surface structures composed of an epidermal cell microstructure and a cuticular wax nanostructure. The hierarchical surface structure of a leaf or a petal does not only play an important role in creating their visual appearance and in defining their light in-coupling properties but also controls their wetting properties through the interplay between the multi-scale structural features. Famously, the leaves of the sacred lotus (*Nelumbo nucifera*) show an extraordinarily efficient self-cleaning ability, often called the lotus-effect (first described in detail by W. Barthlott and C. Neinhuis in 1997 [407]), which stems from the combination of a high water-repellency (high water contact angle and low droplet-adhesion) and a very low adhesive force between contaminant particles and the hierarchically structured leaf surface [407, 408]. The hierarchical surface structure of the lotus leaf is depicted in Fig. 4.4. The cone-shaped epidermal cells are covered with a 3D assembly of wax crystals in the shape of tubules [409]. In case of the lotus-effect, water can neither penetrate the microscale air voids of the hierarchical surface texture nor the

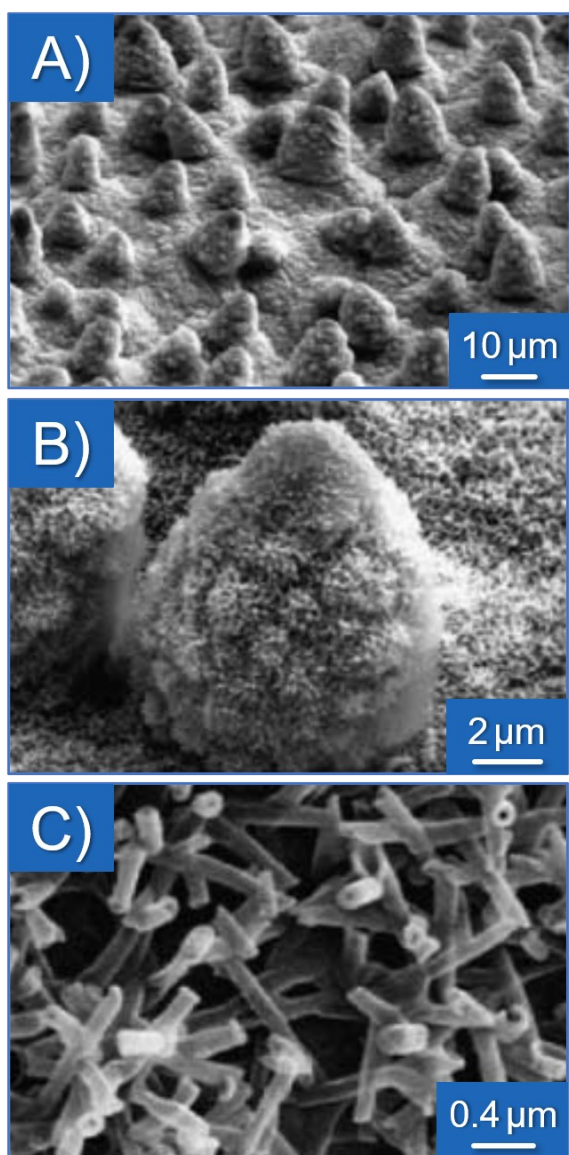


**Fig. 4.4:** SEM images of a lotus leaf's self-cleaning surface structure (*Nelumbo nucifera*) leaf under three different magnification factors. In A) and B), the conical epidermal cells that comprise the microstructure are shown, whereas C) shows a detailed view of the epicuticular wax tubules that form the nanoscale part of the hierarchical surface texture. Adapted with permission from reference [410], © 2009 The Royal Society.

nanoscale ones caused by the wax tubules (see Fig. 4.3). Through combining various epidermal cell microstructures and cuticular wax nanostructures, the surfaces of leaves can be functionalized to exhibit all possible wetting behaviors, covering the whole spectrum from superhydrophilic to superhydrophobic. Which building blocks lead to the various wetting states is schematically summarized in Fig. 4.5.

In contrast to the lotus leaf, which uses superhydrophobicity and low adhesion forces to enable self-cleaning, some other plants exploit their superhydrophilic leaves as the basis for water and nutrient uptake. Superhydrophilic leaves can cause a rapid spreading of water over the whole leaf surface, even overcoming gravitational forces. Considering superhydrophilicity (and superoleophilicity), the leaves of *Ruellia devosiana* are one of the most impressive examples found throughout the plant kingdom [411].

As described in subsection 3.2.1, the hierarchical surface structures found on most flowering plant species' petals can typically be described as a densely packed array of cone-shaped epidermal cells decorated with a nanostructure comprised of cuticular nanofolds [344, 345]. The petals of some varieties of roses, for example, exhibit a very high water contact angle similar to lotus leaves and are therefore

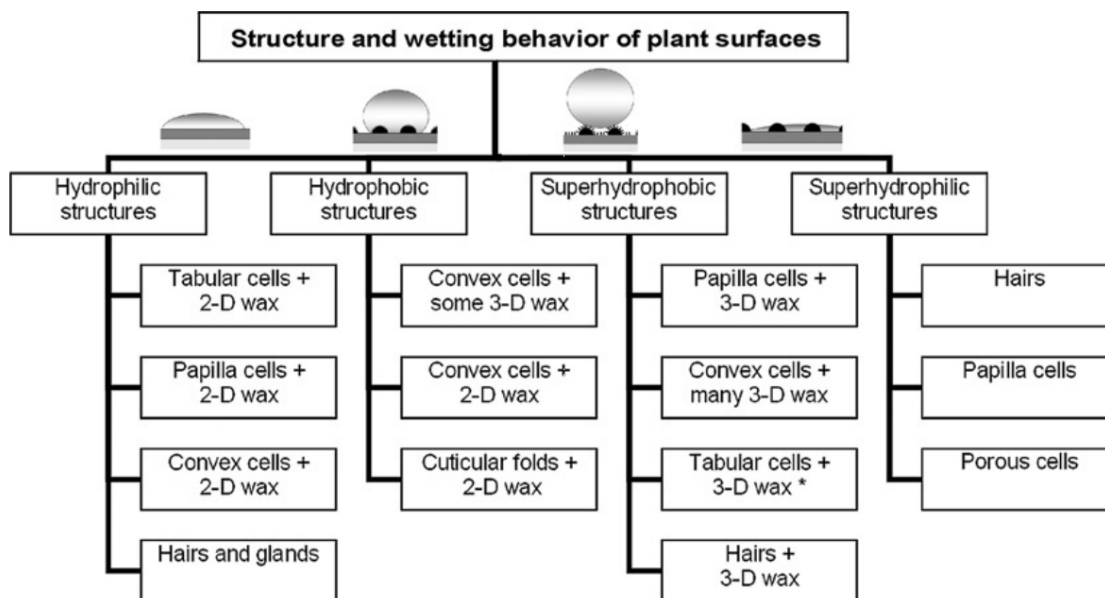


**Fig. 4.5:** Schematic showing which combinations of leaf epidermal cell microstructure and cuticular wax coating lead to different wetting states, covering the whole spectrum from superhydrophilic to superhydrophobic plant leaves. Reprinted with permission from reference [380], © 2008 The Royal Society of Chemistry.

usually categorized as superhydrophobic. However, while the lotus leaf prominently exerts a very low adhesion force to water droplets on its surface, causing the droplets to easily roll off the leaves even at small tilt angles [407, 408], water droplets on rose petals, on the other hand, often strongly stick to the petal surface, even if the petal is turned fully upside down [405]. While for lotus leaves, the water droplets are neither able to impregnate the microscale nor the nanoscale air voids of the hierarchical surface structure, the rose petal structure, on the other hand, although exhibiting a high contact angle due to the water being repelled by the nanoscale structure, still can impregnate the microscale voids of the structure, which creates the strong adhesive force characteristic for the rose petal effect. Studying and artificially recreating this so-called rose petal effect, which describes the wetting regime with a high contact angle combined with a strong adhesive force, has gained many research groups' attention [405, 412–417]. Furthermore, transitions between these high contact angle wetting regimes and hierarchical structures with tunable wetting properties have also been demonstrated [418, 419]. In contrast to rose petals, the flower petals of *Viola tricolor* have been demonstrated to show a lotus-like water repellency [420]. Moreover, the relationship between petal wettability, epidermal cell microstructure, and cuticular nanofold-structure has also been studied theoretically [421].

Next to lotus- and rose-petal-effect, another noteworthy type of wetting behavior can be found on the leaves of the floating water ferns of genus *Salvinia*. The so-called Salvinia-effect describes these leaves' behavior to retain a thin and stable layer of air at their surface when submerged into water, which is achieved through a complex structure comprised of (eggbeater-shaped) superhydrophobic micro-hairs with hydrophilic patches at their tips [422]. Biomimetically recreating these sophisticated wetting properties (for possible applications such as drag reducing ship coatings or low-friction fluid transport) has been demonstrated by producing hydrophobic micropatterns with a predefined level of hydrophilic patches [423]. More information about the vast spectrum of wetting properties encountered throughout the plant (and animal) kingdom can be found, for example, in references [424, 425].

### 4.3 Self-Cleaning Surfaces in Photovoltaics

Solar modules are operated outdoors, usually in a mechanically fixed installation. Therefore, it is inevitable that, over time, their front surface will accumulate various kinds of contaminant particles. Depending on the local climate conditions (like frequency, average duration, and intensity of rainfalls), the PV system's tilt and orientation, and the PV modules' surface texturization, the severity of the resulting dust-coating in terms of module performance degradation can vary greatly. Typically, atmospheric dust particles, often called aeolian dust [426], are comprised of various possible constituents like sand, clay, particles from volcanic activity, pollen, particulate pollutants from power plants, and motor-vehicles textile fibers, vegetation, bacteria, and animal cells [427, 428]. Depending on several location-related parameters of a PV installation site, the local aeolian dust may consist of a mixture of all these different contaminants with varying chemical and particle-size compositions. Fig. 4.6 gives a schematic overview of the various factors that influence the accumulation of dust on solar panels and how these different factors might influence each other. Concerning dust composition, Darwish *et al.* determined that the most severe influence on solar panel performance can be attributed to six distinct types of particulate pollutants: limestone, ash, red soil, calcium carbonate, silica, and sand [427]. Concerning particle size distribution, in the city of Hermosillo (Sonora, Mexico), the diameters of aeolian dust particles were found to range between  $0.4\ \mu\text{m}$  –  $400\ \mu\text{m}$  [428]. However, the most frequently

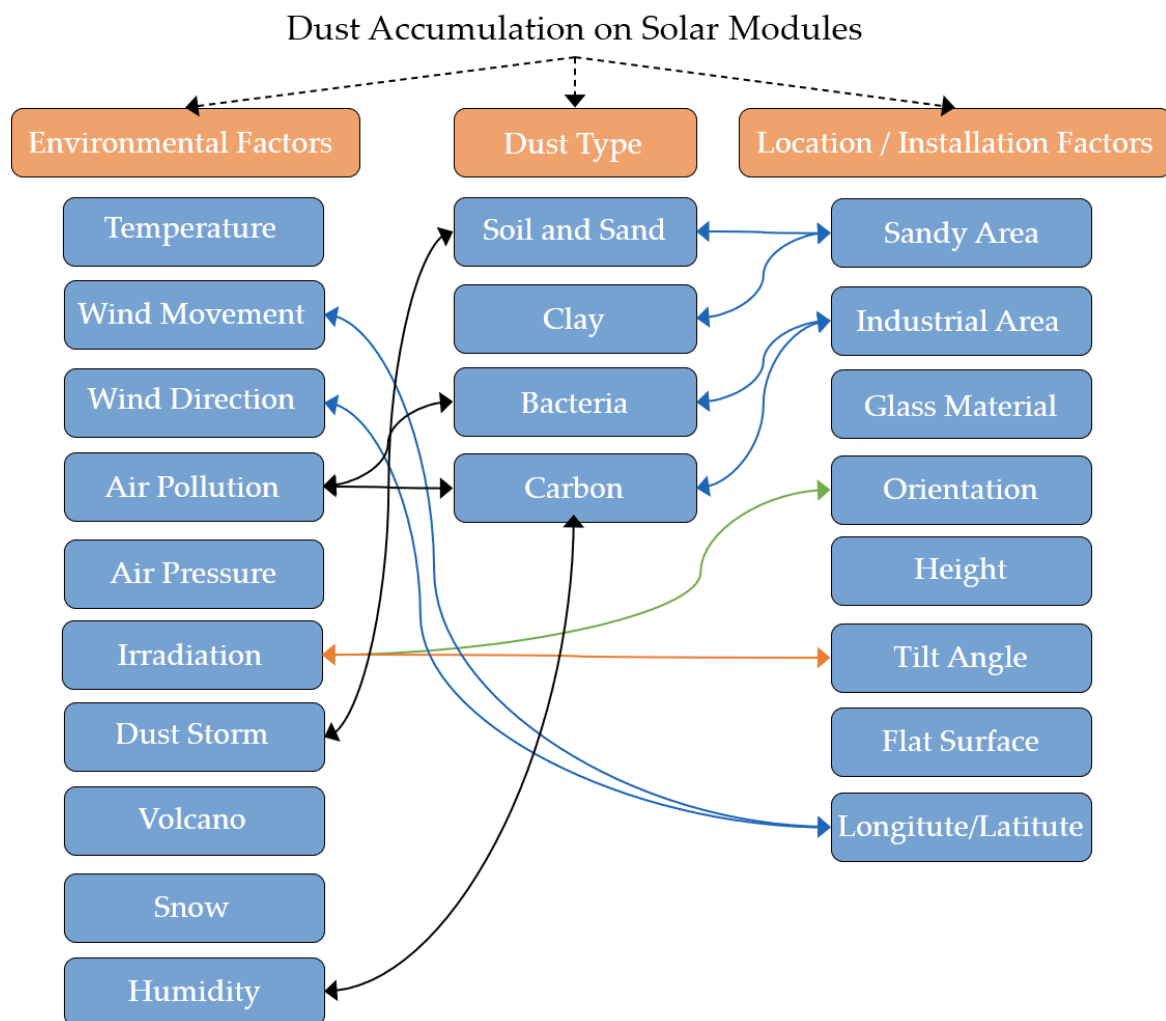


**Fig. 4.6:** Overview of which parameters of a PV installation influence the accumulation of aeolian dust particles on solar modules. Adapted with permission from reference [429], © 2016 The Authors. Published by Elsevier Ltd.

encountered diameter of  $52\ \mu\text{m}$  was found for a total of 11% of all the local aeolian dust particles [428]. Further, particles with a diameter  $\approx 19.8\ \mu\text{m}$  were found to make up the largest fraction of the cumulative volume of all pollutants, and therefore, this particle species is the most impactful in inducing soiling losses through shading effects [428].

In 2017, Micheli and Müller published a study to identify the key parameters for predicting soiling losses based on analyzing possible correlations between 102 environmental and meteorological parameters and experimental soiling-data acquired at 20 measuring stations at various locations in the USA (operating time between 7 and 40 months) [430]. Interestingly, a significant correlation was only found for a small number of parameters. The strongest correlations were found for the parameters that quantify the concentration of airborne dust particles (for

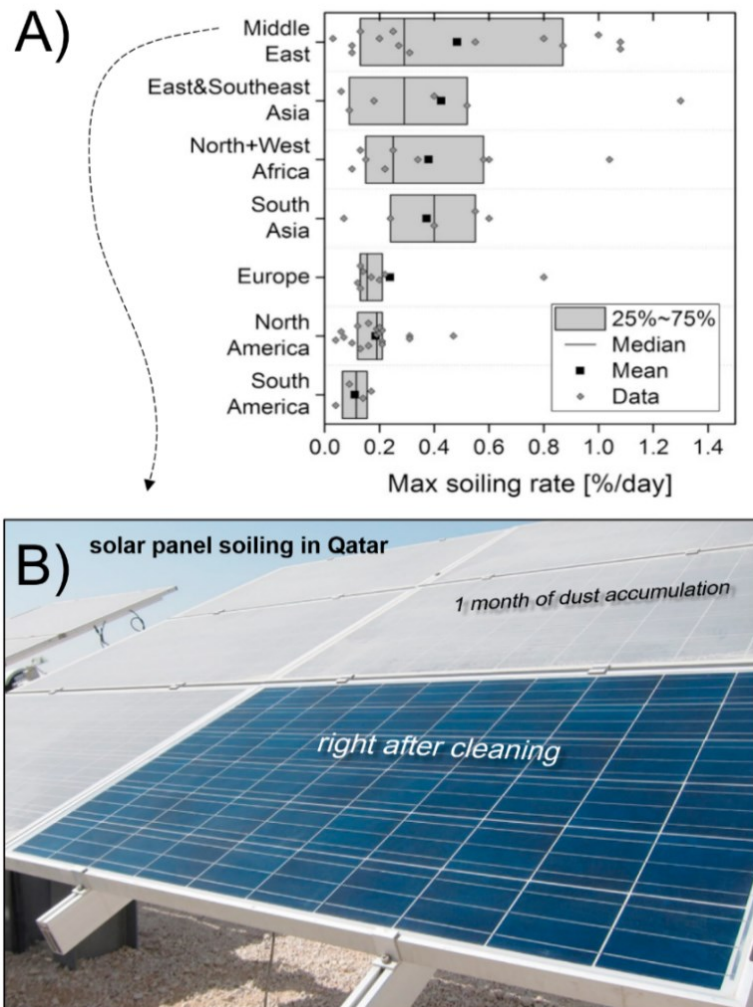


**Fig. 4.7:** Photographic illustration of dust accumulation on PV modules. A) Daily soiling rates (daily loss in power/efficiency) for various regions of the world. This plot is based on the data from 63 publications on soiling (compiled by J. John [431]). Reprinted with permission from [432]. B) Photograph of several solar panels installed in Doha, Qatar. After one month of soiling, only the PV panel in the foreground was cleaned. Photo adapted with permission from [432], © 2018 Elsevier Ltd. All Rights Reserved.

example, the annual average of the daily mean values of the concentration of dust with particle diameters of less than  $10\ \mu\text{m}/2.5\ \mu\text{m}$ , measured at monitoring stations in the vicinity of the PV installation sites). Besides these dust-concentration-related metrics, the remaining parameters with significant correlation to soiling describe the frequency and duration of precipitation (average and maximum number of days between two consecutive rainfalls). A model for making quantitative predictions of PV soiling losses based on environmental variables, however, was not provided by Micheli and Müller. Based on a neural network, such a model to compute the daily change in performance loss of a PV installation due to soiling in dependence of environmental variables was developed by Javed *et al.* [433].

In arid regions, which are often particularly attractive for PV energy production due to the scarcity of rain and the high solar irradiance, PV module soiling can be especially detrimental (as indicated by the worldwide soiling rates shown in Fig. 4.7 A), causing losses in power output of up to 30%–50% through increased reflection and parasitic absorption losses caused by the dust particles (compared to

a clean device), even after only a few weeks or months of operation in the field [434]. The effect of such drastic rates of dust accumulation in arid regions on the visual appearance of solar panels is exemplified by the photograph given in Fig. 4.7 B). In Riyadh, Saudi Arabia (24.71°, 46.72°), a drop in power output of 2%, 14%, and 30% was reported for a PV installation with a 25° tilt towards south after 1, 13, and 32 days of operation respectively [435, 436]. For the case of Kuwait (29.36°, 47.97°), solar panels with a tilt of 30° towards the south even face a 17% decrease in power output after only six days in the field [435, 437]. For efficient PV energy production, it is therefore unavoidable to somehow mitigate the accumulation of dust on solar modules' surfaces, especially in desert regions. The strategies to mitigate PV module soiling can be categorized into two basic classes [438]:

1. **Manual cleaning**, which includes all cleaning schemes that rely (at least partially) on (human) labor.
2. **Self-cleaning**, which covers all methods where an automatized cleaning scheme is exploited.

Employing manual cleaning strategies, PV installations can be thoroughly cleaned, even removing layers of cemented dust or local contaminations such as bird droppings. These methods may vary in the amount of water (and detergent) necessary per cleaning cycle and may employ a variety of cleaning equipment. The cleaning equipment needs to be optimized for the local climatic conditions, aeolian dust compositions, and the morphology of the respective PV panels' front surfaces to reach sufficient cleaning efficiencies [439]. However, all manual cleaning strategies suffer one major drawback, namely the high costs for the manual (human) labor [440, 441]. Next to this financial burden, manual labor can cause several other difficulties for large-scale PV installations since many other factors than the workers' salaries, like occupational safety or government-related issues on labor requirements, also need to be considered [441]. It is yet possible to achieve an economically feasible operation of manually cleaned large-scale PV installations if the cleaning cycles are scheduled properly [442].

Moreover, it is important to note that cleaning tools might cause abrasive damage on PV panel surfaces, which can damage the light-harvesting quality, especially for modules with micro- or nanotextured front surfaces. General recommendations for appropriately mitigating PV soiling losses for different climatic zones have been formulated by Mani and Pillai based on the review of numerous publications from seven decades (1940 – 2010) [443]. A procedure for estimating the optimal cleaning strategy that makes it possible to enhance total PV plant incomes has recently been

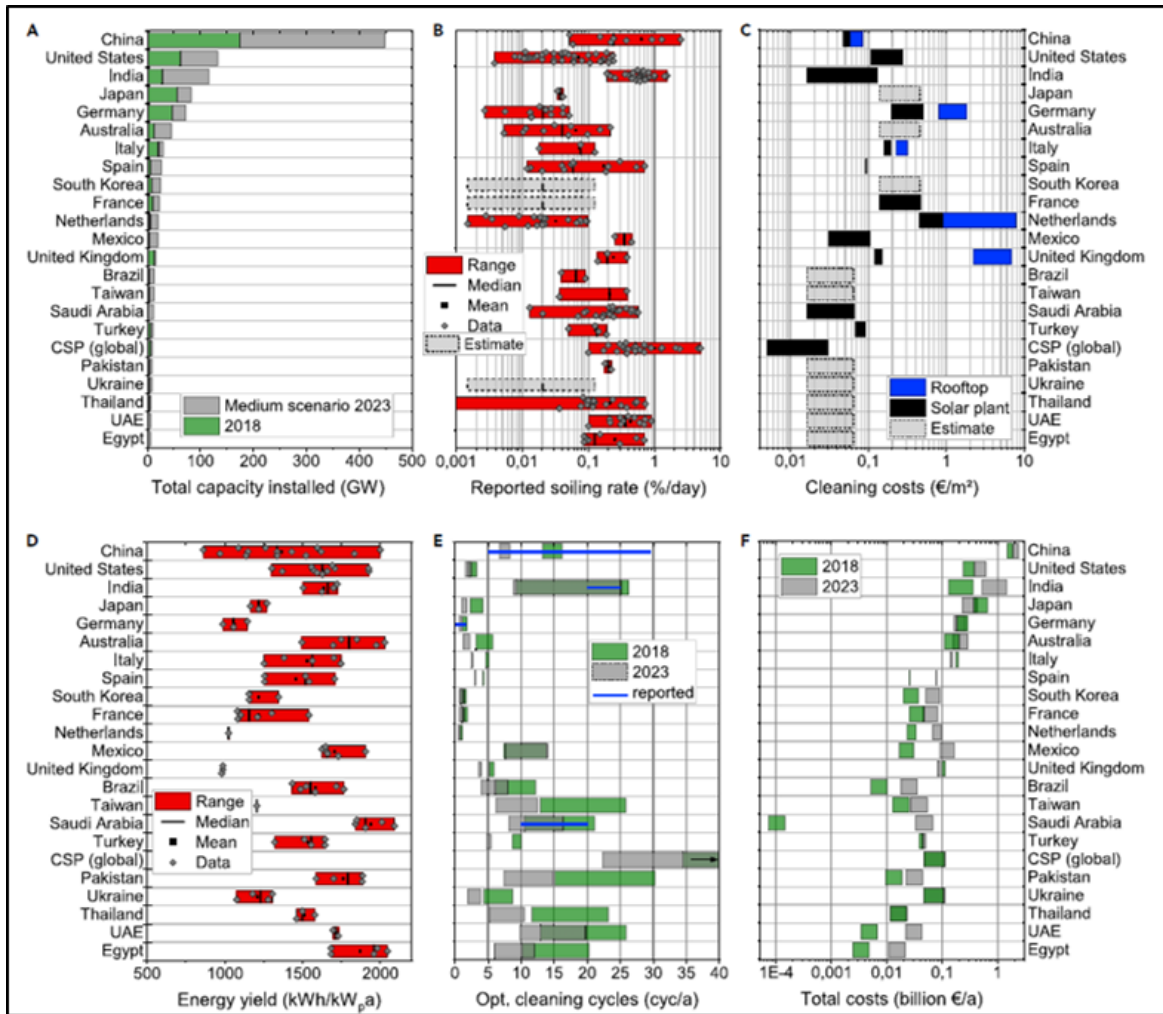


**Fig. 4.8:** Overview of worldwide soiling rates and cleaning costs sorted by country. A) Installed PV capacity in 2018 and medium estimate for 2023. B) Corresponding soiling rates from literature. C) Cleaning costs per cleaning cycle and square meter (reported). D) Typical energy yield for representative locations. E) Calculated range of the optimum number of yearly cleaning cycles and actual range of typical yearly cleaning cycles as reported in the literature. F) Minimum expected financial losses due to soiling, calculated from optimum cleaning cycles. Reprinted with permission from reference [444], © 2019 Elsevier Inc.

proposed [445]. Furthermore, the summary of a 2019 techno-economic assessment of soiling losses and mitigation strategies for solar power generation for various countries worldwide by Ilse *et al.* [444] is depicted in Fig. 4.8.

Following Jamil *et al.* [438], the self-cleaning-based methods of soiling mitigation can be further divided into two categories, namely active and passive self-cleaning schemes. Both can be further sub-categorized, as is depicted in Fig. 4.9. In the case of active self-cleaning methods, auxiliary systems that enable an automatized restoration of PV panels (using mechanical and water-based systems as well as electromagnetic screens) are added to PV installations, cleaning them with an

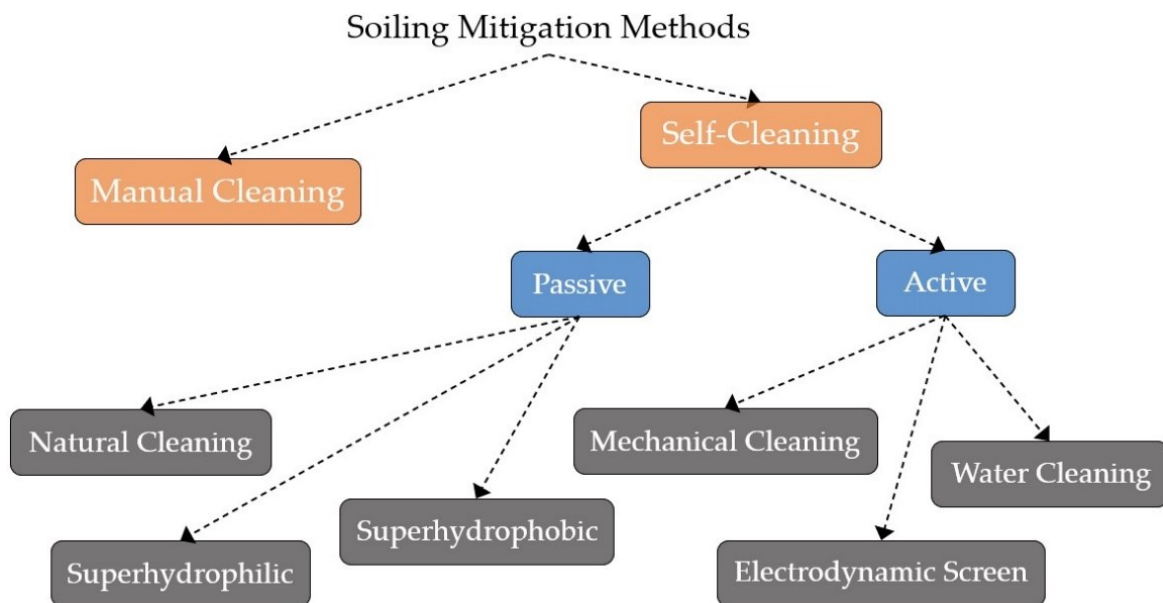


**Fig. 4.9:** Mitigation of PV module soiling. Following the categorization given in reference [438], this figure provides an overview of the different methods to mitigate soiling of solar panels.

appropriate frequency without involving any manual labor (besides maintenance). For example, a recently developed active self-cleaning scheme relies on anisotropic surface microstructures (comprised of hydrophilic features on a hydrophobic background), which, in combination with mechanical vibrations, leads to active driving forces for water droplets along a predefined path [446]. Passive self-cleaning approaches, on the other hand, do not rely on auxiliary systems that actively (help to) clean the modules at certain times. These strategies rather rely on the natural occurrence of rainfall to reduce PV module soiling. Passive self-cleaning, therefore, avoids the costs of manual labor and minimizes the amount of resources necessary (water, detergent) for the cleaning cycles. Disadvantageously and as a result of this reliance on natural rainfalls, controlling and adjusting the cleaning-intensity and -schedule for passive self-cleaning is impossible. There are three different ways to implement a passive self-cleaning scheme:

- 1) Natural cleaning
- 2) Superhydrophilic surfaces
- 3) Superhydrophobic surfaces

Natural cleaning describes the general case where only the climatic conditions at the PV installation site and the modules' orientation and tilt angle are exploited for mitigating PV module soiling, relying only on rain and wind (and melting snow). It has been reported that dust particles smaller than  $10\ \mu\text{m}$  are not removed by natural self-cleaning with rain [447]. Especially light rain is often only able to partially remove dust, while some of it might accumulate at the lower edge of the

PV panels [448]. Smith *et al.* found that relying on natural cleaning by rainfalls only restores about 1/4 of the energy yield that is lost due to soiling, whereas manual cleaning fully restores the module performance [449, 450].

The soiling rate of solar modules depends on the modules' tilt angle (relative to the horizontal plane) [451, 450]. Similarly, module tilt and orientation also influence the effectiveness of the natural cleaning approach. Depending on the latitude angle of a PV installation (as well as on the local geographical/climatic conditions), an optimum module tilt and orientation with respect to soiling losses can thereby be determined by minimizing the rate of dust accumulation and, at the same time, maximizing the efficiency of natural cleaning. However, this sweet-spot in terms of natural soiling reduction might generally differ from the solar modules' optimum tilt and orientation for maximizing sunlight capture (which, as a rule of thumb, can usually be assumed equal to the latitude of the installation site, see subsection 2.1.3). Therefore, effectively exploiting natural cleaning is only possible at locations where the tilt and orientation necessary for soiling-minimization still enables reasonably efficient photon-capture. These geographical restraints can be relaxed by modifying the wetting behavior of PV panels. By designing the PV panels' front surfaces as either superhydrophilic or superhydrophobic, rainwater will efficiently remove contaminants for practically all possible tilt angles and orientations. Both these passive self-cleaning approaches, therefore, assure proper cleaning of PV modules relying only on (wind and) natural rainfalls and a maximized sunlight capture by optimizing module tilt and orientation (even for variable tilt angles and orientations in case solar tracking is utilized to maximize sunlight capture). Designing an efficient superhydrophobic or superhydrophilic self-cleaning scheme for PV module front surfaces, therefore, seems to be a promising pathway for minimizing operational costs of PV installations while still effectively minimizing energy yield losses due to contamination of the modules. Of course, such self-cleaning PV front side coatings need to be designed in a way that simultaneously facilitates an efficient in-coupling and trapping of sunlight for a broad range of wavelengths and AoIs.

In a 2019 contribution, Heckenthaler *et al.* pointed out that nanostructured superhydrophobic self-cleaning surfaces should generally be favored over their superhydrophilic counterparts due to the increased dust removal rates under rainfall that these surfaces tend to exhibit [452]. Heckenthaler *et al.* link this behavior to the combination of reduced particle adhesion forces and an increased

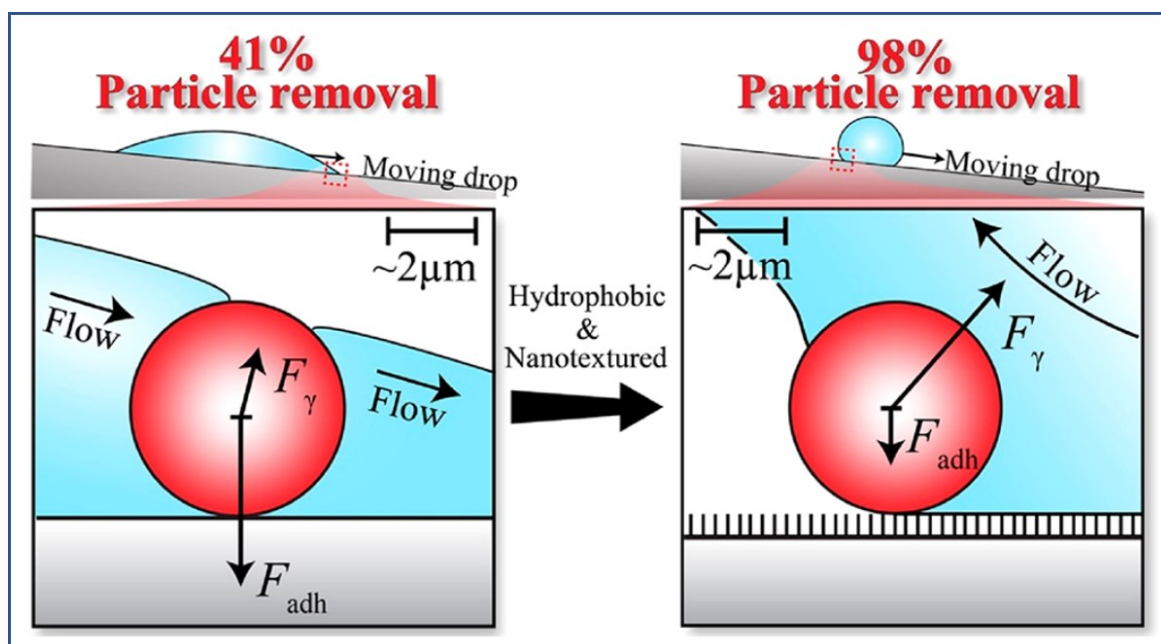


**Fig. 4.10:** Schematic illustration of the main forces acting on a particle during self-cleaning for a hydrophilic (left) and a hydrophobic (right) surface. The adhesion force between dust particles and surface is reduced for nanostructured hydrophobic surfaces, while the lift-off-force exerted by a moving water droplet increases. Reprinted with permission from reference [452], © 2019 American Chemical Society.

lift-off-force exerted by water droplets (due to the altered geometry of the water-particle-air line tension) moving down the inclined superhydrophobic surface, as schematically depicted in Fig. 4.10 [452].

As introduced in chapter 3, many functionalized surfaces are found throughout the plant and animal kingdom, which exhibit highly efficient (superhydrophobic or -philic) self-cleaning properties, almost zero surface reflectance, or extremely high transparency. Some natural surfaces, such as cicada wings [328], or rose petals [13], even exhibit the desired combination of self-cleaning behavior and efficient light in-coupling properties. It therefore seems natural that engineers use such highly functionalized biological surfaces as the source of inspiration for the design of technical materials with a similar portfolio of properties. The following chapter 5 is therefore concerned with the various strategies of how the properties found on plant and animal surfaces can be transferred into technology. Since this dissertation is mainly concerned with replication techniques for templating the properties of functional bio-surfaces, the main focus of the following chapter 5 is bioreplication. The alternative strategies regarding engineered biomimicry (biomimetics and bioinspiration) are also introduced in chapter 5.

---

## 5 Bioreplication, Bioinspiration, and Biomimetics

---

The previous chapters gave an insight into the wealth of (often) hierarchical surface structures that can be found in nature. Moreover, their specific (multiple) functionalities, most notably self-cleaning and antireflection properties, were described. On that basis, the following chapter addresses the question of how multifunctional surface properties found on plants and animals can be transferred into technical materials such as polymers. Especially for cases where the (industrial) fabrication of functionalized surfaces relies on time-consuming or expensive processes (wet/dry etching, ion beam lithography, etc.), the direct replication of a suitable surface texture by a straightforward molding process can be of high scientific and commercial interest. After a detailed introduction of the various bioreplication methodologies in section 5.1, some selected examples of bioinspired and biomimetic functional surfaces are summarized in section 5.2. Lastly, sections 5.3 and 5.4 describe the light-harvesting properties of soft-imprint replicated PV light-harvesting layers and summarize the current state of research concerning plant-replicated PV light-harvesting layers.

### 5.1 Replication of Biological Surface Textures

Replicating the surface morphologies of plants and animals into technical materials has at least a 70-year long history [453]. Since many biological surfaces are simply lacking the mechanical and/or chemical stability (on the micro- or nanoscale) to be directly examined microscopically, imprinting or copying biological surface into suitable materials paved the way towards a detailed topographical analysis of nature's abundant repertoire of micro- and nanotextured surfaces [454], which is, next to analyzing the chemical composition, of key importance in order to understand many of the outstanding physical and chemical properties of plant and animal surfaces. With regards to studying the physical properties of leaf or petal surfaces, which are not only decorated with highly complex topographies but generally also consist of numerous types of (inhomogeneously distributed)

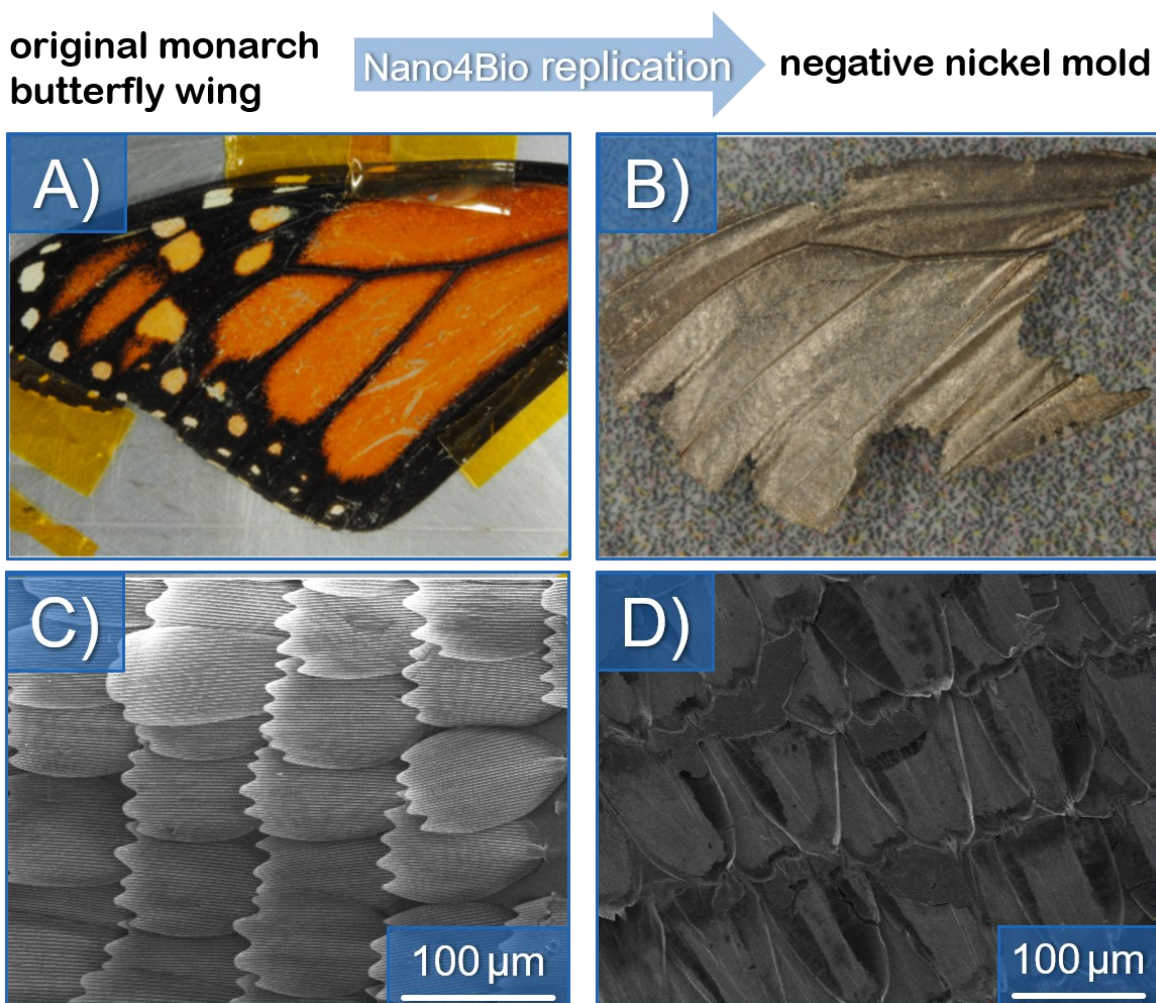


**Fig. 5.1:** Replication of a monarch butterfly wing via Nano4Bio. Photographs of A) a natural wing of a monarch butterfly and B) a negatively textured Ni mold fabricated via the Nano4Bio replication technique (combination of PVD and electroforming). C) and D) depict SEM micrographs of the original wing and the Ni mold. Adapted with permission from reference [455], © 2011 Society of Photo-Optical Instrumentation Engineers (SPIE).

molecules, replication can also be seen as a method to separate the chemistry-induced properties from the ones that are caused only by the surface morphology. Such a strategy has, for example, been utilized in order to study light-focusing in the epidermal cells of green leaves of numerous plant species. By replicating their lens-like epidermal cells into transparent polymers, direct measurements of focal-length and light-intensification-factors within epidermal cells of plants endemic to various habitats were facilitated [376, 456]. In more recent years, polymer replicas of petal surface textures were utilized in order to analyze (possible) structural color effects caused by the cuticular nanofolds that typically cover their epidermal cells [457–459]. These examples already give a hint that bioreplication can not only be employed to gain knowledge about the morphology and functionality of the

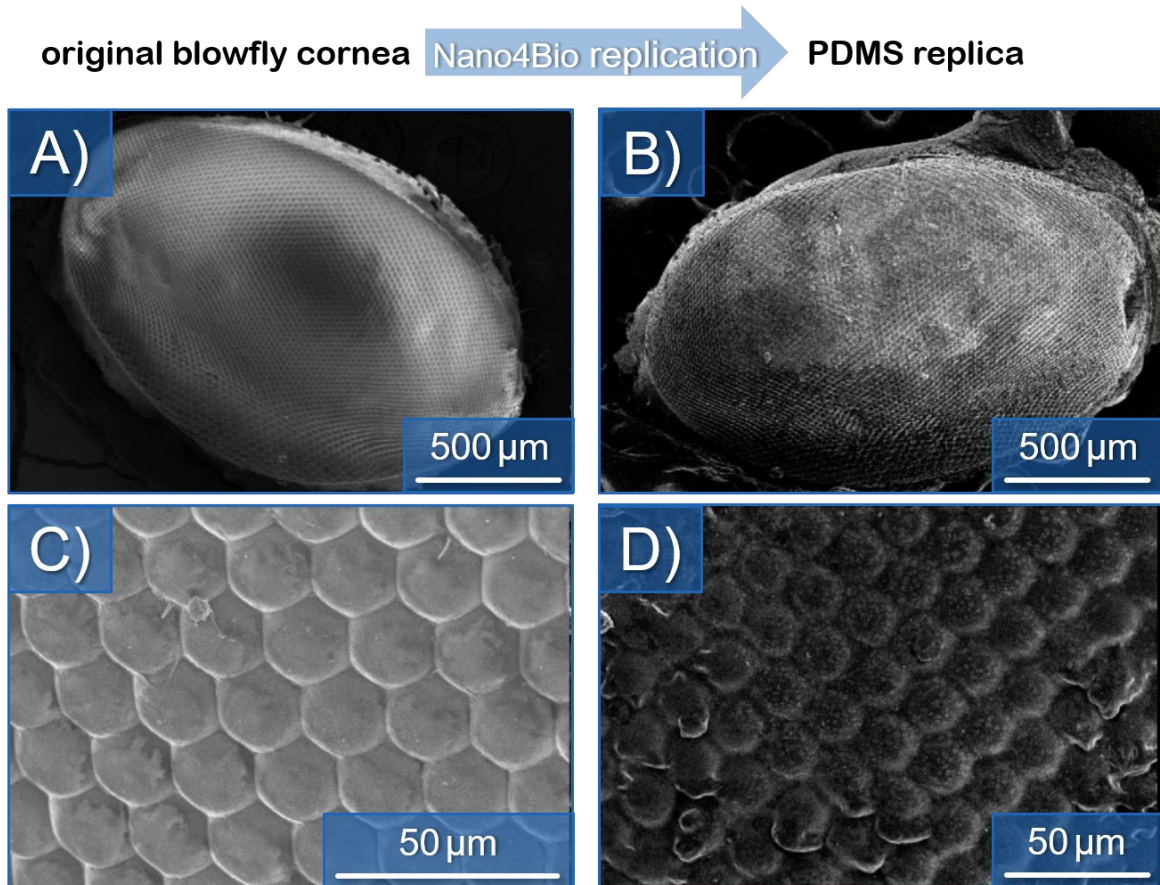


**Fig. 5.2:** Replication of a blowfly cornea via Nano4Bio. SEM micrographs of A) a natural blowfly cornea and B) a PDMS replica fabricated via the Nano4Bio replication technique (combination of PVD and electroforming) and subsequent PDMS casting of a negative Ni mold. C) and D) depict SEM micrographs of the original insect eye and the polymeric replica with larger magnification. Adapted with permission from reference [455], © 2011 Society of Photo-Optical Instrumentation Engineers (SPIE).

original structure but can also be seen as a tool to engineer surfaces that copy one or more specific functions like superhydrophobicity or antireflection from a natural template.

Depending on the 3D morphology and the chemical composition and stability of the template, bioreplication can be achieved with the help of various techniques like atomic layer deposition (ALD), physical vapor deposition (PVD), sol-gel-based approaches, electroforming, or via (a combination of) casting and (soft) imprint lithography [460].

The sub-wavelength microlenses that are found on the eyes of many (nocturnal) insects can be copied into an inorganic, transparent material by employing the conformal-evaporated-film-by-rotation technique (PVD-based), which was demonstrated for *tephritid* flies (common fruit flies) [461]. The same method has

previously been used to transfer the surface structures of butterfly wings (*Battus philenor*) into chalcogenide glasses [462].

Furthermore, insect corneas and butterfly wings can also be transferred into alumina replicas via ALD [463, 464]. While all these approaches are limited to producing only a single replica per biotemplate, an improved technique has been developed, combining the conformal-evaporated-film-by-rotation method with a subsequent Ni electroforming (see chapter 7) step to create a thick, negative mold. This metallic mold can then be used to produce multiple positive polymer replicas by PDMS casting (or imprinting) from a single biotemplate, as has been demonstrated for the wings of the monarch butterfly (*Danaus plexippus*) and the corneas of the common blowfly (*Eucalliphora lilea*) [455, 465]. This replication routine, which is often called 'Nano4Bio' [466], is exemplified for monarch butterfly wings and blowfly corneas in Fig. 5.1 and Fig. 5.2. Following this approach, the subwavelength features of the monarch butterfly wing and the blowfly cornea, although present on the master stamp, were not successfully transferred into the PDMS replica [455, 465]. Following a different approach, a transfer of the nanostructures found on the highly transparent wings of cicadas (*Cryptympana atrata Fabricius*) into gold nanopillars standing on a silicon substrate has been achieved via imprinting the original cicada wing into PMMA and then depositing gold and attaching a silicon wafer before finally removing the PMMA material [327]. Another way of transferring the subwavelength surface structure of a cicada wing was achieved via imprinting the original cicada wing into a PVC layer, which is subsequently coated with a SiO<sub>2</sub> layer and then used as a stamp to replicate the cicada wing nanopillar structure into a UV-curing resist material [467]. Recently, flexible broadband antireflective films with (superhydrophobic) self-cleaning properties have been fabricated based on a cicada wing template by first producing a negative SiO<sub>2</sub> replica via sol-gel-replication with a following second sol-gel step to generate a positive PMMA replica [328]. Furthermore, cicadas' nanostructured compound eyes have also been successfully copied into a polymer via epoxy resin casting [468]. Another example for the bioreplication of an antireflective (micro-) structure into epoxy resin has been demonstrated with blue mussel shells [469].

While replicating transparent butterfly wings and insect corneas has mainly been aimed at studying or copying their highly efficient antireflective properties, studies on plant surface replication have mostly focused on copying/studying wetting properties. To that end, several leaf and petal surfaces have been copied in a variety of ways. The leaf surface structures of bamboo, lovegrass, tulip tree, and silver

maple have also been directly imprinted into UV-curing polymers by using the respective natural leaf itself as a stamper [470]. Natural bamboo (*Phyllostachys pubescence*) leaves have further been metal-coated and galvanically copied into Ni (see chapter 7) in order to fabricate a negatively textured metallic mold that can be repeatedly employed to produce positively textured polymer replicas via UV-NIL or polymer casting [471]. This electroforming-based replication route was further utilized to copy the leaf surface texture of other plants, such as the lotus plant [472] and the rose petal surface texture [458, 473]. Next to using such Ni molds for UV-NIL or for polymer casting, their aptitude for injection molding of replicas has recently been demonstrated for indocalamus leaves [474]. It should be noted that all these plant replication approaches, which rely on directly electroforming a natural leaf or petal template lead to alterations of the epidermal cell convexity due to water loss during metal-coating. Polymer casting and soft-imprint-based molding techniques are a way to ensure the structural integrity of the epidermal cells during the replication process. Historically, however, such a technological approach was often prohibited by the lack of cost-effective molding materials that are able to reliably replicate structural features of small enough size. For many biological templates such as plant surfaces, a proper replication technique additionally needs to be (i) fast enough to prevent topographical changes due to water loss, (ii) avoid any kind of material shrinkage (during drying or curing), and (iii) also keep delicate high AR features intact. Such a replication route for plant surfaces was developed by Koch *et al.* in 2008 [475]. Similar methods have since been widely used throughout academia to replicate various plant (also animal and artificial) surfaces, mainly in order to study or to copy their wetting behavior and/or their optical properties.

The basic procedure for soft-imprint replication of plant surface textures is depicted in Fig. 5.3. A biotemplate (like a rose petal) is fixed onto a planar substrate and cast with PDMS. After heat curing, the solid yet flexible PDMS mold can be detached and cleaned from the residual plant material and can subsequently be used as a negative mold. A droplet of a transparent, liquid, UV-curing resist material is then placed on the target surface (glass substrate or a solar cell) and then carefully covered with the PDMS mold so that no air bubbles are trapped between mold and resist material. The polymerization process is then initiated by UV light exposure (in case of an opaque target surface, as a solar cell, for example, the sample needs to be illuminated through the PDMS). After full curing is achieved, the PDMS mold is removed, leaving a (positive) plant texture replica on the target surface. For the case of the hierarchical rose petal texture, this soft-imprint approach leads to a high

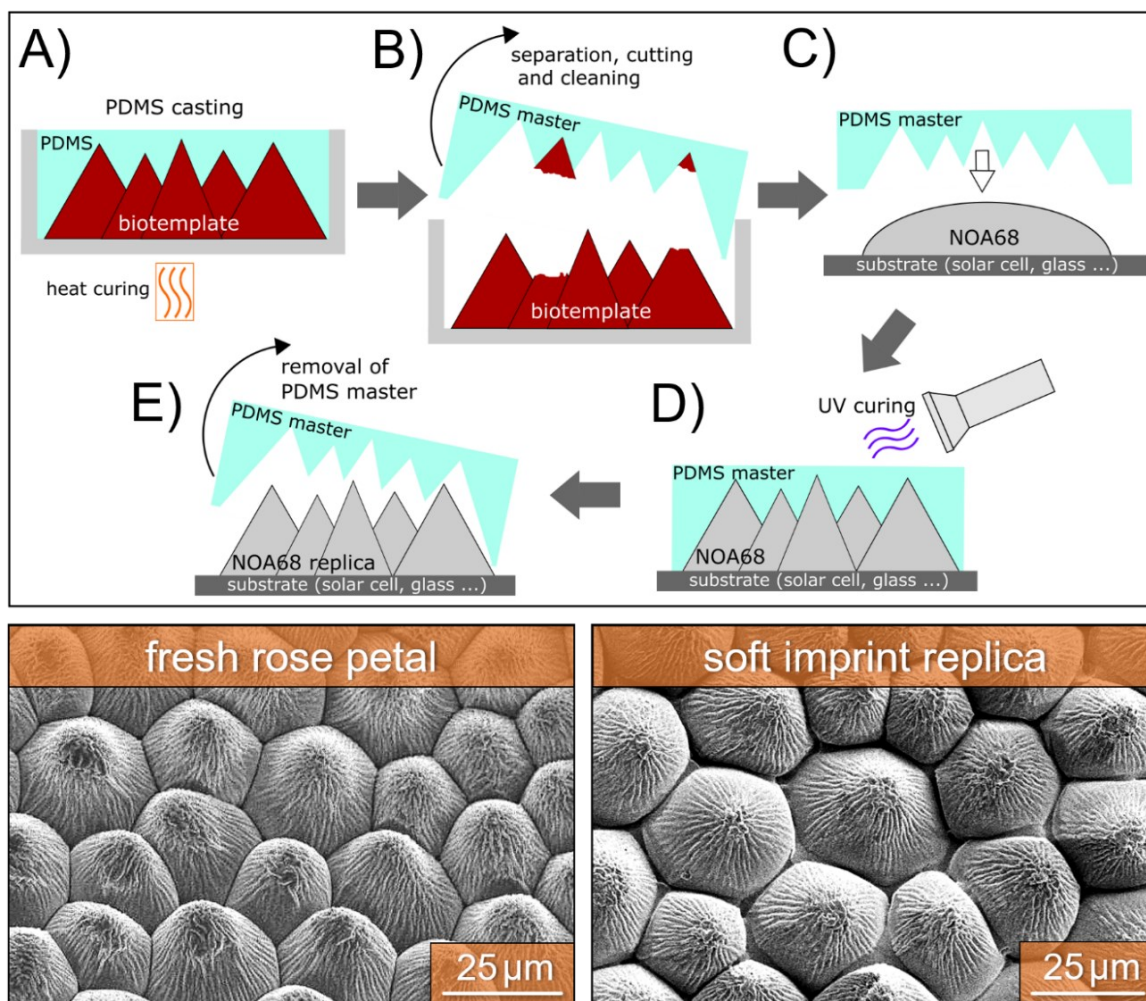


**Fig. 5.3:** Soft-imprint replication of plant surfaces. Top: Schematic depiction of soft-imprint replication of the rose petal surface texture into a transparent, UV-curing resist material. A) A natural rose petal is fixed onto a planar substrate and covered with PDMS. B) After heat-curing, the PDMS layer is removed from the biotemplate and cleaned. C) The PDMS mold is carefully placed onto a droplet of a transparent resist like NOA68. D) Exposure to UV light then starts the polymerization of NOA68. E) After the removal of the PDMS master, a NOA68 rose petal replica is realized. Bottom: SEM micrographs of a fresh rose petal and a soft-imprint replica. The hierarchical texture (epidermal cells decorated with a cuticular wax layer) is well copied into the UV-curing polymer material.

structural fidelity of the resulting polymeric copies, as can be deduced from the SEM images in Fig. 5.3. It is worthy of note that, with a proper surface treatment to enable detachment without causing structural damage, a negative PDMS mold can also be used to fabricate positive PDMS replicas of plant surface structures by direct imprinting/casting [413]. Several similar approaches based on polymer-casting and UV-nanoimprint-lithography steps have been successfully utilized for replicating hierarchical plant surface structures. For rose petals, for example, their

superhydrophobic properties with simultaneous strong adhesive forces have been replicated from natural templates by fabricating a negative master by UV-curing of polyurethane acrylate (PUA) and a following second structure-transfer-step into UV-curing perfluoropolyether (PFPE) [476]. Similarly, the surface texture of rose petals has also been successfully replicated by first pouring polyvinyl alcohol (PVOH) water solution onto a natural petal and letting it dry to produce a PVOH negative mold and a similar second step with polystyrene (PS) chloroform solution to achieve a positive copy of the rose petal structure in PS [412].

The convex epidermal cells combined with 3D epicuticular waxes that are found on, for example, the superhydrophobic leaves of taro (*Colocasia esculenta*) (wax platelets) and lotus (clusters of wax tubules) plants might also qualify as candidates for improving light-harvesting in PV. Unfortunately, a simple PDMS casting approach does not properly copy the highly intricate cuticular surface nanostructures of self-cleaning leaves such as lotus [477, 478], taro [478, 479], or ryegrass [480] and only adequately copies the epidermal microtexture. It is worth noting that electric field-assisted polymer casting methods have already been developed to enable improved polymer casting of such hierarchical plant surface textures [481–483]. Interestingly, it has also been shown that the hierarchical lotus leaf surface structure can be faithfully replicated by extending the standard PDMS casting and soft-imprint lithography approach as follows [484, 485]:

- 1) Removing the cuticular wax layer from the natural leaf template.
- 2) PDMS casting and soft-imprint replication of the lotus leaf epidermal cell microstructure without the cuticular wax structure.
- 3) Deposition of a layer of natural lotus-wax on the replica of the smooth lotus epidermal cells. The nanostructure forms by self-assembly of the wax crystals into tubules.

Lastly, another plant epidermal structure replication approach worth mentioning has recently been demonstrated by Chang *et al.* [486]. They demonstrated a heat-free metal molding technique that can be used directly on soft and delicate substrates such as leaves and petals under ambient conditions. Their process is based on the deposition of undercooled metal (‘undercooled liquid metal core-shell’, ULMCS) particles on a natural rose petal template. A combination of self-filtration and jamming leads to tight packing of the metal particles on the template without damaging the delicate petal underneath. Once densely packed, a subsequent chemical sintering process (‘coalescence of undercooled particles through a chemical trigger’) induces solidification of the molded metal. Although this method doesn’t faithfully reproduce the nanowrinkles which decorate the

micro-cone-shaped epidermal cells of the rose petal, it is still quite remarkable that metallic microstructure replicas can be directly templated under ambient conditions, similar to simple a polymer casting step.

### 5.2 Biomimetic and Bioinspired Materials

As explained in the previous section 5.1, the term ‘bioreplication’ describes all processes aimed at directly copying a structure found on an animal or on a plant. Bioreplication, however, is not the only strategy that can be pursued to transfer specific functionalities found in living nature into technology (engineered biomimicry [455]). Next to such a direct replication approach, two other methodologies of engineered biomimicry, commonly called ‘bioinspiration’ and ‘biomimetics,’ are widely used. In a 2017 review article by R. Martín-Palma and A. Lakhtakia, the authors define these two strategies (the boundary between them is not always easy to establish) as follows [466]:

*‘Bioinspiration aims at reproducing the outcome of a certain functionality of a plant or an animal without reproducing either the physical/chemical mechanism or the biological structure responsible for the outcome. Biomimetics aims at the reproduction of the physical/chemical mechanism underlying a specific functionality of a plant or an animal.’*

This section provides an overview of bioinspired and biomimetic functional materials focusing on topics relevant for optoelectronics, especially for PV, namely self-cleaning and/or antireflective surface structures. The first few of the following paragraphs, however, aim to introduce a broad range of different functional biomimetic or bioinspired materials.

Sharks are known to be incredibly fast swimmers. Their ability to move through water with such ease stems from the special surface structure of their skin, which drastically reduces frictional forces and is the focus of research efforts to develop shark-skin-inspired drag-reducing coatings with anti-bio-fouling properties for ships in order to reduce fuel consumption and reduce maintenance costs [487].

Water-striders can effortlessly walk on water surfaces due to their hierarchically structured water-repellent legs, inspiring the creation of highly superhydrophobic surfaces [488, 489]. Moreover, it is well known that geckos can easily cling to any kind of surface by the combined Van-der-Waals-forces of billions of tiny (branched) hairs of only around 200 nm in diameter, which, simultaneously to this adhesive

property, also cause a self-cleaning effect [490]. These hierarchically structured hair-like objects can serve as an inspiration for the development of, for example, self-cleaning coatings or glue-free adhesives.

Also quite well known, spider capture-silk can serve as an inspiration for a number of functionalized materials, including properties such as stickiness, elasticity, and water-collection ability [491–493]. Spider dragline-silk, on the other hand, shows a number of other interesting properties, such as supercontraction [494, 495] or torsional shape memory [496]. The development of mechanically rigid materials is an example for an area of research, where inspiration can be drawn from many natural materials like, for example, bones or also from some especially tough shells or sponge spicules. Nacre, also commonly known as ‘mother of pearl,’ is such a rigid material, which is found in the shells of some mollusks or, more famously, in pearls. Developing nature-inspired or -mimicking materials, however, is not only valuable in terms of mechanical properties, but researchers have also tried to biomimetically reproduce nacre’s iridescence properties [497, 498]. Silver ants, on the other hand, have inspired the development of textured PDMS layers for improved radiative heat dissipation in devices such as solar cells [499–501]. Inspiration for creating noniridescent structural colors can be drawn from animals such as tarantulas [502] or blue *Morpho* butterflies [503]. In addition to producing angularly stable and bright colors, *Morpho*-inspired materials can also serve other functionalities (relying on structure-based effects as well as chemistry-based effects and combinations of both), such as superhydrophobicity/self-cleaning and directional adhesion [504], or for sensing purposes such as thermal-infrared sensing, vapor, and solvent sensing, or pH sensing [505]. Another variety of butterflies has been mimicked to produce an antireflective layer for boosting the light-harvesting properties of solar cells. The wings of *Pachliopta aristolochiae* butterflies are extraordinarily dark black without glare, which indicates that a low-reflecting surface structure must be present on the micro- and/or nanoscale. R. Siddique *et al.* utilized polymer-blend-lithography and reactive-ion-etching to fabricate a disordered nanohole structure in a-Si:H PV thin-film absorber layers inspired by the nanomorphology of black butterfly wings and thereby achieved a boost in sunlight absorption at large wavelengths [506]. Moreover, subwavelength surface structures which closely resemble the nanonipple-arrays found on the transparent wings of glasswing butterflies and cicadas were recently fabricated on fused silica surfaces by relying on patterning via circularly polarized (femtosecond) laser pulses [507]. Intriguingly, the nanostructures found on cicada wings, due to their ability to kill bacterial cells through mechanical rupture [508], also served as an inspiration for selective anti-bacterial surfaces for medical applications [509].

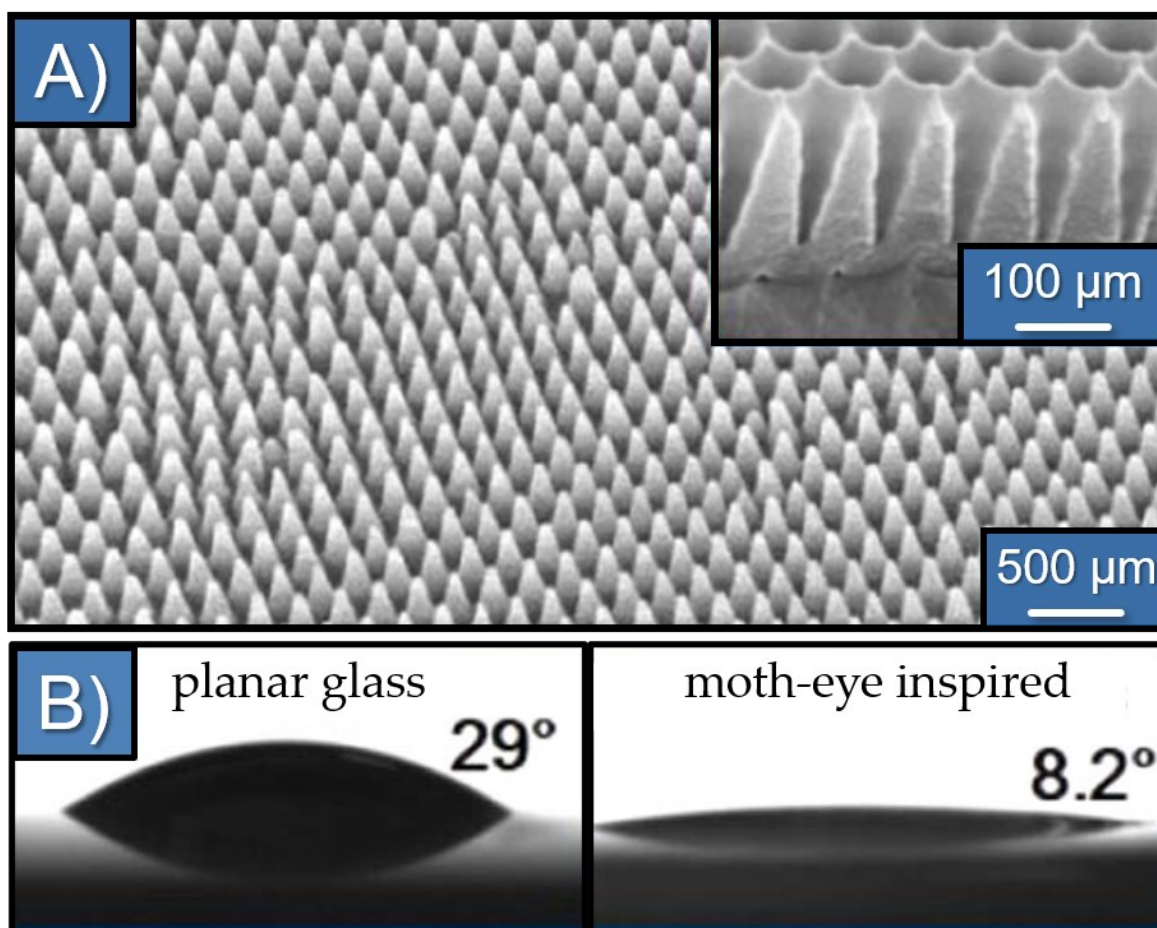


**Fig. 5.4:** Moth-eye-mimicking antireflective structure (AAO-based). **A)** SEM micrograph of a moth-eye-mimicking antireflective nanostructure fabricated by templating an AAO mold, which is displayed as an inset on the upper right. **B)** Photographic depiction of the static water contact angle of planar glass (left) and glass coated with the polymeric moth-eye-inspired nanopillar array. Next to superhydrophilic self-cleaning properties, these coatings also show antifogging and antifouling properties. Adapted with permission from reference [510], © 2019 IOP Publishing Ltd.

Anodic aluminum oxide (AAO) layers exhibit a hexagonal (honeycomb) arrangement of nanopores. By controlling the parameters of the anodization (electrochemical oxidation) process, the arrangement of the AAO-nanoholes can be tuned from disordered to ordered, and the pore-size can be controlled. A popular method to artificially recreate moth-eye-like arrays of subwavelength nanopillars therefore relies on various templating methods based on AAO molds [510–512]. An example of such an AAO-templated antireflective nanostructure, where a (superhydrophilic) self-cleaning nanopillar array was fabricated in a copolymer on glass, is shown in Fig. 5.4. AAO molds have also been integrated into roll-to-roll UV-nanoimprint systems [513]. Another popular route to produce moth-eye AR layers relies on various combinations of nanoparticle-assembly processes, templating, and etching steps [514, 191]. An example of such a fabrication scheme

(resulting in moth-eye-patterned quartz) is shown in Fig. 5.5. A similar fabrication scheme relies on the deposition of a thin Cu layer and a subsequent dewetting step to produce a disordered and subwavelength-scale-structured etching mask to directly etch moth-eye-patterns into glass [515]. Another approach relies on laser-interference-lithography for fabricating a nano-cone-structure in silicon, which is subsequently transferred into PDMS via casting, resulting in a polymeric inverted moth-eye-structure [516]. Positive (highly ordered) moth-eye patterns in PDMS have also been achieved via casting-based replication from Si master molds, fabricated, for example, by photolithography and inductively coupled plasma etching [517]. Moreover, slightly larger moth-eye-like nanostructures that serve as subwavelength broadband antireflective structures for mid-infrared radiation have been successfully transferred into chalcogenide glass via direct imprinting [518]. Further, it has also been demonstrated that moth-eye-inspired antireflective nanostructures can also be transferred onto curved 3D objects (such as lenses) via soft-imprint molding [519], and efforts to upscale the fabrication of such moth-eye-like structures to larger areas have also been undertaken [520]. Using direct laser interference ablation, Wang *et al.* demonstrated that moth-eye-like, tunable, highly-ordered, conical pillar arrays for antireflection can be produced on various material (for example ZnS) surfaces [521]. Interestingly, improving the light-harvesting properties of solar cells using moth-eye-like nanostructures can be realized not only by applying the biomimetic structure on the cover glass (or front side in general) of a PV device as an antireflective coating. For organic solar cells, moth-eye-structures have also been successfully integrated into the device's active layer resulting in significantly improved light-trapping capabilities [522].

A more 'exotic' example for a biomimetic antireflective surface structure takes inspiration from brochosomes, which are soccer-ball-like objects of submicron size (displayed in Fig. 5.6) that leafhoppers produce and actively coat themselves with [523]. Next to their use as a non-stick coating [523], it has been suggested as early as 1936 that part of the function of superoleophobic leafhopper brochosomes might be for camouflaging their eggs for protection against birds or insects [524]. Indeed, artificially produced brochosome-like nanoparticle assemblies have been fabricated (schematic depiction of fabrication scheme is shown in Fig. 5.6 C) and demonstrated to exhibit ultra-antireflective properties [525].

Another example of a biomimetic photonic structure that serves a different purpose than antireflection has been developed by J. Syurik *et al.* with the aim of recreating the brilliant whiteness of some scarab beetles (see Fig. 3.3). The researchers

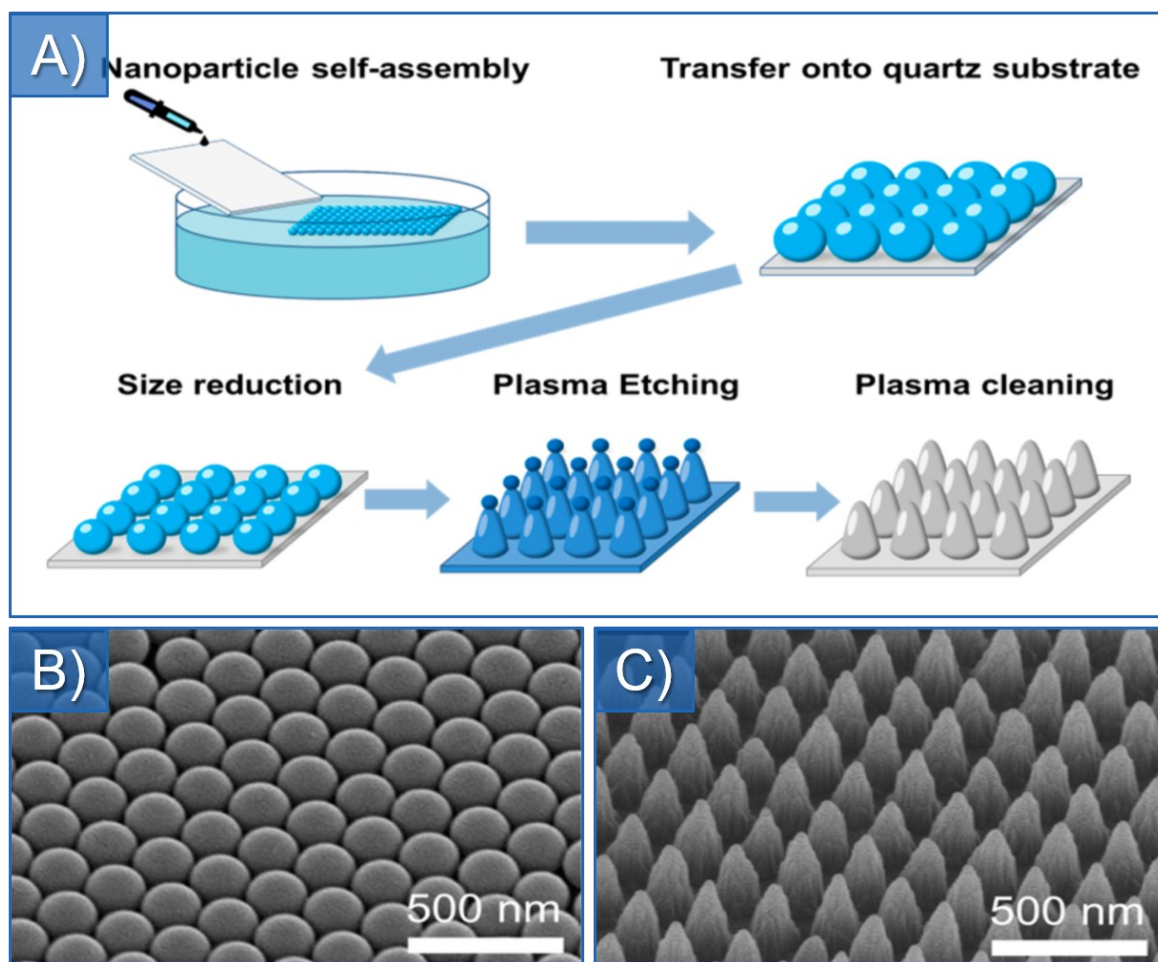


**Fig. 5.5:** Moth-eye-mimicking antireflective structure (nanoparticle-assembly-based). A) Schematic depiction of a fabrication routine for moth-eye-mimicking antireflective layers based on self-assembly of (polystyrene) nanoparticles and subsequent plasma etching. The nanoparticle assembly serves as an etching mask, resulting in a moth-eye-structured quartz substrate. B) SEM micrograph of the self-assembled nanoparticles. C) SEM micrograph of the finished nanopillar array after etching. Adapted with permission from reference [191], © 2013 American Chemical Society.

employed a foaming process in order to produce porous layers of PMMA with broadband and efficient scattering properties [287]. In collaboration with S. Yu *et al.*, similar porous PMMA layers inspired by white beetles as, for example, *Cyphochilus insulanus* were developed within the scope of this doctoral dissertation to be used as host matrices for color-converting quantum dots or dye molecules to achieve efficient, thin, and TiO<sub>2</sub>-nanoparticle-free light-conversion layers [6, 11, 12].

Concerning bioinspired and biomimetic antireflective and/or self-cleaning functional surfaces from the world of plants, one example is given in Fig. 5.7. The so-called nanofur is fabricated by a combination of hot-embossing and hot-pulling

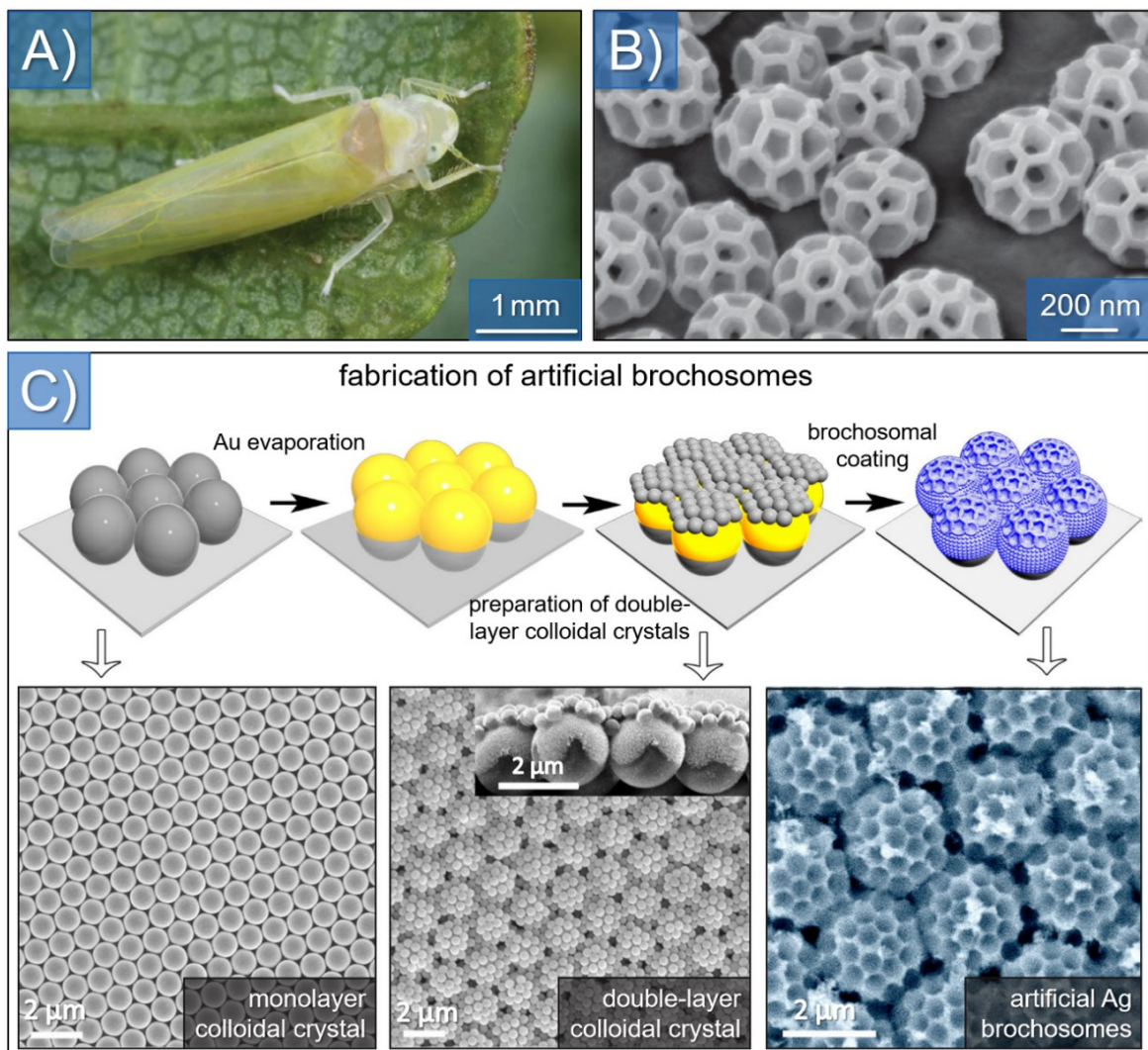


**Fig. 5.6:** Antireflective coating inspired by leafhopper brochosomes. A) Photograph of an adult leafhopper *Alnetoidia alneti* (Dahlbom). B) Close-up SEM micrograph of a forewing of *A. alneti* showing individual brochosomes. C) Schematic depiction of a fabrication process to produce artificial arrays of brochosome-like objects. A) and B) were adapted with permission from reference [523], © 2013 The Authors. Published by the Royal Society. All Rights Reserved. C) was adapted with permission from reference [525], © 2017 The Authors.

of polycarbonate foils with a sandblasted metal plate and mimicks the hairy surface structures found on the leaves of plants such as water fern *Salvinia cucullata* and water lettuce *Pistia stratiotes*. As can be seen from the side-view SEM image in Fig. 5.7 F), nanofur is actually a type of hierarchical structure, with the micro-hairs being arranged around the outlines of microcavities or -indentations, which stem from the hot-embossing part of the fabrication process. Nanofur has been investigated as a possible candidate for oil-spill-cleanup [526, 527] and can be employed as a highly transmissive film for optical applications such

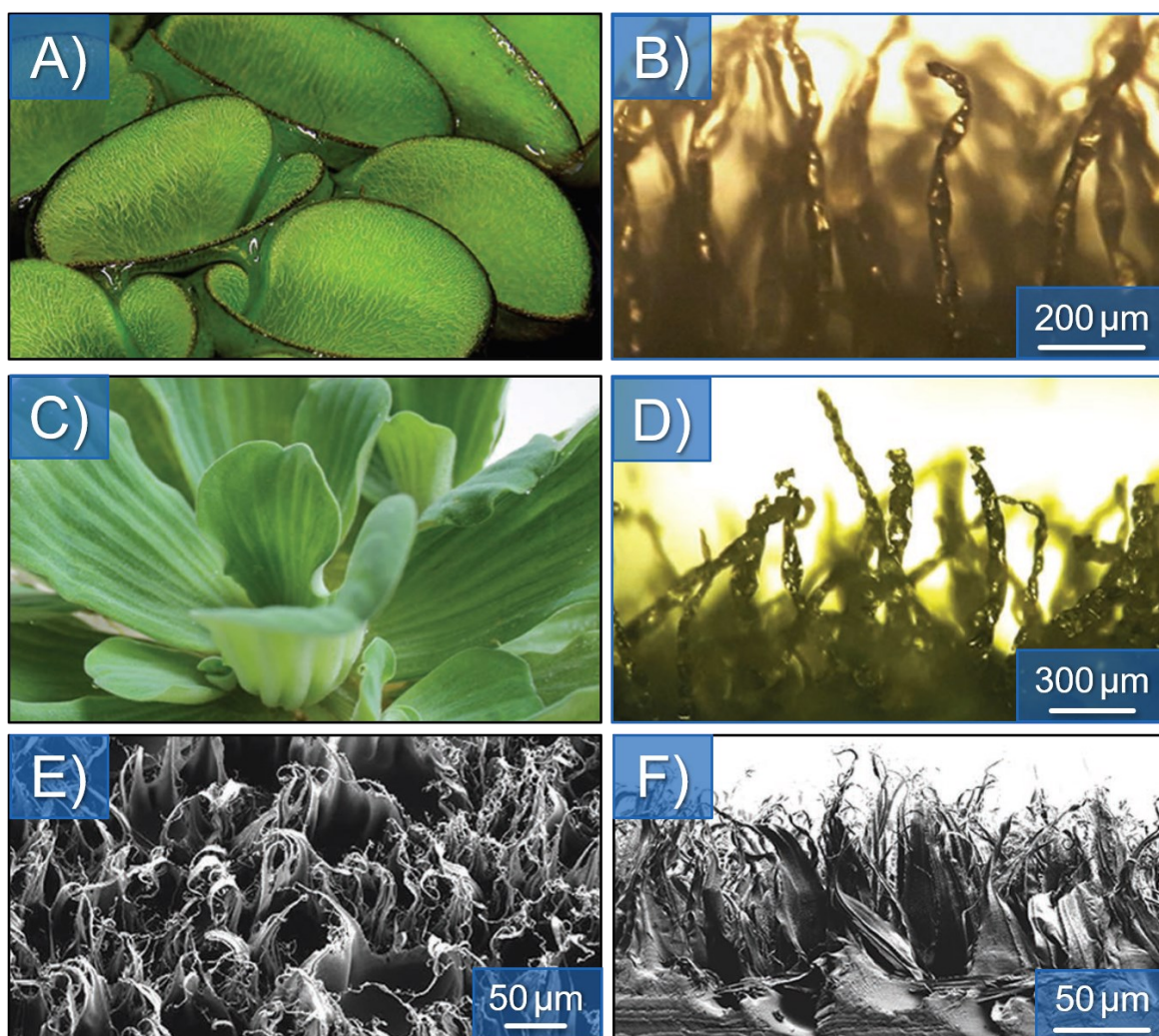


**Fig. 5.7:** Surface structures of water fern, water lettuce, and bioinspired nanofur. A) Photograph of a water fern (*Salvinia cucullate*) leaf and B) cross-sectional optical micrograph of the hairy surface structure of *Salvinia cucullate*. C) Photograph of a water lettuce (*Pistia stratiotes*) leaf and D) cross-sectional optical micrograph of the hairy surface structure of *Pistia stratiotes*. E), F) Top-view and cross-sectional SEM micrographs of bioinspired nanofur, which mimics the hairy surface structures of plants such as water fern or water lettuce. Adapted with permission from reference [528], © 2016 WILEY-VCH Verlag GmbH & Co. KGaA, Weinheim.

as PV [528, 529]. The wetting properties of nanofur can be tuned from hydrophilic to superhydrophobic, and further possible fields of application for nanofur include the fabrication of self-healing surfaces (inspired by pitcher plants) or air-retaining surfaces (mimicking water fern) [530]. Within the scope of this thesis, the nanofur structure was further improved in terms of its applicability to PV in collaboration with F. Vüllers *et al.*, developing a nanofur-based superhydrophobic FEP microcavity array which exhibits enhanced light-harvesting properties compared to the original nanofur with the same quality of self-cleaning properties [8].

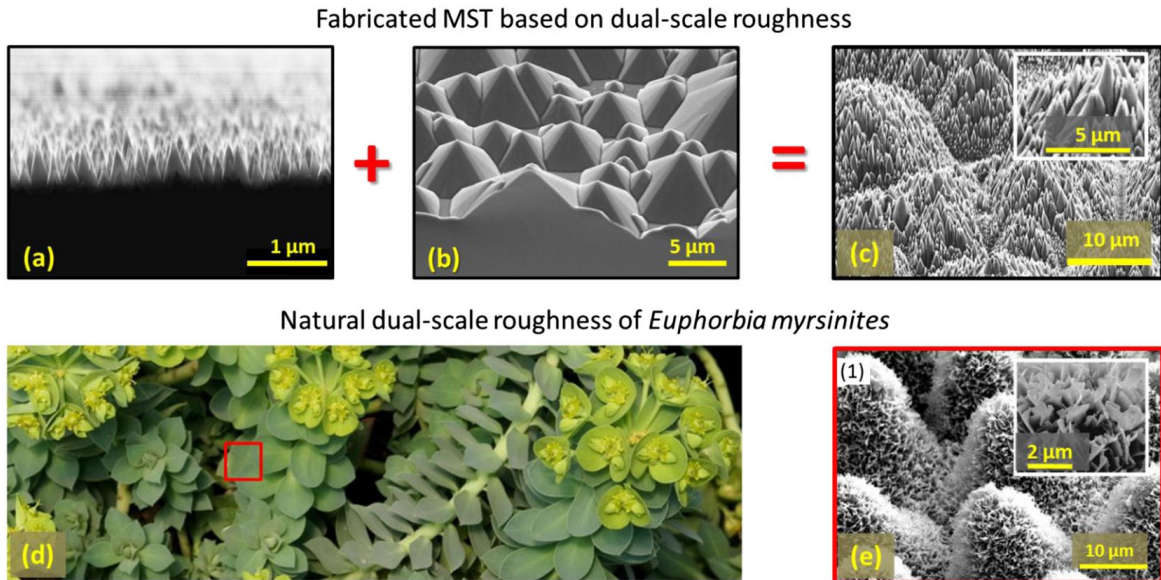


**Fig. 5.8:** Fabrication process for a modulated surface texture (MST) in Si. The hierarchical structure is generated by superimposing the nano-cone-structure depicted in (a) with the micro-pyramid-structure depicted in (b), resulting in the complex topography given in (c). Similar surface structures are found on the leaves of numerous plants. One such example, *Euphorbia myrsinites*, is shown in the photograph in (d), together with an SEM micrograph of the hierarchical leaf surface structure of *E. myrsinites* in (e). Reprinted with permission from reference [531] (SEM images in (e) originally were originally published in reference [532]), © 2015 John Wiley & Sons, Ltd.

Another method to fabricate leaf-mimicking surface structures for antireflection in solar cells has been demonstrated by Ingenito *et al.* [531] and is depicted in Fig. 5.8. First, a wet etching step on a Si wafer produces a disordered micro-pyramid structure on the Si surface. In a second step, a nano-cone-patterning is added to the microstructured Si surface via reactive-ion-etching. Then, instead of using the patterned wafer as a mold for transferring its surface structure into a transparent polymer layer which is then applied on the front side of a PV device, Ingenito *et al.* rely on directly employing the patterned Si wafer as the active/absorber material of a (back-contacted) crystalline Si solar cell. The dual-scale structure formed by the nano-cones and micro-pyramids results in a surface pattern that bears a resemblance to the hierarchical structures found on the leaves of many plants. An example for such a plant (*Euphorbia myrsinites*) is shown in Fig. 5.8, together with SEM micrographs of the Si micro-pyramids, nano-cones, and of the hierarchical Si surface structure. A similar hierarchical surface structure in Si based on a two-step etching technique and the subsequent integration into a solar cell has been demonstrated by Liu *et al.* [533].

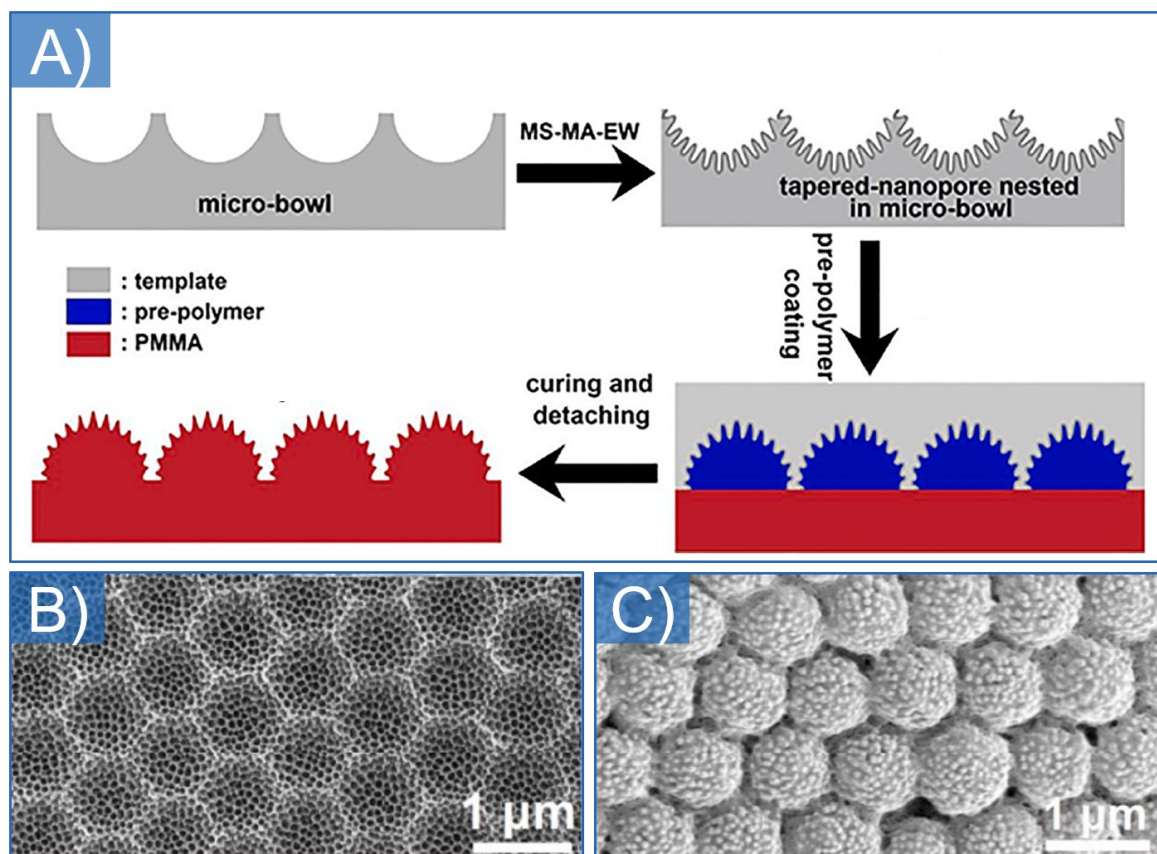


**Fig. 5.9:** Multi-step mild anodization and etching pore widening (MS-MA-EW) process enabling the fabrication of plant-mimicking hierarchical surface structures. A) Schematic depiction of the process. B) SEM image of the negatively structured mold. C) SEM image of the structure positive after templating. Adapted with permission from reference [534], © 2020 Elsevier B.V. All Rights Reserved.

Recently, Ma *et al.* demonstrated a multi-step aluminum anodization approach that enables the fabrication of hierarchically patterned aluminum templates and a subsequent molding step for transferring their surface structure into PMMA [534]. The densely packed assembly of microlenses decorated with subwavelength nanonipples that comprise this dual-scale structure bears a resemblance to the surface structures found on the leaves of some water-repellent plant such as taro (*Colocasia esculenta*). This process is schematically depicted in Fig. 5.9, together with SEM micrographs of the aluminum mold and a corresponding PMMA replica.

Further important techniques that allow the fabrication of a wide variety of hierarchical nature-mimicking structures that can be exploited for their optical and/or their wetting properties on numerous materials surfaces rely on pulsed lasers instead of etching processes [535]. Such pulsed-laser-based methods have been utilized to produce a wide variety of intricate surface structures for all classes of materials. For example, by using ultra-short pulsed (femtosecond) lasers, self-

organized subwavelength structures, so-called laser-induced-periodic-surface-structures (LIPSSs), can be induced. These LIPSSs can be tailored to mimic various functional materials found throughout living nature, including antireflective, structural-color-producing, and superhydrophobic surfaces [536]. The parameters that determine the structural properties of the LIPSSs include the wavelength and fluence of the laser, as well as the polarization properties of the incident laser light, and the total number of pulses hitting the target surface. Furthermore, interference effects and immersion into different (gaseous or liquid) environments may also be exploited by using two-beam-systems [537, 538]. By controlling these parameters, LIPSSs with various morphologies ranging from highly ordered to disordered and even hierarchical LIPSSs have been demonstrated [539–543]. Regarding mimicking functionalized plant surface structures, femtosecond-laser structured steel substrates have been utilized as mold-inserts for injection molding to produce hydrophobic polymer layers with a lotus-leaf-like surface structure [544]. Femtosecond-laser pulses have further been used under reactive gas atmosphere, resulting in a hierarchical surface structure in Si with close resemblance to the natural leaf structure [545].

Besides these ultrafast-pulse approaches, lotus-mimicking surface structures have also been produced on tungsten surfaces by irradiation with a nanosecond-pulsed laser [546]. In addition to these laser-based processes, various other techniques have been explored to mimic the outstanding wetting properties of lotus leaves [547]. Bushan *et al.*, for example, followed a strategy to superimpose micro- and nanostructure by first fabricating micropatterned epoxy substrates decorated with highly ordered micro-pillars and subsequently depositing a layer of wax harvested from natural lotus leaves (as well as from *Tropaeolum majus* and *Leymus arenarius*) onto the micropatterned substrate. The nanostructure is then formed through the wax crystals' self-assembly into nano-tubules [410, 548]. It is worthy of note that, next to lotus leaves, researchers have also drawn inspiration from other superhydrophobic plant surfaces. Biomimetic rice leaf structures, for example, have been shown to combine (superhydrophobic) self-cleaning, drag-reducing, and anti-fouling properties [549, 550].

A method for faithfully biomimicking the typical hierarchical structures found on the surfaces of many flower petals, on the other hand, has yet to be developed. However, it is worthy of note that a method which at least allows the fabrication of densely packed microstructures comprised of disordered arrangements of (smooth) micro-cones on polymer surfaces by laser ablation at UV wavelengths has

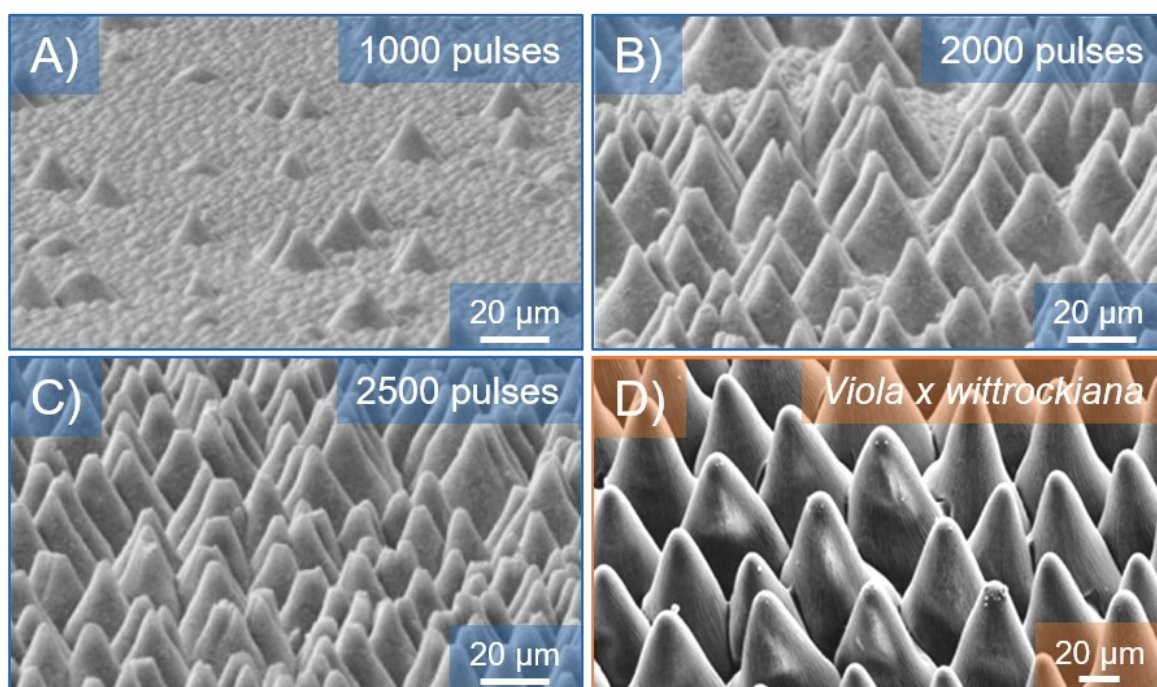


**Fig. 5.10:** Polymeric micro-cones induced via pulsed laser irradiation. A), B) and C) show SEM micrographs of microstructures on a polyimide surface, generated by UV laser ablation with 5 ns pulses and  $150 \text{ mJ/cm}^2$  irradiation after 1000, 2000, and 2500 pulses, respectively. This approach allows the fabrication of a densely packed and disordered assembly of micro-cones, which could be optimized to resemble the petal epidermal cell microstructures of flowers like *Viola x wittrockiana*, which is shown in D). The SEM images in A)-C) were adapted with permission from reference [551], © 2013 Elsevier B.V. All Rights Reserved. The SEM image of the *Viola x wittrockiana* petal structure in D) was adapted with permission from reference [9], © 2017 American Chemical Society.

been known since the 1980s [552]. Such microstructures can resemble the petal surface structures of a small number of plants, namely those with rather high-aspect-ratio conical epidermal cells combined with a negligible cuticular folding pattern. SEM micrographs of cone-microstructures induced by UV laser ablation (after 1000, 2000, and 2500 laser pulses) are depicted in Fig. 5.10, together with an SEM image of a similar-looking petal surface structure (*Viola x wittrockiana*) as a reference. By UV laser ablation, disordered cone-microstructures have been demonstrated for various polymer materials, including polyimide (PI) [551, 552], polyethylene terephthalate (PET) [553], PC [554–556] and allyl diglycol carbonate (CR39) [557]. Individual isolated cones have further been induced on PMMA (with extreme-UV and vacuum-UV wavelengths) [558, 559] and on FEP surfaces (with extreme-UV wavelengths) [558] with nanosecond-pulsed lasers. With ultra-short (femtosecond) laser pulses, on the other hand, similar densely packed, self-organized cone-microstructures have also been induced on the surfaces of various metals, such as stainless steel, Cu, Ti, and Al [560]. Especially for cone-patterned Ti,

the micro-cones are even decorated with subwavelength surface wrinkles [561]. In some instances, the resulting hierarchical structure bears some resemblance to the petal surface structure of viola flowers. These laser-induced cone structures in Ti have further been replicated in PDMS, resulting in a superhydrophobic polymer surface [562]. Concerning light-management in PV, femtosecond-laser-induced micro-cone structures have also been directly implemented into the surfaces of Si wafers, which were then further processed into solar cells [563, 564]. In a recent study, Ackerl *et al.* demonstrated the fabrication of hierarchical surface structures in Cu by combining 2.5D laser ablation for microstructuring (densely packed and highly ordered micro-cones with truncated tips) and ultra-short pulsed laser irradiation for superimposing a LiPSS-nanostructure (periodic wrinkle pattern on the flat top part of the cones and on parts of the flanks) [565]. Upper limits for the production rates of this approach were reported as 100 mm<sup>2</sup>/h for the 2.5D laser ablation and 0.6 m<sup>2</sup>/h for the LIPSS fabrication.

Furthermore, S. Dottermusch *et al.* recently employed direct-laser-writing (DLW) to produce microstructures comprised of densely packed arrays of (more or less smooth) polymeric micro-cones of tunable AR with a resemblance to the epidermal microstructures of petals without the cuticular nanofolds, which were then replicated onto c-Si solar cells by PDMS casting and soft-imprint lithography [566]. These DLW micro-cone structures were also successfully replicated into FEP via Ni electroforming of the DLW template and subsequent hot-embossing, resulting in antireflection and superhydrophobic self-cleaning properties for sufficiently large cone ARs [567]. Interestingly, the sweet-spot for achieving the optimum combination of antireflection and self-cleaning was determined to be AR = 0.7, a value close to the (average) AR of the conical rose petal epidermal cells (AR = 0.61 [568], AR = 0.84 [569]).

It is worth mentioning that a number of procedures have been developed which allow the fabrication of plant-like surface wrinkles without an underlying microstructure in polymer surfaces. Parallel (ordered and disordered) nanofolds similar to those found on petal cuticle of *Queen of the Night* tulips (see Fig. 3.15) can be produced, for example, by surface wrinkling of PDMS [570, 571] or by following the approach developed by S. Schauer *et al.*, which utilizes the unique properties of shape-memory polymers, allowing even the production of hierarchical surface wrinkles and the subsequent application of such polymeric structures for improving light-management in optoelectronic devices [572, 573]. Furthermore, nano-wrinkles on polymer surfaces can also be generated in the form of LIPSSs by using nanosecond-pulsed UV lasers [574, 575].

Lastly, it should be mentioned that Yun *et al.* demonstrated the implementation of omnidirectional antireflection for dye-sensitized solar cells by incorporating leaf-epidermis-mimicking PDMS layers for improved light collection [576]. Since the working principle of dye-sensitized solar cells relies on an energy conversion mechanism similar to photosynthesis in plants [577], the solar cells presented by Yun *et al.* can be considered the first devices that mimic both the light-harvesting mechanism as well as the energy conversion process found in natural leaves.

A detailed discussion of nature-inspired materials with a focus on PV applications can be found, for example, in a 2020 review article by Soudi *et al.* [578].

### 5.3 (Optical) Properties of Soft-Imprint Rose Petal Replicas

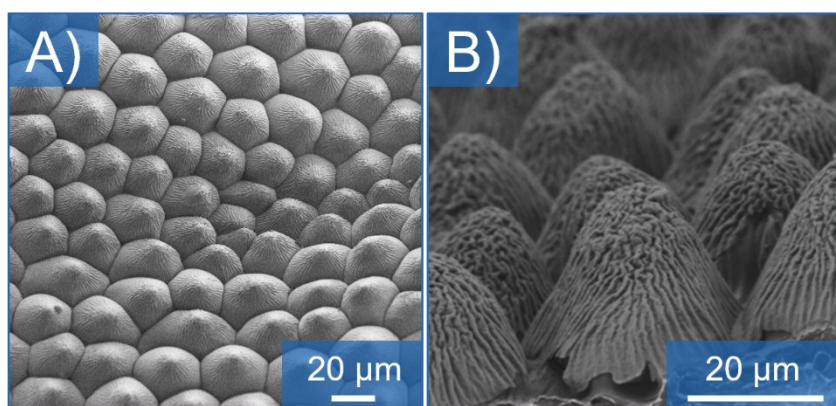
In order to exploit plant surface replicas to improve antireflection and light-trapping in solar cells, the respective biotemplates need to be copied into a sufficiently transparent material of suitable refractive index (over a broad spectral range) with high structural fidelity. Moreover, the replica should be transferable onto glass or onto technical surfaces in general. Based on the facile replication approach introduced by K. Koch *et al.* [475] (see Fig. 5.3 in section 5.1), these fundamental steps towards applying plant surface structure replicas as PV light-harvesting layers were first demonstrated by A. Schulte *et al.* in 2009 [579].

Although green leaves, as opposed to flower petals, host photosynthesis and therefore might seem to be the preferred choice as a biotemplate for boosting sunlight-harvesting in solar cells (see subsection 3.2.4), the systematic analysis of the optical properties of polymer replicas of numerous leaves and petals demonstrated, that the typical surface textures, which are found on the petals of most flowering plant species, actually outperform the textures found on green leaves in terms of minimizing surface reflectance [568, 569, 579–581]. Several key parameters that influence the reflection and transmission properties of petal surface structure replicas have been reported. Since petal microstructures, by their nature, are always comprised of the densely packed and uninterrupted assembly of convex epidermal cells, it seems reasonable that the surface reflectance of petal surface structures was found to generally decrease for increasing ARs of the epidermal cells [568, 569, 579–581]. Overall, petals with cone-shaped epidermal cells exhibit lower surface reflectance compared to petals with lens-like epidermal cells. The AR of conical petal epidermal cells alone, however, does not suffice for

an accurate prediction of the surface reflectance of petal surface structures. Another important influencing factor is the tip-sharpness, defined as a tip-radius, of the conical epidermal cells. With increasing tip-sharpness (decreasing tip-radius), the surface reflectance tends to decrease. Concerning the effects of cuticular nano-folds on the optical properties of petal epidermal cell replicas, the experimental data available to date suggests that their impact on antireflection is somewhat limited compared to the AR and tip radius of the conical epidermal cells. However, since the lowest values for surface reflectance that have been reported thus far were measured exclusively for petal replicas which included cuticular nano-folds, it can be assumed that these folds further facilitate their antireflection properties [568, 569, 580, 581]. In fact, the hierarchical petal surface structures of two types of flowers, namely roses (*Rosa*) and pansies (*Viola*), have repeatedly been demonstrated to effectively minimize surface reflectance for a broad range of AoIs and wavelengths [568, 569, 579–581]. SEM micrographs of the hierarchical structures found on the surfaces of rose petals in a top and a cross-sectional view are depicted in Fig. 5.11 (the hierarchical surface structures of *Viola × wittrockiana* and *Viola tricolor* can be found in Fig. 3.12 C) and Fig. 5.10 D) respectively).

The light-harvesting capabilities of soft-imprint rose petal replicas are exemplified in Fig. 5.12 for the case of CIGS thin-film solar cells. Reflectance spectra for CIGS layer stacks equipped with various top layer configurations were measured for a broad range of AoIs. At normal incidence, the soft-imprint rose petal replica leads to a broadband suppression of reflectance (see Fig. 5.12 A). Although an optimized MgF<sub>2</sub> layer for interference-based antireflection leads to even lower reflection losses for two narrow spectral regions, the AM1.5G (photon-flux-density) weighted reflectance (depicted in Fig. 5.12 B) shows that, even at normal incidence, the rose petal replica slightly outperforms the MgF<sub>2</sub> in terms of minimizing optical losses of the CIGS layer stacks. It should be noted that MgF<sub>2</sub> interference-based antireflective

**Fig. 5.11:** SEM micrographs of the hierarchical surface structure of a rose petal (variety: Red Naomi) NOA68 soft-imprint replica. A) Top-view. B) Cross-sectional view.



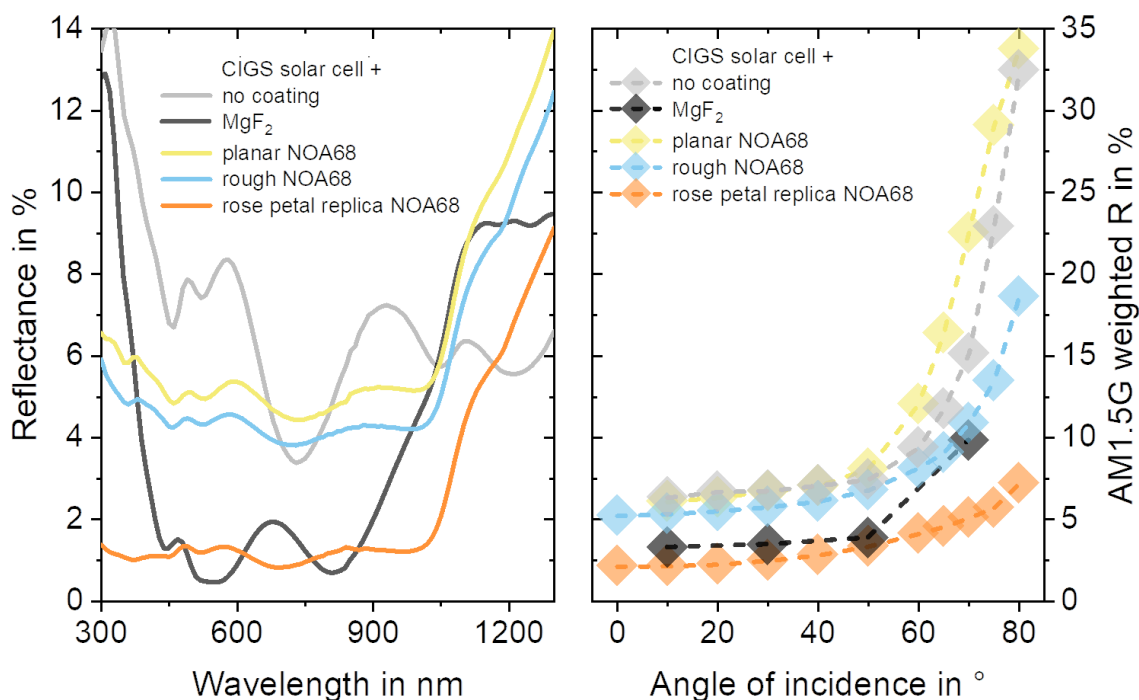


**Fig. 5.12:** Measured reflectance spectra (specular + diffuse) of CIGS solar cells ( $2.5\text{ cm} \times 2.5\text{ cm}$ ) with different cover layer configurations A) at normal incidence of light. The soft-imprint rose petal replica leads to the most effective reduction of reflectance over a broad spectral range. B) AM1.5G(-photon-flux-density)-weighted reflectance in dependence of the AoI.

layers are the state-of-the-art method for reaching highest efficiencies in unencapsulated CIGS solar cells [582–589].

For AoI  $> 50^\circ$ , the weighted reflectance of all the considered configurations, except for the CIGS solar cell equipped with a soft-imprint (NOA68) rose petal replica, begins to increase drastically. Therefore, rose petal replicas show great potential in boosting sunlight-collection, especially for off-normal incidence and under diffuse illumination conditions. Furthermore, the hierarchical surface structure of the rose petal replica causes a distinct black-matte visual appearance for the coated CIGS solar cell, as can be seen in the photographs of CIGS solar cells with various top layers depicted in Fig. 5.13. Next to rose petals, similar light-harvesting capabilities have been reported for the replicas of pansy petals. Mainly due to their larger epidermal cell AR, pansy petal replicas even exhibit slightly lower surface reflectance than rose petal replicas. However, the use of rose petals as a template for bioreplication has several advantages. High-quality roses are available year-round, and the petals of many commercial varieties of roses grow quite large (and in total number per blossom). Furthermore, the hierarchical surface structure of

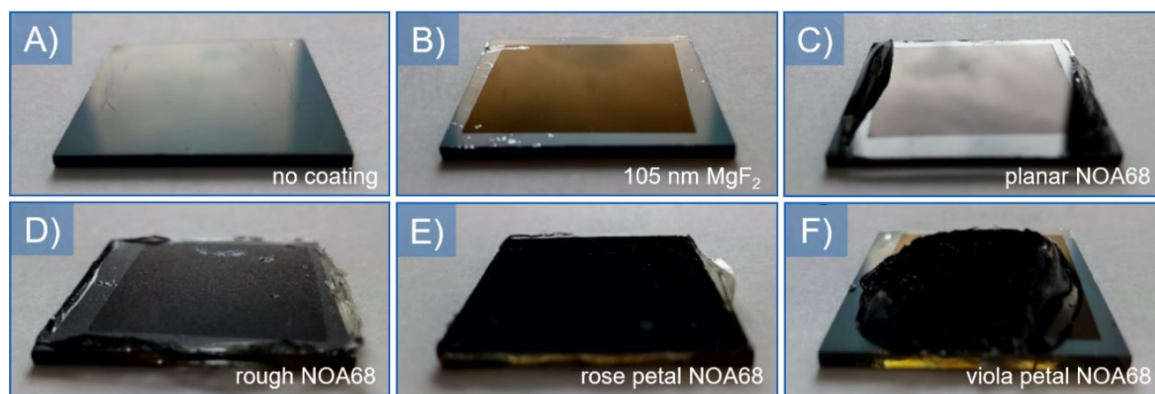


**Fig. 5.13:** Photographs of CIGS solar cells (optical dummies) with various antireflective coatings. CIGS solar cell layer stacks with A) no coating, B) a 105 nm  $\text{MgF}_2$  thin-film antireflective coating, C) a planar layer of NOA68, resembling a simple glass cover layer, D) a rough NOA68 layer, fabricated by soft-imprint replicating sand-blasted steel, E) a soft-imprint NOA68 replica of a rose petal, and F) a soft-imprint NOA68 replica of a viola petal. The central regions of the solar cells in C)-F) are coated with  $\text{MgF}_2$ , except for a narrow uncoated region around their edges. Adapted with permission from reference [581], © 2017 The Author.

pansies is often damaged during soft-imprint replication since the high-AR epidermal cells are easily ripped off. On these grounds, the primary focus of the research efforts described herein was on rose petal replication.

It should be noted that soft-imprint rose petal replicas have recently been shown by Cao *et al.* to delay the growth of bacterial biofilms, a property that could potentially be exploited in biomedical devices [590]. Another useful property of rose petal replicas related to biomedical applications was proposed by Dou *et al.* [591]. They fabricated positive and negative replicas of the rose petal surface structure in PDMS and then, after chemically modifying the structured surfaces, they were able to demonstrate efficient capture and release mechanisms for circulating cancer cells (meaning cancer cells that have detached from the primary tumor and entered the bloodstream). Moreover, the (replicated) surface structure of rose petals has been exploited for its mechanical properties, for example, for flexible strain sensors with possible applications in wearable devices, human motion detection, and soft robotics [592]. Guo *et al.* used negative PDMS rose petal replicas that have been coated with different conductive materials and demonstrated their remarkable qualities as a substrate for omnidirectional, ultra-flexible, stretchable, and wearable (thin-film) electronics [593]. Following a similar approach, Wei *et al.* utilized rose petal replicas to produce electronic skin with a wide range of possible applications. First, they obtained a negative mold of the rose petal surface structure via casting with PVA. The negative mold was then coated

with Cu-Ag-nanowires, and finally, a conductive positive replica was produced by pouring PDMS onto the nanowire-coated PVA mold. Two such conductive PDMS rose petal replicas were then conjoined into a two-layer-system, with the conductive sides of the replicas facing each other, resulting in highly sensitive piezoresistive electronic skin with remarkable electronic properties [594]. The same sandwich architecture has also been followed with Au-coated polymer replicas of mimosa leaves in order to fabricate a flexible pressure sensor with touch sensitivity [595]. Interestingly, due to its roughness, the hierarchical surface structure of PDMS rose petal (as well as lotus leaf and cicada wing) replicas has also been utilized for triboelectric energy harvesting [596]. Lastly, in a 2021 contribution, Zhu *et al.* demonstrated another flexible electronic device based on polymeric rose petal replicas, which they have described as a transparent, self-powered, and antibacterial electronic skin for sensitive tactile sensing [597].

### 5.4 Plant Replicas as PV Light-Harvesting Layers – Current State of Research

The pioneering demonstration of a soft-imprint replication of leaf surfaces onto working solar cells and an experimental demonstration of the reduction of reflection losses and the resulting gain in electrical performance was achieved by Z. Huang *et al.* in 2015 [598]. Motivated by the findings of A. Schulte *et al.*, that the surface textures found on petals typically outperform the structures found on green leaves in terms of minimizing surface reflectance [579, 569], R. Hünig, A. Mertens *et al.* consequently employed soft-imprint replicas of rose petals as cover layers for (high performance) organic solar cells in a 2016 study, achieving a promising 13% relative PCE gain under STC (44% under 80° light incidence) [580, 599]. The following year, instead of following a two-step replication approach via PDMS casting and a subsequent soft-imprint step, K. Li *et al.* directly applied a negatively patterned PDMS rose petal mold on the front surface of PV devices as light-harvesting layers, resulting in (relative) PCE gains of 6.8% for c-Si, 10% for organic, and 15% for perovskite solar cells under STC [600]. Soft-imprint replicas (NOA88) of *Viola × wittrockiana* petals have been applied on c-Si solar cells by R. Schmager *et al.*, resulting in a 6% increase in PCE [9].

After leaf and petal surface structure replicas were first established as PV light-harvesting layers, several studies also focused on investigating the optical

properties for different types of 3D models mimicking plant surface structure replicas via computational methods. Some specific types of hierarchical leaf surface structure models, like, for example, nano-bar-decorated micro-hemispheres, were numerically analyzed by Z. Huang *et al.* via finite-difference-time-domain (FDTD) simulations in 2016 [601]. The following year, Z. Huang *et al.* further employed FDTD simulations in order to study the transmittance and haze of a number of other (simplified) leaf surface structure models, including maize, sugarcane, and lotus [602]. Concerning the typical petal surface structures of conical epidermal cells decorated with cuticular nanofolds, combined ray-tracing and FDTD simulations performed by R. Schmager *et al.* indicated (based on the surface structure of *Viola × wittrockiana* petals) that their ability to efficiently suppress surface reflectance is mainly caused by the epidermal cell microstructure, while the cuticular nanofolds only cause a slight further enhancement of the antireflective effect (as suggested by the experimental data) [9].

The following Table 5.1 lists all publications – as far as the author of this thesis is currently aware – which are concerned with plant surface structure replication to either exploit or to study their light-harvesting properties, without including studies that primarily rely on numerical methods for analyzing the optical properties of plant surface structure replicas.

**Table 5.1: Overview of selected studies that are focused on the optical properties of leaf- and petal-surface-texture replicas where the table entries that are written in blue highlight the studies which utilized plant surface texture replicas as PV light-harvesting layers.**

Reference	Plant species + replica size	Replication technique + material	Impact on PV performance
Schulte <i>et al.</i> (2009) [579]	Various single leaves & petals; Several cm <sup>2</sup>	Soft-imprint Epoxy resin replica	Reflectance + haze reported for free-standing replicas
Schulte (2012) [569]	Various single leaves & petals; Several cm <sup>2</sup>	Soft-imprint Epoxy + injecting resin replica	Reflectance + haze reported for free-standing replicas
Huang <i>et al.</i> (2015) [598]	Various single leaves (some large ones); Several cm <sup>2</sup>	Soft-imprint PMMA replica	c-Si solar cell 17% PCE gain Standard test conditions not applied
Rajput <i>et al.</i> (2016) [603]	Rose petal (red); Several cm <sup>2</sup>	Soft-imprint PDMS replica	Reflectance reported for free-standing replicas
Hünig <i>et al.</i> (2016) [580]	Various single leaves & petals; 2 cm × 2 cm	Soft-imprint NOA68 replica	Rose petal (red) replica on organic solar cell 13% PCE gain at 0°, 44% J <sub>SC</sub> gain at 80°
Li <i>et al.</i> (2017) [600]	Rose petal (yellow); Several cm <sup>2</sup>	Direct use of negative PDMS replica	Various solar cells 6.8% PCE gain (c-Si), 10% PCE gain (organic), 15% PCE gain (perovskite)

continuation on next page

⋮

Schmager <i>et al.</i> (2017) [9]	<i>Viola × wittrockiana</i> petal; 32 mm <sup>2</sup>	Soft-imprint NOA88 replica	c-Si solar cell 6% PCE gain
Bindra <i>et al.</i> (2017) [604]	Rose petal (red), 1 cm × 1 cm	Soft-imprint PDMS replica (positive and negative texture)	Optical properties of free-standing PDMS replicas reported
Huang <i>et al.</i> (2017) [602]	32 kinds of (single) leaves (lotus, sugarcane, maize, ...)	Soft-imprint PMMA replica	Transmittance + haze reported for free standing replicas
Huang <i>et al.</i> (2018) [605]	Leaves: Lotus, bamboo, Indian shot, grape; 5 cm × 5 cm	Soft-imprint NOA63 replica	c-Si solar cell 10.9% PCE gain (lotos)
Fritz <i>et al.</i> (2018) [13]	Rose petal (Red Naomi); 2.5 cm × 2.5 cm	Hot-embossing PMMA, PC, and FEP replicas	Reduction in reflectance reported for CIGS
Mattaparthi and Sharma (2019) [606]	Underside of different leaves; 5 cm × 5 cm	Soft-imprint PDMS replica	Optical properties of free-standing replicas reported
Mattaparthi and Sharma (2019) [607]	Petal of <i>Canna indica</i> ; 5 cm × 5 cm	Soft-imprint PMMA and RF xerogel replica	Optical properties of free-standing replicas reported
Fritz <i>et al.</i> (2020) [3]	Rose petal (Red Naomi); 12.5 cm × 10.0 cm	Hot-embossing PMMA replica	5.7% average PCE gain (0.5 cm <sup>2</sup> CIGS solar cells) Average gain in outdoor performance of 5.4% (100 cm <sup>2</sup> CIGS modules)
Fritz, Horváth <i>et al.</i> (2020) [1]	4 × 5 assembled replicas as in [3] (≅ 50 cm × 50 cm)	Hot-embossing PMMA replica	Polarization properties of reflected light

---

## 6 Light-Harvesting Properties of Disordered Microstructures on Thin-Film Solar Cells – Optical Simulations

---

The following chapter presents a ray-tracing-based simulation methodology developed mainly to analyze the influence of various parameters related to the 3D morphology of plant epidermal cell microstructures on the light-harvesting capabilities of plant surface structure replicas.

The modeling procedure and the numerical results described within this chapter were published as a full research paper in *Bioinspiration & Biomimetics*<sup>1</sup> [10]. Next to the study of antireflective plant surface microstructures, said numerical framework was also utilized for analyzing various other ray-optics-based systems for PV as well as light-emitting diodes (LEDs) and light-emitting electrochemical cells (LECs), leading to several more research paper contributions (F. Vüllers *et al.* *ACS Applied Materials & Interfaces* [8], S. Yu *et al.* *Advanced Optical Materials* [6], N. Jürgensen *et al.* *Advanced Materials Technologies* [4])

### 6.1 Modeling and Simulation Procedures for 3D Disordered Microtextured Surfaces

Polymeric replicas of many flower petals, as discussed in section 5.4, have been experimentally shown to efficiently suppress reflection losses in solar cells over a broad range of wavelengths and incidence angles [568, 569, 579–581]. Previous studies have indicated that their broadband and omnidirectional antireflective and light-trapping properties are primarily caused by the dense arrangement of cone-shaped epidermal cells, while the impact of the superimposed cuticular nanostructure on their light-collection properties seems to be secondary [9, 569]. Moreover, individual epidermal cells on a specific petal exhibit (more or less pronounced) statistical variations in their sizes, tilt angles, and orientations. Also, the conical petal epidermal cells are arranged in a disorganized assembly rather than following a highly-ordered pattern (like, for example, a 2D hexagonal or

---

<sup>1</sup> awarded by the editorial office as one of the journal's 'Highlights of 2017' [15]

rectangular lattice). So far, it has not been established how the optical properties of such disorder-incorporating microstructures compare to their perfectly-ordered counterparts. Due to the large number of (geometry-related) parameters that need to be systematically varied in order to evaluate their influence on the microstructure's optical properties, together with the difficulty of accurately producing such structures within a reasonable timeframe, such a study can only be thoroughly conducted via computational approaches. To this end, a modeling and simulation procedure for disordered microtextures was developed and employed in order to assess the influence of structural disorder on the light-harvesting properties of petal-like microstructures.

As discussed in subsection 3.2.3, several studies have utilized ray-tracing-based approaches for numerically studying light propagation through natural epidermal cells of plant leaves or even through entire leaf cross-sections [373–377]. For such efforts, it is necessary to include a number of different structural features into the simulation models, consisting of various materials with different optical properties. These include, for example, the organelles (especially chloroplasts) and cytosol within the cell-interior, palisade, and spongy cell layers, and air voids. In contrast, the research efforts included in this thesis were concerned with studying the optical properties of plant epidermal structure replicas rather than studying the interaction of light with natural plant parts. Since such replicas only reproduce the topography of plant epidermal structures into a single technical material, the complex scattering and absorption properties caused by the aforementioned constituents of actual plant material can be fully ignored.

Overall, the microtexture modeling routine developed herein is based on the assembly of structure-arrays from basic 3D shapes like cones, square pyramids, hexagonal pyramids, triangular pyramids, and semi-spheroids. The groundwork for this approach was laid during the author's master thesis research [194]. Moreover, this modeling scheme also enables the creation of microstructured surfaces formed by an array of indentations instead of protrusions for all the aforementioned basic 3D shapes. For example, disordered inverse microlens structures were investigated in collaboration with F. Vüllers *et al.* in order to analyze the optical properties of 'improved nanofur', resulting in a disordered array of microcavities [8] (see also section 5.2). Further, modeling of planar layers that include disordered arrangements of spherical air voids within the bulk material was also made possible for the numerical analysis of the scattering properties of nanoparticle-free scattering layers produced via a PMMA foaming

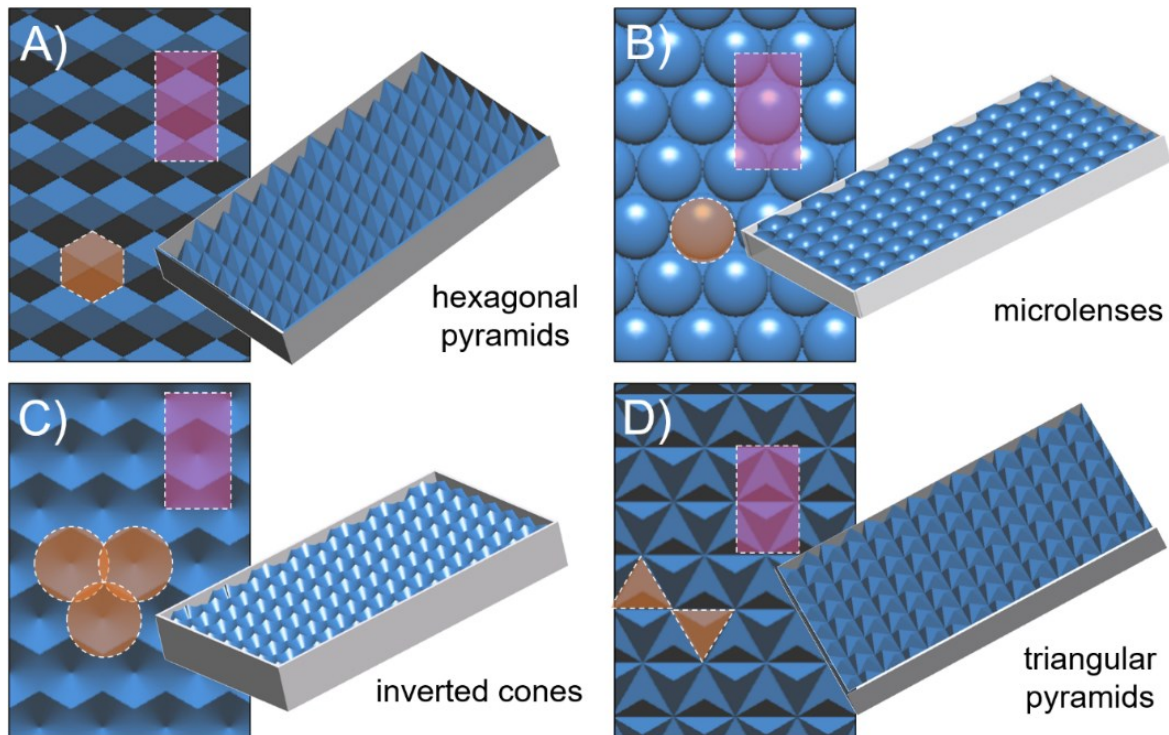


**Fig. 6.1:** Exemplary non-disordered microstructure models assembled from various basic geometries. A) Hexagonal pyramids. B) Microlenses (semi-spheroids). C) Inverted cones. D) Triangular pyramids. While the microlenses in B) are arranged in a hexagonal closest packing configuration, all three other microstructures in A), C), and D) exhibit a full tiling of the base over the entire structured area.

process [6]. Such indentations/voids are created by subtracting the respective basic shapes from the cuboid base of the microstructure models. Some example microstructure models assembled from various basic geometries are shown in Fig. 6.1. However, since the microtexture modeling and simulation efforts that are presented throughout this chapter were mainly targeted at gaining knowledge about the optical properties of the typical epidermal cell microstructures found on petals, microstructure assemblies based on conical protrusions were, by far, the most extensively studied type of microstructures throughout this thesis. In what follows, the general procedures for microtexture modeling and simulation are therefore explained and illustrated with a focus on micro-cones as the basic structural constituents.

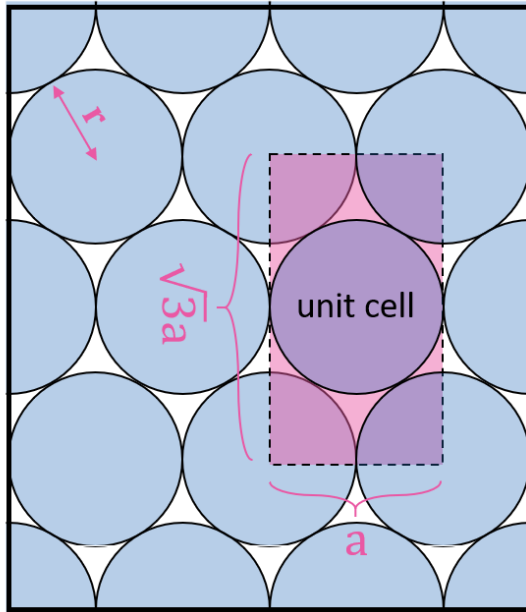
Before providing the detailed explanation of how structural disorder was defined and introduced into the modeling program, the basic procedure of how microstructure models were constructed within the scope of this thesis will first be explained for perfectly ordered (meaning all cones have identical shapes and are arranged in a hexagonal pattern) microstructures. The construction of such non-

disordered 3D microtexture models was carried out by means of a Matlab function relying on the following input parameters:

- Height of the cones  $h$
- Radius of the cones  $r$
- Lattice constant  $a$
- Number of (rectangular) unit cells to be constructed in  $x$ - and in  $y$ -direction  $N_x$  and  $N_y$
- Number of (rectangular) unit cells to be illuminated in  $x$ - and in  $y$ -direction  $M_x$  and  $M_y$

The definition of the (rectangular) unit cells, which constitute the fundamental building blocks of all hexagonal microstructure arrangements discussed within this thesis, is provided in Fig. 6.2 (as well as in Fig. 6.3). The cone height and radius determine the AR of the micro-cones via  $AR = h/2r$ . The cone radius, together with the lattice constant, defines the areal filling fraction (or packing density) of the micro-cones sitting on the cuboid base. If, for example, the lattice constant is chosen as  $a = 2r$ , the cones are arranged in a hexagonal closest packing (hcp) configuration. In this case, nearest neighbors are packed as closely together as possible without having them overlap, resulting in an incomplete tiling of the cuboid base (schematically depicted in Fig. 6.2). Since petal epidermal cell microstructures do not exhibit even the slightest spacing between neighboring cones over the entire structured area, micro-cones are allowed to overlap in the modeling scheme developed herein in order to construct microstructures with a full tiling of the structured surface. For a lattice constant of  $a = 3^{1/2} r$ , the micro-cones are packed together close enough to reach such a full tiling configuration (schematically depicted in Fig. 6.2). If the lattice constant is set to be even smaller compared to the cone radius ( $a < 3^{1/2} r$ ), the resulting microstructure will still be physically equivalent one that is arranged in the full tiling configuration defined by  $a = 3^{1/2} r$ . The reason for this is illustrated in Fig. 6.3. For lattice constants  $a < 3^{1/2} r$ , the increased overlap between neighboring cones leads to a build-up of bulk material which effectively adds to the thickness of the cuboid base since it contains no structural features of refractive index contrasts. Atop this extension of the model base, the tightly packed cones' upper parts still protrude into the surrounding medium, forming an effective microstructure. Since the geodesic lines between a cone's tip and any point on the circumference of its base follow a straight line, the aforementioned effective microstructure is defined by an effective cone height, radius, and lattice constant, which are all linearly downsized by the same factor

hexagonal closest packed (hcp)  
 $a = 2 \cdot r$



hexagonal full tiling  
 $a = \sqrt{3} \cdot r$

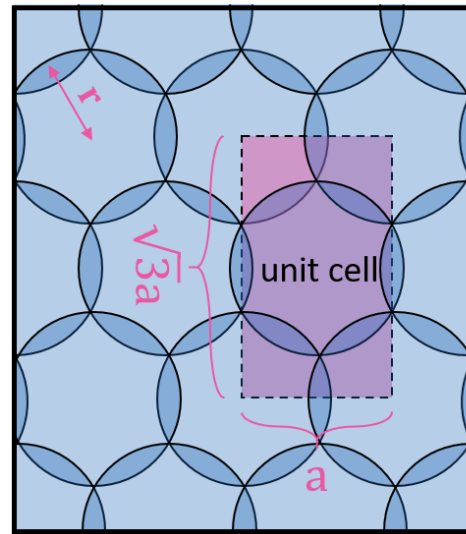


**Fig. 6.2:** Schematic top-view depictions of microstructures comprised of hexagonally arranged cones in two distinctive configurations. On the left, the cones are packed together so closely that nearest neighbors just barely touch each other (hexagonal closest packing). On the right, the lattice constant  $a$  is further reduced to the point that the entire surface area is covered with cones. In such a configuration, all cones will (partially) overlap with their nearest neighbors.

from the values that define the  $a = 3^{1/2} r$  full tiling configuration. Since the absolute scale of the structural features is irrelevant in ray optics (as long as all features are still considerably larger than the wavelength of the incident light), such cone-based microstructures with packing densities defined by  $a < 3^{1/2} r$ , therefore, yield optical properties equivalent to the critical full tiling configuration defined by  $a = 3^{1/2} r$ . Similarly, a micro-cone array in a full tiling configuration does not (effectively) change if the cone height  $h$  and radius  $r$  are isomorphically upscaled by a constant factor, while the lattice constant  $a$  is kept at a fixed value. This property of full tiling configurations was used to circumvent a number of issues that arise when studying microtexture models that include disorder (more details in section 6.2).

The microtexture modeling routine operates according to the following steps (a schematical illustration of the main steps can be found in Fig. 6.4):

- 1) Loading of all input parameters defining the microstructure to be built and connecting Matlab to LightTools via ActiveX interface.

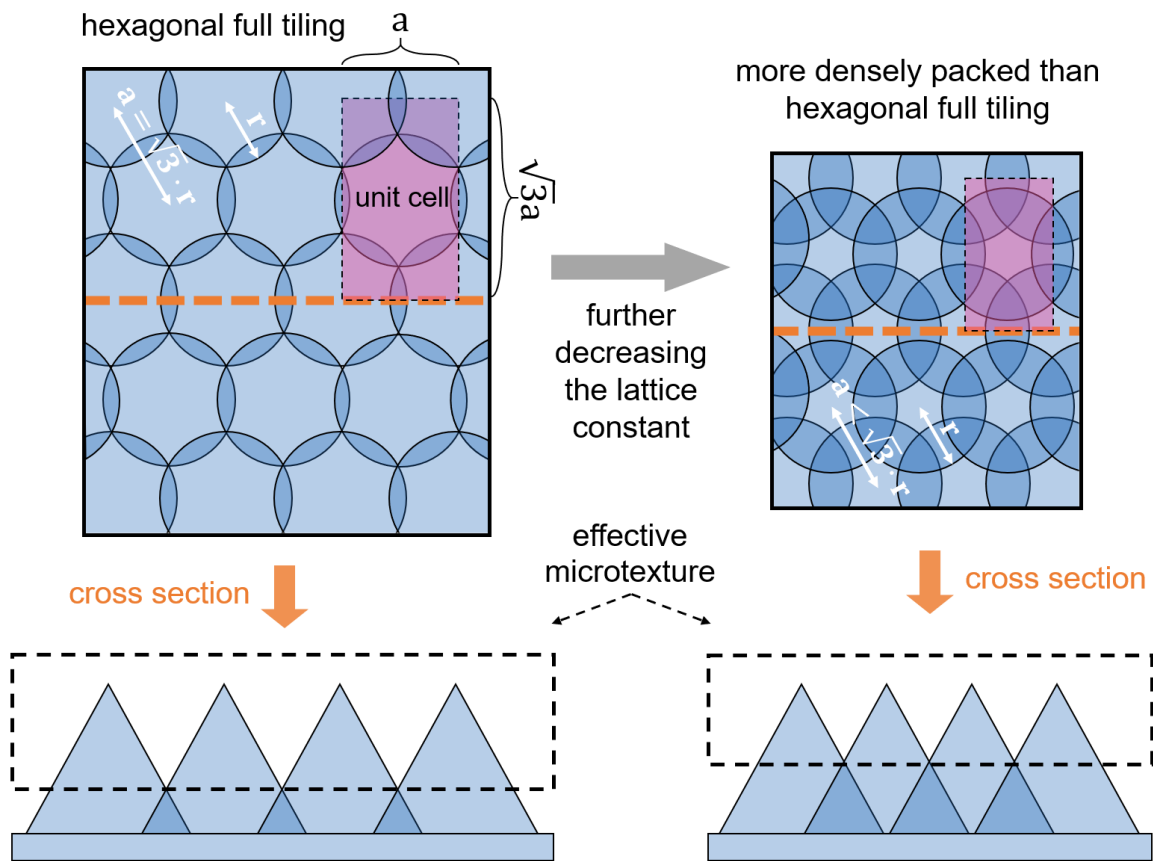


**Fig. 6.3:** Schematic top-view depictions of two highly ordered cone-based microstructures in full tiling configurations. Since in ray optics, the absolute dimensions of the structural features are irrelevant as long as they are much larger than the incident light wavelength, both of these full tiling configurations lead to identical reflection and transmission properties.

- 2) Generation of a cuboid with lateral dimensions of  $N_x \cdot a$  and  $N_y \cdot 3^{1/2} a$  in  $x$ - and in  $y$ -direction as the base of the microstructure model. For all models, the thickness of the cuboid base was (arbitrarily) fixed at  $10 \mu\text{m}$ .
- 3) One by one, all the cones that are needed to construct the overall number of unit cells  $N_x \cdot N_y$  are generated and relocated to their designated lattice position.
- 4) Trimming off all parts of the cones that laterally protrude beyond the cuboid structure base.
- 5) Generation of perfectly reflecting lossless mirrors along the edges of the microtexture model. All the newly created surfaces of the cleaved cones are then set to be either fully transparent or perfectly reflecting in order to realize mirror-like boundary conditions also for light rays propagating within one of the cleaved cones.

- 6) Merging the cuboid base and all of the individual cones into a single 3D object and assigning the desired (wavelength-dependent) complex refractive index to the microtexture.
- 7) Generation of a farfield receiver around the entire model for determining total reflectance and add a planar receiver to the rear side of the microtexture for analyzing the angular distribution of in-coupled light. Further, another four planar receivers are added to (the inside facing surfaces of) the mirrors surrounding the microtexture model in order to evaluate how many light rays have reached the model boundaries.
- 8) Setting the rear side of the merged microtexture model as a perfect absorber in order to prevent in-coupled light rays from back-reflection and consecutive out-coupling from the textured surface. This way, only the reflectance caused by the microtextured front surface is collected by the farfield receiver.
- 9) Setting the optical properties of the entire structured front surface of the microtexture model to follow Fresnel's equations. This means that a light ray that intersects the structured surface is either reflected or transmitted, and the probabilities for these events are calculated from the complex refractive indices of the two interfacing materials, together with the local AoI and polarization state of the incident light ray via Fresnel's equations (17) - (20).
- 10) Generation a rectangular light source with lateral dimensions of  $M_x \cdot a$  and  $M_y \cdot 3^{1/2} a$  in x- and in y-direction. The light source is positioned above the front side of the microtexture model (laterally centered). The distance between the highest cone tip to the emitting surface of the light source is set equal to the height of this highest cone.
- 11) Saving of the generated microtexture model with all of its components in the LightTools format '.lts'.

The Matlab-based script for running the ray-tracing simulations relies on several input parameters:

- Array containing the filenames of the LightTools models to be simulated.
- Array containing all wavelengths.
- Array containing all AoIs.
- Array containing all azimuth angles.
- Array containing the numbers of rays.

The basic steps of the simulation routine can be summed up as follows:

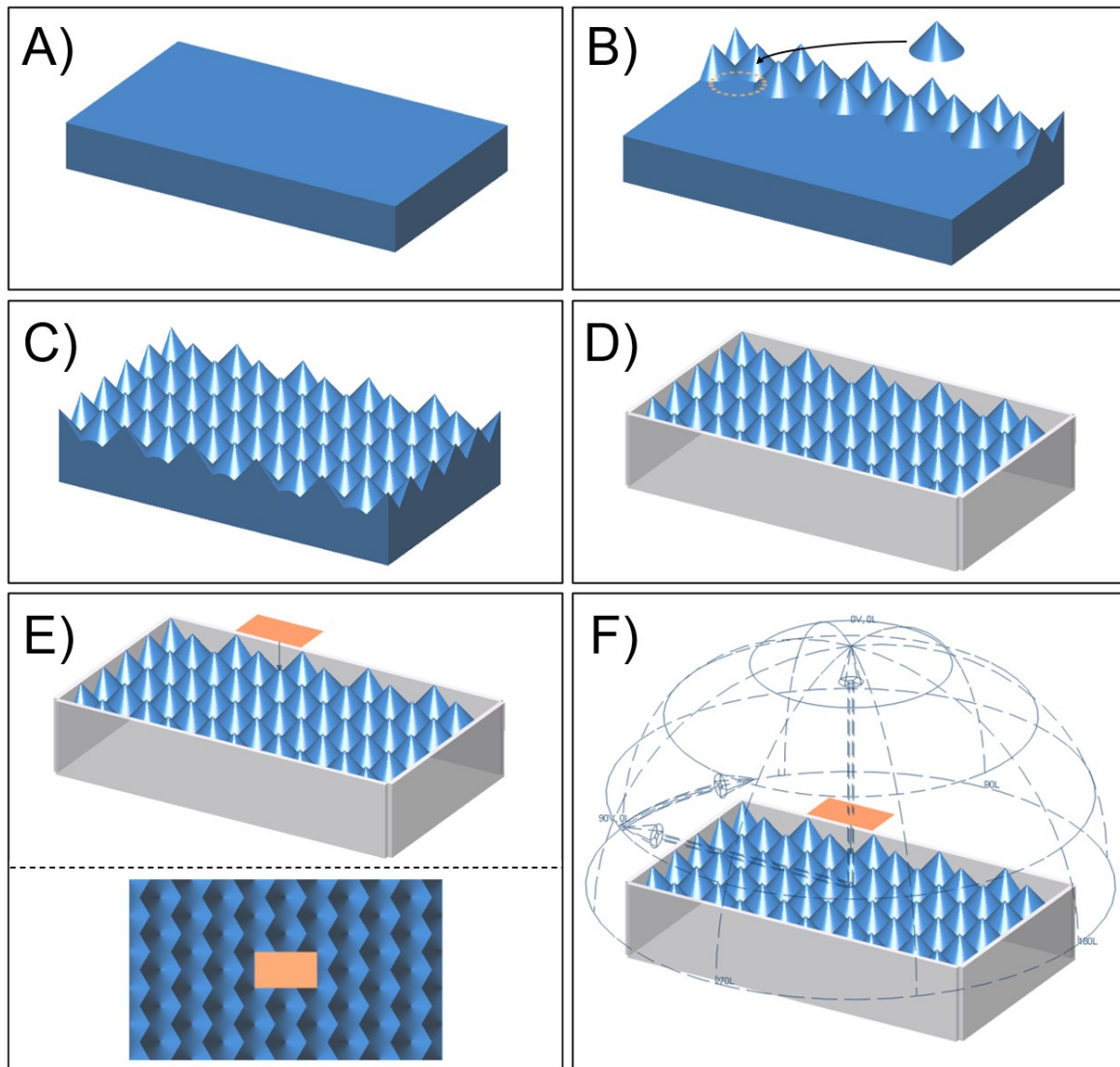


**Fig. 6.4:** Schematic depiction of the main steps of the 3D microtexture modeling routine that was mainly developed for ray-tracing-based studies of disordered microstructured surfaces. For the depicted model (perfectly ordered cones in a full tiling configuration), the input parameters for the modeling routine are  $h = 12 \mu\text{m}$ ,  $r = 10 \mu\text{m}$ ,  $N_x = 5$ ,  $N_y = 5$ ,  $M_x = 1$ ,  $M_y = 1$ .

- 1) Loading of all input parameters that set up the simulations and connecting Matlab to LightTools via ActiveX interface.
- 2) Opening the first microtexture model to be simulated.
- 3) Read-out of the largest height value of all cones of the microtexture. This value is used for calculating the proper lateral displacement of the light source for  $\text{AoI} > 0$  (as depicted in Fig. 6.5).
- 4) In several interleaved for-loops, ray-tracing simulations are launched for all combinations of desired wavelengths, azimuth angles, AoIs, and numbers of rays. The light source, for each simulation, is moved to the proper lateral position according to Fig. 6.5.

- 5) For each individual simulation, the following quantities are extracted and saved as multidimensional arrays: Total reflected power, angular distribution of reflected light rays, angular distribution of transmitted/in-coupled light rays, total power incident on the perfectly reflecting sidewalls of the rectangular microtexture model. The angular distributions of reflected/transmitted light are only recorded at the maximum number of rays for each microtexture model. The total reflected power is recorded for all numbers of rays in order to assess the convergence of the ray-tracing results.
- 6) Formatting the simulation results and saving them as several tables (in Microsoft Excel format).
- 7) Opening the next LightTools microstructure file to be simulated and then repeating steps 3) - 7) until all LightTools models are done.

For all the ray-tracing simulations included in this thesis, only parallel light rays are emitted from (the structure-facing side of) the light source. Further, the light source is always set to emit a total power of 1 W (irrelevant since all results are expressed as relative quantities). As highlighted in Fig. 6.5, if rays are able to reach the perfectly reflecting model boundaries, the angular distribution of in-coupled light will be altered (with respect to azimuth angles and not elevation angle). If necessary, this can be prevented by generating microstructures with an increased number of unit cells and illuminating only a smaller number of unit cells in the model center. This creates a non-illuminated buffer zone that prevents light rays from reaching the model boundaries. Since the reflecting sidewalls are equipped with receivers, the number of rays that reach the boundaries can be explicitly monitored in order to find appropriate dimensions of such a buffer zone.

Before highly complex disordered microtextures were numerically investigated, the validity of the simulations results that are generated by using the (LightTools-controlling) Matlab scripts for generating 3D microtexture models and for running the simulation routine was tested by recreating and simulating the same (non-disordered) surface-microtextures that were already investigated in detail by Deinega *et al.* via FDTD and ray-optical approaches, all performed with the free electromagnetic simulation package Electromagnetic Template Library [190]. To this end, perfectly ordered microstructures composed of cones and square/hexagonal pyramids with ARs ranging from 0.2 to 3 and a refractive index of 1.5 (no absorption losses considered) were constructed, and then their total reflection coefficients (counting specular and diffuse components) were simulated

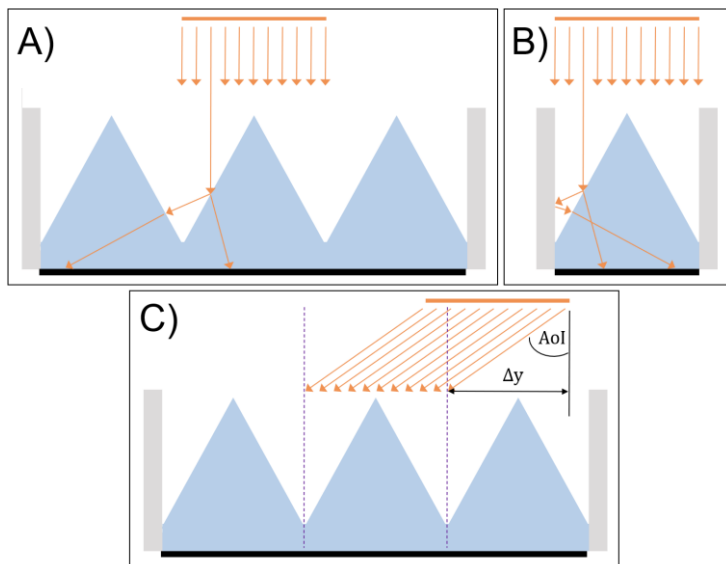


**Fig. 6.5:** Schematic cross-sectional-views of cone-based microstructure models. A) and B) illustrate that the angular distribution of in-coupled light rays is altered if light rays are able to reach the reflecting model boundaries. C) shows how oblique light incidence was implemented by displacing the light source.

for normal incidence of collimated light by using the Matlab/LightTools-based modeling and simulation scripts developed herein. Without exception, the Matlab/LightTools-based routines were able to faithfully reproduce the numerical results of Deinega *et al.* for all the aforementioned microstructure morphologies [190].

## 6.2 Implementation of Structural Disorder

Based on numerous petal surface SEM micrographs of various flowers like roses, violas, pansies, orchids, sunflowers, etc. that were acquired over the course of this thesis (and also numerous examples from literature, as for example in reference [569]), three types of microstructural disorder were defined and implemented into the modeling procedure in order to systematically analyze the light-harvesting properties of petal surface structures:

- 1) Disorder in cone height
- 2) Disorder in cone positioning
- 3) Disorder in cone tilt angle.

The following subsections provide a detailed description of these types of microstructural disorder.

### 6.2.1 Disorder in Cone Height

In order to implement disordered variations in micro-cone height, a parameter  $\sigma_h$ , which plays the role of a standard deviation, was introduced and implemented into the 3D modeling algorithm. The parameter  $h$ , which defines the constant height of all cones in the case of perfectly ordered microtexture models, now plays the role of the average cone height  $\bar{h}$ . In order to create microtexture models with disorder in cone height ( $\sigma_h \neq 0$ ), the modeling algorithm assigns height values to each of the micro-cones, which are randomly generated following a normal distribution defined by the average value  $h$  and the standard deviation  $\sigma_h$ . For fixed cone radii, disorder in cone height, as defined above, directly translates into a normal distribution of the cones' ARs.

The normal distribution defined by  $\bar{h}$  and  $\sigma_h$  generally does not prohibit individual cone height values from taking negative values. For small height average values combined with large standard deviations, the generation of negative height values may appear for a considerable portion of the cones in a microtexture model. Although these negative height values could just be implemented in the form of conical indentations in the cuboid base of the microtexture models, such structural features obviously don't exist for plant epidermal cell microstructures. On this basis, the maximum standard deviation for disorder in height was chosen at

$$\sigma_{h,\max} = 0.3 \cdot \bar{h} \quad (95)$$

in order to keep the probability of generating cones with negative height sufficiently small. Thereby, negative height values were successfully suppressed even for microstructure models consisting of several hundred micro-cones.

### 6.2.2 Disorder in Cone Positioning

In order to implement disordered variations in the positioning of the micro-cone arrangements, another parameter  $\sigma_p$ , also acting as a standard deviation of a normal distribution, was defined. In case of a perfectly ordered cone arrangement ( $\sigma_p = 0$ ), each cone is placed following an exact hexagonal arrangement without any lateral displacement from the lattice points. Disorder in cone positioning ( $\sigma_p \neq 0$ ) is introduced by assigning a lateral displacement to each micro-cone. These lateral displacement values are randomly generated following a normal distribution with the average value of zero and the standard deviation  $\sigma_p$ . The lateral directions in which these cone-displacements are conducted, on the

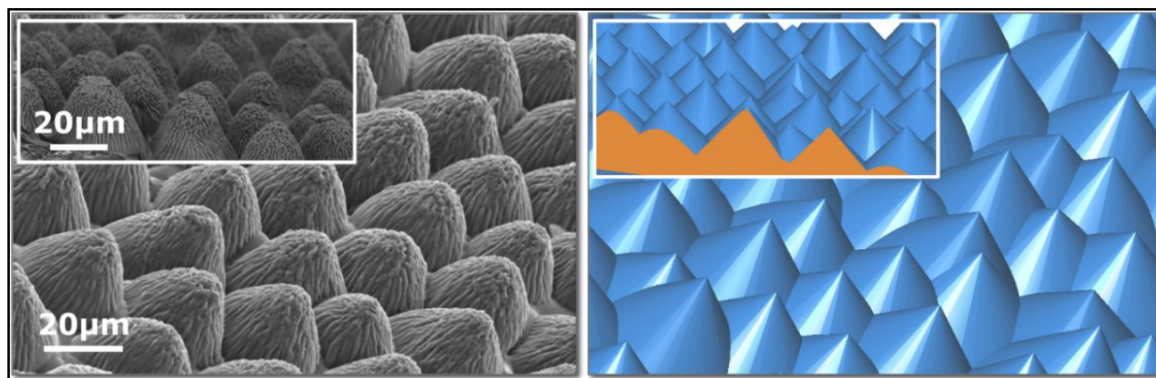


**Fig. 6.6:** Comparison of the disordered microstructure found on rose petals and a generic LightTools microtexture model with disorder in cone height and positioning and an average AR of 0.6, which is similar to rose petal epidermal cells (SEM micrographs of natural structure on the left side; microstructure model screenshots on the right side). The SEM images depicted in this figure were adapted with permission from the aforementioned contribution to *Bioinspiration & Biomimetics* [10], © 2017 IOP Publishing Ltd.

other hand, are chosen to be fully random. Since the  $\sigma_p$  normal distribution produces positive and negative displacement values the random lateral direction is assigned with the help of a uniformly distributed random number between  $0^\circ$  and  $179.9^\circ$ . By gradually ramping up  $\sigma_p$ , the generated disordered microtextures increasingly deviate from hexagonal symmetry. For microtextures with disorder in positioning ( $\sigma_p \neq 0$ ), the parameter  $a$  can not be interpreted as the lattice constant anymore since the structural features do not follow a hexagonal pattern anymore. Yet, together with  $N_x$  and  $N_y$ , the parameter  $a$  still defines the lateral dimensions of the microtexture model and therefore could be described as an effective lattice constant.

When disorder in positioning is introduced to a microtexture with a lattice constant of  $a = 3^{1/2} r$  (the critical value where full tiling of the cuboid base is barely achieved), the probabilistic displacement of cones leads to areas where neighboring cones are so far apart that parts of the planar cuboid base are exposed. This can be prevented by exploiting the aforementioned property of upscaling both the height and radius values of the cones by a constant factor, leading to an effective microstructure with equivalent optical properties as in the  $a = 3^{1/2} r$  configuration (see Fig. 6.3), but with strongly overlapping cones, ensuring that, even for models with disorder in cone positioning, the cuboid base remains fully covered with cones over the entire area.

A reasonable maximum value of  $\sigma_p$  can be given based on the consideration that at a value of

$$\sigma_{p,\max} = 0.5 \cdot a, \quad (96)$$

the resulting microtexture models are equivalent to ones with uniformly distributed, fully random cone arrangements. This was explicitly shown by comparing the positioning patterns of both cases in Fourier-space, as well as their angular distributions of in-coupled light (see supplementary information of [10]). Therefore, by ramping up  $\sigma_p$  from zero to  $\sigma_{p,\max}$ , the full spectrum of cone arrangements between the perfectly ordered hexagonal case and a fully random one can be continuously modeled.

### 6.2.3 Disorder in Cone Tilt Angle

In addition to introducing disorder in the cones' height and arrangement, the conical epidermal cells of many petal surfaces also tend to exhibit a more or less pronounced bending or tilting. Such topographies can be approximated by introducing disorder in the tilt angle of the micro-cones via another standard deviation parameter  $\sigma_t$ . Normally distributed tilt angle values (average zero, standard deviation  $\sigma_t$ ) are generated and assigned to the cones. Initially, positive/negative tilt angle values lead to tilting the cones' tips towards the  $+x/-x$ -direction. As highlighted in Fig. 6.7, two immediate problems arise from such a tilting step. Independent of the choice of the anchor point for the rotation axis, tilted cones will always partially be lifted off the cuboid base, resulting in structural artifacts in the form of air voids at the bases of cones. Moreover, there is

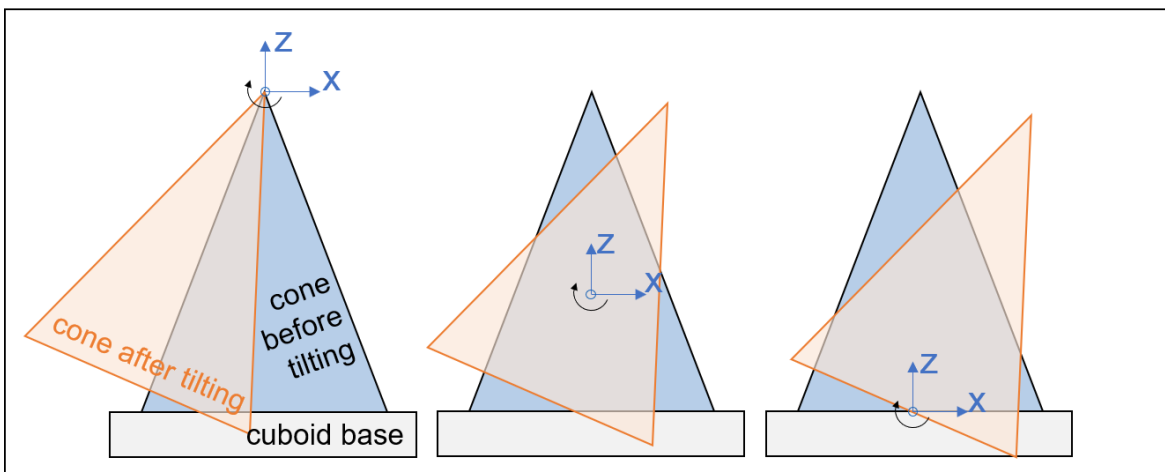


**Fig. 6.7:** Schematic illustration of the issues related to the tilting of micro-cones. Generating cone-based microstructures with  $\sigma_t > 0$  leads to unwanted additional interfaces and 'air inclusions' due to a partial lift-off. By starting the model construction with elongated cones overlapping with the model base even before tilting, such a lift-off scenario can be avoided.

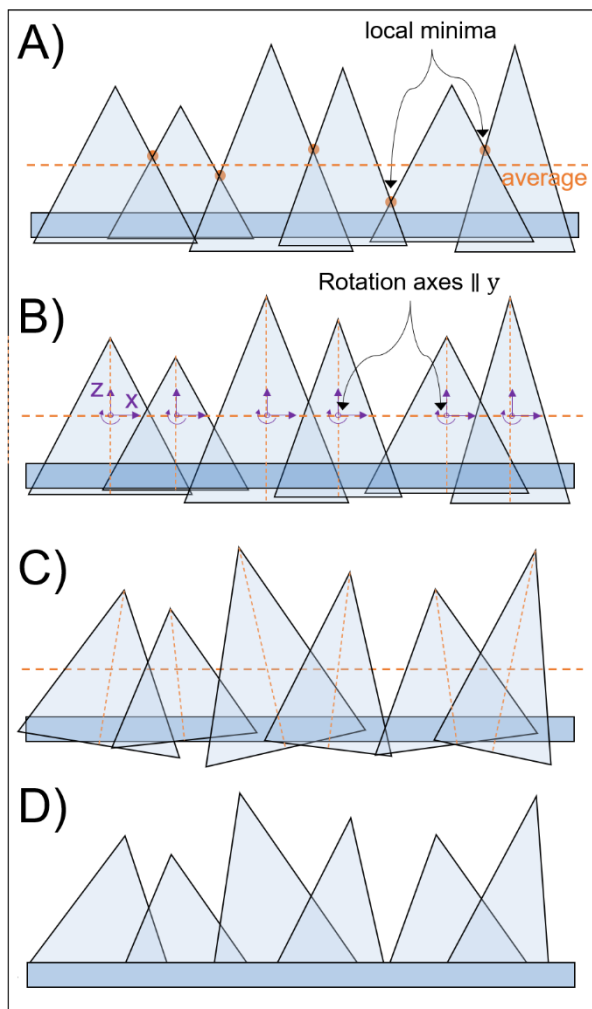


**Fig. 6.8: Schematic illustration of the modeling procedure for cone-based microstructures in case of  $\sigma_t > 0$ .** A) Finding the local minima of the desired microstructure under the assumption  $\sigma_t = 0$ . The plane which shall contain the rotation axes of the micro-cones is given by the average over these minima. B) Positions of the rotation axes for each micro-cone. C) Microstructure after assigning the random tilt angles. D) The overlap of the tilted cones with the cuboid model base is eliminated by accordingly cleaving the cones.

reaching through the cuboid base, as shown in Fig. 6.7. This modification assures that none of the micro-cones can be lifted off the base through the tilting step. After tilting, all cones are laterally cropped right at the cuboid surface. Fig. 6.7 further depicts the routine that was developed to automatically pick appropriate anchor points (z-coordinate) for the cones' tilting-axes. The Matlab-based function for microtexture modeling will if the tilt angle standard deviation is set to a value  $\sigma_t > 0$ , in a first step, determine the locations of all local minima in the microstructure topography prior to the tilting step (see Fig. 6.8 A) and then calculate the average z-value for all these local minima  $z_{min}$ . The anchor points for the cones' tilting axis are then defined as the intersection points of the cones' symmetry axes with the plane defined by  $z = z_{min}$  (see Fig. 6.8 B).

In order to achieve a fully random tilting direction for the cones, the tilted cones further need to be rotated around the z-direction by a uniformly distributed random angle. Similar to the case of assigning a fully random lateral displacement direction for microtexture models with disorder in cone positioning, the fully

still an ambiguity in choosing the anchor point (z-coordinate) of the rotation axis results. The issue of lifting the cones from their base can be resolved by generating cones linearly elongated at their rear sides, even

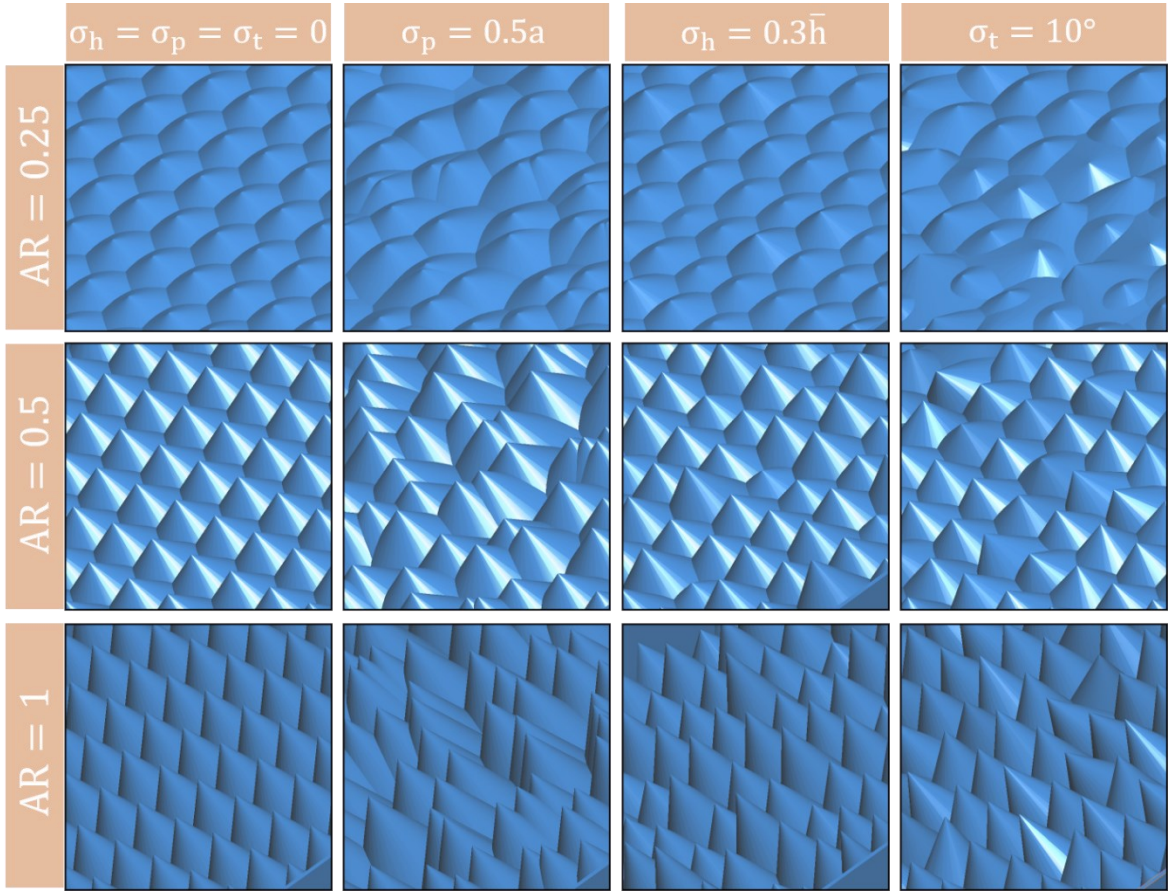


**Fig. 6.9:** Screenshots of exemplary cone-based microstructures in LightTools with ARs of 0.25 (top row), 0.5 (middle row), and 1 (bottom row), each in a non-disordered configuration (first column) and with the maximum disorder in positioning (second column), cone height (third column) and cone tilt (fourth column).

random tilting direction is realized analogously with the help of another uniformly distributed random number between  $0^\circ$  and  $179.9^\circ$ , since the  $\sigma_t$  normal distribution inherently produces positive and negative tilt-angle values with equal probabilities.

The maximum value for the tilt angle standard deviation was chosen at

$$\sigma_{t,\max} = 10^\circ, \quad (97)$$

since such configurations lead to microstructure models with tilt angles which are noticeably more pronounced than what is usually found for the tilting of petal epidermal cells.

For AR = 0.25, 0.5, and 1, 3D microtexture models with the maximum disorder in cone height, positioning, and tilt angle are, together with fully ordered microtexture examples, are depicted in Fig. 6.9.

### 6.3 Model Parameters and Convergence Tests Regarding Number of Rays and Spatial Dimensions

The refractive index of the optically homogeneous cones (and including the cuboid base) was set to  $n = 1.54$  and  $k = 0$ , which is equal to the properties of fully cured NOA68 at  $\lambda = 550$  nm, a material commonly used for the soft-imprint replication of plant surface structures. ARs (or average ARs for disordered configurations) of 0.25, 0.5, and 1 were considered. These configurations were generated by keeping the cone radii fixed at  $r = 10$   $\mu\text{m}$  and only varying the cones' (average) height. The (effective) lattice constant was chosen as  $a = 3^{1/2}r$  (full tiling). For each of these basic configurations, the three types of structural disorder were studied individually by gradually increasing the respective standard deviations introduced in section 6.2. Disorder in cone height was analyzed by ramping up  $\sigma_h$  from  $\sigma_h = 0$  to  $\sigma_{h,\text{max}} = 0.3 \cdot \bar{h}$  (in  $0.1 \cdot \bar{h}$  steps). Disorder in the positioning of the micro-cones was analyzed by ramping up  $\sigma_p$  from  $\sigma_p = 0$  to  $\sigma_{p,\text{max}} = 0.5 \cdot a$  (in  $0.1 \cdot a$  steps). Analogously, disorder in cone tilt was analyzed by ramping up  $\sigma_t$  from  $\sigma_t = 0$  to  $\sigma_{t,\text{max}} = 10^\circ$  (in  $2.5^\circ$  steps). In the case of disorder in tilt angle, the  $\text{AR} = 0.25$  configuration was not analyzed since rather flat cones with disorder in tilt angle only produce reasonable microstructures for very small standard deviations  $\sigma_t$ . Conversely, larger tilt angle standard deviations lead to flat areas on the microstructures (see Fig. 6.9), which are not observed for (petal) epidermal cell microstructures found in nature. For each individual microstructure model, incidence angles of  $0^\circ, 10^\circ, 20^\circ, 30^\circ, 40^\circ, 50^\circ, 60^\circ, 65^\circ, 70^\circ, 75^\circ,$  and  $80^\circ$  were considered (the azimuthal direction was always kept constant). Since light rays change their direction of propagation when reaching the reflecting model boundaries (see Fig. 6.5), all microstructure models were designed to include a sufficiently wide non-illuminated buffer zone around the directly illuminated center region in order to minimize any alterations of the in-coupled light angular distributions. The lateral dimensions of structure models and light sources (defined by  $N_x, N_y, M_x$  and  $M_y$ ) were always chosen such that, for all AoIs considered, less than 1% of all light rays emitted by the light source are able to reach the reflecting sidewalls of the respective microtexture model. Furthermore, ray-tracing models of disordered microstructures must contain a sufficiently large number of illuminated micro-cones so that the statistical nature of the surface structure will be reasonably incorporated into the ray-tracing simulations. If the number of illuminated cones were underestimated, the simulation of two disordered microstructure models generated based on the same set of input parameters would result in slight differences in optical properties (reflectance, angular distribution of in-coupled light, etc.). All the disordered microstructure

models considered herein were therefore laterally upscaled until a second LightTools model based on an identical set of input parameters was explicitly shown to lead to (nearly) identical simulation results. However, it is important to note that the time required for generating microstructure models grows exponentially with an increasing number of structure-elements, which strongly limits the maximum number of structural features that can be generated within a reasonable timeframe. Altogether, these considerations lead to ray-tracing models containing 761 – 1301 cones (corresponding to  $N_x = N_y = 19$  and  $N_x = N_y = 25$ ), with 365 – 613 cones being directly illuminated (corresponding to  $M_x = M_y = 13$  and  $M_x = M_y = 17$ ). Due to these large numbers of structural elements involved, the number of rays to trace needs to be chosen adequately large in order to produce converging simulation results. It was determined that  $10^8$  ray leads to sufficiently accurate ray-tracing results for all the microstructure configurations and at each AoI considered herein. In more detail, it was explicitly found that, for each microstructure model and at each AoI, the first two decimal places of the simulated reflectance coefficient in % did not change when incrementally ramping up the number of rays in the following steps:  $N_{\text{rays},1} = 2.5 \cdot 10^7$ ,  $N_{\text{rays},2} = 5 \cdot 10^7$ ,  $N_{\text{rays},3} = 7.5 \cdot 10^7$  and  $N_{\text{rays},4} = 1 \cdot 10^8$ .

## 6.4 Microtextured Surfaces on Top of Thin-Film Solar Cells

In addition to studying the surface reflectance of microtexture models composed of cones, their properties were further investigated for a configuration where the microtextured layers would be laminated on top of CIGS thin-film solar cells instead of having a perfectly absorbing rear side. This type of configuration mimics the optical properties of, for example, soft-imprint-replicated petal microstructures on top of a thin-film PV device. In such a scenario, a (wavelength-dependent) portion of the light that in-couples into the textured polymer layer will be reflected back towards the textured surface again by the thin film stack, and then either out-coupled or redirected by the microtextured top surface towards the solar cell once more. The total reflectance of such a configuration, therefore, is governed by the complex and wavelength-dependent back-and-forth reflection processes between microtextured interface and thin-film layer stack. Employing a combination of TMM and ray-tracing methods, the optical properties of such a system involving effects on two different length-scales can be properly simulated. Such a routine can be performed by determining the wavelength-, angle- and polarization-dependent

reflection properties of the thin-film stack via TMM calculations and subsequently implementing the resulting reflection properties of the layer stack as the optical response at the rear side of a 3D microtexture model in a ray-tracing software. In LightTools, such a user-defined optical response at a specific surface can be realized via so-called coating files (.coa). It is important to note that the material which constitutes the microtextured light-harvesting layer must be considered as the surrounding/background medium for the TMM calculations. For NOA68 as the microstructured material covering a (standard) CIGS thin-film solar cell, the layer configuration for TMM-simulating the rear side optical response caused by the solar cell is given in the following:

- 1) Surrounding medium: NOA68
- 2) 180 nm Al:ZnO (transparent front contact)
- 3) 85 nm iZnO (transparent front contact)
- 4) 50 nm CdS (buffer layer)
- 5) 2.5  $\mu\text{m}$  CIGS (active layer)
- 6) Substrate: Mo (rear contact)

In more detail, the reflectance (in %) was calculated for this planar stack of thin layers using the TMM software of WVASE for AoIs between  $0^\circ$  and  $89^\circ$  in  $1^\circ$  steps and for a broad range of incident light (vacuum) wavelengths between 300 nm (short wavelength limit of the terrestrial solar irradiance spectrum) and 1300 nm (long wavelength limit defined by the band gap of the absorber layer) in 1 nm steps. These TMM calculations were performed both for s-polarized as well as for p-polarized light. Next, the reflectance properties that were determined this way were implemented as the optical properties of the rear sides of the ray-tracing models in LightTools. By launching a subsequent ray-tracing simulation for such a modified microtexture model, the AoI- and wavelength-dependent optical properties of microtextured light-harvesting layers atop of thin-film solar cells were numerically studied. Due to the increased computational effort for such simulations compared to microtexture models with absorbing rear sides, only the microstructure models with the maximum amounts of disorder in height, positioning, and tilt, as well as the non-disordered configurations, were considered in combined TMM/ray-tracing simulations for each AR. For each microtexture/thin-film stack configuration, only the two extreme cases of  $\text{AoI} = 0^\circ$  and  $\text{AoI} = 80^\circ$  were studied in the combined TMM/ray-tracing approach. At each AoI, wavelengths between 400 nm – 1000 nm (in 20 nm steps) were considered, employing a total number of  $1 \cdot 10^8$  rays. The refractive index of NOA68 was assumed constant at 1.54 over the entire spectral range considered.

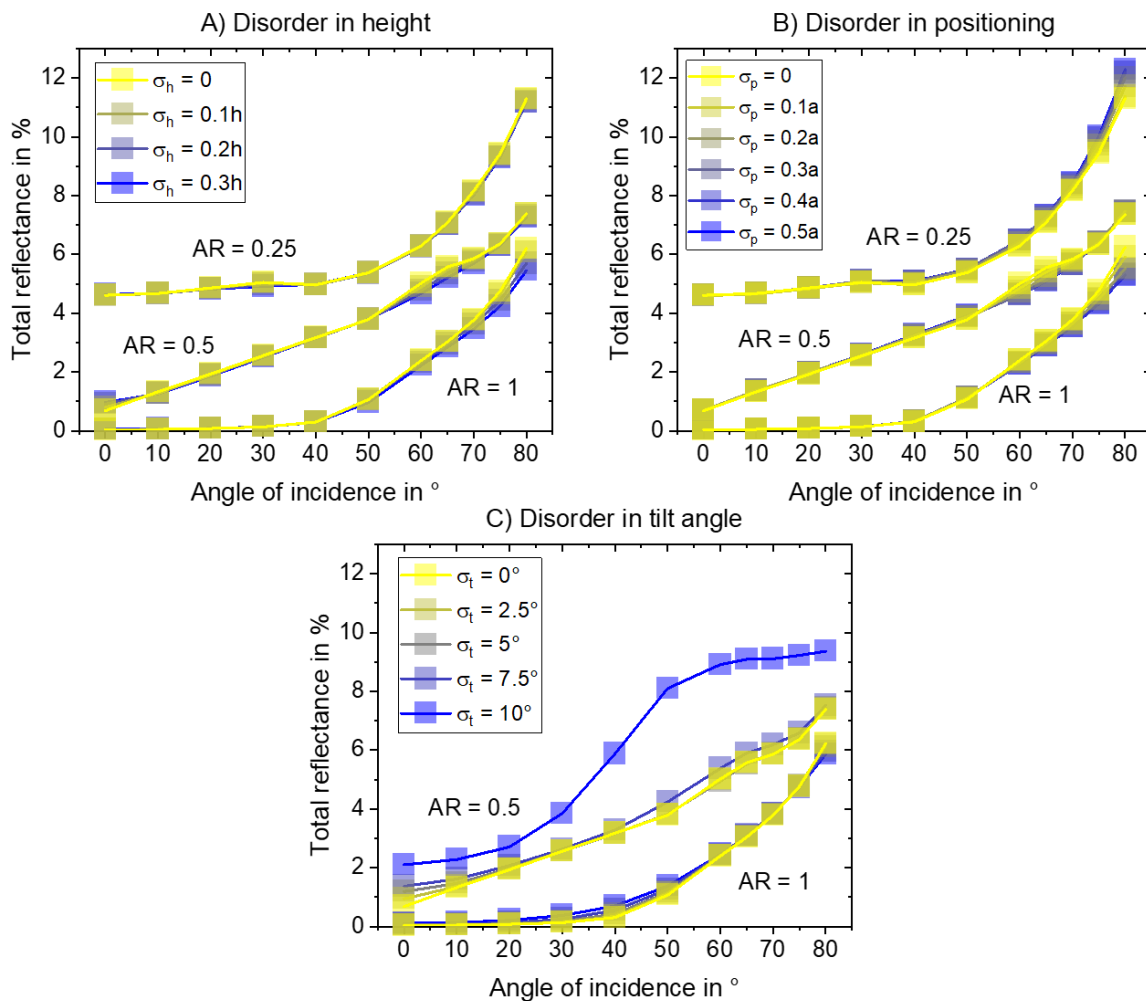
## 6.5 Results – Influence of Structural Disorder on Petal-Like Microstructures

### 6.5.1 Effects of Structural Disorder on Surface Reflectance And In-Coupled Light Angular Distribution

Fig. 6.10 shows the simulated total reflectance (specular + diffuse component) for all the considered microstructure configurations with varying degrees of structural disorder and for different AoIs, as described in section 6.3. The general trend, that reflection losses of petal-structure-replicas decrease with increasing (mean) AR of the conical epidermal cells, which has been established experimentally [569, 580] for petal replicas and also numerically for non-disordered micro-cones at normal incidence [190], is reproduced by these ray-tracing results. It is worthy of note that, for cones with a mean AR of 1, the total reflectance (specular + diffuse) stays well below 1% for AoIs below  $40^\circ$ , which signifies that such high-AR microstructures are well-suited to efficiently collect sunlight under non-diffuse illumination conditions. Astonishingly, introducing disorder to the microstructures only barely changes their surface reflectance, irrespective of the AoI and the type of disorder considered. Except for the extreme case of AR = 0.5 cones with disorder in tilt angle, where the reflectance increases by 4% from the  $\sigma_t = 7.5^\circ$  to the  $\sigma_{t,\max} = 10^\circ$  configuration, the effects of structural disorder on the reflectance are globally limited to  $< 1\%$  (absolute values) and can therefore be regarded as limited (and sometimes even as negligible). Furthermore, this limited effect of structural disorder on reflectance can take place in both directions: For example, for a cone AR of 0.25, ramping up positioning-disorder leads to a slight increase in reflectance for AoIs above  $50^\circ$ . For a cone AR of 1, the same increase in positioning-disorder conversely leads to a slight decrease in reflectance for AoIs above  $50^\circ$ .

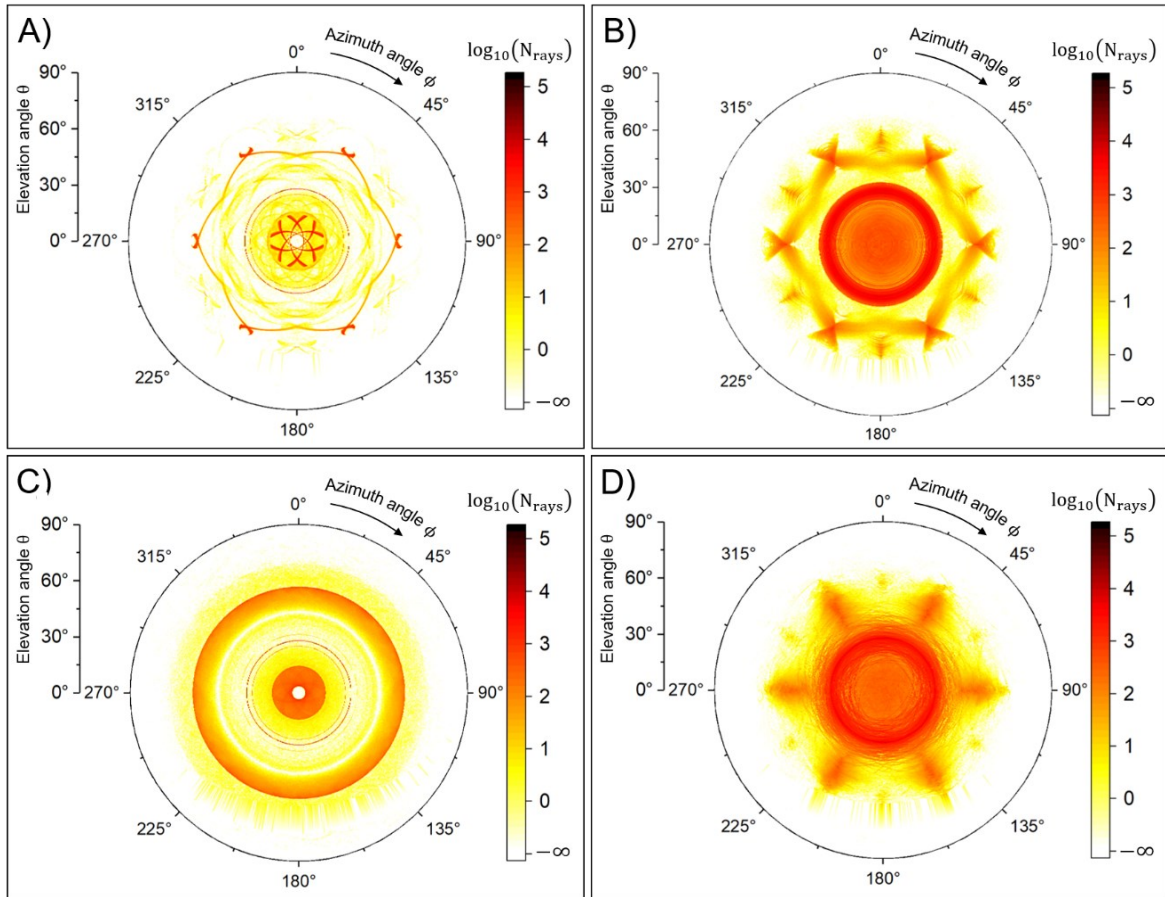
Besides surface reflectance, the angular distribution of in-coupled light rays was also studied for each of the aforementioned microstructure configurations. The propagation direction of in-coupled light rays was measured in a spherical coordinate system. The elevation  $\theta$  is defined as the angle between a light ray and the negative z-axis, while the azimuth  $\phi$  denotes the angle between the ray's projection into the xy-plane and the x-axis (cartesian coordinate system as defined in Fig. 6.7 and Fig. 6.8).

Fig. 6.11 shows exemplary results for micro-cones with AR = 1 under normal incidence of light. For (average) ARs of 0.25 and 0.5, the same basic effects



**Fig. 6.10:** Ray-tracing analysis of the influence of structural disorder on the reflection properties of microstructures comprised of cones, plotted as a function of the incidence angle. Microstructures based on cones with (average) ARs of 0.25, 0.5 and 1 and with varying degrees of disorder in A) cone height, B) positioning, and C) tilt (only for AR = 0.5 and 1) were analyzed. A color-gradient from yellow to blue indicates an increase in magnitude for the respective type of disorder. The data presented in this figure has been previously published in *Bioinspiration & Biomimetics* [10].

were ascertained. In case of a perfectly ordered microstructure configuration (Fig. 6.11 A), the angular distribution of in-coupled light follows a hexagonal symmetry. However, it is important to note that most in-coupled light is concentrated on a narrow circle defined by  $\theta = 27.9^\circ$ . This ring is caused by the rays that reach the receiver on the model backside after only a single interaction, namely the refraction into the first micro-cone that the ray encounters. Due to the rotational symmetry of the micro-cones, light rays that interact with only a single micro-cone lead to features with rotational symmetry in the angular distribution of in-coupled light. Next to the ring defined by  $\theta = 27.9^\circ$ , a second ring at  $\theta = 25.2^\circ$  is caused by rays



**Fig. 6.11:** Ray-tracing results for the angular distribution of in-coupled light for AR = 1 cones (full tiling) with different types of disorder at normal incidence of light. A) No disorder ( $\sigma_{h,p,t} = 0$ ). B) Maximum disorder in cone height ( $\sigma_h = 0.3\bar{h}$ ). C) Maximum disorder in cone positioning ( $\sigma_p = 0.5a$ ). D) Maximum disorder in cone tilt ( $\sigma_t = 10^\circ$ ). The data presented in this figure has been previously published in *Bioinspiration & Biomimetics* [10].

that, after being refracted into the first micro-cone they encountered, are able to reach the opposite sidewall of the same cone again from the inside and are then redirected through TIR. Hexagonal features in the in-coupled light angular distribution, on the other hand, are caused by rays that interacted with more than one of the micro-cones. Light rays that are reflected from the first cone they encounter and thereby redirected towards and refracted into one of the (closest) neighboring micro-cones, for example, cause six discrete features in the in-coupled light angular distribution at  $(\theta, \phi) = (56.8^\circ, m \cdot 60^\circ)$  with  $m = 1, 2, \dots, 5$ . Furthermore, if such light rays, after in-coupling into this secondary cone, can reach the opposite sidewall from within the cone's interior, TIR causes another downwards redirection within the microstructure, leading to six discrete features at  $(\theta, \phi) = (-17.0^\circ, m \cdot 60^\circ)$ .

The introduction of disorder in cone height, positioning, and tilt causes distinct alterations to the unperturbed angular distribution pattern of in-coupled light rays. Ramping up  $\sigma_h$  from zero to  $\sigma_{h,\max} = 0.3\bar{h}$  (Fig. 6.11 B) leads to a broadening of the narrow features found for the perfectly ordered configuration due to the statistical variations of cone heights (and therefore cone AR) and the following slight alterations of propagation angles. Since all cones are still placed in a perfect hexagonal grid, the hexagonal symmetry is still manifested in the in-coupled light's angular distribution. Introducing disorder in cone positioning, on the other hand, does not lead to a peak-broadening effect since all micro-cones are completely identical. Ramping up  $\sigma_p$  from zero to  $\sigma_{p,\max} = 0.5a$  (Fig. 6.11 C), however, breaks the hexagonal symmetry of the cone arrangement and leads to an in-coupled light angular distribution with full azimuthal symmetry (ring pattern). Concerning disorder in tilt angle (Fig. 6.11 D), a similar peak-broadening effect is found as for disorder in cone height.

With respect to assessing light-trapping capabilities in PV devices, the more relevant quantity to analyze is the  $\phi$ -integrated distribution of propagation directions. Again for the (representative) example of  $AR = 1$ , these  $\phi$ -integrated angular distributions of in-coupled light are given in Fig. 6.12 (for all AoIs considered). These integrated distributions indicate that the effects discussed for normal incidence still hold for oblique incidence. While both disorder in cone height and tilt cause a broadening effect for all AoIs, disorder in cone positioning seems to only affect the azimuthal distribution of in-coupled light and therefore does not induce any apparent modifications to the  $\phi$ -integrated angular distribution of in-coupled light.

### 6.5.2 Effects of Structural Disorder on Reflection Losses For Microstructures on CIGS Solar Cells

Although it was found that structural disorder only has a limited impact on surface reflectance, the modifications in the angular distribution of in-coupled light might still affect the light-trapping properties of such structures when applied as solar cell cover layers. Therefore, as explained in section 6.4, combined TMM/ray-tracing simulations were performed to explicitly calculate the effects of microstructural disorder on the antireflection and light-trapping properties of the aforementioned configurations on top of CIGS thin-film solar cells. For all ARs considered, Fig. 6.13 depicts the (combined ray-tracing and TMM) simulated reflectance spectra

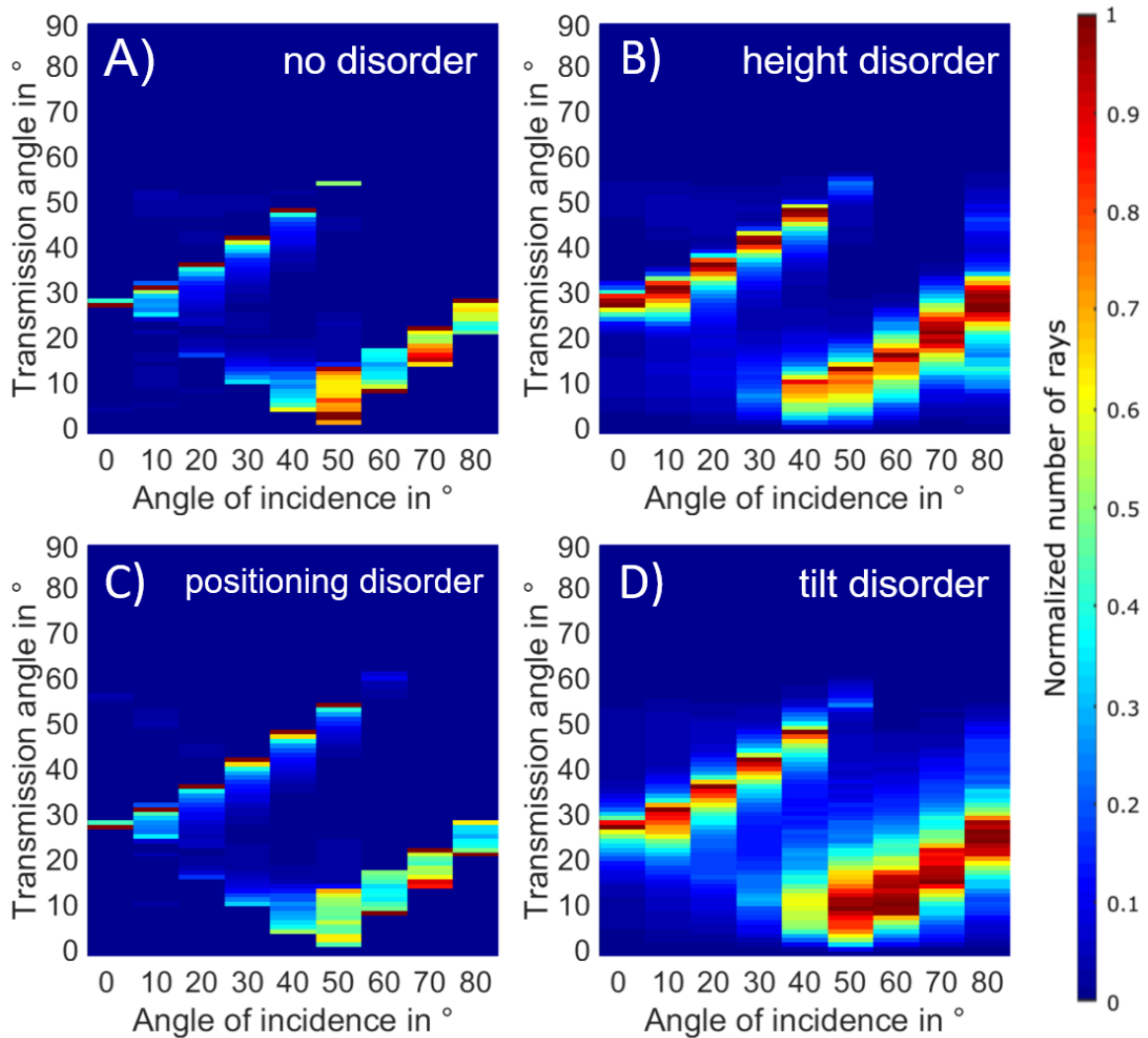


**Fig. 6.12:** Ray-tracing results for the angular distribution of in-coupled light for AR = 1 cones (full tiling) with different types of disorder after integrating over the azimuth angle  $\phi$ . A) No disorder ( $\sigma_{h,p,t} = 0$ ). B) Maximum disorder in cone height ( $\sigma_h = 0.3\bar{h}$ ). C) Maximum disorder in cone positioning ( $\sigma_p = 0.5a$ ). D) Maximum disorder in cone tilt ( $\sigma_t = 10^\circ$ ). Adapted with permission from the aforementioned contribution to *Bioinspiration & Biomimetics* [10], © 2017 IOP Publishing Ltd.

for (NOA68) cone-microstructures atop of CIGS solar cells at normal (AoI =  $0^\circ$ ) and oblique (AoI =  $80^\circ$ ) incidence of light. For benchmarking, simulated reflectance spectra for the uncoated CIGS layer stack, as well as for a CIGS solar cell covered with a (thick) planar layer of NOA68 and another one equipped with an optimized MgF<sub>2</sub> thin-film interference-based antireflective layer were also included. These planar reference configurations, however, were obtained solely by TMM calculations. It should be noted that MgF<sub>2</sub> interference-based antireflective layers are the state-of-the-art method for reaching highest efficiencies for unencapsulated CIGS solar cells [582–589].

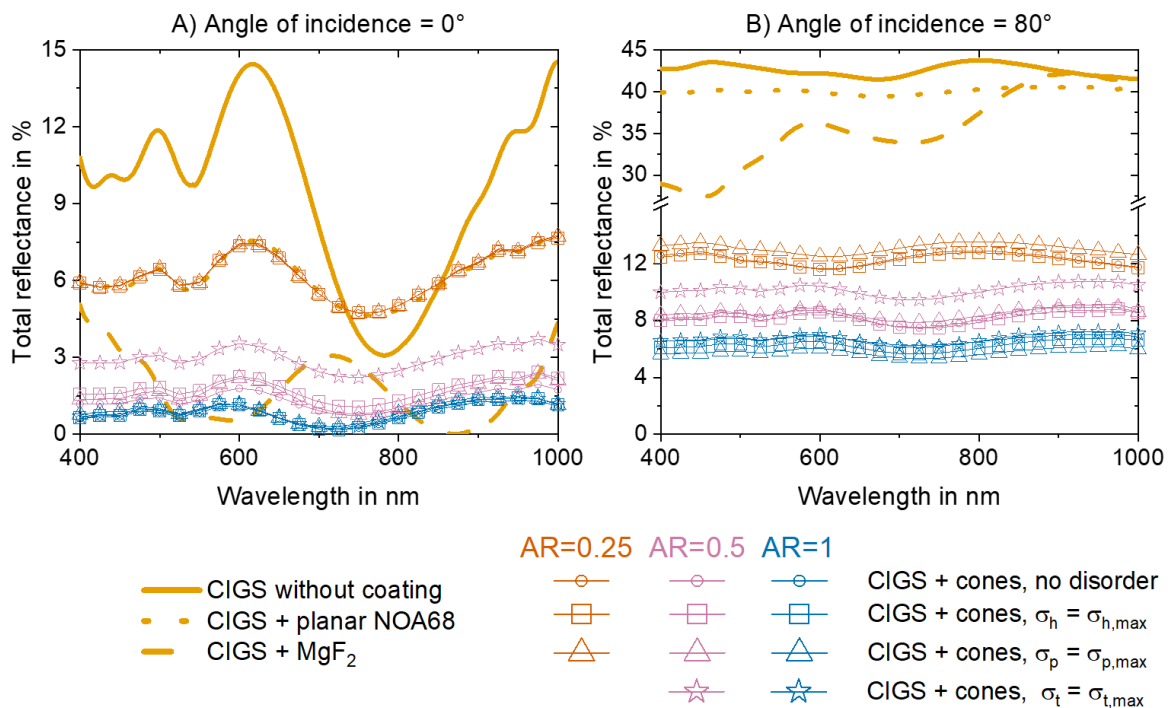


**Fig. 6.13:** Simulation results for the reflection losses of CIGS thin-film solar cells with various top-layer configurations for A) normal incidence and for B) 80° oblique incidence of light. The reflectance spectra of the three planar reference configurations (no coating, thick and planar layer of NOA68, and a 105 nm MgF<sub>2</sub> thin-film coating) were calculated solely via TMM. For all configurations that include a microstructured light-harvesting front-layer, a combined TMM/ray-tracing approach was utilized. For (average) cone ARs of 0.25, 0.5, and 1, non-disordered microstructures and ones with the maximum degree of disorder in cone height, positioning, and tilt were analyzed. Part of these results (AR = 1 case) has been previously published in *Bioinspiration & Biomimetics* [10].

For low AR = 0.25 at normal incidence, the simulated reflectance spectrum equals the TMM results for a planar polymer layer. Only at oblique incidence with AoI = 80°, the low AR cones still exhibit a noticeable antireflection effect, outperforming all reference configurations with planar top layers. With increasing AR, reflection losses are further reduced for all AoIs. For AR = 1, the reflection losses at normal incidence are kept below 2% for the entire spectral range, clearly surpassing the MgF<sub>2</sub> coating in terms of light collection. Furthermore, for ARs of 0.5 and 1, the microstructured top layer configurations considerably smoothen out the reflectance spectra, leading to improved broadband antireflection behavior. This effect is caused by the redistribution of propagation directions upon coupling into the microstructured top layers. The same basic behavior can also be detected in the measured reflectance spectra of rose petal replicas on CIGS solar cells given in Fig. 5.12 A).

For all three ARs considered herein, the introduction of disorder in cone height, positioning, or tilt leaves the simulated reflectance spectra unaltered, similar to what has been reported in Fig. 6.10 for the configurations without a solar cell underneath. Again, the only exemption was found for AR = 0.5 cones with disorder in tilt angle, where a sudden increase in reflection was observed from the  $\sigma_t = 7.5^\circ$  to the  $\sigma_{t,\max} = 10^\circ$  configuration, as previously reported for microstructures with perfectly absorbing rear sides. It can therefore be concluded that the modifications to the angular distribution of in-coupled light rays (as shown for AR = 1 cones in Fig. 6.12) caused by structural disorder are not significant enough to affect the light-harvesting properties of disordered microstructures on top of CIGS solar cells.

Overall, the numerical findings described within this chapter indicate that the antireflection capabilities of petal surface structure replicas are primarily governed by the mean AR of the conical epidermal cells, whereas structural disorder seems to have negligible impact. Even when applied as cover layers for CIGS thin-film solar cells, structural disorder only has limited effects on the overall reflection losses. Concerning the artificial fabrication of similar cone-based microstructures as antireflective surfaces (for example, via direct-laser-writing [566]), this numerical study further indicates that structural disorder can not be engineered in a way that significantly improves the light-harvesting capabilities of PV devices equipped with such microstructures. Conversely, concerning the use of petal surface structure replicas as PV light-harvesting layers, it seems that differences in structural disorder between two petal epidermal cell microstructures (with a comparable average AR of the epidermal cells) are of low importance with respect to minimizing reflection losses.

Inspired by the modeling approach for 3D disordered microstructures discussed throughout this chapter, K. Li *et al.* adopted a similar procedure for numerically studying the light-harvesting properties of negative rose petal replicas on thin-film PV devices [254]. In addition to disorder in (inverted) cone height, positioning and tilt, they further implemented disorder in cone radius (defined similarly to disorder in cone height). Another modification of the modeling approach is their use of parabolic cones as microstructure elements. Furthermore, their combined TMM/ray-tracing simulations were extended to enable the calculation of the power absorbed within each layer of the thin-film solar cell.



---

## 7 Advancing the Replication Techniques of Plant Surface Textures Towards Large-Area and High-Throughput Methods

---

The direct replication of plant surface textures into transparent (UV-curing) polymers via soft-imprint lithography and their subsequent application as antireflective solar cell covers has shown a staggering potential to minimize reflection losses over a broad range of AoIs and wavelengths. However, this approach suffers from several major drawbacks that aggravate its applicability for the PV industry. Next to the obvious issue that a direct replication of a leaf or a petal is always limited by their nature-given shapes and sizes, there are several more drawbacks inherent to the soft-imprint replication of plant surface textures:

- If a plant surface texture is replicated onto a non-(UV-)transparent substrate like a solar cell or a Si wafer, the UV-curing resist needs to be illuminated through the PDMS mold. For many of the widely used UV-curing adhesives like NOA68/88, this might take tens of minutes of UV light exposure through the PDMS mold (under ambient conditions) to achieve full polymerization.
- Accelerated by the UV exposure, the PDMS stamps/masters tend to become brittle after  $\approx 20$  soft-imprint replication cycles, limiting the number of high-quality replicas that can be produced from a single PDMS master.
- Highly transparent, UV-curing adhesives (like NOA88) are rather expensive and therefore not economically feasible for covering the large areas necessary to texture relevant quantities of solar panels.
- Only a limited variety of UV-curing materials are able to meet the high standards regarding transparency that are necessary for solar cell applications. But more importantly, these materials are generally not designed to be able to withstand years of continuous exposure to outdoor conditions. However, such long-term durability is one of the most vital prerequisites to employ plant texture replicas as light-harvesting layers for PV.

The following section 7.1 is focused on overcoming these issues by developing a hot-embossing-based bioreplication routine. To this end, a method to fabricate metallic molds of plant surfaces with high structural quality is demonstrated. These

heat- and force-resistant molds are then integrated into a hot-embossing setup to enable the replication of plant surface textures into polymeric foils. Section 7.2 then deals with the development of an upscaling approach to fabricate large-area hot-embossing molds in order to overcome the nature-given size limitations of molding-based replication techniques. In section 7.3, the process parameters for large-area hot-embossing lithography of the rose petal surface structure into PMMA, PC, and FEP are introduced.

The results presented in this chapter were published in *Proceedings of SPIE* [13] and in *Solar Energy* [3].

## 7.1 Fabrication of Ni Mold Inserts for Rose Petal Replication via Hot-Embossing Lithography

A vital prerequisite for achieving a mass-production of plant surface texture replicas is the development of more durable molds, which would increase the maximum number of (high-quality) polymeric replicas that can be produced from a single natural structure template. As discussed in chapter 5, Ni electroforming of plant surface textures has been utilized in several studies, where the resulting Ni molds were used to structure the target polymer material either via UV-NIL, polymer casting [471, 472], or injection molding [474]. A direct Ni electroforming of natural (air-dried) rose petals has also been realized [458] (for the sake of analyzing structural color effects of rose petal replicas). To date, such Ni molds have not been utilized to demonstrate the replication of plant surface structures via static (plate-to-plate) hot-embossing. Furthermore, all previous approaches suffer a significant disadvantage: Since electroplating requires a conductive surface (plating base), it is necessary to coat the petal surface, for example, with a thin layer of gold. However, the low-pressure conditions during such a deposition process inevitably lead to water loss, causing the epidermal cells to shrink and change shape (see Fig. 7.1). If, however, the fragile surface texture of the natural petal template would be replicated into a material that endures these low-pressure conditions (and is chemically compatible with all components of the electroplating system), such shape-degradation could be avoided. Therefore, a routine for fabricating metallic rose petal molds for static hot-embossing was established, where, instead of directly electroforming the natural petal template, the biotemplate is first replicated under ambient conditions via PDMS casting and a

subsequent molding step. The (first-generation) positive replica can then be metal-coated and electroplated without altering the original template's surface texture. Ryu *et al.* followed a similar route for the fabrication of negatively textured Ni molds from a (positive) polymer replica instead of directly employing the natural rose petal for electroforming [473]. They produced negative polymer replicas by pouring polyurethane-acrylate (PUA) onto the biotemplate and consecutive UV-curing under 5 bar air pressure, which seems to slightly alter the epidermal cell curvature. A negative PUA replica was then used to fabricate a positive one, also via UV-curing of PUA. A separation of the positive and the negative PUA replicas without causing structural damage was only possible if the negative PUA mold receives an anti-adhesive treatment, for example, in the form of a self-assembled monolayer coating. Both the negative and the positive PUA replicas were used for a subsequent Ni electroforming process. Lastly, the Ni molds were then used to transfer the rose petal surface texture into UV-curing perfluoropolyether (PFPE). Advantageously, the Ni mold fabrication routine developed herein does not need to employ elevated air pressure during curing steps, ensuring that the plant epidermal cells do not lose their structural integrity during polymer curing. Furthermore, this novel approach also overcomes the need for any anti-adhesive treatment of the polymer mold surfaces.

The basic fabrication steps necessary from natural rose petal templates to mechanically robust Ni molds for a hot-embossing-based replication of their hierarchical surface texture is schematically depicted in Fig. 7.2 and can be summarized as follows:

- 1) Preparation of a PDMS (negative) mold of a natural rose petal by PDMS casting.

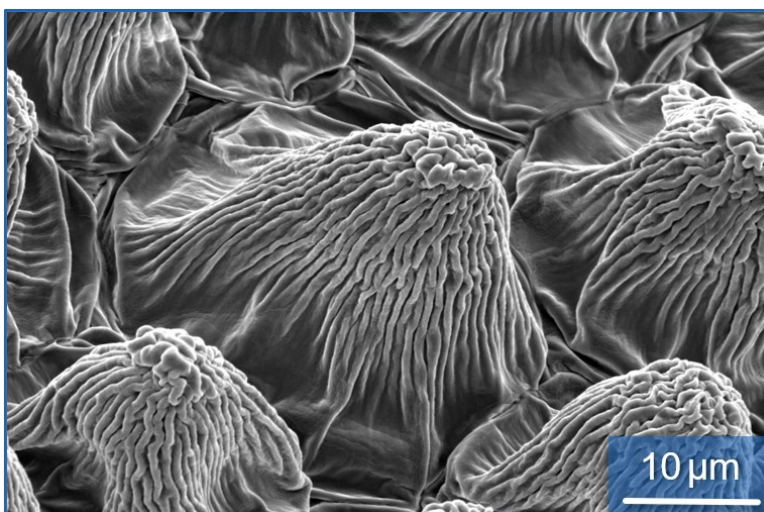


**Fig. 7.1:** SEM image of a natural rose petal surface with shrunken epidermal cells. Such shrinkage occurs when natural rose petals are exposed to low-pressure conditions.

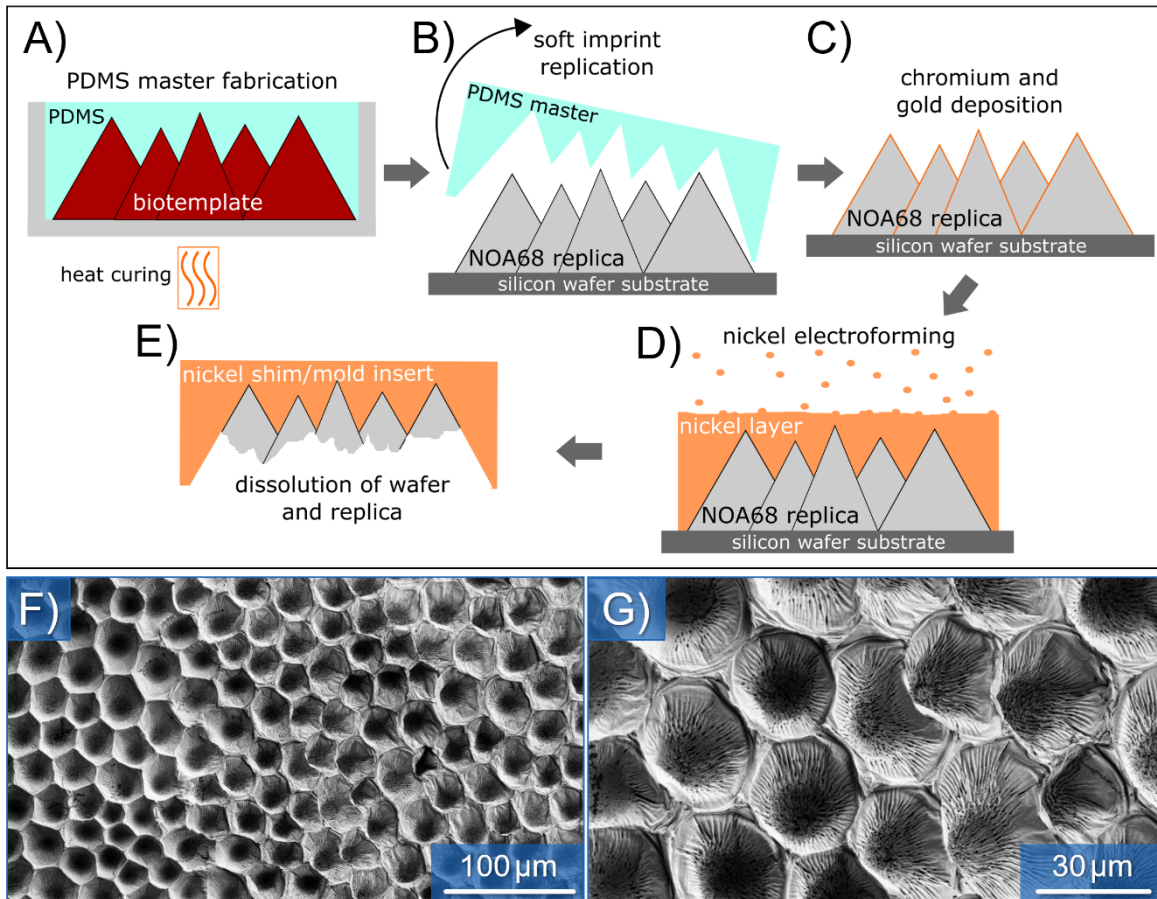


**Fig. 7.2:** Large-area Ni mold insert fabrication for upscaled rose petal replication. A)-E) schematically illustrate the double replication process developed for fabricating leaf and petal surface structure replicas via hot-embossing of polymeric foils using a robust Ni mold insert. F) and G) show SEM micrographs of the Ni mold insert BF05 prior to its first use for hot-embossing. The SEM images in F) and G) were adapted with permission from the abovementioned contribution to *Solar Energy* [3], © 2020 Published by Elsevier Ltd on behalf of International Solar Energy Society.

- 2) Soft-imprint replication of the (positive) rose petal texture onto a Si wafer substrate using NOA68 (as schematically depicted in Fig. 5.3).
- 3) Deposition of a thin layer of Cr (e.g. 15 nm), which acts as an adhesive layer.
- 4) Deposition of a thicker layer of Au (e.g. 100 nm), which acts as a conductive plating base.
- 5) Mounting the wafer substrate onto a homemade plating holder using insulating adhesive tape.
- 6) Immersion into a standard Ni electroplating system until the desired Ni thickness is achieved.
- 7) Planarization of the Ni mold backside by wire electrical discharge machining (wire-EDM) step.
- 8) Removal of the Si substrate by wet chemical dissolution using KOH solution.

- 9) Removal of residual NOA68 by treatment with dichloromethane.
- 10) Realization of the final outer dimensions of the Ni mold by a second wire-EDM step.

Ni electroforming was carried out by Dr. Markus Guttman and colleagues at the Institute of Microstructure Technology (IMT) of the KIT. The Ni electroforming system in 6) was specially developed for thick Ni electroforming of micro- and nanostructures [608, 609]. It includes boric acid with nickel sulfamate electrolyte at  $T = 52^{\circ}\text{C}$  and a pH level of 3.4 – 3.6. A defect-free Ni deposition into the hierarchical micro-/ nanotexture was assured by ramping up the current density from  $0.1 \text{ Adm}^{-2}$  to values up to  $1.75 \text{ Adm}^{-2}$  from start to finish of the electroplating process. Exemplary SEM images of a mold insert clearly show that this fabrication process enables a faithful transfer of the intricate dual-scale surface structure of natural rose petals into Ni. The cuticular nano-wrinkles are even found to be intact in proximity to the base of the epidermal cell micro-cones.

## 7.2 Large-Area Embossing Tool Fabrication – Overcoming the Nature-Given Size Limitations in Templating Plant Surfaces

Quite obviously, when directly templating natural surfaces such as leaves or petals for PV applications, only a small area of a few  $\text{cm}^2$  (depending on the plant species considered) can be patterned. To the best of our knowledge, no method to overcome this natural size limitation of such a direct replication approach has been demonstrated thus far (see section 5.4). Therefore, the following section is dedicated to the development of such an upscaling method. In more detail, the fabrication methodology for (negatively patterned) rose petal Ni molds with high structural fidelity (introduced in the previous section 7.1) was further extended to allow the fabrication of upscaled Ni mold inserts for (static) hot-embossing. In general, the following basic strategy was utilized:

- 1) Manual assembly of natural rose petals on a planar substrate (preferably with seamless stitching).
- 2) PDMS casting of the stitched template.
- 3) Production of a large-area NOA68 replica on Si.
- 4) Ni mold production by following steps 3) - 10) from previous section 7.1.

**Table 7.1: Basic information about the polymer foils that were deployed for the fabrication of large-area rose petal replication via hot-embossing.**

sample name	final status	shape and textured area	nickel thickness
BF01	shim	Ø 95 mm	0.5 mm
BF02	shim	Ø 95 mm	0.5 mm
BF03	shim	Ø 95 mm	0.5 mm
BF04	mold insert	Ø 78 mm	2.5 mm
BF05	mold insert	Ø 78 mm	2.5 mm
BF06	mold insert	25 × 70 mm <sup>2</sup>	2.5 mm
BF07	shim	Ø 136 mm	0.7 mm
BF08	mold insert	Ø 136 mm	3.0 mm
BF09	aborted	Ø 78 mm	-
BF10	mold insert	125 × 100 mm <sup>2</sup>	1.5 mm

A total of ten upscaled Ni shims/mold inserts with variations in shape, size, and stitching quality were produced following this procedure. Table 7.1 provides an overview of the dimensions of these large-area embossing tools. Example photographs of a circular (BF05) and a rectangular (BF06) upscaled mold insert are given in Fig. 7.3. On the basis of BF10 with a structured area of 12.5 cm × 10.0 cm (and a total area of 15.5 cm × 13.0 cm), the main production steps for the metallic mold inserts are illustrated in Fig. 7.4. Fresh rose petals of the ‘Red Naomi’ variety were trimmed into a rectangular shape by using glass slides as stencils. Fifteen such trimmed petals were then manually assembled (in a 3 × 5 matrix) onto a planar metal substrate with double-sided adhesive tape and quickly covered with PDMS (Sylgard ® Elastomer 184, Dow Corning, 10:1 mixture with the respective curing

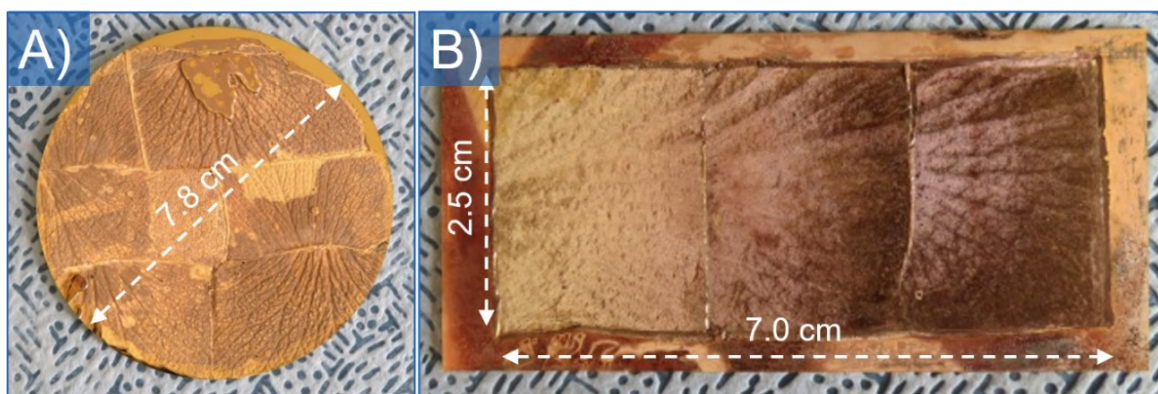


**Fig. 7.3: Large-area Ni mold inserts A) BF05 and B) BF06 for upscaled rose petal replication via hot-embossing of polymeric foils.**

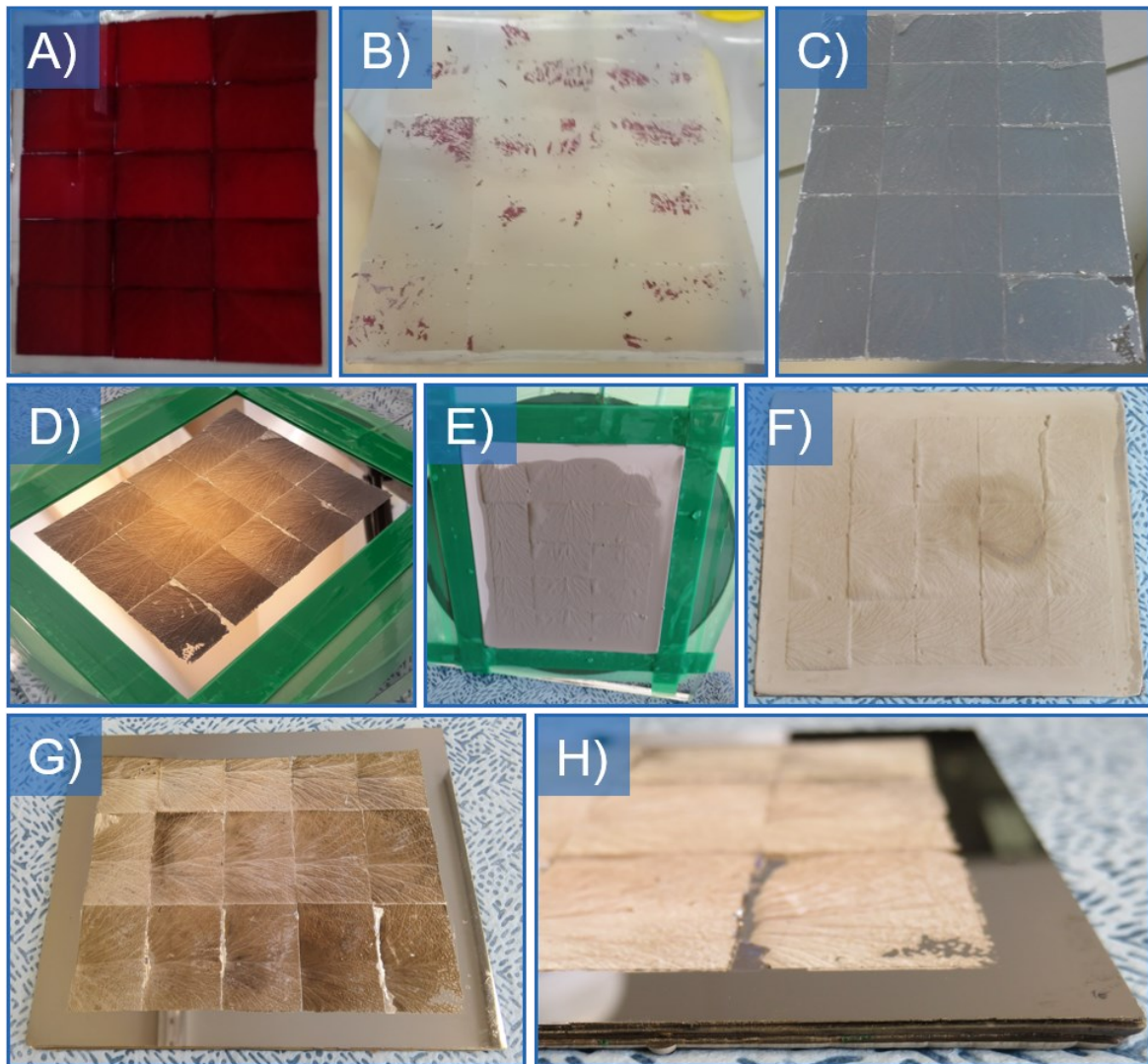


**Fig. 7.4:** Photographs of large-area Ni mold insert BF10 at various stages during its fabrication. A) Stitched array of natural rose petals doused with PDMS. B) Resulting large-area PDMS master mold with residual plant material still attached. C) After cleaning, this PDMS master was used to produce this large-area NOA68 replica on a Si wafer (8-inch diameter). D) Large-area NOA68 replica after Cr and Au deposition. The green tape defines the window for Ni electroforming. E) Large-area NOA68 replica after Ni electroforming. The Ni layer is still attached. F) Rear side of the finalized large-area Ni mold insert. G) Finished large-area Ni mold insert. H) Tilted-view photograph of the completed large-area Ni mold to highlight its evenness at the structural defects.

agent) before the rose petal epidermal cells lose their structural integrity through water evaporation. PDMS curing was carried out at room temperature. Due to structural defects, the resulting large-area PDMS mold was (slightly) trimmed down to a size of 12.5 cm × 10.0 cm, a step which assured proper planarity of PDMS master mold. Macroscopic planarity of the structured area is imperative for the subsequent hot-embossing, assuring a proper thermal contact over the entire

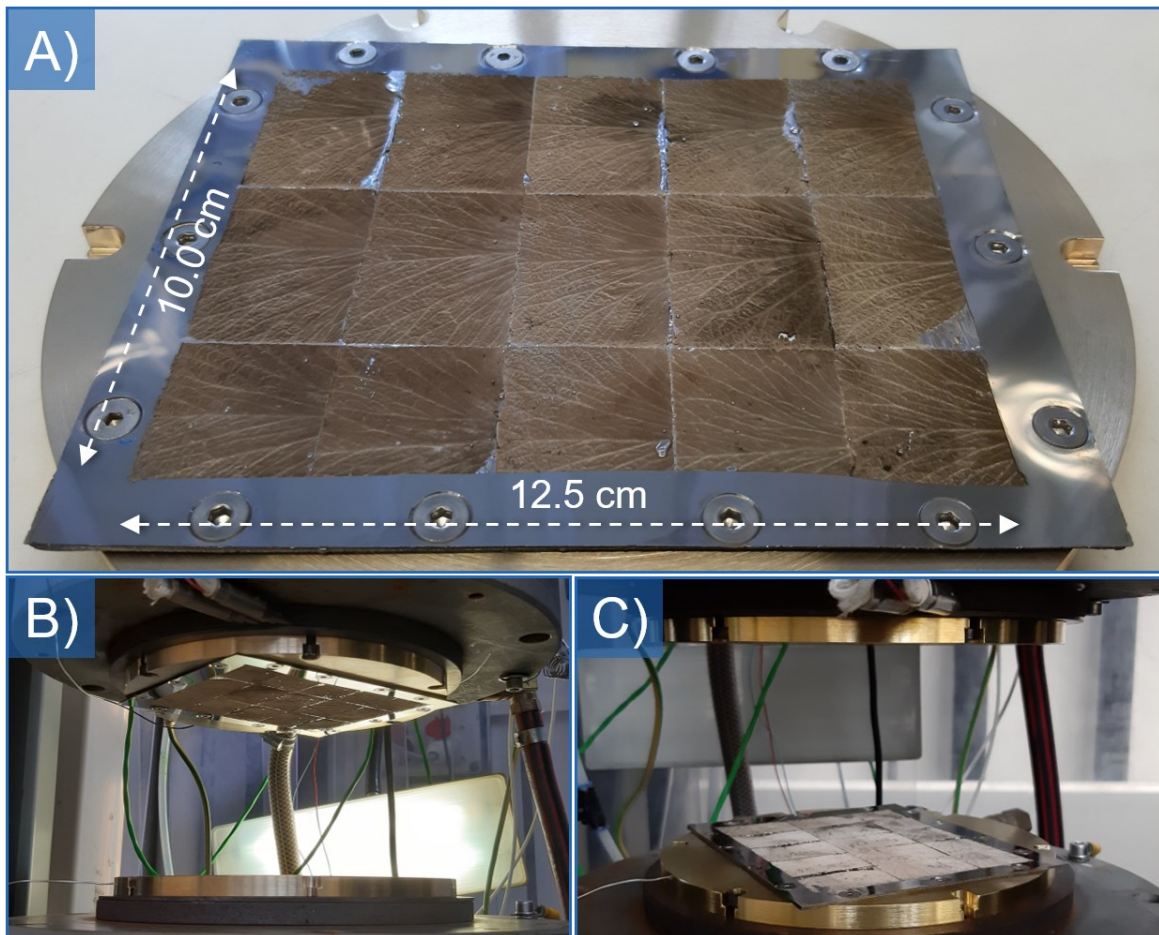


**Fig. 7.5:** Ni mold insert BF10 with a total structured area of 12.5 cm × 10.0 cm. **A)** Pristine Ni mold mounted onto a massive brass substrate prior to the first hot-embossing cycles. **B)** Hot-embossing equipment with Ni mold insert BF10 mounted to the upper side of the setup. **C)** Hot-embossing equipment with Ni mold insert BF10 mounted to the bottom side of the setup. The picture in **A)** was adapted with permission from the abovementioned contribution to *Solar Energy* [3], © 2020 Published by Elsevier Ltd on behalf of International Solar Energy Society.

contact face between the Ni mold insert and the heated substrate (massive brass plate). After thoroughly removing residual plant parts from the upscaled PDMS master, a large-area soft-imprint (NOA68) replica was fabricated on a 1 mm thick Si wafer (8 inches in diameter). This large-area polymer replica was subsequently used to fabricate a large-area (negative) metallic mold via Ni electroforming (following steps 3) - 6) from section 7.1). Lastly, the finished Ni mold insert was mounted onto a massive brass plate using 14 screws (as shown in Fig. 7.5 A) to ensure stability and avoid bending of the mold inserted during hot-embossing.

## 7.3 Large-Area Hot-Embossing for Upscaled Rose Petal Replication

Out of all Ni shims and mold inserts listed in Table 7.1, only BF04, BF05, BF06, and BF10 were utilized for hot-embossing lithography. While only a small number of replicas were produced from BF04 and BF06, the remaining two mold inserts, BF05 and BF10, were extensively used to fabricate hundreds of upscaled hot-embossed rose petal replicas.

Three materials were deployed for hot-embossing-based rose petal replication, namely PMMA, PC, and FEP. The respective manufacturers, foil thicknesses, and refractive indices are given in Table 7.2. It is important to note that the general approach described in this section can straightforwardly be extended to other (thermoplastic) polymer foils by adapting the embossing and demolding temperatures, as well as the applied force.

In principle, static hot-embossing can be performed with the Ni mold insert mounted either to the top or to the bottom plate of the embossing setup, as illustrated in Fig. 7.5 B) and C). Using BF05, hot-embossing was carried out with a polished steel plate at the bottom side, and the mold insert was mounted to the upper plate of the setup. The pristine polymer foils were first trimmed into a circular shape (matching the mold's size) and placed on the bottom plate of the setup. A sheet of polytetrafluoroethylene (PTFE) between the polished steel plate and the pristine foils ensured a smooth rear side of the hot-embossed rose petal replicas. The hot-embossing routine is then carried out according to the following steps:

**Table 7.2: Overview of the three polymeric materials employed for fabricating large-area rose petal replicas through static hot-embossing-lithography.**

material	manufacturer	refractive index @ 588 nm	pristine foil thickness
PC	upag AG, Germany	1.58	0.3 mm
PMMA	Cadillac Plastic GmbH, Germany	1.49	1.0 mm
FEP	RCT Reichelt Chemietechnik GmbH+Co., Germany	1.34	0.25 mm

**Table 7.3: Parameters for the fabrication of large-area rose petal replication via hot-embossing (with Ni mold insert BF05).**

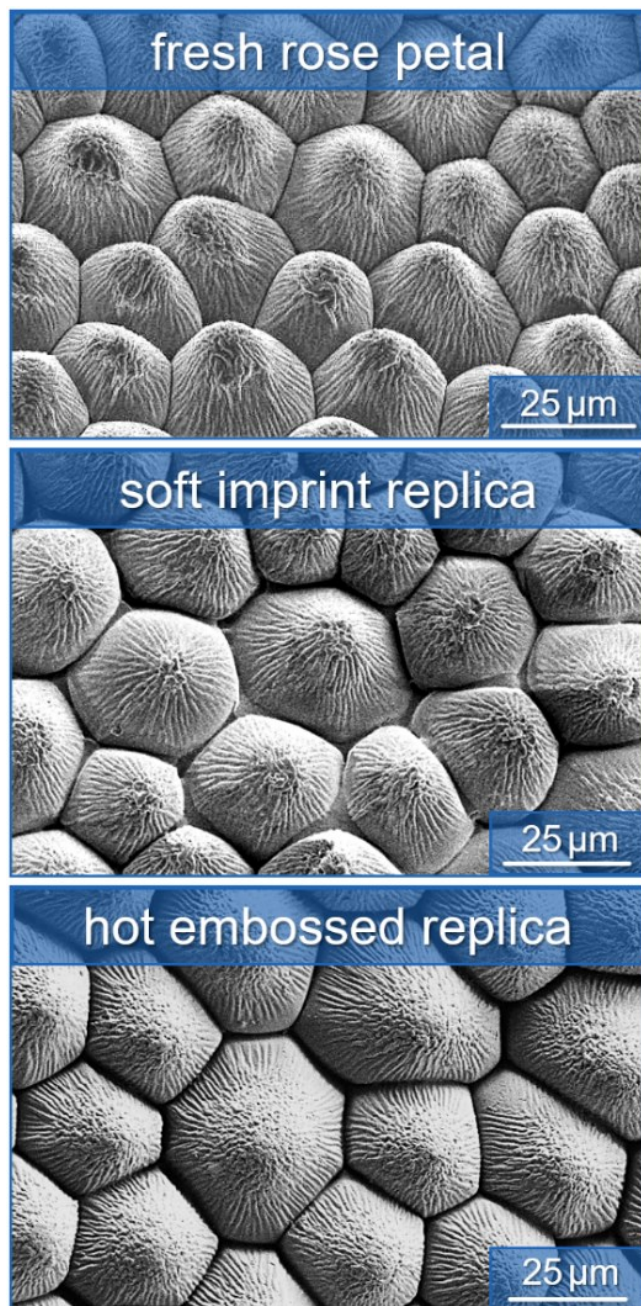
material	embossing temperature	force	demolding temperature
PC	170°C	60 kN	130°C
PMMA	150°C	90 kN	115°C
FEP	275°C	37 kN	235°C

- 1) Both the top and bottom plates of the setup are heated until a target temperature above the respective polymer foil's glass transition temperature is reached.
- 2) Subsequently, the plates are hydraulically pressed together with increasing force until the predefined embossing force is achieved.
- 3) While the embossing force is maintained, the top and bottom plates are cooled down. Due to the thermal contraction of the polymer foil wedged between the two plates, a feedback loop constantly re-adjusts their distance to sustain the embossing force.
- 4) The embossing force is slowly released when the plates' temperatures drop below the predefined demolding temperature (below the respective polymer's glass transition temperature).
- 5) A slowly increasing negative force then pulls the two plates apart.

The plates are moved to their initial positions far apart from each other. The finished replica is then manually delaminated from the mold insert. It should be noted that, since no preheating of the pristine polymer foils was conducted prior to the thermal imprinting, this routine can be considered as a nonisothermal hot-embossing process [610].

The embossing temperatures and forces, as well as the demolding temperatures for large-area rose petal replication using BF05, are given in Table 7.3. These parameter sets assured reproducible replication with high structural quality over the entire patterned area for all three deployed polymer materials. For the case of PMMA, the replication quality is exemplified in Fig. 7.6. SEM micrographs of hot-embossed PC and FEP replicas can be found in Fig. S1 of the supplementary materials. For BF10, which has a considerably larger structured area than BF05, it was found that the embossing forces need to be increased by a factor of 2 – 2.5 to achieve high-quality replication over the entire area. Moreover, it has been found that, especially for PMMA, some slight adjustments to the hot-embossing routine are necessary when using large-scale molds like BF10. Instead of using a polished

**Fig. 7.6:** SEM images comparing the topographies of a fresh rose petal (top), a soft-imprint NOA68 first-generation replica (middle), and a hot-embossed PMMA second-generation replica (bottom).



steel plate (+ PTFE sheet), a sand-blasted brass plate proved to be advantageous for the final step of detaching the replica from the mold insert since the rough brass surface creates an additional pulling force during the retraction of the plates, causing partial delamination of the replica from the Ni mold, which assists the subsequent manual separation. The manual delamination from the (still hot) mold insert was further simplified by mounting the mold to the bottom side of the embossing setup for easier access. After delamination, the PMMA replicas are slightly curved (see Fig. 7.7). This can be avoided by wedging the replicas between two massive, planar metal plates immediately after separation from the mold insert.

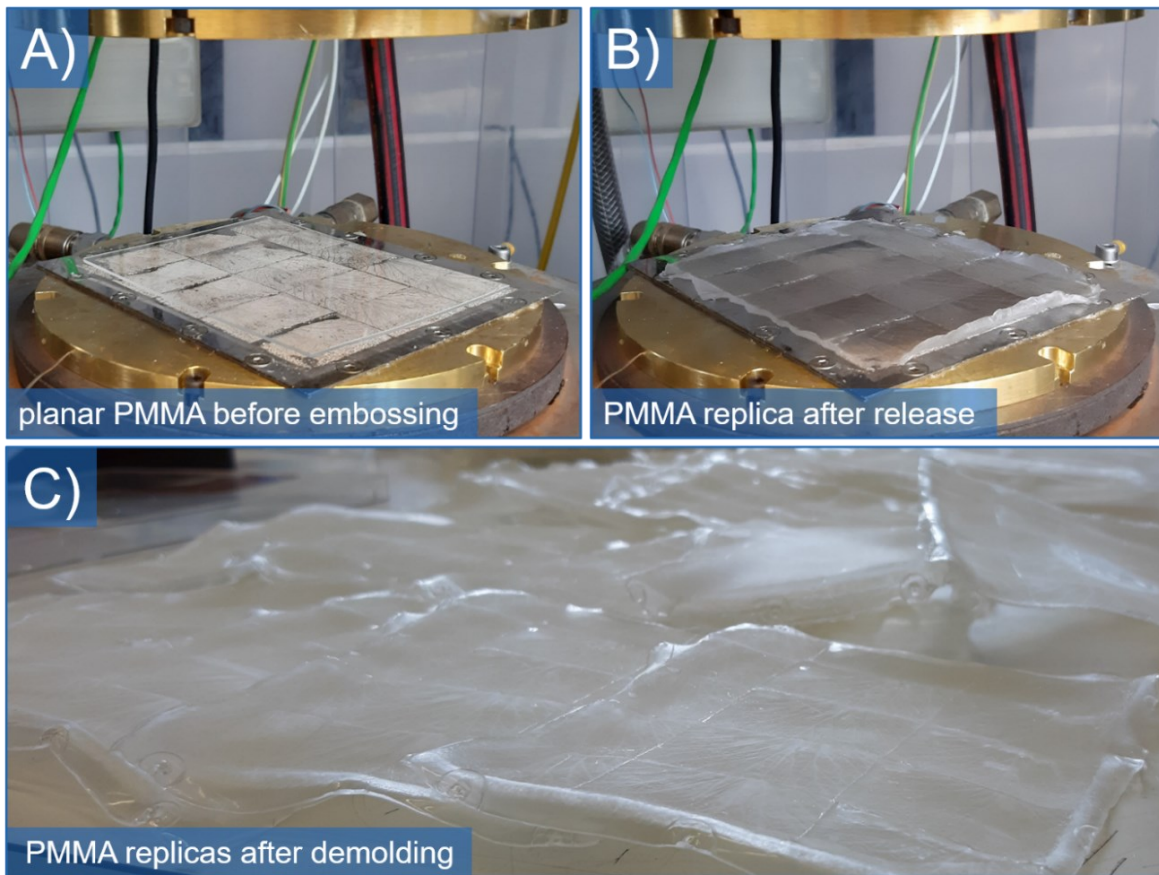


**Fig. 7.7:** Photographs of the large-area Ni mold insert BF10 mounted to the bottom side of the hot-embossing setup and at different stages of the embossing routine. In A), a pristine (planar) PMMA sheet is placed atop BF10. In B), the PMMA layer is depicted immediately after hot-embossing while still firmly attached to the structured Ni mold surface. C) shows several PMMA large-area rose petal replicas after removal from BF10.

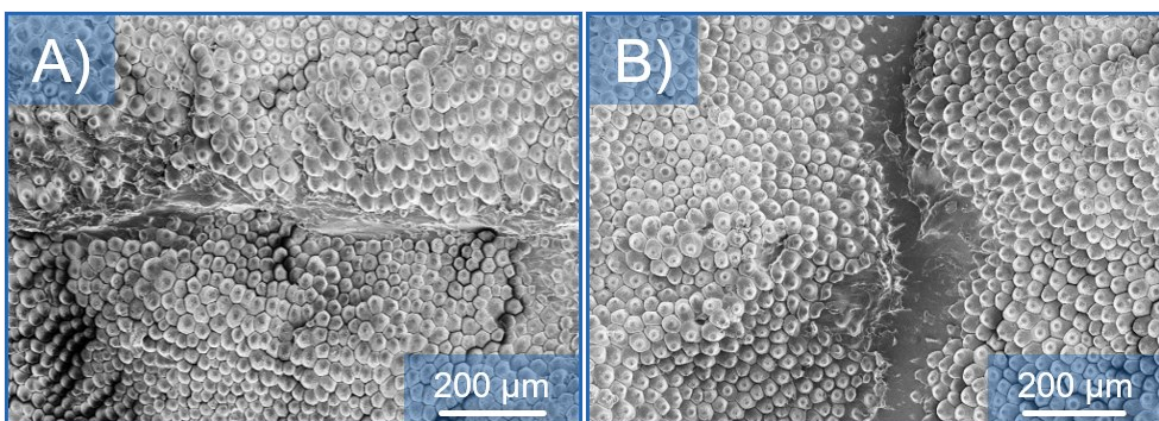


**Fig. 7.8:** Top-view SEM micrographs of the stitching between neighboring patches of a large-area rose petal replica, fabricated by hot-embossing PMMA with the mold insert BF10. A) Stitching line of exceptional quality. B) Average stitching quality. The image in B) was adapted with permission from the abovementioned contribution to *Solar Energy* [3], © 2020 Published by Elsevier Ltd on behalf of International Solar Energy Society.

Due to the manual stitching approach of natural rose petals utilized for upscaling the (PDMS and Ni) mold fabrication processes, a narrow streak with improper structurization can be found around the edges of the rectangular petal patches. The stitching quality is illustrated in Fig. 7.8. By analyzing the topography of (BF10-based) large-area rose petal replicas via SEM, it was determined that these streaks have an average width of  $\approx 100 \mu\text{m}$  (Fig. 7.8 B). However, it is important to note that some of the stitching lines even exhibit a negligible loss in textured area (Fig. 7.8 A).



---

## 8 Light-Harvesting and Wetting Properties of Hot-Embossed Rose Petal Replicas – Experimental Analysis

---

The upscaling approach discussed in the previous chapter 7 enables the fabrication of large-area Ni mold inserts and their subsequent use for large-area rose petal replication via hot-embossing. The following chapter deals with the experimental characterization of several PV-relevant properties of such hot-embossed rose petal replicas. First, the antireflection capabilities of rose petal textured PMMA, PC, and FEP foils on CIGS solar cells are assessed in section 8.1 via optical measurements. The characterization of the patterned foils' respective wetting properties then follows in section 8.2. Finally, section 8.3 explores the opto-electrical properties of hot-embossed rose petal replicas on top of highly efficient CIGS solar cells and (mini) modules.

The results presented in the following sections 8.1 and 8.2 were published in *Proceedings of SPIE* [13]. Moreover, parts of the results described in section 8.3 were included in a full research paper published in *Solar Energy* [3].

### 8.1 Antireflection Properties of Hot-Embossed Rose Petal Replicas on CIGS Single Solar Cells

PMMA, PC, and FEP foils, both planar and rose petal textured, were applied to the front surfaces of CIGS solar cells (active area of  $2.5\text{ cm} \times 2.5\text{ cm}$ ) by using UV-curing NOA88 as a bonding agent. The large-area rose petal replicas, which were fabricated by hot-embossing using mold insert BF05, were trimmed down to match the solar cells' active areas. For all of the deployed polymer materials, identical sections were cut out from the pristine, circularly shaped replicas to assure direct comparability. The CIGS solar cells were fabricated by the ZSW in an in-line three-stage process [611], with the following layer configuration (identical to the CIGS solar cells previously introduced in Fig. 5.12 and Fig. 5.13):

**specular + diffuse reflectance measurement**

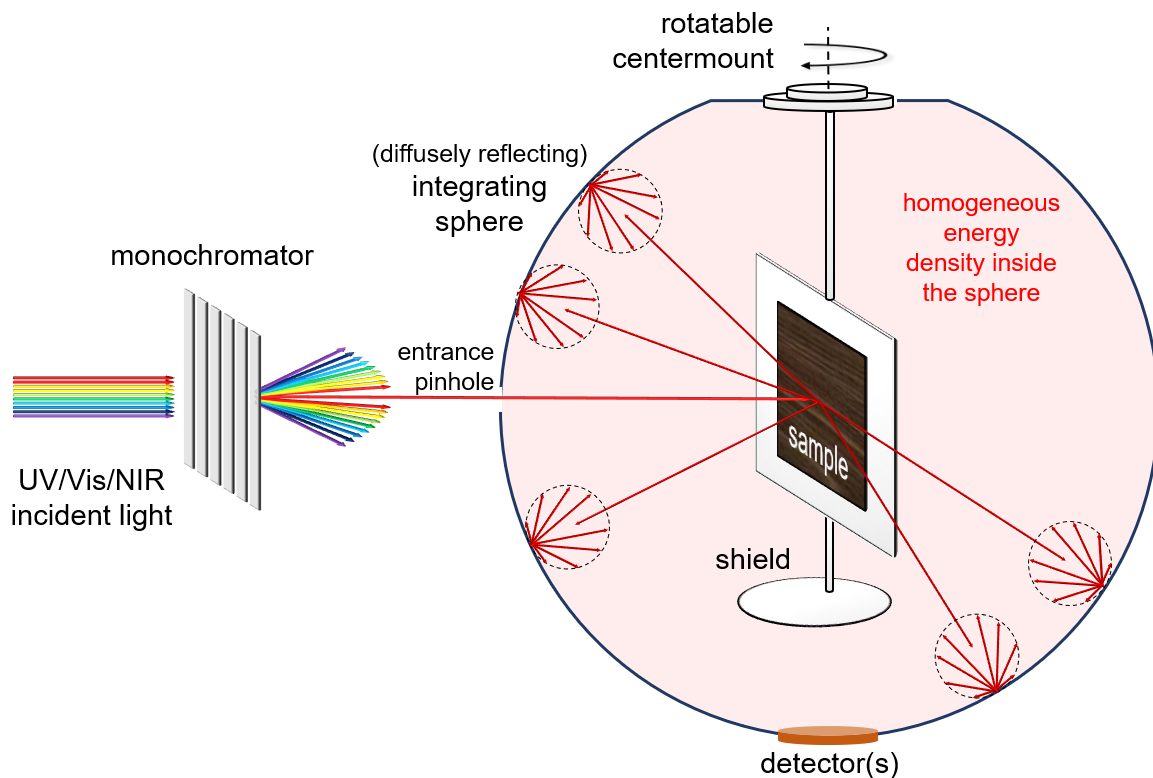


**Fig. 8.1:** Schematic illustration of spectrally resolved reflectance measurements using an integrating sphere.

- 1) 180 nm Al:ZnO (transparent front contact)
- 2) 80 nm iZnO (transparent front contact)
- 3) 50 nm CdS (buffer layer)
- 4) 2.5  $\mu\text{m}$  CIGS (active layer)
- 5) 500 nm Mo (rear contact)

It should be noted that these devices lack metallic fingers for contacting the front and back electrodes and, therefore, can be described as 'optical dummies'. Next to configurations with planar and rose petal textured polymer foils as cover layers, CIGS solar cells with a 105 nm  $\text{MgF}_2$  antireflective coating as well as uncoated devices were also considered for benchmarking. The  $\text{MgF}_2$  layer thickness was optimized via TMM calculations to minimize AM1.5G (photon-flux-density) weighted reflectance (instead of minimizing the reflectance at a single wavelength) at normal incidence of light. For these eight different cover layer configurations, reflection losses were measured for five AoIs between  $0^\circ$  and  $70^\circ$  and the entire relevant spectral range between 300 nm and 1200 nm (CIGS band gap) in 10 nm steps by using a UV/Vis/NIR spectrophotometer (Lambda 1050, PerkinElmer, USA) with an integrating sphere and a pivotable center-mount. The use of an integrating sphere allows the direct measurement of the total reflection losses (meaning

specular + diffuse component) of the abovementioned CIGS solar cells for the various cover layers. The basic functionality of such a setup is schematically depicted in Fig. 8.1. Monochromatic light enters the integrating sphere – which is a hollow sphere with its inside surface being coated with a diffusely (Lambertian) reflecting material – through a small pinhole and hits the sample, which is located at the center of the sphere, under the desired AoI. All light reflected from the sample will inevitably be directed towards a diffusely reflecting surface and, due to the spherical shape of the chamber, randomized over the entire volume of the integrating sphere, leading to a homogeneous energy density over the whole interior of the sphere. Detectors at the bottom of the sphere are then used to quantify the total amount of reflected light (relative to a chopped reference beam that enters the sphere without directly hitting the sample), irrespective of its initial angular distribution. Reflectance spectra were acquired for AoI = 0°, 10°, 30°, 50°, and 70°. However, this type of setup does not allow measuring the reflectance of smooth, planar samples at normal incidence since all the (specularly) reflected light would just be redirected and exit the integrating sphere through the entrance pinhole. Therefore, the case of AoI = 0° was not considered for all the configurations with planar top layers. Measured reflectance spectra for (close to) normal incidence under 10°, and for oblique incidence under 70° are shown in Fig. 8.2 A) and B). Furthermore, for each top layer configuration and for every AoI, the ‘sunlight reflectance’ – the appropriate quantity to assess reflection losses in PV – was calculated by weighting the spectrally resolved reflectance with the AM1.5G solar spectrum (photon flux density). These values were then further used to compute the relative change in sunlight reflectance compared to uncoated devices, as shown in Fig. 8.2 C) (where positive values indicate a reduction in reflectance compared to the uncoated reference).

Even though the MgF<sub>2</sub> coating, under normal incidence of light, leads to the most effective minimization of reflection losses for visible light wavelengths, rose petal textured PC and PMMA light-harvesting layers still lead to comparable weighted reflection losses as the destructive-interference-based coating, due to the improved broadband stability of their antireflective behavior at UV and near-infrared wavelengths. The configuration with the rose petal textured PMMA cover layer even slightly surpasses the antireflection capabilities of the optimized MgF<sub>2</sub> layer. While the devices with MgF<sub>2</sub> and rose petal textured PC antireflective coating exhibit a 48.7% and 48.2% decrease in weighted reflectance at normal incidence, the rose petal textured PMMA cover layer even leads to a 51.7% relative reduction of reflection losses. Since MgF<sub>2</sub> thin-film antireflective layers are the state-of-the-art method for reaching world record efficiencies for unencapsulated CIGS

solar cells [582–589], these findings suggest that rose petal textured PMMA cover layers could, in principle, be a candidate for surpassing the current PCE record for CIGS solar cells by relying solely on improving light-management of the devices with the help of an external layer. It must be noted, however, that the relative reductions in sunlight reflectance (caused by applying various external layers) discussed within this section can not be directly translated 1:1 into a relative increase in  $J_{SC}$  or in PCE, since not every additional photon that gets trapped in a device will necessarily be absorbed in its active material. Therefore, it is imperative to directly analyze the impact of the reduction in reflection losses on the electrical performance of working solar cells under STC and via EQE measurements. Such an opto-electrical characterization of hot-embossed rose petal replicas on top of high-efficiency CIGS solar cells and modules was conducted at ZSW with the help of Dr. Ruben Hünig, and are discussed in detail in section 8.3.

For off-normal incidence of light under an AoI  $> 50^\circ$ , both rose petal textured PC, and PMMA layers outperformed the  $MgF_2$  coated configuration by a considerable margin. Rose petal textured PMMA was found to reduce the spectrally weighted reflectance by (relative) 63.5% at AoI =  $70^\circ$  compared to uncoated devices, outperforming the  $MgF_2$  coated device by a factor of 1.8. As previously demonstrated for soft-imprint NOA68 rose petal replicas [581, 194, 612], the hot-embossed PC and PMMA rose petal replicas show outstanding potential to maximize sunlight-collection in situations where, for example, solar panels can not be installed under appropriate tilt angle and orientation (for example in building-integrated-photovoltaics, BIPV), as well as for strongly diffuse irradiation conditions. Overall, the most efficient reduction of (spectrally weighted) reflectance was clearly achieved with the rose petal textured PMMA cover layer, with its antireflection properties slightly surpassing the optimized  $MgF_2$  thin-film coating even under normal incidence of light.

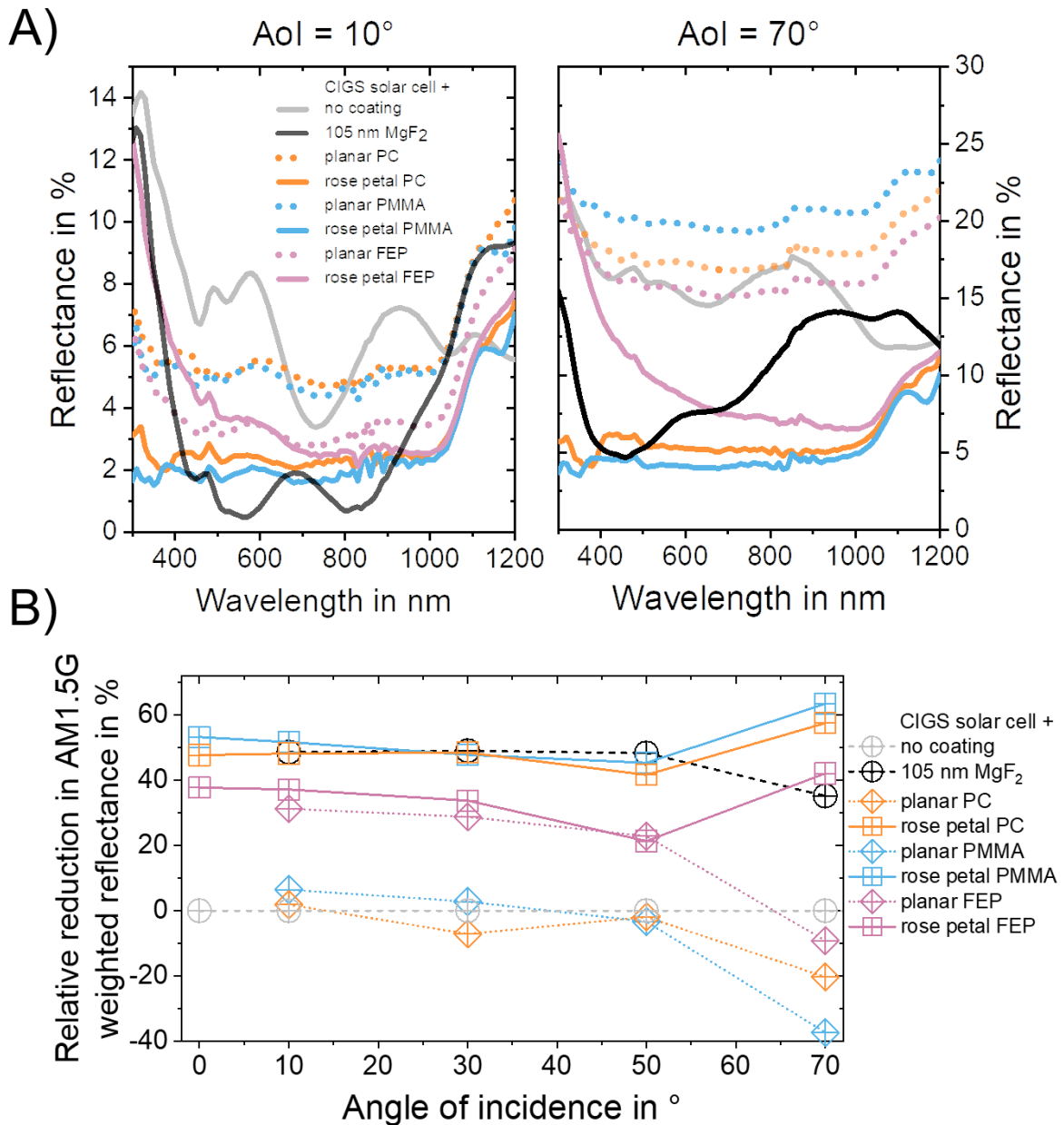


**Fig. 8.2:** Light-harvesting properties of CIGS thin-film solar cells with hot-embossed (using mold insert BF05) rose petal textured PC, PMMA and FEP cover layers, as well as corresponding planar reference foils. Furthermore, the cases of the pristine CIGS device layout with and without an  $MgF_2$  thin-film antireflective coating are also included for benchmarking. A) depicts measured reflectance spectra (specular + diffuse components) of all these device configurations for normal ( $AoI = 10^\circ$ ) and oblique ( $AoI = 70^\circ$ ) incidence of light. For all  $AoI$ s considered, the reflectance spectra were then weighted with the photon-flux-density of the AM1.5G spectrum, and the relative change in weighted reflectance compared to uncoated devices was computed and plotted in B). The data presented in this figure has been previously included in a contribution to *Proceedings of SPIE* [13].

## 8.2 Wetting Properties of Hot-Embossed Rose Petal Replicas

While the previous section 8.1 focused on hot-embossed rose petal replicas' ability to minimize reflection losses when applied atop solar cells, the following section presents a basic experimental assessment of their wetting properties.

With the help of Aiman Roslizar (IMT, KIT), static water contact angles were measured for both planar and rose petal textured PC, PMMA, and FEP layers, which were fabricated via hot-embossing with Ni mold insert BF05, using a contact angle goniometer (OCA 15Pro, Dataphysics, Germany) and a water droplet volume of 10  $\mu\text{l}$ . At least six individual measurements per sample were conducted and averaged. All these results are provided in Table 8.1. For all three polymer materials considered, the hot-embossed foils possess noticeably larger static water contact angles than their untreated/planar counterparts, as can be seen from the photographs depicted in Fig. 8.3. Remarkably, rose petal textured PMMA was found to be hydrophobic with a static water contact angle well above the critical value of  $90^\circ$ , despite PMMA being intrinsically hydrophilic, as indicated by the contact angle of  $72.2^\circ$  measured for the planar PMMA reference layer. Such a structure-induced transition between the hydrophilic and the hydrophobic wetting regimes can not be explained by the classical models for describing the wetting properties of rough surfaces (see section 4.1) since increasing the surface roughness of a solid material will, according to the equations introduced by Wenzel [401] and Cassie & Baxter [402], only render intrinsically hydrophilic materials more hydrophilic, and intrinsically hydrophobic materials more hydrophobic. Interestingly, Ma *et al.* previously demonstrated a porous PMMA structure that even leads to superhydrophobicity. They proposed two main reasons for this behavior, namely (i) the interplay between micro- and nanostructure features and (ii) a reorientation of surface (hydrophobic and hydrophilic) groups of the PMMA chain molecules [613]). Indeed, similar structure-induced transitions from (intrinsically) hydrophilic to hydrophobic properties have further been demonstrated for other polymers such as PVA [614], as well as for semiconductors like (hydrogen-terminated) Si [615] and metals like Cu [565].

Due to FEP having a particularly low surface free energy, rose petal textured FEP foils expectedly exhibited the maximum static contact angle out of all the tested surfaces, averaging at  $134.4^\circ \pm 4.3^\circ$ . However, assuming that the high contact angle value of rose petal textured FEP might be equivalent with a pronounced self-cleaning quality is a fallacy since it has been demonstrated that, in fact, some natural rose petal surfaces exhibit a high value for the static water contact

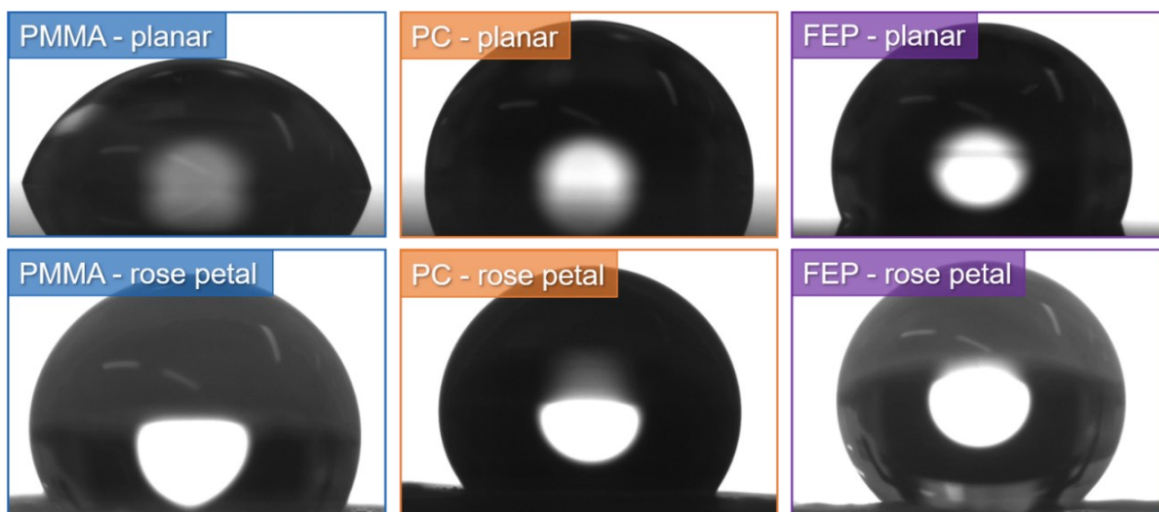


**Fig. 8.3:** Water droplets on planar and rose petal textured PMMA, PC, and FEP, fabricated via hot-embossing with Ni mold insert BF05. For all three materials, the texturization results in a noticeable increase in static water contact angle. Interestingly, for the case of PMMA, the hierarchical rose petal patterning leads to a transition from the hydrophilic to the hydrophobic wetting regime.

angle ( $> 150^\circ$ ) but, at the same time, a strong adhesion force between the surface and the water droplet keeps droplets from rolling/sliding/bouncing off the surface. As discussed in chapter 4, this seemingly contradictory set of properties is often

**Table 8.1:** Results of the static contact angle measurements for planar and rose petal textured PMMA, PC, and FEP.

	planar PMMA	rose PMMA	planar PC	rose PC	planar FEP	rose FEP
static water contact angle / °	68.8	126.3	93.9	125.0	113.0	131.3
	71.3	124.3	93.6	115.3	111.5	131.3
	75.0	111.0	97.5	129.2	111.5	136.6
	71.5	114.6	92.7	121.4	107.9	134.0
	73.8	128.1	95.3	131.7	108.5	145.6
	72.8	124.3	97.6	136.3	114.4	133.6
			118.3	92.9	123.6	
						131.1
						134.4
	$72.2 \pm 2.0$	$121.0 \pm 6.0$	$94.8 \pm 1.9$	$126.1 \pm 6.4$	$110.6 \pm 1.8$	$134.4 \pm 4.3$

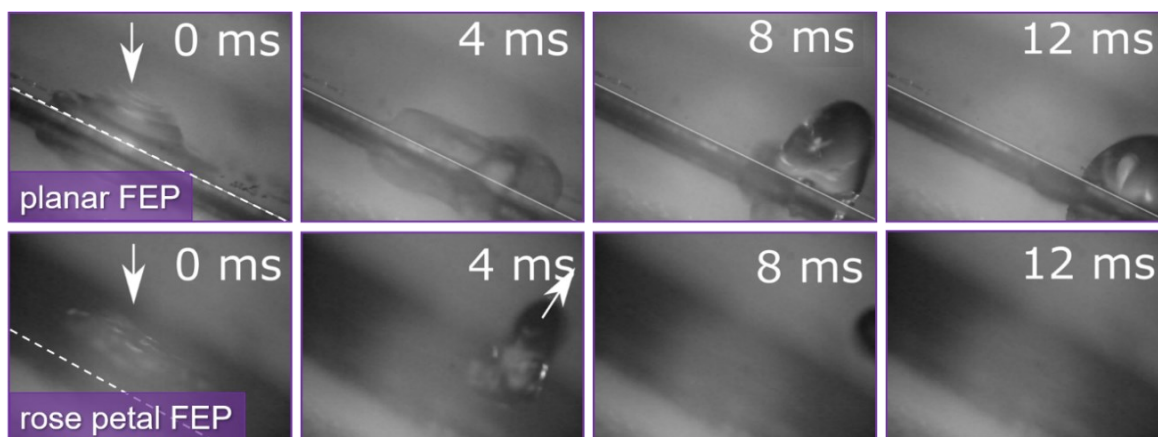


**Fig. 8.4:** High-speed camera analysis of 5  $\mu\text{l}$  water droplets falling onto 30° tilted planar (top row) and rose petal textured (bottom row) FEP foils, fabricated via hot-embossing with Ni mold insert BF05. Screenshots at four instants in time show that after slightly sliding down the surface, the droplets ultimately get stuck at the planar FEP foil. After impact on a rose petal textured FEP surface, on the other hand, water droplets immediately bounce off the surface again. Adapted from the abovementioned contribution to *Proceedings of SPIE* [13], © 2018 Society of Photo-Optical Instrumentation Engineers (SPIE).

called the (rose-) ‘petal effect’ [405, 412–416]. Placing a single water droplet onto a test surface and then carefully and slowly tilting this surface until the gravitational force (possibly) overcompensates the adhesion force, causing the water droplet to start rolling downwards and off the surface. Therefore, this so-called roll-off angle can be exploited as a measure for the adhesion force between a water droplet and a (textured) surface.

To assess their self-cleaning capabilities concerning PV applications, the behavior of 5  $\mu\text{l}$  water droplets when falling onto 30° tilted layers after a 7 cm drop was analyzed, mimicking rain droplets falling onto tilted PV modules. A module tilt angle of around 30° is the realistic inclination needed for a year-round optimized PV energy production in Karlsruhe, Germany [616, 89, 617]. Using high-speed camera recordings (VW-6000E, Keyence, Japan), water droplets were found to always stick to the tilted PC and PMMA surfaces, both for planar and rose petal textured layers. Both these materials, therefore, do not qualify as self-cleaning light-harvesting coatings. The same behavior was found for planar FEP reference layers. In the case of rose petal textured FEP, however, it was found that all of the droplets immediately bounce off the tilted surface. Fig. 8.4 depicts these findings through screenshots at different instances in time. It should be noted that, even for tilt angles as low as 10°, all droplets were still found to bounce off the rose petal textured FEP surfaces immediately.

Although rose petal textured FEP was shown to be less efficient in terms of minimizing reflection losses when used as PV cover layers (see section 8.1), its additional potential to introduce self-cleaning to solar panels still makes rose petal textured FEP a relevant candidate for PV applications.

### 8.3 Opto-Electrical Properties of Hot-Embossed Rose Petal Replicas on CIGS Solar Cells and Modules

Although the broadband and angle-tolerant reduction in reflectance caused by rose petal textured polymer cover layers (relative to a planar cover layer of the same material) on top of CIGS solar cells already indicate that these cover layers should also improve the opto-electrical performance of solar cells. However, due to multiple loss mechanisms, the relative gain in the number of in-coupled photons does not result in an equally large gain in photocurrent or PCE. Only in the ideal case where all the surplus photons that couple into the device due to the surface patterning would be absorbed in the appropriate (active) layer of the device, and none of the resulting excitons would recombine before reaching the contacts. This chapter is therefore dedicated to explicitly measure the opto-electrical properties of CIGS single solar cells and modules, covered with hot-embossed rose petal PMMA antireflective layers, under laboratory conditions. All measurements discussed in this section were performed at ZSW with the help of Dr. Ruben Hünig.

For the high-efficiency CIGS single solar cells, 18 individual cells, each with an active area of  $0.5 \text{ cm}^2$  were characterized under Standard Test Conditions (STC) before and after applying various coatings/cover layers. More specifically, their IV characteristics were measured using a WACOM Solar Simulator WXS-90S-5, 1.5G (spectrum is in coincidence with AM1.5G IEC-60904-9, ClassA) in forward direction (no hysteresis observed), and on this basis, the PCE,  $V_{OC}$ , FF and  $I_{SC}$  were determined. In their pristine/uncoated state, the transparent front electrode constitutes the uppermost layer of these devices. Details about their fabrication can be found in reference [618]. An average PCE of the 18 pristine cells of  $19.8\% \pm 1.0\%$  was measured (lowest PCE at 17.6% and highest PCE at 21.4% for the pristine cells). Six of the solar cells were then equipped with a 105 nm thick layer of  $\text{MgF}_2$ , another six with cutout pieces of rose petal textured PC, and the remaining six with cutout pieces of rose petal textured PMMA. The PC and the PMMA replicas were

**Table 8.2: Changes in PCE,  $I_{SC}$ ,  $V_{OC}$ , and FF caused by various light-harvesting layers on top of highly efficient CIGS solar cells relative to the respective uncoated devices.**

	105 nm MgF <sub>2</sub>	rose petal PC	rose petal PC + 105 nm MgF <sub>2</sub>	rose petal PMMA
$\Delta PCE / \%$	+ 4.5 ± 1.6	+ 4.6 ± 0.9	+ 6.3 ± 0.8	+ 5.7 ± 0.6
$\Delta I_{SC} / \text{mA}$	+ 4.2 ± 1.3	+ 5.2 ± 0.7	+ 7.2 ± 0.7	+ 5.4 ± 0.6
$\Delta V_{OC} / \text{mV}$	+ 0.4 ± 0.1	+ 0.1 ± 0.2	- 0.6 ± 0.1	+ 0.2 ± 0.2
$\Delta FF / \%$	- 0.1 ± 0.3	- 0.7 ± 0.3	- 0.2 ± 0.3	+ 0.1 ± 0.6

fabricated by hot-embossing with Ni mold insert BF05 and bonded onto the CIGS solar cells by using UV-curing NOA88, which is highly transparent even into the UV spectral range. After another STC characterization of all 18 coated solar cells, (only) the six samples covered with rose petal textured PC (due to  $n_{PC} > n_{PMMA}$ ) were additionally coated with a 105 nm MgF<sub>2</sub> layer, and their IV characteristics were acquired once more. For all four cover layer configurations, the relative change in PCE,  $V_{OC}$ , FF and in  $I_{SC}$  (compared to the pristine/uncoated cells) was determined. Rose petal textured FEP layers were not considered for the opto-electrical analysis discussed in this subsection, mainly since the low refractive index  $n_{FEP} = 1.34$  leads to inferior light in-coupling and light-trapping capabilities compared to rose petal textured PMMA or PC cover layers (see reflectance spectra in Fig. 8.2). In addition to the measurement of IV characteristics, EQE measurements were performed for normal incidence of light (using a PVE300 Photovoltaic Device Characterisation System by Bentham Instruments, UK) in order to gain further insight into the spectrally resolved response of the CIGS single solar cells with their various top layer configurations.

The results of the IV-characterizations are summarized in Table 8.2. The complete set of measured data can be found in Table S1 - Table S14. Overall, the highest PCE that was reached for an MgF<sub>2</sub> coated device was measured at 22.2%. For the rose petal textured PMMA covered solar cells, the overall highest measured PCE was 21.6%. The highest efficiency reached with rose petal textured PC combined with an MgF<sub>2</sub> coating was found at 21.3%. Before applying the MgF<sub>2</sub> coating to the PC rose petal replica, the highest PCE with the bare rose petal textured PC cover layer was measured at 20.9%. For the case of MgF<sub>2</sub>, as well as for rose petal textured PMMA and PC, measured EQE spectra of the solar cells with the highest PCE are presented in Fig. 8.5 A). Although rose petal textured PMMA, as discussed in

section 8.1, exhibited lower reflectance for near-infrared and UV wavelengths than the MgF<sub>2</sub> coating, the EQE measurements clarify that the additional in-coupled UV photons are parasitically absorbed within the PMMA layer. For wavelengths < 400 nm, a rapid decrease in EQE is found for both polymeric cover layer materials but is especially pronounced for PC.

Although the overall highest efficiency was reached with an MgF<sub>2</sub> coated device, this configuration, on average, leads to a relative increase in PCE of only 4.5%, while rose petal textured PMMA cover layers cause an average PCE boost of 5.7%. The findings presented in Table 8.2 further indicate that FF and V<sub>OC</sub> remain almost unaffected upon lamination of rose petal textured PMMA onto the devices. It can therefore be concluded that the performance increase induced by the hot-embossed rose petal replicas is primarily caused by optical effects, namely (i) the suppression of surface reflectance and (ii) a more efficient trapping of the collected light, both effects resulting in an increased photon-absorption-rate in the active material of the PV devices.

While for MgF<sub>2</sub>, the PCE gains reached for the six individual solar cells tend to vary quite strongly, rose petal textured PMMA cover layers, on the other hand, seem to boost device performance more reliably (as indicated by the standard deviations provided in Table 8.2). With an average increase in PCE of 4.6%, rose petal textured PC layers lead to a comparable performance enhancement as MgF<sub>2</sub> coatings under normal incidence of AM1.5G simulated light. Interestingly, an additional MgF<sub>2</sub> coating applied onto the PC rose petal replicas leads to another considerable improvement of the device performance under STC, resulting in an average increase in PCE of 6.3% relative to uncoated devices. Considering that the refractive index of MgF<sub>2</sub> ( $n_{\text{MgF}_2} \approx 1.38$  [138]) does not quite match the ideal refractive index for suppressing reflection losses at an air-PC interface, which is given by  $(n_{\text{air}}n_{\text{PC}})^{1/2} = (1 \cdot 1.58)^{1/2} \approx 1.26$  (assuming a wavelength around 588 nm), the combination of polymeric rose petal replicas with a superimposed thin-film antireflective coating made from a low refractive index material such as porous silica, which can be prepared with refractive indices between 1.44 and 1.22 [150] and even below [151], might be a promising strategy for surpassing the current CIGS record efficiency of 23.35% [588, 589] through improved light-management. It is important to note, however, that even though the MgF<sub>2</sub> coated rose petal PC cover layer caused the most pronounced PCE increase of 6.3%, the relevance of this configuration for the PV industry is limited nonetheless since MgF<sub>2</sub> is a relatively soft material and not well-suited for withstanding outdoor conditions [619].

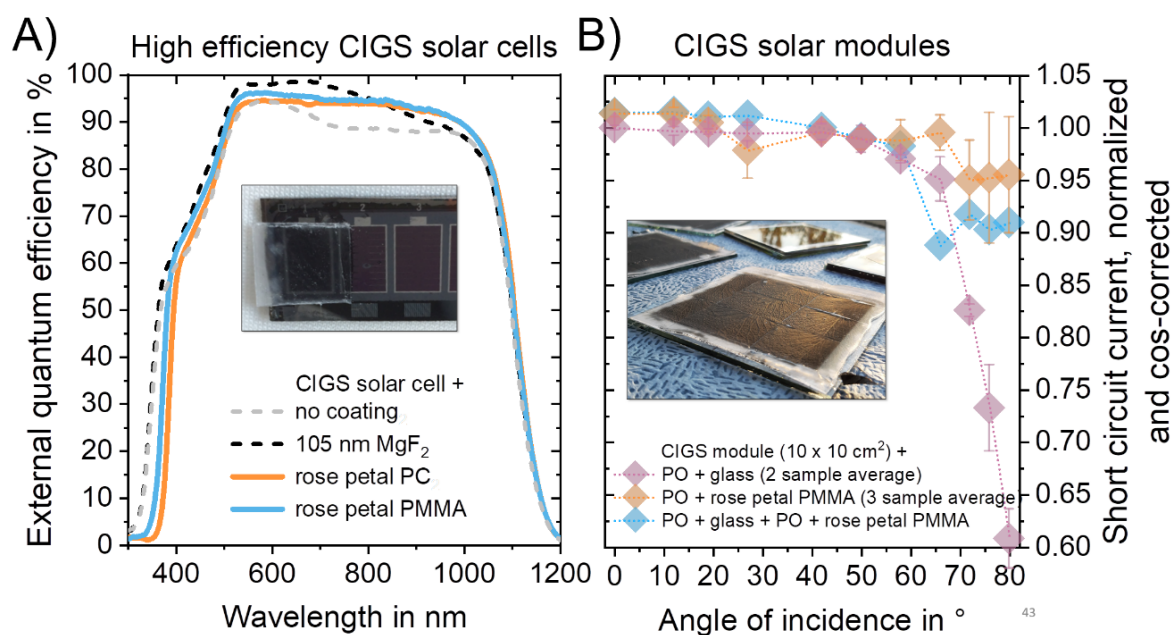


**Fig. 8.5:** Opto-electrical properties of high-performance CIGS single solar cells with various cover layer configurations. **A)** EQE of CIGS solar cells with various cover layer configurations. The solar cells were fabricated in a strip-layout (see inset), and the PC and PMMA replicas were attached with the UV-curing resist NOA88. **B)** Angle-dependent short circuit current of CIGS solar modules with various cover layer configurations. All these layers were bonded atop each other via lamination with PO foil. Part of the data presented in this figure has been previously published in the abovementioned contribution to *Solar Energy* [3].

Next to studying the opto-electrical properties of hot-embossed rose petal replicas only on small-scaled single solar cells, similar experiments were also conducted for large-area (125 cm<sup>2</sup>) rose petal replicas, fabricated by hot-embossing using Ni mold insert BF10 (see sections 7.2 and 7.3), on top of CIGS modules. 10 cm × 10 cm CIGS mini-modules were fabricated at ZSW in a co-evaporation process [620]. For ten uncoated (no glass cover) CIGS mini-modules, IV-measurements were carried out under STC after 10 min of cold light soaking (using a WACOM Solar Simulator WXS-90S-5 again), leading to an average device efficiency of PCE = (13.4 ± 0.3)%. In addition to STC-based testing, the same setup was further utilized for characterizing CIGS modules with various top layer configurations under oblique incidence (up to 80°) of AM1.5G simulated light. Since the tilted modules could not be adequately cooled, only the angle-dependent photocurrent could be regarded as meaningful in these experiments.

Since rose petal textured PMMA was determined to be the most well-suited candidate for enhancing PV device performance, both through angle-dependent

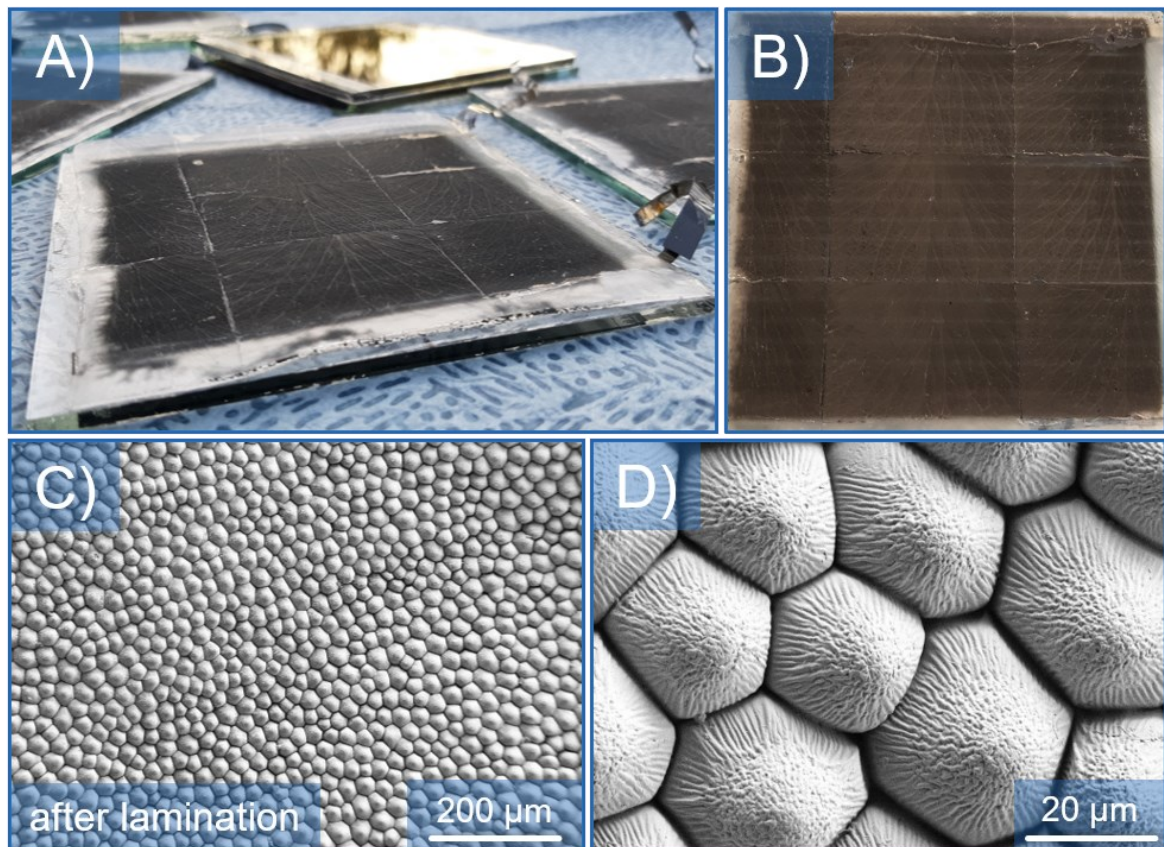


**Fig. 8.6:** Planar and rose petal textured PMMA laminated onto CIGS solar modules. A) Photograph of several identical CIGS solar modules equipped with planar and rose petal textured PMMA, fabricated by hot-embossing with Ni mold insert BF10. B) Top-view photo of a CIGS module equipped with rose petal textured PMMA. C), D) SEM images of a hot-embossed PMMA rose petal replica after the lamination onto a CIGS solar module. Neither the epidermal microstructure nor the cuticular nanostructure was affected by the pressure at elevated temperatures during the lamination process. The SEM images in C) and D) were adapted with permission from the abovementioned contribution to *Solar Energy* [3], © 2020 Published by Elsevier Ltd on behalf of International Solar Energy Society.

reflectance spectra (see Fig. 8.2), as well as through IV- (see Table 8.2) and EQE-measurements (see Fig. 8.5 A), all experiments concerning CIGS mini-modules were focused only on PMMA light-harvesting layers. Large-area hot-embossed PMMA rose petal replicas (as well as planar reference foils and glass cover sheets) were bonded onto the 10 cm × 10 cm CIGS mini-modules via lamination using polyolefin foil (PO8110) and an SPI Laminator 240 (Spire Solar Inc., USA). At an elevated temperature of 140°C and under vacuum conditions (10 min at 10 mbar, then 20 min at 0.5 bar), a force is applied normally to the layer stack, resulting in a homogeneous and robust bonding over the entire area. Photographs of CIGS mini-modules with laminated rose petal textured PMMA cover layers can be found in Fig. 8.6 A) and B). Moreover, the SEM images depicted in Fig. 8.6 C) and D) clearly

show that the employed lamination process does not cause any degradation of the bioreplicated hierarchical surface structure. Next to PO, other possible PV-relevant bonding materials include – for example – polyvinyl butyral (PVB), ethylene-vinyl acetate (EVA), or thermoplastic polyurethane (TPU) [621, 622]. Regarding the specific example of a PMMA-glass-interface, it should be noted that (atmospheric-pressure-plasma-treated) PDMS has also been successfully utilized to achieve strong bonding between PMMA and glass [623].

In order to correct the measured currents for the decrease in irradiance at oblique incidence angles (due to the enlarged irradiated area for tilted modules), all measured photocurrents were divided by  $\cos(\text{AoI})$ . Furthermore, since the deployed CIGS solar modules exhibited slight variations in performance under STC in their pristine and uncoated state, comparability between individual modules was ensured by dividing the cosine-corrected current values by the  $I_{\text{SC}}$  value measured under STC for the respective module in its pristine/uncoated state. For three different cover layer configurations, the normalized and cosine-corrected  $I_{\text{SC}}$  values in dependence of the AoI are displayed in Fig. 8.5 B). Large-area rose petal textured PMMA replicas were directly laminated onto the transparent front electrode of CIGS modules, as well as onto the cover glass of glass-encapsulated devices. CIGS modules with a standard glass cover laminated directly onto the transparent front electrode of the devices were included as a reference configuration.

Both configurations equipped with rose petal textured PMMA on the front side exhibit an increased current generation compared to the glass encapsulated reference configuration. As prompted by the experimental findings for small-scale single solar cells, the upscaled PMMA light-harvesting layers lead to a noticeable gain in photocurrent under normal incidence of light and a much more drastic improvement for incidence angles above  $50^\circ$  (compared to a glass-covered module). These measurements show, for the first time, that upscaled replicas of natural rose petals can straightforwardly be integrated into finished and working solar modules by a simple lamination step onto their glass cover layers, and thereby induce the same performance-boosting effects that have been previously reported numerous times on the scale of single solar cells.

---

## 9 Outdoor Performance and Long-Term Stability of Hot-Embossed Rose Petal Replicas as PV Light-Harvesting Layers

---

After the development of an upscaling technique for enabling the fabrication of large-area polymeric replicas of plant surface structures, which was discussed in chapter 7, the previous chapter 8 showed that the resulting upscaled, hot-embossed rose petal replicas could be exploited for enhancing the PCE of PV devices through improved light-management, as well as for implementing self-cleaning properties for the mitigation of soiling losses. While the results discussed in chapter 8 were solely acquired under laboratory conditions, the following chapter 9 focuses on experimentally assessing the applicability of large-area, hot-embossed plant surface structure replicas as PV cover layers under realistic operating conditions. Section 9.1 is therefore concerned with monitoring the performance of CIGS and Si solar modules with and without rose petal textured PMMA cover layers in the field. Next to outdoor performance monitoring, several accelerated aging tests were conducted on hot-embossed rose petal replicas for evaluating the deterioration of their beneficial properties after long-term field use. The results of these durability tests are introduced in section 9.2.

Part of the results presented within chapter 9 were published in *Solar Energy* as a full research paper [3].

### 9.1 Outdoor Performance Monitoring of Rose Petal Textured PMMA on CIGS and Si Solar Modules

The opto-electrical properties measured under laboratory conditions (STC and beyond), which were discussed in section 8.3, provide universally comparable units of measure for the performance of PV devices with hot-embossed rose petal replicas as cover layers. However, these quantities – which are all derived from the (AoI-dependent) IV characteristics and  $\text{EQE}(\lambda)$ -spectra – can not straightforwardly be exploited for predicting the performance of rose petal textured PV devices under

outdoor operational conditions due to the large number of interdependent influencing factors related to the geographical, environmental, and climatic conditions at the installation site, as well as to module orientation and tilt. Since the relative performance enhancement in CIGS solar modules induced by polymeric replicas of the hierarchical rose petal surface structure increases with increasing AoI (see Fig. 8.5 B), it should be expected that rose petal textured PV cover layers might lead to relative gains in power output which even exceed the previously reported values for  $\Delta PCE$  (see section 8.3), especially under conditions with strongly diffuse irradiance or for suboptimal module tilt and orientation. Moreover, it might also be suspected that, contrary to the measurements under STC with controlled device temperature, the increased absorption induced by the textured light-harvesting layers could cause a rise in module temperature compared to a planar reference device under field conditions, an effect which would decrease the device efficiency and thereby counteract the performance gain caused by the increase in light in-coupling. Outdoor performance monitoring experiments were therefore conducted to quantitatively assess the influence of hot-embossed rose petal replicas on PV device performance under realistic operational conditions. To this end, an experimental setup was developed, enabling the simultaneous logging of the photocurrents generated by several solar modules with the help of two analog 4-channel data loggers (HOBO UX120-006M). The setup, mainly comprised of a cubic box with solar modules mounted to its flat surfaces, is photographically depicted in Fig. 9.1. For each of the monitored modules equipped with rose petal replicas as cover layers, a second pristine module of the same type was installed under identical tilt and orientation to determine relative gains in device performance. Based on the findings of chapter 8 that PMMA rose petal replicas, compared to ones made from FEP and PC foils, lead to the most pronounced increase in PV device performance, all the experiments described in chapter 9 were focused solely on PMMA light-harvesting layers for outdoor PV performance monitoring, whereas large-area PC and FEP rose petal replicas were not considered for testing in the field. Ohmic resistors ( $R = 10 \Omega$ ) were connected to the front and rear electrodes of each module. Since the voltage at these resistors is proportional to the respective module's photocurrent, this quantity was collected in 10 s intervals by the data loggers as a direct measure for the photogenerated current. All resistors, cables, and data loggers were stored inside the cube for protection against damage. Shading effects by buildings and vegetation (close to sunrise and sunset) were avoided by placing the performance monitoring setup on the roof of Light Technology Institute (LTI, KIT).



**Fig. 9.1:** Photograph of the setup developed for outdoor performance monitoring of PV modules with and without rose petal textured PMMA light-harvesting cover layers. The depicted modules were installed under  $30^\circ$  and  $90^\circ$  tilt towards the south, as well as under  $90^\circ$  tilt towards the east.

The coordinates (longitude, latitude) of the performance monitoring site were determined via Google Maps as  $49^\circ 0' 42.4''$  N,  $8^\circ 24' 46.6''$  E). Overall, performance tracking was continuously performed for nine months between August 2019 and May 2020. For this entire period, the solar modules were never manually cleaned in any way, including the devices used several times under different orientations and tilt angles.

The outdoor performance was monitored for  $10\text{ cm} \times 10\text{ cm}$  CIGS and Si solar modules. The CIGS modules, which were identical to the modules described in section 8.3 (depicted in Fig. 8.6), were equipped with rose petal textured PMMA cover layers by employing the lamination method with PO foil described in section 8.3. The CIGS reference modules were fabricated by laminating a planar glass cover layer (for protection against moisture) onto the respective pristine module (uppermost layer: transparent front contact), also using PO foil as a bonding material. By using a second (equivalent) lamination step with PO foil, the rose petal textured PMMA layers were then laminated onto such glass encapsulated devices in order to produce encapsulated modules with bioreplicated light-harvesting cover layers. The commercial Si modules, on the other hand, were encapsulated with a polymeric material by the manufacturer. Therefore, the Si modules did not need a glass cover layer as a moisture barrier. The rose petal textured PMMA layers were then glued onto this polymeric encapsulant by using UV-curing NOA68. All

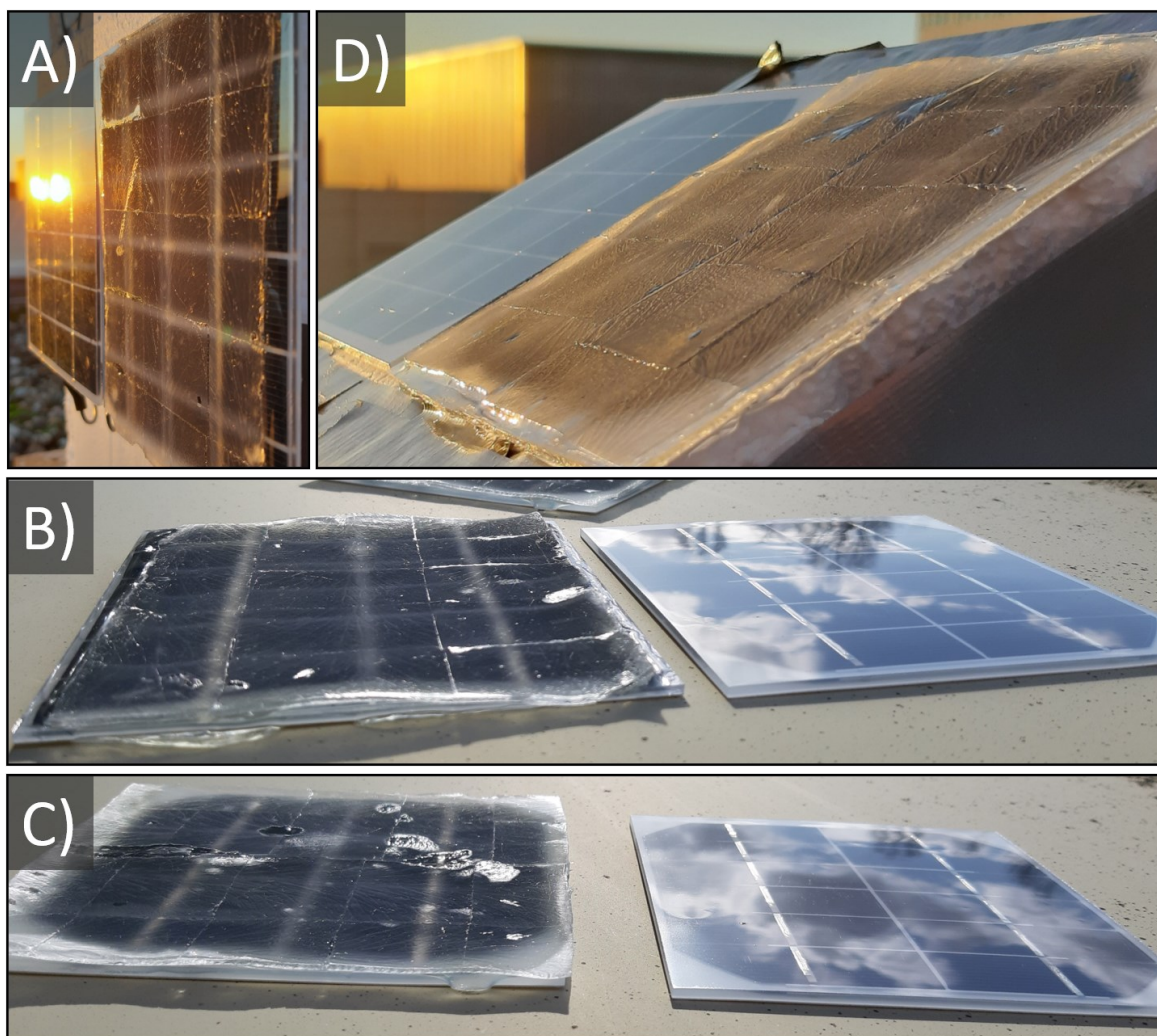


**Fig. 9.2:** Photographs of the commercial Si solar modules used in the outdoor performance monitoring experiments. A) Si module 1. B) Si module 2. C) Si module 3. D) Si module 4.

four of the analyzed Si modules are photographically depicted in Fig. 9.2, together with the respective pristine reference modules. As can be seen in these photographs, the addition of the rose petal textured layer induces a color change from blueish to black for the Si modules. Furthermore, specular reflection is strongly suppressed, leading to an anti-glare effect. Moreover, a (kind of) cloaking effect is induced by visually blurring the metallic contact fingers (or the interconnection lines of thin-film modules).

As discussed in section 8.3, the CIGS modules exhibited slight variations in performance in their pristine state. Similar to the normalization performed for the data shown in Fig. 8.5 B), all the photocurrents measured for the CIGS modules under outdoor operational conditions were divided by their STC photocurrent to assure comparability. By integrating these corrected photocurrent signals over a specific time interval, the total amount of extracted charge can be calculated for the

respective period. In contrast to the CIGS devices, the commercial Si modules (PCE  $\approx$  15%), in their pristine state, did not exhibit any noticeable variations in performance under STC, and therefore, a normalization of the measured photocurrents was unnecessary for the Si modules.

Measured photocurrent signals, together with the time-resolved relative gain and AoI are given in Fig. 9.3 A) and B) for the two consecutive days of Jan 24<sup>th</sup> and Jan 25<sup>th</sup> 2020 for the example of Si solar modules with a 90° tilt towards the south, and in Fig. 9.3 C) and D) for the two consecutive days of Feb 09<sup>th</sup> and Feb 10<sup>th</sup> 2020 for the same Si modules but with a 90° tilt towards the north. The time-resolved performance gain with a 10 s resolution was calculated as the ratio of the measured signals of a rose petal textured module and the respective reference device. The time-resolved AoI was calculated for the exact geographical location of the setup and calendrical date of the respective measurements by using

$$\text{AoI} = \arccos(\sin \alpha_S \cdot \cos \beta + \cos \alpha_S \cdot \sin \beta \cdot \cos(\gamma_S - \gamma)), \quad (98)$$

where  $\beta$  (here:  $\beta = 90^\circ$ ) describes the module tilt angle against the horizontal and  $\gamma$  (here:  $\gamma = 0^\circ$ ) its azimuthal orientation (south =  $0^\circ$ , east =  $-90^\circ$ ), while  $\alpha_S$  and  $\gamma_S$  denote the altitude and azimuth angles of the sun's position.  $\text{AoI} > 90^\circ$  means that the sun is behind the surface and no direct irradiance takes place. The time-dependent angles  $\alpha_S$  and  $\gamma_S$  describing the solar position were calculated via

$$\alpha_S = \arcsin(\cos \phi \cdot \cos \delta \cdot \cos \omega + \sin \phi \cdot \sin \delta), \quad (99)$$

and

$$\gamma_S = \text{sign}(\omega) \left| \arccos\left(\frac{\sin \alpha_S \sin \phi - \sin \delta}{\cos \alpha_S \cos \phi}\right) \right|, \quad (100)$$

with the hour angle  $\omega$ , the day of the year  $n$  ( $n = 1$ : Jan 1<sup>st</sup>), the solar declination  $\delta$ , and the local geographical latitude  $\phi$ . The solar declination was approximated via the widely used relation introduced by Cooper [624]

$$\delta = 23.45^\circ \cdot \sin\left(360 \cdot \frac{284+n}{365}\right). \quad (101)$$

More details about these calculations can, for example, be found in reference [625].

As should be expected, the data presented in Fig. 9.3 A) and B) indicates that relative performance gains for modules oriented southwards tend to be more significant around sunrise and sunset due to the large AoIs (of the direct component of the solar irradiance). The same general trend was also confirmed for CIGS modules (time-resolved signals for two exemplary days of measurement can

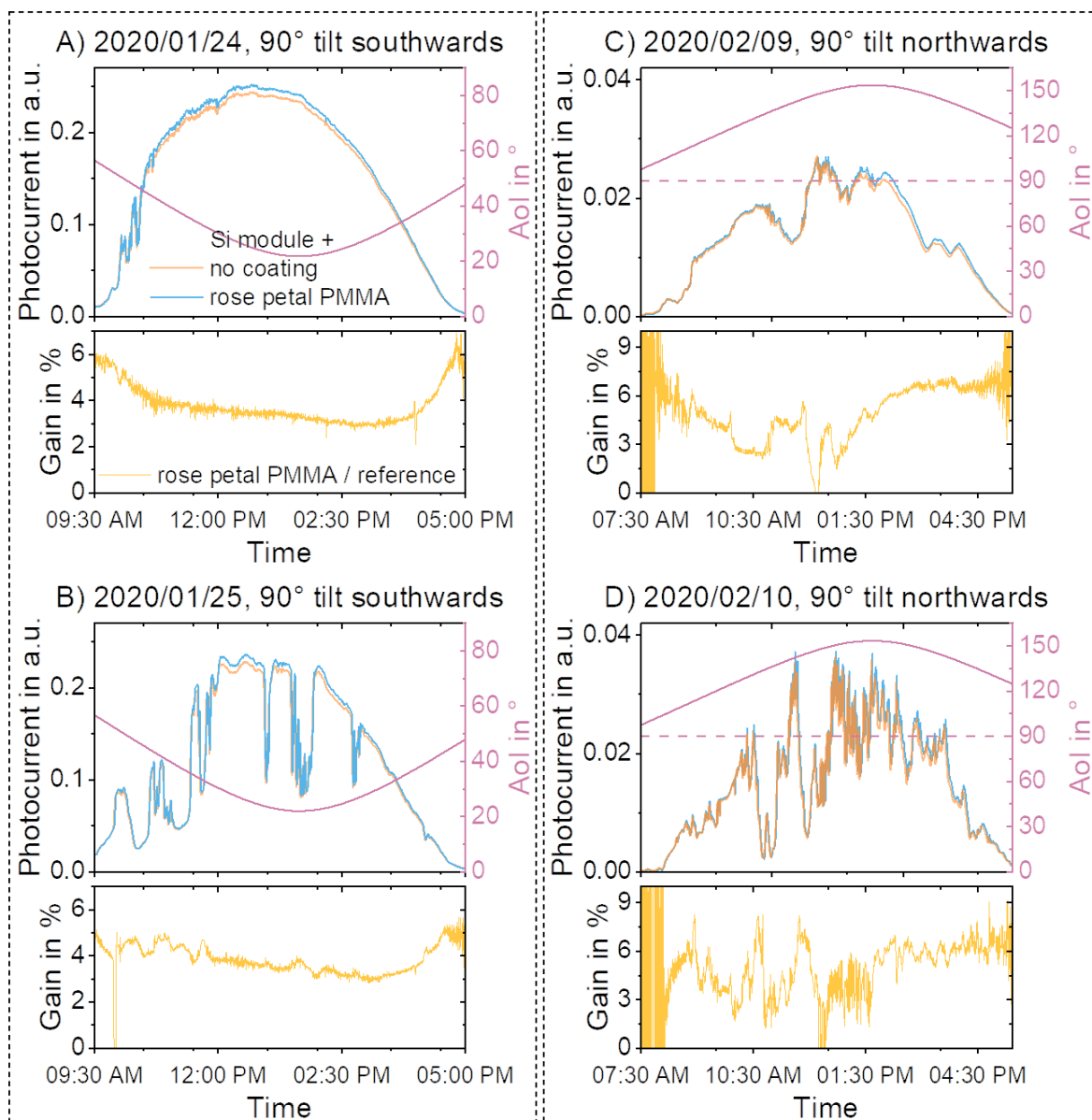


**Fig. 9.3:** Time-resolved photocurrent of a pristine Si module and one with a rose petal textured PMMA cover layer for A), B) two consecutive days in January 2020 and a 90° tilt (vertical installation) southwards. As well as for two consecutive days in February 2020 and a 90° tilt northwards. Besides the measured photocurrents, the time-resolved AoIs and performance gain are also displayed. The (relative) gains in generated electricity per day for these four exemplary days were A) 3.5%, B) 3.6%, C) 4.4%, and D) 4.8%.

be found in [3]). Si module 1 with a 90° tilt towards the north, as illustrated in Fig. 9.3 C) and D), exemplifies the scenario where no direct sunlight can reach the modules' surfaces over the entire day. Next to the configurations with 90° tilt towards south and north, solar modules were also mounted horizontally (tilt 0°), 30° tilted towards the south, as well as with a 90° tilt towards the north, east, and west.

For each day of measurement, the ratio of the total extracted charge with and without a rose petal textured PMMA cover layer was calculated, yielding a daily (relative) performance gain. For the CIGS modules, these daily gains are displayed in Fig. 9.4 A). For the Si solar modules, the respective daily gains are plotted in Fig. 9.4 B). In addition to these daily performance gains, total performance gains were also determined for the entire respective measurement periods for each of the solar modules and the various tilt angles and orientations considered. It is important to note that these total performance gains were not calculated by averaging the individual daily performance gains since the resulting quantity would not consider the large fluctuations of the daily generated power due to varying weather conditions. Therefore, total performance gains were calculated as the ratio of the total extracted charge for the module with rose petal textured PMMA and the respective reference module over the entire measurement period under constant installation conditions. For each measurement period shown in Fig. 9.4, the respective total performance gains are displayed as colored dashed lines. Furthermore, the gains in overall power output for each of the respective measurement intervals are also summarized in Table 9.1.

Concerning CIGS, two different glass-covered CIGS modules were equipped with hot-embossed PMMA rose petal replicas, and two further glass-covered CIGS modules were utilized as reference devices. Textured CIGS module 1 was mounted horizontally directly next to one of the reference devices, and their photocurrent was monitored from Aug 07<sup>th</sup> 2019 till Sep 17<sup>th</sup> 2019, yielding a total performance gain of 5.4% (these measurements were included in a *Solar Energy* publication [3]). For the period from Sep 19<sup>th</sup> 2019 till Jan 16<sup>th</sup> 2020 and with a 30° tilt southwards, which is close to the optimum installation conditions for the location of the setup, rose petal textured CIGS module 2 exhibited a power output increase of 4.7% compared to the first reference device and 4.4% compared to the second reference.

The overall highest total performance gain of 12.0% was found for rose petal textured Si module 3 for the period between Mar 17<sup>th</sup> 2020 and May 6<sup>th</sup> 2020 and a 90° tilt towards the south. The overall lowest total performance gain of 3.1%, on the other hand, was found measured for rose petal textured Si module 1, also for a 90° tilt towards the south, measured over the (relatively short) period from Mar 04<sup>th</sup> till Mar 17<sup>th</sup>. Over the same period, rose petal textured Si module 3 was mounted with a 90° tilt eastwards and exhibited another rather high total performance gain of 10.3%. Overall, rose petal textured Si module 3 exhibited exceptionally high gains

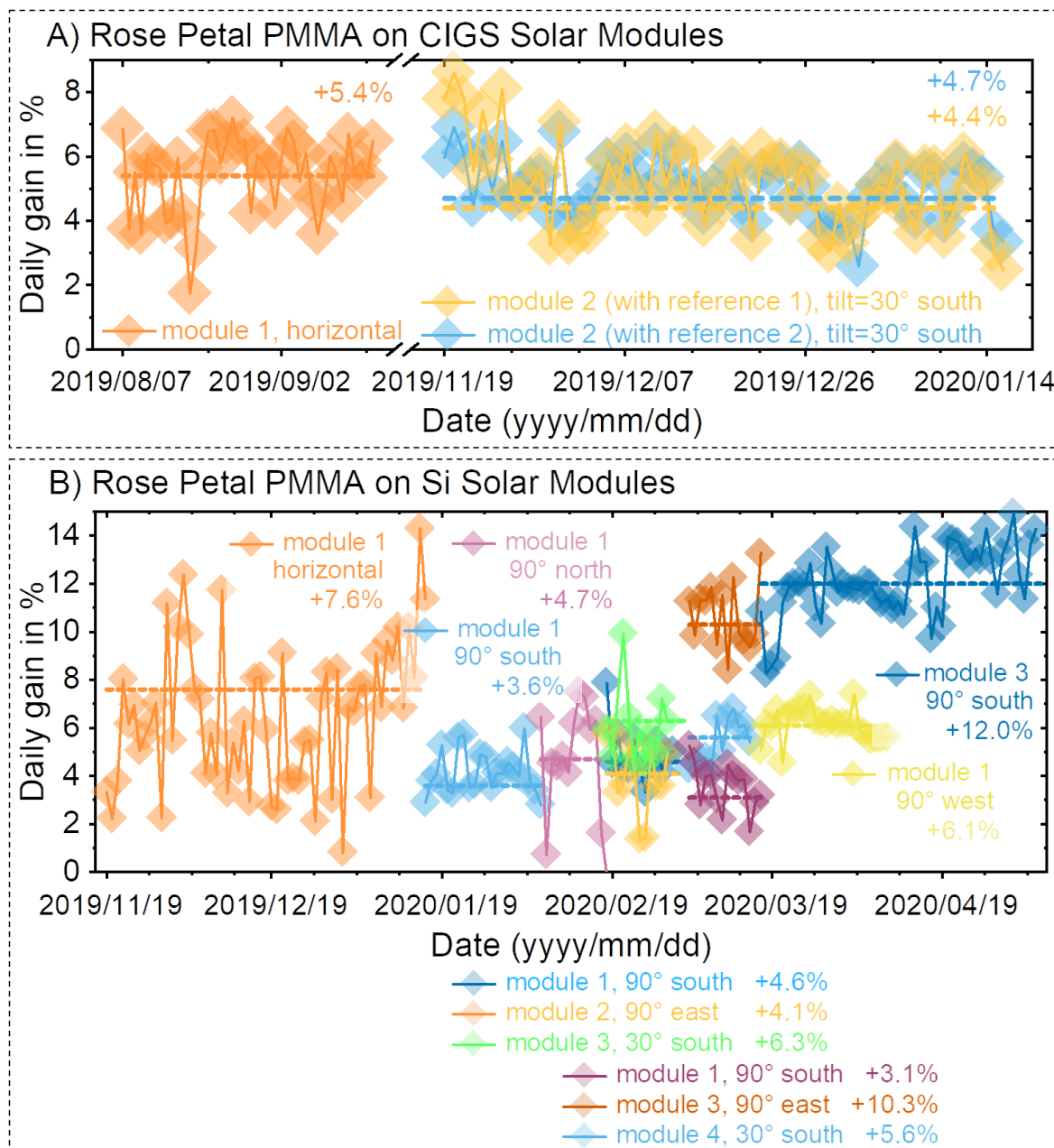


**Fig. 9.4:** Daily relative gain in device performance for A) CIGS and B) Si solar modules with and without rose petal textured PMMA cover layers under outdoor conditions and for different module orientations. Since CIGS module 2 was mounted next to two glass-covered reference modules, the relative daily gains for both references were determined. The daily gains for the horizontally placed CIGS modules have been previously included in the abovementioned contribution to *Solar Energy* [3].

in performance for all three installation conditions that were considered for this specific module. Next to the abovementioned 10.3% and 12.0% performance gains, rose petal textured Si module 3 was further found to outperform the respective reference module by 6.3% for a 30° tilt towards the south, measured between Feb 18<sup>th</sup> and Mar 01<sup>st</sup>.

**Table 9.1: Outdoor performance monitoring of CIGS and Si solar modules, performed in Karlsruhe, Germany.**

start	stop	module	orientation	gain
2019/08/07	2019/09/17	CIGS 1	0° –	+5.4%
2019/11/19	2020/01/16	“ 2 / 1	30° south	+4.4%
“	“	“ 2 / 2	30° south	+4.7%
“	“	Si 1	0° –	+7.6%
2020/01/16	2020/02/06	“ 1	90° south	+3.6%
2020/02/06	2020/02/18	“ 1	90° north	+4.7%
2020/02/18	2020/03/01	“ 1	90° south	+4.6%
“	“	“ 2	90° east	+4.1%
“	“	“ 3	30° south	+6.3%
2020/03/04	2020/03/17	“ 1	90° south	+3.1%
“	“	“ 3	90° east	+10.3%
“	“	“ 4	30° south	+5.6%
2020/03/17	2020/04/09	“ 1	90° west	+6.1%
“	2020/05/06	“ 3	90° south	+12.0%

For the particular case where no direct solar irradiation can reach the PV devices, due to a 90° tilt towards the north, an overall gain in power output of 4.7% was determined for rose petal textured Si module 1 from Feb 06<sup>th</sup> till Feb 18<sup>th</sup> 2020 (the measured photocurrent signals for two days from this period are depicted in Fig. 9.3 C) and D).

Rose petal textured Si modules 2 and 4 were both only used for a single measurement period. Si module 2 was mounted 90° tilted eastwards from Feb 18<sup>th</sup> till Mar 01<sup>st</sup> and exhibited a 4.1% gain in power output relative to a pristine device. Si module 4, on the other hand, was used from Mar 04<sup>th</sup> till Mar 17<sup>th</sup> under a 30° tilt towards the south, resulting in a 5.6% increase in power output.

Based on the outdoor performance monitoring data presented herein, the general conclusion can be drawn that the hot-embossed PMMA rose petal replicas on CIGS and Si solar modules were able to endure the outdoor conditions in Karlsruhe over several months without any delamination or damaging of the hierarchical surface structure of the light-harvesting layers taking place. To assess the extent of soiling and abrasive structural damage on the textured PMMA layers at the installation site, a PMMA rose petal replica was exposed to the local outdoor conditions under

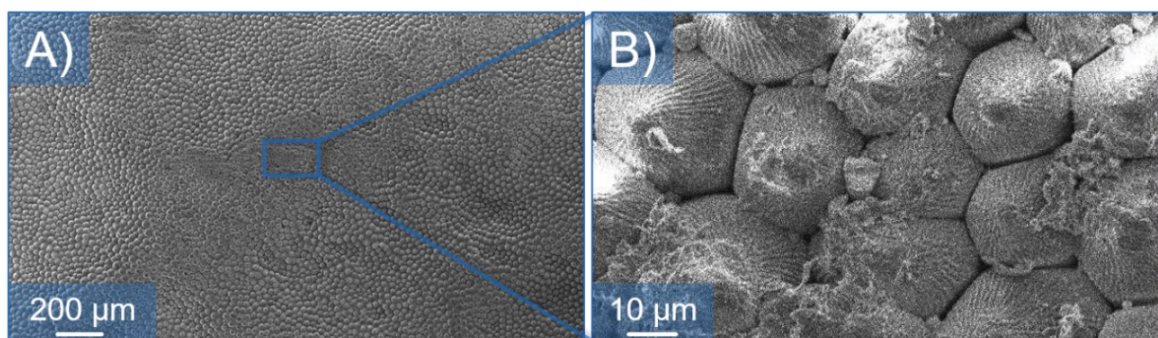


**Fig. 9.5:** SEM micrographs of rose petal textured PMMA after six months (Nov 2019 - May 2020) of continuous exposure to the outdoor conditions in Karlsruhe (Germany) under a 30° tilt towards the south. The densely packed microcone array (A) and the micro- and nanotextural features of the epidermal cell replicas (B) are still intact, but agglomerations of tiny dust particles are spread over the entire replica surface.

a 30° tilt southwards for the entire six-month period between Nov 2019 - May 2020. SEM micrographs, examples of which are displayed in Fig. 9.5, were then acquired for the uncleaned rose petal replica. It was found that the hierarchical surface structure exhibited no abrasive damage at all. Concerning soiling, however, the SEM evaluation showed some accumulation of dust particles with diameters  $< 10 \mu\text{m}$  over the entire sample surface. It was found that, with the help of a water-based high-pressure cleaner, these dust particles could be entirely removed without damaging the hierarchical surface structure (see also section 9.2).

To further analyze the conditions under which high gains in power output can be achieved, for each day of measurement, the power output was deconstructed into the relative contributions from the various AoIs appearing over each respective day. The results of such calculations for rose petal textured Si module 3 are given in Fig. 9.6. For  $\text{AoI} \leq 90^\circ$ , a  $1^\circ$  resolution was chosen for generating the bar charts in Fig. 9.6. All scenarios with an  $\text{AoI} > 90^\circ$  (only diffuse irradiance) were added up and displayed at a value of  $\text{AoI} = 91^\circ$ . Analogous plots for rose petal textured Si module 1 are given in Fig. S3. Together with the AoI-dependent opto-electrical properties measured (for CIGS modules) under laboratory conditions and reported in section 8.3, the following main conclusion can be deduced. Overall, the most significant gains were found for module orientations which expose the PV devices to direct sunlight under oblique incidence angles above  $40^\circ$  for a preferably extended period. Moreover, for installation conditions where most of the power is generated from diffuse solar irradiance, performance gains tend to be more moderate. As should be expected based on the AoI-dependent properties measured for CIGS devices with rose petal textured and planar cover layers under laboratory conditions (reflectance spectra shown in Fig. 8.2, photocurrent measurements

summarized in Fig. 8.5 B), the lowest relative gains in power output were found for installation conditions where most of the power was generated from direct sunlight with  $\text{AoI} < 40^\circ$ . These findings indicated that the increase in energy yield induced by polymeric rose petal replicas should be especially pronounced in situations where PV modules can not be installed under optimum tilt and/or orientation conditions, as is the case for building-integrated and building-attached/applied PV (BIPV/BAPV) [626].

It is important to note that, due to the vast number of parameters that impact PV device performance in the field, direct quantitative comparisons of the measured PV performance gains under outdoor conditions presented herein to similar studies from the scientific literature should generally be treated with caution. However, it is still relevant to provide some generic numbers from the literature for roughly comparing the performance gains measured for rose petal textured PMMA light-harvesting layers on CIGS and Si solar modules with other relevant antireflection concepts. Currently, concerning commercially available antireflective coatings for PV, the industry relies primarily on cover glasses coated with thin-film antireflective coatings based on porous silica. The current market leader DSM Advanced Solar (Netherlands), has, as of 2020, provided porous-silica-based thin-film antireflective coatings for  $\approx 250$  mio. panels ( $70 \text{ GW}_p$  of installed capacity). Their most widely-used coating leads to a long-term gain in power output of  $\approx 3\%$  for optimally oriented solar panels (while causing a blueish color). Their top product for improved antireflection (causing no unwanted blueish coloration) reaches a long-term gain in power output of  $\approx 4\%$  for optimally oriented panels [147]. As introduced in chapter 2 of this thesis, due to the limited angular and spectral tolerance of such interference-based antireflective coatings, approaches based on surface micro- and nanostructures should, in principle, be able to induce higher gains in energy yield through their broadband and omnidirectional antireflection properties. In 2017, Huh *et al.* indeed demonstrated an increase in monthly generated electricity of  $7.24\% - 7.88\%$  for  $1644 \text{ mm} \times 955 \text{ mm}$  (Si) solar modules equipped with a moth-eye-mimicking ( $\text{SiO}_x$ -based) antireflective patterned protective glass and installed with a tilt angle of  $35^\circ$  southwards on a rooftop located at  $37^\circ 58' \text{ N}, 127^\circ 23' \text{ E}$  [627]. Moreover, Nishioka *et al.* recently studied the long-term reliability of CIGS modules (similar findings for Si modules) with a moth-eye-mimicking cover glass for 3.5 years in Miyazaki (Japan), resulting in a  $3.9\%$  increase in collected energy for the structured modules [628]. Since nanostructured antireflective layers based on the moth-eye-principle, as discussed in chapter 2, inherently exhibit light-trapping capabilities inferior to those found for microstructured surfaces, it can be suspected that

polymeric rose petal light-harvesting layers should, in principle, be able to induce similar or even higher long-term gains in PV energy yield compared to moth-eye-like subwavelength structures. In the future, similar performance monitoring experiments for solar modules covered with hot-embossed (PMMA) rose petal replicas should be extended over longer periods to provide a reliable measure for the long-term average of the energy yield increase under optimum tilt and orientation. Furthermore, similar experiments should also be conducted for other latitudes and climatic conditions. Besides PMMA replicas, other polymers (such as PC) should also be considered for outdoor performance monitoring experiments. More detailed analyses concerning dust accumulation on polymeric rose petal replicas and adequate strategies for soiling mitigation should further be conducted.

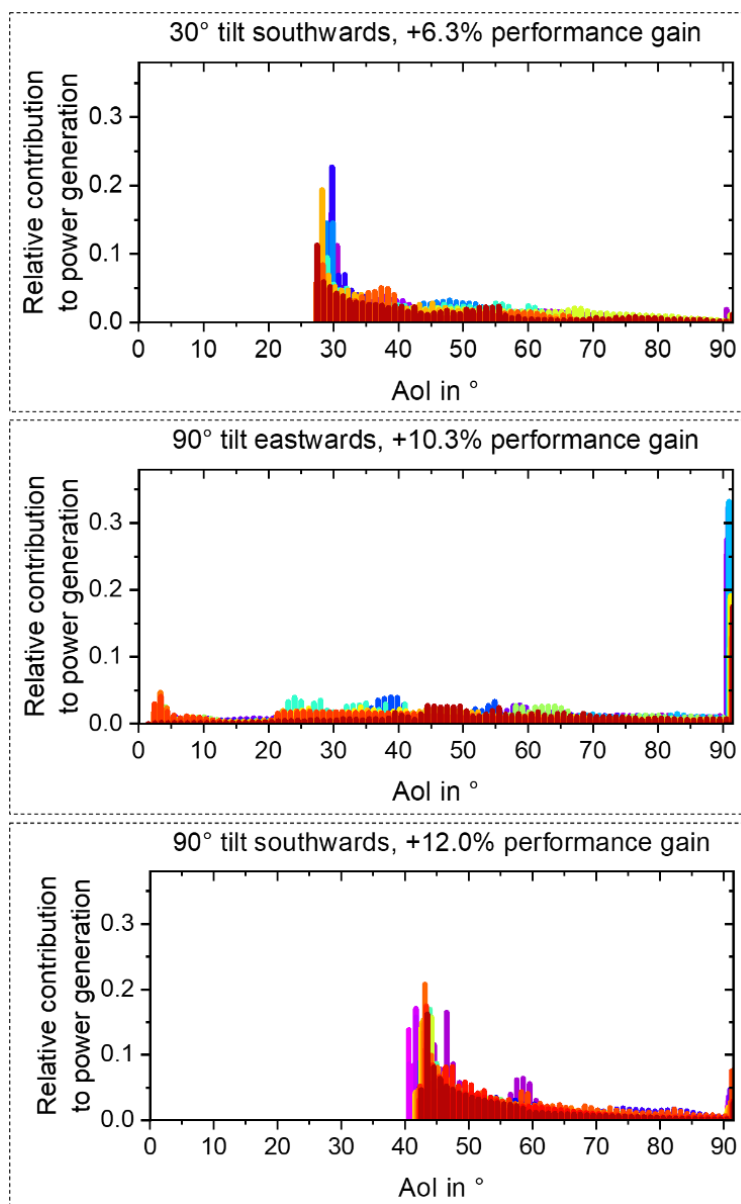


**Fig. 9.6:** Relative contributions of different AoIs (of the direct sunlight component) to the total generated power for rose petal textured Si module 3 at each day of performance monitoring. Each day is displayed in a different color. The summarized relative contributions of AoI > 90° (only diffuse irradiance) were included in these plots at a value of AoI = 91°.

## 9.2 Long-Term Durability of Rose Petal Textured PMMA Light-Harvesting Layers

Although the nine months of outdoor performance monitoring discussed in section 9.1 can be considered as a proof of principle for the applicability of hot-embossed PMMA rose petal replicas for PV energy production, their durability over the typical (guaranteed) lifetime of commercial PV modules of typically (at least) 25 years by far exceeds the duration of the outdoor experiments discussed above. Therefore, accelerated aging tests need to be performed to further substantiate the stability of the PMMA-glass bonding and the hierarchical surface structure of the PMMA layer within a reasonable timeframe. It should be noted that the long-term applicability of PMMA for concentrator-PV lenses has already been demonstrated [629].

A variety of accelerated aging tests are necessary to proof the long-term stability of PMMA rose petal replicas applied as PV light-harvesting layers. The following (climatic) aging tests were performed:

**Damp-heat test ‘DH-1000’ (as specified in IEC 61215 10.13):** 1000 h at an elevated temperature of 85°C and relative humidity of 85%. DH-1000 testing was executed at LTI.

**Temperature cycle test ‘TC-200’ (as specified in IEC 61215 10.11):** 200 temperature cycles from –40°C to 85°C and back are executed with an aging chamber. The TC-200 routine was carried out at the Material Research Center for Energy Systems (MZE, KIT) with the kind help of PD Dr. Alexander Colsmann and Dr. Holger Röhm.

**UV preconditioning (as specified in IEC 61215 10.10):** For the pretreatment with UV light, a total dose of 15 kWh/m<sup>2</sup> for the spectral range between 280 nm and 385 nm is defined as the target. For the UV-B portion of the spectrum (280 nm – 320 nm), the total dose should reach a minimum of 5 kWh/m<sup>2</sup>. During irradiation, the sample temperature is fixed at 60°C. Further, the lamp power (UV-A + UV-B) should not exceed 250 W/m<sup>2</sup>. UV-preconditioning was performed at ZSW with the kind help of Dr. Oliver Kiowski and Dr. Ruben Hünig.

**Long-term UV exposure (as specified in IEC 61345 / IEC 61646 10.10):** For long-term UV exposure, the target dose for UV-B is set at 7.5 kWh/m<sup>2</sup> and for UV-A radiation, a minimum dose of 15 kWh/m<sup>2</sup>. Module temperature of 60°C. The UV-B target was reached after ≈ 922 h of UV exposure, leading to a total UV-A dose of

106.4 kWh/m<sup>2</sup>. Long-term UV exposure testing was performed at ZSW with the kind help of Dr. Oliver Kiowski and Dr. Ruben Hünig.

Next to these climatic aging procedures, abrasion tests were also performed for pristine as well as aged samples for testing the structural stability under extreme conditions such as sand storms. The following testing schemes, both performed at LTI, were used:

**Sandblasting (as specified in UN-R112 Annex 6 – Appendix 2):** A continuous and moving stream of a sand-water-mix following the recipe of 25 g of standardized sand per liter of water is shot at the samples from a 1.3 mm nozzle with a pressure of 6 bar. This treatment is usually performed for simulating the long-term abrasive damages that car headlights need to endure during years of driving. For PV devices, this procedure might lead to overestimating the abrasive damaging that PV panels typically need to endure over their lifetimes.

**Sand tickling (as specified in DIN 52348):** To emulate severe abrasive damaging through sand storms, a total of 3 kg of (standardized) sand are falling from a height of 1.65 m guided by a pipe of standardized diameter and equipped with two integrated sieves onto a 45°-tilted test surface. Similar to the sandblasting test discussed above, sand tickling was originally not developed with PV in mind and can be considered excessively destructive compared to PV abrasive damaging under typical operating conditions. In addition to this standard procedure, other surface tilt angles were also tested. Furthermore, two types of sand were used for sand tickling, namely quartz sand with sharply-edged, irregularly shaped grains and Sahara desert sand with rather small and spherical grains. Both types of sand were used in quantities of even up to 10 kg per sample.

After these abrasion procedures, test surfaces are heavily soiled with residual sand grains. Next to characterizing the reflection properties of such soiled samples, several straightforward cleaning methods, including pressurized air, water, or an ultrasonic bath treatment, were employed both to assess the efficacy of these cleaning strategies and to characterize the deterioration of the antireflective effect through structural damages isolated from the impact of dust contamination after abrasion testing.

The key conclusions from these tests can be summarized as follows:

- The bonding of rose petal textured PMMA cover layers to the module cover glass (via the lamination process described in section 8.3) endured all the aging procedures (long-term UV, UV preconditioning + DH-1000, UV preconditioning + TC-200) without showing any signs of deterioration.

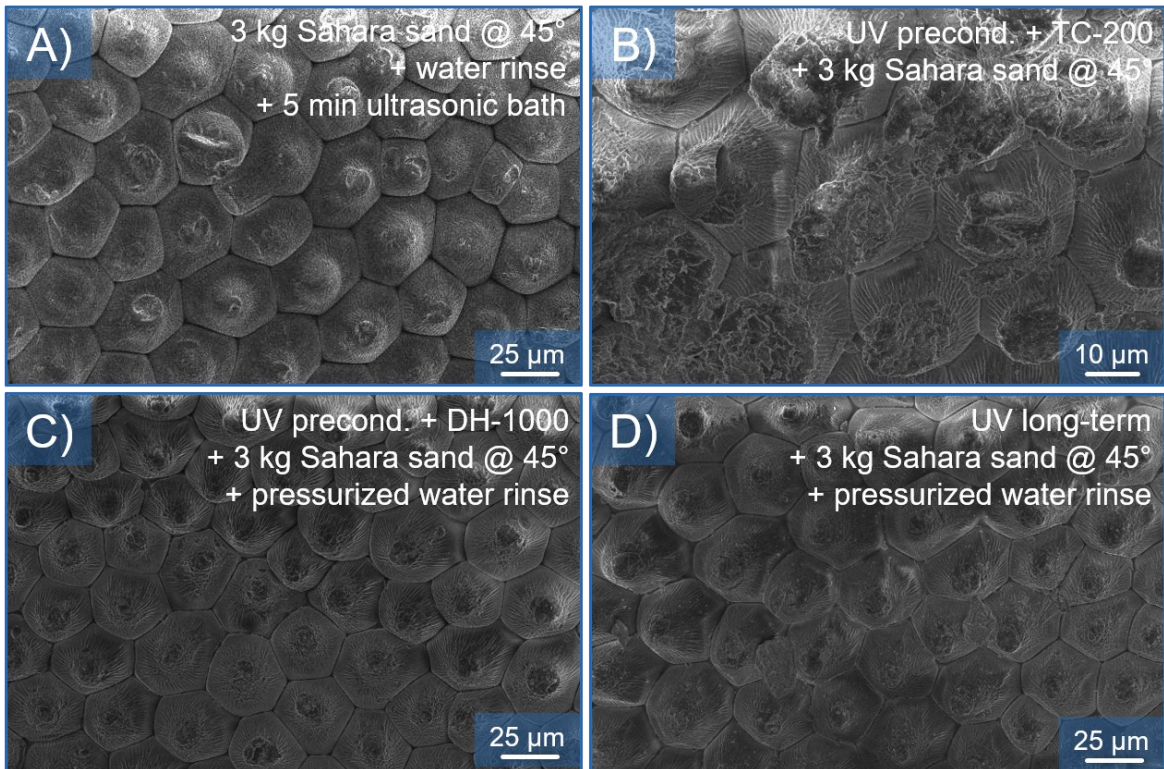


**Fig. 9.7:** SEM micrographs of (cleaned) rose petal textured PMMA after various accelerated aging and abrasion tests.

- A minor yellowing of the PMMA material was detected only after long-term UV exposure. Contrary, UV preconditioning + DH-1000 and UV preconditioning + TC-200 left the optical properties of the textured PMMA layers almost unchanged.
- Sand tickling with 3 kg of Sahara desert sand under 45° tilt did not cause pronounced structural damaging to the PMMA rose petal replicas, not even if the structured layers endured various accelerated aging routines prior to abrasion testing (see Fig. 9.7). Not even sand tickling with 10 kg of Sahara desert sand under 45° could cause significant damage to the PMMA rose petal replicas (see Fig. 9.8).
- For tilt angles below 45°, the structural damage caused by the falling sand decreases, and more and more sand accumulates on the surface (in case there is no wind to remove parts of the dust). For tilt angles above 45°, the structural damage caused by the falling sand was also decreased, but in this case, more and more sand just falls off the tilted surface.
- Replacing Sahara desert sand with sharp-edged quartz sand in the sand tickling routine lead to increased damaging of the aged and PMMA replicas, with 45° tilted surfaces treated with 10 kg quartz sand exhibiting a significant polishing of the epidermal micro-cones' tips, as can be seen in Fig. 9.8.

- After between five and fifteen minutes of ultrasonic bath-soaking almost no residual dust particles of Sahara desert sand can be found on the PMMA rose petal replica under the SEM. Even at 45° tilt, where the most structural damage is expected, sand tickling with Sahara desert sand leaves the microstructured PMMA almost unharmed, which is shown by the SEM images in Fig. 9.7 and Fig. 9.8
- The influence of these various accelerated aging and abrasion tests on the antireflective properties of rose petal textured PMMA was measured for normal and oblique light incidence. The results are summarized in Fig. 9.9. Except for the case of long-term UV exposure followed by the sandblasting test, the pristine reflectance spectra before aging and abrasion testing could almost be fully restored simply by rinsing the aged and soiled replicas thoroughly with (pressurized) water.
- Generally, sandblasting and sand tickling were both found to cause more abrasive damage to the microstructure after long-term exposure to UV light. The abrasive damage was assessed with SEM scans after removing residual dust from aged surfaces. This observation is illustrated by the SEM micrographs given in Fig. 9.10.

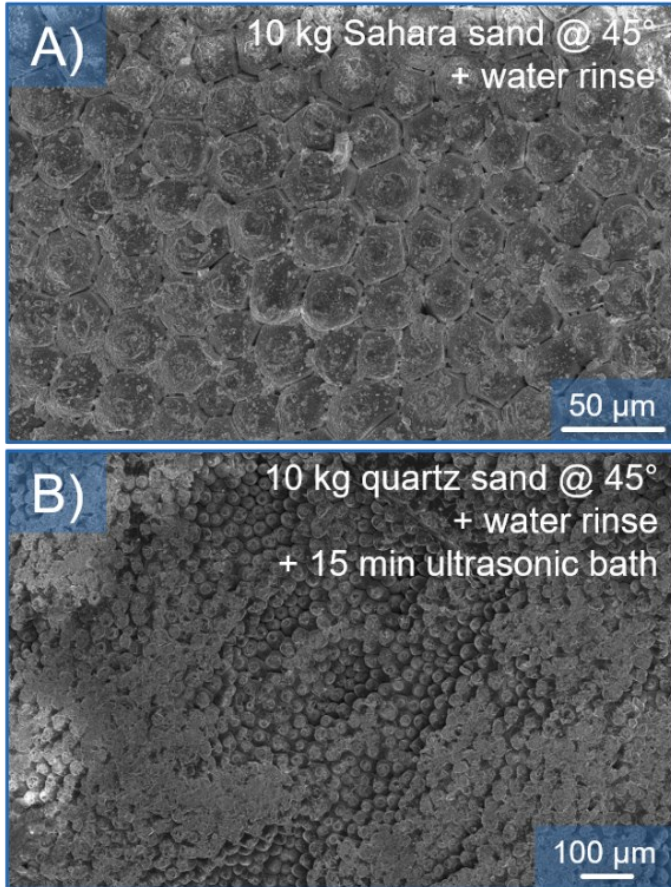


**Fig. 9.8:** SEM micrographs of rose petal textured PMMA after sand tickling with 10 kg of A) Sahara desert sand as well as B) quartz sand.

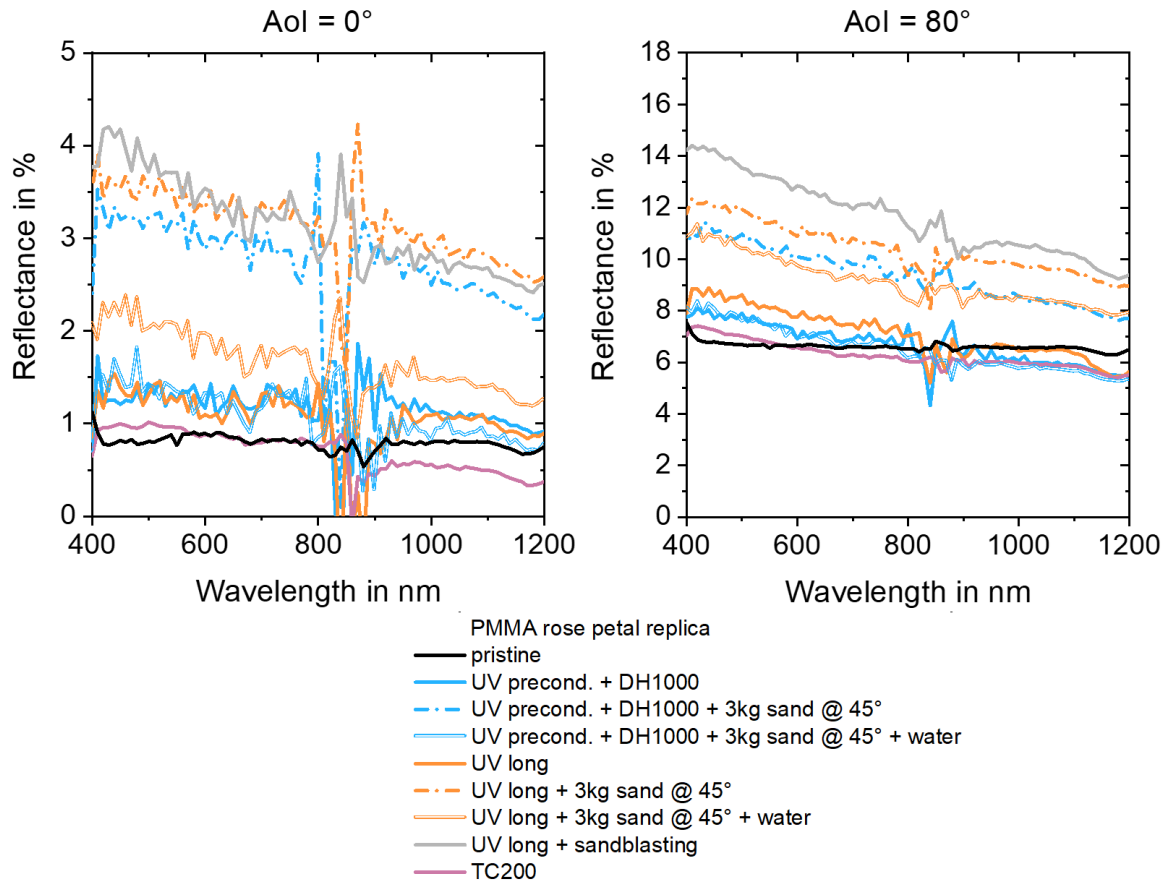


**Fig. 9.9:** Measured (surface) reflectance spectra of rose petal textured PMMA after various durability tests under normal and oblique light incidence under 80°. The rear sides of the replicas were blackened using acrylic paint such that only the surface reflectance contributed to the measured signal.

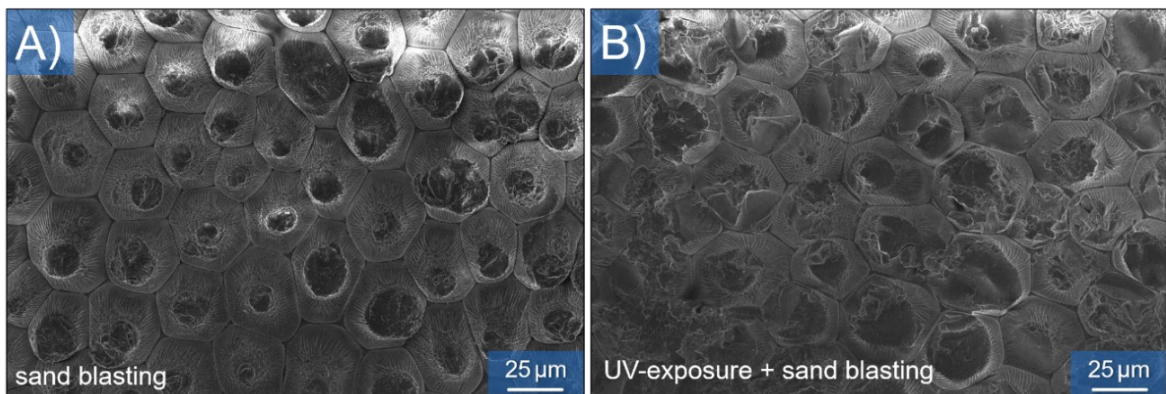


**Fig. 9.10:** SEM micrographs of rose petal textured PMMA after an abrasive sandblasting test as specified in UN-R112 Annex 6 – Appendix 2. The sample in A) was blasted with sand without any prior treatment, while the sample in B) endured an exposure to UV radiation prior to sandblasting. The SEM images show that PMMA rose petal replicas become more susceptible to abrasive damaging after long-term exposure to UV light.

Overall, hot-embossed PMMA rose petal replicas are quite robust against abrasive damage, even after aging via DH, TC, or UV exposure. The bonding of the PMMA replicas to the module cover glasses remained unharmed by the climatic aging routines considered herein, indicating that such cover layer configurations could possibly even withstand a continuous outdoor operation for several years without significant deterioration of the light-harvesting properties.

---

## 10 Polarized Light Pollution of Solar Panels – Are Polarotactic Insects Maladaptively Attracted by Microtextured Light-Harvesting Layers?

---

As discussed in chapter 2, the front surfaces of solar panels should facilitate various properties in order to maximize device performance. These include, for example, the two rather obvious qualities of antireflection and self-cleaning, as well as more ‘exotic’ traits such as (passive) radiative cooling. Although numerous such multifunctional PV cover layers have been fabricated and characterized over the previous decades, the possibility/probability of environmental repercussions caused by the mass deployment of PV technology in various ecosystems all around the globe has rarely been discussed. Therefore, the following chapter focuses on studying the impact of rose petal replicated PV cover layers on the ecology and conservation of polarotactic insect species through an effect often termed ‘polarized light pollution’ (PLP), which is introduced in detail in section 10.1 [630]. In collaboration with Prof. Dr. Gábor Horváth, Dr. Ádám Pereszlényi, Dr. Ádám Egri, and Dr. György Kriska from the ELTE Eötvös Loránd University in Budapest (Hungary), the maladaptive attractiveness of rose petal textured PMMA layers to polarotactic mayflies and horseflies was studied experimentally in the field with a focus on two specific polarotactic aquatic insect taxa, namely mayflies (*Ephemera danica*) and horseflies (Diptera: Tabanidae), which function as indicators of PLP [631]. The details of these experimental procedures, as well as the respective outcomes, are discussed in section 10.2. Subsequently, the results of these field studies are interpreted on the basis of the reflection-polarization properties of the three deployed test surfaces, which were obtained and studied based on imaging polarimetric measurements (see section 10.3) as well as through ray-tracing simulations (see section 10.4).

The results presented in this chapter were published as full research papers in *PLOS ONE* [1] and in *Parasitology Research* [2].

## 10.1 Introduction to Polarized Light Pollution

Many polarotactic insect species use the characteristic farfield patterns in the angle and degree of (linear) polarization – denoted as AoP and DoLP, respectively – of surface-reflected light for object identification [632–637]. Calm water surfaces, for example, reflect (nearly) horizontally polarized light (AoP = 0°) with a DoLP that (assuming unpolarized incident light) spans the entire possible range between fully unpolarized (for a normal/perpendicular viewing direction) and full linear polarization (if viewed under the Brewster angle). As a direct consequence of the Fresnel equations (17) and (18), such reflection-polarization characteristics are typical for (perfectly) planar surfaces. Besides calm water surfaces, other natural surfaces are usually not smooth and do not exhibit this specific kind of reflection-polarization pattern. Many aquatic insects (orders: Coleoptera, Collembola, Diptera, Ephemeroptera, Hemiptera, Hymenoptera, Lepidoptera, Mecoptera, Megaloptera, Neuroptera, Odonata, Plecoptera, Trichoptera) have therefore evolved to utilize such a visual cue to identify bodies of water by detecting the (partial) horizontal polarization of surface-reflected daylight [633, 634]. Various artificial surfaces such as asphalt roads [630–634, 638], dark car paints [639], or the glass or polymer covers of PV panels [640, 641], have been found to disruptively affect the behavior of polarization-sensitive insects by inducing a maladaptive attraction, which can be especially dangerous for populations of water-seeking polarotactic aquatic insects like mayflies, dragonflies, stoneflies, or caddisflies, if a respective insect either can not escape the visual stimulus of horizontally polarized light anymore (polarization trap) or if the egg-batches of these insects are laid, for example, onto PV modules, where they irredeemably perish due to dehydration [634]. For mayflies and horseflies, for example, G. Kriska *et al.* reported that surfaces that both show a DoLP > 15% and a polarization direction which only deviates from the horizontal by  $\pm 10\%$ , leads to a misdetection as a water surface [631]. It is important to note that this kind of erroneous interpretation of the reflected light polarization properties of artificial human-made objects is not restricted to horizontally placed surfaces (like a PV panel laying flat on the ground) but can also occur for tilted or even fully vertical surfaces [2, 642]. In 2009, G. Horváth *et al.* introduced the term ‘polarized light pollution’ (PLP) to describe this specific type of ecological photopollution [630]. In the same contribution, the authors identify PV panels as a possible source of PLP (schematically illustrated in Fig. 10.1). The next year, Horváth *et al.* conducted the first experiments aimed at reducing the maladaptive attractiveness of PV panels to polarotactic insects by

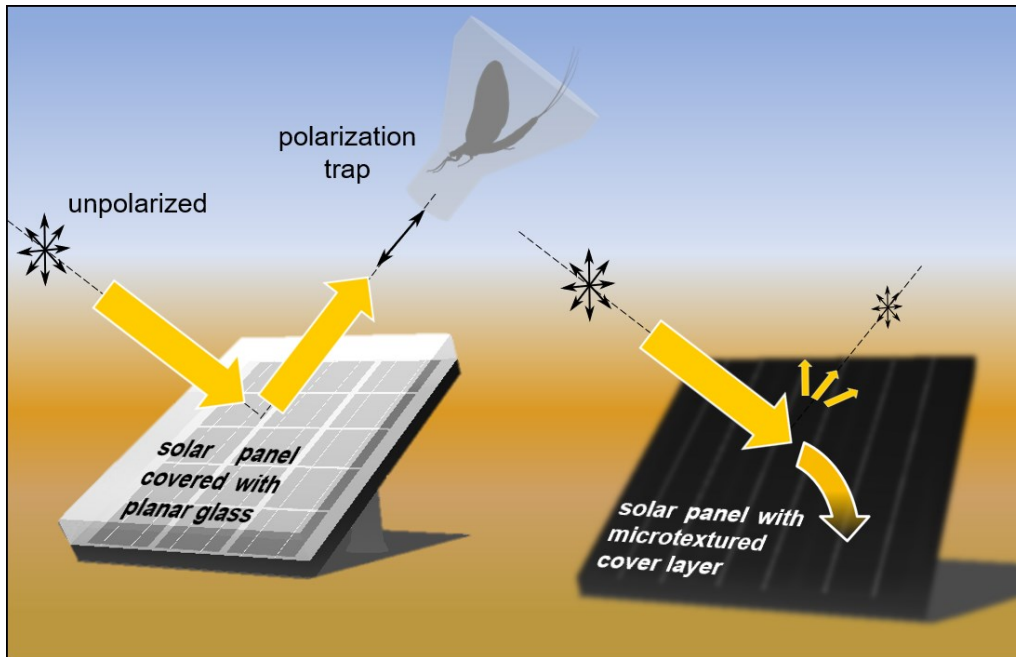


**Fig. 10.1:** Schematic illustration highlighting that PV modules equipped with a planar cover layer act as polarization traps for polarotactic insects if the panel-reflected light is (partially or completely) horizontally polarized, whereas an appropriate surface (micro-) structure of the cover layer not only improves sunlight-harvesting but simultaneously also strongly reduces PLP.

painting a non-polarizing white grid pattern on the panels' front surfaces [640]. The additional grid pattern, however, causes an additional shaded active area of 1% – 5%, depending on the density and width of the grid lines. Similar values have recently been reported by Black and Robertson [643]. It is worthy of note that this strategy towards reducing PLP basically mimics the unattractive appearance of spotted or striped animal coats to polarotactic insects [644–646]. A second approach towards minimizing the PLP caused by solar panels was demonstrated in 2016 by D. Száz *et al.* and is based on the reduction of the amount of surface-reflected light in general via applying an antireflective coating (more specifically a commercial solar glass equipped with a nanoporous silica single-layer antireflective coating produced the Danish company Sunarc Technology A/S) and therefore doesn't induce any additional shading (or other) losses [647]. It should be noted that, although such an antireflective glass was found to significantly decrease maladaptive attractiveness for polarotactic mayflies, horseflies, and non-biting midges under most weather conditions, mayflies actually preferred the matte solar glass under overcast sky conditions and therefore, while beneficial for some polarotactic insect species, such antireflective glass covers could still cause harm to some aquatic insect populations. The following sections 10.2-10.4 show that a consistent mitigation of PLP independent of polarotactic insect species and weather conditions can be achieved via microtextured front surfaces.

## 10.2 Field Experiments for Studying the Maladaptive Attractiveness of PV Cover Layers to Polarotactic Mayflies and Horseflies

To test the attractiveness of different PV cover layer configurations to *E. danica* mayflies, Prof. Dr. G. Horváth and Dr. Á. Pereszlényi performed field experiments in the North Hungarian Mountains close to the village of Dömörkapu at a bridge overarching the Bükkös Creek (47° 41' 45'' N, 18° 59' 50'' E) on six warm days between July 6<sup>th</sup> and July 13<sup>th</sup> 2019 (average maximum daily temperatures  $\approx 25 - 35^\circ\text{C}$ ) from 18:30 to 21:00 local summer time (UTC + 2h). The three test surfaces (each with dimensions of 50 cm  $\times$  50 cm) were deployed on an asphalt road running parallel to the creek (with a 1 m spacing between the test surfaces, a value optimal to simultaneously ensure the independence and the minimization of the side effect of the reactions to neighboring test surfaces [631, 632, 638–640, 647]). A photographic depiction of the experimental site can be found in Fig. 10.2 A). The experimental site was surrounded by trees so that the test surfaces were illuminated by the down-welling skylight and by light reflected from the green vegetation. The three test surfaces were

- a 50 cm  $\times$  50 cm hot-embossed PMMA rose petal replica, assembled from  $4 \times 5 = 20$  individual hot-embossed rose petal replicas (of dimensions 12.5 cm  $\times$  10.0 cm) fabricated with the help of Ni mold insert BF10 (following the approach described in chapter 7),
- another such 50 cm  $\times$  50 cm hot-embossed PMMA rose petal replica but covered with a 3 mm thick glass sheet, as well as
- a planar PMMA sheet of identical size as a reference surface, assembled from four individual quadratic elements with 25 cm side length.

For all these test surfaces, three layers of black acrylic paint (Decorlack 073, Marabu GmbH & Co. KG, Germany) were applied to their backsides in order to suppress the reflection of in-coupled light at the polymer-air interface at the rear side, thereby mimicking the appearance of highly absorbing PV modules. The order of the test surfaces was changed by cyclic permutation every 14 min (taking

## 10.2 Field Experiments for Studying the Maladaptive Attractiveness of PV Cover Layers to Polarotactic Mayflies and Horseflies

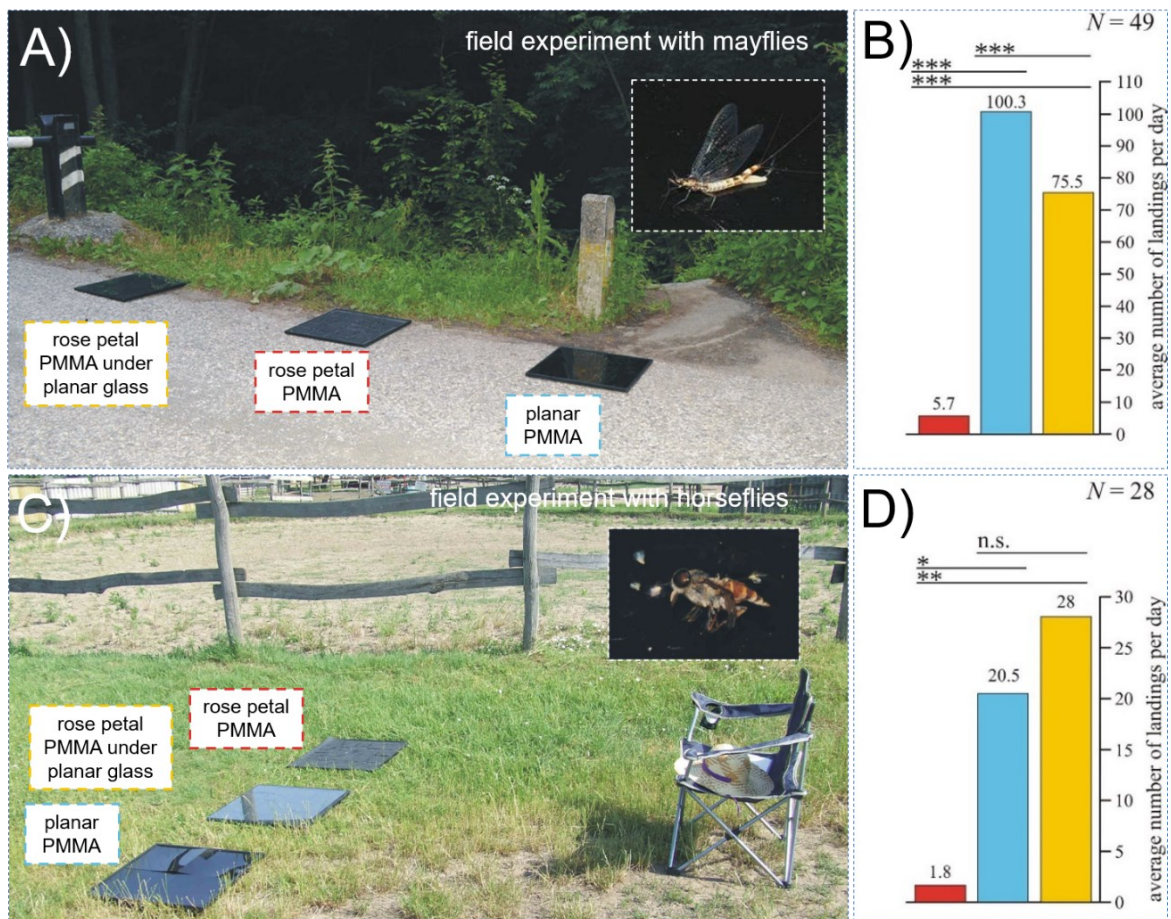


**Fig. 10.2:** Photographs of the experimental sites for the field experiments with mayflies and horseflies, together with the respective results, summarized as the average daily numbers of landings and including the results of the Wilcoxon signed-rank test. N: number of observations per category, n.s.: not significant with  $p > 0.05$ , \*:  $0.001 < p < 0.05$ , \*\*:  $0.0001 < p < 0.001$ , \*\*\*:  $p < 0.0001$ . Adapted with permission from the abovementioned *PLOS ONE* contribution [1], © 2020 Fritz *et al.*

no longer than 10 s for the switch and waiting 1 min so that the mayflies' behavior has fully recovered from any disruptive effects caused by humans moving around the test panels). A more detailed description of the field study with mayflies can be found in the aforementioned *PLOS ONE* contribution [1].

Similar to the field experiments with mayflies, on four sunny and warm days (again, the average maximum daily temperatures were  $\approx 25 - 35^\circ\text{C}$ ) in June of 2019 on a Hungarian horse farm in Szokolya ( $47^\circ 52' \text{N}$ ,  $19^\circ 00' \text{E}$ ), G. Horváth *et al.* also conducted a similar study with a focus on horseflies. The experimental site for the field experiments with horseflies is depicted in Fig. 10.2 C). The exact same three test surfaces as in the field experiments with mayflies were placed on the grassy ground along a straight line with a 50 cm spacing (optimum distance based on numerous previous field experiments with horseflies conducted by

G. Horváth *et al.* [631, 639, 640, 644–649]) between each other. In contrast to the field experiments with mayflies, here, all test surfaces were exposed to unobstructed direct sunlight. The order of the test surfaces was changed by cyclic permutation after every 29 min (taking no longer than 10 s for the switch and waiting 1 min so that the horseflies can fully recover their normal behavior). Since the horseflies were not captured, species-level identification of all the horseflies that landed on the test surfaces was practically impossible. Thus, in contrast to the field experiments with mayflies, the possibility of pseudoreplication due to repeated visits by some individuals could not be fully ruled out. Based on their experiences in previous field experiments at the identical location, G. Horváth *et al.* determined the following horsefly species to occur [648, 649]: *Tabanus tergustinus*, *T. bromius*, *T. bovinus*, *T. autumnalis*, *Atylotus fulvus*, *A. loewianus*, *A. rusticus*, and *Haematopota italica*. More experimental details concerning the field study with horseflies, as well as further information on the subsequent statistical data analysis (Friedman test with Kendall's *W* effect size and Wilcoxon signed-rank test with Bonferroni's correction), are provided in the [PLOS ONE](#) [1] (and [Parasitology Research](#) [2]) contribution mentioned above.

The results of the field studies with horseflies and mayflies are summarized in Fig. 10.2. It can be deduced from Fig. 10.2 that the planar PMMA reference layer was the most attractive to mayflies, while the attractiveness of the glass-covered PMMA rose petal replica was slightly lower, and the PMMA rose petal replica was practically unattractive to *Ephemera danica*, an observation that can be explained by considering that

- (i) *Ephemera danica* mayflies rely on the horizontal polarization of object-reflected light for water-detection [632, 638],
- (ii) the attractiveness of a respective surface to polarotactic mayflies increases with an increase in the degree of horizontal polarization of the reflected light received from the respective surface [631, 632], and
- (iii) through imaging polarimetric measurements, the degree of horizontal polarization of light reflected from the test surfaces was found to decrease following the order  
reference → glass-covered rose replica → rose replica.

In the field experiments with horseflies, a similar behavior was found, with the difference that no statistically significant difference in the attractiveness of the two configurations with planar top surfaces was found. A reason for this distinction between the two polarotactic insect species may be the different illumination

conditions during the field experiments (as well as species-dependent reactions to the planar test surfaces).

As previously mentioned in section 10.1, the PLP caused by a PV light-harvesting layer has so far only been studied for a commercial solar glass coated with a thin-film antireflective layer based on nanoporous silica [647]. Although effectively reducing the maladaptive attractiveness to horseflies, mayflies (studied at the identical experimental site as in the field experiment described herein) were significantly more attracted to the solar glass than a planar reference layer without antireflective coating. Therefore, the hierarchically textured PV cover layer investigated herein exhibits the novel property of fully alleviating PLP (at least) for the studied mayflies and horseflies. This result is further discussed in the following sections 10.3 and 10.4. Moreover, it should be mentioned that a detailed discussion of the dependence of this maladaptive attractiveness to horseflies on the surface tilt angle as well as on surface temperature (also using the 50 cm × 50 cm PMMA rose petal replica discussed in this chapter) can be found in the contribution to *Parasitology Research* mentioned above [2].

### 10.3 Imaging Polarimetric Measurements of the Reflection-Polarization Properties of Microstructured PV Light-Harvesting Layers

Imaging polarimetry was utilized for measuring the reflection-polarization properties (meaning DoLP and AoP patterns) of solar panel mimicking surfaces under various irradiation conditions and for various observer positions. It was conducted by G. Horváth using a digital camera (NIKON D3200 DSLR) outfitted with a (rotatable) linear polarizer (W-Tianya Slim MCCPL, circular filter frame, 2 mm thick). Furthermore, the camera was fixed to a tripod to minimize motion artifacts. Reflection-polarization properties were measured via rotating-analyzer sequential (serial) imaging polarimetry in the red (650 nm), green (550 nm), and blue (450 nm) spectral regions from different directions of view and under various illumination conditions. In the following, only the polarization patterns measured at 450 nm are displayed since all the green and red channels lead to practically identical results and since many aquatic insect species are sensitive to the polarization of reflected light at shorter wavelengths [634, 650, 651].

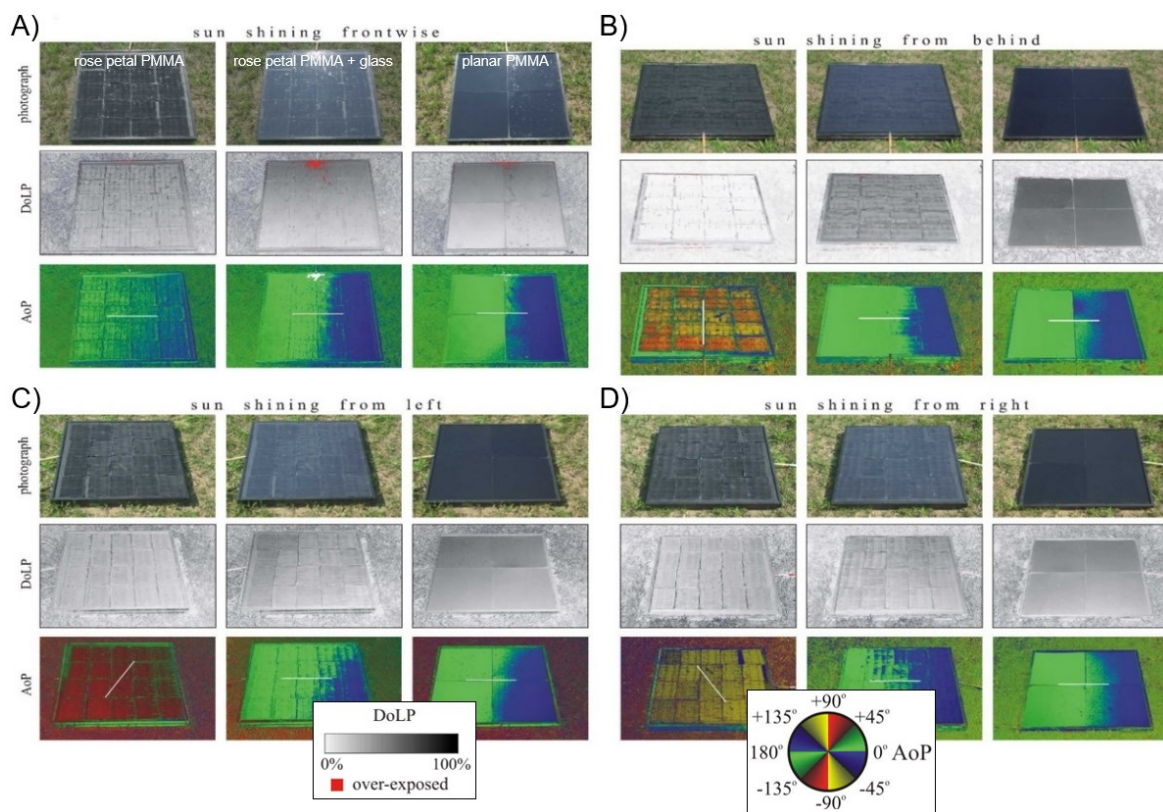


**Fig. 10.3:** Photographs of the three test surfaces used in the field experiments with horseflies and corresponding patterns of the DoLP and AoP, measured with imaging polarimetry in the blue (450 nm) spectral region. During these measurements, the sky was cloudless and clear, and the sun shone A) from in front of the observer ( $\phi = 0^\circ$ ), B) from behind the observer ( $\phi = 180^\circ$ ), C) from the left ( $\phi = 90^\circ$ ) and D) from the right ( $\phi = -90^\circ$ ) as the direct sunlight was reflected off the different surfaces. The optical axis was tilted by  $\theta = 55^\circ$  (a value close to the Brewster angle of PMMA). In the AoP patterns, the white bars show the average directions of polarization of the test surfaces. Adapted with permission from (the supplementary materials of) the abovementioned *PLOS ONE* contribution [1], © 2020 Fritz *et al.*

The observer positions in the farfield are defined by the (tilt) angle  $\theta$  between the optical axis and the horizontal plane and the azimuthal angle  $\phi$  relative to the solar position. Concerning the azimuthal position of the observer, four characteristic perspectives are chosen for all imaging polarimetric investigations discussed herein: Sun shining from in front of the observer ( $\phi = 0^\circ$ ), from behind the observer ( $\phi = 180^\circ$ ), from the left ( $\phi = 90^\circ$ ) or from the right ( $\phi = -90^\circ$ ) relative to the observer (schematic illustration is provided in Fig. 10.6 of the next section 10.4). More experimental details concerning the imaging polarimetric measurements discussed herein can be found in the aforementioned *PLOS ONE* publication [1].

### 10.3 Imaging Polarimetric Measurements of the Reflection-Polarization Properties of Microstructured PV Light-Harvesting Layers

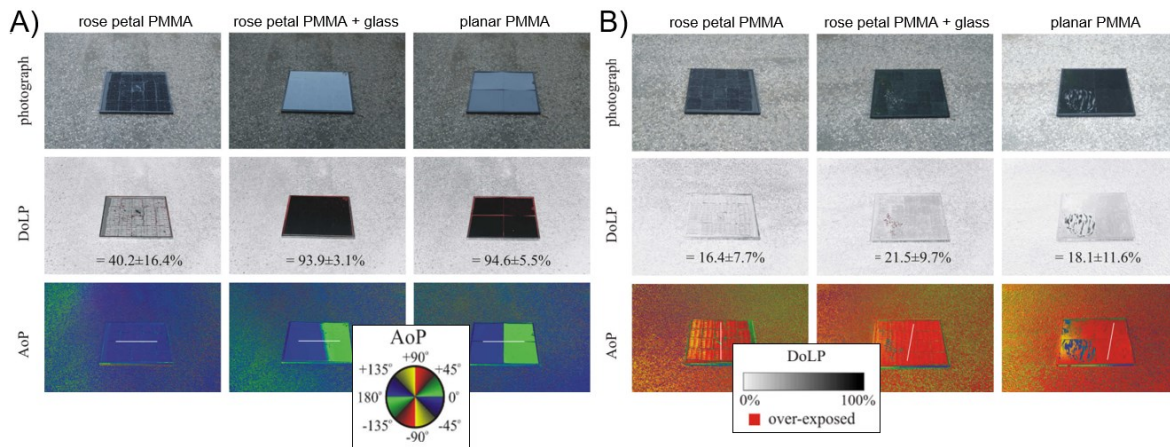


**Fig. 10.4:** Photographs and patterns of the DoLP and AoP of the three test surfaces as utilized in the field experiments with mayflies and measured with imaging polarimetry at 450 nm and a tilt of the camera's optical axis of  $55^\circ$  (a value close to the Brewster angle of PMMA). In A), the polarimeter's optical axis pointed eastwards, approximately parallel to the antisolar meridian. Here, light from the clear sky was reflected off the surfaces. In B), the polarimeter's optical axis pointed southwards, approximately perpendicular to the antisolar meridian. Here, light from the forest vegetation was reflected off the layers surfaces. The DoLP-values given in the middle rows represent average values for the entire respective test surface. In the AoP patterns, the white bars show the average directions of the polarization of reflected light for each of the surfaces. Adapted with permission from (the supplementary materials of) the abovementioned *PLOS ONE* contribution [1], © 2020 Fritz *et al.*

The reflection-polarization properties of the 50 cm  $\times$  50 cm PMMA rose petal replica (and the two planar reference surfaces) under unobstructed direct sunlight irradiance during the field experiments with horseflies are shown in Fig. 10.3.

While both configurations with planar uppermost surfaces reflect (partially) horizontally polarized light for all azimuthal viewing directions of an observer, the PMMA rose petal replica exhibits a fundamentally different reflection-polarization characteristic under direct sunlight illumination, which can be summed up as follows:

- If the sun shines from in front of the observer, polymeric rose petal replicas reflect horizontally polarized light (like the planar top layer configurations).
- If the sun shines from behind the observer, polymeric rose petal replicas reflect vertically polarized light (with a rather low DoLP).
- If the sun shines from the observer's left- or right-hand side, polymeric rose petal replicas reflect diagonally polarized light.

It should be noted that the reflection-polarization characteristics of PMMA rose petal replicas do not change under rotation of the test surfaces (for constant

irradiation conditions and a fixed observer position), which is shown in supplementary Fig. S4. The disordered hierarchical surface structure of rose petals, therefore, does not exhibit any kind of preferential direction.

The reflection-polarization properties of the three test surfaces were again measured at the experimental site of the field experiments with mayflies, where the test surfaces were placed in close proximity to vegetation without direct solar irradiance of the test surfaces. The results are summarized in Fig. 10.4. If blue skylight is reflected from the surface, which is displayed in Fig. 10.4. A), all three test surfaces reflect horizontally polarized light, while the PMMA rose petal replica is the least polarizing of the test surfaces by far. If light originating from sunlight reflected by the forest vegetation is reflected off the test surfaces, all three show a vertical direction of polarization (which is the least attractive linear polarization state for mayflies [636]) in combination with a relatively low DoLP. A detailed discussion about how these reflection-polarization patterns are formed can be found in the *PLOS ONE* publication mentioned above [1].

For an upscaled PMMA rose petal replica laminated onto a 10 cm × 10 cm CIGS solar module (unencapsulated optical dummies with an architecture identical to the devices discussed in chapters 8 and 9), the same behavior of the polarization directions in dependence of the observer viewing direction as for the test surfaces with blackened rear sides is found, as can be seen in Fig. 10.5. These similarities provide an a posteriori justification for using black paint at the rear side of PV cover layers for mimicking actual PV modules in the field experiments with polarotactic mayflies and horseflies. Interestingly, the same reflection-polarization pattern (including the AoP and the DoLP properties) as the hierarchically structured rose petal replicas can also be observed for densely packed and highly ordered arrays of smooth microlenses (also shown in Fig. 10.5), which indicates that this property might be a microstructure-related effect, and the cuticular nanofolds which decorate the epidermal cells of rose petals only play a limited role for the reflection-polarization properties of petal structure replicas. It is worthy of mention that, as should be expected, a planar PMMA layer laminated on top of a CIGS module causes a horizontal direction of polarization irrespective of the observer's azimuthal viewing direction (also see Fig. 10.5).

Based on the measured reflection-polarization patterns discussed within this section, it can be concluded that the low PLP caused by rose petal replicated light-harvesting layers in the previously described field experiments (see section 10.2) can be ascribed to two factors:

### 10.3 Imaging Polarimetric Measurements of the Reflection-Polarization Properties of Microstructured PV Light-Harvesting Layers

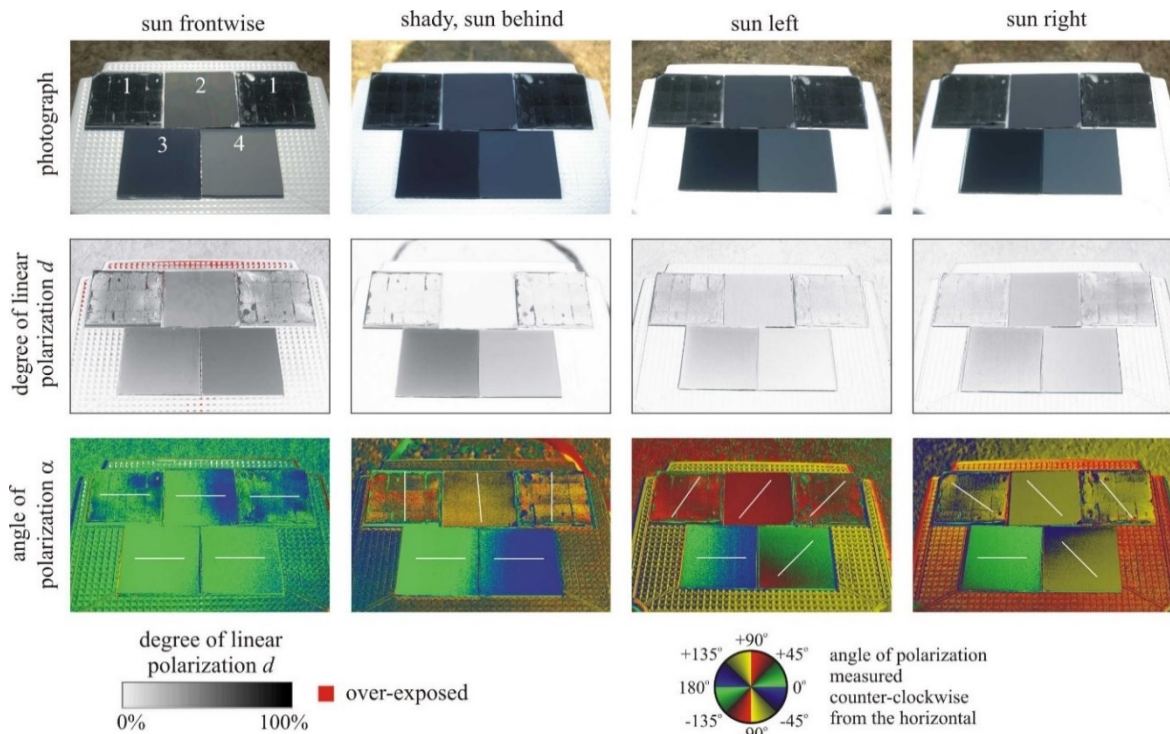


**Fig. 10.5:** Photographs and patterns of the DoLP and AoP of the three test surfaces in the field experiments with mayflies measured with imaging polarimetry (at 450 nm). In A), the polarimeter’s optical axis pointed eastwards, approximately parallel to the antisolar meridian, when light from the clear sky was reflected from the test surfaces. In B), the polarimeter’s optical axis pointed southwards (approximately orthogonal to the antisolar meridian) with a tilt of  $55^\circ$  (close to the Brewster angle of PMMA), and light from the forest vegetation was reflected from the tested layers. The DoLP-values given in the middle rows are the average values for the entire respective test surface. In the AoP patterns, white bars show the average directions of the polarization of reflected light for each of the test surfaces. Reprinted with permission from the abovementioned *PLOS ONE* contribution [1], © 2020 Fritz *et al.*

- Rose petal textured PV cover layers reflect non-horizontally polarized light for most illumination conditions and observation directions, which makes it easily distinguishable from water surfaces, especially if the observer (polarotactic insect) is moving.
- Even in cases where the light reflected from rose petal replicas is horizontally polarized and could potentially be confused for a water surface, the rather low DoLP compared to the planar reference configurations still renders the microtextured layers considerably less attractive to polarotactic insects.

Lastly, the superior PLP reduction exhibited by rose petal replicated light-harvesting layers compared to the commercial solar glass based on nanoporous

silica previously studied by Száz *et al.* [647] can be attributed to the more effective DoLP minimization of the bioreplicated surfaces.

## 10.4 Ray-Tracing-Based Analysis of the Reflection-Polarization Properties of Microstructured Surfaces

The following section discusses a computational analysis of the reflection-polarization properties of (petal-like) microstructured surfaces via Monte-Carlo ray-tracing calculations based on the modeling and simulation framework previously described in chapter 6 with some additional modifications in order to enable the analysis of the polarization state of reflected light rays in the farfield. Since terrestrial illumination conditions with their variable direct and diffuse components are rather diverse and complex, only the clear-sky reflection-polarization patterns were considered herein, modeling the (mostly) direct sunlight as parallel light rays. Cone-based microstructures (full tiling of the base) in perfectly ordered configurations were considered as well as textures that incorporate increasing amounts of structural disorder in cone height or positioning. Microtexture models were generated with cone ARs between 0.3 and 1 (0.1-steps). However, only the results for AR = 0.3, 0.6, and 1 are explicitly depicted in this thesis. Concerning disorder in cone height, the previously introduced standard deviation parameter  $\sigma_h$  (see also subsection 6.2.1) was ramped up from  $\sigma_h = 0$  to  $\sigma_h = 0.3\bar{h}$  in  $0.1\bar{h}$  steps. Disorder in cone positioning, on the other hand, was increased by ramping up the standard deviation  $\sigma_p$  (see also subsection 6.2.2) from  $\sigma_p = 0$  to  $\sigma_p = 0.5a$  (which corresponds to an entirely random arrangement, see chapter 6) in  $0.125a$  steps. All ray-tracing simulations discussed in this section were performed for a fixed wavelength of  $\approx 550$  nm by defining the material refractive index in the 3D microtexture models as  $n_{\text{PMMA } 550 \text{ nm}} = 1.49$ . For each microstructure model, the reflection-polarization properties were simulated for incidence angles  $\text{AoI} = 0^\circ, 20^\circ, 40^\circ, 60^\circ$ , and  $80^\circ$ . A series of convergence tests proved that configurations with 753 cones (419 of which are directly illuminated) lead to reliable and statistically relevant results, which was explicitly tested by repeating the simulations for each disordered microstructure configuration with another 3D model generated from the identical set of parameters and comparing the total amount of reflected power, the farfield intensity distribution of reflected light, as well as the farfield distributions of the DoLP and AoP. A generic cone-

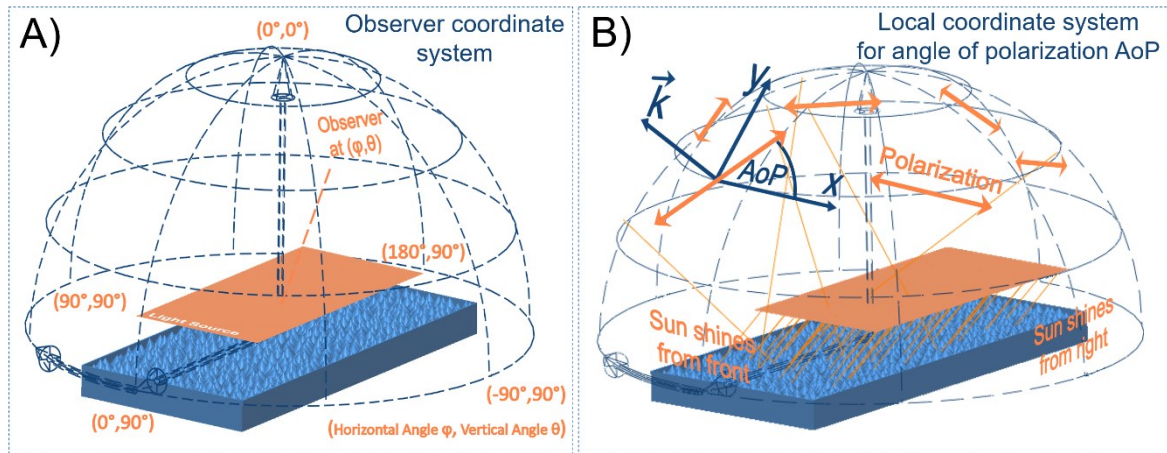


**Fig. 10.6:** Illustration of a ray-tracing-based simulation approach for studying the polarization properties of light reflected from disordered microstructures. A) Illustration of the (spherical) coordinate system for describing observer viewing directions (in the farfield). B) At every observer viewing direction  $(\phi, \theta)$ , the incoming rays' propagation direction  $\vec{k}$  defines the z-axis of a local reference frame used for measuring the AoP of reflected light in the farfield. The y-axis is defined as parallel to the local  $\phi = \text{const}$  curve. The AoP (of the electric field vector of light) is then measured relative to the local x-axis (mathematically positive). Several generic ray paths are depicted as faint orange lines

based microstructure model of full size is shown in Fig. 10.6. The number of rays again (see chapter 6) was chosen at  $10^8$  (unpolarized and parallel). The observer positions in the farfield were described in spherical coordinates by an azimuth angle  $\phi$  and a zenith angle  $\theta$ , which were defined following the illustrations given in Fig. 10.6. At every  $(\phi, \theta)$  in the farfield, the intensity of the collected light rays and the respective polarization state in terms of DoLP and AoP were observed. The AoP in the farfield was measured relative to the local  $\theta = \text{const}$  line, following the illustration provided in Fig. 10.6 B). In LightTools, both DoLP and AoP can be calculated either directly using the Stokes' parameters for each light ray combined with its respective propagation direction or indirectly using a locally defined linear polarizer as a 'filter' which can be added to the farfield detector in LightTools. All data presented in the following was acquired following the indirect approach, which can be summed up as follows: After fully tracing all of the light rays through the 3D model, a linear polarizer is rotated for all observer viewing directions  $(\phi, \theta)$  around the local z-axis defined as is shown Fig. 10.6 B). For each of the farfield positions  $(\phi, \theta)$ , the specific polarizer rotation angles for which the total collected power at the respective farfield position  $(\phi, \theta)$  reaches its maximum and minimum values. The rotation angle of the polarizing filter in the case where the maximum power is observed at the respective farfield position directly translates into the  $\text{AoP}(\phi, \theta)$ . The farfield DoLP at each specific  $(\phi, \theta)$ , on the other hand, can be

deduced from the power values  $P_{\max}$  and  $P_{\min}$ , which denote the overall highest and lowest power values observed at the respective farfield position  $(\phi, \theta)$  during the full rotation of the (locally defined) linear polarizer, by utilizing the relation

$$\text{DoLP}(\phi, \theta) = \frac{P_{\max}(\phi, \theta) - P_{\min}(\phi, \theta)}{P_{\max}(\phi, \theta) + P_{\min}(\phi, \theta)} \quad (102)$$

Interestingly, the optical simulations discussed within this section qualitatively reproduce the reflection-polarization pattern of rose petal textured PMMA under direct sunlight illumination (as in the field experiment with horseflies, see section 10.2 and 10.3). Since approaching polarotactic insects can track the polarization state of object-reflected light during flight, they will always observe object surfaces from varying viewing angles. If a PV cover layer reflects horizontally polarized light only for a narrow range of viewing directions (or illumination conditions), such as the various cone-based (ordered and disordered) microstructure models presented within this section, it is highly improbable for these kinds of densely packed microstructures to be confused for bodies of water by polarotactic insects [633, 634].

It should be pointed out that, due to the complexity and wide range of possibilities regarding terrestrial illumination conditions and the drastically simplified assumption of parallel incident light rays in the ray-tracing approach, a direct quantitative comparison has to be handled cautiously. A graphical display of selected simulation results for the farfield intensity, DoLP, and AoP for all possible observer positions is given in Fig. 10.7, Fig. 10.8, and Fig. 10.9. These figures present the simulated reflection-polarization properties of densely packed microstructures based on cones with an (average)  $\text{AR} = 0.6$ , a value close to the average AR of rose petal epidermal cells [568, 569], for the extreme cases of no structural disorder  $\sigma_h = \sigma_p = \sigma_t = 0$ , maximum disorder in cone height  $\sigma_h = 0.3\bar{h}$  as well as maximum disorder in cone positioning  $\sigma_p = 0.5a$ . Furthermore, similar figures for  $\text{AR} = 0.3$  and  $\text{AR} = 1$  are given in Fig. S5, Fig. S6, Fig. S7, Fig. S8, Fig. S9, and Fig. S10 of the supplementary information of this thesis. In these graphical displays, the farfield distributions of three different quantities, namely the reflected light intensity, DoLP, and AoP, are collectively presented for several different microtextures and illumination conditions. The intensity was normalized by the peak value of each intensity distribution and displayed as a cartesian colormap, where the horizontal viewing direction  $\phi$  is plotted along the x-direction, and the vertical viewing direction  $\theta$  is plotted along the y-axis. Furthermore, the polarization state for each observer position  $(\phi, \theta)$  is represented in the form of white arrows, where the length

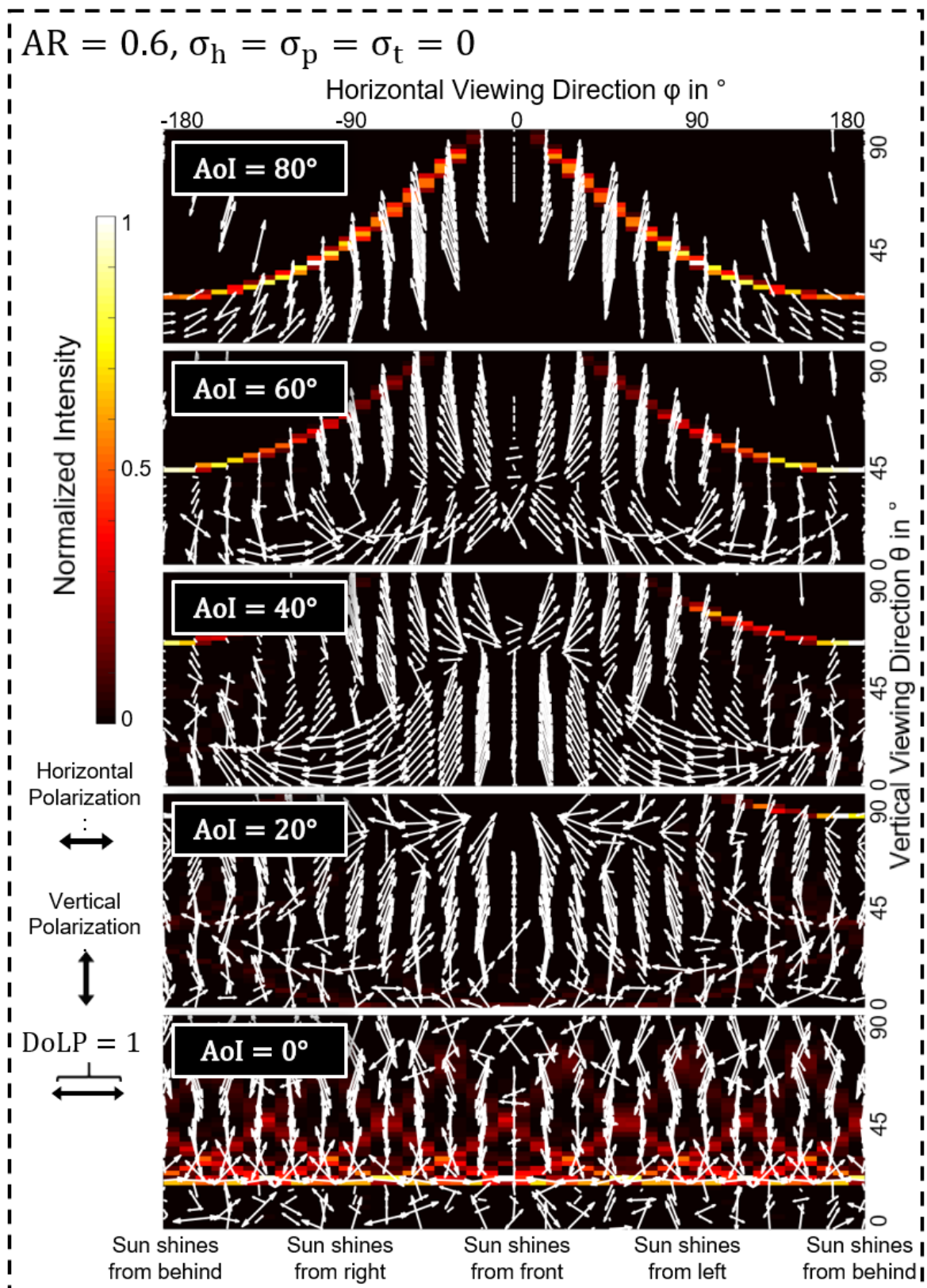


Fig. 10.7: Simulated farfield intensity, DoLP, and AoP distribution of densely packed micro-cones with an AR of 0.6 and no disorder. Adapted with permission from (the supplementary materials of) the abovementioned *PLOS ONE* publication [1], © 2020 Fritz *et al.*

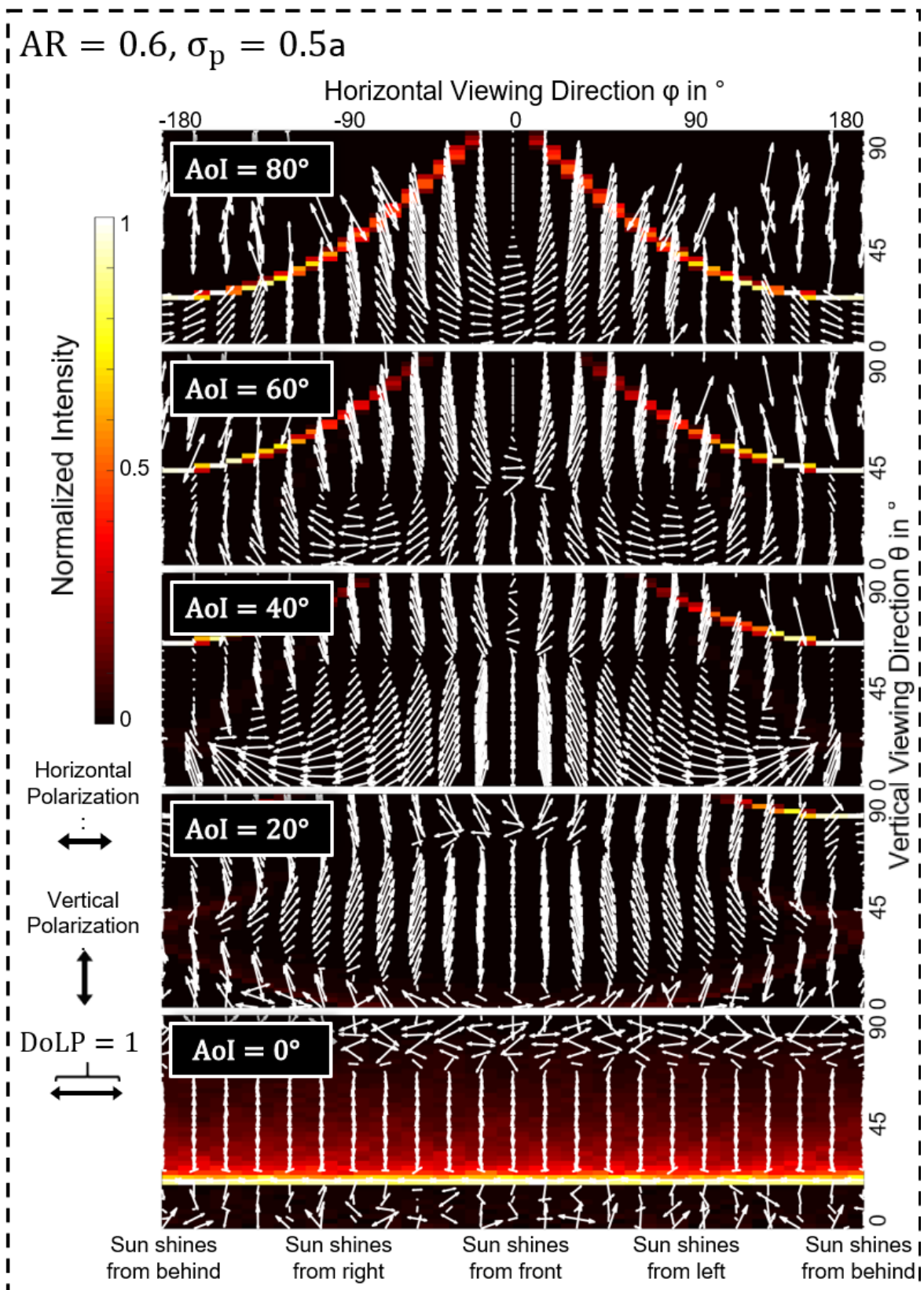


Fig. 10.8: Simulated farfield intensity, DoLP, and AoP distribution of densely packed micro-cones with an AR of 0.6 and maximum disorder in positioning. Adapted with permission from (the supplementary materials of) the abovementioned *PLOS ONE* publication [1], © 2020 Fritz *et al.*

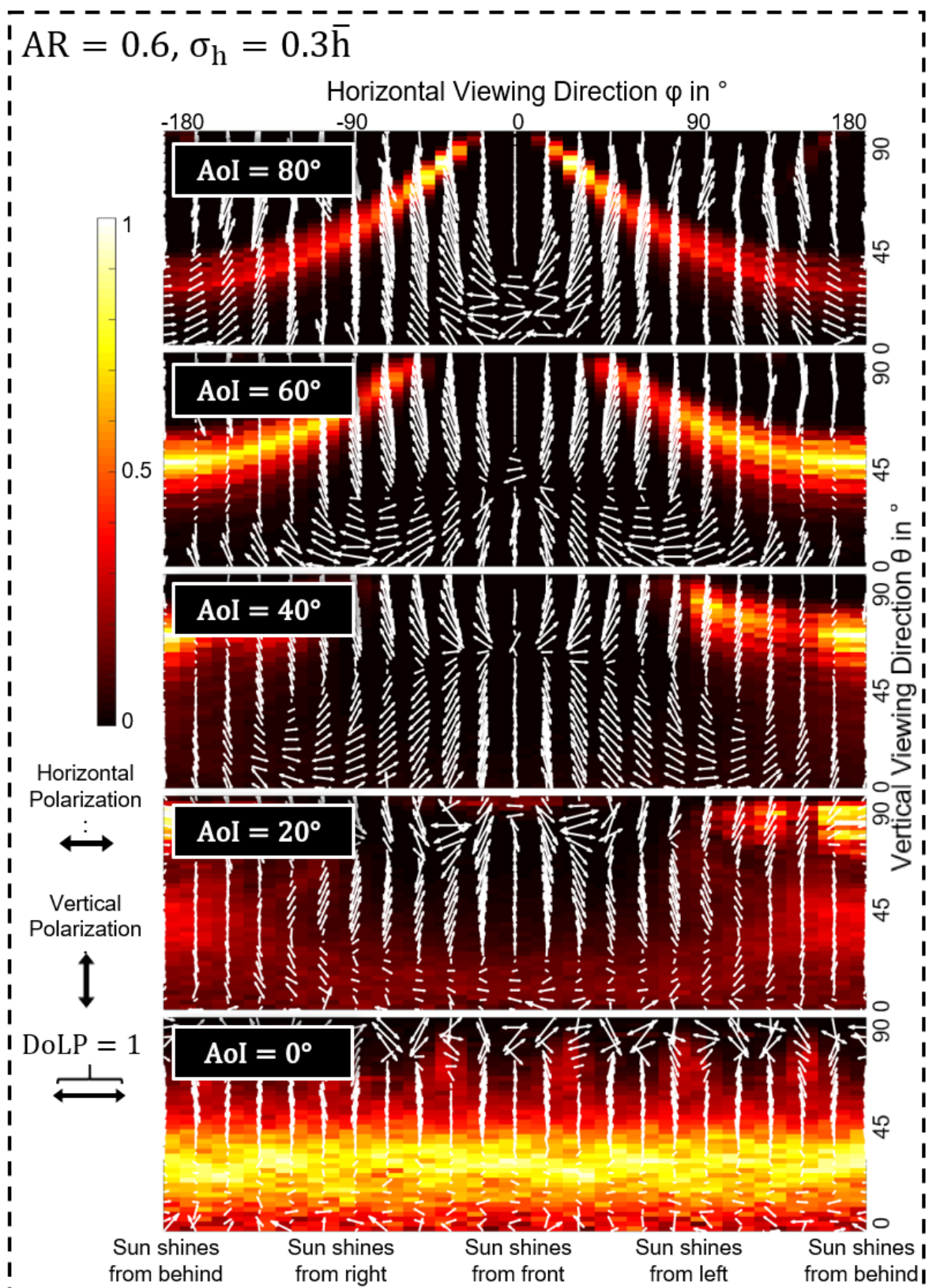
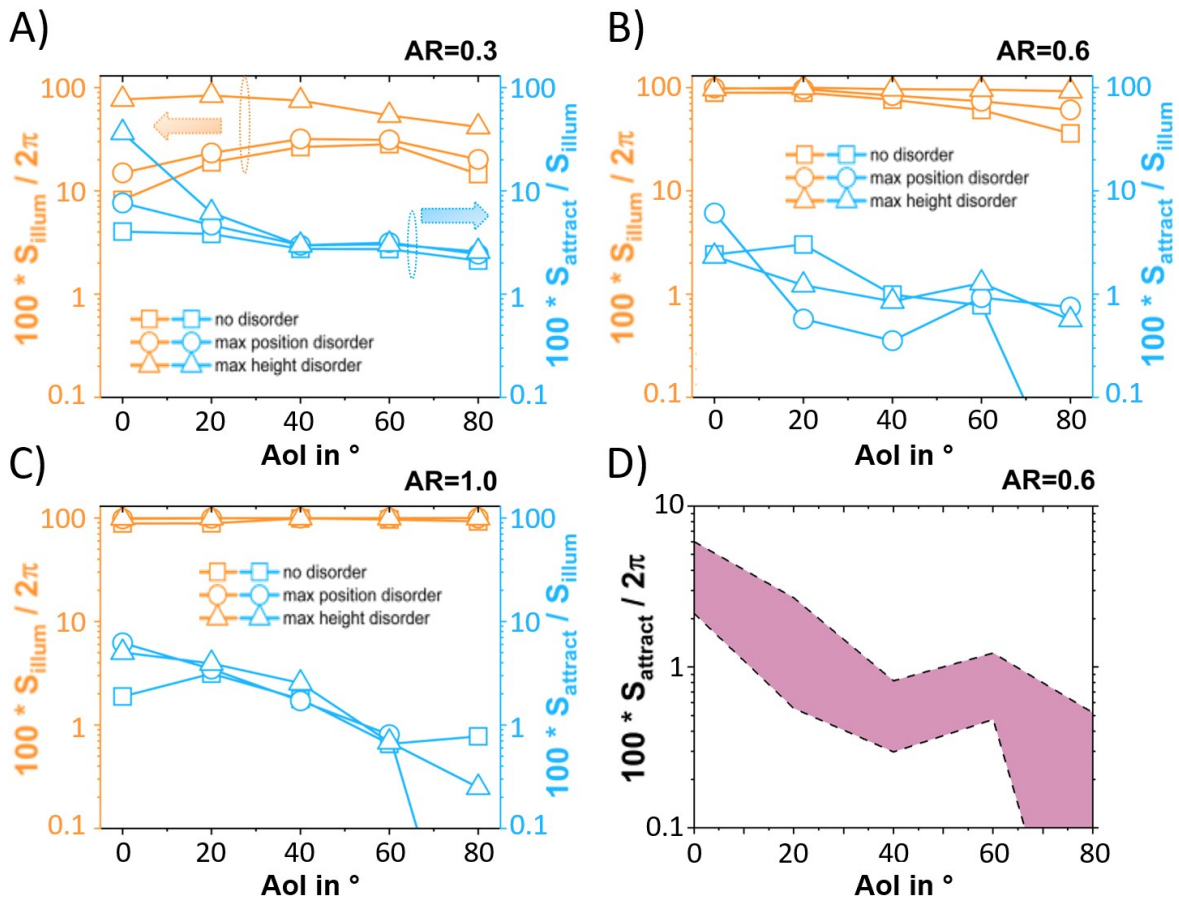


Fig. 10.9: Simulated farfield intensity, DoLP, and AoP distribution of densely packed micro-cones with an AR of 0.6 and maximum disorder in height. Adapted with permission from (the supplementary materials of) the abovementioned *PLOS ONE* publication [1], © 2020 Fritz *et al.*

of each arrow is proportional to the DoLP, while the AoP is given by the arrow's rotation angle of the arrow relative to the  $x$ -axis. With these definitions, the polarization arrows are displayed in the same way as an observer at  $(\phi, \theta)$  in the farfield looking directly into the center of the microstructure would perceive the orientation of the linearly polarized component of the microstructure-reflected light. This methodology, therefore, allows direct comparisons between the orientations of the polarization of surface-reflected light obtained either experimentally via imaging polarimetry or numerically by Monte-Carlo ray-tracing simulations.

The farfield DoLP and AoP patterns of surface-reflected light were reduced to a more accessible form by processing the farfield data based on considerations described in the following. According to a 2009 report by Kriska *et al.* [631], surfaces that reflect light with a DoLP  $< 15\%$  and an AoP deviating from the horizontal by less than  $\pm 10^\circ$  cause a maladaptive attractiveness to mayflies and horseflies because of misidentification of such surfaces as calm bodies of water. These thresholds were exploited to quantify the polarized light pollution (and its dependence on several structural parameters) caused by the reflection of direct sunlight from microtextured surfaces. It is assumed that the microtextured surface is placed horizontally because only then can it be observed from all positions on the  $2\pi$  hemisphere. It was further assumed that none of the possible viewing directions over the entire hemisphere is favored by the polarotactic insects for spotting water surfaces (assumption based on the experience of G. Horváth and colleagues from their numerous field experiments [631, 632, 639, 640, 647–649]). Three numbers for characterizing the PLP caused by a reflecting surface were then calculated from the farfield distributions of reflected light intensity, DoLP, and AoP, namely

- the solid angle ratio  $S_{\text{illum}}/2\pi$ , where  $S_{\text{illum}}$  denotes the total solid angle within which a nonzero intensity of reflected light was collected, which can be considered as a measure of the spread or concentration of reflected light over the hemisphere of observer positions,
- the solid angle ratio  $S_{\text{attract}}/S_{\text{illum}}$ , where  $S_{\text{attract}}$  denotes the total solid angle for which both a DoLP  $> 15\%$  as well as a polarization direction that only deviates from the horizontal by a maximum of  $\pm 10^\circ$  (which are) were found simultaneously, which describes the fraction of viewing directions that can be suspected to cause mayflies and horseflies to identify a respective surface as water (relative to the part of the observer hemisphere that is reached by reflected light rays), and



**Fig. 10.10:** Numerical assessment of the influence of structural disorder on the polarized light pollution caused by microtextured surfaces. For ARs of 0.3 (A), 0.6 (B), and 1 (C), the two characteristic solid angle ratios  $S_{\text{illum}}/2\pi$  and  $S_{\text{attract}}/S_{\text{illum}}$  are plotted as a function of incidence angle. D) Depicts the solid angle fraction  $S_{\text{attract}}/2\pi$  versus AoI for which horseflies and mayflies would detect the reflecting surface as a water surface with respect to the entire hemisphere of possible observer viewing directions for  $AR = 0.6$ . The colored area in panel D) indicates the full range of numerical results found when ramping up both height and position disorder. Reprinted with permission from the abovementioned contribution to *PLOS ONE* [1], © 2020 Fritz *et al.*

— the product of the first two ratios yields  $S_{\text{attract}}/2\pi$  which describes the total solid angle from which a misdetection of the textured surface as water can be expected (relative to the entire observer hemisphere).

These three quantities were calculated for all of the ray-tracing simulations discussed within this chapter. For micro-cones with an (average) AR of 0.3, 0.6, and 1, the results of these considerations are depicted in Fig. 10.10.

Both disorder in cone height and positioning lead to a spread of the reflected light over more extensive parts of the observer hemisphere. The slight variations in micro-cone height lead to alterations of the local incidence angles, resulting in a peak-broadening effect in the farfield intensity distribution of surface-reflected

light. Only for very few exceptions, namely the cases of (at least close to) perfectly ordered microstructures and cones with low (average) AR, the microtextured surfaces can spread the parallel light rays over most of the farfield hemisphere. The calculated solid angle fractions of possible farfield viewing directions  $(\phi, \theta)$  that lead to an erroneous detection as a water surface relative to the entire hemisphere are summarized in Fig. 10.10. The purple-shaded area in Fig. 10.10 D) indicates (for the example of  $AR = 0.6$ ) the entire range of numerical results encountered when ramping up both height and position disorder from zero to their respective maximum values. For the entire parameter ranges of the AR, AoI, as well as the types and degrees of structural disorder that were investigated herein, the conditions for a misdetection of a microstructured surface as water were only met for a relatively limited fraction of the observer hemisphere: According to Fig. 10.10 D), across all AoIs, less than 10% of the  $2\pi$  hemisphere would exhibit a harmful attractiveness to polarotactic mayflies and horseflies. For oblique light incidence, this fraction even falls below 1%. These findings indicate that the ability of hierarchically textured cover layers such as polymeric petal replicas to greatly reduce polarized light pollution is not (strongly) susceptible to changes in the illumination conditions and variations of microstructure geometry-related parameters like the AR or the type and degree of structural disorder.

---

## 11 Summary and Outlook

---

This thesis reported on the optical and wetting properties of petal surface structure replicas and their application as multifunctional cover layers for solar panels. Experimental and computational analyses aimed at improving the understanding of the light-harvesting and wetting properties of petal-replicated plant epidermal cell microstructures were presented. Moreover, this thesis covered the development of an upscaling method that enables the fabrication of large-area metallic mold inserts for plant surface structure replication via static hot-embossing. It was further shown that hot-embossed polymeric rose petal replicated PV cover layers can combine broadband and omnidirectional light-capture with water-repellency and a minimized impact on the ecology and conservation of polarotactic insect species by nearly eliminating polarized light pollution.

In **chapter 6**, a [ray-tracing-based assessment of the impact of microstructural disorder on the light-harvesting properties of plant surface structure replicas](#) was discussed. As the main conclusion, the numerical results suggest that the light in-coupling properties of petal-like microstructures are remarkably robust against introducing different structural disorder types. Irrespective of the degree of disorder in epidermal cell height, positioning, or tilt angle, the angle-dependent reflectance of such microstructures is mainly governed by the average AR of the epidermal cell micro-cones (as well as by their packing density).

**Chapter 7** described [advancements regarding experimental techniques for plant surface structure replication](#), aiming towards large-area applications and high-throughput methods. A fabrication route based on hot-embossing lithography for replicating the surface micro- and nanostructures of leaves and petals into large-area (up to 125 cm<sup>2</sup>) thermoplastic polymer foils for application as multifunctional PV cover layers was developed. This bioreplication route is straightforwardly extendable to other biological surfaces, polymers, PV technologies, or other optical devices such as organic LEDs. Since static plate-to-plate hot-embossing is a relatively slow process, it is not economically feasible for the PV industry, where relatively cheap antireflective coatings are the current standard. A transfer to a faster roll-to-roll-based approach, therefore, seems inevitable to reach a competitive level. It should be noted that, in collaboration with Dr. Ruben Hünig, Dr. Markus Guttmann, and Dr. Guillaume Gomard, a patent concerning the fabrication of, for

example, rose petal structured embossing rollers for such a roll-to-roll process has been submitted to the German Patent and Trade Mark Office (Deutsches Patent- und Markenamt, DPMA) and is currently under review (as of March 2021).

For three different polymeric materials (PC, PMMA, FEP), the experimentally obtained [angle-dependent reflectance spectra of rose petal replicas as cover layers for CIGS thin-film solar cells](#) were discussed in **chapter 8**, together with a [characterization of the self-cleaning properties of hot-embossed rose petal replicas](#) via contact angle measurements and falling droplet experiments. For all three materials, adding the hierarchical rose petal surface structure leads to a considerable increase in static water contact angle, even for the intrinsically hydrophilic material PMMA. For rose petal replicas based on the low surface free energy material FEP, the overall highest (static) water contact angle out of the three polymeric materials considered is found at  $134.4^\circ \pm 4.3^\circ$ . Moreover, for FEP rose petal replicas, falling droplet experiments demonstrated their potential to implement self-cleaning properties in PV devices. For minimizing reflection losses, on the other hand, rose petal textured PMMA was found to be the most effective cover layer candidate, outperforming optimized  $\text{MgF}_2$  thin-film antireflective coatings – the state-of-the-art antireflective coating for reaching world record efficiencies in unencapsulated CIGS solar cells [582–589] – even for normal incidence of light. [Opto-electrical characterizations \(IV and EQE\) of high-efficiency CIGS solar cells equipped with hot-embossed rose petal replicas as light-harvesting layers under STC](#) revealed an average increase in CIGS solar cell efficiency of  $5.7\% \pm 0.6\%$  caused by adding rose petal textured PMMA cover layers, whereas  $\text{MgF}_2$  coatings were determined to improve device performance by  $4.5\% \pm 1.6\%$ .

The performance of [large-area hot-embossed rose petal replicas as PV light-harvesting layers under field conditions](#) was discussed in **chapter 9** for c-Si and CIGS thin-film solar modules (10 cm × 10 cm) installed under various tilt and orientation angles in Karlsruhe, Germany. The highest daily performance gains (above 10%) were found for situations with much direct sunlight reaching the modules under oblique AoIs above  $50^\circ$ . Accelerated aging tests DH-1000, TC-200 (with and without a UV preconditioning), as well as long-term UV light exposure, left the bonding (lamination) between glass-encapsulated CIGS mini-modules and large-area PMMA rose petal replicas perfectly intact. Moreover, SEM-based topographical analyses and AoI-dependent reflectance spectra further indicated that the bioreplicated light-harvesting layers' light-collection capabilities were almost unharmed by these climatic aging procedures. Only the long-term UV exposure led to a non-negligible deterioration of the textured PMMA layers' optical

quality. Sandblasting and sand tickling of several pristine and artificially aged demonstrated a clear difference in abrasive damage depending on the accumulated UV exposure endured by the respective polymeric light-harvesting layer. Further climatic aging protocols such as humidity-freeze testing or assessing the damage through the impact of hail should follow to further assess the long-term durability of PMMA rose petal replicas as PV cover layers also for colder climatic conditions.

Numerical and experimental studies concerning the [maladaptive attractiveness of rose-petal-replicated PV light-harvesting layers to polarotactic insects](#) were presented in **chapter 10**. Field experiments with polarotactic mayflies and horseflies strongly indicated that rose petal replicated PMMA does not cause any harmful PLP. It should be pointed out that such behavior had not been demonstrated for any PV cover layer configuration thus far. Imaging polarimetric measurements, as well as simplified ray-tracing calculations on disordered cone-based microstructures, show that this type of light-harvesting layer exhibits pronounced variations in AoP and DoLP depending on the observer viewing direction as well as the illumination conditions and only rarely reflects a considerable amount of horizontally polarized light. This somewhat chaotic fluctuation of the polarization direction for an observer moving around the microtextured layer prevents any misidentification by polarotactic water-seeking insects. In the future, the impact of PV light-harvesting layers on insect conservation should further be discussed for other cover layer concepts. Furthermore, since birds can also visually perceive polarized light [652], future studies should determine if an equivalent to polarized light pollution might also exist for some species of birds.



## Supplementary Information

orange = these cells are either defective or kept in their pristine state.

**Table S1: Test strip XLS1057-3, pristine.**

solar cell no.	1	2	3	4	5	6	7	8	9	10
PCE / %		20.66			20.72	20.23	21.00	20.83	21.43	
V <sub>OC</sub> / mV		726			717	713	711	711	707	
FF / %		79.90			79.50	78.80	79.70	79.50	79.10	
I <sub>SC</sub> / mA		17.79			18.19	18.00	18.53	18.43	19.15	
ΔJ <sub>SC</sub> / mA cm <sup>-2</sup>		35.58			36.37	36.01	37.06	36.87	38.29	

**Table S2: Test strip XLS1057-3 + 105 nm MgF<sub>2</sub>.**

solar cell no.	1	2	3	4	5	6	7	8	9	10
PCE / %		21.56			22.20	21.44	21.78	21.39	22.11	
V <sub>OC</sub> / mV		728			721	715	713	715	709	
FF / %		79.90			79.60	79.00	79.60	79.00	79.00	
I <sub>SC</sub> / mA		18.51			19.34	18.97	19.17	18.93	19.73	
ΔJ <sub>SC</sub> / mA cm <sup>-2</sup>		37.03			38.68	37.93	38.33	37.86	39.47	

**Table S3: Test strip XLS1057-3, relative enhancement due to MgF<sub>2</sub>.**

solar cell no.	1	2	3	4	5	6	7	8	9	10
ΔPCE / %		+4.39			+7.16	+5.98	+3.74	+2.67	+3.14	
ΔV <sub>OC</sub> / mV		+0.28			+0.56	+0.28	+0.28	+0.56	+0.28	
ΔFF / %		+0.00			+0.13	+0.25	-0.13	-0.63	-0.13	
ΔI <sub>SC</sub> / mA		+4.05			+6.32	+5.39	+3.45	+2.71	+3.03	
ΔJ <sub>SC</sub> / mA cm <sup>-2</sup>		+4.08			+6.35	+5.33	+3.43	+2.69	+3.08	

**Table S4: Test strip XLS1058-3, pristine.**

solar cell no.	1	2	3	4	5	6	7	8	9
PCE / %			19.73	19.51	19.07	19.26	19.89	19.78	
V <sub>OC</sub> / mV			694	689	682	683	685	680	
FF / %			78.50	77.30	76.30	76.30	78.40	79.30	
I <sub>SC</sub> / mA			18.09	18.30	18.33	18.49	18.53	18.34	
J <sub>SC</sub> / mA cm <sup>-2</sup>			36.19	36.61	36.67	36.99	37.06	36.67	

**Table S5: Test strip XLS1058-3 + NOA88 + rose petal textured PC:**

solar cell no.	1	2	3	4	5	6	7	8	9
PCE / %			20.88	20.26	19.99	20.05	20.58	20.85	
$V_{OC}$ / mV			694	691	683	684	684	682	
FF / %			78.10	76.60	76.10	75.80	77.40	78.80	
$I_{SC}$ / mA			19.25	19.13	19.23	19.34	19.44	19.41	
$J_{SC}$ / mA cm <sup>-2</sup>			38.50	38.26	38.46	38.68	38.87	38.82	

**Table S6: Test strip XLS1058-3 + NOA88 + rose petal textured PC + 105 nm MgF<sub>2</sub>.**

solar cell no.	1	2	3	4	5	6	7	8	9
PCE / %			21.28	20.73	20.29	20.26	21.04	21.05	
$V_{OC}$ / mV			690	686	677	679	680	676	
FF / %			78.50	76.90	76.50	76.10	78.00	79.00	
$I_{SC}$ / mA			19.63	19.65	19.59	19.60	19.85	19.70	
$J_{SC}$ / mA cm <sup>-2</sup>			39.27	39.31	39.17	39.20	39.70	39.39	

**Table S7: Test strip XLS1058-3, relative enhancement due to rose petal textured PC.**

solar cell no.	1	2	3	4	5	6	7	8	9
$\Delta PCE$ / %			+5.85	+3.85	+4.78	+4.10	+3.45	+5.40	
$\Delta V_{OC}$ / mV			+0.00	+0.29	+0.15	+0.15	-0.15	+0.29	
$\Delta FF$ / %			-0.51	-0.91	-0.26	-0.66	-1.28	-0.63	
$\Delta I_{SC}$ / mA			+6.41	+4.54	+4.91	+4.60	+4.91	+5.83	
$\Delta J_{SC}$ / mA cm <sup>-2</sup>			+6.38	+4.51	+4.88	+4.57	+4.88	+5.86	

**Table S8: Test strip XLS1058-3, relative enhancement due to rose petal textured PC + 105 nm MgF<sub>2</sub>.**

solar cell no.	1	2	3	4	5	6	7	8	9
$\Delta PCE$ / %			+7.86	+6.25	+6.36	+5.19	+5.79	+6.44	
$\Delta V_{OC}$ / mV			-0.58	-0.44	-0.73	-0.59	-0.73	-0.59	
$\Delta FF$ / %			+0.00	-0.52	+0.26	-0.26	-0.51	-0.38	
$\Delta I_{SC}$ / mA			+8.51	+7.38	+6.87	+6.00	+7.12	+7.42	
$\Delta J_{SC}$ / mA cm <sup>-2</sup>			+8.51	+7.38	+6.82	+5.97	+7.12	+7.42	

**Table S9: Test strip 9680524, pristine.**

solar cell no.	1	2	3	4	5	6	7	8	9	10
PCE / %	17.69		19.38							
V <sub>OC</sub> / mV	653		661							
FF / %	72.20		77.10							
I <sub>SC</sub> / mA	18.78		19.02							

**Table S10: Test strip 9680524 + NOA88 + rose petal textured PMMA.**

solar cell no.	1	2	3	4	5	6	7	8	9	10
PCE / %	18.73		20.3							
V <sub>OC</sub> / mV	656		660							
FF / %	72.7		76.6							
I <sub>SC</sub> / mA	19.64		20.08							

**Table S11: Test strip 9680524, relative enhancement due to rose petal textured PMMA.**

solar cell no.	1	2	3	4	5	6	7	8	9	10
ΔPCE / %	+5.86		+4.74							
ΔV <sub>OC</sub> / mV	+0.46		-0.15							
ΔFF / %	+0.69		-0.65							
ΔI <sub>SC</sub> / mA	+4.58		+5.57							

**Table S12: Test strip 9680575, pristine.**

solar cell no.	1	2	3	4	5	6	7	8	9	10
PCE / %	17.64	18.96		19.92			20.24			
V <sub>OC</sub> / mV	645	673		694			693			
FF / %	67.80	76.60		78.90			79.30			
I <sub>SC</sub> / mA	20.18	18.39		18.19			18.42			

**Table S13: Test strip 9680575 + NOA88 + rose petal textured PMMA.**

solar cell no.	1	2	3	4	5	6	7	8	9	10
PCE / %	18.71	20.03		21.01			21.57			
V <sub>OC</sub> / mV	645	675		695			695			
FF / %	68.40	76.80		78.50			79.20			
I <sub>SC</sub> / mA	21.20	19.33		19.26			19.61			

**Table S14: Test strip 9680575, relative enhancement due to rose petal textured PMMA.**

solar cell no.	1	2	3	4	5	6	7	8	9	10
$\Delta PCE / \%$	+6.04	+5.63		+5.46			+6.55			
$\Delta I_{SC} / \text{mA}$	+0.00	+0.30		+0.14			+0.29			
$\Delta V_{OC} / \text{mV}$	+0.88	+0.26		-0.51			-0.13			
$\Delta FF / \%$	+5.05	+5.11		+5.88			+6.46			

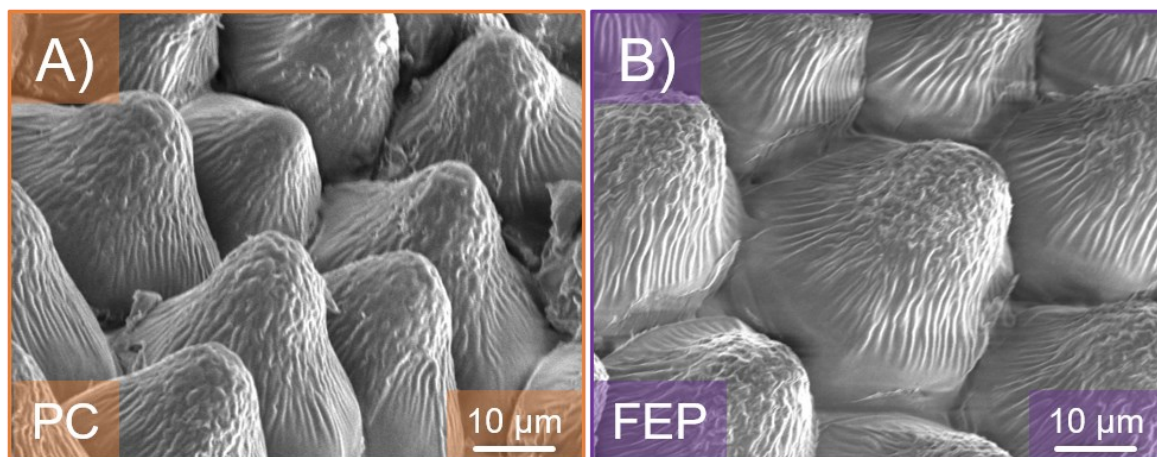


**Fig. S1: SEM micrographs of hot-embossed rose petal replicas, fabricated by using mold insert BF05. A) PC replica. B) FEP replica.**

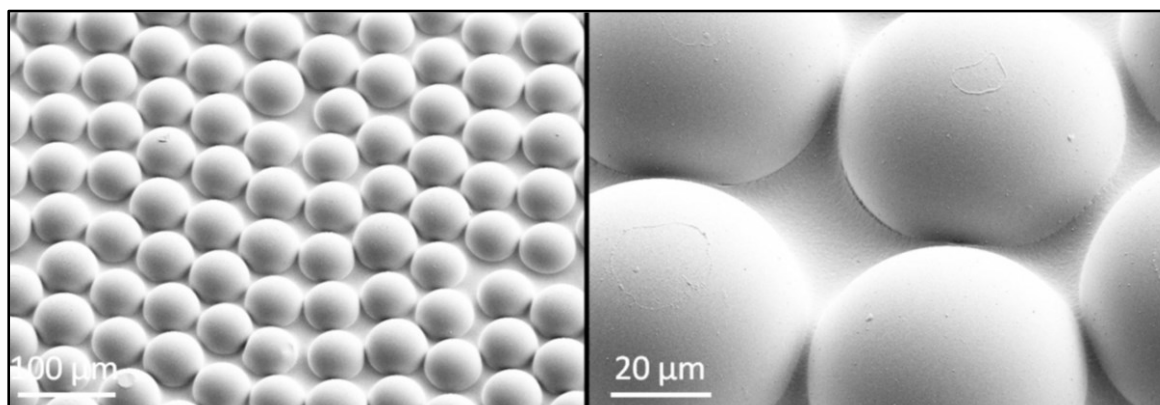


**Fig. S2: SEM images of the commercial microlens array foil used as a CIGS solar module cover layer, resulting in AoP and DoLP patterns very similar to polymeric rose petal surface structure replicas. Reprinted with permission from the aforementioned *PLOS ONE* publication [1], © 2020 Fritz *et al.***

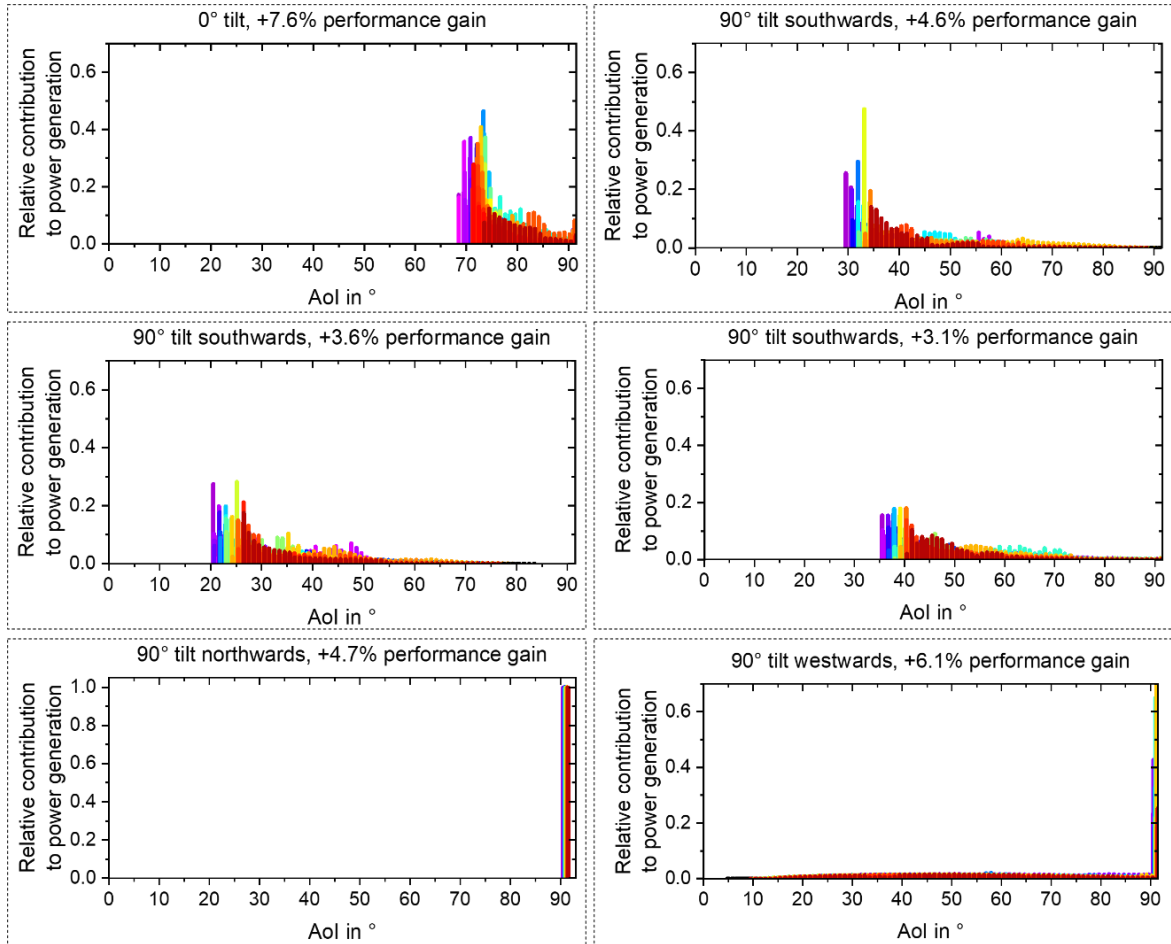


**Fig. S3:** Bar chart illustrating the relative contributions of different AoIs (of the direct sunlight component) to the total power generated for each individual day for rose petal textured Si module 1. Each individual day of performance monitoring is displayed in a different color. The summarized relative contributions of AoI > 90° (only diffuse irradiance) were included in these plots at a value of AoI = 91°.

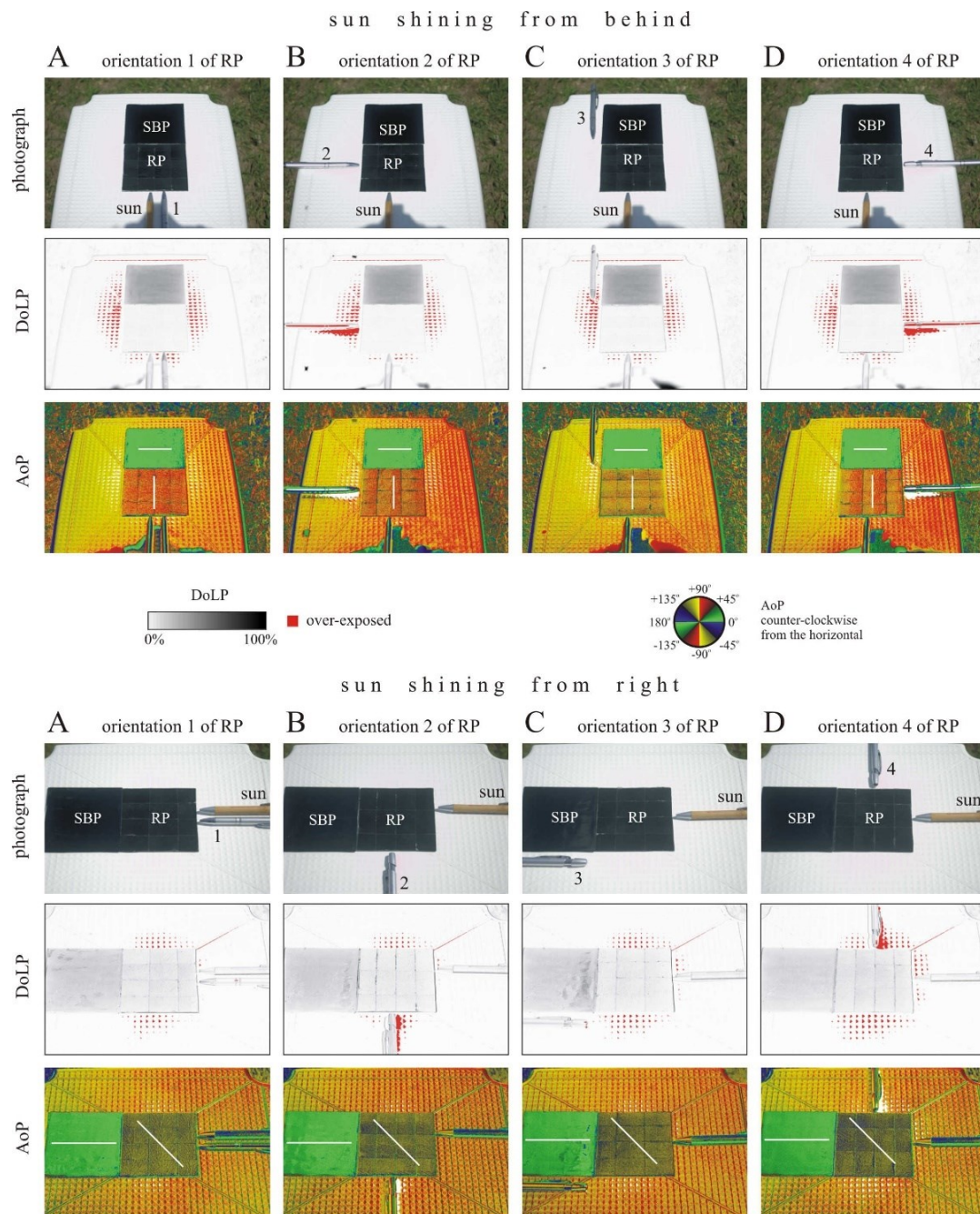


**Fig. S4:** Photographs and patterns of the degree and angle of polarization of the rose petal replica and the planar PMMA reference layer used in the field experiments with mayflies and horseflies for four different orientations of the rose petal replica. Polarization patterns were measured using imaging polarimetry in the 450 nm spectral range when the sun shone from behind (top) and from the left (bottom), with light from the clear sky being reflected from the test surfaces. The camera's optical axis was tilted by  $55^\circ$  (a value close to the Brewster angle of PMMA). In the AoP patterns, the white bars show the average directions of the reflected light polarization of the test surfaces. In the photographs, SBP (=shiny black plastic) denotes the planar PMMA reference, and RP denotes the PMMA rose petal replica. Reprinted with permission from (the supplementary materials of) the abovementioned *PLOS ONE* publication [1], © 2020 Fritz *et al.*

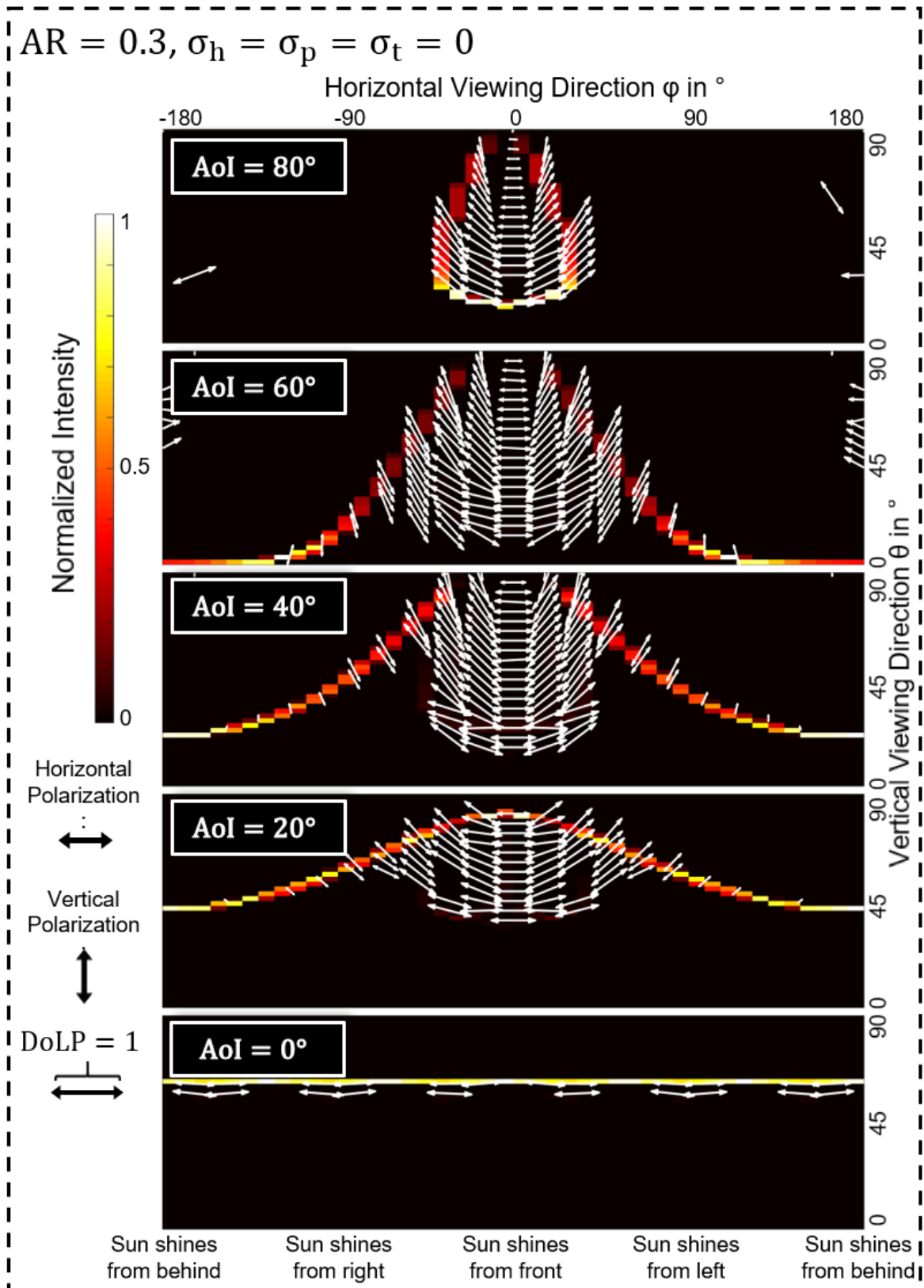


Fig. S5: Simulated farfield intensity, DoLP, and AoP distribution of densely packed micro-cones with an AR of 0.3 and no disorder. Reprinted with permission from (the supplementary materials of) the aforementioned *PLOS ONE* publication [1], © 2020 Fritz *et al.*

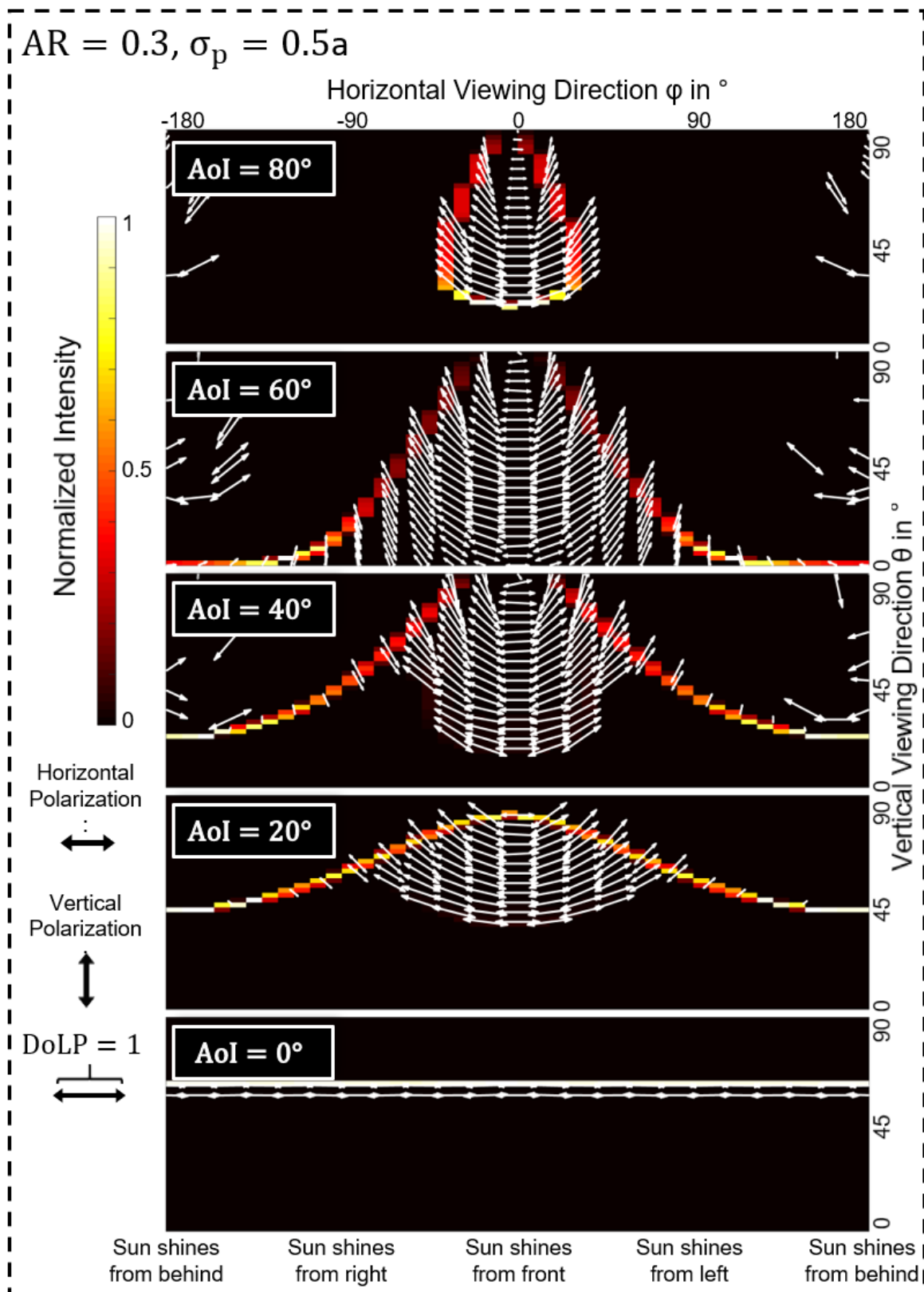


Fig. S6: Simulated farfield intensity, DoLP, and AoP distribution of densely packed micro-cones with an AR of 0.3 and maximum disorder in positioning. Reprinted with permission from (the supplementary materials of) the aforementioned *PLOS ONE* publication [1], © 2020 Fritz *et al.*

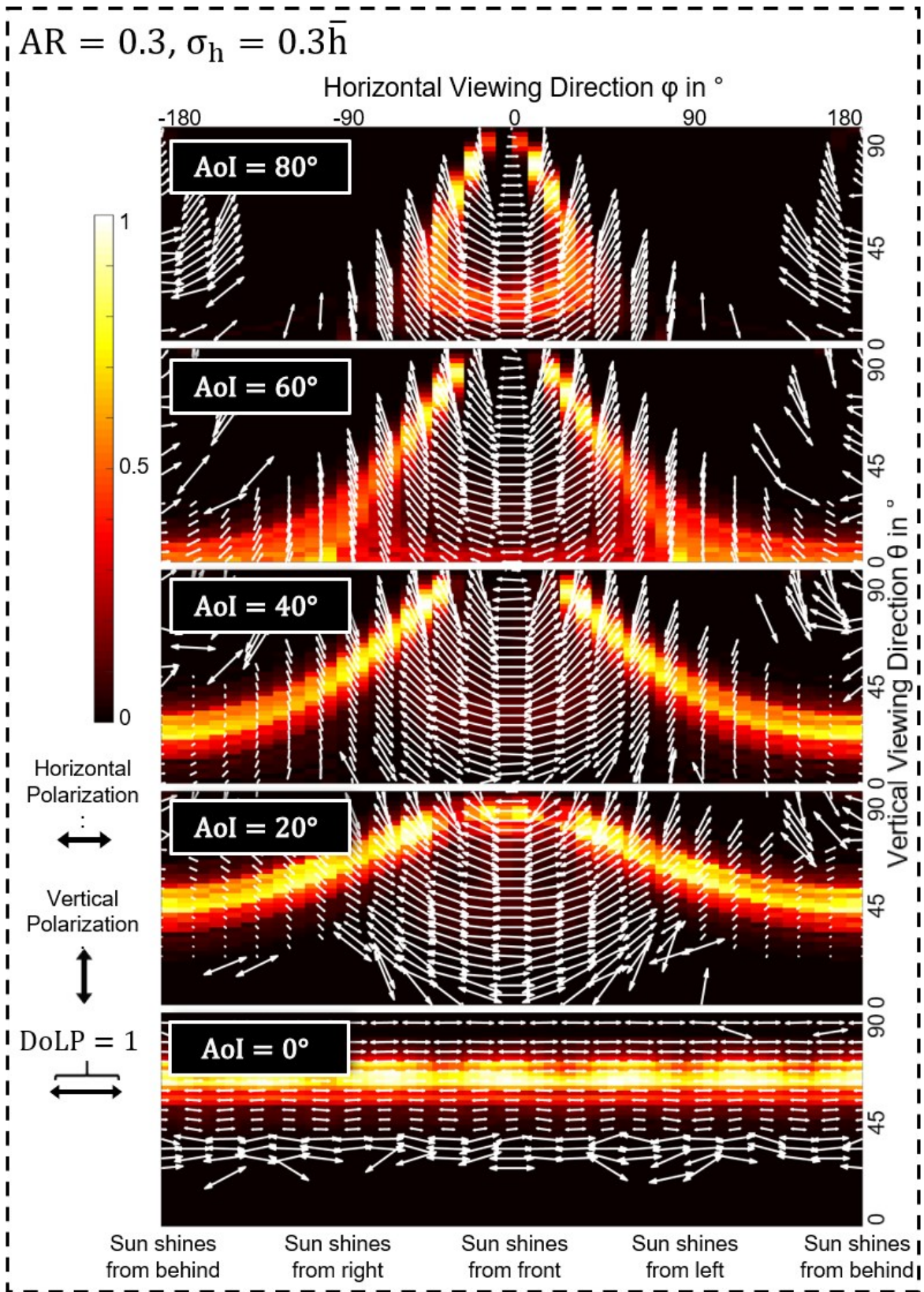


Fig. S7: Simulated farfield intensity, DoLP, and AoP distribution of densely packed micro-cones with an AR of 0.3 and maximum disorder in height. Reprinted with permission from (the supplementary materials of) the aforementioned *PLOS ONE* publication [1], © 2020 Fritz *et al.*

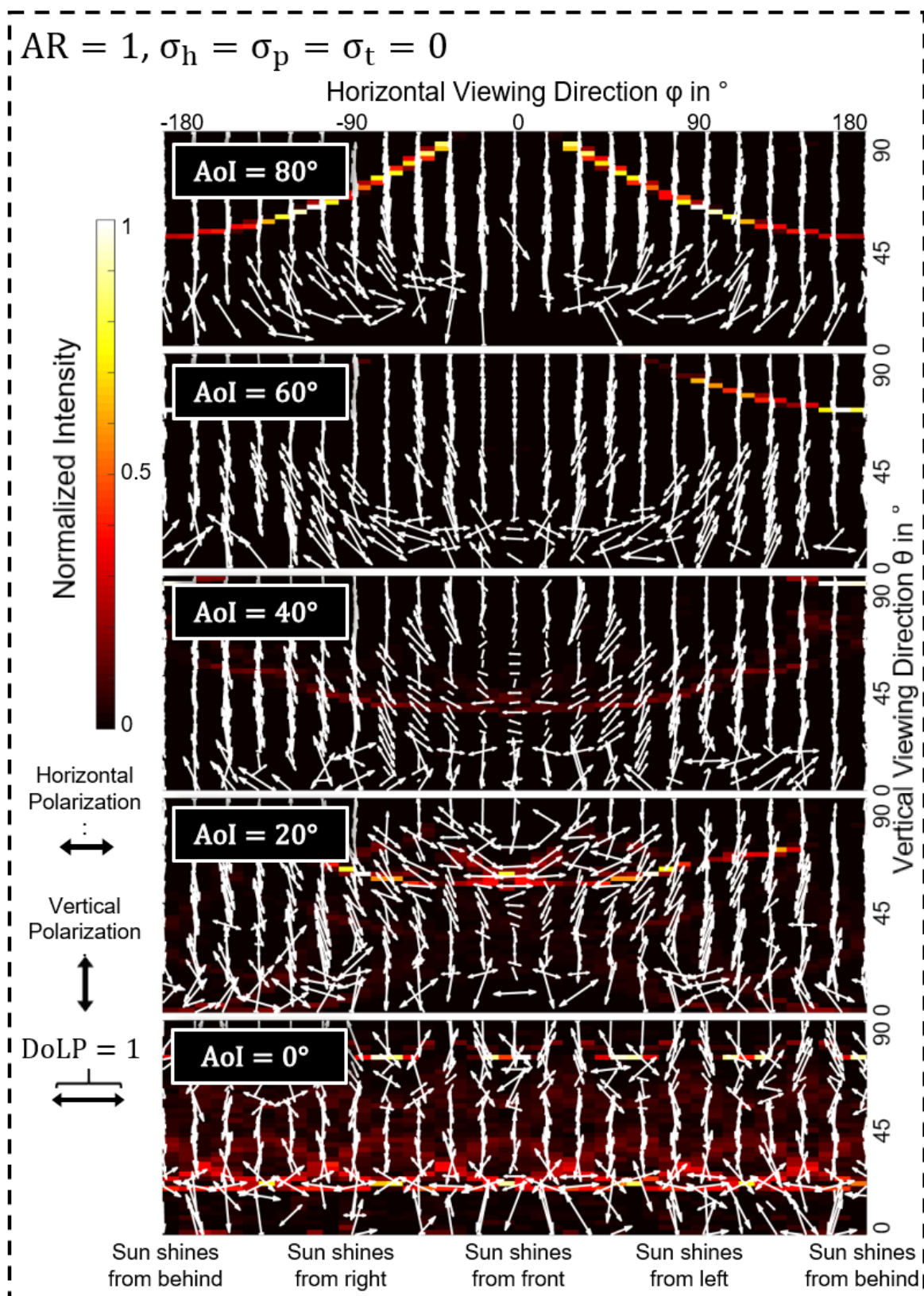
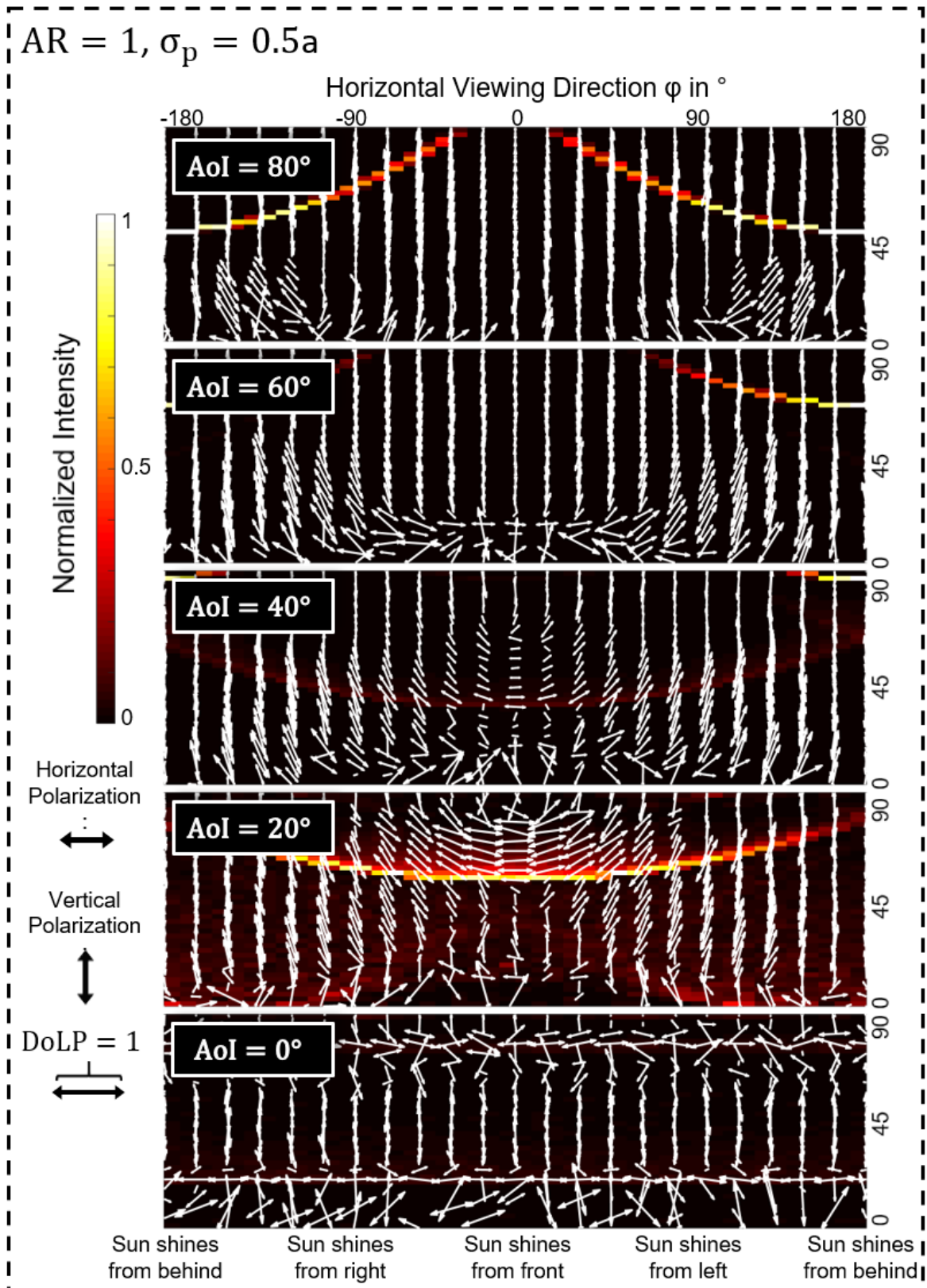


Fig. S8: Simulated farfield intensity, DoLP, and AoP distribution of densely packed micro-cones with an AR of 1 and no disorder. Reprinted with permission from (the supplementary materials of) the aforementioned *PLOS ONE* publication [1], © 2020 Fritz *et al.*



**Fig. S9:** Simulated farfield intensity, DoLP, and AoP distribution of densely packed micro-cones with an AR of 1 and maximum disorder in positioning. Reprinted with permission from (the supplementary materials of) the aforementioned *PLOS ONE* publication [1], © 2020 Fritz *et al.*

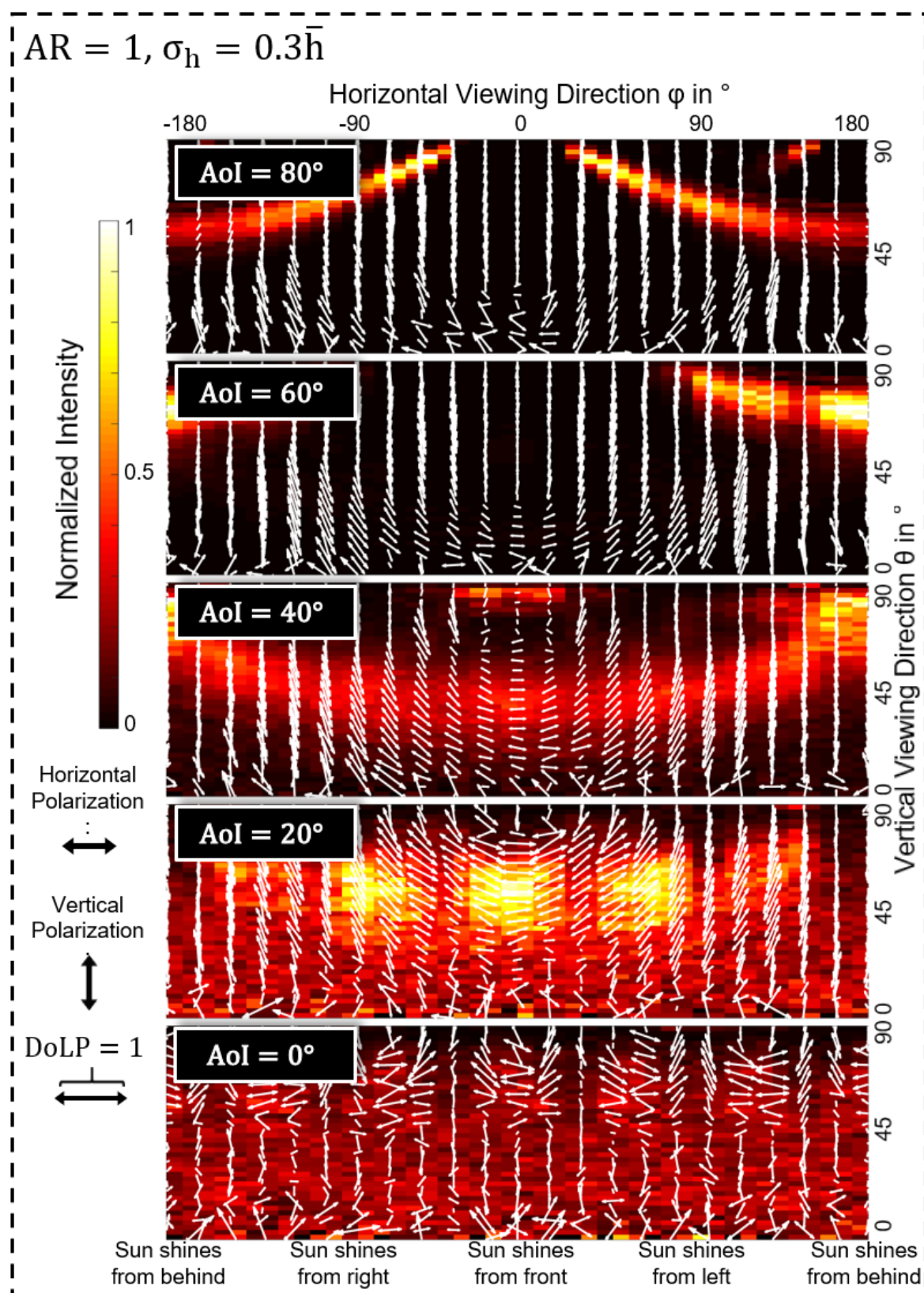


Fig. S10: Simulated farfield intensity, DoLP, and AoP distribution of densely packed micro-cones with an AR of 1 and maximum disorder in height. Reprinted with permission from (the supplementary materials of) the aforementioned *PLOS ONE* publication [1], © 2020 Fritz *et al.*

---

## List of Figures

---

Fig. 1.1:	Recent records for lowest prices achieved for PV-generated electricity, together with a compilation of projections for the future development of the globally installed cumulative capacity.....	10
Fig. 2.1:	Basic opto-electrical properties of solar cells.....	17
Fig. 2.2:	Schematic depictions of a selection of high efficiency c-Si solar cell architectures. ....	19
Fig. 2.3:	Intrinsic loss mechanisms in single-junction solar cells.....	22
Fig. 2.4:	Intrinsic loss mechanisms in multi-junction solar cells.....	24
Fig. 2.5:	Incidence angle distribution and direct solar irradiance for a solar module tilted 30° southwards,.....	26
Fig. 2.6:	Schematic illustration of the definitions of the (real) angles $\theta_i$ and $\Psi_i$ for describing inhomogeneous plane waves.....	31
Fig. 2.7:	Working principle of single-layer antireflective coatings.....	36
Fig. 2.8:	SEM micrographs of various thin-film antireflective coatings .....	41
Fig. 2.9:	Light transmission spectra through planar glass (with $n = 1.52$ ) coated on both sides with different thin-film antireflective layers .....	42
Fig. 2.10:	Comparison of the reflectance spectra a single-layer $\text{TiO}_2$ , double-layer $\text{SiO}_2/\text{TiO}_2$ , and a $\text{SiO}_2/\text{SiO}_2\text{-TiO}_2/\text{TiO}_2$ triple-layer antireflective coating on Si solar cells .....	45
Fig. 2.11:	Calculated reflectance spectra of different gradient-index antireflective coatings. ....	47
Fig. 2.12:	Schematic illustration of the working principle of subwavelength nanostructures as antireflective layers. ....	49
Fig. 2.13:	Optical properties of moth-eye-like antireflective nanostructures. ....	50
Fig. 2.14:	Schematic depiction of the working principle of antireflective layers based on microstructured surfaces. ....	51
Fig. 2.15:	AoI-dependent reflectance of a selection of microtextured surfaces based on cones, pyramids, inverted cones, and inverted pyramids.....	52
Fig. 2.16:	Anisotropic etching of Si for producing random micro-pyramids for antireflection and light-trapping. ....	54

## LIST OF FIGURES

---

Fig. 2.17: SEM micrographs of Si wafers with different microstructured surfaces:.....	55
Fig. 2.18: Combined antireflection and radiative cooling effect of random micro-pyramids. ....	58
Fig. 2.19: Schematic illustration of two strategies to utilize nighttime radiative cooling. ....	59
Fig. 2.20: Schematic illustration of normally incident light propagating through a planar multilayer system. ....	61
Fig. 2.21: Schematic illustration of light propagation through a planar material boundary under oblique incidence for p-polarized and s-polarized light.....	63
Fig. 2.22: Ray propagation in materials with gradually changing refractive indices.....	66
Fig. 3.1: Structural vs. pigment-based coloration in butterflies.....	73
Fig. 3.2: Structural coloration of a <i>Callophrys rubi</i> butterfly, also known as the green hairstreak. ....	75
Fig. 3.3: Exceptionally white scarab beetle <i>Cyphochilus insulanus</i> . ....	76
Fig. 3.4: Scarab beetles with metal-like structural coloration. ....	78
Fig. 3.5: Highly transparent wings of the glasswing butterfly ( <i>Greta oto</i> ). ....	80
Fig. 3.6: Highly transparent cicada ( <i>Megapomponia intermedia</i> ) wings. ....	81
Fig. 3.7: Highly transparent wings of hawkmoths ( <i>Cephonodes hylas</i> ).....	82
Fig. 3.8: SEM images of a compound eye of a silkworm <i>Philosamia cynthia ricini</i> at different magnifications. ....	83
Fig. 3.9: 3D morphology of plant epidermal cells (without the cuticula). ....	85
Fig. 3.10: Schematic cross-sectional depiction of possible shapes of plant epidermal cells .....	86
Fig. 3.11: SEM micrographs of four exemplary leaf surfaces showing different types of epicuticular waxes.....	87
Fig. 3.12: SEM micrographs of epidermal cells covered with cuticular nanofolds. ....	87
Fig. 3.13: Cuticular surface textures caused by sub-cuticular insertions. ....	88
Fig. 3.14: Basic varieties of hierarchically structured plant surfaces, .....	88
Fig. 3.15: Iridescent tulip variety <i>Queen of the Night</i> .....	90

---

Fig. 3.16: Structurally colored fruits of <i>Pollia condensata</i> and <i>Margaritaria nobilis</i> . .....	91
Fig. 3.17: Overview of the various functional structures typically found on the surfaces of plants from different habitats. ....	93
Fig. 3.18: Influence of epidermal cell shape on the flower color saturation in <i>Antirrhinum majus</i> petals. ....	95
Fig. 4.1: Definition of the (water) contact angle. Both an example for a hydrophobic surface (left schematic) and a hydrophilic surface (right schematic). ....	98
Fig. 4.2: Schematics displaying the three classical wetting regimes of rough surfaces. ....	99
Fig. 4.3: Schematic depiction of the nine different types of wetting regimes of hierarchically textured surfaces. ....	100
Fig. 4.4: SEM images of a lotus leaf's self-cleaning surface structure ( <i>Nelumbo nucifera</i> ) leaf under three different magnification factors. ....	101
Fig. 4.5: Schematic showing which combinations of leaf epidermal cell microstructure and cuticular wax coating lead to different wetting states, covering the whole spectrum from superhydrophilic to superhydrophobic plant leaves. ....	102
Fig. 4.6: Overview of which parameters of a PV installation influence the accumulation of aeolian dust particles on solar modules. ....	104
Fig. 4.7: Photographic illustration of dust accumulation on PV modules. ....	105
Fig. 4.8: Overview of worldwide soiling rates and cleaning costs sorted by country. ....	107
Fig. 4.9: Mitigation of PV module soiling. ....	108
Fig. 4.10: Schematic illustration of the main forces acting on a particle during self-cleaning for a hydrophilic (left) and a hydrophobic (right) surface. ....	110
Fig. 5.1: Replication of a monarch butterfly wing via Nano4Bio. ....	112
Fig. 5.2: Replication of a blowfly cornea via Nano4Bio. ....	113
Fig. 5.3: Soft-imprint replication of plant surfaces. Top: Schematic depiction of soft-imprint replication of the rose petal surface texture into a transparent, UV-curing resist material. ....	116
Fig. 5.4: Moth-eye-mimicking antireflective structure (AAO-based). ....	120

---

## LIST OF FIGURES

---

Fig. 5.5: Moth-eye-mimicking antireflective structure (nanoparticle-assembly-based).....	122
Fig. 5.6: Antireflective coating inspired by leafhopper brochosomes. ....	123
Fig. 5.7: Surface structures of water fern, water lettuce, and bioinspired nanofur.....	124
Fig. 5.8: Fabrication process for a modulated surface texture (MST) in Si. ....	125
Fig. 5.9: Multi-step mild anodization and etching pore widening (MS-MA-EW) process enabling the fabrication of plant-mimicking hierarchical surface structures.....	126
Fig. 5.10: Polymeric micro-cones induced via pulsed laser irradiation. ....	128
Fig. 5.11: SEM micrographs of the hierarchical surface structure of a rose petal (variety: Red Naomi) NOA68 soft-imprint replica.....	131
Fig. 5.12: Measured reflectance spectra (specular + diffuse) of CIGS solar cells (2.5 cm × 2.5 cm) with different cover layer configurations.....	132
Fig. 5.13: Photographs of CIGS solar cells (optical dummies) with various antireflective coatings. ....	133
Fig. 6.1: Exemplary non-disordered microstructure models assembled from various basic geometries. ....	139
Fig. 6.2: Schematic top-view depictions of microstructures comprised of hexagonally arranged cones in two distinctive configurations.....	141
Fig. 6.3: Schematic top-view depictions of two highly ordered cone-based microstructures in full tiling configurations. ....	142
Fig. 6.4: Schematic depiction of the main steps of the 3D microtexture modeling routine that was mainly developed for ray-tracing-based studies of disordered microstructured surfaces. ....	144
Fig. 6.5: Schematic cross-sectional-views of cone-based microstructure models.....	146
Fig. 6.6: Comparison of the disordered microstructure found on rose petals and a generic LightTools microtexture model with disorder in cone height and positioning.....	148
Fig. 6.7: Schematic illustration of the issues related to the tilting of micro-cones.....	149
Fig. 6.8: Schematic illustration of the modeling procedure for cone-based microstructures in case of $\sigma_t > 0$ . ....	150

---

Fig. 6.9: Screenshots of exemplary cone-based microstructures in LightTools .....	151
Fig. 6.10: Ray-tracing analysis of the influence of structural disorder on the reflection properties of microstructures comprised of cones, plotted as a function of the incidence angle. ....	156
Fig. 6.11: Ray-tracing results for the angular distribution of in-coupled light for AR = 1 cones (full tiling) with different types of disorder at normal incidence of light. ....	157
Fig. 6.12: Ray-tracing results for the angular distribution of in-coupled light for AR = 1 cones (full tiling) with different types of disorder after integrating over the azimuth angle $\phi$ . ....	159
Fig. 6.13: Simulation results for the reflection losses of CIGS thin-film solar cells with various top-layer configurations .....	160
Fig. 7.1: SEM image of a natural rose petal surface with shrunken epidermal cells. Such shrinkage occurs when natural rose petals are exposed to low-pressure conditions. ....	165
Fig. 7.2: Large-area Ni mold insert fabrication for upscaled rose petal replication. ....	166
Fig. 7.3: Large-area Ni mold inserts A) BF05 and B) BF06 for upscaled rose petal replication via hot-embossing of polymeric foils. ....	168
Fig. 7.4: Photographs of large-area Ni mold insert BF10 at various stages during its fabrication. ....	169
Fig. 7.5: Ni mold insert BF10 with a total structured area of 12.5 cm $\times$ 10.0 cm. ....	170
Fig. 7.6: SEM images comparing the topographies of a fresh rose petal (top), a soft-imprint NOA68 first-generation replica (middle), and a hot-embossed PMMA second-generation replica (bottom). ....	173
Fig. 7.7: Photographs of the large-area Ni mold insert BF10 mounted to the bottom side of the hot-embossing setup and at different stages of the embossing routine. ....	174
Fig. 7.8: Top-view SEM micrographs of the stitching between neighboring patches of a large-area rose petal replica, fabricated by hot-embossing PMMA with the mold insert BF10. ....	174
Fig. 8.1: Schematic illustration of spectrally resolved reflectance measurements using an integrating sphere. ....	178

---

Fig. 8.2:	Light-harvesting properties of CIGS thin-film solar cells with hot-embossed (using mold insert BF05) rose petal textured PC, PMMA and FEP cover layers, as well as corresponding planar reference foils. ....	181
Fig. 8.3:	Water droplets on planar and rose petal textured PMMA, PC, and FEP, fabricated via hot-embossing with Ni mold insert BF05. ....	183
Fig. 8.4:	High-speed camera analysis of 5 $\mu$ l water droplets falling onto 30° tilted planar (top row) and rose petal textured (bottom row) FEP foils, fabricated via hot-embossing with Ni mold insert BF05.....	184
Fig. 8.5:	Opto-electrical properties of high-performance CIGS single solar cells with various cover layer configurations.....	188
Fig. 8.6:	Planar and rose petal textured PMMA laminated onto CIGS solar modules.....	189
Fig. 9.1:	Photograph of the setup developed for outdoor performance monitoring of PV modules.....	193
Fig. 9.2:	Photographs of the commercial Si solar modules used in the outdoor performance monitoring experiments. ....	194
Fig. 9.3:	Time-resolved photocurrent of a pristine Si module and one with a rose petal textured PMMA cover layer .....	196
Fig. 9.4:	Daily relative gain in device performance for A) CIGS and B) Si solar modules with and without rose petal textured PMMA cover layers under outdoor conditions and for different module orientations.....	198
Fig. 9.5:	SEM micrographs of rose petal textured PMMA after six months (Nov 2019 - May 2020) of continuous exposure to the outdoor conditions in Karlsruhe (Germany) .....	200
Fig. 9.6:	Relative contributions of different AoIs (of the direct sunlight component) to the total generated power for rose petal textured Si module 3 at each day of performance monitoring. ....	202
Fig. 9.7:	SEM micrographs of (cleaned) rose petal textured PMMA after various accelerated aging and abrasion tests. ....	205
Fig. 9.8:	SEM micrographs of rose petal textured PMMA after sand tickling with 10 kg of A) Sahara desert sand as well as B) quartz sand.....	206
Fig. 9.9:	Measured (surface) reflectance spectra of rose petal textured PMMA after various durability tests under normal and oblique light incidence under 80°.....	207

---

Fig. 9.10: SEM micrographs of rose petal textured PMMA after an abrasive sandblasting test .....	207
Fig. 10.1: Schematic illustration highlighting that PV modules equipped with a planar cover layer act as polarization traps for polarotactic insects if the panel-reflected light is (partially or completely) horizontally polarized, whereas an appropriate surface (micro-) structure of the cover layer not only improves sunlight-harvesting but simultaneously also strongly reduces PLP. ....	211
Fig. 10.2: Photographs of the experimental sites for the field experiments with mayflies and horseflies, together with the respective results, summarized as the average daily numbers of landings and including the results of the Wilcoxon signed-rank test.....	213
Fig. 10.3: Photographs of the three test surfaces used in the field experiments with horseflies and corresponding patterns of the DoLP and AoP, measured with imaging polarimetry in the blue (450 nm) spectral region.....	216
Fig. 10.4: Photographs and patterns of the DoLP and AoP of the three test surfaces as utilized in the field experiments with mayflies and measured with imaging polarimetry at 450 nm and a tilt of the camera's optical axis of 55°.....	217
Fig. 10.5: Photographs and patterns of the DoLP and AoP of the three test surfaces in the field experiments with mayflies measured with imaging polarimetry (at 450 nm).....	219
Fig. 10.6: Illustration of a ray-tracing-based simulation approach for studying the polarization properties of light reflected from disordered microstructures. ....	221
Fig. 10.7: Simulated farfield intensity, DoLP, and AoP distribution of densely packed micro-cones with an AR of 0.6 and no disorder.....	223
Fig. 10.8: Simulated farfield intensity, DoLP, and AoP distribution of densely packed micro-cones with an AR of 0.6 and maximum disorder in positioning.....	224
Fig. 10.9: Simulated farfield intensity, DoLP, and AoP distribution of densely packed micro-cones with an AR of 0.6 and maximum disorder in height.....	225
Fig. 10.10: Numerical assessment of the influence of structural disorder on the polarized light pollution caused by microtextured surfaces.....	227

## Supplementary Information

Fig. S1:	SEM micrographs of hot-embossed rose petal replicas, fabricated by using mold insert BF05. ....	236
Fig. S2:	SEM images of the commercial microlens array foil used as a CIGS solar module cover layer, resulting in AoP and DoLP patterns very similar to polymeric rose petal surface structure replicas.....	236
Fig. S3:	Bar chart illustrating the relative contributions of different AoIs (of the direct sunlight component) to the total power generated for each individual day for rose petal textured Si module 1.....	237
Fig. S4:	Photographs and patterns of the degree and angle of polarization of the rose petal replica and the planar PMMA reference layer used in the field experiments with mayflies and horseflies for four different orientations of the rose petal replica. ....	238
Fig. S5:	Simulated farfield intensity, DoLP, and AoP distribution of densely packed micro-cones with an AR of 0.3 and no disorder.....	239
Fig. S6:	Simulated farfield intensity, DoLP, and AoP distribution of densely packed micro-cones with an AR of 0.3 and maximum disorder in positioning.....	240
Fig. S7:	Simulated farfield intensity, DoLP, and AoP distribution of densely packed micro-cones with an AR of 0.3 and maximum disorder in height.....	241
Fig. S8:	Simulated farfield intensity, DoLP, and AoP distribution of densely packed micro-cones with an AR of 1 and no disorder.....	242
Fig. S9:	Simulated farfield intensity, DoLP, and AoP distribution of densely packed micro-cones with an AR of 1 and maximum disorder in positioning.....	243
Fig. S10:	Simulated farfield intensity, DoLP, and AoP distribution of densely packed micro-cones with an AR of 1 and maximum disorder in height.....	244

---

## List of Tables

---

Table 5.1: Overview of selected studies that are focused on the optical properties of leaf- and petal-surface-texture replicas.....	135
Table 7.1: Basic information about the polymer foils that were deployed for the fabrication of large-area rose petal replication via hot-embossing. ....	168
Table 7.2: Overview of the three polymeric materials employed for fabricating large-area rose petal replicas through static hot-embossing-lithography. ....	171
Table 7.3: Parameters for the fabrication of large-area rose petal replication via hot-embossing.....	172
Table 8.1: Results of the static contact angle measurements for planar and rose petal textured PMMA, PC, and FEP. ....	183
Table 8.2: Changes in PCE, $I_{SC}$ , $V_{OC}$ , and FF caused by various light-harvesting layers on top of highly efficient CIGS solar cells relative to the respective uncoated devices.....	186
Table 9.1: Outdoor performance monitoring of CIGS and Si solar modules, performed in Karlsruhe, Germany.....	199

### Supplementary Information

Table S1: Test strip XLS1057-3, pristine.....	233
Table S2: Test strip XLS1057-3 + 105 nm $MgF_2$ . ....	233
Table S3: Test strip XLS1057-3, relative enhancement due to $MgF_2$ .....	233
Table S4: Test strip XLS1058-3, pristine.....	233
Table S5: Test strip XLS1058-3 + NOA88 + rose petal textured PC: .....	234
Table S6: Test strip XLS1058-3 + NOA88 + rose petal textured PC + 105 nm $MgF_2$ .....	234
Table S7: Test strip XLS1058-3, relative enhancement due to rose petal textured PC.....	234
Table S8: Test strip XLS1058-3, relative enhancement due to rose petal textured PC + 105 nm $MgF_2$ .....	234

## LIST OF TABLES

---

Table S9: Test strip 9680524, pristine.....	235
Table S10:Test strip 9680524 + NOA88 + rose petal textured PMMA.....	235
Table S11:Test strip 9680524, relative enhancement due to rose petal textured PMMA.....	235
Table S12:Test strip 9680575, pristine.....	235
Table S13:Test strip 9680575 + NOA88 + rose petal textured PMMA.....	235
Table S14:Test strip 9680575, relative enhancement due to rose petal textured PMMA.....	236

---

## List of Abbreviations

---

Ag	silver
Al	aluminum
ALD	atomic layer deposition
AM1.5G	air mass 1.5 global
AoI	angle of incidence
AoP	angle of polarization
AR	aspect ratio
As	arsenic
Au	gold
BAPV	building-attached/applied photovoltaics
BIPV	building-integrated-photovoltaics
BSF	back surface field
Cd	cadmium
CIGS	copper indium gallium diselenide, $\text{Cu}(\text{In}, \text{Ga})\text{Se}_2$
Cr	chromium
CR39	allyl diglycol carbonate
Cu	copper
DH	damp-heat
DLW	direct laser writing
DoLP	degree of linear polarization
DPMA	Deutsches Patent- und Markenamt
EQE	external quantum efficiency
F	fluorine
FDTD	finite-difference time-domain
FEP	fluorinated ethylene propylene
FF	fill factor
Ga	gallium
Ge	germanium
H	hydrogen
IMT	Institute of Microstructure Technology
In	indium

## LIST OF ABBREVIATIONS

---

$I_{sc}$	short circuit current
IV	current-voltage
$J_{sc}$	short-circuit current density
K	potassium
KIT	Karlsruhe Institute of Technology
LEC	light-emitting electrochemical cell
LED	light-emitting diode
LIPSS	laser-induced periodic surface structure
LTI	Light Technology Institute
Mg	magnesium
MLA	micro-lens array
Mo	molybdenum
MPP	maximum power point
MZE	Materialwissenschaftliches Zentrum für Energiesysteme
$\mu c$	microcrystalline
Na	sodium
Ni	nickel
NIL	nanoimprint lithography
NIR	near-infrared
NOA	Norland Optical Adhesive
O	oxygen
PC	polycarbonate
PCE	power conversion efficiency
PDMS	polydimethylsiloxane
PET	polyethylene terephthalate
PFPE	perfluoropolyether
PI	polyimide
PLP	polarized light pollution
PMMA	polymethyl methacrylate
PPA	power purchase agreement
PS	polystyrene
PTFE	polytetrafluorethylen
PUA	polyurethane acrylate
PV	photovoltaic(s)
PVA	polyvinyl acetate

## LIST OF ABBREVIATIONS

---

PVC		polyvinyl chloride
PVD		physical vapor deposition
PVOH		polyvinyl alcohol
SCUT	South China University of Technology	
Se		selenium
SEM		scanning electron microscopy
Si		silicon
STC		standard test conditions
TC		temperature-cycle
Te		tellurium
Ti		titanium
TIR		total internal reflection
TMM		transfer matrix method
UV		ultraviolet
Vis		visible (light)
V <sub>OC</sub>		open-circuit voltage
W <sub>p</sub>		watt-peak
Zn		zinc
ZSW	Zentrum für Sonnenenergie- und Wasserstoff-Forschung Baden-Württemberg	

---



---

## References

---

- [1] **Fritz, B., Horváth, G., Hünig, R., Pereszlényi, Á., Egri, Á., Guttman, M., Schneider, M., Lemmer, U., Kriska, G. and Gomard, G. (2020)** ‘Bioreplicated coatings for photovoltaic solar panels nearly eliminate light pollution that harms polarotactic insects’, *PLOS ONE* **15**(12): e0243296. <https://doi.org/10.1371/journal.pone.0243296>
- [2] **Horváth, G., Pereszlényi, Á., Egri, A., Fritz, B., Guttman, M., Lemmer, U., Gomard, G. and Kriska, G. (2020)** ‘Horsefly reactions to black surfaces: attractiveness to male and female tabanids versus surface tilt angle and temperature’, *Parasitology Research* **119**(8): 2399-2409. <https://doi.org/10.1007/s00436-020-06702-7>
- [3] **Fritz, B., Hünig, R., Guttman, M., Schneider, M., Reza, K. S., Salomon, O., Jackson, P., Powalla, M., Lemmer, U. and Gomard, G. (2020)** ‘Upscaling the fabrication routine of bioreplicated rose petal light harvesting layers for photovoltaic modules’, *Solar Energy* **201**: 666-673. <https://doi.org/10.1016/j.solener.2020.03.020>
- [4] **Jürgensen, N., Fritz, B., Mertens, A., Tisserant, J.-N., Kolle, M., Gomard, G. and Hernandez-Sosa, G. (2020)** ‘A Single-Step Hot Embossing Process for Integration of Microlens Arrays in Biodegradable Substrates for Improved Light Extraction of Light-Emitting Devices’, *Advanced Materials Technologies*: 1900933. <https://doi.org/10.1002/admt.201900933>
- [5] **Chen, J., Fritz, B., Liang, G., Ding, X., Lemmer, U. and Gomard, G. (2019)** ‘Microlens arrays with adjustable aspect ratio fabricated by electrowetting and their application to correlated color temperature tunable light-emitting diodes’, *Optics Express* **27**(4): A25-A38. <https://doi.org/10.1364/OE.27.000A25>
- [6] **Yu, S., Fritz, B., Johnsen, S., Busko, D., Richards, B. S., Hippler, M., Wiegand, G., Tang, Y., Li, Z., Lemmer, U., Hölscher, H. and Gomard, G. (2019)** ‘Enhanced Photoluminescence in Quantum Dots–Porous Polymer Hybrid Films Fabricated by Microcellular Foaming’, *Advanced Optical Materials* **7**(12): 1900223. <https://doi.org/10.1002/adom.201900223>

- [7] **Schumann, M. F., Fritz, B., Eckstein, R., Lemmer, U., Gomard, G. and Wegener, M. (2018)** 'Cloaking of metal grid electrodes on Lambertian emitters by free-form refractive surfaces', *Optics Letters* **43**(3): 527-530. <https://doi.org/10.1364/OL.43.000527>
- [8] **Vüllers, F., Fritz, B., Roslizar, A., Striegel, A., Guttman, M., Richards, B. S., Hölscher, H., Gomard, G., Klampaffis, E. and Kavalenka, M. N. (2018)** 'Self-Cleaning Microcavity Array for Photovoltaic Modules', *ACS Applied Materials & Interfaces* **10**(3): 2929-2936. <https://doi.org/10.1021/acsami.7b15579>
- [9] **Schmager, R., Fritz, B., Hünig, R., Ding, K., Lemmer, U., Richards, B. S., Gomard, G. and Paetzold, U. W. (2017)** 'Texture of the Viola Flower for Light Harvesting in Photovoltaics', *ACS Photonics* **4**(11): 2687-2692. <https://doi.org/10.1021/acsphotonics.7b01153>
- [10] **Fritz, B., Hünig, R., Schmager, R., Hetterich, M., Lemmer, U. and Gomard, G. (2017)** 'Assessing the influence of structural disorder on the plant epidermal cells' optical properties: a numerical analysis', *Bioinspiration & Biomimetics* **12**(3): 36011. <https://doi.org/10.1088/1748-3190/aa6c46>
- [11] **Yu, S., Fritz, B., Theobald, D., Johnsen, S., Busko, D., Richards, B. S., Hippler, M., Wiegand, G., Tang, Y., Li, Z., Lemmer, U., Hölscher, H. and Gomard, G. (2019)** 'Foamed polymer/quantum dots composite films with enhanced photoluminescence efficiency', *Proceedings of OSA Optical Devices and Materials for Solar Energy and Solid-state Lighting: PT2C.4*. <https://doi.org/10.1364/PVLED.2019.PT2C.4>
- [12] **Yu, S., Fritz, B., Theobald, D., Wu, K., Johnsen, S., Busko, D., Richards, B. S., Wiegand, G., Tang, Y., Li, Z., Lemmer, U., Holscher, H. and Gomard, G. (2019)** 'Enhanced color conversion of quantum dots - polymer hybrid films in light emitting diodes', *Proceedings of ICEPT Hong Kong 2019*. <https://doi.org/10.1109/ICEPT47577.2019.245231>
- [13] **Fritz, B., Guttman, M., Soler, P. C., Roslizar, A., Langenhorst, M., Schneider, M., Paetzold, U. W., Richards, B. S., Lemmer, U., Hünig, R. and Gomard, G. (2018)** 'Towards mass fabrication of hot embossed plant surface texture replicas as photovoltaic cover layers', *Proceedings of SPIE* **10730**: 107300J. <https://doi.org/10.1117/12.2320555>
- [14] **Fritz, B., Guttman, M., Gomard, G. and Hünig, R. (2020)** 'Hot embossed large-area plant microstructures for improved photovoltaic light

- harvesting', *WOMAG* (Band 9). [https://www.wotech-technical-media.de/womag/ausgabe/2020/05/20\\_guttmann\\_struktur\\_05j2020/20\\_guttmann\\_struktur\\_05j2020.php](https://www.wotech-technical-media.de/womag/ausgabe/2020/05/20_guttmann_struktur_05j2020/20_guttmann_struktur_05j2020.php)
- [15] **Bioinspiration & Biomimetics (2018)** 'Highlights of 2017' [accessed 30 November 2020]. <https://iopscience.iop.org/journal/1748-3190/page/Highlights-of-2017>
- [16] **Creutzig, F., Agoston, P., Goldschmidt, J. C., Luderer, G., Nemet, G. and Pietzcker, R. C. (2017)** 'The underestimated potential of solar energy to mitigate climate change', *Nature Energy* **2**(9). <https://doi.org/10.1038/nenergy.2017.140>
- [17] **Bloomberg New Energy Finance (16 January 2019)** 'Clean Energy Investment Exceeded \$300 Billion Once Again in 2018'. <https://about.bnef.com/blog/clean-energy-investment-exceeded-300-billion-2018/> [accessed 25 March 2021]
- [18] **Green, M. A. (2019)** 'Photovoltaic technology and visions for the future', *Progress in Energy* **1**(1): 13001. <https://doi.org/10.1088/2516-1083/ab0fa8>
- [19] **Renewable Energy World (2020)** '142 GW of global solar capacity will be added in 2020, says IHS' [accessed 25 March 2021]. <https://www.renewableenergyworld.com/solar/142-gw-of-solar-capacity-will-be-added-to-the-global-market-in-2020-says-ihs/#gref>
- [20] **Deign, J. (2018)** 'Xcel Attracts 'Unprecedented' Low Prices for Solar and Wind Paired With Storage' [accessed 25 March 2021]. <https://www.greentechmedia.com/articles/read/record-low-solar-plus-storage-price-in-xcel-solicitation>
- [21] **Shell Global (2018-2021)** 'The *Sky* Scenario' [accessed 25 March 2021]. <https://www.shell.com/energy-and-innovation/the-energy-future/scenarios/shell-scenario-sky.html>
- [22] **Yang, L., Gao, X., Lv, F., Hui, X., Ma, L. and Hou, X. (2017)** 'Study on the local climatic effects of large photovoltaic solar farms in desert areas', *Solar Energy* **144**: 244-253. <https://doi.org/10.1016/j.solener.2017.01.015>
- [23] **Grippo, M., Hayse, J. W. and O'Connor, B. L. (2015)** 'Solar energy development and aquatic ecosystems in the southwestern United States: potential impacts, mitigation, and research needs', *Environmental Management* **55**(1): 244-256. <https://doi.org/10.1007/s00267-014-0384-x>

- [24] **Turney, D. and Fthenakis, V. (2011)** 'Environmental impacts from the installation and operation of large-scale solar power plants', *Renewable and Sustainable Energy Reviews* **15**(6): 3261-3270. <https://doi.org/10.1016/j.rser.2011.04.023>
- [25] **Katzner, T., Johnson, J. A., Evans, D. M., Garner, T. W. J., Gompper, M. E., Altwegg, R., Branch, T. A., Gordon, I. J. and Pettorelli, N. (2013)** 'Challenges and opportunities for animal conservation from renewable energy development', *Animal Conservation* **16**(4): 367-369. <https://doi.org/10.1111/acv.12067>
- [26] **Hernandez, R. R., Easter, S. B., Murphy-Mariscal, M. L., Maestre, F. T., Tavassoli, M., Allen, E. B., Barrows, C. W., Belnap, J., Ochoa-Hueso, R., Ravi, S. and Allen, M. F. (2014)** 'Environmental impacts of utility-scale solar energy', *Renewable and Sustainable Energy Reviews* **29**: 766-779. <https://doi.org/10.1016/j.rser.2013.08.041>
- [27] **Walston, L. J., Rollins, K. E., LaGory, K. E., Smith, K. P. and Meyers, S. A. (2016)** 'A preliminary assessment of avian mortality at utility-scale solar energy facilities in the United States', *Renewable Energy* **92**: 405-414. <https://doi.org/10.1016/j.renene.2016.02.041>
- [28] **Gasparatos, A., Doll, C. N., Esteban, M., Ahmed, A. and Olang, T. A. (2017)** 'Renewable energy and biodiversity: Implications for transitioning to a Green Economy', *Renewable and Sustainable Energy Reviews* **70**: 161-184. <https://doi.org/10.1016/j.rser.2016.08.030>
- [29] **Hochkirch, A. (2016)** 'The insect crisis we can't ignore', *Nature* **539**(7628): 141. <https://doi.org/10.1038/539141a>
- [30] **Hallmann, C. A., Sorg, M., Jongejans, E., Siepel, H., Hofland, N., Schwan, H., Stenmans, W., Müller, A., Sumser, H., Hörren, T., Goulson, D. and Kroon, H. de (2017)** 'More than 75 percent decline over 27 years in total flying insect biomass in protected areas', *PLOS ONE* **12**(10): e0185809. <https://doi.org/10.1371/journal.pone.0185809>
- [31] **Forister, M. L., Pelton, E. M. and Black, S. H. (2019)** 'Declines in insect abundance and diversity: We know enough to act now', *Conservation Science and Practice* **1**(8). <https://doi.org/10.1111/csp2.80>
- [32] **Sánchez-Bayo, F. and Wyckhuys, K. A. (2019)** 'Worldwide decline of the entomofauna: A review of its drivers', *Biological Conservation* **232**: 8-27. <https://doi.org/10.1016/j.biocon.2019.01.020>

- 
- [33] **Gong, J., Sumathy, K., Qiao, Q. and Zhou, Z. (2017)** 'Review on dye-sensitized solar cells (DSSCs): Advanced techniques and research trends', *Renewable and Sustainable Energy Reviews* **68**: 234-246. <https://doi.org/10.1016/j.rser.2016.09.097>
- [34] **Schmager, R. (2020)** 'Advanced light management concepts for perovskite photovoltaics'. *Dissertation*. Karlsruhe Institute of Technology. <https://doi.org/10.5445/IR/1000119647>
- [35] **Smith, W. (1873)** 'Effect of Light on Selenium During the Passage of An Electric Current \*', *Nature* **7**(173): 303. <https://doi.org/10.1038/007303e0>
- [36] **Adams, W. G. and Day, R. E. (1877)** 'V. The action of light on selenium', *Proceedings of the Royal Society of London* **25**(171-178): 113-117. <https://doi.org/10.1098/rspl.1876.0024>
- [37] **Fritts, C. E. (1883)** 'On a new form of selenium cell, and some electrical discoveries made by its use', *American Journal of Science* **s3-26**(156): 465-472. <https://doi.org/10.2475/ajs.s3-26.156.465>
- [38] **Perlin, J. (2004)** 'The Silicon Solar Cell Turns 50' [accessed 20 January 2021]. <https://www.nrel.gov/docs/fy04osti/33947.pdf>
- [39] **Yoshikawa, K., Kawasaki, H., Yoshida, W., Irie, T., Konishi, K., Nakano, K., Uto, T., Adachi, D., Kanematsu, M., Uzu, H. and Yamamoto, K. (2017)** 'Silicon heterojunction solar cell with interdigitated back contacts for a photoconversion efficiency over 26%', *Nature Energy* **2**(5): 17032. <https://doi.org/10.1038/nenergy.2017.32>
- [40] **Sunpower** 'X-series solar panels' [accessed 20 January 2021]. <https://us.sunpower.com/solar-panels-technology/x-series-solar-panels>
- [41] **Hadar, I., Song, T.-B., Ke, W. and Kanatzidis, M. G. (2019)** 'Modern Processing and Insights on Selenium Solar Cells: The World's First Photovoltaic Device', *Advanced Energy Materials* **9**(16): 1802766. <https://doi.org/10.1002/aenm.201802766>
- [42] **Green, M., Dunlop, E., Hohl-Ebinger, J., Yoshita, M., Kopidakis, N. and Hao, X. (2021)** 'Solar cell efficiency tables (version 57)', *Progress in Photovoltaics: Research and Applications* **29**(1): 3-15. <https://doi.org/10.1002/pip.3371>
- [43] **Fraunhofer ISE (2020)** 'Photovoltaics Report 2020' [accessed 25 January 2021]. <https://www.ise.fraunhofer.de/de/veroeffentlichungen/studien/photovoltaics-report.html>
-

- [44] **Nayak, P. K., Mahesh, S., Snaith, H. J. and Cahen, D. (2019)** 'Photovoltaic solar cell technologies: analysing the state of the art', *Nature Reviews Materials* **4**(4): 269-285. <https://doi.org/10.1038/s41578-019-0097-0>
- [45] **Hirst, L. C. and Ekins-Daukes, N. J. (2011)** 'Fundamental losses in solar cells', *Progress in Photovoltaics: Research and Applications* **19**(3): 286-293. <https://doi.org/10.1002/pip.1024>
- [46] **Markvart, T. (2008)** 'Solar cell as a heat engine: energy-entropy analysis of photovoltaic conversion', *Physica Status Solidi A* **205**(12): 2752-2756. <https://doi.org/10.1002/pssa.200880460>
- [47] **Landsberg, P. T. and Baruch, P. (1989)** 'The thermodynamics of the conversion of radiation energy for photovoltaics', *Journal of Physics A: Mathematical and General* **22**(11): 1911-1926. <https://doi.org/10.1088/0305-4470/22/11/028>
- [48] **Kirchhoff, G. (1859)** 'Über den Zusammenhang zwischen Emission und Absorption von Licht und Wärme', *Monatsberichte der Königlich Preussische Akademie des Wissenschaften zu Berlin*: 783-787
- [49] **Kirchhoff, G. (1859)** 'Über den Zusammenhang zwischen Emissionsvermögen und dem Absorptionsvermögen der Körper für Wärme und Licht', *Monatsberichte der Königlich Preussische Akademie des Wissenschaften zu Berlin* **1**(2)
- [50] **Shockley, W. and Read, W. T. (1952)** 'Statistics of the Recombinations of Holes and Electrons', *Physical Review* **87**(5): 835-842. <https://doi.org/10.1103/PhysRev.87.835>
- [51] **Hall, R. N. (1952)** 'Electron-Hole Recombination in Germanium', *Physical Review* **87**(2): 387. <https://doi.org/10.1103/PhysRev.87.387>
- [52] **Auger, P. (1923)** 'Sur les rayons  $\beta$  secondaires produits dans un gaz par des rayons X', *Comptes rendus de l'Académie des sciences* **177**: 169. <https://ci.nii.ac.jp/naid/10003469554/>
- [53] **Kosyachenko, L. A., Lytvynenko, V. Y. and Maslyanchuk, O. L. (2016)** 'Quantitative analysis of optical and recombination losses in Cu(In,Ga)Se<sub>2</sub> thin-film solar cells', *Semiconductors* **50**(4): 508-516. <https://doi.org/10.1134/S1063782616040138>
- [54] **Kosyachenko, L. A., Grushko, E. V. and Mathew, X. (2012)** 'Quantitative assessment of optical losses in thin-film CdS/CdTe solar cells', *Solar Energy*

- 
- Materials and Solar Cells* **96**: 231-237.  
<https://doi.org/10.1016/j.solmat.2011.09.063>
- [55] Nakane, A., Tampo, H., Tamakoshi, M., Fujimoto, S., Kim, K. M., Kim, S., Shibata, H., Niki, S. and Fujiwara, H. (2016) 'Quantitative determination of optical and recombination losses in thin-film photovoltaic devices based on external quantum efficiency analysis', *Journal of Applied Physics* **120**(6): 64505. <https://doi.org/10.1063/1.4960698>
- [56] McIntosh, K. R., Kho, T. C., Fong, K. C., Baker-Finch, S. C., Wan, Y., Zin, N., Franklin, E. T., Wang, D., Abbott, M. D., Grant, N. E., Wang, E., Stocks, M. and Blakers, A. W. (2014) 'Quantifying the Optical Losses in Back-contact Solar Cells', *IEEE 40th Photovoltaic Specialist[s] Conference (PVSC 2014)*. <https://doi.org/10.1109/pvsc.2014.6925360>
- [57] Berginski, M., Hüpkes, J., Gordijn, A., Reetz, W., Wätjen, T., Rech, B. and Wuttig, M. (2008) 'Experimental studies and limitations of the light trapping and optical losses in microcrystalline silicon solar cells', *Solar Energy Materials and Solar Cells* **92**(9): 1037-1042. <https://doi.org/10.1016/j.solmat.2008.03.005>
- [58] Polman, A., Knight, M., Garnett, E. C., Ehrler, B. and Sinke, W. C. (2016) 'Photovoltaic materials: Present efficiencies and future challenges', *Science* **352**(6283): aad4424. <https://doi.org/10.1126/science.aad4424>
- [59] Schmid, M. (2017) 'Review on light management by nanostructures in chalcopyrite solar cells', *Semiconductor Science and Technology* **32**(4): 43003. <https://doi.org/10.1088/1361-6641/aa59ee>
- [60] Ruppel, W. and Wurfel, P. (1980) 'Upper limit for the conversion of solar energy', *IEEE Transactions on Electron Devices* **27**(4): 877-882. <https://doi.org/10.1109/T-ED.1980.19950>
- [61] Shockley, W. and Queisser, H. J. (1961) 'Detailed Balance Limit of Efficiency of p-n Junction Solar Cells', *Journal of Applied Physics* **32**(3): 510-519. <https://doi.org/10.1063/1.1736034>
- [62] Tiedje, T., Yablonovitch, E., Cody, G. D. and Brooks, B. G. (1984) 'Limiting efficiency of silicon solar cells', *IEEE Transactions on Electron Devices* **31**(5): 711-716. <https://doi.org/10.1109/T-ED.1984.21594>
- [63] Rühle, S. (2016) 'Tabulated values of the Shockley–Queisser limit for single junction solar cells', *Solar Energy* **130**: 139-147. <https://doi.org/10.1016/j.solener.2016.02.015>
-

- [64] **Kenning, T. (2018)** 'Alta Devices sets GaAs solar cell efficiency record at 29.1%, joins NASA space station testing' [accessed 25 January 2021]. <https://www.pv-tech.org/news/alta-devices-sets-gaas-solar-cell-efficiency-record-at-29.1-joins-nasa-spac>
- [65] **Endo, T., Reddy, L., Nishikawa, H., Kaneko, S., Nakamura, Y. and Endo, K. (2017)** 'Composite Engineering – Direct Bonding of plastic PET Films by Plasma Irradiation', *Procedia Engineering* **171**: 88-103. <https://doi.org/10.1016/j.proeng.2017.01.315>
- [66] **Ferry, D. K. (2019)** 'In search of a true hot carrier solar cell', *Semiconductor Science and Technology* **34**(4): 44001. <https://doi.org/10.1088/1361-6641/ab0bc3>
- [67] **Nelson, C. A., Monahan, N. R. and Zhu, X.-Y. (2013)** 'Exceeding the Shockley–Queisser limit in solar energy conversion', *Energy & Environmental Science* **6**(12): 3508. <https://doi.org/10.1039/c3ee42098a>
- [68] **Luque, A. and Martí, A. (1997)** 'Increasing the Efficiency of Ideal Solar Cells by Photon Induced Transitions at Intermediate Levels', *Physical Review Letters* **78**(26): 5014-5017. <https://doi.org/10.1103/PhysRevLett.78.5014>
- [69] **Ramiro, I. and Martí, A. (2020)** 'Intermediate band solar cells: Present and future', *Progress in Photovoltaics: Research and Applications*: 1-9. <https://doi.org/10.1002/pip.3351>
- [70] **Snyder, W. C., Wan, Z. and Li, X. (1998)** 'Thermodynamic Constraints on Reflectance Reciprocity and Kirchhoff's Law', *Applied Optics* **37**(16): 3464-3470. <https://doi.org/10.1364/ao.37.003464>
- [71] **Green, M. A. (2012)** 'Time-asymmetric photovoltaics', *Nano Letters* **12**(11): 5985-5988. <https://doi.org/10.1021/nl3034784>
- [72] **Mann, S. A., Grote, R. R., Osgood, R. M., Alù, A. and Garnett, E. C. (2016)** 'Opportunities and Limitations for Nanophotonic Structures To Exceed the Shockley-Queisser Limit', *ACS Nano* **10**(9): 8620-8631. <https://doi.org/10.1021/acsnano.6b03950>
- [73] **Xu, Y., Gong, T. and Munday, J. N. (2015)** 'The generalized Shockley-Queisser limit for nanostructured solar cells', *Scientific Reports* **5**: 13536. <https://doi.org/10.1038/srep13536>
- [74] **Rephaeli, E. and Fan, S. (2009)** 'Absorber and emitter for solar thermophotovoltaic systems to achieve efficiency exceeding the Shockley-

- 
- Queisser limit', *Optics Express* **17**(17): 15145-15159. <https://doi.org/10.1364/oe.17.015145>
- [75] **Wang, Y., Liu, H. and Zhu, J. (2019)** 'Solar thermophotovoltaics: Progress, challenges, and opportunities', *APL Materials* **7**(8): 80906. <https://doi.org/10.1063/1.5114829>
- [76] **Martí, A. and Araújo, G. L. (1996)** 'Limiting efficiencies for photovoltaic energy conversion in multigap systems', *Solar Energy Materials and Solar Cells* **43**(2): 203-222. [https://doi.org/10.1016/0927-0248\(96\)00015-3](https://doi.org/10.1016/0927-0248(96)00015-3)
- [77] **Baruch, P. and Parrott, J. E. (1987)** 'A Carnot Cycle for the Solar Cell'. In: A. Goetzberger, W. Palz, and G. Willeke, eds. Dordrecht: Springer, pp. 1122-1126. 10.1007/978-94-009-3817-5
- [78] **Markvart, T. (2007)** 'Thermodynamics of losses in photovoltaic conversion', *Applied Physics Letters* **91**(6): 64102. <https://doi.org/10.1063/1.2766857>
- [79] **Markvart, T. and Bauer, G. H. (2012)** 'What is the useful energy of a photon?', *Applied Physics Letters* **101**(19): 193901. <https://doi.org/10.1063/1.4766177>
- [80] **Würfel, P. (2002)** 'Thermodynamic limitations to solar energy conversion', *Physica E: Low-dimensional Systems and Nanostructures* **14**(1-2): 18-26. [https://doi.org/10.1016/S1386-9477\(02\)00355-7](https://doi.org/10.1016/S1386-9477(02)00355-7)
- [81] IEC (2019). IEC 60904-3, *Measurement principles for terrestrial photovoltaic (PV) solar devices with reference spectral irradiance data*. <https://www.vde-verlag.de/normen/0100547/din-en-iec-60904-3-vde-0126-4-3-2020-01.html>
- [82] ASTM International (2020). G173-03(2020), *Standard Tables for Reference Solar Spectral Irradiances: Direct Normal and Hemispherical on 37° Tilted Surface*. [https://compass.astm.org/EDIT/html\\_annot.cgi?G173+03\(2020\)](https://compass.astm.org/EDIT/html_annot.cgi?G173+03(2020)). <https://doi.org/10.1520/G0173-03R20>
- [83] **King, D. L., Boyson, W. E. and Kratochvil, J. A. (2002)** 'Analysis of factors influencing the annual energy production of photovoltaic systems', *Photovoltaic Specialists Conference, Institute of Electrical and Electronics Engineers*: 1356-1361. <https://doi.org/10.1109/PVSC.2002.1190861>
- [84] **Parretta, A., Sarno, A. and Vicari, L. R. (1998)** 'Effects of solar irradiation conditions on the outdoor performance of photovoltaic modules', *Optics Communications* **153**(1-3): 153-163. [https://doi.org/10.1016/S0030-4018\(98\)00192-8](https://doi.org/10.1016/S0030-4018(98)00192-8)
-

- [85] **Martin, N. and Ruiz, J. M. (2001)** 'Calculation of the PV modules angular losses under field conditions by means of an analytical model', *Solar Energy Materials and Solar Cells* **70**(1): 25-38. [https://doi.org/10.1016/S0927-0248\(00\)00408-6](https://doi.org/10.1016/S0927-0248(00)00408-6)
- [86] **Martín, N. and Ruiz, J. M. (2005)** 'Annual angular reflection losses in PV modules', *Progress in Photovoltaics: Research and Applications* **13**(1): 75-84. <https://doi.org/10.1002/pip.585>
- [87] **Ebert, M., Stascheit, H., Haedrich, I. and Eitner, U. (2014)** 'The Impact of Angular Dependent Loss Measurement on PV Module Energy Yield Prediction', *29th European Photovoltaic Solar Energy Conference*: 3244-3247. <https://doi.org/10.4229/EUPVSEC20142014-5CV.2.10>
- [88] **Lave, M. and Kleissl, J. (2011)** 'Optimum fixed orientations and benefits of tracking for capturing solar radiation in the continental United States', *Renewable Energy* **36**(3): 1145-1152. <https://doi.org/10.1016/j.renene.2010.07.032>
- [89] **Beringer, S., Schilke, H., Lohse, I. and Seckmeyer, G. (2011)** 'Case study showing that the tilt angle of photovoltaic plants is nearly irrelevant', *Solar Energy* **85**(3): 470-476. <https://doi.org/10.1016/j.solener.2010.12.014>
- [90] **Chen, X. M., Li, Y., Zhao, B. Y. and Wang, R. Z. (2020)** 'Are the optimum angles of photovoltaic systems so important?', *Renewable and Sustainable Energy Reviews* **124**: 109791. <https://doi.org/10.1016/j.rser.2020.109791>
- [91] **Nishioka, K., Hatayama, T., Uraoka, Y., Fuyuki, T., Hagihara, R. and Watanabe, M. (2003)** 'Field-test analysis of PV system output characteristics focusing on module temperature', *Solar Energy Materials and Solar Cells* **75**(3-4): 665-671. [https://doi.org/10.1016/S0927-0248\(02\)00148-4](https://doi.org/10.1016/S0927-0248(02)00148-4)
- [92] **Sunpower** 'E-series solar panels' [accessed 20 January 2021]. <https://us.sunpower.com/solar-panels-technology/e-series-solar-panels>
- [93] **Dash, P. K. and Gupta, N. C. (2015)** 'Effect of temperature on power output from different commercially available photovoltaic modules', *International Journal of Engineering Research and Applications* **5**(1): 148-151
- [94] **Klugmann-Radziemska, E. and Wcisło-Kucharek, P. (2017)** 'Photovoltaic module temperature stabilization with the use of phase change materials', *Solar Energy* **150**: 538-545. <https://doi.org/10.1016/j.solener.2017.05.016>

- 
- [95] **Sun, V., Asanakham, A., Deethayat, T. and Kiatsiriroat, T. (2020)** 'Study on phase change material and its appropriate thickness for controlling solar cell module temperature', *International Journal of Ambient Energy* **41**(1): 64-73. <https://doi.org/10.1080/01430750.2018.1443500>
- [96] **Sun, X., Silverman, T. J., Zhou, Z., Khan, M. R., Bermel, P. and Alam, M. A. (2017)** 'Optics-Based Approach to Thermal Management of Photovoltaics: Selective-Spectral and Radiative Cooling', *IEEE Journal of Photovoltaics* **7**(2): 566-574. <https://doi.org/10.1109/JPHOTOV.2016.2646062>
- [97] **Zhu, L., Raman, A., Wang, K. X., Anoma, M. A. and Fan, S. (2014)** 'Radiative cooling of solar cells', *Optica* **1**(1): 32-38. <https://doi.org/10.1364/OPTICA.1.000032>
- [98] **Gentle, A. R. and Smith, G. B. (2016)** 'Is enhanced radiative cooling of solar cell modules worth pursuing?', *Solar Energy Materials and Solar Cells* **150**: 39-42. <https://doi.org/10.1016/j.solmat.2016.01.039>
- [99] **Kumar, A. and Chowdhury, A. (2019)** 'Reassessment of different antireflection coatings for crystalline silicon solar cell in view of their passive radiative cooling properties', *Solar Energy* **183**: 410-418. <https://doi.org/10.1016/j.solener.2019.03.060>
- [100] **Lee, E. and Luo, T. (2019)** 'Black body-like radiative cooling for flexible thin-film solar cells', *Solar Energy Materials and Solar Cells* **194**: 222-228. <https://doi.org/10.1016/j.solmat.2019.02.015>
- [101] **Long, L., Yang, Y. and Wang, L. (2019)** 'Simultaneously enhanced solar absorption and radiative cooling with thin silica micro-grating coatings for silicon solar cells', *Solar Energy Materials and Solar Cells* **197**: 19-24. <https://doi.org/10.1016/j.solmat.2019.04.006>
- [102] **Lu, Y., Chen, Z., Ai, L., Zhang, X., Zhang, J., Li, J., Wang, W., Tan, R., Dai, N. and Song, W. (2017)** 'A Universal Route to Realize Radiative Cooling and Light Management in Photovoltaic Modules', *Solar RRL* **1**(10): 1700084. <https://doi.org/10.1002/solr.201700084>
- [103] **Born, M. and Wolf, E. (1959)** 'Principles of optics'. 6. ed., reprinted with corrections (1983) Oxford: Pergamon Press. ISBN: 0080264824
- [104] **Hecht, E. and Ganesan, A. R. (2012)** 'Optics'. Fourth edition New Delhi: Pearson. ISBN: 9788131718070
-

- [105] **Macleod, H. A. (2010)** 'Thin-film optical filters'. 4th ed. Boca Raton FL: CRC Press/Taylor & Francis. Series in optics and optoelectronics. ISBN: 9781420073027
- [106] **Mistrik, J., Kasap, S., Ruda, H. E., Koughia, C. and Singh, J.** 'Optical Properties of Electronic Materials: Fundamentals and Characterization', pp. 47-83
- [107] **Lekner, J. (2016)** 'Theory of Reflection'. Second Edition: Springer International Publishing. Springer series on atomic, optical, and plasma physics. ISBN: 978-3-319-23626-1. <https://doi.org/10.1007/978-3-319-23627-8>
- [108] **Orfanidis, S. J., Ramaccia, D. and Toscano, A. (2002)** 'Electromagnetic Waves and Antennas'. Revised 2016 version [accessed 20 January 2021]. [www.ece.rutgers.edu/~orfanidi/ewa](http://www.ece.rutgers.edu/~orfanidi/ewa)
- [109] **Feynman, R., Leighton, R. and Sands, M. (1963)** 'The Feynman Lectures on Physics, The Feynman Lectures on Physics, Vol. 2, Chapter 33': Pearson/Addison-Wesley
- [110] **Weber, H. (2014)** 'The Fresnel equations for lossy dielectrics and conservation of energy', *Journal of Modern Optics* **61**(15): 1219-1224. <https://doi.org/10.1080/09500340.2014.928375>
- [111] **Canning, F. X. (2011)** 'Corrected Fresnel coefficients for lossy materials'. Piscataway, NJ: IEEE, pp. 2123-2126
- [112] **Canning, F. X. (2011)** 'Reply to: Comment on the "Corrected Fresnel Coefficients for Lossy Materials"', *Antennas and Propagation Magazine IEEE* **53**(4): 165-168. <https://scholar.google.com/citations?user=htzc12aaaaaj&hl=en&oi=sra>
- [113] **Canning, F. X. (2015)** 'On Fresnel coefficients for transmission into a lossy medium'. Piscataway, NJ: IEEE, pp. 165-168
- [114] **Roy, J. E. (2003)** 'New results for the effective propagation constants of nonuniform plane waves at the planar interface of two lossy media', *IEEE Transactions on Antennas and Propagation* **51**(6): 1206-1215. <https://doi.org/10.1109/TAP.2003.812247>
- [115] **Besieris, I. M. (2011)** 'Comment on the "Corrected Fresnel Coefficients for Lossy Materials"', *IEEE Antennas and Propagation Magazine* **53**(4): 161-164. <https://doi.org/10.1109/MAP.2011.6097314>

- 
- [116] **Dupertuis, M. A., Acklin, B. and Proctor, M. (1994)** 'Generalized energy balance and reciprocity relations for thin-film optics', *Journal of the Optical Society of America A* **11**(3): 1167-1174. <https://doi.org/10.1364/JOSAA.11.001167>
- [117] **Radcliff, R. D. and Balanis, C. A. (1982)** 'Modified Propagation Constants for Nonuniform Plane Wave Transmission through Conducting Media', *IEEE Transactions on Geoscience and Remote Sensing* **GE-20**(3): 408-411. <https://doi.org/10.1109/TGRS.1982.350463>
- [118] **Dupertuis, M. A., Proctor, M. and Acklin, B. (1994)** 'Generalization of complex Snell-Descartes and Fresnel laws', *Journal of the Optical Society of America A* **11**(3): 1159-1166. <https://doi.org/10.1364/JOSAA.11.001159>
- [119] **Guimarães, L. G. and Sampaio, E. E. S. (2008)** 'A note on Snell laws for electromagnetic plane waves in lossy media', *Journal of Quantitative Spectroscopy and Radiative Transfer* **109**(11): 2124-2140. <https://doi.org/10.1016/j.jqsrt.2008.03.014>
- [120] **Frezza, F. and Tedeschi, N. (2012)** 'On the electromagnetic power transmission between two lossy media: discussion', *Journal of the Optical Society of America A* **29**(11): 2281-2288. <https://doi.org/10.1364/JOSAA.29.002281>
- [121] **Frezza, F. and Tedeschi, N. (2012)** 'Deeply penetrating waves in lossy media', *Optics Letters* **37**(13): 2616-2618. <https://doi.org/10.1364/OL.37.002616>
- [122] **Fedorov, V. Y. and Nakajima, T. (2014)** 'Negative refraction of inhomogeneous waves in lossy isotropic media', *Journal of Optics* **16**(3): 35103. <https://doi.org/10.1088/2040-8978/16/3/035103>
- [123] **Schake, M. C. (2018)** 'Comparison of recent results for the determination of effective propagation constants at attenuating interfaces', *European Journal of Physics* **39**(1): 15302. <https://doi.org/10.1088/1361-6404/aa94e6>
- [124] **Zhang, S., Liu, L. and Liu, Y. (2020)** 'Generalized laws of Snell, Fresnel and energy balance for a charged planar interface between lossy media', *Journal of Quantitative Spectroscopy and Radiative Transfer* **245**: 106903. <https://doi.org/10.1016/j.jqsrt.2020.106903>
- [125] **Ivlev, E. I. (1987)** 'Structure and Properties of Inhomogeneous Waves', *Journal of Modern Optics* **34**(12): 1559-1569. <https://doi.org/10.1080/09500348714551491>
-

- [126] **Oughstun, K. E. and Palombini, C. L. (2018)** 'Fresnel Reflection and Transmission Coefficients for Temporally Dispersive Attenuative Media', *Radio Science* **53**(11): 1382-1397. <https://doi.org/10.1029/2018RS006646>
- [127] **Frezza, F. and Tedeschi, N. (2015)** 'Electromagnetic inhomogeneous waves at planar boundaries: tutorial', *Journal of the Optical Society of America A* **32**(8): 1485-1501. <https://doi.org/10.1364/JOSAA.32.001485>
- [128] **Vitela, J. E. (2004)** 'Electromagnetic waves in dissipative media revisited', *American Journal of Physics* **72**(3): 393-403. <https://doi.org/10.1119/1.1639010>
- [129] **Oughstun, K. E. (2020)** 'Modified Brewster and pseudo-Brewster angles at the interface between isotropic lossy media', *Journal of the Optical Society of America A* **37**(9): 1505-1511. <https://doi.org/10.1364/JOSAA.398423>
- [130] **Chang, P. C., Walker, J. G. and Hopcraft, K. I. (2005)** 'Ray tracing in absorbing media', *Journal of Quantitative Spectroscopy and Radiative Transfer* **96**(3-4): 327-341. <https://doi.org/10.1016/j.jqsrt.2005.01.001>
- [131] **Rousseau, E. and Felbacq, D. (2020)** 'Concept of a Generalized Law of Refraction: A Phenomenological Model', *ACS Photonics* **7**(7): 1649-1654. <https://doi.org/10.1021/acsp Photonics.0c00639>
- [132] **Lommel, E. v. (1888)** 'Joseph von Fraunhofer's gesammelte Schriften. Versuche über die Ursachen des Anlaufens und Mattwerdens des Glases und die Mittel denselben zuvorzukommen (1817, Appendix 1819).' München. <http://publikationen.badw.de/en/003056526>
- [133] **Maxwell, J. C. (1865)** 'VIII. A dynamical theory of the electromagnetic field', *Philosophical Transactions of the Royal Society of London* **155**: 459-512. <https://doi.org/10.1098/rstl.1865.0008>
- [134] **Lord Rayleigh (1887)** 'IV. On the intensity of light reflected from certain surfaces at nearly perpendicular incidence', *Proceedings of the Royal Society of London* **41**(246-250): 275-294. <https://doi.org/10.1098/rspl.1886.0094>
- [135] **Taylor, H. D. (1904)**. 'A method of increasing the brilliancy of the images formed by lenses'. United Kingdom. Patent 29561
- [136] **Thelen, A. (2005)** 'Milestones in optical coating technology: from A. Smakula / John Strong until today'. In: Claude Amra, Norbert Kaiser, and H. Angus Macleod, eds.: SPIE, p. 596301

- [137] **Boden, S. A. and Bagnall, D. M. (2009)** 'Sunrise to sunset optimization of thin film antireflective coatings for encapsulated, planar silicon solar cells', *Progress in Photovoltaics: Research and Applications* **17**(4): 241-252. <https://doi.org/10.1002/pip.884>
- [138] **Dodge, M. J. (1984)** 'Refractive properties of magnesium fluoride', *Applied Optics* **23**(12): 1980. <https://doi.org/10.1364/AO.23.001980>
- [139] **Treharne, R. E., Seymour-Pierce, A., Durose, K., Hutchings, K., Roncallo, S. and Lane, D. (2011)** 'Optical Design and Fabrication of Fully Sputtered CdTe/CdS Solar Cells', *Journal of Physics: Conference Series* **286**: 12038. <https://doi.org/10.1088/1742-6596/286/1/012038>
- [140] **Bao, L., Ji, Z., Wang, H. and Chen, R. (2017)** 'Hollow Rodlike MgF<sub>2</sub> with an Ultralow Refractive Index for the Preparation of Multifunctional Antireflective Coatings', *Langmuir* **33**(25): 6240-6247. <https://doi.org/10.1021/acs.langmuir.7b00737>
- [141] **Prevo, B. G., Hwang, Y. and Velev, O. D. (2005)** 'Convective Assembly of Antireflective Silica Coatings with Controlled Thickness and Refractive Index', *Chemistry of Materials* **17**(14): 3642-3651. <https://doi.org/10.1021/cm050416h>
- [142] **Löbmann, P. (2017)** 'Antireflective coatings by sol-gel processing: commercial products and future perspectives', *Journal of Sol-Gel Science and Technology* **83**(2): 291-295. <https://doi.org/10.1007/s10971-017-4408-x>
- [143] **Scheurell, K., Kemnitz, E., Garcia-Juan, P., Eicher, J., Lintner, B., Hegmann, J., Jahn, R., Hofmann, T. and Löbmann, P. (2015)** 'Porous MgF<sub>2</sub> antireflective  $\lambda/4$  films prepared by sol-gel processing: comparison of synthesis approaches', *Journal of Sol-Gel Science and Technology* **76**(1): 82-89. <https://doi.org/10.1007/s10971-015-3754-9>
- [144] **Ankit Rohatgi.** Web Plot Digitizer. (2020). <https://automeris.io/WebPlotDigitizer/> [accessed 6 January 2020]
- [145] **Shivola, A. H. (1989)** 'Self-consistency aspects of dielectric mixing theories', *IEEE Transactions on Geoscience and Remote Sensing* **27**(4): 403-415. <https://doi.org/10.1109/36.29560>
- [146] **Bruggeman, D. A. G. (1935)** 'Berechnung verschiedener physikalischer Konstanten von heterogenen Substanzen. I. Dielektrizitätskonstanten und Leitfähigkeiten der Mischkörper aus isotropen Substanzen', *Annalen der Physik* **416**(7): 636-664. <https://doi.org/10.1002/ANDP.19354160705>

- [147] **DSM (2020)** 'Antireflective and Anti-Soiling Coatings' [accessed 29 December 2020]. [https://www.dsm.com/dsm-in-solar/en\\_US/technologies/anti-reflective-coatings.html](https://www.dsm.com/dsm-in-solar/en_US/technologies/anti-reflective-coatings.html)
- [148] **Raut, H. K., Nair, A. S., Dinachali, S. S., Ganesh, V. A., Walsh, T. M. and Ramakrishna, S. (2013)** 'Porous SiO<sub>2</sub> anti-reflective coatings on large-area substrates by electrospinning and their application to solar modules', *Solar Energy Materials and Solar Cells* **111**: 9-15. <https://doi.org/10.1016/j.solmat.2012.12.023>
- [149] **Ballif, C., Dicker, J., Borchert, D. and Hofmann, T. (2004)** 'Solar glass with industrial porous SiO<sub>2</sub> antireflection coating: measurements of photovoltaic module properties improvement and modelling of yearly energy yield gain', *Solar Energy Materials and Solar Cells* **82**(3): 331-344. <https://doi.org/10.1016/j.solmat.2003.12.004>
- [150] **Thomas, I. M. (1992)** 'Method for the preparation of porous silica antireflection coatings varying in refractive index from 1.22 to 1.44', *Applied Optics* **31**(28): 6145-6149
- [151] **Xi, J.-Q., Schubert, M. F., Kim, J. K., Schubert, E. F., Chen, M., Lin, S.-Y., Liu, W. and Smart, J. A. (2007)** 'Optical thin-film materials with low refractive index for broadband elimination of Fresnel reflection', *Nature Photonics* **1**(3): 176-179. <https://doi.org/10.1038/nphoton.2007.26>
- [152] **Chi, F., Liu, D., Wu, H. and Lei, J. (2019)** 'Mechanically robust and self-cleaning antireflection coatings from nanoscale binding of hydrophobic silica nanoparticles', *Solar Energy Materials and Solar Cells* **200**: 109939. <https://doi.org/10.1016/j.solmat.2019.109939>
- [153] **Zhang, J., Ai, L., Lin, S., Lan, P., Lu, Y., Dai, N., Tan, R., Fan, B. and Song, W. (2019)** 'Preparation of humidity, abrasion, and dust resistant antireflection coatings for photovoltaic modules via dual precursor modification and hybridization of hollow silica nanospheres', *Solar Energy Materials and Solar Cells* **192**: 188-196. <https://doi.org/10.1016/j.solmat.2018.12.032>
- [154] **Li, W., Tan, X., Zhu, J., Xiang, P., Xiao, T., Tian, L., Yang, A., Wang, M. and Chen, X. (2019)** 'Broadband antireflective and superhydrophobic coatings for solar cells', *Materials Today Energy* **12**: 348-355. <https://doi.org/10.1016/j.mtener.2019.03.006>

- [155] **Du, G., Zhang, Y., Li, W., Chen, N., Liu, B. and Sun, J. (2015)** 'Performance enhancement of multicrystalline silicon solar cells and modules using double-layered SiN<sub>x</sub>:H antireflection coatings', *Progress in Photovoltaics: Research and Applications* **23**(12): 1806-1814. <https://doi.org/10.1002/pip.2623>
- [156] **Tao, W. and Du, Y. (2015)** 'The optical properties of solar cells before and after encapsulation', *Solar Energy* **122**: 718-726. <https://doi.org/10.1016/j.solener.2015.10.007>
- [157] **Chandra Sekhar Reddy, K., Karthik, D., Bhanupriya, D., Ganesh, K., Ramakrishna, M. and Sakthivel, S. (2018)** 'Broad band antireflective coatings using novel in-situ synthesis of hollow MgF<sub>2</sub> nanoparticles', *Solar Energy Materials and Solar Cells* **176**: 259-265. <https://doi.org/10.1016/j.solmat.2017.12.010>
- [158] **Chattopadhyay, S., Huang, Y. F., Chen, K.-H. and Chen, L.-C.** 'Optical biomimetics'. *Materials and applications* **48**
- [159] **Han, Z. W., Wang, Z., Feng, X. M., Li, B., Mu, Z. Z., Zhang, J. Q., Niu, S. C. and Ren, L. Q. (2016)** 'Antireflective surface inspired from biology: A review', *Biosurface and Biotribology* **2**(4): 137-150. <https://doi.org/10.1016/j.bsbt.2016.11.002>
- [160] **Han, Z., Jiao, Z., Niu, S. and Ren, L. (2019)** 'Ascendant bioinspired antireflective materials: Opportunities and challenges coexist', *Progress in Materials Science* **103**: 1-68. <https://doi.org/10.1016/j.pmatsci.2019.01.004>
- [161] **Zhao, J. and Green, M. A. (1991)** 'Optimized antireflection coatings for high-efficiency silicon solar cells', *IEEE Transactions on Electron Devices* **38**(8): 1925-1934. <https://doi.org/10.1109/16.119035>
- [162] **Yang, T., Wang, X., Liu, W., Shi, Y. and Yang, F. (2013)** 'Double-layer anti-reflection coating containing a nanoporous anodic aluminum oxide layer for GaAs solar cells', *Optics Express* **21**(15): 18207-18215. <https://doi.org/10.1364/OE.21.018207>
- [163] **Li, J., Lu, Y., Lan, P., Zhang, X., Xu, W., Tan, R., Song, W. and Choy, K.-L. (2013)** 'Design, preparation, and durability of TiO<sub>2</sub>/SiO<sub>2</sub> and ZrO<sub>2</sub>/SiO<sub>2</sub> double-layer antireflective coatings in crystalline silicon solar modules', *Solar Energy* **89**: 134-142. <https://doi.org/10.1016/j.solener.2012.12.011>
- [164] **Lin, W., Zheng, J., Yan, L. and Zhang, X. (2018)** 'Sol-gel preparation of self-cleaning SiO<sub>2</sub>-TiO<sub>2</sub>/SiO<sub>2</sub>-TiO<sub>2</sub> double-layer antireflective coating for

- solar glass', *Results in Physics* **8**: 532-536. <https://doi.org/10.1016/j.rinp.2017.12.058>
- [165] **Jung, J., Jannat, A., Akhtar, M. S. and Yang, O.-B. (2018)** 'Sol-Gel Deposited Double Layer TiO<sub>2</sub> and Al<sub>2</sub>O<sub>3</sub> Anti-Reflection Coating for Silicon Solar Cell', *Journal of nanoscience and nanotechnology* **18**(2): 1274-1278. <https://doi.org/10.1166/jnn.2018.14928>
- [166] **Lien, S., Wu, D., Yeh, W. and Liu, J. (2006)** 'Tri-layer antireflection coatings (SiO<sub>2</sub>/SiO<sub>2</sub>-TiO<sub>2</sub>/TiO<sub>2</sub>) for silicon solar cells using a sol-gel technique', *Solar Energy Materials and Solar Cells* **90**(16): 2710-2719. <https://doi.org/10.1016/j.solmat.2006.04.001>
- [167] **Richards, B. S., Rowlands, S. F., Honsberg, C. B. and Cotter, J. E. (2003)** 'TiO<sub>2</sub> DLAR coatings for planar silicon solar cells', *Progress in Photovoltaics: Research and Applications* **11**(1): 27-32. <https://doi.org/10.1002/pip.474>
- [168] **Kuo, T.-W., Wang, N.-F., Tsai, Y.-Z., Hung, P.-K. and Houng, M.-P. (2014)** 'Broadband triple-layer SiO<sub>x</sub>/SiO<sub>x</sub>N<sub>y</sub>/SiN<sub>x</sub> antireflective coatings in textured crystalline silicon solar cells', *Materials Science in Semiconductor Processing* **25**: 211-218. <https://doi.org/10.1016/j.mssp.2013.11.035>
- [169] **Cox, J. T. and Hass, G. (1968)** 'Antireflection coatings for optical and infrared materials', *Physics of Thin Films* **2**: 239
- [170] **Ye, L., Zhang, Y., Zhang, X., Hu, T., Ji, R., Ding, B. and Jiang, B. (2013)** 'Sol-gel preparation of SiO<sub>2</sub>/TiO<sub>2</sub>/SiO<sub>2</sub>-TiO<sub>2</sub> broadband antireflective coating for solar cell cover glass', *Solar Energy Materials and Solar Cells* **111**: 160-164. <https://doi.org/10.1016/j.solmat.2012.12.037>
- [171] **Epstein, L. I. (1952)** 'The Design of Optical Filters', *Journal of the Optical Society of America* **42**(11): 806. <https://doi.org/10.1364/JOSA.42.000806>
- [172] **Young, P. A. (1970)** 'Extension of Herpin's Theorem', *Journal of the Optical Society of America* **60**(10): 1422. <https://doi.org/10.1364/JOSA.60.001422>
- [173] **Schallenberg, U. B. (2006)** 'Antireflection design concepts with equivalent layers', *Applied Optics* **45**(7): 1507-1514. <https://doi.org/10.1364/ao.45.001507>
- [174] **Schulz, U., Schallenberg, U. B. and Kaiser, N. (2003)** 'Symmetrical periods in antireflective coatings for plastic optics', *Applied Optics* **42**(7): 1346-1351. <https://doi.org/10.1364/ao.42.001346>

- 
- [175] **Schulz, U., Schallenberg, U. B. and Kaiser, N. (2002)** 'Antireflection coating design for plastic optics', *Applied Optics* **41**(16): 3107-3110. <https://doi.org/10.1364/ao.41.003107>
- [176] **Aiken, D. J. (2000)** 'High performance anti-reflection coatings for broadband multi-junction solar cells', *Solar Energy Materials and Solar Cells* **64**(4): 393-404. [https://doi.org/10.1016/S0927-0248\(00\)00253-1](https://doi.org/10.1016/S0927-0248(00)00253-1)
- [177] **Selj, J. H., Mongstad, T. T., Søndena, R. and Marstein, E. S. (2011)** 'Reduction of optical losses in colored solar cells with multilayer antireflection coatings', *Solar Energy Materials and Solar Cells* **95**(9): 2576-2582. <https://doi.org/10.1016/j.solmat.2011.03.005>
- [178] **Southwell, W. H. (1983)** 'Gradient-index antireflection coatings', *Optics Letters* **8**(11): 584-586. <https://doi.org/10.1364/ol.8.000584>
- [179] **Zhang, J.-C., Xiong, L.-M., Fang, M. and He, H.-B. (2013)** 'Wide-angle and broadband graded-refractive-index antireflection coatings', *Chinese Physics B* **22**(4): 44201. <https://doi.org/10.1088/1674-1056/22/4/044201>
- [180] **Grann, E. B., Moharam, M. G. and Pommet, D. A. (1995)** 'Optimal design for antireflective tapered two-dimensional subwavelength grating structures', *Journal of the Optical Society of America A* **12**(2): 333. <https://doi.org/10.1364/JOSAA.12.000333>
- [181] **Du, Y., Luna, L. E., Tan, W. S., Rubner, M. F. and Cohen, R. E. (2010)** 'Hollow silica nanoparticles in UV-visible antireflection coatings for poly(methyl methacrylate) substrates', *ACS Nano* **4**(7): 4308-4316. <https://doi.org/10.1021/nn101033y>
- [182] **Ma, L. L., Zhou, Y. C., Jiang, N., Lu, X., Shao, J., Lu, W., Ge, J., Ding, X. M. and Hou, X. Y. (2006)** 'Wide-band "black silicon" based on porous silicon', *Applied Physics Letters* **88**(17): 171907. <https://doi.org/10.1063/1.2199593>
- [183] **Kuo, M.-L., Poxson, D. J., Kim, Y. S., Mont, F. W., Kim, J. K., Schubert, E. F. and Lin, S.-Y. (2008)** 'Realization of a near-perfect antireflection coating for silicon solar energy utilization', *Optics Letters* **33**(21): 2527-2529. <https://doi.org/10.1364/ol.33.002527>
- [184] **Li, D., Wan, D., Zhu, X., Wang, Y., Han, Z., Han, S., Shan, Y. and Huang, F. (2014)** 'Broadband antireflection TiO<sub>2</sub>-SiO<sub>2</sub> stack coatings with refractive-index-grade structure and their applications to Cu(In,Ga)Se<sub>2</sub>
-

- solar cells', *Solar Energy Materials and Solar Cells* **130**: 505-512. <https://doi.org/10.1016/j.solmat.2014.07.042>
- [185] **Raguin, D. H. and Morris, G. M. (1993)** 'Analysis of antireflection-structured surfaces with continuous one-dimensional surface profiles', *Applied Optics* **32**(14): 2582-2598. <https://doi.org/10.1364/AO.32.002582>
- [186] **Garnett, J. C. M. (1904)** 'XII. Colours in metal glasses and in metallic films', *Philosophical Transactions of the Royal Society of London. Series A, Containing Papers of a Mathematical or Physical Character* **203**(359-371): 385-420. <https://doi.org/10.1098/rsta.1904.0024>
- [187] **Kubota, S., Kanomata, K., Suzuki, T., Ahmmad, B. and Hirose, F. (2015)** 'Hybrid antireflection structure with moth eye and multilayer coating for organic photovoltaics', *Journal of Coatings Technology and Research* **12**(1): 37-47. <https://doi.org/10.1007/s11998-014-9614-7>
- [188] **Song, Y. M., Jeong, Y., Yeo, C. I. and Lee, Y. T. (2012)** 'Enhanced power generation in concentrated photovoltaics using broadband antireflective coverglasses with moth eye structures', *Optics Express* **20 Suppl 6**: A916-23. <https://doi.org/10.1364/OE.20.00A916>
- [189] **Yeo, C. I., Kang, E. K., Lee, S. K., Song, Y. M. and Lee, Y. T. (2014)** 'Efficiency Enhancement of III-V Triple-Junction Solar Cell Using Nanostructured Bifunctional Coverglass With Enhanced Transmittance and Self-Cleaning Property', *IEEE Photonics Journal* **6**(3): 1-9. <https://doi.org/10.1109/JPHOT.2014.2319100>
- [190] **Deinega, A., Valuev, I., Potapkin, B. and Lozovik, Y. (2011)** 'Minimizing light reflection from dielectric textured surfaces', *Journal of the Optical Society of America A* **28**(5): 770-777. <https://doi.org/10.1364/JOSAA.28.000770>
- [191] **Ji, S., Song, K., Nguyen, T. B., Kim, N. and Lim, H. (2013)** 'Optimal moth eye nanostructure array on transparent glass towards broadband antireflection', *ACS Applied Materials & Interfaces* **5**(21): 10731-10737. <https://doi.org/10.1021/am402881x>
- [192] **Wilson, S. J. and Hutley, M. C. (1982)** 'The Optical Properties of 'Moth Eye' Antireflection Surfaces', *Optica Acta: International Journal of Optics* **29**(7): 993-1009. <https://doi.org/10.1080/713820946>
- [193] **Hua, X.-S., Zhang, Y.-J. and Wang, H.-W. (2010)** 'The effect of texture unit shape on silicon surface on the absorption properties', *Solar Energy*

- 
- Materials and Solar Cells* **94**(2): 258-262.  
<https://doi.org/10.1016/j.solmat.2009.09.011>
- [194] **Fritz, B. (2016)** 'Raytracing-basierte Untersuchung der optischen Eigenschaften panzeninspirierter Antireexbeschichtungen'. *Master's thesis*. Karlsruhe Institute of Technology Karlsruhe, Germany
- [195] **Muller, J., Herman, A., Mayer, A. and Deparis, O. (2015)** 'A fair comparison between ultrathin crystalline-silicon solar cells with either periodic or correlated disorder inverted pyramid textures', *Optics Express* **23**(11): A657-70. <https://doi.org/10.1364/OE.23.00A657>
- [196] **Dewan, R., Vasilev, I., Jovanov, V. and Knipp, D. (2011)** 'Optical enhancement and losses of pyramid textured thin-film silicon solar cells', *Journal of Applied Physics* **110**(1): 13101. <https://doi.org/10.1063/1.3602092>
- [197] **Her, T.-H., Finlay, R. J., Wu, C., Deliwala, S. and Mazur, E. (1998)** 'Microstructuring of silicon with femtosecond laser pulses', *Applied Physics Letters* **73**(12): 1673-1675. <https://doi.org/10.1063/1.122241>
- [198] **Abdullah, M. F., Alghoul, M. A., Naser, H., Asim, N., Ahmadi, S., Yatim, B. and Sopian, K. (2016)** 'Research and development efforts on texturization to reduce the optical losses at front surface of silicon solar cell', *Renewable and Sustainable Energy Reviews* **66**: 380-398. <https://doi.org/10.1016/j.rser.2016.07.065>
- [199] **Kim, J., Inns, D., Fogel, K. and Sadana, D. K. (2010)** 'Surface texturing of single-crystalline silicon solar cells using low density SiO<sub>2</sub> films as an anisotropic etch mask', *Solar Energy Materials and Solar Cells* **94**(12): 2091-2093. <https://doi.org/10.1016/j.solmat.2010.06.026>
- [200] **Peng, Y.-J., Huang, H.-X. and Xie, H. (2017)** 'Rapid fabrication of antireflective pyramid structure on polystyrene film used as protective layer of solar cell', *Solar Energy Materials and Solar Cells* **171**: 98-105. <https://doi.org/10.1016/j.solmat.2017.06.013>
- [201] **Eisenhauer, D., Trinh, C. T., Amkretz, D. and Becker, C. (2019)** 'Light management in crystalline silicon thin-film solar cells with imprint-textured glass superstrate', *Solar Energy Materials and Solar Cells* **200**: 109928. <https://doi.org/10.1016/j.solmat.2019.109928>
- [202] **Wooh, S., Yoon, H., Jung, J.-H., Lee, Y.-G., Koh, J. H., Lee, B., Kang, Y. S. and Char, K. (2013)** 'Efficient light harvesting with micropatterned 3D
-

- pyramidal photoanodes in dye-sensitized solar cells', *Advanced Materials* **25**(22): 3111-3116. <https://doi.org/10.1002/adma.201300085>
- [203] **Papet, P., Nichiporuk, O., Kaminski, A., Rozier, Y., Kraiem, J., Lelievre, J.-F., Chaumartin, A., Fave, A. and Lemiti, M. (2006)** 'Pyramidal texturing of silicon solar cell with TMAH chemical anisotropic etching', *Solar Energy Materials and Solar Cells* **90**(15): 2319-2328. <https://doi.org/10.1016/j.solmat.2006.03.005>
- [204] **Nagpal, P., Lindquist, N. C., Oh, S.-H. and Norris, D. J. (2009)** 'Ultrasoother patterned metals for plasmonics and metamaterials', *Science* **325**(5940): 594-597. <https://doi.org/10.1126/science.1174655>
- [205] **Chen, W., Liu, Y., Yang, L., Wu, J., Chen, Q., Zhao, Y., Wang, Y. and Du, X. (2018)** 'Difference in anisotropic etching characteristics of alkaline and copper based acid solutions for single-crystalline Si', *Scientific Reports*: 3408. <https://doi.org/10.1038/s41598-018-21877-x>
- [206] **You, J. S., Kim, D., Huh, J. Y., Park, H. J., Pak, J. J. and Kang, C. S. (2001)** 'Experiments on anisotropic etching of Si in TMAH', *Solar Energy Materials and Solar Cells* **66**(1-4): 37-44. [https://doi.org/10.1016/S0927-0248\(00\)00156-2](https://doi.org/10.1016/S0927-0248(00)00156-2)
- [207] **Lindquist, N. C., Nagpal, P., McPeak, K. M., Norris, D. J. and Oh, S.-H. (2012)** 'Engineering metallic nanostructures for plasmonics and nanophotonics', *Reports on Progress in Physics* **75**(3): 36501. <https://doi.org/10.1088/0034-4885/75/3/036501>
- [208] **King, D. L. and Buck, M. E. (1991)** 'Experimental optimization of an anisotropic etching process for random texturization of silicon solar cells'. New York, NY: Inst. of Electrical and Electronics Engineers, pp. 303-308
- [209] **Garnett, E. and Yang, P. (2010)** 'Light trapping in silicon nanowire solar cells', *Nano Letters* **10**(3): 1082-1087. <https://doi.org/10.1021/nl100161z>
- [210] **Demésy, G. and John, S. (2012)** 'Solar energy trapping with modulated silicon nanowire photonic crystals', *Journal of Applied Physics* **112**(7): 74326. <https://doi.org/10.1063/1.4752775>
- [211] **Pastorelli, F., Romero-Gomez, P., Betancur, R., Martinez-Otero, A., Mantilla-Perez, P., Bonod, N. and Martorell, J. (2015)** 'Enhanced Light Harvesting in Semitransparent Organic Solar Cells using an Optical Metal Cavity Configuration', *Advanced Energy Materials* **5**(2): 1400614. <https://doi.org/10.1002/aenm.201400614>

- [212] **Sergeant, N. P., Hadipour, A., Niesen, B., Cheyns, D., Heremans, P., Peumans, P. and Rand, B. P. (2012)** 'Design of transparent anodes for resonant cavity enhanced light harvesting in organic solar cells', *Advanced Materials* **24**(6): 728-732. <https://doi.org/10.1002/adma.201104273>
- [213] **Enrichi, F., Quandt, A. and Righini, G. C. (2018)** 'Plasmonic enhanced solar cells: Summary of possible strategies and recent results', *Renewable and Sustainable Energy Reviews* **82**: 2433-2439. <https://doi.org/10.1016/j.rser.2017.08.094>
- [214] **Wang, K. X., Yu, Z., Sandhu, S., Liu, V. and Fan, S. (2014)** 'Condition for perfect antireflection by optical resonance at material interface', *Optica* **1**(6): 388. <https://doi.org/10.1364/OPTICA.1.000388>
- [215] **Wang, K. X. and Fan, S. (2015)** 'Theory and Practice of Resonant Antireflection'. Washington, DC: OSA The Optical Society, SW11.3
- [216] **Brongersma, M. L., Cui, Y. and Fan, S. (2014)** 'Light management for photovoltaics using high-index nanostructures', *Nature Materials* **13**(5): 451-460. <https://doi.org/10.1038/nmat3921>
- [217] **Babicheva, V. E., Petrov, M. I., Baryshnikova, K. V. and Belov, P. A. (2017)** 'Reflection compensation mediated by electric and magnetic resonances of all-dielectric metasurfaces [Invited]', *Journal of the Optical Society of America B* **34**(7): D18. <https://doi.org/10.1364/JOSAB.34.000D18>
- [218] **Pecora, E. F., Cordaro, A., Kik, P. G. and Brongersma, M. L. (2018)** 'Broadband Antireflection Coatings Employing Multiresonant Dielectric Metasurfaces', *ACS Photonics* **5**(11): 4456-4462. <https://doi.org/10.1021/acsp Photonics.8b00913>
- [219] **Cordaro, A., van de Groep, J., Raza, S., Pecora, E. F., Priolo, F. and Brongersma, M. L. (2019)** 'Antireflection High-Index Metasurfaces Combining Mie and Fabry-Pérot Resonances', *ACS Photonics* **6**(2): 453-459. <https://doi.org/10.1021/acsp Photonics.8b01406>
- [220] **Yasuda, H., Matsuno, R., Koito, N., Hosoda, H., Tani, T. and Naya, M. (2017)** 'Anti-reflective coating for visible light using a silver nanodisc metasurface with a refractive index of less than 1.0', *Applied Physics Letters* **111**(23): 231105. <https://doi.org/10.1063/1.5000531>
- [221] **Roberts, C. M., Cook, T. A. and Podolskiy, V. A. (2017)** 'Metasurface-enhanced transparency', *Journal of the Optical Society of America B* **34**(7): D42. <https://doi.org/10.1364/JOSAB.34.000D42>

- [222] **Maas, R., Mann, S. A., Sounas, D. L., Alù, A., Garnett, E. C. and Polman, A. (2016)** 'Generalized antireflection coatings for complex bulk metamaterials', *Physical Review B* **93**(19): 195433. <https://doi.org/10.1103/PhysRevB.93.195433>
- [223] **Schumann, M. F., Wiesendanger, S., Goldschmidt, J. C., Bläsi, B., Bittkau, K., Paetzold, U. W., Sprafke, A., Wehrspohn, R. B., Rockstuhl, C. and Wegener, M. (2015)** 'Cloaked contact grids on solar cells by coordinate transformations: designs and prototypes', *Optica* **2**(10): 850. <https://doi.org/10.1364/OPTICA.2.000850>
- [224] **Schumann, M. F., Langenhorst, M., Smeets, M., Ding, K., Paetzold, U. W. and Wegener, M. (2017)** 'All-Angle Invisibility Cloaking of Contact Fingers on Solar Cells by Refractive Free-Form Surfaces', *Advanced Optical Materials* **5**(17): 1700164. <https://doi.org/10.1002/adom.201700164>
- [225] **Saive, R., Borsuk, A. M., Emmer, H. S., Bukowsky, C. R., Lloyd, J. V., Yalamanchili, S. and Atwater, H. A. (2016)** 'Effectively Transparent Front Contacts for Optoelectronic Devices', *Advanced Optical Materials* **4**(10): 1470-1474. <https://doi.org/10.1002/adom.201600252>
- [226] **Chen, F.-H., Pathreker, S., Kaur, J. and Hosein, I. D. (2016)** 'Increasing light capture in silicon solar cells with encapsulants incorporating air prisms to reduce metallic contact losses', *Optics Express* **24**(22): A1419-A1430. <https://doi.org/10.1364/OE.24.0A1419>
- [227] **Garnett, E. C., Ehrler, B., Polman, A. and Alarcon-Llado, E. (2021)** 'Photonics for Photovoltaics: Advances and Opportunities', *ACS Photonics* **8**(1): 61-70. <https://doi.org/10.1021/acsp Photonics.0c01045>
- [228] **van Sark, W. G., Wild, J. de, Rath, J. K., Meijerink, A. and Schropp, R. E. (2013)** 'Upconversion in solar cells', *Nanoscale research letters* **8**(1): 81. <https://doi.org/10.1186/1556-276X-8-81>
- [229] **La Mora, M. B. de, Amelines-Sarria, O., Monroy, B. M., Hernández-Pérez, C. D. and Lugo, J. E. (2017)** 'Materials for downconversion in solar cells: Perspectives and challenges', *Solar Energy Materials and Solar Cells* **165**: 59-71. <https://doi.org/10.1016/j.solmat.2017.02.016>
- [230] **Klampafitis, E., Ross, D., McIntosh, K. R. and Richards, B. S. (2009)** 'Enhancing the performance of solar cells via luminescent down-shifting of the incident spectrum: A review', *Solar Energy Materials and Solar Cells* **93**(8): 1182-1194. <https://doi.org/10.1016/j.solmat.2009.02.020>

- [231] **Upping, J., Bielawny, A., Wehrspohn, R. B., Beckers, T., Carius, R., Rau, U., Fahr, S., Rockstuhl, C., Lederer, F., Kroll, M., Pertsch, T., Steidl, L. and Zentel, R. (2011)** 'Three-dimensional photonic crystal intermediate reflectors for enhanced light-trapping in tandem solar cells', *Advanced Materials* **23**(34): 3896-3900. <https://doi.org/10.1002/adma.201101419>
- [232] **Raman, A. P., Li, W. and Fan, S. (2019)** 'Generating Light from Darkness', *Joule* **3**(11): 2679-2686. <https://doi.org/10.1016/j.joule.2019.08.009>
- [233] **Li, W., Dong, M., Fan, L., John, J. J., Chen, Z. and Fan, S. (2021)** 'Nighttime Radiative Cooling for Water Harvesting from Solar Panels', *ACS Photonics* **8**(1): 269-275. <https://doi.org/10.1021/acsp Photonics.0c01471>
- [234] **Byrnes, S. J., Blanchard, R. and Capasso, F. (2014)** 'Harvesting renewable energy from Earth's mid-infrared emissions', *Proceedings of the National Academy of Sciences* **111**(11): 3927-3932. <https://doi.org/10.1073/pnas.1402036111>
- [235] **Buddhiraju, S., Santhanam, P. and Fan, S. (2018)** 'Thermodynamic limits of energy harvesting from outgoing thermal radiation', *Proceedings of the National Academy of Sciences* **115**(16): E3609-E3615. <https://doi.org/10.1073/pnas.1717595115>
- [236] **Li, W., Buddhiraju, S. and Fan, S. (2020)** 'Thermodynamic limits for simultaneous energy harvesting from the hot sun and cold outer space', *Light, science & applications* **9**: 68. <https://doi.org/10.1038/s41377-020-0296-x>
- [237] **O'Regan, B. and Grätzel, M. (2005)** 'A low-cost, high-efficiency solar cell based on dye-sensitized colloidal TiO<sub>2</sub> films', *Nature* **353**(6346): 737-740
- [238] **Park, N.-G. (2010)** 'Light management in dye-sensitized solar cell', *Korean Journal of Chemical Engineering* **27**(2): 375-384. <https://doi.org/10.1007/s11814-010-0112-z>
- [239] **Wu, W.-Q., Feng, H.-L., Rao, H.-S., Xu, Y.-F., Kuang, D.-B. and Su, C.-Y. (2014)** 'Maximizing omnidirectional light harvesting in metal oxide hyperbranched array architectures', *Nature Communications* **5**: 3968. <https://doi.org/10.1038/ncomms4968>
- [240] **Mangini, F. and Frezza, F. (2016)** 'Analysis of the electromagnetic reflection and transmission through a stratified lossy medium of an elliptically polarized plane wave', *Mathematics and Mechanics of Complex Systems* **4**(2): 153-167. <https://doi.org/10.2140/memocs.2016.4.153>

- [241] **Khorasani, S. and Rashidian, B. (2002)** 'Modified transfer matrix method for conducting interfaces', *Journal of Optics A: Pure and Applied Optics* **4**(3): 251-256. <https://doi.org/10.1088/1464-4258/4/3/306>
- [242] **Yeh, P. (1979)** 'Electromagnetic propagation in birefringent layered media', *Journal of the Optical Society of America* **69**(5): 742. <https://doi.org/10.1364/JOSA.69.000742>
- [243] **Berkhout, A. and Koenderink, A. F. (2020)** 'A simple transfer-matrix model for metasurface multilayer systems', *Nanophotonics* **9**(12): 3985-4007. <https://doi.org/10.1515/nanoph-2020-0212>
- [244] **Troparevsky, M. C., Sabau, A. S., Lupini, A. R. and Zhang, Z. (2010)** 'Transfer-matrix formalism for the calculation of optical response in multilayer systems: from coherent to incoherent interference', *Optics Express* **18**(24): 24715-24721. <https://doi.org/10.1364/OE.18.024715>
- [245] **Katsidis, C. C. and Siapkias, D. I. (2002)** 'General transfer-matrix method for optical multilayer systems with coherent, partially coherent, and incoherent interference', *Applied Optics* **41**(19): 3978-3987. <https://doi.org/10.1364/ao.41.003978>
- [246] **Mitsas, C. L. and Siapkias, D. I. (1995)** 'Generalized matrix method for analysis of coherent and incoherent reflectance and transmittance of multilayer structures with rough surfaces, interfaces, and finite substrates', *Applied Optics* **34**(10): 1678-1683. <https://doi.org/10.1364/AO.34.001678>
- [247] **Simonot, L., Hersch, R. D., Hébert, M. and Mazauric, S. (2015)** 'Multilayer four-flux matrix model accounting for directional-diffuse light transfers', *Applied Optics* **55**(1): 27-37. <https://doi.org/10.1364/AO.55.000027>
- [248] **Pereyra, P. and Robledo-Martinez, A. (2009)** 'On the equivalence of the summation and transfer-matrix methods in wave propagation through multilayers of lossless and lossy media', *European Journal of Physics* **30**(2): 393-401. <https://doi.org/10.1088/0143-0807/30/2/018>
- [249] **Kulowski, A. (1985)** 'Algorithmic representation of the ray tracing technique', *Applied Acoustics* **18**(6): 449-469. [https://doi.org/10.1016/0003-682X\(85\)90024-6](https://doi.org/10.1016/0003-682X(85)90024-6)

- 
- [250] **Ortiz, S., Siedlecki, D., Remon, L. and Marcos, S. (2009)** 'Three-dimensional ray tracing on Delaunay-based reconstructed surfaces', *Applied Optics* **48**(20): 3886-3893. <https://doi.org/10.1364/ao.48.003886>
- [251] **Lipovsek, B., Krc, J. and Topic, M. (2014)** 'Optimization of Microtextured Light-Management Films for Enhanced Light Trapping in Organic Solar Cells Under Perpendicular and Oblique Illumination Conditions', *IEEE Journal of Photovoltaics* **4**(2): 639-646. <https://doi.org/10.1109/JPHOTOV.2013.2293875>
- [252] **Lipovsek, B., Krc, J. and Topic, M. (2018)** 'Microtextured Light-Management Foils and Their Optimization for Planar Organic and Perovskite Solar Cells', *IEEE Journal of Photovoltaics* **8**(3): 783-792. <https://doi.org/10.1109/JPHOTOV.2018.2810844>
- [253] **Lipovsek, B., Krc, J. and Topic, M. (2014)** 'Micro-scale textures for enhanced performance of organic solar cells'. <https://doi.org/10.1109/PVSC.2014.6925454>
- [254] **Li, K., Wu, R., Ruan, Y., Zhang, L. and Zhen, H. (2018)** 'Numerical analysis of the angular insensitive photovoltaic light harvesting with the biomimetic scattering film inspired by the rose petal epidermal topography', *Solar Energy* **170**: 800-806. <https://doi.org/10.1016/j.solener.2018.05.098>
- [255] **J.A. Woollam Co. WVASE. (2016).** <https://www.jawoollam.com/ellipsometry-software/wvase> [accessed 22 November 2020]
- [256] **Synopsys Inc. LightTools. Version 8.5.2-8.7.0. (2016-2020).** <https://www.synopsys.com/optical-solutions/lighttools.html> [accessed 22 November 2020]
- [257] **The MathWorks, I. Matlab. Version 2016b-2019b. (2016-2019).** <https://de.mathworks.com/products/matlab.html> [accessed 22 November 2020]
- [258] **Hooke, R. (1665)** 'Micrographia', *London: Martyn and Allestry*
- [259] **Newton, I. (1704)** 'Opticks', *Mineola, NY: Dover Publications*
- [260] **Mason, C. W. (1923)** 'Structural Colors in Feathers. I', *The Journal of Physical Chemistry* **27**(3): 201-251. <https://doi.org/10.1021/j150228a001>
- [261] **Mason, C. W. (1923)** 'Structural Colors in Feathers. II', *The Journal of Physical Chemistry* **27**(5): 401-448. <https://doi.org/10.1021/j150230a001>
-

- [262] **Mason, C. W. (1926)** 'Structural Colors in Insects. I', *The Journal of Physical Chemistry* **30**(3): 383-395. <https://doi.org/10.1021/j150261a009>
- [263] **Mason, C. W. (1927)** 'Structural Colors in Insects. II', *The Journal of Physical Chemistry* **31**(3): 321-354. <https://doi.org/10.1021/j150273a001>
- [264] **Mason, C. W. (1927)** 'Structural Colors in Insects. III', *The Journal of Physical Chemistry* **31**(12): 1856-1872. <https://doi.org/10.1021/j150282a008>
- [265] **Anderson, T. F. and Richards, A. G. (1942)** 'An Electron Microscope Study of Some Structural Colors of Insects', *Journal of Applied Physics* **13**(12): 748-758. <https://doi.org/10.1063/1.1714827>
- [266] **Neville, A. C. and Caveney, S. (1969)** 'Scarabaeid beetle exocuticle as an optical analogue of cholesteric liquid crystals', *Biological Reviews of the Cambridge Philosophical Society* **44**(4): 531-562. <https://doi.org/10.1111/j.1469-185x.1969.tb00611.x>
- [267] **McNamara, M. E., Briggs, D. E. G., Orr, P. J., Noh, H. and Cao, H. (2012)** 'The original colours of fossil beetles', *Proceedings of the Royal Society B* **279**(1731): 1114-1121. <https://doi.org/10.1098/rspb.2011.1677>
- [268] **Vargas, W. E., Avendano, E., Hernández-Jiménez, M., Azofeifa, D. E., Libby, E., Solís, Á. and Barboza-Aguilar, C. (2018)** 'Photonic Crystal Characterization of the Cuticles of *Chrysina chrysargyrea* and *Chrysina optima* Jewel Scarab Beetles', *Biomimetics* **3**(4). <https://doi.org/10.3390/biomimetics3040030>
- [269] **Ghiradella, H. (1991)** 'Light and color on the wing: structural colors in butterflies and moths', *Applied Optics* **30**(24): 3492-3500. <https://doi.org/10.1364/AO.30.003492>
- [270] **Kinoshita, S., Yoshioka, S. and Kawagoe, K. (2002)** 'Mechanisms of structural colour in the *Morpho* butterfly: cooperation of regularity and irregularity in an iridescent scale', *Proceedings of the Royal Society B* **269**(1499): 1417-1421. <https://doi.org/10.1098/rspb.2002.2019>
- [271] **Yoshioka, S. and Kinoshita, S. (2004)** 'Wavelength-selective and anisotropic light-diffusing scale on the wing of the *Morpho* butterfly', *Proceedings of the Royal Society B* **271**(1539): 581-587. <https://doi.org/10.1098/rspb.2003.2618>
- [272] **Lee, R. T. and Smith, G. S. (2009)** 'Detailed electromagnetic simulation for the structural color of butterfly wings', *Applied Optics* **48**(21): 4177-4190. <https://doi.org/10.1364/ao.48.004177>

- [273] **Siddique, R. H., Diewald, S., Leuthold, J. and Hölscher, H. (2013)** 'Theoretical and experimental analysis of the structural pattern responsible for the iridescence of *Morpho* butterflies', *Optics Express* **21**(12): 14351-14361. <https://doi.org/10.1364/OE.21.014351>
- [274] **Noh, H., Liew, S. F., Saranathan, V., Mochrie, S. G. J., Prum, R. O., Dufresne, E. R. and Cao, H. (2010)** 'How noniridescent colors are generated by quasi-ordered structures of bird feathers', *Advanced Materials* **22**(26-27): 2871-2880. <https://doi.org/10.1002/adma.200903699>
- [275] **Saranathan, V., Narayanan, S., Sandy, A., Dufresne, E. R. and Prum, R. O. (2021)** 'Evolution of single gyroid photonic crystals in bird feathers', *Proceedings of the National Academy of Sciences* **118**(23). <https://doi.org/10.1073/pnas.2101357118>
- [276] **Gur, D., Palmer, B. A., Leshem, B., Oron, D., Fratzl, P., Weiner, S. and Addadi, L. (2015)** 'The mechanism of color change in the neon tetra fish: a light-induced tunable photonic crystal array', *Angewandte Chemie* **54**(42): 12426-12430. <https://doi.org/10.1002/anie.201502268>
- [277] **McCoy, D. E., McCoy, V. E., Mandsberg, N. K., Shneidman, A. V., Aizenberg, J., Prum, R. O. and Haig, D. (2019)** 'Structurally assisted super black in colourful peacock spiders', *Proceedings of the Royal Society B* **286**(1902): 20190589. <https://doi.org/10.1098/rspb.2019.0589>
- [278] **Chandler, C. J., Wilts, B. D., Brodie, J. and Vignolini, S. (2016)** 'Structural Color in Marine Algae', *Advanced Optical Materials* **5**(5): 1600646. <https://doi.org/10.1002/adom.201600646>
- [279] **Smith, G. S. (2009)** 'Structural color of *Morpho* butterflies', *American Journal of Physics* **77**(11): 1010-1019. <https://doi.org/10.1119/1.3192768>
- [280] **Zhang, S. and Chen, Y. (2015)** 'Nanofabrication and coloration study of artificial *Morpho* butterfly wings with aligned lamellae layers', *Scientific Reports* **5**: 16637. <https://doi.org/10.1038/srep16637>
- [281] **Kinoshita, S., Yoshioka, S. and Miyazaki, J. (2008)** 'Physics of structural colors', *Reports on Progress in Physics* **71**(7): 76401. <https://doi.org/10.1088/0034-4885/71/7/076401>
- [282] **Morris, R. B. (1975)** 'Iridescence from diffraction structures in the wing scales of *Callophrys rubi*, the Green Hairstreak', *Journal of Entomology Series A, General Entomology* **49**(2): 149-154. <https://doi.org/10.1111/j.1365-3032.1975.tb00079.x>

- [283] **Winter, B., Butz, B., Dieker, C., Schröder-Turk, G. E., Mecke, K. and Spiecker, E. (2015)** 'Coexistence of both gyroid chiralities in individual butterfly wing scales of *Callophrys rubi*', *Proceedings of the National Academy of Sciences of the United States of America* **112**(42): 12911-12916. <https://doi.org/10.1073/pnas.1511354112>
- [284] **Corkery, R. W. and Tyrode, E. C. (2017)** 'On the colour of wing scales in butterflies: iridescence and preferred orientation of single gyroid photonic crystals', *Interface Focus* **7**(4): 20160154. <https://doi.org/10.1098/rsfs.2016.0154>
- [285] **Kertész, K., Bálint, Z., Vértesy, Z., Márk, G. I., Lousse, V., Vigneron, J. P., Rassart, M. and Biró, L. P. (2006)** 'Gleaming and dull surface textures from photonic-crystal-type nanostructures in the butterfly *Cyanophrys remus*', *Physical Review E* **74**(2 Pt 1): 21922. <https://doi.org/10.1103/PhysRevE.74.021922>
- [286] **Márk, G. I., Vértesy, Z., Kertész, K., Bálint, Z. and Biró, L. P. (2009)** 'Order-disorder effects in structure and color relation of photonic-crystal-type nanostructures in butterfly wing scales', *Physical Review E* **80**(5 Pt 1): 51903. <https://doi.org/10.1103/PhysRevE.80.051903>
- [287] **Syurik, J., Siddique, R. H., Dollmann, A., Gomard, G., Schneider, M., Worgull, M., Wiegand, G. and Hölscher, H. (2017)** 'Bio-inspired, large scale, highly-scattering films for nanoparticle-alternative white surfaces', *Scientific Reports* **7**: 46637. <https://doi.org/10.1038/srep46637>
- [288] **Vukusic, P., Hallam, B. and Noyes, J. (2007)** 'Brilliant Whiteness in Ultrathin Beetle Scales', *Science* **315**(5810): 348. <https://doi.org/10.1126/science.1134666>
- [289] **Luke, S. M., Hallam, B. T. and Vukusic, P. (2010)** 'Structural optimization for broadband scattering in several ultra-thin white beetle scales', *Applied Optics* **49**(22): 4246-4254. <https://doi.org/10.1364/AO.49.004246>
- [290] **Burresti, M., Cortese, L., Pattelli, L., Kolle, M., Vukusic, P., Wiersma, D. S., Steiner, U. and Vignolini, S. (2014)** 'Bright-white beetle scales optimise multiple scattering of light', *Scientific Reports* **4**: 6075. <https://doi.org/10.1038/srep06075>
- [291] **Cortese, L., Pattelli, L., Utel, F., Vignolini, S., Burresti, M. and Wiersma, D. S. (2015)** 'Anisotropic Light Transport in White Beetle Scales', *Advanced Optical Materials* **3**(10): 1337-1341. <https://doi.org/10.1002/adom.201500173>

- [292] **Wilts, B. D., Sheng, X., Holler, M., Diaz, A., Guizar-Sicairos, M., Raabe, J., Hoppe, R., Liu, S.-H., Langford, R., Onelli, O. D., Chen, D., Torquato, S., Steiner, U., Schroer, C. G., Vignolini, S. and Sepe, A. (2018)** 'Evolutionary-Optimized Photonic Network Structure in White Beetle Wing Scales', *Advanced Materials* **30**(19): 1702057. <https://doi.org/10.1002/adma.201702057>
- [293] **Jacucci, G., Schertel, L., Zhang, Y., Yang, H. and Vignolini, S. (2020)** 'Light Management with Natural Materials: From Whiteness to Transparency', *Advanced Materials*: e2001215. <https://doi.org/10.1002/adma.202001215>
- [294] **Michelson, A. A. (1911)** 'LXI. On metallic colouring in birds and insects', *The London, Edinburgh, and Dublin Philosophical Magazine and Journal of Science* **21**(124): 554-567. <https://doi.org/10.1080/14786440408637061>
- [295] **Gaubert, P. (1924)** 'Sur la polarisation circulaire de la lumière réfléchie par les Insectes', *Comptes rendus* **179**: 1148-1150
- [296] **Mathieu, J. P. and Faraggi, N. (1937)** 'Étude de la lumière polarisée circulairement réfléchie par certains coléoptères', *Comptes rendus* **205**: 1378-1380
- [297] **Bouligand, Y. (1972)** 'Twisted fibrous arrangements in biological materials and cholesteric mesophases', *Tissue and Cell* **4**(2): 189-217. [https://doi.org/10.1016/S0040-8166\(72\)80042-9](https://doi.org/10.1016/S0040-8166(72)80042-9)
- [298] **Vries, H. de (1951)** 'Rotatory power and other optical properties of certain liquid crystals', *Acta Crystallographica* **4**(3): 219-226. <https://doi.org/10.1107/S0365110X51000751>
- [299] **Prum, R. O. and Torres, R. H. (2004)** 'Structural colouration of mammalian skin: convergent evolution of coherently scattering dermal collagen arrays', *The Journal of Experimental Biology* **207**(Pt 12): 2157-2172. <https://doi.org/10.1242/jeb.00989>
- [300] **Hsiung, B.-K., Deheyn, D. D., Shawkey, M. D. and Blackledge, T. A. (2015)** 'Blue reflectance in tarantulas is evolutionarily conserved despite nanostructural diversity', *Science Advances* **1**(10): e1500709. <https://doi.org/10.1126/sciadv.1500709>
- [301] **Wilts, B. D., Otto, J. and Stavenga, D. G. (2020)** 'Ultra-dense, curved, grating optics determines peacock spider coloration', *Nanoscale Advances* **2**(3): 1122-1127. <https://doi.org/10.1039/C9NA00494G>

- [302] **Shi, N. N., Tsai, C.-C., Camino, F., Bernard, G. D., Yu, N. and Wehner, R. (2015)** 'Keeping cool: Enhanced optical reflection and radiative heat dissipation in Saharan silver ants', *Science* **349**(6245): 298-301. <https://doi.org/10.1126/science.aab3564>
- [303] **Willot, Q., Simonis, P., Vigneron, J.-P. and Aron, S. (2016)** 'Total Internal Reflection Accounts for the Bright Color of the Saharan Silver Ant', *PLOS ONE* **11**(4): e0152325. <https://doi.org/10.1371/journal.pone.0152325>
- [304] **Goldstein, D. H. (2006)** 'Polarization properties of Scarabaeidae', *Applied Optics* **45**(30): 7944-7950. <https://doi.org/10.1364/ao.45.007944>
- [305] **Finlayson, E. D., McDonald, L. T. and Vukusic, P. (2017)** 'Optically ambidextrous circularly polarized reflection from the chiral cuticle of the scarab beetle *Chrysina resplendens*', *Journal of The Royal Society Interface* **14**(131): 20170129. <https://doi.org/10.1098/rsif.2017.0129>
- [306] **Mencattelli, L. and Pinho, S. T. (2020)** 'Ultra-thin-ply CFRP Bouligand bio-inspired structures with enhanced load-bearing capacity, delayed catastrophic failure and high energy dissipation capability', *Composites Part A: Applied Science and Manufacturing* **129**: 105655. <https://doi.org/10.1016/j.compositesa.2019.105655>
- [307] **Zi, J., Yu, X., Li, Y., Hu, X., Xu, C., Wang, X., Liu, X. and Fu, R. (2003)** 'Coloration strategies in peacock feathers', *Proceedings of the National Academy of Sciences of the United States of America* **100**(22): 12576-12578. <https://doi.org/10.1073/pnas.2133313100>
- [308] **Vigneron, J. P., Colomer, J.-F., Rassart, M., Ingram, A. L. and Lousse, V. (2006)** 'Structural origin of the colored reflections from the black-billed magpie feathers', *Physical Review E* **73**(2 Pt 1): 21914. <https://doi.org/10.1103/PhysRevE.73.021914>
- [309] **Welch, V., Vigneron, J. P., Lousse, V. and Parker, A. (2006)** 'Optical properties of the iridescent organ of the comb-jellyfish *Beroë cucumis* (Ctenophora)', *Physical Review E* **73**(4 Pt 1): 41916. <https://doi.org/10.1103/PhysRevE.73.041916>
- [310] **Welch, V. L., Vigneron, J. P. and Parker, A. R. (2005)** 'The cause of colouration in the ctenophore *Beroë cucumis*', *Current Biology* **15**(24): R985-6. <https://doi.org/10.1016/j.cub.2005.11.060>
- [311] **Mäthger, L. M., Denton, E. J., Marshall, N. J. and Hanlon, R. T. (2009)** 'Mechanisms and behavioural functions of structural coloration in

- cephalopods', *Journal of The Royal Society Interface* **6 Suppl 2**: S149-63. <https://doi.org/10.1098/rsif.2008.0366.focus>
- [312] **McPhedran, R., Nicorovici, N., McKenzie, D., Rouse, G., Botten, L., Welch, V., Parker, A., Wohlgennant, M. and Vardeny, V. (2003)** 'Structural colours through photonic crystals', *Physica B: Condensed Matter* **338**(1-4): 182-185. [https://doi.org/10.1016/S0921-4526\(03\)00483-6](https://doi.org/10.1016/S0921-4526(03)00483-6)
- [313] **Welch, V. L. and Vigneron, J.-P. (2007)** 'Beyond butterflies—the diversity of biological photonic crystals', *Optical and Quantum Electronics* **39**(4-6): 295-303. <https://doi.org/10.1007/S11082-007-9094-4>
- [314] **Parker, A. R., Welch, V. L., Driver, D. and Martini, N. (2003)** 'Structural colour: opal analogue discovered in a weevil', *Nature* **426**(6968): 786-787. <https://doi.org/10.1038/426786a>
- [315] **Cai, C., Tihelka, E., Pan, Y., Yin, Z., Jiang, R., Xia, F. and Huang, D. (2020)** 'Structural colours in diverse Mesozoic insects', *Proceedings of the Royal Society B* **287**(1930): 20200301. <https://doi.org/10.1098/rspb.2020.0301>
- [316] **D'Alba, L., Wang, B., Vanthournout, B. and Shawkey, M. D. (2019)** 'The golden age of arthropods: ancient mechanisms of colour production in body scales', *Journal of The Royal Society Interface* **16**(159): 20190366. <https://doi.org/10.1098/rsif.2019.0366>
- [317] **McDonald, L. T., Narayanan, S., Sandy, A., Saranathan, V. and McNamara, M. E. (2020)** 'Brilliant angle-independent structural colours preserved in weevil scales from the Swiss Pleistocene', *Biology Letters* **16**(4): 20200063. <https://doi.org/10.1098/rsbl.2020.0063>
- [318] **McNamara, M. E., Briggs, D. E. G., Orr, P. J., Field, D. J. and Wang, Z. (2013)** 'Experimental maturation of feathers: implications for reconstructions of fossil feather colour', *Biology Letters* **9**(3): 20130184. <https://doi.org/10.1098/rsbl.2013.0184>
- [319] **Teyssier, J., Saenko, S., van der Marel, D. and Milinkovitch, M. C. (2015)** 'Photonic crystals cause active colour change in chameleons', *Nature Communications* **6**: 6368
- [320] **Thayer, G. H. (1909)** 'Concealing-coloration in the animal kingdom: an exposition of the laws of disguise through color and pattern': Macmillan Company
- [321] **Kjernsmo, K., Hall, J. R., Doyle, C., Khuzayim, N., Cuthill, I. C., Scott-Samuel, N. E. and Whitney, H. M. (2018)** 'Iridescence impairs object

- recognition in bumblebees', *Scientific Reports* **8**(1): 8095. <https://doi.org/10.1038/s41598-018-26571-6>
- [322] **Kjernsmo, K., Whitney, H. M., Scott-Samuel, N. E., Hall, J. R., Knowles, H., Talas, L. and Cuthill, I. C. (2020)** 'Iridescence as Camouflage', *Current Biology* **30**(3): 551-555.e3. <https://doi.org/10.1016/j.cub.2019.12.013>
- [323] **Siddique, R. H., Gomard, G. and Hölscher, H. (2015)** 'The role of random nanostructures for the omnidirectional anti-reflection properties of the glasswing butterfly', *Nature Communications* **6**: 6909. <https://doi.org/10.1038/ncomms7909>
- [324] **Gale, M. (1989)** 'Diffraction, beauty and commerce', *Physics World* **2**(10): 24-29. <https://doi.org/10.1088/2058-7058/2/10/20>
- [325] **Binetti, V. R., Schiffman, J. D., Leaffer, O. D., Spanier, J. E. and Schauer, C. L. (2009)** 'The natural transparency and piezoelectric response of the *Greta oto* butterfly wing', *Integrative Biology* **1**(4): 324-329. <https://doi.org/10.1039/b820205b>
- [326] **Narasimhan, V., Siddique, R. H., Lee, J. O., Kumar, S., Ndjamen, B., Du, J., Hong, N., Sretavan, D. and Choo, H. (2018)** 'Multifunctional biophotonic nanostructures inspired by the longtail glasswing butterfly for medical devices', *Nature Nanotechnology* **13**(6): 512-519. <https://doi.org/10.1038/s41565-018-0111-5>
- [327] **Zhang, G., Zhang, J., Xie, G., Liu, Z. and Shao, H. (2006)** 'Cicada wings: a stamp from nature for nanoimprint lithography', *Small* **2**(12): 1440-1443. <https://doi.org/10.1002/sml.200600255>
- [328] **Han, Z., Wang, Z., Li, B., Feng, X., Jiao, Z., Zhang, J., Zhao, J., Niu, S. and Ren, L. (2019)** 'Flexible Self-Cleaning Broadband Antireflective Film Inspired by the Transparent Cicada Wings', *ACS Applied Materials & Interfaces* **11**(18): 17019-17027. <https://doi.org/10.1021/acsami.9b01948>
- [329] **Yoshida, A., Motoyama, M., Kosaku, A. and Miyamoto, K. (1996)** 'Nanoprotuberance Array in the Transparent Wing of a Hawkmoth, *Cephonodes hylas*', *Zoological Science* **13**(4): 525-526. <https://doi.org/10.2108/zsj.13.525>
- [330] **Yoshida, A., Motoyama, M., Kosaku, A. and Miyamoto, K. (1997)** 'Antireflective Nanoprotuberance Array in the Transparent Wing of a Hawkmoth, *Cephonodes hylas*', *Zoological Science* **14**(5): 737-741. <https://doi.org/10.2108/zsj.14.737>

- [331] **Bernhard, C. G. and Miller, W. H. (1962)** 'A corneal nipple pattern in insect compound eyes', *Acta Physiologica Scandinavica* **56**: 385-386. <https://doi.org/10.1111/j.1748-1716.1962.tb02515.x>
- [332] **Clapham, P. B. and Hutley, M. C. (1973)** 'Reduction of Lens Reflexion by the "Moth Eye" Principle', *Nature* **244**(5414): 281-282. <https://doi.org/10.1038/244281a0>
- [333] **Bernhard, C. G., Miller, W. H. and Moller, A. R. (1963)** 'Function of the corneal nipples in the compound eyes of insects', *Acta Physiologica Scandinavica* **58**: 381-382. <https://doi.org/10.1111/j.1748-1716.1963.tb02661.x>
- [334] **Bernhard, C. G., Miller, W. H. and Moller, A. R. (1965)** 'The insect corneal nipple array. A biological broad-band impedance transformer that acts as an antireflection coating', *Acta Physiologica Scandinavica Supplementum*: SUPPL 243:1-79
- [335] **Miller, W. H., Bernard, G. D. and Allen, J. L. (1968)** 'The optics of insect compound eyes', *Science* **162**(3855): 760-767. <https://doi.org/10.1126/science.162.3855.760>
- [336] **Bernhard, C. G., Gemne, G. and Moller, A. R. (1968)** 'Modification of specular reflexion and light transmission by biological surface structures', *Quarterly Reviews of Biophysics* **1**(1): 89-105. <https://doi.org/10.1017/s0033583500000470>
- [337] **Bernhard, C. G., Gemne, G. and Sllstrm, J. (1970)** 'Comparative ultrastructure of corneal surface topography in insects with aspects on phylogenesis and function', *Zeitschrift fr Vergleichende Physiologie* **67**(1): 1-25. <https://doi.org/10.1007/BF00298117>
- [338] **Stavroulakis, P. I., Boden, S. A., Johnson, T. and Bagnall, D. M. (2013)** 'Suppression of backscattered diffraction from sub-wavelength 'moth-eye' arrays', *Optics Express* **21**(1): 1. <https://doi.org/10.1364/OE.21.000001>
- [339] **Aizenberg, J., Tkachenko, A., Weiner, S., Addadi, L. and Hendler, G. (2001)** 'Calcitic microlenses as part of the photoreceptor system in brittlestars', *Nature* **412**(6849): 819-822. <https://doi.org/10.1038/35090573>
- [340] **Kuo, W.-K., Hsu, J.-J., Nien, C.-K. and Yu, H. H. (2016)** 'Moth-Eye-Inspired Biophotonic Surfaces with Antireflective and Hydrophobic Characteristics', *ACS Applied Materials & Interfaces* **8**(46): 32021-32030. <https://doi.org/10.1021/acsami.6b10960>

- [341] **Barthlott, W., Neinhuis, C., Cutler, D., Ditsch, F., Meusel, I., Theisen, I. and Wilhelmi, H. (1998)** 'Classification and terminology of plant epicuticular waxes', *Botanical Journal of the Linnean Society* **126**(3): 237-260. <https://doi.org/10.1006/bojl.1997.0137>
- [342] **Koch, K., Bhushan, B. and Barthlott, W. (2009)** 'Multifunctional surface structures of plants: An inspiration for biomimetics', *Progress in Materials Science* **54**(2): 137-178. <https://doi.org/10.1016/j.pmatsci.2008.07.003>
- [343] **Antoniou Kourouniotti, R. L., Band, L. R., Fozard, J. A., Hampstead, A., Lovrics, A., Moyroud, E., Vignolini, S., King, J. R., Jensen, O. E. and Glover, B. J. (2013)** 'Buckling as an origin of ordered cuticular patterns in flower petals', *Journal of The Royal Society Interface* **10**(80): 20120847. <https://doi.org/10.1098/rsif.2012.0847>
- [344] **Kay, Q. O. N., Daoud, H. S. and Stirton, C. H. (1981)** 'Pigment distribution, light reflection and cell structure in petals', *Botanical Journal of the Linnean Society* **83**: 57-83. <https://doi.org/10.1111/j.1095-8339.1981.tb00129.x>
- [345] **Christensen, K. I. and Hansen, H. V. (1998)** 'SEM-studies of epidermal patterns of petals in the angiosperms' Copenhagen: Council for Nordic Publ. in Botany. Opera Botanica. 135. ISBN: 8788702634
- [346] **Thomas, K. R., Kolle, M., Whitney, H. M., Glover, B. J. and Steiner, U. (2010)** 'Function of blue iridescence in tropical understorey plants', *Journal of The Royal Society Interface* **7**(53): 1699-1707. <https://doi.org/10.1098/rsif.2010.0201>
- [347] **Vignolini, S., Moyroud, E., Glover, B. J. and Steiner, U. (2013)** 'Analysing photonic structures in plants', *Journal of The Royal Society Interface* **10**(87): 20130394. <https://doi.org/10.1098/rsif.2013.0394>
- [348] **Jacobs, M., Lopez-Garcia, M., Phrathep, O.-P., Lawson, T., Oulton, R. and Whitney, H. M. (2016)** 'Photonic multilayer structure of *Begonia* chloroplasts enhances photosynthetic efficiency', *Nature Plants* **2**(11): 16162. <https://doi.org/10.1038/nplants.2016.162>
- [349] **van de Kerkhof, G. T., Schertel, L., Poon, R. N., Jacucci, G., Glover, B. J. and Vignolini, S. (2020)** 'Disordered wax platelets on *Tradescantia pallida* leaves create golden shine', *Faraday Discussions* **223**: 207-215. <https://doi.org/10.1039/d0fd00024h>

- [350] **Steiner, L. M., Ogawa, Y., Johansen, V. E., Lundquist, C. R., Whitney, H. and Vignolini, S. (2019)** 'Structural colours in the frond of *Microsorium thailandicum*', *Interface Focus* **9**(1): 20180055. <https://doi.org/10.1098/rsfs.2018.0055>
- [351] **Whitney, H. M., Kolle, M., Andrew, P., Chittka, L., Steiner, U. and Glover, B. J. (2009)** 'Floral Iridescence, Produced by Diffractive Optics, Acts As a Cue for Animal Pollinators', *Science* **323**(5910): 130-133. <https://doi.org/10.1126/science.1166256>
- [352] **Vignolini, S., Moyroud, E., Hingant, T., Banks, H., Rudall, P. J., Steiner, U. and Glover, B. J. (2015)** 'The flower of *Hibiscus trionum* is both visibly and measurably iridescent', *The New Phytologist* **205**(1): 97-101. <https://doi.org/10.1111/nph.12958>
- [353] **Bradshaw, E., Rudall, P. J., Devey, D. S., Thomas, M. M., Glover, B. J. and Bateman, R. M. (2010)** 'Comparative labellum micromorphology of the sexually deceptive temperate orchid genus *Ophrys*: diverse epidermal cell types and multiple origins of structural colour', *Botanical Journal of the Linnean Society* **162**(3): 504-540. <https://doi.org/10.1111/j.1095-8339.2010.01033.x>
- [354] **Whitney, H. M., Reed, A., Rands, S. A., Chittka, L. and Glover, B. J. (2016)** 'Flower Iridescence Increases Object Detection in the Insect Visual System without Compromising Object Identity', *Current Biology* **26**(6): 802-808. <https://doi.org/10.1016/j.cub.2016.01.026>
- [355] **Fernandes, S. N., Geng, Y., Vignolini, S., Glover, B. J., Trindade, A. C., Canejo, J. P., Almeida, P. L., Brogueira, P. and Godinho, M. H. (2013)** 'Structural Color and Iridescence in Transparent Sheared Cellulosic Films', *Macromolecular Chemistry and Physics* **214**(1): 25-32. <https://doi.org/10.1002/macp.201200351>
- [356] **van der Kooi, C. J., Wilts, B. D., Leertouwer, H. L., Staal, M., Elzenga, J. T. M. and Stavenga, D. G. (2014)** 'Iridescent flowers? Contribution of surface structures to optical signaling', *The New Phytologist* **203**(2): 667-673. <https://doi.org/10.1111/nph.12808>
- [357] **Vignolini, S., Davey, M. P., Bateman, R. M., Rudall, P. J., Moyroud, E., Tratt, J., Malmgren, S., Steiner, U. and Glover, B. J. (2012)** 'The mirror crack'd: both pigment and structure contribute to the glossy blue appearance of the mirror orchid, *Ophrys speculum*', *The New Phytologist* **196**(4): 1038-1047. <https://doi.org/10.1111/j.1469-8137.2012.04356.x>

- [358] **Vignolini, S., Thomas, M. M., Kolle, M., Wenzel, T., Rowland, A. V., Rudall, P. J., Baumberg, J. J., Glover, B. J. and Steiner, U. (2012)** 'Directional scattering from the glossy flower of *Ranunculus*: how the buttercup lights up your chin', *Journal of The Royal Society Interface* **9**(71): 1295-1301. <https://doi.org/10.1098/rsif.2011.0759>
- [359] **van der Kooi, C. J., Dyer, A. G. and Stavenga, D. G. (2015)** 'Is floral iridescence a biologically relevant cue in plant-pollinator signaling?', *The New Phytologist* **205**(1): 18-20. <https://doi.org/10.1111/nph.13066>
- [360] **van der Kooi, C. J., Dyer, A. G., Kevan, P. G. and Lunau, K. (2019)** 'Functional significance of the optical properties of flowers for visual signalling', *Annals of Botany* **123**(2): 263-276. <https://doi.org/10.1093/aob/mcy119>
- [361] **Morehouse, N. I. and Rutowski, R. L. (2009)** 'Comment on "Floral iridescence, produced by diffractive optics, acts as a cue for animal pollinators"', *Science* **325**(5944): 1072; author reply 1072. <https://doi.org/10.1126/science.1173324>
- [362] **Whitney, H. M., Kolle, M., Andrew, P., Chittka, L., Steiner, U. and Glover, B. J. (2009)** 'Response to Comment on "Floral Iridescence, Produced by Diffractive Optics, Acts As a Cue for Animal Pollinators"', *Science* **325**(5944): 1072. <https://doi.org/10.1126/science.1173503>
- [363] **Heather M. Whitney, Alison Reed, Sean A. Rands, Lars Chittka and Beverley J. Glover (2016)** 'Flower Iridescence Increases Object Detection in the Insect Visual System without Compromising Object Identity', *Current Biology* **26**(6): 802-808. <https://doi.org/10.1016/j.cub.2016.01.026>
- [364] **Garcia, J. E., Shrestha, M., Howard, S. R., Petersen, P. and Dyer, A. G. (2019)** 'Signal or cue: the role of structural colors in flower pollination', *Current Zoology* **65**(4): 467-481. <https://doi.org/10.1093/cz/zoy096>
- [365] **Garcia, J. E., Shrestha, M., Ospina-Rozo, L., Dekiwadia, C., Field, M. R., Ma, J. S., Tran, N., Dyer, A. G., Fox, K. and Greentree, A. D. (2020)** 'Iridescence and hydrophobicity have no clear delineation that explains flower petal micro-surface', *Scientific Reports* **10**(1): 10685. <https://doi.org/10.1038/s41598-020-67663-6>
- [366] **Moyroud, E., Wenzel, T., Middleton, R., Rudall, P. J., Banks, H., Reed, A., Mellers, G., Killoran, P., Westwood, M. M., Steiner, U., Vignolini, S. and Glover, B. J. (2017)** 'Disorder in convergent floral nanostructures

- enhances signalling to bees', *Nature* **550**(7677): 469-474.  
<https://doi.org/10.1038/nature24285>
- [367] **Daumer, K. (1958)** 'Blumenfarben, wie sie die Bienen sehen', *Zeitschrift für vergleichende Physiologie* **41**(1): 49-110
- [368] **Lee, D. W. (1991)** 'Ultrastructural basis and function of iridescent blue colour of fruits in *Elaeocarpus*', *Nature* **349**(6306): 260-262.  
<https://doi.org/10.1038/349260A0>
- [369] **Lee, D. W., Taylor, G. T. and Irvine, A. K. (2000)** 'Structural Fruit Coloration in *Delaribrea michieana* (Araliaceae)', *International Journal of Plant Sciences* **161**(2): 297-300. <https://doi.org/10.1086/314249>
- [370] **Vignolini, S., Rudall, P. J., Rowland, A. V., Reed, A., Moyroud, E., Faden, R. B., Baumberg, J. J., Glover, B. J. and Steiner, U. (2012)** 'Pointillist structural color in *Pollia* fruit', *Proceedings of the National Academy of Sciences of the United States of America* **109**(39): 15712-15715.  
<https://doi.org/10.1073/pnas.1210105109>
- [371] **Vignolini, S., Gregory, T., Kolle, M., Lethbridge, A., Moyroud, E., Steiner, U., Glover, B. J., Vukusic, P. and Rudall, P. J. (2016)** 'Structural colour from helicoidal cell-wall architecture in fruits of *Margaritaria nobilis*', *Journal of The Royal Society Interface* **13**(124).  
<https://doi.org/10.1098/rsif.2016.0645>
- [372] **Chandler, C. J., Wilts, B. D., Vignolini, S., Brodie, J., Steiner, U., Rudall, P. J., Glover, B. J., Gregory, T. and Walker, R. H. (2015)** 'Structural colour in *Chondrus crispus*', *Scientific Reports* **5**: 11645.  
<https://doi.org/10.1038/srep11645>
- [373] **Bone, R. A., Lee, D. W. and Norman, J. M. (1985)** 'Epidermal cells functioning as lenses in leaves of tropical rain-forest shade plants', *Applied Optics* **24**(10): 1408-1412. <https://doi.org/10.1364/AO.24.001408>
- [374] **Kumar, R. and Silva, L. (1973)** 'Light ray tracing through a leaf cross section', *Applied Optics* **12**(12): 2950-2954.  
<https://doi.org/10.1364/AO.12.002950>
- [375] **Martin, G., Josserand, S. A., Bornman, J. F. and Vogelmann, T. C. (1989)** 'Epidermal focussing and the light microenvironment within leaves of *Medicago sativa*', *Physiologia Plantarum* **76**(4): 485-492.  
<https://doi.org/10.1111/j.1399-3054.1989.tb05467.x>

- [376] **Poulson, M. E. and Vogelmann, T. C. (1990)** 'Epidermal focussing and effects upon photosynthetic light-harvesting in leaves of *Oxalis*', *Plant, Cell & Environment* **13**(8): 803-811. <https://doi.org/10.1111/j.1365-3040.1990.tb01096.x>
- [377] **Xiao, Y., Tholen, D. and Zhu, X.-G. (2016)** 'The influence of leaf anatomy on the internal light environment and photosynthetic electron transport rate: exploration with a new leaf ray tracing model', *Journal of Experimental Botany* **67**(21): 6021-6035. <https://doi.org/10.1093/jxb/erw359>
- [378] **Vogelmann, T. C., Bornman, J. F. and Yates, D. J. (1996)** 'Focusing of light by leaf epidermal cells', *Physiologia Plantarum* **98**(1): 43-56. <https://doi.org/10.1034/j.1399-3054.1996.980106.x>
- [379] **Brodersen, C. R. and Vogelmann, T. C. (2007)** 'Do epidermal lens cells facilitate the absorptance of diffuse light?', *American Journal of Botany* **94**(7): 1061-1066. <https://doi.org/10.3732/ajb.94.7.1061>
- [380] **Koch, K., Bhushan, B. and Barthlott, W. (2008)** 'Diversity of structure, morphology and wetting of plant surfaces', *Soft Matter* **4**(10): 1943-1963. <https://doi.org/10.1039/b804854a>
- [381] **Exner, F. and Exner, S. (1910)** 'Die physikalischen Grundlagen der Blütenfärbungen'
- [382] **Bernhard, C. G., Gemne, G. and Moller, A. R. (1968)** 'Modification of specular reflexion and light transmission by biological surface structures', *Quarterly Reviews of Biophysics* **1**(1): 89-105. <https://doi.org/10.1017/s0033583500000470>
- [383] **Marloth, R. (1915)** 'The Flora of South Africa: With Synopical Tables of the Genera of the Higher Plants': Darter bros. & Company. Bd. 4. <https://books.google.de/books?id=u2pBAQAIAAJ>
- [384] **Whitney, H. M., Glover, B. J., Walker, R. H. and Ellis, A. G. (2011)** 'The contribution of epidermal structure to flower colour in the South African flora', *Curtis's Botanical Magazine* **28**(4): 349-371. <https://doi.org/10.1111/j.1467-8748.2011.01762.x>
- [385] **Gkikas, D., Argiropoulos, A. and Rhizopoulou, S. (2015)** 'Epidermal focusing of light and modelling of reflectance in floral-petals with conically shaped epidermal cells', *Flora - Morphology, Distribution, Functional Ecology of Plants* **212**: 38-45. <https://doi.org/10.1016/j.flora.2015.02.005>

- [386] **Noda, K.-I., Glover, B. J., Linstead, P. and Martin, C. (1994)** 'Flower colour intensity depends on specialized cell shape controlled by a Myb-related transcription factor', *Nature* **369**(6482): 661-664. <https://doi.org/10.1038/369661a0>
- [387] **Whitney, H. M. and Glover, B. J. (2007)** 'Morphology and development of floral features recognised by pollinators', *Arthropod-Plant Interactions* **1**(3): 147-158. <https://doi.org/10.1007/s11829-007-9014-3>
- [388] **Dyer, A. G., Whitney, H. M., Arnold, S. E. J., Glover, B. J. and Chittka, L. (2007)** 'Mutations perturbing petal cell shape and anthocyanin synthesis influence bumblebee perception of *Antirrhinum majus* flower colour', *Arthropod-Plant Interactions* **1**(1): 45-55. <https://doi.org/10.1007/s11829-007-9002-7>
- [389] **Whitney, H. M., Poetes, R., Steiner, U., Chittka, L. and Glover, B. J. (2011)** 'Determining the contribution of epidermal cell shape to petal wettability using isogenic *Antirrhinum* lines', *PLOS ONE* **6**(3): e17576. <https://doi.org/10.1371/journal.pone.0017576>
- [390] **Rudall, P. J. (2020)** 'Colourful cones: how did flower colour first evolve?', *Journal of Experimental Botany* **71**(3): 759-767. <https://doi.org/10.1093/jxb/erz479>
- [391] **Whitney, H. M., Federle, W. and Glover, B. J. (2009)** 'Grip and slip: mechanical interactions between insects and the epidermis of flowers and flower stalks', *Communicative & Integrative Biology* **2**(6): 505-508. <https://doi.org/10.4161/cib.2.6.9479>
- [392] **Whitney, H. M., Chittka, L., Bruce, T. J. A. and Glover, B. J. (2009)** 'Conical epidermal cells allow bees to grip flowers and increase foraging efficiency', *Current Biology* **19**(11): 948-953. <https://doi.org/10.1016/j.cub.2009.04.051>
- [393] **Rands, S. A., Glover, B. J. and Whitney, H. M. (2011)** 'Floral epidermal structure and flower orientation: getting to grips with awkward flowers', *Arthropod-Plant Interactions* **5**(4): 279-285. <https://doi.org/10.1007/s11829-011-9146-3>
- [394] **Alcorn, K., Whitney, H. M. and Glover, B. (2012)** 'Flower movement increases pollinator preference for flowers with better grip', *Functional Ecology* **26**(4): 941-947. <https://doi.org/10.1111/j.1365-2435.2012.02009.x>

- [395] **Prüm, B., Seidel, R., Bohn, H. F. and Speck, T. (2012)** 'Plant surfaces with cuticular folds are slippery for beetles', *Journal of The Royal Society Interface* **9**(66): 127-135. <https://doi.org/10.1098/rsif.2011.0202>
- [396] **Prüm, B., Seidel, R., Bohn, H. F. and Speck, T. (2012)** 'Impact of cell shape in hierarchically structured plant surfaces on the attachment of male Colorado potato beetles (*Leptinotarsa decemlineata*)', *Beilstein Journal of Nanotechnology* **3**: 57-64. <https://doi.org/10.3762/bjnano.3.7>
- [397] **Whitney, H. M., Bennett, K. M. V., Dorling, M., Sandbach, L., Prince, D., Chittka, L. and Glover, B. J. (2011)** 'Why do so many petals have conical epidermal cells?', *Annals of Botany* **108**(4): 609-616. <https://doi.org/10.1093/aob/mcr065>
- [398] **Frisch, K. V. (1949)** 'Die Polarisation des Himmelslichtes als orientierender Faktor bei den Tänzen der Bienen', *Experientia* **5**(4): 142-148. <https://doi.org/10.1007/BF02174424>
- [399] **Foster, J. J., Sharkey, C. R., Gaworska, A. V. A., Roberts, N. W., Whitney, H. M. and Partridge, J. C. (2014)** 'Bumblebees learn polarization patterns', *Current Biology* **24**(12): 1415-1420. <https://doi.org/10.1016/j.cub.2014.05.007>
- [400] **Horváth, G., Gál, J., Labhart, T. and Wehner, R. (2002)** 'Does reflection polarization by plants influence colour perception in insects? Polarimetric measurements applied to a polarization-sensitive model retina of Papilio butterflies', *The Journal of Experimental Biology* **205**(21): 3281-3298. <https://doi.org/10.5167/uzh-647>
- [401] **Wenzel, R. N. (1936)** 'Resistance of solid surfaces to wetting by water', *Industrial & Engineering Chemistry* **28**(8): 988-994. <https://doi.org/10.1021/ie50320a024>
- [402] **Cassie, A. B. D. and Baxter, S. (1944)** 'Wettability of porous surfaces', *Trans. Faraday Soc.* **40**: 546-551. <https://doi.org/10.1039/TF94444000546>
- [403] **unav (1805)** 'III. An essay on the cohesion of fluids', *Philosophical Transactions of the Royal Society of London* **95**: 65-87. <https://doi.org/10.1098/RSTL.1805.0005>
- [404] **Marmur, A. (2003)** 'Wetting on Hydrophobic Rough Surfaces: To Be Heterogeneous or Not To Be?', *Langmuir* **19**(20): 8343-8348. <https://doi.org/10.1021/la0344682>

- [405] **Bhushan, B. and Nosonovsky, M. (2010)** 'The rose petal effect and the modes of superhydrophobicity', *Philosophical Transactions of the Royal Society A* **368**(1929): 4713-4728. <https://doi.org/10.1098/rsta.2010.0203>
- [406] **Marmur, A. (2004)** 'The Lotus effect: superhydrophobicity and metastability', *Langmuir* **20**(9): 3517-3519. <https://doi.org/10.1021/la036369u>
- [407] **Barthlott, W. and Neinhuis, C. (1997)** 'Purity of the sacred lotus, or escape from contamination in biological surfaces', *Planta* **202**(1): 1-8. <https://doi.org/10.1007/s004250050096>
- [408] **Ensikat, H. J., Ditsche-Kuru, P., Neinhuis, C. and Barthlott, W. (2011)** 'Superhydrophobicity in perfection: the outstanding properties of the lotus leaf', *Beilstein Journal of Nanotechnology* **2**: 152-161. <https://doi.org/10.3762/bjnano.2.19>
- [409] **Koch, K., Dommisse, A. and Barthlott, W. (2006)** 'Chemistry and Crystal Growth of Plant Wax Tubules of Lotus ( *Nelumbonucifera* ) and Nasturtium ( *Tropaeolummajus* ) Leaves on Technical Substrates', *Crystal Growth & Design* **6**(11): 2571-2578. <https://doi.org/10.1021/cg060035w>
- [410] **Bhushan, B., Jung, Y. C. and Koch, K. (2009)** 'Micro-, nano- and hierarchical structures for superhydrophobicity, self-cleaning and low adhesion', *Philosophical Transactions of the Royal Society A* **367**(1894): 1631-1672. <https://doi.org/10.1098/rsta.2009.0014>
- [411] **Koch, K., Blecher, I. C., König, G., Kehraus, S. and Barthlott, W. (2009)** 'The superhydrophilic and superoleophilic leaf surface of *Ruellia devosiana* (Acanthaceae): a biological model for spreading of water and oil on surfaces', *Functional plant biology : FPB* **36**(4): 339-350. <https://doi.org/10.1071/FP08295>
- [412] **Feng, L., Zhang, Y., Xi, J., Zhu, Y., Wang, N., Xia, F. and Jiang, L. (2008)** 'Petal effect: a superhydrophobic state with high adhesive force', *Langmuir* **24**(8): 4114-4119. <https://doi.org/10.1021/la703821h>
- [413] **Ghosh, U. U., Nair, S., Das, A., Mukherjee, R. and DasGupta, S. (2019)** 'Replicating and resolving wetting and adhesion characteristics of a Rose petal', *Colloids and Surfaces A: Physicochemical and Engineering Aspects* **561**: 9-17. <https://doi.org/10.1016/j.colsurfa.2018.10.028>

- [414] **Bhushan, B. and Her, E. K. (2010)** 'Fabrication of Superhydrophobic Surfaces with High and Low Adhesion Inspired from Rose Petal', *Langmuir* **26**(11): 8207-8217. <https://doi.org/10.1021/la904585j>
- [415] **Yeh, K.-Y., Cho, K.-H., Yeh, Y.-H., Promraksa, A., Huang, C.-H., Hsu, C.-C. and Chen, L.-J. (2014)** 'Observation of the rose petal effect over single- and dual-scale roughness surfaces', *Nanotechnology* **25**(34): 345303. <https://doi.org/10.1088/0957-4484/25/34/345303>
- [416] **Chakraborty, M., Weibel, J. A., Schaber, J. A. and Garimella, S. V. (2019)** 'The Wetting State of Water on a Rose Petal', *Advanced Materials Interfaces* **6**(17): 1900652. <https://doi.org/10.1002/admi.201900652>
- [417] **Wong, W. S. Y., Nasiri, N., Liu, G., Rumsey-Hill, N., Craig, V. S. J., Nisbet, D. R. and Tricoli, A. (2015)** 'Flexible Transparent Hierarchical Nanomesh for Rose Petal-Like Droplet Manipulation and Lossless Transfer', *Advanced Materials Interfaces* **2**(9): 1500071. <https://doi.org/10.1002/admi.201500071>
- [418] **Mahanta, U., Khandelwal, M. and Deshpande, A. S. (2019)** 'Wetting Transition from Lotus Leaf to Rose Petal using Modified Fly Ash', *ChemistrySelect* **4**(27): 7936-7942. <https://doi.org/10.1002/slct.201901535>
- [419] **Fernández, A., Francone, A., Thamdrup, L. H., Johansson, A., Bilenberg, B., Nielsen, T., Guttman, M., Sotomayor Torres, C. M. and Kehagias, N. (2017)** 'Design of Hierarchical Surfaces for Tuning Wetting Characteristics', *ACS Applied Materials & Interfaces* **9**(8): 7701-7709. <https://doi.org/10.1021/acsami.6b13615>
- [420] **Schulte, A. J., Droste, D. M., Koch, K. and Barthlott, W. (2011)** 'Hierarchically structured superhydrophobic flowers with low hysteresis of the wild pansy (*Viola tricolor*) - new design principles for biomimetic materials', *Beilstein Journal of Nanotechnology* **2**: 228-236. <https://doi.org/10.3762/bjnano.2.27>
- [421] **Taneda, H., Watanabe-Taneda, A., Chhetry, R. and Ikeda, H. (2015)** 'A theoretical approach to the relationship between wettability and surface microstructures of epidermal cells and structured cuticles of flower petals', *Annals of Botany* **115**(6): 923-937. <https://doi.org/10.1093/aob/mcv024>
- [422] **Barthlott, W., Schimmel, T., Wiersch, S., Koch, K., Brede, M., Barczewski, M., Walheim, S., Weis, A., Kaltenmaier, A., Leder, A. and**

- Bohn, H. F. (2010)** 'The salvinia paradox: superhydrophobic surfaces with hydrophilic pins for air retention under water', *Advanced Materials* **22**(21): 2325-2328. <https://doi.org/10.1002/adma.200904411>
- [423] **Hunt, J. and Bhushan, B. (2011)** 'Nanoscale biomimetics studies of *Salvinia molesta* for micropattern fabrication', *Journal of Colloid and Interface Science* **363**(1): 187-192. <https://doi.org/10.1016/j.jcis.2011.06.084>
- [424] **Wang, G., Guo, Z. and Liu, W. (2014)** 'Interfacial effects of superhydrophobic plant surfaces: A review', *Journal of Bionic Engineering* **11**(3): 325-345. [https://doi.org/10.1016/S1672-6529\(14\)60047-0](https://doi.org/10.1016/S1672-6529(14)60047-0)
- [425] **Webb, H. K., Crawford, R. J. and Ivanova, E. P. (2014)** 'Wettability of natural superhydrophobic surfaces', *Advances in Colloid and Interface Science* **210**: 58-64. <https://doi.org/10.1016/j.cis.2014.01.020>
- [426] **Pye, K. (1987)** 'Aeolian Dust and Dust Deposits': Elsevier. ISBN: 9780125686907
- [427] **Darwish, Z. A., Kazem, H. A., Sopian, K., Al-Goul, M. A. and Alawadhi, H. (2015)** 'Effect of dust pollutant type on photovoltaic performance', *Renewable and Sustainable Energy Reviews* **41**: 735-744. <https://doi.org/10.1016/j.rser.2014.08.068>
- [428] **Cabanillas, R. E. and Munguía, H. (2011)** 'Dust accumulation effect on efficiency of Si photovoltaic modules', *Journal of Renewable and Sustainable Energy* **3**(4): 43114. <https://doi.org/10.1063/1.3622609>
- [429] **Maghami, M. R., Hizam, H., Gomes, C., Radzi, M. A., Rezadad, M. I. and Hajighorbani, S. (2016)** 'Power loss due to soiling on solar panel: A review', *Renewable and Sustainable Energy Reviews* **59**: 1307-1316. <https://doi.org/10.1016/j.rser.2016.01.044>
- [430] **Micheli, L. and Muller, M. (2017)** 'An investigation of the key parameters for predicting PV soiling losses', *Progress in Photovoltaics: Research and Applications* **25**(4): 291-307. <https://doi.org/10.1002/pip.2860>
- [431] **John, J. J. (2015)** 'Characterization of soiling loss on photovoltaic modules, and development of a novel cleaning system'. *Dissertation*. Indian Institute of Technology Bombay
- [432] **Ilse, K. K., Figgis, B. W., Naumann, V., Hagendorf, C. and Bagdahn, J. (2018)** 'Fundamentals of soiling processes on photovoltaic modules', *Renewable and Sustainable Energy Reviews* **98**: 239-254. <https://doi.org/10.1016/j.rser.2018.09.015>

- [433] **Javed, W., Guo, B. and Figgis, B. (2017)** 'Modeling of photovoltaic soiling loss as a function of environmental variables', *Solar Energy* **157**: 397-407. <https://doi.org/10.1016/j.solener.2017.08.046>
- [434] **Sayyah, A., Horenstein, M. N. and Mazumder, M. K. (2014)** 'Energy yield loss caused by dust deposition on photovoltaic panels', *Solar Energy* **107**: 576-604. <https://doi.org/10.1016/j.solener.2014.05.030>
- [435] **Al-Hasan, A. Y. (1998)** 'A new correlation for direct beam solar radiation received by photovoltaic panel with sand dust accumulated on its surface', *Solar Energy* **63**(5): 323-333. [https://doi.org/10.1016/S0038-092X\(98\)00060-7](https://doi.org/10.1016/S0038-092X(98)00060-7)
- [436] **Sayigh, A., Charchafchi, S., & Al-Habali, A. (1979)** 'Experimental evaluation of solar cells in arid zones', *Proceedings of the Izmir International Symposium on Solar Energy Fundamentals and Applications, Izmir, Turkey*: 1-5
- [437] **Wakim, F. (1981)** 'Introduction of PV power generation to Kuwait', *Kuwait Institute for Scientific Researchers, Kuwait City*
- [438] **Jamil, W. J., Abdul Rahman, H., Shaari, S. and Salam, Z. (2017)** 'Performance degradation of photovoltaic power system: Review on mitigation methods', *Renewable and Sustainable Energy Reviews* **67**: 876-891. <https://doi.org/10.1016/j.rser.2016.09.072>
- [439] **Chen, E. Y.-T., Chen, Y., Guo, B. and Liang, H. (2019)** 'Effects of surface morphological parameters on cleaning efficiency of PV panels', *Solar Energy* **194**: 840-847. <https://doi.org/10.1016/j.solener.2019.10.087>
- [440] **Naeem, M. H. (2014)** 'Soiling of Photovoltaic Modules: Modelling and Validation of Location-Specific Cleaning Frequency Optimization'. *Master Thesis*. Arizona State University
- [441] **Al-Jawah, M. J. (2014)** 'A Decision Aiding Framework for Investing in Cleaning Systems for Solar Photovoltaic (PV) Power Plants in Arid Regions'. *Dissertation*. George Washington University
- [442] **Al-Sabounchi, A. M., Yalyali, S. A. and Al-Thani, H. A. (2013)** 'Design and performance evaluation of a photovoltaic grid-connected system in hot weather conditions', *Renewable Energy* **53**: 71-78. <https://doi.org/10.1016/j.renene.2012.10.039>
- [443] **Mani, M. and Pillai, R. (2010)** 'Impact of dust on solar photovoltaic (PV) performance: Research status, challenges and recommendations',

- 
- Renewable and Sustainable Energy Reviews* **14**(9): 3124-3131.  
<https://doi.org/10.1016/j.rser.2010.07.065>
- [444] **Ilse, K., Micheli, L., Figgis, B. W., Lange, K., Daßler, D., Hanifi, H., Wolfertstetter, F., Naumann, V., Hagendorf, C. and Gottschalg, R. (2019)** 'Techno-economic assessment of soiling losses and mitigation strategies for solar power generation', *Joule* **3**(10): 2303-2321.  
<https://doi.org/10.1016/j.joule.2019.08.019>
- [445] **Alvarez, D. L., Al-Sumaiti, A. S. and Rivera, S. R. (2020)** 'Estimation of an Optimal PV Panel Cleaning Strategy Based on Both Annual Radiation Profile and Module Degradation', *IEEE Access* **8**: 63832-63839.  
<https://doi.org/10.1109/ACCESS.2020.2983322>
- [446] **Di Sun and Böhringer, K. F. (2020)** 'An active self-cleaning surface system for photovoltaic modules using anisotropic ratchet conveyors and mechanical vibration', *Microsystems & Nanoengineering* **6**(1).  
<https://doi.org/10.1038/s41378-020-00197-z>
- [447] **Appels, R., Lefevre, B., Herteleer, B., Goverde, H., Beerten, A., Paesen, R., Medts, K. de, Driesen, J. and Poortmans, J. (2013)** 'Effect of soiling on photovoltaic modules', *Solar Energy* **96**: 283-291.  
<https://doi.org/10.1016/j.solener.2013.07.017>
- [448] **Schill, C., Brachmann, S., Heck, M., Weiss, K.-A. and Koehl, M. (2011)** 'Impact of heavy soiling on the power output of PV modules'. In: Neelkanth G. Dhere, John H. Wohlgemuth, and Kevin W. Lynn, eds.: SPIE, p. 811207
- [449] **Smith, M. K., Wamser, C. C., James, K. E., Moody, S., Sailor, D. J. and Rosenstiel, T. N. (2013)** 'Effects of Natural and Manual Cleaning on Photovoltaic Output', *Journal of Solar Energy Engineering* **135**(3).  
<https://doi.org/10.1115/1.4023927>
- [450] **Azouzoute, A., Garoum, M., Jeffali, F., Ghali Bennouna, E. and Ghennioui, A. (2020)** 'Experimental study of dust effect on the transmission of a glass PV panel for a fixed and tracking system', *Materials Today: Proceedings* **27**: 3091-3094.  
<https://doi.org/10.1016/j.matpr.2020.03.646>
- [451] **Cano, J., John, J. J., Tatapudi, S. and TamizhMani, G. (2014)** 'Effect of tilt angle on soiling of photovoltaic modules'. Piscataway, NJ: IEEE Service Center, pp. 3174-3176
-

- [452] **Heckenthaler, T., Sadhujan, S., Morgenstern, Y., Natarajan, P., Bashouti, M. and Kaufman, Y. (2019)** 'Self-Cleaning Mechanism: Why Nanotexture and Hydrophobicity Matter', *Langmuir* **35**(48): 15526-15534. <https://doi.org/10.1021/acs.langmuir.9b01874>
- [453] **Crisp, D. J. and Thorpe, W. H. (1950)** 'A simple replica technique suitable for the study of surface structures', *Nature* **165**(4190): 273. <https://doi.org/10.1038/165273a0>
- [454] **Sampson, J. (1961)** 'A method of replicating dry or moist surfaces for examination by light microscopy', *Nature* **191**: 932-933. <https://doi.org/10.1038/191932a0>
- [455] **Pulsifer, D. P., Lakhtakia, A., Martín-Palma, R. J. and Pantano, C. G. (2011)** 'Engineered biomimicry: polymeric replication of surface features found on insects', *Proc. SPIE 7975, Bioinspiration, Biomimetics, and Bioreplication*: 79750O. <https://doi.org/10.1117/12.876479>
- [456] **Martin, G., Myres, D. A. and Vogelmann, T. C. (1991)** 'Characterization of Plant Epidermal Lens Effects by a Surface Replica Technique', *Journal of Experimental Botany* **42**(5): 581-587. <https://doi.org/10.1093/jxb/42.5.581>
- [457] **Feng, L., Zhang, Y., Li, M., Zheng, Y., Shen, W. and Jiang, L. (2010)** 'The Structural Color of Red Rose Petals and Their Duplicates', *Langmuir* **26**(18): 14885-14888. <https://doi.org/10.1021/la102406u>
- [458] **Lee, S.-M., Üpping, J., Bielawny, A. and Knez, M. (2010)** 'Structure-Based Color of Natural Petals Discriminated by Polymer Replication', *ACS Applied Materials & Interfaces* **3**(1): 30-34. <https://doi.org/10.1021/am1007968>
- [459] **Schulte, A. J., Mail, M., Hahn, L. A. and Barthlott, W. (2019)** 'Ultraviolet patterns of flowers revealed in polymer replica - caused by surface architecture', *Beilstein Journal of Nanotechnology* **10**: 459-466. <https://doi.org/10.3762/bjnano.10.45>
- [460] **Pulsifer, D. P. and Lakhtakia, A. (2011)** 'Background and survey of bioreplication techniques', *Bioinspiration & Biomimetics* **6**(3): 31001. <https://doi.org/10.1088/1748-3182/6/3/031001>
- [461] **Martín-Palma, R. J., Pantano, C. G. and Lakhtakia, A. (2008)** 'Replication of fly eyes by the conformal-evaporated-film-by-rotation technique', *Nanotechnology* **19**(35): 355704. <https://doi.org/10.1088/0957-4484/19/35/355704>

- 
- [462] **Martín-Palma, R. J., Pantano, C. G. and Lakhtakia, A. (2008)** 'Biomimetization of butterfly wings by the conformal-evaporated-film-by-rotation technique for photonics', *Applied Physics Letters* **93**(8): 83901. <https://doi.org/10.1063/1.2973167>
- [463] **Huang, J., Wang, X. and Wang, Z. L. (2006)** 'Controlled replication of butterfly wings for achieving tunable photonic properties', *Nano Letters* **6**(10): 2325-2331. <https://doi.org/10.1021/nl061851t>
- [464] **Huang, J., Wang, X. and Wang, Z. L. (2008)** 'Bio-inspired fabrication of antireflection nanostructures by replicating fly eyes', *Nanotechnology* **19**(2): 25602. <https://doi.org/10.1088/0957-4484/19/02/025602>
- [465] **Pulsifer, D. P., Lakhtakia, A., Martín-Palma, R. J. and Pantano, C. G. (2010)** 'Mass fabrication technique for polymeric replicas of arrays of insect corneas', *Bioinspiration & Biomimetics* **5**(3): 36001. <https://doi.org/10.1088/1748-3182/5/3/036001>
- [466] **Martín-Palma, R. J. and Lakhtakia, A. (2017)** 'Progress on bioinspired, biomimetic, and bioreplication routes to harvest solar energy', *Applied Physics Reviews* **4**(2): 21103. <https://doi.org/10.1063/1.4981792>
- [467] **Hong, S.-H., Hwang, J. and Lee, H. (2009)** 'Replication of cicada wing's nano-patterns by hot embossing and UV nanoimprinting', *Nanotechnology* **20**(38): 385303. <https://doi.org/10.1088/0957-4484/20/38/385303>
- [468] **Gao, H., Liu, Z., Zhang, J., Zhang, G. and Xie, G. (2007)** 'Precise replication of antireflective nanostructures from biotemplates', *Applied Physics Letters* **90**(12): 123115. <https://doi.org/10.1063/1.2715094>
- [469] **Pan, E. and Zhang, G. (2020)** 'Natural Antireflective Microstructure of Blue Mussel Shells and Biomimetic Replication', *Langmuir* **36**(15): 4065-4070. <https://doi.org/10.1021/acs.langmuir.0c00418>
- [470] **Lee, S.-M., Lee, H. S., Kim, D. S. and Kwon, T. H. (2006)** 'Fabrication of hydrophobic films replicated from plant leaves in nature', *Surface and Coatings Technology* **201**(3-4): 553-559. <https://doi.org/10.1016/j.surfcoat.2005.12.006>
- [471] **Lee, S.-M. and Kwon, T. H. (2006)** 'Mass-producible replication of highly hydrophobic surfaces from plant leaves', *Nanotechnology* **17**(13): 3189-3196. <https://doi.org/10.1088/0957-4484/17/13/019>
- [472] **Lee, S.-M. and Kwon, T. H. (2007)** 'Effects of intrinsic hydrophobicity on wettability of polymer replicas of a superhydrophobic lotus leaf', *Journal*
-

- of Micromechanics and Microengineering* **17**(4): 687-692. <https://doi.org/10.1088/0960-1317/17/4/003>
- [473] **Ryu, S., Choo, S., Choi, H.-J., Kim, C.-H. and Lee, H. (2014)** 'Replication of rose petal surfaces using a nickel electroforming process and UV nanoimprint lithography', *Applied Surface Science* **322**: 57-63. <https://doi.org/10.1016/j.apsusc.2014.10.063>
- [474] **Weng, C., Wang, F., Zhou, M., Yang, D. and Jiang, B. (2018)** 'Fabrication of hierarchical polymer surfaces with superhydrophobicity by injection molding from nature and function-oriented design', *Applied Surface Science* **436**: 224-233. <https://doi.org/10.1016/j.apsusc.2017.11.268>
- [475] **Koch, K., Schulte, A. J., Fischer, A., Gorb, S. N. and Barthlott, W.** 'A fast, precise and low-cost replication technique for nano- and high-aspect-ratio structures of biological and artificial surfaces', *Bioinspiration & Biomimetics* **3**(4): 46002. <https://doi.org/10.1088/1748-3182/3/4/046002>
- [476] **Choo, S., Choi, H.-J. and Lee, H. (2014)** 'Replication of rose-petal surface structure using UV-nanoimprint lithography', *Materials Letters* **121**: 170-173. <https://doi.org/10.1016/j.matlet.2014.01.037>
- [477] **Sun, M., Luo, C., Xu, L., Ji, H., Ouyang, Q., Yu, D. and Chen, Y. (2005)** 'Artificial lotus leaf by nanocasting', *Langmuir* **21**(19): 8978-8981. <https://doi.org/10.1021/la050316q>
- [478] **Verbanic, S., Brady, O., Sanda, A., Gustafson, C. and Donhauser, Z. J. (2014)** 'A Novel General Chemistry Laboratory: Creation of Biomimetic Superhydrophobic Surfaces through Replica Molding', *Journal of Chemical Education* **91**(9): 1477-1480. <https://doi.org/10.1021/ed4007056>
- [479] **Yuan, Z., Chen, H., Tang, J., Gong, H., Liu, Y., Wang, Z., Shi, P., Zhang, J. and Chen, X. (2007)** 'A novel preparation of polystyrene film with a superhydrophobic surface using a template method', *Journal of Physics D: Applied Physics* **40**(11): 3485-3489. <https://doi.org/10.1088/0022-3727/40/11/033>
- [480] **Guo, P., Zheng, Y., Liu, C., Ju, J. and Jiang, L. (2012)** 'Directional shedding-off of water on natural/bio-mimetic taper-ratchet array surfaces', *Soft Matter* **8**(6): 1770-1775. <https://doi.org/10.1039/C1SM06631E>
- [481] **Kim, G. H., Jeon, H. J. and Yoon, H. (2009)** 'Electric field-aided formation combined with a nanoimprinting technique for replicating a plant leaf',

- Macromolecular rapid communications* **30**(12): 991-996.  
<https://doi.org/10.1002/marc.200900076>
- [482] **Jin, G. and Kim, G. (2011)** 'Pressure/electric-field-assisted micro/nanocasting method for replicating a lotus leaf', *Langmuir* **27**(2): 828-834. <https://doi.org/10.1021/la1040954>
- [483] **Jin, G., Jeon, H. and Kim, G. (2011)** 'Hydrophobic polymer surfaces by lotus leaf replication using an alternating current electric field with an interdigitated electrode', *Soft Matter* **7**(10): 4723. <https://doi.org/10.1039/c0sm01388a>
- [484] **Koch, K., Bhushan, B., Jung, Y. C. and Barthlott, W. (2009)** 'Fabrication of artificial Lotus leaves and significance of hierarchical structure for superhydrophobicity and low adhesion', *Soft Matter* **5**(7): 1386. <https://doi.org/10.1039/b818940d>
- [485] **Bhushan, B., Jung, Y. C. and Koch, K. (2009)** 'Self-cleaning efficiency of artificial superhydrophobic surfaces', *Langmuir* **25**(5): 3240-3248. <https://doi.org/10.1021/la803860d>
- [486] **Chang, J. J., Martin, A., Du, C., Pauls, A. M. and Thuo, M. (2020)** 'Heat-Free Biomimetic Metal Molding on Soft Substrates', *Angewandte Chemie* **59**(38): 16346-16351. <https://doi.org/10.1002/anie.202008621>
- [487] **Ball, P. (1999)** 'Engineering shark skin and other solutions', *Nature* **400**(6744): 507-509. <https://doi.org/10.1038/22883>
- [488] **Gao, X. and Jiang, L. (2004)** 'Water-repellent legs of water striders', *Nature* **432**(7013): 36. <https://doi.org/10.1038/432036a>
- [489] **Zhou, Z. and Liu, Z. (2009)** 'Fabrication of Biomimetic Water Strider Legs Covered with Setae', *Journal of Bionic Engineering* **6**(1): 1-6. [https://doi.org/10.1016/S1672-6529\(08\)60098-0](https://doi.org/10.1016/S1672-6529(08)60098-0)
- [490] **Hansen, W. R. and Autumn, K. (2005)** 'Evidence for self-cleaning in gecko setae', *Proceedings of the National Academy of Sciences of the United States of America* **102**(2): 385-389. <https://doi.org/10.1073/pnas.0408304102>
- [491] **Zheng, Y., Bai, H., Huang, Z., Tian, X., Nie, F.-Q., Zhao, Y., Zhai, J. and Jiang, L. (2010)** 'Directional water collection on wetted spider silk', *Nature* **463**(7281): 640-643. <https://doi.org/10.1038/nature08729>
- [492] **Becker, N., Oroudjev, E., Mutz, S., Cleveland, J. P., Hansma, P. K., Hayashi, C. Y., Makarov, D. E. and Hansma, H. G. (2003)** 'Molecular

- nanosprings in spider capture-silk threads', *Nature Materials* **2**(4): 278-283. <https://doi.org/10.1038/nmat858>
- [493] **Swanson, B. O., Blackledge, T. A. and Hayashi, C. Y. (2007)** 'Spider capture silk: performance implications of variation in an exceptional biomaterial', *Journal of Experimental Zoology Part A, Ecological Genetics and Physiology* **307**(11): 654-666. <https://doi.org/10.1002/jez.420>
- [494] **Liu, Y., Shao, Z. and Vollrath, F. (2005)** 'Relationships between supercontraction and mechanical properties of spider silk', *Nature Materials* **4**(12): 901-905. <https://doi.org/10.1038/nmat1534>
- [495] **Bell, F. I., McEwen, I. J. and Viney, C. (2002)** 'Supercontraction stress in wet spider dragline', *Nature* **416**(6876): 37. <https://doi.org/10.1038/416037a>
- [496] **Emile, O., Le Floch, A. and Vollrath, F. (2006)** 'Biopolymers: shape memory in spider draglines', *Nature* **440**(7084): 621. <https://doi.org/10.1038/440621a>
- [497] **Tan, T., Wong, D. and Lee, P. (2004)** 'Iridescence of a shell of mollusk *Haliotis Glabra*', *Optics Express* **12**(20): 4847-4854. <https://doi.org/10.1364/opex.12.004847>
- [498] **Mayer, G. (2005)** 'Rigid biological systems as models for synthetic composites', *Science* **310**(5751): 1144-1147. <https://doi.org/10.1126/science.1116994>
- [499] **Lin, S., Ai, L., Zhang, J., Bu, T., Li, H., Huang, F., Zhang, J., Lu, Y. and Song, W. (2019)** 'Silver ants-inspired flexible photonic architectures with improved transparency and heat radiation for photovoltaic devices', *Solar Energy Materials and Solar Cells* **203**: 110135. <https://doi.org/10.1016/j.solmat.2019.110135>
- [500] **Wu, W., Lin, S., Wei, M., Huang, J., Xu, H., Lu, Y. and Song, W. (2020)** 'Flexible passive radiative cooling inspired by Saharan silver ants', *Solar Energy Materials and Solar Cells* **210**: 110512. <https://doi.org/10.1016/j.solmat.2020.110512>
- [501] **Jeong, S. Y., Tso, C. Y., Wong, Y. M., Chao, C. and Huang, B. (2020)** 'Daytime passive radiative cooling by ultra emissive bio-inspired polymeric surface', *Solar Energy Materials and Solar Cells* **206**: 110296. <https://doi.org/10.1016/j.solmat.2019.110296>
- [502] **Hsiung, B.-K., Siddique, R. H., Jiang, L., Liu, Y., Lu, Y., Shawkey, M. D. and Blackledge, T. A. (2017)** 'Tarantula-Inspired Noniridescent Photonics

- with Long-Range Order', *Advanced Optical Materials* 5(2): 1600599. <https://doi.org/10.1002/adom.201600599>
- [503] **Chung, K., Yu, S., Heo, C.-J., Shim, J. W., Yang, S.-M., Han, M. G., Lee, H.-S., Jin, Y., Lee, S. Y., Park, N. and Shin, J. H. (2012)** 'Flexible, Angle-Independent, Structural Color Reflectors Inspired by *Morpho* Butterfly Wings', *Advanced Materials* 24(18): 2375-2379. <https://doi.org/10.1002/adma.201200521>
- [504] **Nishimoto, S. and Bhushan, B. (2013)** 'Bioinspired self-cleaning surfaces with superhydrophobicity, superoleophobicity, and superhydrophilicity', *RSC Advances* 3(3): 671-690. <https://doi.org/10.1039/C2RA21260A>
- [505] **Li, Q., Zeng, Q., Shi, L., Zhang, X. and Zhang, K.-Q. (2016)** 'Bio-inspired sensors based on photonic structures of *Morpho* butterfly wings: a review', *Journal of Materials Chemistry C* 4(9): 1752-1763. <https://doi.org/10.1039/C5TC04029A>
- [506] **Siddique, R. H., Donie, Y. J., Gomard, G., Yalamanchili, S., Merdzhanova, T., Lemmer, U. and Hölscher, H. (2017)** 'Bioinspired phase-separated disordered nanostructures for thin photovoltaic absorbers', *Science Advances* 3(10). <https://doi.org/10.1126/sciadv.1700232>
- [507] **Papadopoulos, A., Skoulas, E., Mimidis, A., Perrakis, G., Kenanakis, G., Tsibidis, G. D. and Stratakis, E. (2019)** 'Biomimetic Omnidirectional Antireflective Glass via Direct Ultrafast Laser Nanostructuring', *Advanced Materials* 31(32): e1901123. <https://doi.org/10.1002/adma.201901123>
- [508] **Ivanova, E. P., Hasan, J., Webb, H. K., Truong, V. K., Watson, G. S., Watson, J. A., Baulin, V. A., Pogodin, S., Wang, J. Y., Tobin, M. J., Löbbe, C. and Crawford, R. J. (2012)** 'Natural bactericidal surfaces: mechanical rupture of *Pseudomonas aeruginosa* cells by cicada wings', *Small* 8(16): 2489-2494. <https://doi.org/10.1002/smll.201200528>
- [509] **Diu, T., Faruqui, N., Sjöström, T., Lamarre, B., Jenkinson, H. F., Su, B. and Ryadnov, M. G. (2014)** 'Cicada-inspired cell-instructive nanopatterned arrays', *Scientific Reports* 4: 7122. <https://doi.org/10.1038/srep07122>
- [510] **Feng, C., Gou, T., Li, J., Cai, Y., He, P., Huang, J., Wen, Y., Ma, Y. and Zhang, Z. (2019)** 'A highly transparent polymer coating on the glass with broadband antireflection, antifogging and antifouling properties',

- Materials Research Express* 6(7): 75319. <https://doi.org/10.1088/2053-1591/ab122d>
- [511] **Deniz, H., Khudiyev, T., Buyukserin, F. and Bayindir, M. (2011)** 'Room temperature large-area nanoimprinting for broadband biomimetic antireflection surfaces', *Applied Physics Letters* 99(18): 183107. <https://doi.org/10.1063/1.3657766>
- [512] **Tsui, K.-H., Lin, Q., Chou, H., Zhang, Q., Fu, H., Qi, P. and Fan, Z. (2014)** 'Low-Cost, Flexible, and Self-Cleaning 3D Nanocone Anti-Reflection Films for High-Efficiency Photovoltaics', *Advanced Materials* 26(18): 2805-2811. <https://doi.org/10.1002/adma.201304938>
- [513] **Chuang, C.-H., Lu, D.-M., Wang, P.-H., Lee, W.-Y. and Shaikh, M. O. (2018)** 'Antireflective polymer films via roll to roll UV nanoimprint lithography using an AAO mold', *Microsystem Technologies* 24(1): 389-395. <https://doi.org/10.1007/s00542-017-3299-7>
- [514] **Sun, C.-H., Min, W.-L., Linn, N. C., Jiang, P. and Jiang, B. (2007)** 'Templated fabrication of large area subwavelength antireflection gratings on silicon', *Applied Physics Letters* 91(23): 231105. <https://doi.org/10.1063/1.2821833>
- [515] **Luo, X., Lu, L., Yin, M., Fang, X., Chen, X., Li, D., Yang, L., Li, G. and Ma, J. (2019)** 'Antireflective and self-cleaning glass with robust moth-eye surface nanostructures for photovoltaic utilization', *Materials Research Bulletin* 109: 183-189. <https://doi.org/10.1016/j.materresbull.2018.09.029>
- [516] **Leem, J. W., Kim, S., Lee, S. H., Rogers, J. A., Kim, E. and Yu, J. S. (2014)** 'Efficiency Enhancement of Organic Solar Cells Using Hydrophobic Antireflective Inverted Moth-Eye Nanopatterned PDMS Films', *Advanced Energy Materials* 4(8): 1301315. <https://doi.org/10.1002/aenm.201301315>
- [517] **Kim, M., Jang, S., Choi, J., Kang, S. M. and Choi, M. (2019)** 'Moth-eye Structured Polydimethylsiloxane Films for High-Efficiency Perovskite Solar Cells', *Nano-Micro Letters* 11(1). <https://doi.org/10.1007/s40820-019-0284-y>
- [518] **Lotz, M. R., Petersen, C. R., Markos, C., Bang, O., Jakobsen, M. H. and Taboryski, R. (2018)** 'Direct nanoimprinting of moth-eye structures in chalcogenide glass for broadband antireflection in the mid-infrared', *Optica* 5(5): 557. <https://doi.org/10.1364/OPTICA.5.000557>

- 
- [519] **Haslinger, M., Moharana, A. R. and Mühlberger, M. (17.06.2019 - 19.06.2019)** 'Antireflective moth-eye structures on curved surfaces fabricated by nanoimprint lithography'. In: Uwe F. Behringer and Jo Finders, eds.: SPIE, p. 31
- [520] **Yano, T., Sugawara, H. and Taniguchi, J. (2020)** 'Moth-eye structured mold using sputtered glassy carbon layer for large-scale applications', *Micro and Nano Engineering* **9**: 100077. <https://doi.org/10.1016/j.mne.2020.100077>
- [521] **Wang, L., Xu, B.-B., Chen, Q.-D., Ma, Z.-C., Zhang, R., Liu, Q.-X. and Sun, H.-B. (2011)** 'Maskless laser tailoring of conical pillar arrays for antireflective biomimetic surfaces', *Optics Letters* **36**(17): 3305-3307. <https://doi.org/10.1364/OL.36.003305>
- [522] **Chen, J.-D., Zhou, L., Ou, Q.-D., Li, Y.-Q., Shen, S., Lee, S.-T. and Tang, J.-X. (2014)** 'Enhanced Light Harvesting in Organic Solar Cells Featuring a Biomimetic Active Layer and a Self-Cleaning Antireflective Coating', *Advanced Energy Materials* **4**(9): 1301777. <https://doi.org/10.1002/aenm.201301777>
- [523] **Rakitov, R. and Gorb, S. N. (2013)** 'Brochosomes protect leafhoppers (Insecta, Hemiptera, Cicadellidae) from sticky exudates', *Journal of The Royal Society Interface* **10**(87): 20130445. <https://doi.org/10.1098/rsif.2013.0445>
- [524] **Swain, R. B. (1936)** 'Notes on the oviposition and life history of *Phlepsius Decorus* O.& B. (Cicadellidae)', *The Canadian Entomologist* **68**(12): 280-281. <https://doi.org/10.4039/Ent68280b-12>
- [525] **Yang, S., Sun, N., Stogin, B. B., Wang, J., Huang, Y. and Wong, T.-S. (2017)** 'Ultra-antireflective synthetic brochosomes', *Nature Communications* **8**(1): 1285. <https://doi.org/10.1038/s41467-017-01404-8>
- [526] **Zeiger, C., Rodrigues da Silva, I. C., Mail, M., Kavalenka, M. N., Barthlott, W. and Hölscher, H. (2016)** 'Microstructures of superhydrophobic plant leaves - inspiration for efficient oil spill cleanup materials', *Bioinspiration & Biomimetics* **11**(5): 56003. <https://doi.org/10.1088/1748-3190/11/5/056003>
- [527] **Zeiger, C., Kumberg, J., Vüllers, F., Worgull, M., Hölscher, H. and Kavalenka, M. N. (2017)** 'Selective filtration of oil/water mixtures with
-

- bioinspired porous membranes', *RSC Advances* 7(52): 32806-32811. <https://doi.org/10.1039/C7RA05385A>
- [528] **Vüllers, F., Gomard, G., Preinfalk, J. B., Klampaftis, E., Worgull, M., Richards, B. S., Hölscher, H. and Kavalenka, M. N. (2016)** 'Bioinspired Superhydrophobic Highly Transmissive Films for Optical Applications', *Small* 12(44): 6144-6152. <https://doi.org/10.1002/sml.201601443>
- [529] **Vüllers, F. (2018)** 'Bioinspired superhydrophobic nano- and microstructured surfaces for drag reduction and optoelectronics'. *Dissertation*. Karlsruhe Institute of Technology. <https://doi.org/10.5445/KSP/1000084178>
- [530] **Röhrig, M., Mail, M., Schneider, M., Louvin, H., Hopf, A., Schimmel, T., Worgull, M. and Hölscher, H. (2014)** 'Nanofur for Biomimetic Applications', *Advanced Materials Interfaces* 1(4): 1300083. <https://doi.org/10.1002/admi.201300083>
- [531] **Ingenito, A., Isabella, O. and Zeman, M. (2015)** 'Nano-cones on micro-pyramids: modulated surface textures for maximal spectral response and high-efficiency solar cells', *Progress in Photovoltaics: Research and Applications* 23(11): 1649-1659. <https://doi.org/10.1002/pip.2606>
- [532] **Koch, K. and Barthlott, W. (2009)** 'Superhydrophobic and superhydrophilic plant surfaces: an inspiration for biomimetic materials', *Philosophical Transactions of the Royal Society A* 367(1893): 1487-1509. <https://doi.org/10.1098/rsta.2009.0022>
- [533] **Liu, Y., Das, A., Lin, Z., Cooper, I. B., Rohatgi, A. and Wong, C. P. (2014)** 'Hierarchical robust textured structures for large scale self-cleaning black silicon solar cells', *Nano Energy* 3: 127-133. <https://doi.org/10.1016/j.nanoen.2013.11.002>
- [534] **Ma, Y., Gou, T., Feng, C., Li, J., Li, Y., Huang, J., Li, R., Zhang, Z. and Gao, X. (2021)** 'Facile fabrication of biomimetic films with the microdome and tapered nanonipple hierarchical structure possessing high haze, high transmittance, anti-fouling and moisture self-cleaning functions', *Chemical Engineering Journal* 404: 127101. <https://doi.org/10.1016/j.cej.2020.127101>
- [535] **Stratakis, E., Bonse, J., Heitz, J., Siegel, J., Tsibidis, G. D., Skoulas, E., Papadopoulos, A., Mimidis, A., Joel, A.-C., Comanns, P., Krüger, J., Florian, C., Fuentes-Edfuf, Y., Solis, J. and Baumgartner, W. (2020)** 'Laser

- engineering of biomimetic surfaces', *Materials Science and Engineering: R: Reports* **141**: 100562. <https://doi.org/10.1016/j.mser.2020.100562>
- [536] **Müller, F. A., Kunz, C. and Gräf, S. (2016)** 'Bio-Inspired Functional Surfaces Based on Laser-Induced Periodic Surface Structures', *Materials* **9**(6): 476. <https://doi.org/10.3390/ma9060476>
- [537] **Ganeev, R. A. (2014)** 'Optical modification of semiconductor surfaces through the nanoripples formation using ultrashort laser pulses: Experimental aspects', *Optics and Spectroscopy* **117**(2): 320-340. <https://doi.org/10.1134/S0030400X14080098>
- [538] **Albu, C., Dinescu, A., Filipescu, M., Ulmeanu, M. and Zamfirescu, M. (2013)** 'Periodical structures induced by femtosecond laser on metals in air and liquid environments', *Applied Surface Science* **278**: 347-351. <https://doi.org/10.1016/j.apsusc.2012.11.075>
- [539] **Wang, J. and Guo, C. (2006)** 'Formation of extraordinarily uniform periodic structures on metals induced by femtosecond laser pulses', *Journal of Applied Physics* **100**(2): 23511. <https://doi.org/10.1063/1.2214464>
- [540] **Reif, J., Varlamova, O. and Costache, F. (2008)** 'Femtosecond laser induced nanostructure formation: self-organization control parameters', *Applied Physics A* **92**(4): 1019-1024. <https://doi.org/10.1007/s00339-008-4671-3>
- [541] **Vorobyev, A. Y. and Guo, C. (2011)** 'Antireflection effect of femtosecond laser-induced periodic surface structures on silicon', *Optics Express* **19**(S5): A1031. <https://doi.org/10.1364/OE.19.0A1031>
- [542] **Ding, K., Wang, C., Zheng, Y., Xie, Z., Luo, Z., Man, S., Wu, B. and Duan, J. (2019)** 'One-step fabrication of multifunctional fusiform hierarchical micro/nanostructures on copper by femtosecond laser', *Surface and Coatings Technology* **367**: 244-251. <https://doi.org/10.1016/j.surfcoat.2019.04.005>
- [543] **Zhang, D., Ranjan, B., Tanaka, T. and Sugioka, K. (2020)** 'Multiscale Hierarchical Micro/Nanostructures Created by Femtosecond Laser Ablation in Liquids for Polarization-Dependent Broadband Antireflection', *Nanomaterials (Basel, Switzerland)* **10**(8). <https://doi.org/10.3390/nano10081573>
- [544] **Wu, P. H., Cheng, C. W., Chang, C. P., Wu, T. M. and Wang, J. K. (2011)** 'Fabrication of large-area hydrophobic surfaces with femtosecond-laser-

- structured molds', *Journal of Micromechanics and Microengineering* **21**(11): 115032. <https://doi.org/10.1088/0960-1317/21/11/115032>
- [545] **Zorba, V., Stratakis, E., Barberoglou, M., Spanakis, E., Tzanetakis, P., Anastasiadis, S. H. and Fotakis, C. (2008)** 'Biomimetic Artificial Surfaces Quantitatively Reproduce the Water Repellency of a Lotus Leaf', *Advanced Materials* **20**(21): 4049-4054. <https://doi.org/10.1002/adma.200800651>
- [546] **He, H., Qu, N. and Zeng, Y. (2016)** 'Lotus-leaf-like microstructures on tungsten surface induced by one-step nanosecond laser irradiation', *Surface and Coatings Technology* **307**: 898-907. <https://doi.org/10.1016/j.surfcoat.2016.10.033>
- [547] **Yan, Y. Y., Gao, N. and Barthlott, W. (2011)** 'Mimicking natural superhydrophobic surfaces and grasping the wetting process: a review on recent progress in preparing superhydrophobic surfaces', *Advances in Colloid and Interface Science* **169**(2): 80-105. <https://doi.org/10.1016/j.cis.2011.08.005>
- [548] **Bhushan, B., Jung, Y. C., Niemietz, A. and Koch, K. (2009)** 'Lotus-like biomimetic hierarchical structures developed by the self-assembly of tubular plant waxes', *Langmuir* **25**(3): 1659-1666. <https://doi.org/10.1021/la802491k>
- [549] **Bixler, G. D. and Bhushan, B. (2014)** 'Rice- and butterfly-wing effect inspired self-cleaning and low drag micro/nanopatterned surfaces in water, oil, and air flow', *Nanoscale* **6**(1): 76-96. <https://doi.org/10.1039/c3nr04755e>
- [550] **Bixler, G. D., Theiss, A., Bhushan, B. and Lee, S. C. (2014)** 'Anti-fouling properties of microstructured surfaces bio-inspired by rice leaves and butterfly wings', *Journal of Colloid and Interface Science* **419**: 114-133. <https://doi.org/10.1016/j.jcis.2013.12.019>
- [551] **Least, B. T. and Willis, D. A. (2013)** 'Modification of polyimide wetting properties by laser ablated conical microstructures', *Applied Surface Science* **273**: 1-11. <https://doi.org/10.1016/j.apsusc.2012.12.141>
- [552] **Dyer, P. E., Jenkins, S. D. and Sidhu, J. (1986)** 'Development and origin of conical structures on XeCl laser ablated polyimide', *Applied Physics Letters* **49**(8): 453-455. <https://doi.org/10.1063/1.97113>

- [553] **Andrew, J. E., Dyer, P. E., Forster, D. and Key, P. H. (1983)** 'Direct etching of polymeric materials using a XeCl laser', *Applied Physics Letters* **43**(8): 717-719. <https://doi.org/10.1063/1.94488>
- [554] **Hopp, B., Bor, Z., Homolya, E. and Mihalik, E. (1997)** 'Investigation of conical structures created by ArF excimer laser irradiation of polycarbonate', *Applied Surface Science* **109-110**: 232-235. [https://doi.org/10.1016/S0169-4332\(96\)00915-4](https://doi.org/10.1016/S0169-4332(96)00915-4)
- [555] **Kazemi, S. S., Jelvani, S., Ehsani, H., Silakhori, K. and Hantehzadeh, M. (2014)** 'Sem Study of Conical Structures on Polycarbonate Surface Induced by ArF Laser', *Journal of Applied Spectroscopy* **81**(5): 801-806. <https://doi.org/10.1007/s10812-014-0008-5>
- [556] **Dyer, P. E., Walton, C. D. and Zakaria, R. (2009)** 'Interference effects in 157 nm laser ablated cones in polycarbonate and application to spatial coherence measurement', *Applied Physics A* **95**(2): 319-323. <https://doi.org/10.1007/s00339-009-5102-9>
- [557] **Zakaria, R. and Dyer, P. E. (2010)** 'Cone evolution on VUV laser ablated polymers', *Applied Physics A* **101**(1): 13-18. <https://doi.org/10.1007/s00339-010-5803-0>
- [558] **Bartnik, A., Fiedorowicz, H., Jarocki, R., Kostecki, J. and Szczurek, M. (2010)** 'PMMA and FEP surface modifications induced with EUV pulses in two selected wavelength ranges', *Applied Physics A* **98**(1): 61-65. <https://doi.org/10.1007/s00339-009-5406-9>
- [559] **Dyer, P. E., Maswadi, S. M., Snelling, H. V. and Walton, C. D. (2002)** 'Glass micromachining using the VUV F 2 laser'. In: Koji Sugioka, Malcolm C. Gower, Jr. Richard F. Haglund, Alberto Pique, Frank Traeger, Jan J. Dubowski, and Willem Hoving, eds.: SPIE, p. 218
- [560] **Nayak, B. K. and Gupta, M. C. (2010)** 'Self-organized micro/nano structures in metal surfaces by ultrafast laser irradiation', *Optics and Lasers in Engineering* **48**(10): 940-949. <https://doi.org/10.1016/j.optlaseng.2010.04.010>
- [561] **Nayak, B. K., Gupta, M. C. and Kolasinski, K. W. (2008)** 'Formation of nano-textured conical microstructures in titanium metal surface by femtosecond laser irradiation', *Applied Physics A* **90**(3): 399-402. <https://doi.org/10.1007/s00339-007-4349-2>

- [562] **Nayak, B. K., Caffrey, P. O., Speck, C. R. and Gupta, M. C. (2013)** 'Superhydrophobic surfaces by replication of micro/nano-structures fabricated by ultrafast-laser-microtexturing', *Applied Surface Science* **266**: 27-32. <https://doi.org/10.1016/j.apsusc.2012.11.052>
- [563] **Nayak, B. K., Iyengar, V. and Gupta, M. C. (2008)** 'Ultrafast Laser Textured Silicon Solar Cells', *MRS Proceedings* **1123**. <https://doi.org/10.1557/PROC-1123-1123-P07-09>
- [564] **Nayak, B. K., Iyengar, V. V. and Gupta, M. C. (2011)** 'Efficient light trapping in silicon solar cells by ultrafast-laser-induced self-assembled micro/nano structures', *Progress in Photovoltaics: Research and Applications* **19**(6): 631-639. <https://doi.org/10.1002/pip.1067>
- [565] **Ackerl, N., Boerner, P. and Wegener, K. (2019)** 'Toward application of hierarchical structures by ultrashort pulsed laser ablation', *Journal of Laser Applications* **31**(2): 22501. <https://doi.org/10.2351/1.5096079>
- [566] **Dottermusch, S., Schmager, R., Klampaftis, E., Paetel, S., Kiowski, O., Ding, K., Richards, B. S. and Paetzold, U. W. (2019)** 'Micro-cone textures for improved light in-coupling and retroreflection-inspired light trapping at the front surface of solar modules', *Progress in Photovoltaics: Research and Applications*. <https://doi.org/10.1002/pip.3133>
- [567] **Roslizar, A., Dottermusch, S., Schmager, R., Guttman, M., Gomard, G., Hölscher, H., Richards, B. S. and Paetzold, U. W. (2020)** 'Hot-embossed microcone-textured fluoropolymer as self-cleaning and anti-reflective photovoltaic module covers', *Solar Energy Materials and Solar Cells* **214**: 110582. <https://doi.org/10.1016/J.SOLMAT.2020.110582>
- [568] **Stephan, M. (2015)** 'Optische Charakterisierung pflanzlicher Oberflächenstrukturen für den Einsatz auf Solarzellen'. *Master's thesis*. Karlsruhe Institute of Technology Karlsruhe
- [569] **Schulte, A. J. (2012)** 'Light-trapping and superhydrophobic plant surfaces-optimized multifunctional biomimetic surfaces for solar cells'. *Dissertation*. Rheinische Friedrich-Wilhelms-Universität Bonn. [urn:nbn:de:hbz:5n-29855](https://nbn-resolving.org/urn:nbn:de:hbz:5n-29855)
- [570] **Schweikart, A., Zimin, D., Handge, U. A., Bennemann, M., Altstädt, V., Fery, A. and Koch, K. (2010)** 'Fabrication of Artificial Petal Sculptures by Replication of Sub-micron Surface Wrinkles', *Macromolecular Chemistry and Physics* **211**(2): 259-264. <https://doi.org/10.1002/macp.200900543>

- [571] **Oh, J. H., Woo, J. Y., Jo, S. and Han, C.-S. (2019)** 'Iridescent and Glossy Effect on Polymer Surface Using Micro-/Nanohierarchical Structure: Artificial Queen of the Night Tulip Petals', *ACS Applied Materials & Interfaces* **11**(29): 26442-26447. <https://doi.org/10.1021/acsami.9b06376>
- [572] **Schauer, S., Schmager, R., Hünig, R., Ding, K., Paetzold, U. W., Lemmer, U., Worgull, M., Hölscher, H. and Gomard, G. (2018)** 'Disordered diffraction gratings tailored by shape-memory based wrinkling and their application to photovoltaics', *Optical Materials Express* **8**(1): 184. <https://doi.org/10.1364/OME.8.000184>
- [573] **Schauer, S. R. (2017)** 'Shape-Memory Polymers for Bioinspired, Tunable Photonic Structures'. *Dissertation*. Karlsruhe Institute of Technology. <https://doi.org/10.5445/IR/1000078106>
- [574] **Heitz, J., Reisinger, B., Fahrner, M., Romanin, C., Siegel, J. and Svorcik, V. (02.07.2012 - 05.07.2012)** 'Laser-induced periodic surface structures (LIPSS) on polymer surfaces': IEEE, pp. 1-4
- [575] **Parvin, P., Refahizadeh, M., Mortazavi, S. Z., Silakhori, K., Mahdilo, A. and Aghaii, P. (2014)** 'Regular self-microstructuring on CR39 using high UV laser dose', *Applied Surface Science* **292**: 247-255. <https://doi.org/10.1016/j.apsusc.2013.11.125>
- [576] **Yun, M. J., Sim, Y. H., Cha, S. I. and Lee, D. Y. (2019)** 'Omnidirectional Light Capture by Solar Cells Mimicking the Structures of the Epidermal cells of Leaves', *Scientific Reports* **9**(1): 12773. <https://doi.org/10.1038/s41598-019-49046-8>
- [577] **McConnell, I., Li, G. and Brudvig, G. W. (2010)** 'Energy conversion in natural and artificial photosynthesis', *Chemistry & biology* **17**(5): 434-447. <https://doi.org/10.1016/j.chembiol.2010.05.005>
- [578] **Soudi, N., Nanayakkara, S., Jahed, N. M. and Naahidi, S. (2020)** 'Rise of nature-inspired solar photovoltaic energy convertors', *Solar Energy* **208**: 31-45. <https://doi.org/10.1016/j.solener.2020.07.048>
- [579] **Schulte, A. J., Koch, K., Spaeth, M. and Barthlott, W. (2009)** 'Biomimetic replicas: Transfer of complex architectures with different optical properties from plant surfaces onto technical materials', *Acta Biomaterialia* **5**(6): 1848-1854. <https://doi.org/10.1016/j.actbio.2009.01.028>
- [580] **Hünig, R., Mertens, A., Stephan, M., Schulz, A., Richter, B., Hetterich, M., Powalla, M., Lemmer, U., Colsmann, A. and Gomard, G. (2016)**

- 'Flower Power: Exploiting Plants' Epidermal Structures for Enhanced Light Harvesting in Thin-Film Solar Cells', *Advanced Optical Materials* 4(10): 1487-1493. <https://doi.org/10.1002/adom.201600046>
- [581] **Hünig, R. (2017)** 'Lichtmanagement in Cu(In,Ga)Se<sub>2</sub>-Dünnschichtsolarzellen'. *Dissertation*. Karlsruhe Institute of Technology. <https://doi.org/10.5445/IR/1000075888>
- [582] **Wallin, E., Malm, U., Jarmar, T., Lundberg, O., Edoff, M. and Stolt, L. (2012)** 'World-record Cu(In,Ga)Se<sub>2</sub>-based thin-film sub-module with 17.4% efficiency', *Progress in Photovoltaics: Research and Applications* 20(7): 851-854. <https://doi.org/10.1002/pip.2246>
- [583] **Hiroi, H., Iwata, Y., Adachi, S., Sugimoto, H. and Yamada, A. (2016)** 'New World-Record Efficiency for Pure-Sulfide Cu(In,Ga)S<sub>2</sub> Thin-Film Solar Cell With Cd-Free Buffer Layer via KCN-Free Process', *IEEE Journal of Photovoltaics* 6(3): 760-763. <https://doi.org/10.1109/jphotov.2016.2537540>
- [584] **Kamada, R., Yagioka, T., Adachi, S., Handa, A., Tai, K. F., Kato, T. and Sugimoto, H. (2016)** 'New world record Cu(In, Ga)(Se, S)<sub>2</sub> thin film solar cell efficiency beyond 22%'. Piscataway, NJ: IEEE, pp. 1287-1291
- [585] **Jackson, P., Hariskos, D., Lotter, E., Paetel, S., Wuerz, R., Menner, R., Wischmann, W. and Powalla, M. (2011)** 'New world record efficiency for Cu(In,Ga)Se<sub>2</sub> thin-film solar cells beyond 20%', *Progress in Photovoltaics: Research and Applications* 19(7): 894-897. <https://doi.org/10.1002/pip.1078>
- [586] **Jackson, P., Hariskos, D., Wuerz, R., Kiowski, O., Bauer, A., Friedlmeier, T. M. and Powalla, M. (2015)** 'Properties of Cu(In,Ga)Se<sub>2</sub> solar cells with new record efficiencies up to 21.7%', *Physica Status Solidi – Rapid Research Letters* 9(1): 28-31. <https://doi.org/10.1002/pssr.201409520>
- [587] **Solar Frontier (2017)** 'Solar Frontier Achieves World Record Thin-Film Solar Cell Efficiency of 22.9%' [accessed 16 December 2020]. [http://www.solar-frontier.com/eng/news/2017/1220\\_press.html](http://www.solar-frontier.com/eng/news/2017/1220_press.html)
- [588] **Solar Frontier (2019)** 'Solar Frontier Achieves World Record Thin-Film Solar Cell Efficiency of 22.9%' [accessed 16 December 2020]. [http://www.solar-frontier.com/eng/news/2019/0117\\_press.html](http://www.solar-frontier.com/eng/news/2019/0117_press.html)
- [589] **Nakamura, M., Yamaguchi, K., Kimoto, Y., Yasaki, Y., Kato, T. and Sugimoto, H. (2019)** 'Cd-Free Cu(In,Ga)(Se,S)<sub>2</sub> Thin-Film Solar Cell With Record Efficiency of 23.35%', *IEEE Journal of Photovoltaics* 9(6): 1863-1867. <https://doi.org/10.1109/JPHOTOV.2019.2937218>

- [590] **Cao, Y., Jana, S., Bowen, L., Tan, X., Liu, H., Rostami, N., Brown, J., Jakubovics, N. S. and Chen, J. (2019)** 'Hierarchical Rose Petal Surfaces Delay the Early-Stage Bacterial Biofilm Growth', *Langmuir* **35**(45): 14670-14680. <https://doi.org/10.1021/acs.langmuir.9b02367>
- [591] **Dou, X., Li, P., Jiang, S., Bayat, H. and Schönherr, H. (2017)** 'Bioinspired Hierarchically Structured Surfaces for Efficient Capture and Release of Circulating Tumor Cells', *ACS Applied Materials & Interfaces* **9**(10): 8508-8518. <https://doi.org/10.1021/acsami.6b16202>
- [592] **Teng, F.-R., Ren, Q., Lai, T.-C., Liu, C. and Li, A.-D. (2020)** 'A stretchable petal patterned strain sensor comprising Ir nanoparticles-modified multi-walled carbon nanotubes for human-motion detection', *Journal of Physics D: Applied Physics* **53**(50): 505402. <https://doi.org/10.1088/1361-6463/abb1e5>
- [593] **Guo, R., Yu, Y., Zeng, J., Liu, X., Zhou, X., Niu, L., Gao, T., Li, K., Yang, Y., Zhou, F. and Zheng, Z. (2015)** 'Biomimicking Topographic Elastomeric Petals (E-Petals) for Omnidirectional Stretchable and Printable Electronics', *Advanced Science* **2**(3): 1400021. <https://doi.org/10.1002/advs.201400021>
- [594] **Wei, Y., Chen, S., Lin, Y., Yang, Z. and Liu, L. (2015)** 'Cu–Ag core–shell nanowires for electronic skin with a petal molded microstructure', *Journal of Materials Chemistry C* **3**(37): 9594-9602. <https://doi.org/10.1039/C5TC01723H>
- [595] **Su, B., Gong, S., Ma, Z., Yap, L. W. and Cheng, W. (2015)** 'Mimosa-inspired design of a flexible pressure sensor with touch sensitivity', *Small* **11**(16): 1886-1891. <https://doi.org/10.1002/smll.201403036>
- [596] **Seol, M.-L., Woo, J.-H., Lee, D.-I., Im, H., Hur, J. and Choi, Y.-K. (2014)** 'Nature-Replicated Nano-in-Micro Structures for Triboelectric Energy Harvesting', *Small* **10**(19): 3887-3894. <https://doi.org/10.1002/smll.201400863>
- [597] **Zhu, M., Wang, Y., Lou, M., Yu, J., Li, Z. and Ding, B. (2021)** 'Bioinspired transparent and antibacterial electronic skin for sensitive tactile sensing', *Nano Energy* **81**: 105669. <https://doi.org/10.1016/j.nanoen.2020.105669>
- [598] **Huang, Z., Yang, S., Zhang, H., Zhang, M. and Cao, W. (2015)** 'Replication of Leaf Surface Structures for Light Harvesting', *Scientific Reports* **5**: 14281. <https://doi.org/10.1038/srep14281>

- [599] **Hünig, R., Mertens, A., Hetterich, M., Powalla, M., Lemmer, U., Colsmann, A. and Gomard, G. (2016)** 'Plant epidermal structures for enhanced sunlight harvesting in solar cells', *SPIE Newsroom*. <https://doi.org/10.1117/2.1201611.006701>
- [600] **Li, K., Zhang, Y., Zhen, H., Wang, H., Liu, S., Yan, F. and Zheng, Z. (2017)** 'Versatile biomimetic haze films for efficiency enhancement of photovoltaic devices', *Journal of Materials Chemistry A* **5**(3): 969-974. <https://doi.org/10.1039/C6TA07586J>
- [601] **Huang, Z., Shi, T., Zhang, H., Zhang, M., Huttula, M. and Cao, W. (2016)** 'A computational study of antireflection structures bio-mimicked from leaf surface morphologies', *Solar Energy* **131**: 131-137. <https://doi.org/10.1016/j.solener.2016.02.041>
- [602] **Huang, Z., Cai, C., Shi, X., Li, T., Huttula, M. and Cao, W. (2017)** 'Leaf-mimicking polymers for hydrophobicity and high transmission haze', *Proceedings of the Estonian Academy of Sciences* **66**(4): 444. <https://doi.org/10.3176/proc.2017.4.24>
- [603] **Rajput, D., Bindra, H. S., Saha, A. and Nayak, R. (2016)** 'A simple low-cost approach of fabricating nanostructured polydimethylsiloxane layer for application in solar cell encapsulation', *Advanced Science, Engineering and Medicine* **8**(7): 533-537. <https://doi.org/10.1166/ase.2016.1829>
- [604] **Bindra, H. S., Kumar, A. K. and Nayak, R. (2017)** 'Optical properties of a biomimetically prepared hierarchical structured polydimethyl siloxane template for potential application in anti-reflection and photovoltaic encapsulation', *Materials Research Express* **4**(5): 55501. <https://doi.org/10.1088/2053-1591/aa6365>
- [605] **Huang, Z., Cai, C., Kuai, L., Li, T., Huttula, M. and Cao, W. (2018)** 'Leaf-structure patterning for antireflective and self-cleaning surfaces on Si-based solar cells', *Solar Energy* **159**: 733-741. <https://doi.org/10.1016/j.solener.2017.11.020>
- [606] **Mattaparthi, S. and Sharma, C. S. (2019)** 'Fabrication of Self-cleaning Antireflective Polymer Surfaces by Mimicking Underside Leaf Hierarchical Surface Structures', *Journal of Bionic Engineering* **16**(3): 400-409. <https://doi.org/10.1007/s42235-019-0032-5>
- [607] **Mattaparthi, S. and Sharma, C. S. (2019)** 'Mimicking flower petals to fabricate self-cleaning and antireflective polymer surfaces', *Bioinspired*,

- Biomimetic and Nanobiomaterials* **9**(1): 45-52.  
<https://doi.org/10.1680/jbibn.19.00017>
- [608] **Schanz, G. and Bade, K. (2008)** 'Microelectroforming of metals', *Microengineering of Metals and Ceramics: Special Replication Techniques, Automation, and Properties*
- [609] **Leach, R., Giusca, C., Guttman, M., Jakobs, P.-J. and Rubert, P. (2015)** 'Development of low-cost material measures for calibration of the metrological characteristics of areal surface texture instruments', *CIRP Annals* **64**(1): 545-548. <https://doi.org/10.1016/j.cirp.2015.03.002>
- [610] **Yao, D., Virupaksha, V. L. and Kim, B. (2005)** 'Study on squeezing flow during nonisothermal embossing of polymer microstructures', *Polymer Engineering & Science* **45**(5): 652-660. <https://doi.org/10.1002/pen.20322>
- [611] **Powalla, M., Jackson, P., Witte, W., Hariskos, D., Paetel, S., Tschamber, C. and Wischmann, W. (2013)** 'High-efficiency Cu(In,Ga)Se<sub>2</sub> cells and modules', *Solar Energy Materials and Solar Cells* **119**: 51-58. <https://doi.org/10.1016/j.solmat.2013.05.002>
- [612] **Schmager, R. (2016)** 'Einfluss der Nanostruktur auf die optischen Eigenschaften hierarchischer Pflanzenoberflächen'. *Master's thesis*. Karlsruhe Institute of Technology Karlsruhe, Germany
- [613] **Ma, Y., Cao, X., Feng, X., Ma, Y. and Zou, H. (2007)** 'Fabrication of superhydrophobic film from PMMA with intrinsic water contact angle below 90°', *Polymer* **48**(26): 7455-7460. <https://doi.org/10.1016/j.polymer.2007.10.038>
- [614] **Li, X.-M., Reinhoudt, D. and Crego-Calama, M. (2007)** 'What do we need for a superhydrophobic surface? A review on the recent progress in the preparation of superhydrophobic surfaces', *Chemical Society Reviews* **36**(8): 1350-1368. <https://doi.org/10.1039/b602486f>
- [615] **Cao, L., Hu, H.-H. and Di Gao (2007)** 'Design and fabrication of microtextures for inducing a superhydrophobic behavior on hydrophilic materials', *Langmuir* **23**(8): 4310-4314. <https://doi.org/10.1021/la063572r>
- [616] **Huld, T., Šúri, M. and Dunlop, E. D. (2008)** 'Comparison of potential solar electricity output from fixed-inclined and two-axis tracking photovoltaic modules in Europe', *Progress in Photovoltaics: Research and Applications* **16**(1): 47-59. <https://doi.org/10.1002/pip.773>

- [617] **Jacobson, M. Z. and Jadhav, V. (2018)** 'World estimates of PV optimal tilt angles and ratios of sunlight incident upon tilted and tracked PV panels relative to horizontal panels', *Solar Energy* **169**: 55-66. <https://doi.org/10.1016/j.solener.2018.04.030>
- [618] **Jackson, P., Wuerz, R., Hariskos, D., Lotter, E., Witte, W. and Powalla, M. (2016)** 'Effects of heavy alkali elements in Cu(In,Ga)Se<sub>2</sub> solar cells with efficiencies up to 22.6%', *Physica Status Solidi – Rapid Research Letters* **10(8)**: 583-586. <https://doi.org/10.1002/pssr.201600199>
- [619] **Womack, G., Kaminski, P. M., Abbas, A., Isbilir, K., Gottschalg, R. and Walls, J. M. (2017)** 'Performance and durability of broadband antireflection coatings for thin film CdTe solar cells', *Journal of Vacuum Science & Technology A: Vacuum, Surfaces, and Films* **35(2)**: 21201. <https://doi.org/10.1116/1.4973909>
- [620] **Powalla, M., Voorwinden, G., Hariskos, D., Jackson, P. and Kniese, R. (2009)** 'Highly efficient CIS solar cells and modules made by the co-evaporation process', *Thin Solid Films* **517(7)**: 2111-2114. <https://doi.org/10.1016/j.tsf.2008.10.126>
- [621] **Gorter, T. and Reinders, A. (2012)** 'A comparison of 15 polymers for application in photovoltaic modules in PV-powered boats', *Applied Energy* **92**: 286-297. <https://doi.org/10.1016/j.apenergy.2011.10.042>
- [622] **Martín, M., Centelles, X., Solé, A., Barreneche, C., Fernández, A. I. and Cabeza, L. F. (2020)** 'Polymeric interlayer materials for laminated glass: A review', *Construction and Building Materials* **230**: 116897. <https://doi.org/10.1016/j.conbuildmat.2019.116897>
- [623] **Bagiatis, V., Critchlow, G. W., Price, D. and Wang, S. (2019)** 'The effect of atmospheric pressure plasma treatment (APPT) on the adhesive bonding of poly(methyl methacrylate) (PMMA)-to-glass using a polydimethylsiloxane (PDMS)-based adhesive', *International Journal of Adhesion and Adhesives* **95**: 102405. <https://doi.org/10.1016/j.ijadhadh.2019.102405>
- [624] **Cooper, P. I. (1969)** 'The absorption of radiation in solar stills', *Solar Energy* **12(3)**: 333-346. [https://doi.org/10.1016/0038-092X\(69\)90047-4](https://doi.org/10.1016/0038-092X(69)90047-4)
- [625] **Duffie, J. A. and Beckman, W. A. (1980)** 'Solar engineering of thermal processes'. 4th edition (2013): Wiley New York. ISBN: 978-0-470-87366-3

- 
- [626] **Ghosh, A. (2020)** 'Potential of building integrated and attached/applied photovoltaic (BIPV/BAPV) for adaptive less energy-hungry building's skin: A comprehensive review', *Journal of Cleaner Production* **276**: 123343. <https://doi.org/10.1016/j.jclepro.2020.123343>
- [627] **Huh, D., Shin, J.-H., Byun, M., Son, S., Jung, P.-H., Choi, H.-J., Kim, Y.-D. and Lee, H. (2017)** 'Analysis of long-term monitoring data of PV module with SiO<sub>x</sub>-based anti-reflective patterned protective glass', *Solar Energy Materials and Solar Cells* **170**: 33-38. <https://doi.org/10.1016/j.solmat.2017.05.031>
- [628] **Nishioka, K., Moe, S. P. and Ota, Y. (2019)** 'Long-Term Reliability Evaluation of Silica-Based Coating with Antireflection Effect for Photovoltaic Modules', *Coatings* **9**(1): 49. <https://doi.org/10.3390/coatings9010049>
- [629] **Fassbender, B., Ackermann, J., Rattenhausen, P., Colburn, P., Loffler, U. and Marks, P. A. (2011)** 'Reliability of PMMA for CPV Lens Applications', *30th ISES Biennial Solar World*: 722-733. <https://doi.org/10.18086/swc.2011.03.04>
- [630] **Horváth, G., Kriska, G., Malik, P. and Robertson, B. (2009)** 'Polarized light pollution: a new kind of ecological photopollution', *Frontiers in Ecology and the Environment* **7**(6): 317-325. <https://doi.org/10.1890/080129>
- [631] **Kriska, G., Bernáth, B., Farkas, R. and Horváth, G. (2009)** 'Degrees of polarization of reflected light eliciting polarotaxis in dragonflies (Odonata), mayflies (Ephemeroptera) and tabanid flies (Tabanidae)', *Journal of Insect Physiology* **55**: 1167-1173. <https://doi.org/10.1016/j.jinsphys.2009.08.013>
- [632] **Kriska, G., Horváth, G. and Andrikovics, S. (1998)** 'Why do mayflies lay their eggs en masse on dry asphalt roads? Water-imitating polarized light reflected from asphalt attracts Ephemeroptera', *The Journal of Experimental Biology* **201**(15): 2273-2286. <https://jeb.biologists.org/content/201/15/2273>
- [633] **Horváth, G. and Varjú, D. (2004)** 'Polarized Light in Animal Vision: Polarization Patterns in Nature' Berlin, New York: Springer. ISBN: 978-3-642-07334-2
- [634] **Horváth, G. (2014)** 'Polarized Light and Polarization Vision in Animal Sciences'. 2nd ed. 2014: Springer Berlin Heidelberg. Springer Series in
-

- Vision Research. 2. ISBN: 9783642547188. <https://doi.org/10.1007/978-3-642-54718-8>
- [635] **Horváth, G., Majer, J., Horváth, L., Szivák, I. and Kriska, G. (2008)** 'Ventral polarization vision in tabanids: horseflies and deerflies (Diptera: Tabanidae) are attracted to horizontally polarized light', *Naturwissenschaften* **95**(11): 1093-1100. <https://doi.org/10.1007/s00114-008-0425-5>
- [636] **Farkas, A., Száz, D., Egri, A., Barta, A., Mészáros, Á., Hegedüs, R., Horváth, G. and Kriska, G. (2016)** 'Mayflies are least attracted to vertical polarization: A polarotactic reaction helping to avoid unsuitable habitats', *Physiology & Behavior* **163**: 219-227. <https://doi.org/10.1016/j.physbeh.2016.05.009>
- [637] **Horváth, G., Szörényi, T., Pereszlényi, Á., Gerics, B., Hegedüs, R., Barta, A. and Akesson, S. (2017)** 'Why do horseflies need polarization vision for host detection? Polarization helps tabanid flies to select sunlit dark host animals from the dark patches of the visual environment', *Royal Society Open Science* **4**(11): 170735. <https://doi.org/10.1098/rsos.170735>
- [638] **Egri, A., Pereszlényi, Á., Farkas, A., Horváth, G., Penksza, K. and Kriska, G. (2017)** 'How can Asphalt Roads Extend the Range of In Situ Polarized Light Pollution? A Complex Ecological Trap of *Ephemera danica* and a Possible Remedy', *Journal of Insect Behavior* **30**(4): 374-384. <https://doi.org/10.1007/s10905-017-9623-3>
- [639] **Blaho, M., Herczeg, T., Kriska, G., Egri, A., Szaz, D., Farkas, A., Tarjanyi, N., Czinke, L., Barta, A. and Horváth, G. (2014)** 'Unexpected attraction of polarotactic water-leaving insects to matt black car surfaces: mattness of paintwork cannot eliminate the polarized light pollution of black cars', *PLOS ONE* **9**(7): e103339. <https://doi.org/10.1371/journal.pone.0103339>
- [640] **Horváth, G., Blahó, M., Egri, A., Kriska, G., Seres, I. and Robertson, B. (2010)** 'Reducing the maladaptive attractiveness of solar panels to polarotactic insects', *Conservation Biology* **24**(6): 1644-1653. <https://doi.org/10.1111/j.1523-1739.2010.01518.x>
- [641] **Blahó, M., Egri, A., Barta, A., Antoni, G., Kriska, G. and Horváth, G. (2012)** 'How can horseflies be captured by solar panels? A new concept of tabanid traps using light polarization and electricity produced by photovoltaics', *Veterinary Parasitology* **189**(2-4): 353-365. <https://doi.org/10.1016/j.vetpar.2012.04.016>

- [642] **Malik, P., Hegedüs, R., Kriska, G. and Horváth, G. (2008)** 'Imaging polarimetry of glass buildings: why do vertical glass surfaces attract polarotactic insects?', *Applied Optics* **47**(24): 4361-4374. <https://doi.org/10.1364/ao.47.004361>
- [643] **Black, T. V. and Robertson, B. A. (2020)** 'How to disguise evolutionary traps created by solar panels', *Journal of Insect Conservation* **24**(2): 241-247. <https://doi.org/10.1007/s10841-019-00191-5>
- [644] **Blahó, M., Egri, Á., Száz, D., Kriska, G., Akesson, S. and Horváth, G. (2013)** 'Stripes disrupt odour attractiveness to biting horseflies: Battle between ammonia, CO<sub>2</sub>, and colour pattern for dominance in the sensory systems of host-seeking tabanids', *Physiology & Behavior* **119**: 168-174. <https://doi.org/10.1016/j.physbeh.2013.06.013>
- [645] **Blaho, M., Egri, A., Bahidszki, L., Kriska, G., Hegedus, R., Akesson, S. and Horváth, G.** 'Spottier Targets Are Less Attractive to Tabanid Flies: On the Tabanid-Repellency of Spotty Fur Patterns', *PLOS ONE* **7**(8): 1-10. <https://doi.org/10.1371/journal.pone.0041138>
- [646] **Egri, A., Blahó, M., Kriska, G., Farkas, R., Gyurkovszky, M., Akesson, S. and Horváth, G.** 'Polarotactic tabanids find striped patterns with brightness and/or polarization modulation least attractive: an advantage of zebra stripes', *The Journal of Experimental Biology* **215**(5): 736-745. <https://doi.org/10.1242/jeb.065540>
- [647] **Száz, D., Mihályi, D., Farkas, A., Egri, A., Barta, A., Kriska, G., Robertson, B. and Horváth, G. (2016)** 'Polarized light pollution of matte solar panels: anti-reflective photovoltaics reduce polarized light pollution but benefit only some aquatic insects', *Journal of Insect Conservation* **20**(4): 663-675. <https://doi.org/10.1007/s10841-016-9897-3>
- [648] **Herczeg, T., Blahó, M., Száz, D., Kriska, G., Gyurkovszky, M., Farkas, R. and Horváth, G. (2014)** 'Seasonality and daily activity of male and female tabanid flies monitored in a Hungarian hill-country pasture by new polarization traps and traditional canopy traps', *Parasitology Research* **113**(11): 4251-4260. <https://doi.org/10.1007/s00436-014-4103-6>
- [649] **Herczeg, T., Száz, D., Blahó, M., Barta, A., Gyurkovszky, M., Farkas, R. and Horváth, G. (2015)** 'The effect of weather variables on the flight activity of horseflies (Diptera: Tabanidae) in the continental climate of Hungary', *Parasitology Research* **114**(3): 1087-1097. <https://doi.org/10.1007/s00436-014-4280-3>

- [650] **Schwind, R. (1995)** 'Spectral regions in which aquatic insects see reflected polarized light', *Zeitschrift fr Vergleichende Physiologie* **177**(4). <https://doi.org/10.1007/bf00187480>
- [651] **Meglič, A., Ilić, M., Pirih, P., Škorjanc, A., Wehling, M. F., Kreft, M. and Belušič, G. (2019)** 'Horsefly object-directed polarotaxis is mediated by a stochastically distributed ommatidial subtype in the ventral retina', *Proceedings of the National Academy of Sciences* **116**(43): 21843-21853. <https://doi.org/10.1073/pnas.1910807116>
- [652] **Muheim, R., Sjöberg, S. and Pinzon-Rodriguez, A. (2016)** 'Polarized light modulates light-dependent magnetic compass orientation in birds', *Proceedings of the National Academy of Sciences* **113**(6): 1654-1659. <https://doi.org/10.1073/pnas.1513391113>

---

## Acknowledgments / Danksagung

---

First and foremost, I am sincerely grateful to Prof. Dr. Ulrich Lemmer for giving me the opportunity to pursue my Ph.D. and for all his great support during the past years. Furthermore, I would like to thank Prof. Dr. Mathias Kolle from the Massachusetts Institute of Technology (MIT) for agreeing to take the role of the second referee in the examination process of this dissertation.

I am also profoundly grateful to Dr. Guillaume Gomard and Dr. Ruben Hünig for their scientific mentoring and guidance during my years as a Master's and Ph.D. student at LTI.

I would like to thank Dr. Markus Guttman from the Institute of Microstructure Technology for his expertise in electroplating techniques and his numerous contributions over the past years of close collaboration on the development of metallic embossing tools for replicating the hierarchical surface structures found on flower petals. Furthermore, I am thankful to Marc Schneider (IMT, KIT) for all his help during the development of the large-area hot-embossing process for upscaled petal structure replication. I also thank all the colleagues from the IMT workshop for their excellent work and support in processing the numerous metallic shims and mold inserts into high-quality hot-embossing tools.

I would also like to thank all the colleagues from IMT I had the pleasure to work with over the last years, including Dr. Felix Vüllers, Dr. Ulrich W. Paetzold, Prof. Dr. Bryce S. Richards, Dr. Efthimios Klampaftis, and Dr. Maryna Kavalenka. I am further grateful to Dr. Nils Jürgensen and the colleagues from InnovationLab in Heidelberg for the collaboration on biodegradable light-management layers. I am also thankful to the many researchers from ZSW who supported my research efforts over the years, especially Prof. Dr. Michael Powalla, Dr. Philip Jackson, and Dr. Oliver Salomon. Dr. Martin Schumann from the Institute of Applied Physics (APH, KIT) also deserves my gratitude for the exciting collaboration on optical cloaking of OLED contact fingers. I would also like to kindly thank PD Dr. Alexander Colsmann (MZE) and Dr. Holger Röhm (MZE) for their support in executing the TC-200 accelerated aging routine. Thanks also to Dr. Dieter Kooß (LTI Prüfstelle) for his tremendous support in conducting various standardized abrasion procedures. Special thanks also go out to Aiman Roslizar for help with all the measurements concerning the wetting properties of structured polymer layers.

Also, Dr. m Pereszenyi, Dr. m Egri, Dr. Gyorgy Kriszkan and especially Prof. Dr. Gabor Horvath (ELTE Eotvos Lorand University, Budapest) deserve my gratitude for the exciting and fruitful collaboration on the harmful effects of solar panels on water-seeking insects.

Special thanks goes out to the entire team of the Karlsruhe School of Optics and Photonics (KSOP), which made this research possible by financially supporting me through their scholarship program during the first two years as a Ph.D. student at LTI.

I would further like to thank the Karlsruhe Nano Micro Facility (KNMF) for providing resources and granting me access to various types of state-of-the-art equipment like micro-/nanofabrication technologies over the years of my Ph.D. studies.

I thankfully acknowledge the Karlsruhe House of Young Scientists (KHYS) for supporting me by providing the funding for two international research stays. Especially Jutta Klein-Hitpa was helpful in organizing these trips. A kind thank you goes out to Prof. Peter Bermel and Dr. Zhiguang Zhou for the opportunity to visit Purdue University. Similarly, I would like to thank Prof. Dr. Yong Tang for inviting me to visit his research group at the South China University of Technology (SCUT). Mainly thanks to Dr. Shudong Yu and Junchi Chen, who simply were the most excellent hosts one could wish for, our visit to China was an especially memorable travel experience for me. I also want to thank my travel buddies Dominik Theobald and Andres Rosch, who were a fantastic company during these trips.

Thanks to all my other colleagues and friends from LTI that I've left out so far: Dr. Raphael Schmager, Dr. Adrian Mertens, Dr. Andreas Arndt, Yidenekachew Donie, Dr. Jan Preinfalk, Robert Huber, Dr. Carsten Eschenbaum, Dr. Anne Habermehl, and my ubungsleiter-buddy Henning Mescher. It was a pleasure to work with all of you guys!

Finally, my closest colleagues and flower enthusiasts Dr. Guillaume Gomard, Dr. Ruben Hunig, and Dr. Raphael Schmager, deserve another special mentioning. Thanks for the uncounted hours of discussing, measuring, proofreading, and especially for all the fun times we spent together in Karlsruhe and abroad.

*Meiner Familie, vor allem meinen lieben Eltern Anita und Andreas, danke ich für den Rückhalt und die Unterstützung über all die Jahre. Besonderer Dank gebührt auch meiner Ehefrau Seyda, die mich während meiner Promotionszeit über viele Höhen und Tiefen hinweg stets treu begleitet und angespornt hat.*